Energy harvesting on flexible UAVs

Romain Jan

Université Fédérale
Toulouse Midi-Pyrénées

THÈSE

En vue de l'obtention du

DOCTORAT DE L'UNIVERSITÉ DE TOULOUSE

Délivré par :

Institut Supérieur de l'Aéronautique et de l'Espace

Présentée et soutenue par :
Romain JAN
le lundi 16 octobre 2023

Titre :

Récupération d'énergie sur drone à voilure souple

École doctorale et discipline ou spécialité :
ED AA : Dynamique des fluides

Unité de recherche :
Équipe d'accueil ISAE-ONERA EDyF

Directeur(s) de Thèse :

M. Jean-Marc MOSCHETTA (directeur de thèse)
M. Jean-Philippe CONDOMINES (co-directeur de thèse)

Jury :
M. Éric LAURENDEAU, Polytechnique Montréal - Examinateur, Président
M. Murat BRONZ, ENAC - Examinateur
M. Jean-Philippe CONDOMINES, ENAC - Co-directeur de thèse
M. Mark DRELA, Massachusetts Institute of Technology - Rapporteur
M. Jean-Marc MOSCHETTA, ISAE-SUPAERO - Directeur de thèse
M. Rafael PALACIOS, Imperial College London - Rapporteur

Remerciements

À Toulouse, le 15/01/2024,

Beaucoup et à la fois peu d'entre vous le savent, mais cet exercice de thèse fut compliqué à achever. J'aimerais donc, à travers les prochaines lignes, remercier les personnes qui ont compté dans ce projet, et qui m'ont porté tout au long de ces trois (quatre) années.

Reussir cet exercice n'aurait pu être mené correctement sans l'aide d'un encadrement, rigoureux et assidu. Je remercie donc Jean-Philippe de m'avoir incité à l'autonomie, pour sa diplomatie et l'énergie qu'il a déployé pour essayer de mener cette thèse sur le plan expérimental. Je tiens également à remercier Jean-Marc de m'avoir orienté dans les bonnes directions. Je pense que sans vous, je serais encore là à coder mes petits modèles de début de thèse. La recherche s'appuie sur le travail passé de ses pairs et vous me l'avez fait comprendre avec justesse. Vous m'avez également prouvé très tôt que montrer qu'une idée ne fonctionne pas est un résultat scientifique et qu'en aucun cas il ne doit être occulté par notre égo. J'ai su apprécier nos échanges et vos précieux conseils lors de ma phase de rédaction. Merci de m'avoir poussé et encouragé à constituer ce jury. Jury dont j'aimerais remercier les membres qui m'ont fait l'honneur d'accepter d'évaluer mon travail. Merci donc à Mark Drela et Rafael Palacios pour leurs relectures et à Eric Laurendeau d'avoir présidé le jury. Merci Murat d'avoir été présent. J'aurais tant aimé plus travailler à tes côtés, surtout sur le plan expérimental. Je tiens particulièrement à remercier aussi les professeurs Oliver Gehan, Mohammed M'Saad, Johannes Reuter et David Saussié. Même si nos échanges se sont raréfiés avec les années, ces personnes restent les premières à m'avoir donné l'envie de faire une thèse, probablement inconsciemment. J'ai une pensée particulière pour Mohammed M'Saad, qui fut une réelle source d'inspiration lors de mes études et m'ayant le plus encouragé à poursuivre mon cycle universitaire. Professeur, ô combien attaché à la rigueur et à la transmission. Ancien militant, même 40 ans plus tard, n'hésitait pas à rendre hommage dans ses manuscrits à son camarade de lutte, qui aurait aimé devenir comme lui, un brillant ingénieur. Il reste et restera un modèle.

Achever ce travail ne pouvait se faire sans l'aide que j'ai reçue au quotidien. Merci à la 38.128, d'abord collègues, puis solides amis. Merci, mon Sam, je pense qu'on ne pourrait se parler qu'avec des répliques de films et avoir une discussion cohérente. Notre histoire commence avec une énorme boite en skate, à espérer qu'elle se poursuivra avec des moins violentes (sauf si c'est dans de la grosse POOOOOOWWWW). Merci pour ton aide et tes mots, tu as toujours été là dans les moments compliqués. À Maxime, je ski toujours les chaussures ouvertes, ça refroidit mes tibias, tu devrais essayer. Merci pour nos discussions à chaque fois passionnantes et ta créativité au jeu du rond. Tu me dois un pantalon d'ailleurs. Tu es un modèle de rigueur, d'efficacité et d'éthique. Tu me fais tellement rire, saches-le ! Merci. Massyl. Après 4 ans, je ne comprends toujours pas ce que c'est le marxisme. Tu ne dois pas assez en parler, je pense. Merci pour les mots rassurants durant la thèse. Je me souviendrai toujours de ta soutenance, la turbo machine, elle était sur le zoom ce jour-là (et je ne parle pas de Drela). Merci Alessio, pour ton sérieux et ta bienséance italienne. Toujours là pour transmettre avec brio ta langue maternelle. Tu restes un modèle de pédagogie. Merci, Adrien, pour le partage de ta passion des danses modernes, et de l'empathie quotidienne dont tu fais preuve. Grâce à toi, je sais résoudre un Rubik's cube et j'ai déjà oublié. Merci à Greta, j'ai lancé des calculs CFD récemment pour éviter l'apparition des chocs supersoniques sur tes chaussures de ski. Ça doit être un peu relou à force. Merci pour ton optimisme quotidien à toute épreuve. Merci Manu, le plus sage de

tous, toujours aussi intéressant d'échanger avec toi ! Merci Simao pour ton humour fou que je ne comprends pas toujours. Tu avais toujours les mots justes quand ça n'allait pas. Merci à Christopher, machine de travail ! Toujours là pour résoudre les problèmes de dernières minutes. Merci Julien pour ton aide. Promis, prochaine sortie en falaise, je te donnerai du mou en temps voulu. Et merci au Tibs, machine de travail, serein et toujours prêt à aider. Autour de la 38, ont gravité des personnes d'intérêt. Chloé, évidemment, merci pour tous les moments hilarants. Je ne les compte plus, mais j'espère qu'ils vont se multiplier à l'avenir. Merci à Yaya pour ta folie, on se fait un atelier dégustation Selecto quand tu veux. Merci aux inséparables Marta et Vic, vos départs ont créé un vrai vide. Mais Giovanni et sa trottinette répondront toujours à l'appel. Merci Jean pour le soutien, la prise de recul, les cours de voile et l'apport de motivation à la natation. Un jour, je vais me décider à aller à Londres. Merci aux autres copains du labo, Florian, Thomas, Pierre, Julien, Anaïs, Claudia, Michele, Oriol, Juan, Miguel et Suzanne. Merci aux autres personnes du laboratoire, vos mots et vos attentions ont été précieuses. Je pense notamment à Nicolas B, T.J, Xavier C et Sylvain. Enfin, merci aux personnes de mon nouveau laboratoire dans lequel j'ai pu finir l'écriture de ce manuscrit. Merci donc à Scott, Thomas, Antoine, Felix, Valérian, Valentine, Younes, Florent, Giulia et Paco.

Clôturer ce chapitre universitaire n'aurait pas été possible sans l'aide précieuse de mes chères collègues de bureau : Yuchen et Nikola. Yuchen c'est comme avoir un professeur d'université, mais pour soi tout seul. Merci infiniment, j'ai énormément appris à tes côtés. J'ai toujours été impressionné par la précision constante de tes explications. Nos tours à vélo où nous souffrions avec Nikola et nos séances de Flight Simulator me manquent. Nikola, merci à toi également, les précédents commentaires s'appliquent à ton égard. Ta meilleure contribution restera ma découverte du Dude ! La boussole dont chacun doit se servir pour aller mieux, « I can only hope that one day, you'll have a nice marmot ! ».

Merci aux copains d'avant et de toujours ! Le plus vieux et le plus fidèle, Léo, ce manuscrit t'est dédié ! Tu resteras le plus fou et brillant que j'ai connu. Je chéris nos moments gamins, à manquer de se tuer chaque seconde par notre téméraire stupidité ou stupide témérité. Dans toute cette folie, on avait le temps de moins être bêtes et de s'intéresser aux sciences. Mon goût pour ces dernières, je te le dois largement. Viennent ensuite les copains de Prépa ! Merci Louis, pour les moments de dingues passés ensemble. Si je veux de l'aventure, je sais toujours qui appeler. Merci Père Picsou, le plus filou. Deux ans de prépa (trois), c'est court, mais les souvenirs les plus fous et hilarants sont concentrés dans cette période où tu as été tellement drôle, emphatique et d'un soutien inconditionnel. Promis qu'un jour, je t'accompagne voir Mylène dans la fosse. À toi Thomas ! Si on me demandait d'inventer un nouveau mot qui décrit une personne brillante, attentionnée, dévouée et empathique au souhait, je proposerais : Tomish ! Je t'attends pour le Toulouse Saint-Malo sur nos vélos pour se paumer à chaque rond-point et en rire jusqu'aux larmes. À toi, mon Juju aka Jack, quel immense soutien tu m'as apporté, je ne saurais te remercier assez. Un jour, on ira faire de l'apnée et tu me montreras tes talents ! Jean Réno n'aura qu'à bien se tenir. Merci aux copains de la team de St-Malo : Phéphé, Marie, Victor, Flo. Merci Nico, je pense que je ne rencontrai jamais quelqu'un comme toi de nouveau. Bon sang, que j'ai ri avec toi ! Ton soutien fut si précieux, sache le. Merci Gardan, la team internat restera la meilleure, surtout avec le collègue précédent et ses escapades sur des grues de chantier. Enfin, remerciement aux sœurs Bruand de m'avoir fait changer d'air à chaque fois que l'on se voyait et que l'on se verra.

Obtenir le titre de docteur n'aurait jamais été possible sans l'aide inconditionnelle et la plus importante de ma famille. Merci Papa de m'avoir donné le goût des sciences, de la rigueur et de la pratique. Je n'ai jamais embrassé le monde du modélisme comme tu l'aurais peut-être souhaité, mais c'est assez ironique finalement de défendre une thèse de doctorat sur le sujet. Je ne serais jamais assez reconnaissant de l'aide que tu m'as apporté sur cette thèse, en particulier sur le plan technique et scientifique. On pourrait même parler d'un troisième encadrant. Merci, maman, de m'avoir inculqué le goût des arts, la créativité et la folie, qui sont des notions bien étrangères au monde scientifique (hormis la folie). Les quelques dessins de ce manuscrit qui tentent de donner un peu de chaleur à l'ensemble te sont dédiés. Merci au frangin Alexandre, tu es une source d'inspiration quotidienne. Je n'ai jamais connu quelqu'un d'autre que toi d'aussi attaché au détail et à la rigueur. Tu es toujours d'une précision chirurgicale et je t'envie ces qualités. Ton avis extérieur a toujours été précieux et d'une grande aide. Merci à Grand-Mère, source d'inspiration quotidienne, un modèle de résilience et de combativité. Sortir de nos discussions dominicales me remplissait et me remplit toujours de sagesse et de sérénité.

Bon vent et bonne lecture.

Contents

List of Figures

List of Tables

Part I

The UAV context and soaring techniques

Chapter 1

The UAV context and endurance improvement techniques

Abstract

This chapter introduces the concepts underlying the thesis through a semantic analysis of the subject. First, a historical overview of the use of UAVs is given. Then, the classification of fixed-wing UAVs is recalled and illustrated with numerous cases of civil, academic and military applications. In view of the strong growth of the UAV market, the main characteristics of an attractive UAV are identified. This is followed by a list of possible permanent improvements, highlighted by recent work in the literature. These are compared with so-called intermittent improvement techniques and their potential. Techniques aimed at harvesting energy from the atmospheric environment seem to be particularly attractive, especially for UAVs. The different objectives and the roadmap of the manuscript are presented.

Contents

Acronyms

UAV	Unmanned Aerial Vehicule
SUAV	Suicide Unmanned Aerial Vehicule
KUAV	Kamikaze Unmanned Aerial Vehicule
RPV	Remotely Piloted Vehicule
LM	Loitering Munition
m-UAV	micro Unmanned Aerial Vehicule
M-UAV	Mini Unmanned Aerial Vehicule
HALE	High Altitude Long Endurance
LH2	Liquid hydrogen
GH2	gaz hydrogen
SAF	Sustainable Aviation Fuel
DT	Delair-Tech
NASA	National Aeronautics and Space Administration
NACA	National Advisory Committee for Aeronautics
SNCF	Société Nationale des Chemins de Fer

Résumé du chapitre en français

Ce chapitre via une analysise sémantique du sujet, permet d'introduire les concepts sous jacents à la thèse. Une revue historique de l'utilisation des drones est faite en premier lieu. Puis la classification des drones à voilure fixe est rappelée et illustrée avec de nombreux cas d'applications civiles, académiques et militaires. A la lumière de la forte croissance du marché des drones, les caractéristiques principales d'un drone dit attactif sont identifiées. En découle alors une liste des différentes améliorations possibles dites permanentes, mises en avant par les récents travaux de la littérature. Ces dernières sont mise en comparaison avec les améliorations dites intermitentes et leur potentiel. Les techniques visant à exploiter les phénomènes aérologiques se révèlent particulièrement attractives, en particulier sur les drones motivant ainsi le sujet. Sur ce constat, les différents objectifs et la feuille de route du manuscrit sont présentés.

1.1 The UAV context

This chapter introduces the concepts underlying the thesis through a semantic analysis of the subject. The document starts with some basic definitions.

1.1.1 Definition and historical background

Definition:
An Unmanned Aerial Vehicle (UAV), or more commonly a drone, is a flying aircraft without a pilot on board. They can be either remotely or automatically piloted, the former being referred to as RPVs (remotely piloted vehicles). The term UAV does not include missiles, as they are designed to be recoverable. However, there is an intermediate category of UAV that becomes a missile once it has detected its target. They are called Loitering Munition (LM) or Suicide/Kamikaze Drone (SUAV, KUAV).

Historical background:
UAVs have been used since before the dawn of aviation. In fact, their first use could be attributed to the invention of the kite or (wooden bird) by Lu Ban (500 BC), who used them in battle to send messages, lift soldiers and even set fire to enemy installations. Another example is the Austrian incendiary balloon used during the attack on Venice in 1849, known as the first offensive UAV. They carried a small charge of explosives and, once launched, drifted with the wind until they reached their target. This last feature made them very imprecise and historical reports mention that only one bomb was dropped over the city and the rest drifted back towards the Austrian battle lines. After the first powered flight by the Wright brothers in 1903, and with war looming, interest in UAVs began to grow. As a result, remotely piloted aircraft were used to attack zeppelins during the First World War. The most famous UAVs used during this conflict were the Hewiit-Sperry Automatic Airplane and the Kettering Bug. Then came World War II, when many more drones were developed, such as the Radioplane QQ-2, which was primarily used to train anti-aircraft weapons. A total of 15,000 were produced and supplied to the US Army. Even before the war began, the US Army Air Forces (USAAF) used the Culver PQ-8 and PQ-14 as anti-aircraft target drones. The TDN-1 was used by the same army as the UAV bomber, but was never widely used. Finally, the most sadly famous UAV of the Second World War is the Wernher von Braun's V1, an LM flying at 640km/h, launched from a rail system with a range of 250km, with the purpose of targeting and bombing London. Shortly afterwards the USAAF received its equivalent, the TD2D-1 Katydid. During the Cold War, UAVs were used as reconnaissance and radioactive data collectors, such as the modified B-17 Flying Fortresses used in Operation Crossroads. They were also used to study the blast and shock waves of nuclear bombs. Aerojet UAVs such as the Ryan Model 147 were used to spy on North Vietnam and Korea during the Vietnam War. The USSR also developed military UAVs. However, historical reports are difficult to find, so the information is still rather sketchy. In the 1980s and beyond, a new type of UAV emerged that collected much more data, had a better autopilot and so on, with the development of computer science and the miniaturisation of electronics. The missions remain quite similar, but they implement new technologies more adapted to modern warfare, such as stealth systems, high-resolution cameras and radar... The most famous modern models are the Northrop Grumman RQ-4 Global Hawk and the MQ-1 Predator, both shown in the figure 1.1. They can fly for many hours (see figure 1.2) and can be remotely controlled from a secure base via a satellite link. Historically, UAVs have been developed mainly for military purposes, but fortunately modern applications are no longer limited to warfare. Nowadays, UAVs are used for various civilian applications such as agriculture, mining, railways, dams, construction, nuclear power plant inspection and monitoring (Ren et al., Banić et al., Rahman and Mammeri, Winkvist et al., Almalki et al., Buffi et al.). High-altitude UAVs, introduced in the later section, are also used for internet broadcasting and weather monitoring (Cravey et al.-2006). The author proposes to classify the different types of UAVs that exist, mainly illustrated by the figure 1.2. These are illustrated with modern academic and civil applications.

1.1.2 UAV categories

1.1.2.1 micro UAV

The micro UAV category can be defined in different ways, but the main characteristics used to describe them are either mass or wingspan, but the mass is prefered as it can include more planforms such as quadcopters etc. Thus, micro UAVs are usually defined by any flying planform with a mass of less than 1kg. Two models from Aerovironement are shown in figure 1.3, with their respective endurance and range shown in figure 1.2. They are typically used for short range reconnaissance or for development in very small and restrictive environments, their embedded electronics

(a) Northrop Grumman RQ-4 Global Hawk
Image source : Global Hawk

(b) General Atomics MQ-1 Predator
Image source : Predator

Figure 1.1: Long endurance/range military UAVs

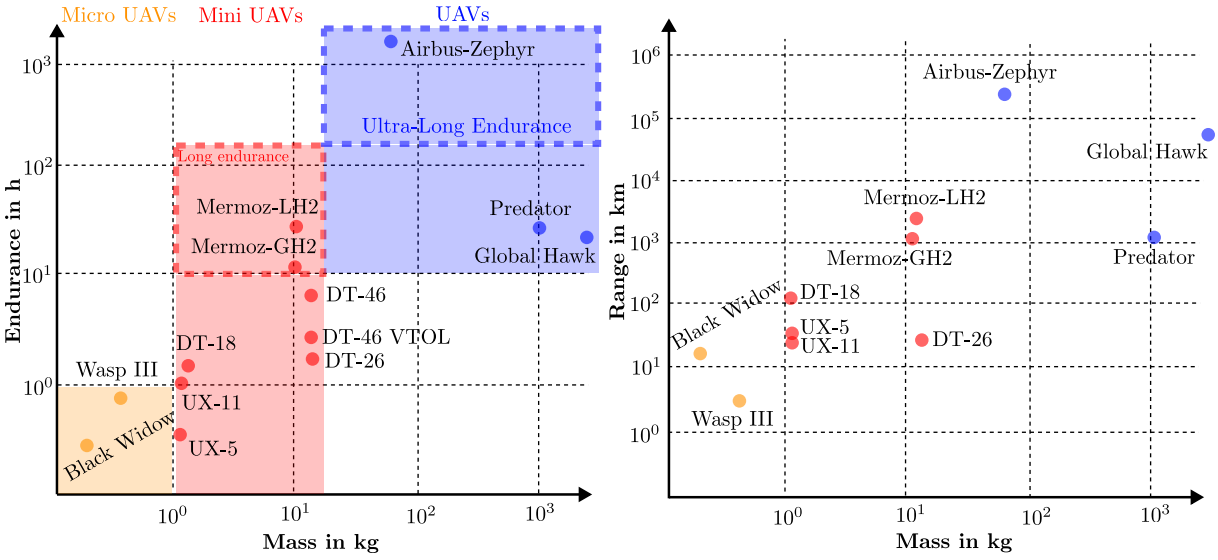

Figure 1.2: Endurance (left) and Range (right) versus mass for various modern UAVs covering the entire classification (Micro, Mini, long endurance, long range etc)

are quite limited due to the low payload capabilities, limiting their potential applications.

1.1.2.2 Mini UAV

Mini UAVs are defined with a mass in the range of 1 to 20 kg, their endurance usually varies from 1 to several hours on traditional layout [1]. The lower and upper limits of this category are illustrated by the solutions proposed by Delair-Tech. The DT UX-5 and its upgraded version UX-11 are shown in figure 1.4 for the micro/mini limit and the DT-26 and DT-46 (figure 1.6) for the upper limit. Note that the DT-46 exists in 2 configurations (vertical take-off and landing and traditional layout), whose endurance is highlighted in figure 1.2. Some models in the mid-range category are shown in figure 1.5. Because the mini-UAVs are heavier, they can carry more electronics and sensors. Their range is also extended, and their cruising speed is low enough to make them attractive for reconnaissance and surveillance. For example, the French national railway company (SNCF), in partnership with Delair Tech, is using the DT-26 and UX-11 coupled with AI software to detect and predict when trees near railway lines need to be pruned.

1.1.2.3 Long Endurance Mini-UAV

Within the Mini-UAV category there is a subcategory called Long Endurance Mini-UAV, defined by an endurance of more than 10 hours as shown in the figure 1.2. This usually incorporates a very efficient aerodynamic layout using gasoline or liquid/gaseous hydrogen as an energy source. The ISAE-Mermoz [2]. LH2 and GH2 (liquid or gaseous hydrogen) are shown in the figure 1.7 are modern academic prototypes (without payload) whose objective is to cross the Atlantic Ocean on the Aeropostale Mermoz flight path from Dakar to Natal (3500km) (Gavrilovic et al. 2021 and 2023). This project aims to demonstrate the feasibility of using hydrogen combined with a fuel cell as a solution for future UAV layouts. The use of sustainable aviation fuel (SAF) or hydrogen opens up a new range of long-range sustainable missions such as weather monitoring, migratory bird tracking, etc. The author will take an important interest in the last 2 categories in the following work (mini and long endurance mini UAVs).

[1] by traditional layout it means that the main lifting component comes from a lifting surface (wing) such as flying wing, planes, tandem, etc.

[2] Jean Mermoz (9 December 1901, Aubenton, Aisne - 7 December 1936) was a French aviator, considered a hero and pioneer by other pilots such as Saint-Exupéry, he is best known for being the first to cross the Atlantic Ocean as a pilot for the Compagnie aéropostale in a Latecoere 28 in 1930

1.1.2.4 High Altitude Long Endurance UAV

The last category of interest is the High Altitude Long Endurance UAV (HALE), figure 1.8 shows 2 prototypes. The Airbus Zephyr-S is known to have broken range and endurance records over the last few decades. As it flies above the clouds and carries a set of solar cells on its wing, the UAV is able to recharge its battery during the day and use it during the night. Being durable enough, it has broken records by flying for more than a month and covering more than 1 million km without landing or refuelling. The main application for this type of aircraft is to provide internet and communications to remote areas of the planet. These are presented as an alternative to satellites, which are expansive solutions. Note that the Airbus Zephyr is also equipped with high-resolution sensors for atmospheric and weather monitoring. HALE UAVs can easily be brought down to the ground for maintenance, changing to a more advanced system, making them extremely attractive and versatile.

1.1.3 Market growth and needs

As UAVs have reached civilian applications, the overall market has seen an increase in the last few decades, with a growth rate in the double to triple digits. The market size is expected to exceed $30 billion by the end of 2030 Mazur et al.-2016. Many different small companies are emerging offering different solutions from micro to HALE UAVs, but regardless of the category, to remain competitive, endurance and payload mass must be as high as possible. Consequently, the implementation of technologies that improve the performance and reduce the mass of the aircraft is quite critical and motivates this work. In consequence, the next sections present the various methods currently applied or studied that improve the overall endurance/range of the aircraft and those of interest in this thesis work.

As UAVs tend to be small, they are less expensive to design and manufacture. Consequently, they provide a good opportunity to test and implement new ideas that may be common to manned aircraft, such as laminar flow control devices, wingtip devices, new types of layouts and high lift devices, etc. In addition, UAVs are less subject to restrictive safety standards as they do not carry human life. As a result, it is easier and quicker to implement new technologies and make them good incubators of ideas.

(a) Aerovironment's Blackwidow
Image source : Blackwidow

(b) Aerovironment's WASP III
Image source : WASP III

Figure 1.3: Long endurance/range military UAVs

(a) Delair Tech UX5
Image source : UX-5

(b) Delair Tech UX11
Image source : UX-11

Figure 1.4: UAV example close to the lower bound of Mini UAV's category using Flying wing layout. Low endurance models

(a) Delair Tech DT-18
Image source : DT-18

(b) The University of Sydney SBXC (glider configuration)
Image source : [Lawrence]

Figure 1.5: UAV examples closed tp the lower bound of Mini UAVs, classic layout

(a) Delair Tech DT-26
Image source : DT-26

(b) Delair Tech DT-46
Image source : DT-46

Figure 1.6: Examples close to the higher bound of the Mini UAV's category using classic layout, mid endurance models

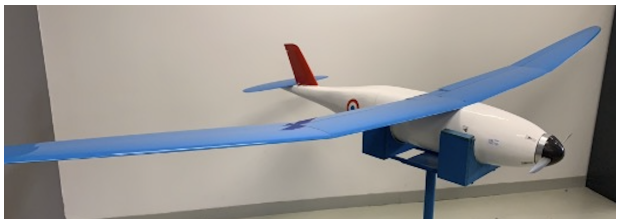

(a) ISAE : Mermoz-GH2
Image source : Mermoz-GH2

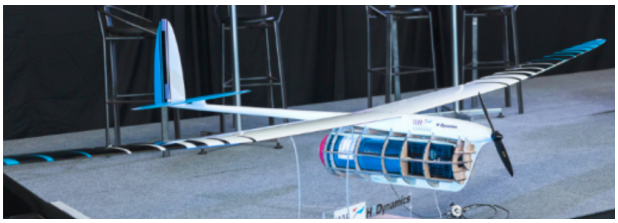

(b) ISAE : Mermoz-LH2
Image source : Mermoz-LH2

Figure 1.7: Long endurance mini UAV's low emission prototypes enabled by hydrogen.

(a) Airbus-Zephyr S
Image credit : Christian Otto
Image source : Airbus Zephyr-S

(b) Swift Engineering HALE prototype
Image credit : Swift Engineering
Image source : Swift Engineering

Figure 1.8: Ultra Long endurance UAV' prototypes flying at high altitude (HALE)

1.2 Steady and permanent endurance improvement techniques

This section discusses the different methods that currently exist to improve the endurance of drones. Continuous/permanent improvement methods are defined as those that permanently increase endurance and do not depend on exogenous parameters. They are usually optimised for the cruise state. They include drag reduction, propulsion efficiency optimisation, mass reduction, power source selection, etc.

1.2.1 Flying at low Reynolds number

The biggest problem with UAVs is usually low Reynolds number flight, which degrades the aerodynamic performance of the aircraft. In fact, the flow around the airfoil of a small UAV is more prone to transition to turbulent flow in its boundary layer, drastically increasing the drag of the aircraft. As a result, mini and micro UAVs are inherently much less aerodynamically efficient than manned aircraft. The figure 1.9 illustrates the differences between the sources of drag on a mini UAV and a commercial aircraft. Despite the fact that there are fewer drag sources on a mini UAV. The total non-dimensionalised contribution is higher than for the commercial airliner because the UAV flies at a much lower Reynolds number.

1.2.2 UAV drag reduction methods

As seen in the previous section, there are different sources of drag and for each there are devices and methods to reduce their contributions. For the sake of readability, we will focus on reducing interference drag, lift induced drag and profile drag (the most common drag sources for mini UAVs). Lift induced drag can be reduced in many ways, by increasing the wing span and trying to achieve an elliptical lift distribution. The use of wingtip devices is known to virtualy increase the wingspan. Lift-induced drag is also related to the wing wake. The latter can interact with the downstream surfaces to increase the overall drag. Tandem aircraft are particularly susceptible to these effects. However, optimum geometric parameters can be used to reduce these effects.
Interference drag generally occurs in a zone of connection between the lifting surfaces (fuselage/wing). As the change in geometry is quite sharp, the flow can be subject to turbulence, which increases the aircraft drag. Von Karman transitions are used to provide a smoother change in geometry, avoiding the above phenomenon.
Several methods can be used to reduce profile drag, for example the airfoil shape can be optimised for the target cruise condition as shown by Bronz-2012. Then, drag related to the turbulent boundary layer or laminar bubble formation can be reduced using different devices such as surface rugosity distribution (Jaroslawski et al., Scarano et al.), advanced heat-

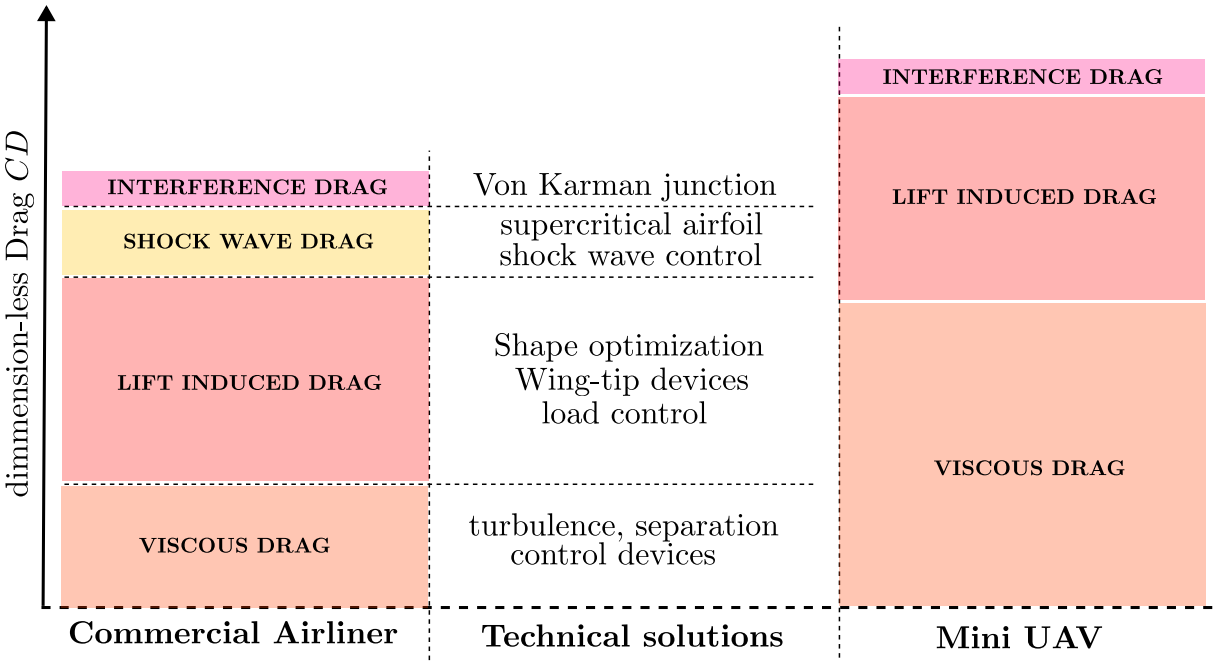

Figure 1.9: Comparison of the different sources of drag between a commercial airliner (high Reynolds number, transonic flight) and a Mini UAV (low Reynolds and Mach number)

ing devices (Yeh and Taira-2019) and boundary layer suction devices (Messing and Kloker-2010).

1.2.3 Propulsion efficiency

Another vector for improvement is to look at the efficiency of the propulsion chain used on any aircraft. First of all, the propeller or ducted fan (most likely to be used) can see its geometry optimised for a given flight condition as shown for example by Li Volsi et al.-2022.

As for fixed wing aircraft, boundary layer control devices can be used on propellers, but because of integration problems they are fewer. Similarly, rugosity distribution can be used to improve the efficiency of a given propeller, as shown by Jaroslawski et al.-2022.

Then there is the question of propeller/engine coupling. Indeed, electric engines are optimal at a given speed, multidisciplinary optimisation can be performed to find the best fit as suggested for example by Bronz et al.-2012.

Finally, there is the problem of integrating the propeller into an aircraft. The latter, which produces a jet with a swirl, can drastically affect the aerodynamic performance of the aircraft. It can also affect its aeroelastic response (whirl flutter). The correct placement of the propulsion devices can therefore dramatically improve the performance. For example, Veldhuis-2005, Runyan and Sewall-1948 have studied the problems experimentally.

1.2.4 Lighter structure

The structure of an aircraft has a significant impact on its performance. A lighter structure would result in a smaller wetted area as less lift has to be generated by the lifting surfaces, reducing the overall drag. For the same wetted area, the lift required to maintain a level flight would be lower and, by reducing the angle of attack, the 3D induced drag would be lower. As lift-induced drag varies with the square of lift, a 10% saving in mass would result in a 19% saving in lift-induced drag. Saving weight would in most cases be beneficial to endurance performance. However, reducing the mass of the structure has its drawbacks, as it usually increases flexibility. This leads to various undesirable aeroelastic phenomena such as torsional divergence, aileron reversal, flutter, etc. [3]. These phenomena reduce the flight envelope of the drone, making it less attractive. As a consequence, a compromise has to be found and usually the benefit of mass saving is quickly limited. Also, as mentioned earlier, the mass of the payload is very important to be competitive as a UAV manufacturer. As a result, the mass saved on the structure is usually used to increase the payload. Consequently, in this work it is assumed that a change in flexibility does not affect the mass characteristics of the aircraft.

[3] These phenomena are discussed in detail in a separate chapter.

1.2.5 Energy source matters

The energy vector used on a UAV or manned aircraft plays a significant role in the overall endurance. Figure 1.10 shows the gravimetric and volumetric energy of the sources commonly used in aircraft. The graph is based on data from Stura and Nicolini-2006 and Jeong et al.-2015 for battery technology.

Note that additional data (dashed lines) have been added to show the usable energy for each source after it has been integrated into a modern solution. For example, for hydrogen, the efficiency of the fuel cell plus the losses in the entire propulsion chain have been taken into account. However, in terms of hydrogen efficiency and volumetric density, more volume is needed to carry the same amount of energy provided by kerosene, despite the fact that its gravimetric density is 7 times greater. Increasing the volume to carry hydrogen means increasing the size of the tanks or the fuselage containing the tanks, thus increasing the wetted surface of the aircraft.

1.3 Intermittent endurance improvement strategies

In addition to the improvement methods mentioned above, it is still possible to increase the endurance of a drone. In fact, there are several sources of energy, known as exogenous, that can be used during flight. The table 1.1 shows the main sources and the forms of end energy that can be used.

1.3.1 Solar Energy

A significant amount of energy can be harvested from solar radiation. Figure 1.11 shows the mean daily and annual Global Horizontal Irradiance (GHI)[4] available. . This incoming energy can be used to increase endurance. On the ISAE-Mermoz GH2 and LH2, for example, flexible solar cells are glued to the wing and slightly extend endurance by recharging the buffer battery. This means that less hydrogen is used during the day. The author claims that the installation of solar cells on the windward side of the wing would also increase performance, as the sun's rays would be reflected off the Atlantic Ocean and hit the panels. Some experimental tests (unpublished) carried out over a lake showed that 10% of the equivalent energy harvested on the leeward side was extracted. HALE UAVs also rely heavily on solar power; for example, the Airbus Zephyr-S recharges its battery using solar panels and can fly all night until the next day. The amount of incoming energy is usually greater than the amount used to power the aircraft. Authors have also explored using solar panels on the HALE prototype to electrolyse water produced by the fuel cell to produce hydrogen, which would be reused in the propulsion chain (Cha et al.-2015 and 2016. However, this appears to be less efficient than a solar panel battery solution because of losses along the loop. So far, only HALE can achieve almost infinite range and endurance because they are extremely efficient and have large exposed surfaces. Also, because they fly extremely high, they are not subject to cloud cover, so the solar panels are always exposed during the day. For the lower category of UAVs, the use of solar energy remains interesting and is used, for example, in the XSUN commercial solution. Unfortunately, it can only be used with a battery and electric motors. And given the gravimetric and volumetric density of the battery, the advantage is quite limited and it is difficult to compete with SAF or hydrogen. For example, XSUN and Mermoz-LH2 have the same mass, around 10-15 kg, with both solar panels, but the XSUN's endurance is announced at 11 hours, while the Mermoz prototype of the liquid hydrogen version is almost 40 hours.

[4]GHI is the total irradiance of the Sun on a horizontal surface on Earth. It is the sum of direct and diffuse horizontal irradiance. For more details see GHI

1.3.2 Wind field

For any aircraft flying through an environment that is unlikely to be calm, many atmospheric phenomena (thermals, gusts, wind shear, etc.) can occur that provide a significant amount of energy. Harvesting energy from the wind field can lead to two forms of final energy on the aircraft. The first is electrical, which can be produced using methods such as kite soaring, using the aircraft propeller as a windmill, or using piezoelectric harvesters in the structure during turbulence and gust encounters. Note that these methods have a very low potential in UAV applications due to the small amount of energy harvested. The second type of final energy is mechanical, either potential or kinematic, or both. There are three main strategies, static, dynamic and gust soaring. The latter will be discussed in detail in the next chapter. They provide much more energy than the first two types of final energy strategies.
As we have seen in the previous sections, the first vector of aerodynamic improvement is usually to increase the span, which reduces the lift-induced drag. This inevitably leads to a lighter and more flexible structure. These characteristics need to be discussed in terms of energy harvesting strategies.

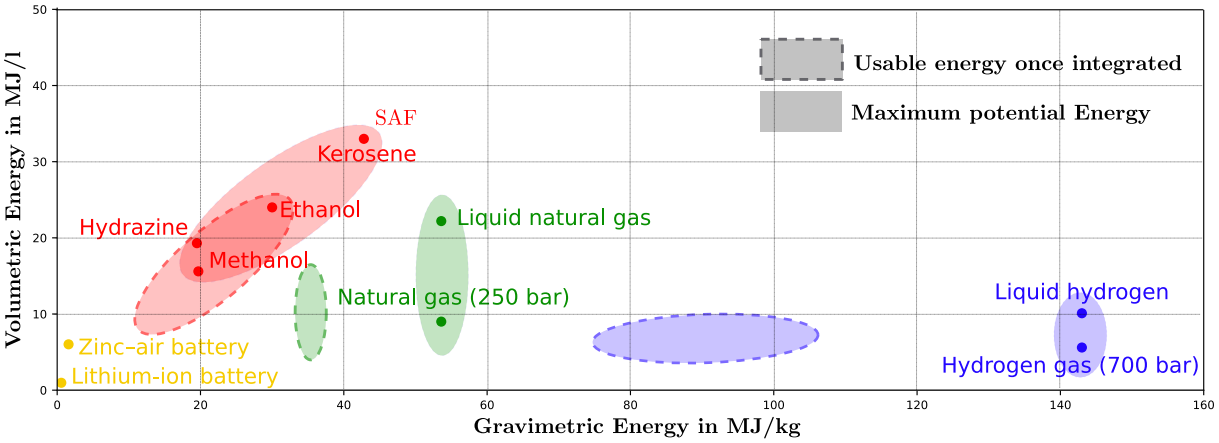

Figure 1.10: Volumetric versus gravimetric energy of different sources of energy, efficiencies effect of existing integration technologies are highlighted

	Electrical final energy	Mechanical final energy
Radiation	- Solar panels	
Windfield	- Kite Soaring - Propeller used as a wind mill - Piezoelectric generator	- Static soaring - Dynamic soaring - Gust soaring

Table 1.1: Exegeous engergy types versus final energy on the aircraft

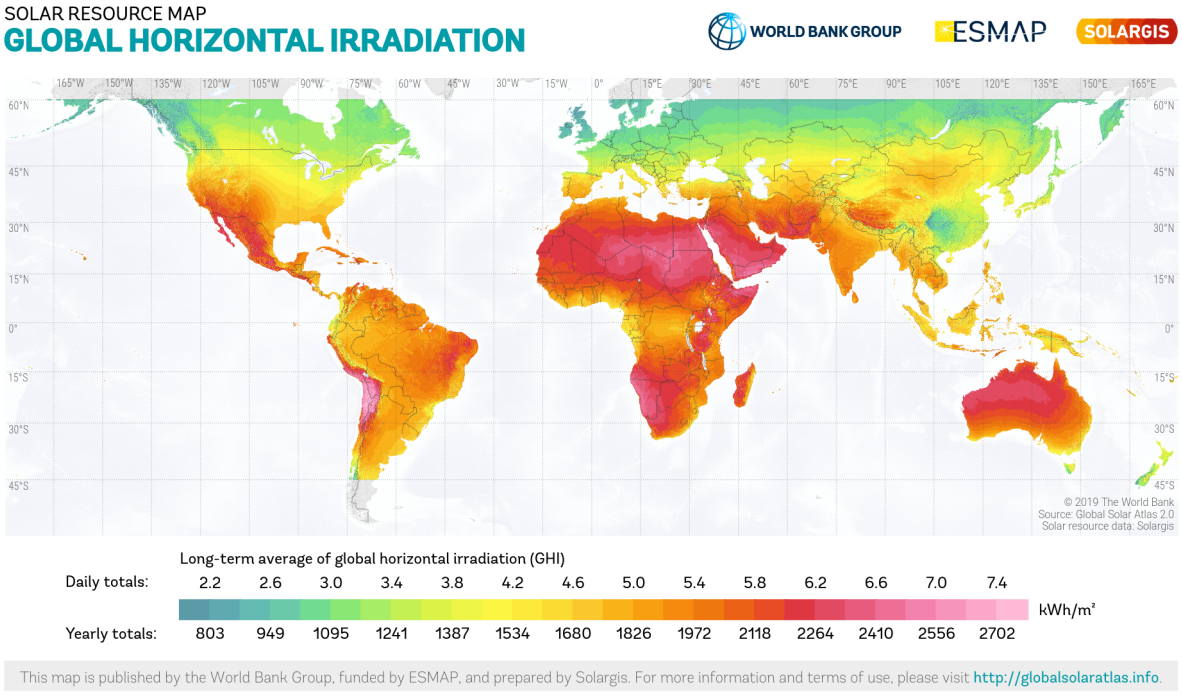

Figure 1.11: Daily and Yearly global horizontal irradiation on the planet
Original image source : Global Solar Atlas

1.4 Thesis overview

As we have seen in the previous section, we have reduced the scope of UAV endurance improvement methods to energy harvesting strategies on flexible geometries. Hence the title of the thesis: *"Energy harvesting on flexible UAVs: design of robust control laws"* The first main term (*"Energy Harvesting"*) was rather vague at the beginning, as it has been seen in the previous sections, but in this case we will only evaluate the energy harvesting strategies that involve using the surrounding wind field to increase the UAV's endurance.
The second term (*"flexible UAV"*) is also quite large, but only examples of UAVs with sufficient endurance will be considered. According to figure 1.2 and the different layouts presented, these usually have a high aspect ratio fixed planform, as this drastically reduces the 3D lift-induced drag. These characteristics usually result in a weaker and more flexible structure. In this work it is assumed that one has sufficient degrees of freedom to consider this flexibility variable in a reasonable range so that one can assess its effects on the overall performance.
The last term (*"robust control law"*) underlies the need for automated strategies that are sufficiently robust to different types of disturbances and parametric uncertainties. From this brief semantic analysis, it can be concluded that this topic raises three main questions:

Question 1: *"Can tailoring* [5] *and the flexibility of a planform improves the performance of energy harvesting strategies..."*

Question 2: *"Are optimal tailoring and stiffness parameters compatible with the flight conditions of the UAV mission? Do they adversely affect the cruise aerodynamic performance and the size of the flight envelope? "*

Question 3: *"The stiffness and tailoring properties are fixed, how to develop a control law that satisfies energy harvesting strategies and deals with the aeroelastic phenomenon that can threaten its stability and health?"* Thus, during the last three years, I have tried to contribute to the thesis topic. The three questions above require experimental and numerical needs to be able to answer them. Consequently, the following thesis roadmap is proposed, summarising the work done.

PART I: BACKGROUND

Chapter 1 reviewed the various methods available for improving the endurance of UAVs and the one of interest in this thesis.

Chapter 2 presents the basics of the soaring technique, the physics behind it, the most recent work from the community and what are the metrics of performance that the author needs to evaluate the three previous questions. In view of the content of the chapter, the numerical requirements for dealing with the subject are presented in the last section, and the chosen framework (ASWING/XFOIL/QPROP) is introduced.

PART II : THESIS FRAMEWORK
Since small performance gains or losses were expected, the numerical framework had to be precise enough to draw reasonable conclusions. In addition, as the software proposed many features that were not necessarily used in the thesis, we proposed an experimental evaluation as suggested in chapters 3, 4, 5 and 6.

Chapter 3 focuses on the aerodynamic model of the ASWING and proposes modifications in the light of modern literature. Each aerodynamic feature is then evaluated against experimental data from the literature. It also proposes computational time and prediction benchmarks with other numerical methods.

Chapter 4 presents the experimental evaluation of the propeller model against experimental data. Some modifications are proposed in the light of the prediction performance.

Chapter 5 focuses on the experimental evaluation of the structural model. Stressful cases have allowed the limits of the model to be identified.

Chapter 6 finally couples the aerodynamic, propeller and structural models and proposes the evaluation of some of the aeroelasticity characteristics against various experimental reports.

PART III: CONTRIBUTIONS The aim of this part is to present the contributions to the main topic, which is the energy harvesting strategy. The contributions are divided into 2 chapters. For both, the same aircraft has been used as an application example.

Chapter 7: proposes an optimisation of a UAV structure and tail in order to maximise the energy harvested in thermal soaring. ASWING is used directly in the optimisation loop. In the light of the solutions found, a discussion of the implications for the full flight envelope is proposed.

Chapter 8: presents how ASWING has been used as an out-of-loop analysis tool to study the perfor-

[5] Tailoring refers to the way the composite is made, for a given stiffness property, the planform can have different elastic/tension axis position and cross-coupling stiffness terms. This concept is introduced in Chapters 3 and 5

mance of UAVs in a dynamic soaring strategy. A completely new formulation of the problem is proposed to assess whether or not flexibility improves the performance of the aircraft in dynamic soaring flight.

1.5 Conclusions

Chapter one has provided some definitions of what a UAV is, its historical background, what are its modern uses and what are the problems arising from the expansion of the market. Increasing a UAV's range and endurance is crucial to stay competitive, so the different techniques to improve them have been summed up in 2 categories, permanent and intermittent. Among the intermittent ones, the energy contained in the surrounding wind field has a high potential to improve the performance of any aircraft. Or UAVs with long endurance are mainly characterised by a high aspect ratio and a flexible wing, and the author believes that there are 3 main issues to be assessed. In the light of these, the roadmap of the thesis has been introduced.

Bibliography

[1] Almalki, F. A., Soufiene, B. O., Alsamhi, S. H., and Sakli, H. (2021). A low-cost platform for environmental smart farming monitoring system based on iot and uavs. *Sustainability*, 13(11):5908. 26

[2] Banić, M., Miltenović, A., Pavlović, M., and Ćirić, I. (2019). Intelligent machine vision based railway infrastructure inspection and monitoring using uav. *Facta Universitatis, Series: Mechanical Engineering*, 17(3):357–364. 26

[3] Bronz, M. (2012). A contribution to the design of long-endurance mini aerial vehicles. 30

[4] Bronz, M., Moschetta, J.-M., and Hattenberger, G. (2012). Multi-point optimisation of a propulsion set as applied to a multi-tasking mav. In *IMAV 2012, International Micro Aerial Vehicle Conference and Competition*, pages pp–xxxx. 31

[5] Buffi, G., Manciola, P., Grassi, S., Barberini, M., and Gambi, A. (2017). Survey of the ridracoli dam: Uav–based photogrammetry and traditional topographic techniques in the inspection of vertical structures. *Geomatics, natural hazards and risk*, 8(2):1562–1579. 26

[6] Cha, M.-Y., Kim, M., and Sohn, Y.-J. (2015). A design of size of regenerative fuel cell system used for a high altitude long endurance unmanned aerial vehicle. *AFORE*, pages 359–359. 32

[7] Cha, M.-Y., Kim, M., Sohn, Y.-J., Yang, T.-H., and Kim, S.-G. (2016). Flight paths for a regenerative fuel cell based high altitude long endurance unmanned aerial vehicle. *Journal of Mechanical Science and Technology*, 30:3401–3409. 32

[8] Cravey, R. L., Vedeler, E., Goins, L., Young, W. R., and Lawrence, R. W. (2006). Structurally integrated antenna concepts for hale uavs. Technical report. 26

[9] Gavrilovic, N., Leelaburanathanakul, P., Cuadrado, J., and Moschetta, J.-M. (2021). Aero-propulsive performance improvement of h2 powered uas. 28

[10] Gavrilovic, N., Moschetta, J.-M., and Barascud, Q. (2023). Development of a Hydrogen-powered UAV System for Crossing the Atlantic Ocean. In *AIAA SCITECH 2023 Forum*, National Harbor, MD & Online. American Institute of Aeronautics and Astronautics. 28

[11] Jaroslawski, T., Forte, M., Moschetta, J.-M., Delattre, G., and Gowree, E. R. (2022). Characterisation of boundary layer transition over a low reynolds number rotor. *Experimental Thermal and Fluid Science*, 130:110485. 31

[12] Jaroslawski, T., Forte, M., Vermeersch, O., Moschetta, J.-M., and Gowree, E. R. (2023). Disturbance growth in a laminar separation bubble subjected to free-stream turbulence. *Journal of Fluid Mechanics*, 956:A33. 30

[13] Jeong, G., Kim, H., Park, J. H., Jeon, J., Jin, X., Song, J., Kim, B.-R., Park, M.-S., Kim, J. M., and Kim, Y.-J. (2015). Nanotechnology enabled rechargeable Li–SO2 batteries: another approach towards post-lithium-ion battery systems. *Energy & Environmental Science*, 8(11):3173–3180. Publisher: The Royal Society of Chemistry. 32

[14] Li Volsi, P., Gomez-Ariza, D., Gojon, R., Jardin, T., and Moschetta, J.-M. (2022). Aeroacoustic optimization of mav rotors. *International Journal of Micro Air Vehicles*, 14:17568293211070827. 31

[15] Mazur, M., Wisniewski, A., McMillan, J., et al. (2016). Clarity from above: Pwc global report on the commercial applications of drone technology. *Warsaw: Drone Powered Solutions, PriceWater house Coopers*. 28

[16] Messing, R. and Kloker, M. J. (2010). Investigation of suction for laminar flow control of three-dimensional boundary layers. *Journal of Fluid Mechanics*, 658:117–147. 31

[17] Rahman, M. A. and Mammeri, A. (2021). Vegetation detection in uav imagery for railway monitoring. In *Vehits*, pages 457–464. 26

[18] Ren, H., Zhao, Y., Xiao, W., and Hu, Z. (2019). A review of uav monitoring in mining areas: Current status and future perspectives. *International Journal of Coal Science & Technology*, 6:320–333. 26

[19] Runyan, H. L. and Sewall, J. L. (1948). Experimental investigation of the effects of concentrated weights on flutter characteristics of a straight cantilever wing. NACA Technical Note 1594, NACA, Langley Memorial Aeronautical Laboratory, Langley Field. 31

[20] Scarano, F., Jacob, M. C., Gojon, R., Carbonneau, X., and Gowree, E. R. (2022). Modification of a turbulent boundary layer by circular cavities. *Physics of Fluids*, 34(6):065134. 30

[21] Stura, E. and Nicolini, C. (2006). New nanomaterials for light weight lithium batteries. *Analytica Chimica Acta*, 568(1):57–64. 32

[22] Veldhuis, L. L. M. (2005). *Propeller wing aerodynamic interference*. s.n., S.l. OCLC: 840392156. 31

[23] Winkvist, S., Rushforth, E., and Young, K. (2013). Towards an autonomous indoor aerial inspection vehicle. *Industrial Robot: An International Journal*, 40(3):196–207. 26

[24] Yeh, C.-A. and Taira, K. (2019). Resolvent-analysis-based design of airfoil separation control. *Journal of Fluid Mechanics*, 867:572–610. 31

Chapter 2

Soaring techniques

Abstract

This chapter aims to give the reader a better understanding of energy harvesting strategies using atmospheric phenomena. To this end, a 6-degree-of-freedom point aircraft model is introduced to present static and dynamic/gradient soaring techniques. The specific power of the aircraft is derived to highlight the effect of a time frozen wind field. Then, by isolating each field component, static and dynamic soaring techniques are presented. For the static soaring strategy, atmospheric phenomena that can be used in such techniques are presented. Speed polars, minimum sink and optimum cruise speed are then introduced as basic performance metrics.
Secondly, the components of the specific performance equation of the aircraft that involve the wing slope are isolated to present the different dynamic soaring strategies. Each atmospheric phenomenon involving a different component of the spatial wind gradient is presented and the associated optimal strategies are recalled. In the light of the literature work on dynamic soaring strategies, 2 main classes of trajectories are introduced, namely high and low G manoeuvres. The first is disqualified for flexible aircraft.
Then, in the third part, the gust and turbulence soaring strategies are presented and illustrated. The 3 strategies presented constitute a set of characteristics to be mastered by the numerical framework to be able to status if the flexibility of an aircraft can bring performance improvements or not.
Fourthly, a common methodology is proposed to correctly assess the problem and the final numerical needs arise.
In the light of the different needs presented in this chapter, the chosen numerical framework is presented.

Contents

List of Symbols

(x_b, y_b, z_b)	body frame coordinates
(x_a, y_a, z_a)	air-relative frame coordinates
(x_i, y_i, z_i)	inertial frame coordinates
$\mathcal{E}_{tot}$	total aircraft energy
$\mathcal{E}_{k,a}$	kinematic energy into the air-relative frame
$\mathcal{E}_{p,i}$	potential energy into inertial frame
$\mathcal{P}$	specific power
Π	normalized specific power
V	air-relative speed
D	aircraft drag
L	aircraft lift
T	aircraft thrust
(ϕ, ψ, γ)	bank, heading and climb angle
∇W	wind jacobian
λ	aspect ratio

Résumé du chapitre en français

Avant de se lancer dans l'étude de l'impact de la flexibilité d'une voilure sur les performances d'extractions d'énergie aérologique, il convient de les définir. En ce sens, ce chapitre propose de donner au lecteur une description des différentes méthodes qui existent, les phénomènes atmosphériques qu'elles font intervenir et leurs mise en perspectives face au sujet. Pour ce faire, un modèle avion simplifié est présenté pour expliquer le principe du vol d'ascendance et de gradient. Les notions de polaires de vitesse, ainsi que vitesse de chute et parcours optimales sont introduites. Une revue exhaustive de la littérature est présentée permettant de mettre en évidence les points clefs d'analyse de ces methodes. Pour le vol de gradient, l'ensemble des phénomènes atmosphériques exploitables est présenté. A savoir, la couche limite planétaire, les ondes orographiques, les vortex de sillage, les contractions de tube de courant dans les cayons, les allées de Von Karman planétaires, les cyclones etc. Pour chacun d'entre eux, les conditions minimales d'extraction ainsi que les travaux de la littérature sur le sujet sont présentés. A la lumière de ces derniers, nous distinguerons 2 types de trajectoires. Par la suite, l'exploitation de rafales et de turbulence sont présentées et illustrés. De la même manière, les métriques de performances et les besoins numériques associés sont introduits.
Puis une méthodologie d'analyse de l'impact de la flexibilité sur les performances globales invariante avec les stratégies considérées est présentée afin de répondre en toute rigueur aux questions soulevées par la thèse. Enfin à la lumière des pré-requis présentés, l'outil numérique retenu dans ce travail de thèse est introduit ainsi que les différents travaux concernant ce dernier à entreprendre pour aborder le sujet sereinement.
Conclusions générales:
Pour le vol d'ascendance, la polaire de vitesse (ou virage) d'un aéronef, est la métrique de performance la plus adaptée, elle permet de donner l'intensité et la taille (via le rayon de virage) des thermiques exploitables par un aéronef donné. Celle ci peut être bornée par différentes limites en vitesse (décrochage, divergence aéroélastique) et facteur de charge (rupture de la structure). Pour étudier l'impact de la flexiblité de l'aéronef sur cette méthode, il faut donc un outil en mesure de calculer les grandeurs physiques mentionnées précédemment. Pour le vol de gradient, on parle plus de problématique d'optimisation de trajectoire. Il a été démontré que ces dernières peuvent être catégorisées en 2 grandes classes qui sont les trajectoires à très fort et faible facteur de charge. Les premières étant de toute évidence disqualifiées sur un drone flexible, les secondes si le facteur de charge est relativement faible peuvent être étudiées en utilisant la polaire de vitesse mentionnée plus haut (quasi stationnaire).
Pour l'exploitation de rafales ou de turbulences, ici une simulation temporelle de l'aéronef considéré doit être effectuée. De plus les phénomènes atmosphériques en jeux impliquent une composante instationnaire de l'écoulement. L'outil retenu doit donc être en mesure de les modéliser.
Quelque soit la stratégie considérée, si un jeu de paramètre optimal est trouvé, il doit être mis en perspective avec son impact sur les performances en vol de croisière et sur la mission complète du drone. Seulement à l'issue de cette analyse, il sera possible de statuer sur l'apport ou non de la flexibilité sur les performances d'endurance globales de l'aéronef.
En ce sens, l'espace numérique retenue doit être en mesure de prodiguer toutes les fonctionnalités mentionnées plus haut. L'outil se verra particulièrement attractif s'il est efficace sur le plan du temps calcul , permettant une exploration exhaustive de l'effet des différents paramètres de flexibilité. A la lumières de tous ces pré-requis et des solutions existantes dans la littérature, ASWING a été choisi pour cette étude. Couplé à XFOIL et QPROP, il présente toutes les fonctionnalités nécessaires mentionnées précédemment et plus encore. En revanche, après une étude bibliographique de son utilisation, ce dernier contrairement à XFOIL et QPROP n'a fait l'objet que d'une évaluation expérimentale très limitée motivant une méthodologie de validation séparée en 4 chapitres distincts. A noter que je n'ai pas évalué uniquement les fonctionnalités nécessaires pour ce travail de thèse mais presque la totalité proposée par l'outil.

2.1 Introduction

This chapter aims to provide the reader with a better understanding of energy harvesting strategies using atmospheric phenomena. To this end, a 6 degree of freedom point mass aircraft model is introduced to present static and dynamic/-gradient soaring techniques. The specific power of the aircraft is derived to highlight the effect of a time frozen wind field. Then, by isolating each field component, static and dynamic soaring techniques are presented. For the static soaring strategy, atmospheric phenomena that can be used in such techniques are presented. Speed polars, minimum sink and optimum travel speed are then introduced as basic performance metrics. In the light of various works in the literature, a set of minimal required analysis features is summarised to be able to answer the questions arising from the thesis for each specific strategy.
Secondly, the components involved in the specific performance equation of the aircraft are isolated in order to present the different dynamic soaring strategies. Each atmospheric phenomenon involving a different component of the spatial wind gradient is presented and the associated optimal strategies are recalled. In the light of the literature work on dynamic soaring strategies, 2 main classes of trajectories are introduced, high and low G manoeuvres, and the performance metrics are recalled.
Then, in the third part, the gust and turbulence soaring strategies are presented and illustrated. These specific strategies represent a new set of features to be mastered by the numerical framework in order to be able to assess whether or not the flexibility of an aircraft can bring performance improvements.
Whether or not all the strategies are studied in this thesis, a common methodology is proposed. In particular, it is shown that there is an extra need for a tool capable of performing flight mission performance analysis.
In view of the different needs presented in this chapter, the chosen numerical framework is presented. Despite the numerous features it proposes, a literature review shows that it has not been much evaluated against experimental data motivivating the next chapters of this manuscript

2.2 Energy of a 6 degrees of freedom point mass aircraft

To give the reader a better insight into the energy harvesting strategies and how they work, a point mass model with 6 degrees of freedom is introduced. Also for the sake of readability, the equations development is omitted.
There are several reference frames of interest for the following analysis
Body reference frame $\mathcal{F}_b$, whose origin is fixed to the centre of gravity of the aircraft. The x_b is in the plane of symmetry of the aircraft and faces forward. Usually the thrust is defined as lying with this vector, which is considered here in this analysis as shown in the figure 2.1. The z_b also lies in the symmetry plane, but points downwards. The y_b vector is obtained using the right hand rule to ensure the orthogonality of the frame.

North-East-Down (NED) Inertial Reference Frame $\mathcal{F}_i$: Using a flat Earth assumption, since the radius of the Earth is 3 orders of magnitude greater than the altitude of the aircraft, the inertial position of the centre of gravity of the aircraft is expressed using the North-East-Down frame. Its origin is arbitrary as long as it lies in the ground plane, the vector z_i points to the ground, x_e to the north and y_e to the east to respect the right hand rule. This frame is usually of interest if you are travelling in an aircraft, as it gives your position and speed relative to the ground. It is also very convenient for expressing the potential energy of the aircraft, which is denoted as $\mathcal{E}_{p,i}$.

Air-relative frame $\mathcal{F}_a$: The air-relative frame represents the motion of the airplane with respect to the air surrounding it. It indicates how strong the aerodynamic forces acting on the aircraft would be. Secondly, expressing the total kinematic energy of the aircraft in this frame gives an indication of the energy contributed by the surrounding wind field. To better understand why this frame is more convenient for calculating the kinematic energy of the aircraft, we can take an example. Imagine the aircraft is anchored in a wind tunnel, if the kinematic energy is calculated in the inertial frame, it would be zero as the ground speed is taken into account. However, energy is added to the aircraft as the wind tunnel blows. If we now consider the airspeed, the kinematic energy would be non-zero.

Aircraft energy : The main objective of gliding is to maximise the energy extracted from the atmospheric phenomenon encountered. Let us express the total energy of the glider. This is defined as the sum of the potential energy and the kinematic energy, expressed respectively in the inertial frame and in the air relative frame, as follows

$$\mathcal{E}_{tot} = \mathcal{E}_{p,i} + \mathcal{E}_{k,a} = -\,\mathrm{mg}\, z_i + \frac{1}{2} m V^2 \tag{2.1}$$

where V, z_i and m in equation 2.1 are the air-relative velocity, the inertial altitude and the mass of the

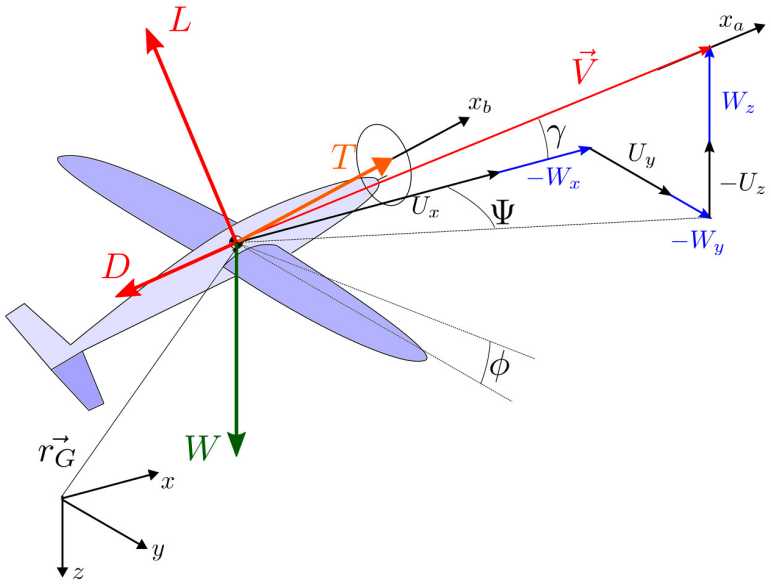

Figure 2.1: Applied forces and air relative velocity on a 6-degree of freedom point mass aircraft

aircraft. The power of the aircraft is expressed by deriving the equation 2.1 with respect to time

$$\mathcal{P} = \dot{\mathcal{E}_{tot}} = -mg\dot{z_i} + mV\frac{dV}{dt} \tag{2.2}$$

From now on, the aim is to express the equations 2.2 as a function of the wind field and the different sources of power losses and gains. The aim of this chapter is to be as concise as possible, so the derivation leading to the next equations is not given. Instead, the methodology is given in a few lines. For further details, the reader can refer to the work of Lawrance and Gavrilovic. First of all, the air relative speed is the sum of opposite inertial and wind speed. The air relative speed can be expressed in the inertial frame using the climb and yaw angles shown in the figure 2.1. Using Newton's law, the contributions of lift, drag and thrust to power losses and gains can be recovered. Then the variation of the wind field velocity with respect to time can be expressed as the product of the wind spatial gradient time the inertial velocity. Taking all these steps into account, the power of the aircraft is given by

$$\begin{aligned}\frac{\dot{\mathcal{E}_{tot}}}{m} &= V\frac{(-D + T\vec{x_b}\cdot\vec{x_a})}{m} - gW_z \\ &\quad - V\begin{Bmatrix}\cos\psi\cos\gamma\\ \sin\psi\cos\gamma\\ -\sin\gamma\end{Bmatrix}^T \nabla W \\ &\quad \begin{Bmatrix}V\cos\psi\cos\gamma + W_x\\ V\sin\psi\cos\gamma + W_y\\ -V\sin\gamma + W_z\end{Bmatrix} \\ \mathcal{P} &= \frac{\dot{\mathcal{E}_{tot}}}{m} = \mathcal{P}_D + \mathcal{P}_T + \mathcal{P}_{W_z} + \mathcal{P}_{\nabla W}\end{aligned} \tag{2.3}$$

where $\mathcal{P}$ has been introduced as the aircraft specific power flying into a space varying wind field frozen in time. $\mathcal{P}$ is the contribution of 4 different components, the power loss due to drag denoted as $\mathcal{P}_D$, the power invested by the thrust $\mathcal{P}_T$, the power gain due to rising air motion $\mathcal{P}_{W_z}$, and the loss or gain due to the spatial acceleration of the wind field denoted as $\mathcal{P}_{\nabla W}$. Finally, ∇W, in the equation 2.3, is the wind field spatial gradient expressed in the inertial frame.

2.3 Static Soaring

The specific power equation 2.3 allows the introduction of the first energy harvesting strategy, static soaring. This bio-inspired technique consists of harvesting energy from atmospheric phenomena that are considered to be stationary. These include thermals, ridges, upward wind motion and lee waves. Note that the steadineess of the phenomena must be defined in relation to the dynamics of the glider. For example, a Lee wave or thermal on a mini UAV or manned glider can be considered as a steady upward motion of the air. However, for a commercial airliner such as a Boeing 737 or a fighter jet, these phenomena are not steady due to the speed of flight. They can even be considered as gusts under certain conditions. Nevertheless, the atmospheric phenomena considered here are considered as steady, spatially frozen and bounded, leading to a simplified specific power equation

$$\frac{\dot{\mathcal{E}_{tot}}}{m} = -\frac{VD}{m} - gW_z \tag{2.4}$$

Note that in the above equation the thrust contribution has been omitted. This does not make the analysis conservative and makes it easier to understand. To measure the performance of an aircraft in static soaring, the speed and turn polars are popularly used. This polar is constructed by calculating any steady climb angle that will give a steady glide for a given airspeed and bank angle.
As this is only a simplified 6 degree of freedom point mass aircraft model, only lift, drag and weight are considered as applied forces, where lift is given as

$$L = \frac{1}{2}\rho C_L S V^2$$

where C_L is the 3D lift coefficient of the aircraft, S is the wetted surface area and ρ is the air density. The drag is given as

$$D = \frac{1}{2}\rho S C_D V^2 = \frac{1}{2}\rho S \left(C_{D0} + \frac{C_L^2}{\pi\lambda e}\right) V^2$$

where C_{D0} is the parasitic drag coefficient, λ is the aspect ratio and e is the Oswald coefficient of the wing. The drag is reasonably approximated by the contribution of the parasitic drag and the induced drag. The parasitic drag is assumed to be constant over a wide range of angles of attack because its contribution is an order of magnitude smaller than the lift induced drag. In practice, parasitic drag varies quadratically with the angle of attack. The main aerodynamic forces are introduced, and to spare the reader the development, the steady climb angle that ensures a steady glide for a given bank angle and airspeed is given by

$$\sin\gamma = \frac{1}{2mg}\left[qS\cos^2\phi k - \sqrt{(qS\pi k)^2\cos^2\phi\,(\pi k + 4C_{Do}) + 4(mg)^2}\right] \tag{2.5}$$

where $k = \lambda e$, $q = 1/2\rho V_\infty^2$ is the dynamic pressure and ϕ is the bank angle. This result was demonstrated in *chapter 3* of Lawrance and has been extended to a steady glide in turn. From equation 2.5 and by recalling that in steady glide, the drag compensates the projected component of the weight against x_a, the specific power equations can be expressed as

$$\frac{\dot{\mathcal{E}_{tot}}}{m} = -Vg\sin\gamma - gW_z \tag{2.6}$$

where $V\sin\gamma$ is actually the steady sink rate U_z. Usually the first step from the equation 2.5 is to calculate 2 main speeds of interest, the minimum sink speed and the optimum forward speed. The first will ensure that for a given bank angle, the sink rate of the aircraft into the atmospheric phenomena is minimised, thus maximising the energy harvested into it. While the second is not necessarily related to energy harvesting, it is important to know the distance the aircraft can travel before touching the ground. In other words, the optimal travel speed gives some indication of how efficient the aircraft will be in reaching other exploitable atmospheric phenomena. These 2 speeds are solutions of different optimisation problems defined in *chapter 3* of Lawrance, whose solutions are simply recalled below

	SBXC	**ASW28-18**
m **in kg**	5.44	345
AR	19.54	27.27
e	0.85	0.85 (estimated)
S **in** m^2	0.957	11.88
C_{D0}	0.017	0.005 (estimated)
C_{Lmax}	1.2	1.4

Table 2.1: illustrive example aircrafts parameters

$$V_{opt,travel} = \sqrt[4]{\frac{4m^2g^2}{\rho^2 S^2 C_{D,0}(\pi\lambda e + 4C_{D,0})}} \tag{2.7}$$

From the equation 2.7, it is highlighted that the optimal travel speed is the best one in a straight glide (no turn).
The minimal sink speed in a steady glide turn is given by equation 2.8. Equations 2.5, 2.7 and 2.8 could be a good start to evaluate the performances of an aircraft in static soaring manoeuvres. However, when it comes to flexible Mini UAVs different problems arise.

Flying at low Reynolds number:
Because of their small mass, mini UAVs tend to fly at low speeds and therefore low Reynolds numbers. As a result, the airfoil is less aerodynamically efficient (they produce more drag) and they stall earlier (lower angle of attack) than manned aircraft. To illustrate this problem, the speed polar based on the equations 2.5, 2.7 and 2.8 of a mini UAV and a manned glider are presented, using the properties summarised in 2.1. Note that the SBXC glider was used in the work of Lawrance. The speed polars are shown in figures 2.2 (a) and (b), where the first is of interest as it shows that the stall speed of the SBXC is greater than the minimum sink speed given by the equation 2.8, regardless of the bank angle. Therefore, the minimum sink speed is not the correct performance metric for a Mini UAV in static soaring. The SBXC speed polar also highlights another problem related to control theory. In fact, to maximise the energy of a Mini UAV, it is very likely to fly close to the stall speed, as the sink speed is lowest in this range. There is therefore a greater need for a robust controller that can perform trajectory control while rejecting perturbations to prevent the aircraft from stalling and crashing.

$$V_{min,sink} = \sqrt[4]{\frac{2m^2g^2\left[\pi\lambda e\cos^2\phi - 8C_{D,0} + \sqrt{\pi\lambda e\cos^2\phi\left(\pi\lambda e\cos^2\phi - 32C_{D,0}\right)}\right]}{3\rho^2S^2\pi\lambda e\cos^2\phi C_{D,0}\left(\pi\lambda e\cos^2\phi + 4C_{D,0}\right)}} \tag{2.8}$$

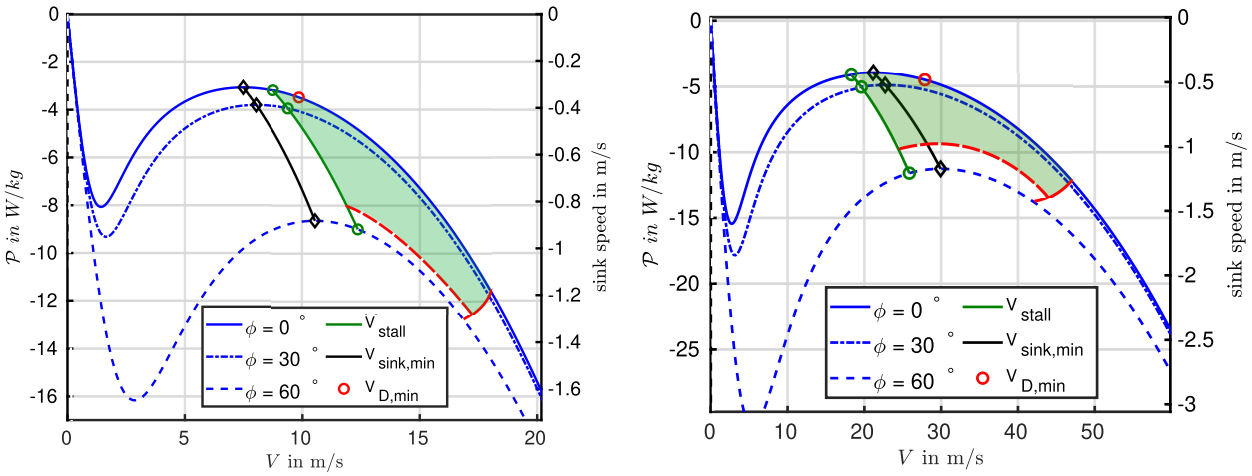

(a) SBXC (b) ASW28

Figure 2.2: Specific power and sink speed of 2 gliders in steady glidding turn green zone define the usable speed polars on a flexible aircraft (illustration)

Structural failure and aeroelastic divergence:
As the aircraft of interest in this work are flexible, they are subject to 2 main constraints that will limit the speed polar presented earlier. Firstly, there is the torsional divergence and the flutter speed, which define an upper limit to the polars. One can occur before the other, but it is mainly related to the structural tailoring and is difficult to predict. So the first one to appear will define the limit. This limit has been (arbitrarily) illustrated in figures 2.2(a) and (b) by the solid red lines. Another quantity of interest is the control reversal speed. This quantity (not shown) is of interest from a control theory perspective as it provides information on the controllability of the aircraft. Finally, the last quantity that will define an upper bound on the speed polar is the maximum load factor. Mini UAVs are made of composite materials (or not), which are usually brittle. As a result, they can be stretched or compressed to a maximum before total failure. When a UAV is in steady turn, its structure is subjected to greater loads and can therefore break if they are too great. Therefore, the green areas in the figures2.2(a) and (b) show the usable speed polars of the respective gliders, where the red dash lines are the load factor bound.

What else does the speed polar tell you?
Another very important piece of information provided by the speed polar is the turn radius, which is a function of the bank angle and the airspeed, given as

$$R(\phi, V) = \frac{V^2 cos^2\gamma}{g\tan\phi} \tag{2.9}$$

Note that the above equation is valid for both rigid and flexible aircraft. The turning radius is a very important piece of information as it gives the size of the atmospheric phenomena that can be exploited. If thermals are considered as an application example, using the radius of turn with the speed polar will provide the minimum intensity required for a given size. For example, if a thermal with a radius of 20m and a maximum velocity peak amplitude of 3.0 m/s is considered, figures 2.3 (a) and (b) show that the ASW28 manned glider will not be able to stay in it and thus harvest energy. However, figure (a) shows the optimum turning radius of the SBXC to be maintained in order to maximise the energy gain. It is extremely important to note that figure 2.3 (b) only explains that the ASW28 cannot use static soaring techniques in this thermal. However, it can harvest energy by flying straight into the thermal. Due to the size of the thermal and the speed of flight, we will talk more about gust-soaring, as it involves unsteady aerodynamics. This strategy will be introduced later in the manuscript.

What does the speed polar not tell ?
The most important information that the speed polar does not provide is how stable and controllable the aircraft is after it has been trimmed to obtain the speed polar. By examining the flap/aileron

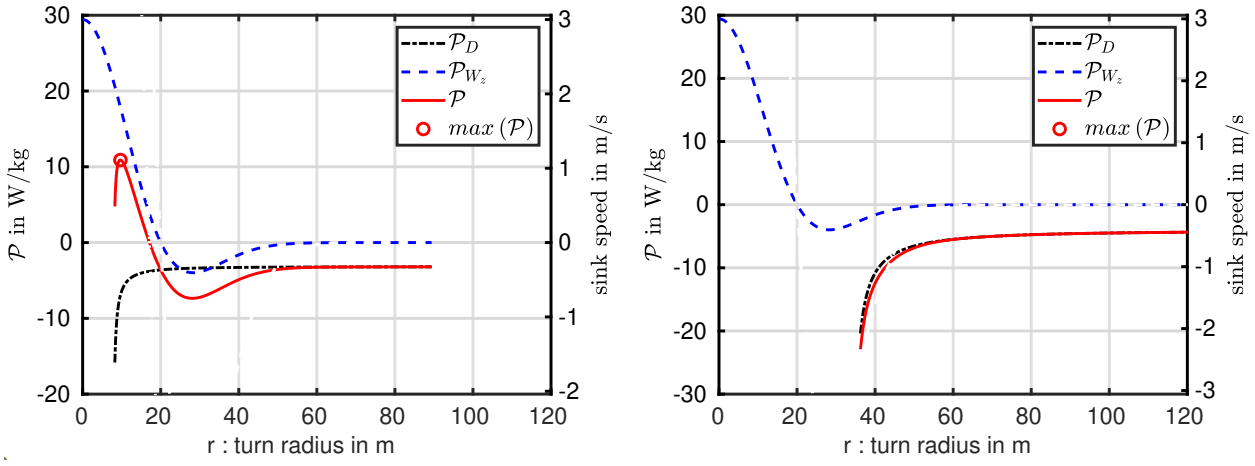

(a) SBXC (b) ASW28

Figure 2.3: Specific static soaring power of 2 gliders in steady turn into a thermal of $R_t = 20m$ and $W_{z,max} = 3.0m/s$. Classification of exploitable thermals

deflections required to trim the aircraft for a given steady glide turn condition, the controllability of the aircraft can be discussed. For example, conditions where the deflections are close to their saturation are considered difficult to control. It is also important to consider how stable or unstable the aircraft is in the turn, as this will give an indication of how much effort the controller will have to make to maintain the desired trajectory.

Summary of the numerical requirements for static soaring analysis:
In the light of the previous sections, a numerical framework with the following characteristics must be used to properly assess the issues arising from the thesis in static soaring strategy. First, it must be able to model flexible UAVs or aircraft. Secondly, it must be able to correctly predict their performance and the effect of structural tailoring on it. Speed polars, torsional divergence and flutter speed must be calculable. Linear stability and controllability as well as aileron/flap effectiveness analysis must be considered. Finally, for all the above requirements, the quality of the predictions must be qualitative as well as the computational time required to investigate a wide range of stiffness parameters.

2.4 Dynamic or wind gradient soaring

In the section on static soaring, the wind gradient has been neglected under a time and space frozen assumption. In this section a review of the potential of the $\mathcal{P}_{\nabla W}$ term in the equation 2.3 is proposed. The main goal of dynamic soaring techniques is to maximise $\mathcal{P}_{\nabla W}$ by choosing the appropriate bank, heading and climb angle as a function of the local wind gradient ∇W. The problem is not trivial because ∇W is a 3 by 3 matrix. Fortunately, its shape can be drastically simplified by examining the different atmospheric phenomena defined by a time-freezed spatial wind field and the simplifications they imply. For each of them, the minimum conditions for the extraction of energy are recalled

Planetary Boundary Layer and Ridge Wind Field
The Planetary Boundary Layer is formed by high-altitude winds accelerating layers of air due to shear stress. Figure 2.4 shows an illustration of what the PBL speed profile might be over Egypt due to the high altitude jet stream. The PBL can be quite thick, from 100m to 2km (Hanna). Most of the time the PBL is turbulent and therefore difficult to use. However, over the sea the PBL is much less turbulent and the velocity profile is almost laminar. In the PBL, the strongest gradient can be found from the ground to 200 metres, mostly dominated by horizontal wind components, so the Jacobian can be reduced to

$$\nabla W_{PBL} = \begin{pmatrix} \frac{\partial W_x}{\partial x} & \frac{\partial W_x}{\partial y} & \frac{\partial W_x}{\partial z} \\ \frac{\partial W_y}{\partial x} & \frac{\partial W_y}{\partial y} & \frac{\partial W_y}{\partial z} \\ \frac{\partial W_z}{\partial x} & \frac{\partial W_z}{\partial y} & \frac{\partial W_z}{\partial z} \end{pmatrix} \tag{2.10}$$

Without loss of generality, the specific power equation can be rewritten neglecting $\frac{\partial W_y}{\partial z}$. Let us introduce P_{xz} and Π_{xz} the specific and normalized specific power brought by a horizontal wind shear gradient. P_{xz} is

expressed from the specific power equation 2.3.

$$\begin{aligned} P_{xz} &= -V\cos\psi\cos\gamma\frac{\partial W_x}{\partial z}\left(-V\sin\gamma + W_Z\right) \\ \Pi_{xz} &= \frac{P_{xz}}{\frac{\partial W_x}{\partial z}V^2} \end{aligned} \tag{2.11}$$

Figures 2.5 (a) shows the variation of Π_{xz} with climb and heading angle. It can be seen that the more the glider faces the wind, the greater the Π_{xz}. Secondly, a minimum condition for power extraction is to climb in a positive horizontal wind shear and dive in a negative one. Figure 2.5 (b) shows the optimal climb and dive angles (dashed and solid green lines) proposed by Lawrance and their variation with vertical wind speed. Since the PBL wind profile varies with space and the optimal climb angle varies with vertical speed, the problem is transformed into one of optimal trajectory planning. Therefore, gradient soaring cannot be considered as steady soaring as it strongly depends on the UAV internial position.

Canyon/Valley Contraction:
Canyons and valleys can affect the wind field. For example, figure 2.6 shows a satellite view of the Great Canyon. Suppose a strong wind blows into the canyon. As the canyon throat/section contracts or expands along its path line, the wind field is spatially accelerated or decelerated due to the conservation of mass flow. The wind Jacobian is mostly dominated by horizontal wind accelerations as follows

$$\nabla W_{CC} = \begin{pmatrix} \frac{\partial W_x}{\partial x} & \frac{\partial W_x}{\partial y} & \frac{\partial W_x}{\partial z} \\ \frac{\partial W_y}{\partial x} & \frac{\partial W_y}{\partial y} & \frac{\partial W_y}{\partial z} \\ \frac{\partial W_z}{\partial x} & \frac{\partial W_z}{\partial y} & \frac{\partial W_z}{\partial z} \end{pmatrix} \tag{2.12}$$

Note that the blue components in the above equation are second order terms. They represent the potential low speed profile near the canyon wall (boundary layer). Again neglecting $\frac{\partial W_x}{\partial y}$ without loss of generality, the contribution of the horizontal wind acceleration to the aircraft specific power is given by

$$\begin{aligned} P_{xx} &= -V\cos\psi\cos\gamma\frac{\partial W_x}{\partial x}\left(V\cos\psi\cos\gamma + W_x\right) \\ \Pi_{xx} &= \frac{P_{xx}}{\frac{\partial W_x}{\partial x}V^2} \end{aligned} \tag{2.13}$$

Figures 2.6 (a) and (b) show the Π_{xx} variation with heading and climb angle. From the latter it can be concluded that it is not possible to extract energy from the horizontal wind acceleration. Cayon or valley contractions are therefore disqualified.

Planetary Von Karman Street and Hurricane (Horizontal Plane Vorticity)
A Von Karman street is a phenomenon that occurs when a fluid, such as air or water, flows past a solid object and creates a series of vortices in its wake. These vortices are named after the Hungarian-American physicist Theodore von Kármán, who first described the phenomenon in 1911. The Von Karman street is characterised by alternating vortices that form in a periodic pattern behind the object. The size and frequency of the vortices depend on the size, shape and speed of the object and the properties of the fluid. Von Karman vortices can occur over islands whose shape and size can be favourable to their appearance. Figure 2.8 shows a satellite view of one of these over the Juan Fernandez Islands.
A cyclone, including a hurricane (as shown in the figure 2.9), has a characteristic wind field surrounding a central eye. Near the eye, the winds are relatively calm, but as you move away from the centre, the winds increase in speed. This region of increasing winds is called the eyewall, and is where the strongest winds, heaviest rainfall, and most severe weather are found. Beyond the eyewall, there is another region of decreasing wind speed, known as the outer rain bands. The wind field in a cyclone is caused by the force of the pressure gradient, which pushes air from areas of higher pressure to areas of lower pressure. In addition, the rotation of the Earth and the difference in azimuthal speed causes the wind to deflect (Coriolis effect), resulting in the characteristic circular motion of the wind field.
Overall, planetary Von Karman tracks and hurricanes/cyclones are 2 atmospheric phenomena that can produce a wind field dominated by a horizontal plane shear component (strong horizontal plane vorticity), giving the wind the Jacobian

$$\nabla W_{H,VKS} = \begin{pmatrix} \frac{\partial W_x}{\partial x} & \frac{\partial W_x}{\partial y} & \frac{\partial W_x}{\partial z} \\ \frac{\partial W_y}{\partial x} & \frac{\partial W_y}{\partial y} & \frac{\partial W_y}{\partial z} \\ \frac{\partial W_z}{\partial x} & \frac{\partial W_z}{\partial y} & \frac{\partial W_z}{\partial z} \end{pmatrix} \tag{2.14}$$

As in the previous cases, this results in the specific power contribution of horizontal wind shear as follows

$$\begin{aligned} P_{xy} &= -V\cos\psi\cos\gamma\frac{\partial W_x}{\partial y}\left(V\sin\psi\cos\gamma + W_y\right) \\ \Pi_{xy} &= \frac{P_{xy}}{\frac{\partial W_x}{\partial y}V^2} \end{aligned} \tag{2.15}$$

Figures 2.10 (a) and (b) show the variation of Π_{xy}. As can be seen, the maximum power contribution occurs when the climb angle of the aircraft is zero, while the optimal heading angle solution varies with the lateral speed W_y. It is also interesting to note that the specific power potential is the same as for the PBL shown earlier in figures 2.5 (a) and (b).

Commercial aircraft wing-tip vortex and Kelvin Helmholtz instability (vertical plane vorticity)

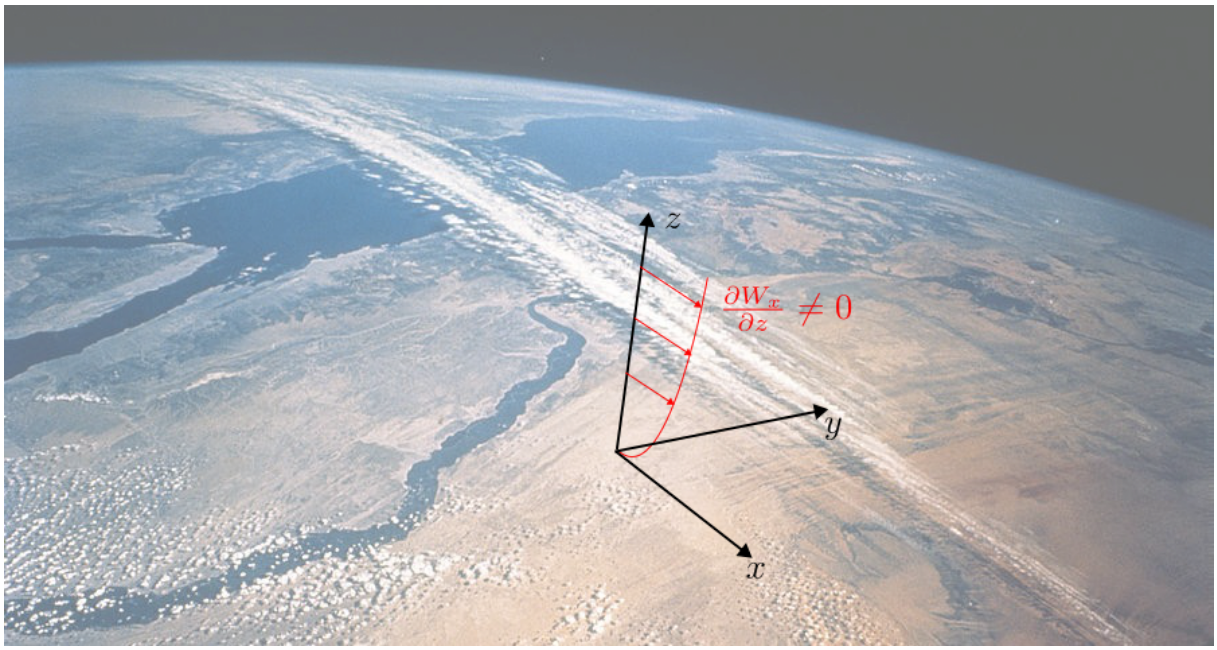

Figure 2.4: Jet stream horizontal wind shear vectorial field representation
Satellite view of the jet stream over Egypt
Original image source : Jet Stream

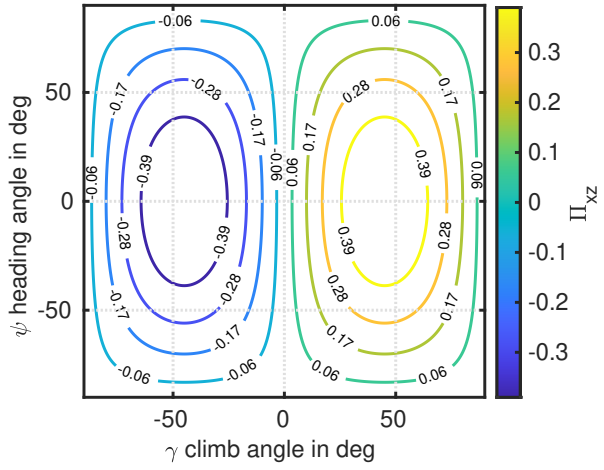

(a) Dimensionless specific power Π_{xz} due to $\frac{\partial W_x}{\partial z}$ function of heading γ and climb γ angle (computed for $W_z = 0$)

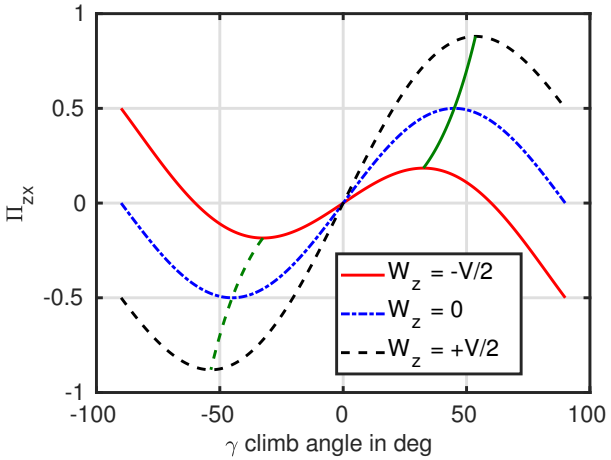

(b) Effect of W_z on the dimensionless specific power Π_{xz} due to $\frac{\partial W_x}{\partial z}$ (computed at $\phi = 0°$)

Figure 2.5: Dimensionless power Π_{xz} due to $\frac{\partial W_x}{\partial z}$

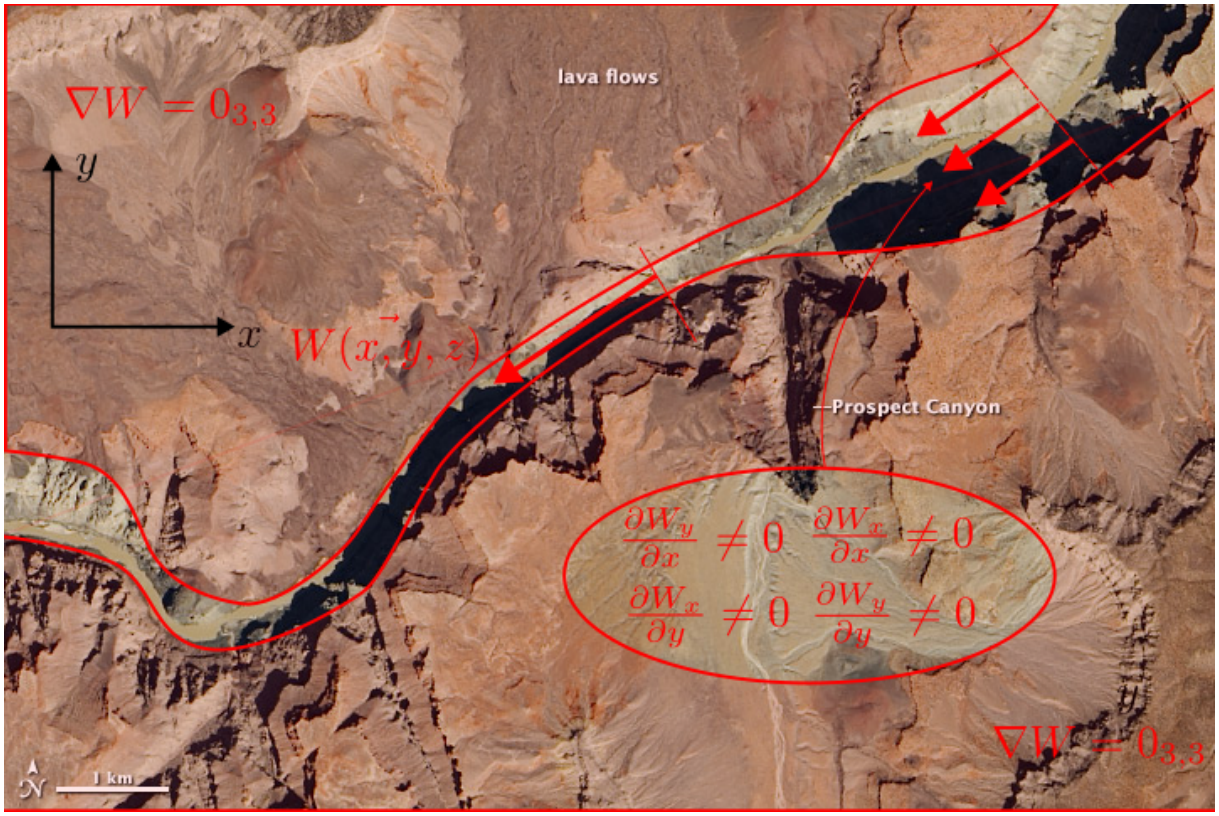

Figure 2.6: Horinzontal wind acceleration vector field representation
Satellite view of the contraction of the throat section of the Great Canyon, March 2013
Original image source : Cayon contraction

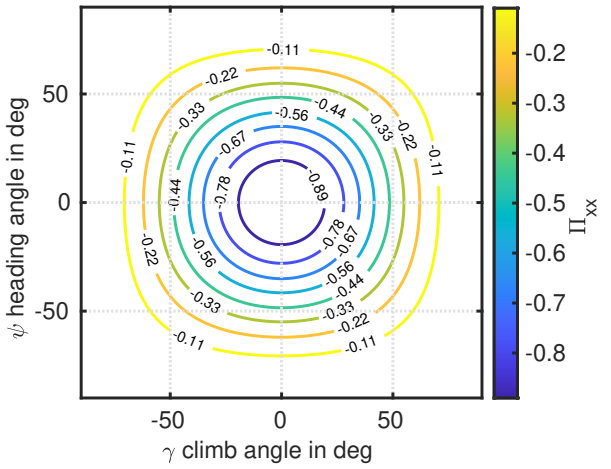

(a) Dimensionless specific power Π_{xx} due to $\frac{\partial W_x}{\partial x}$ function of heading γ and climb γ angle (computed for $W_x = 0$)

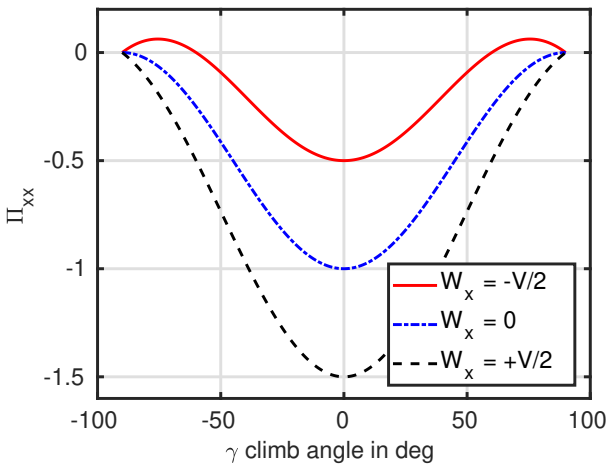

(b) Effect of W_x on the dimensionless specific power Π_{zz} due to $\frac{\partial W_z}{\partial z}$ (computed at $\gamma = 0°$)

Figure 2.7: Dimensionless power Π_{xx} due to $\frac{\partial W_x}{\partial x}$

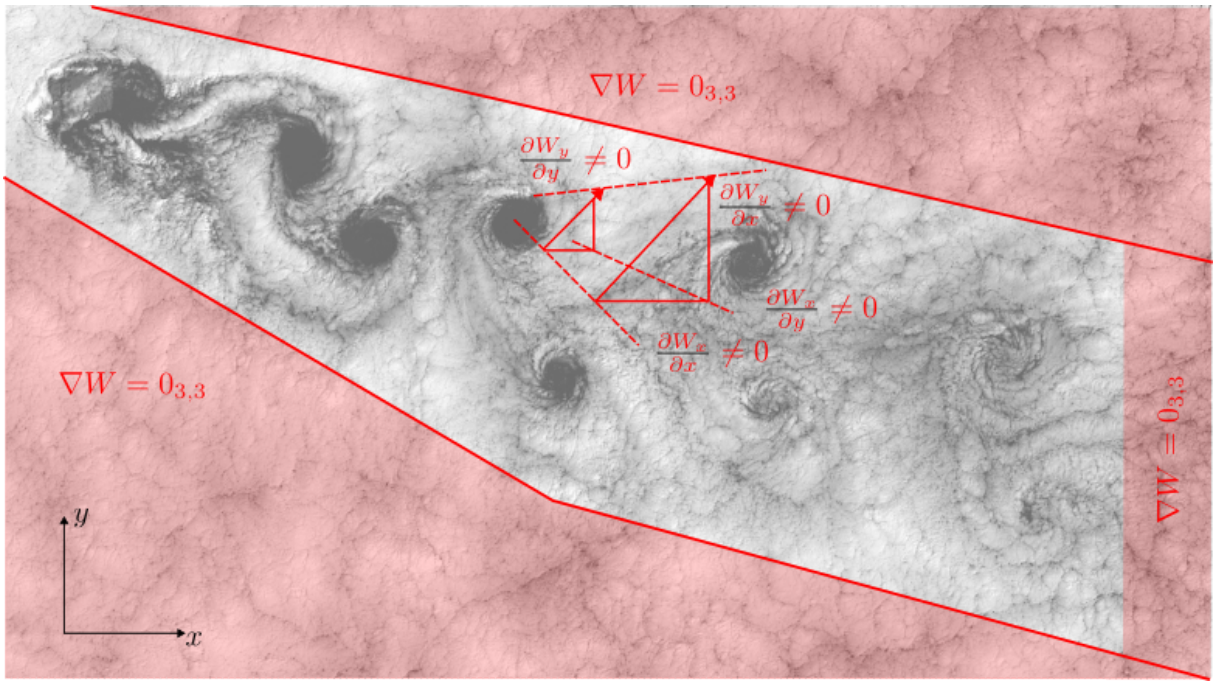

Figure 2.8: Planetary Von Karman street vector wind field representation
Landsat 7 image of clouds off the Chilean coast near the Juan Fernandez Islands, showing a Von Karman Street Pattern, September 1999
Original image source : Von Karman Street

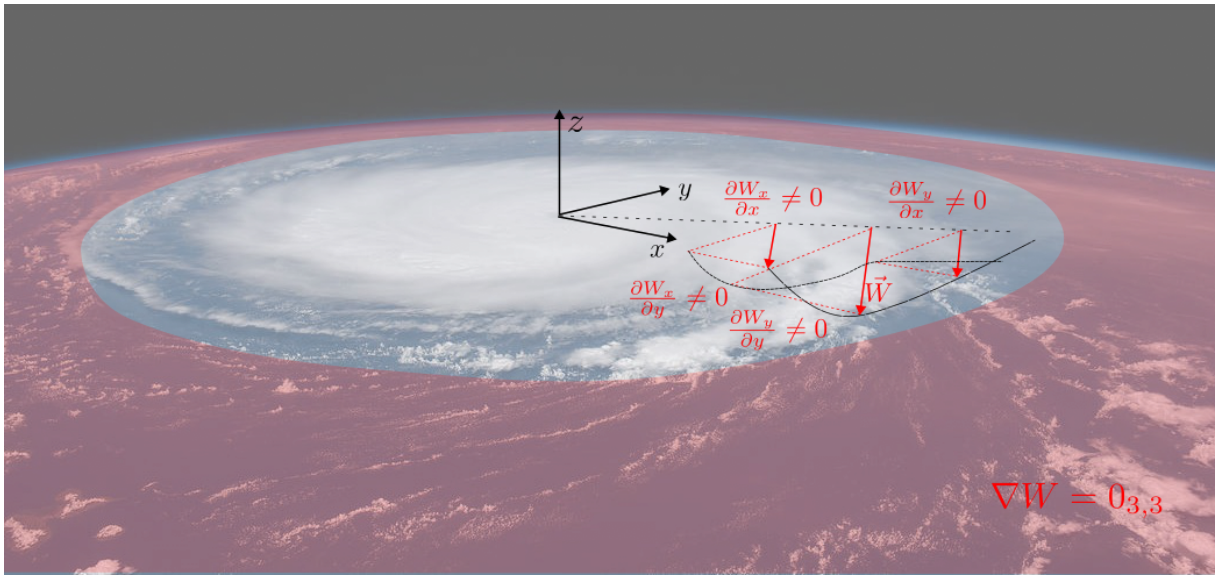

Figure 2.9: Hurricane vectorial wind field representation
Hurricane Sam churns in the Atlantic Ocean
Original image source : Hurricane

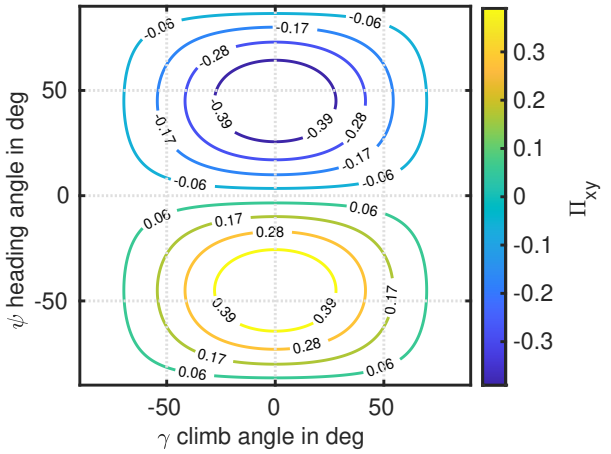

(a) Dimensionless specific power Π_{xy} due to $\frac{\partial W_x}{\partial y}$ function of heading ψ and climb γ angle (computed for $W_y = 0$)

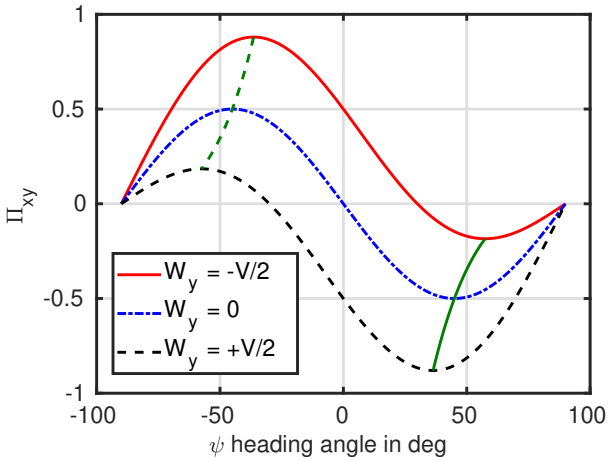

(b) Effect of W_y on the dimensionless specific power Π_{xy} due to $\frac{\partial W_x}{\partial y}$ (computed at $\gamma = 0°$)

Figure 2.10: Dimensionless power Π_{xy} due to $\frac{\partial W_x}{\partial y}$

Every flying aircraft generates wing-tip vortices. Because they all have finite wings, the pressure difference between the leeward and windward sections creates a tip vortex that lies in the vertical plane and is dissipated by the incoming flow. Tip vortices can persist in an area for a long time after the aircraft has entered it. Typically, the airport control tower imposes a 2 minute delay between each landing on a runway before a new landing is authorised. Figure 2.11 (a) shows an Airbus A340-642 landing where the weather conditions were favourable for visualising the tip vortices. Surprising as it may seem, it is possible to harvest energy from the wake of an airliner, as will be seen in the literature review section.

The Kelvin-Helmholtz instability in clouds is also a phenomenon that exhibits vertical plane vorticity. They usually occur in the planetary boundary layer at high altitudes and are caused by a faster stream of air moving above slower winds.

Thus, wingtip vortices and Kelvin-Helmholtz instability in cloud wind fields are strongly dominated by vertical and horizontal wind gradients, as summarised in the following wind Jacobian matrix

$$\nabla W_{WV} = \begin{pmatrix} \frac{\partial W_x}{\partial x} & \frac{\partial W_x}{\partial y} & \frac{\partial W_x}{\partial z} \\ \frac{\partial W_y}{\partial x} & \frac{\partial W_y}{\partial y} & \frac{\partial W_y}{\partial z} \\ \frac{\partial W_z}{\partial x} & \frac{\partial W_z}{\partial y} & \frac{\partial W_z}{\partial z} \end{pmatrix} \tag{2.16}$$

As the horizontal wind shear has already been discussed, only the vertical wind shear is presented in the following lines. The contribution of vertical wind shear to specific power is given by

$$\begin{aligned} P_{zx} &= -V\cos\psi\cos\gamma\frac{\partial W_z}{\partial x}\left(V\cos\psi\cos\gamma + W_x\right) \\ \Pi_{xy} &= \frac{P_{xy}}{\frac{\partial W_x}{\partial y}V^2} \end{aligned} \tag{2.17}$$

Figures 2.11 (a) and (b) show the energy harvesting potential in a vertical shear wind. Again, the optimum climb angle is a function of the horizontal wind. In summary, to harvest energy in positive wind shear, the aircraft must dive into it and otherwise climb. This conclusion is not consistent with figure 2.11 (a) and (b) simply because of the W_z sign convention, please refer to figure 2.1

Lee Waves and Thermals:

Two final atmospheric phenomena are introduced to discuss the final component of the wind Jacobian, the vertical wind acceleration. Thermals are spatially confined, and the vertical velocity is very strong near the ground where convection is important, and decreases slowly with altitude until the thermal disappears.

When air flows over a mountain, it is forced to rise and cool as it encounters the mountain's slope. As the air rises, it can cool to its dew point, causing water vapour to condense into clouds. When the air reaches the top of the mountain, it begins to descend on the leeward side. This descending air warms and dries, and its pressure increases as it moves towards the lower regions downstream. This rapid increase in pressure causes the air to oscillate, or wave, back and forth. These waves can travel downstream, sometimes hundreds of miles from the mountain range or island

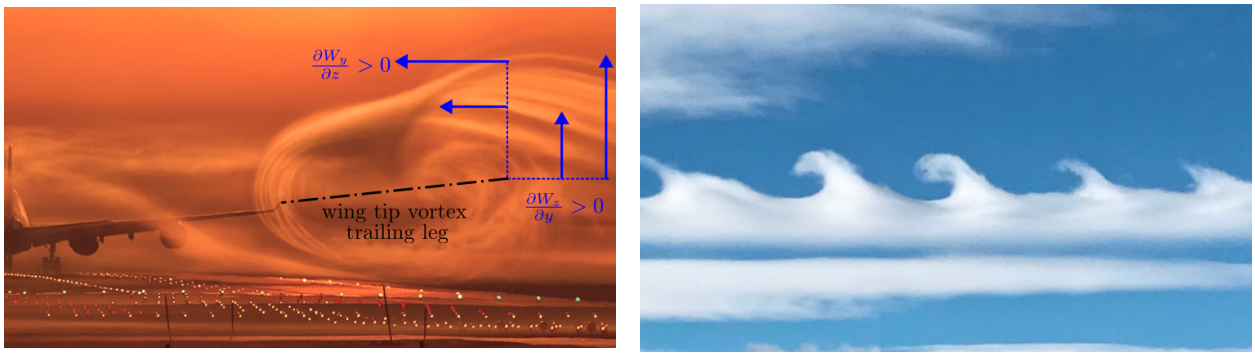

(a) (b)

Figure 2.11: Vertical plane vorticity
(a) Tip Vortices vectorial field représentation
Tip vortices detaching from the wings of an Airbus 340-642 while landing in Munich airport
Original image source : Tip Vortices
(b) Kelvin Helmholtz instability in clouds caused by a faster stream of air moving above slower winds (picture credit: Hannah Martin

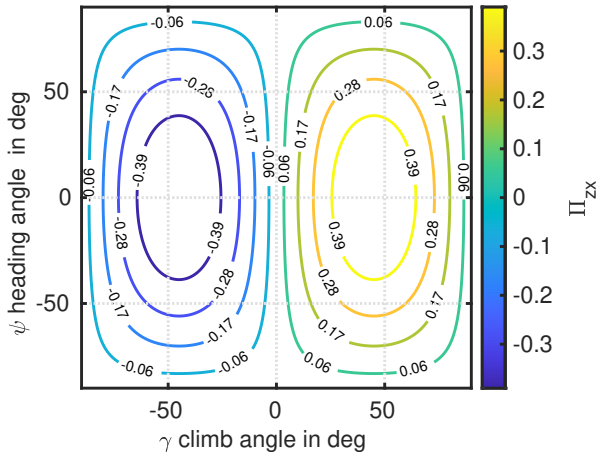

(a) Dimensionless specific power Π_{zx} due to $\frac{\partial W_z}{\partial x}$ function of heading ψ and climb γ angle (computed for $W_x = 0$)

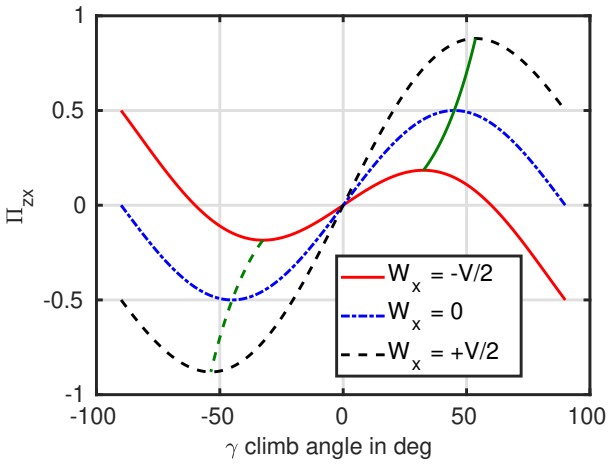

(b) Effect of W_x on the dimensionless specific power Π_{zx} due to $\frac{\partial W_z}{\partial z}$ (computed at $\gamma = 0°$)

Figure 2.12: Dimensionless power Π_{zx} due to $\frac{\partial W_z}{\partial x}$

that caused them. For example, figure 2.13 shows one of them over an island. These waves are called lee waves, and they can produce spectacular cloud formations, including lenticular clouds (see figure 2.13-b), which can be seen downwind of the mountain range. These lee waves are extremely dangerous for motorised aircraft, because if you are caught in a negative vertical speed zone, the thrust of the aircraft is usually not sufficient to prevent a descent, leading to a crash. However, they are used by glider pilots as the positive vertical speed can remain interesting even at high altitudes (10000m). In fact, the world altitude record has been broken many times using these phenomena. Jean-Mermoz, Henri Guillaumet and Antoine De St-Exupery are also said to have used them to cross the Pyrenees or the Andes (de Saint-Exupéry). However, Lee waves are mostly dominated by vertical and horizontal wind shear. Here, our interest is in the vertical speed acceleration, the blue component in the next Wind Jacobian.

$$\nabla W_{LW} = \begin{pmatrix} \frac{\partial W_x}{\partial x} & \frac{\partial W_x}{\partial y} & \frac{\partial W_x}{\partial z} \\ \frac{\partial W_y}{\partial x} & \frac{\partial W_y}{\partial y} & \frac{\partial W_y}{\partial z} \\ \frac{\partial W_z}{\partial x} & \frac{\partial W_z}{\partial y} & \frac{\partial W_z}{\partial z} \end{pmatrix} \tag{2.18}$$

Thus if only the vertical wind acceleration is considered, its contribution to the specific power is given as follows:

$$\begin{aligned} P_{zz} &= V \sin\gamma \frac{\partial W_z}{\partial z} \left(V \sin\gamma + W_z\right) \\ \Pi_{zz} &= \frac{P_{zz}}{\frac{\partial W_z}{\partial z} V^2} \end{aligned} \tag{2.19}$$

Figures 2.14(a) and (b) provide a stark conclusion, the potential energy gain with vertical wind acceleration is very limited. It is therefore recommended that static soaring should be preferred to the search for a dynamic trajectory. Consequently, static soaring techniques should only be used in Lee waves and thermals.

Summary of the literature on dynamic soaring:

As it has been introduced, dynamic soaring is a promising way to harvest energy from various atmospheric phenomena. This section proposes a brief literature review of dynamic soaring techniques. The most common work proposed focuses on horizontal wind shear, and in particular to harvest energy from the planetary boundary layer or the low speed profile of ridges (similar). Basically, all the works, initially bio-inspired by the flight of albatrosses near the South American coast, propose trajectory optimisation under constraints (maximum load factor, flying in the linear lift range, minimum and maximum altitude, flying above a maximum speed, etc). The numerical analysis of Liu et al., Gao et al., Cutler et al., Mears, Bonnin et al., Deittert et al., Bencatel et al. (2012a and 2012b) can be mentioned. The approach remains the same, a point mass or inertial simplified aircraft model is used to run an optimisation program for a given bounded wind shear profile. The aircraft and wind profiles vary, but they all show the feasibility of dynamic soaring on mini-UAVs. The latter work has been confirmed experimentally by Bronz et al. (2021a and 2021b). As shown by Lawrance and Bonnin et al., there are 4 main families of trajectories, the inclined ellipse and 3 open cycle trajectories, which allow to fly toward, backward and across the wind. On each elliptical cycle, the UAV gains kinematic energy, by repeating the process, the world record in speed was broken with a reported ground speed greater than 800km/h. At this speed, and in such a compressed trajectory, the drone faced a load factor of up to 100G, as reported by Richardson. Apart from this case, the "travelling" trajectories mentioned earlier imply a reasonable load factor of up to 2G to 6G. Also, Zikmund and Zikmund showed that it was possible for a fighter jet, or what they called a transonic glider, to "surf" into the wake of an airliner. As the latter conclusion is entirely numerical, it is considered exotic.

Dynamic soaring is possible in hurricanes, cyclones or planetary Von Karman streets, where an optimal trajectory can be established, as shown by Grenestedt et al.. However, according to the author, the existence of a solution depends on the nature and intensity of the atmospheric phenomena mentioned. Due to the high level of turbulence in a hurricane, no experimental evaluation has yet been proposed.

Grenestedt and Spletzer has shown numerically that it is possible to perform perpetual flight in shear layers of the jet stream.

Finally, Long et al. suggested using dynamic soaring to recharge the UAV's battery using the propeller in windmill mode. Thus the kinematic energy gain in a dynamic cycle is transformed into electric energy.

Summary of the numerical requirements for the analysis of dynamic soaring:

Overall, dynamic soaring shows a real interest and the planetary boundary layer or low speed ridge profiles seem to be the most promising atmospheric phenomena. We have also seen that there are low and high G manoeuvres. It is reasonable to assume that flexible UAVs are automatically disqualified for the high-G trajectory. All in all, the topic of dynamic soaring can be summarised as a multi-objective optimal path planning problem. Therefore, in order to assess the performance improvement of flexibility in this type of strategy, a numerical framework is needed. The latter must be able to model the above atmospheric phenomena and flexible aircraft. Time marching simulations need to be performed

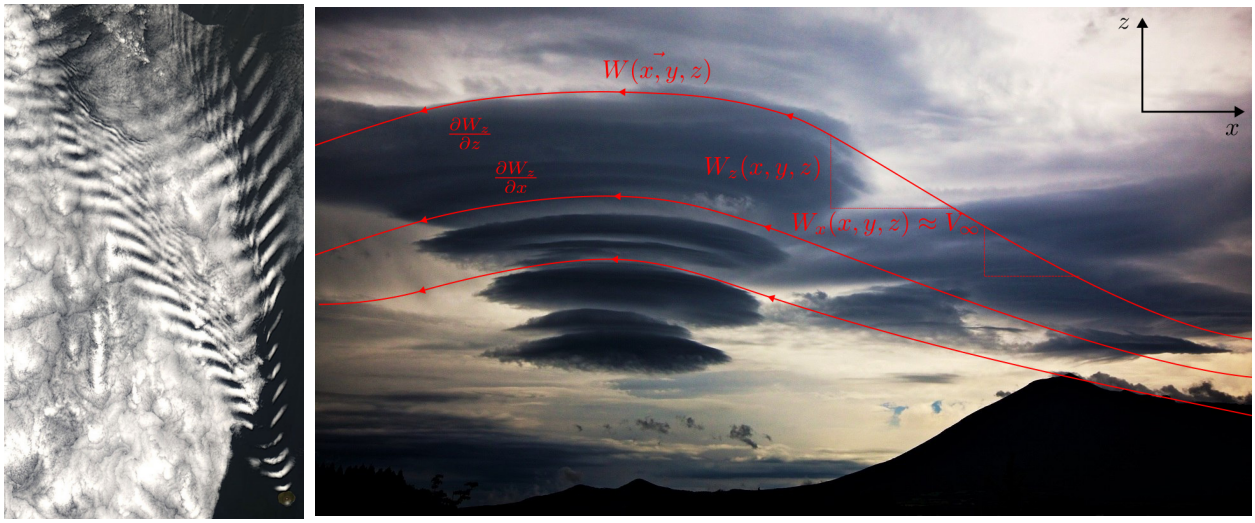

(a) (b)

Figure 2.13: Lee waves
(a) Lee waves vectorial wind speed field representation
Lee Waves lenticular clouds near Amsterdam island in the far southern Indian Ocean, December 2005
Original image source : Kelvin Lee wave
(b) Lee waves vectorial wind speed field representation
Lenticular clouds due to the lee waves over Iwate Mount, Japan
Original image source : Lenticular clouds

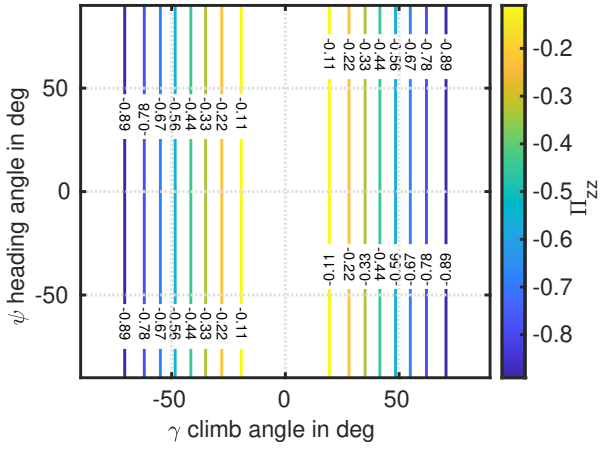

(a) Dimensionless specific power Π_{zz} due to $\frac{\partial W_z}{\partial z}$ function of heading ψ and climb γ angle (computed for $W_z = 0$)

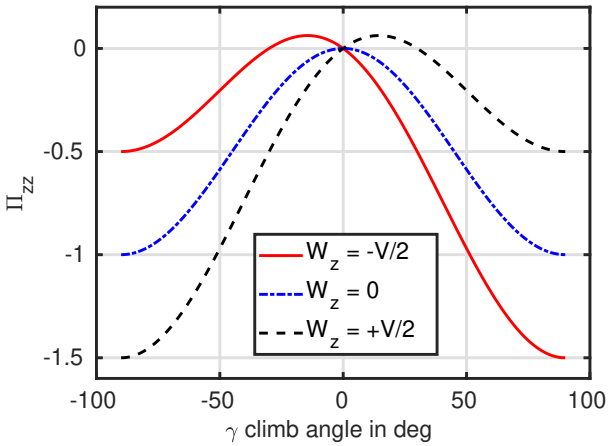

(b) Effect of W_z on the dimensionless specific power Π_{zz} due to $\frac{\partial W_z}{\partial z}$ (computed at $\psi = 0°$)

Figure 2.14: Dimensionless power Π_{xy} due to $\frac{\partial W_z}{\partial z}$

relatively quickly in order to converge to an optimal trajectory. The framework must also be able to provide the aeroelastic divergence speed, as this will define a constraint for the various optimisation algorithms. Finally, it must provide a control toolbox to implement an autopilot capable of following the computed trajectories.

2.5 gust/turbulence soaring

In this section the last interesting energy harvesting strategy is presented. Gust/turbulence soaring differs from static and dynamic soaring in that it involves temporally and spatially varying phenomena. The gust/turbulence soaring strategy deeply involves unsteady aerodynamic flow. To illustrate the main idea, take a look at figures 2.15 (a) and (b). For the sake of simplicity, only one wing is considered here. Now consider a plunging airfoil with no incidence, equivalent to an airfoil facing a vertical gust or turbulence. The plunging motion is assumed to be sinusoidal for simplicity.Figure 2.15 shows the different phases of the dive. Depending on whether the airfoil is plunging up or down, the air relative velocity vector is tilted in the opposite direction. The lift orthogonal to the air speed vector can be generated positively or negatively. The aerodynamic load resultant R_a, when projected onto the horizontal axis ($R_{a,x}$), shows a propulsive component. This problem has recently been treated experimentally by Floryan et al. (2017 and 2018) where optimal heave amplitude and frequency were provided. In the same paper, the author performed the same analysis for pitching only. Then he provided a coupled analysis where pitching and heaving are simultaneous (Van Buren et al., 2019). In particular, he showed that there are optimal amplitude-frequency and phase delays. Finally, he provided a large amplitude analysis to constrain the numerical simulation comparison he performed in the aforementioned papers Floryan et al.. This work was done to find the optimal parameters for dolphin kicks, so that professional swimmers could improve their dives in competition. In the water, however, your buoyancy is sufficient to keep you from drowning, so there is no need to generate a vertical hydrodynamic component $R_{a,z}$. In the case of a UAV, lift must be generated, so the situation shown in figure 2.15 (a) no longer applies. However, the problem remains the same, except that the airfoil will have a propulsive component only in the half of the dive period (see figure 2.15-b). Assuming that the heave amplitude is not controlled (exogenous input: gust), an optimal pitch amplitude and lag can be found to maximise drag reduction as demonstrated by Gavrilovic et al. (2017). After that, an optimal controller can be designed to actively harvest energy from a sinusoidal gust as done in Gavrilovic-2018. The experimental tests were performed on UAV in Australia and presented by Gavrilovic et al. in 2018 with a completion in 2020. The experiments showed promising results. The last paragraph is dedicated to a special case of thermal soaring. As we saw at the beginning of the chapter, gliders, because of their manoeuvrability, sometimes cannot stay in a thermal. However, they can fly through them in a straight line. Depending on the size of the thermal and the speed of the glider, the latter can be considered as a gust and the previous explanation applies. This particular case will be of interest in this thesis.

Numerical needs to treat gust soaring strategies: In the light of the previous lines, the numerical features needed to assess whether the flexibility of an aircraft can bring performances in gust soaring are summarised. The framework must be able to capture the unsteady aerodynamics correctly, also gusts, turbulence and small thermals must be implemented. Finally, it must be possible to perform time marching calculations with an attractive computational time in order to investigate the widest possible range of structural parameters.

2.6 Methodology

The 3 different energy harvesting strategies have been presented. Regardless of the one considered in this thesis, it is not yet known if the flexibility of an aircraft can bring better performances than a rigid one. Assuming that it does, that is, the analysis has converged on an optimal set of structural parameters that ensure better performances in a given energy harvesting strategy. Can we conclude yet? The answer is obviously no, because the optimal set of parameters must be studied on the UAV flight mission. In fact, the energy harvesting strategies must be considered as a bonus. A small part of the flight time is dedicated to them. Therefore, it does not make sense to design and optimise a UAV for energy harvesting strategies without considering their impact on the flight mission. An example is proposed to illustrate this point.
Let η_T be the amount of flight time devoted to energy harvesting strategies. Let $\mathcal{P}^R_{EH}$ be the average specific power harvested during the strategy on the rigid aircraft. Let $\mathcal{P}^R_S$ be the average power consumed by the aircraft to complete its mission flight (level flight or steady turn level flight). The total energy of the rigid aircraft during the flight time T can be written as follows

$$\mathcal{E}^{\mathcal{R}} = (1-\eta_T)\mathcal{P}^R_S T - \eta_T \mathcal{P}^R_{EH} T \qquad (2.20)$$

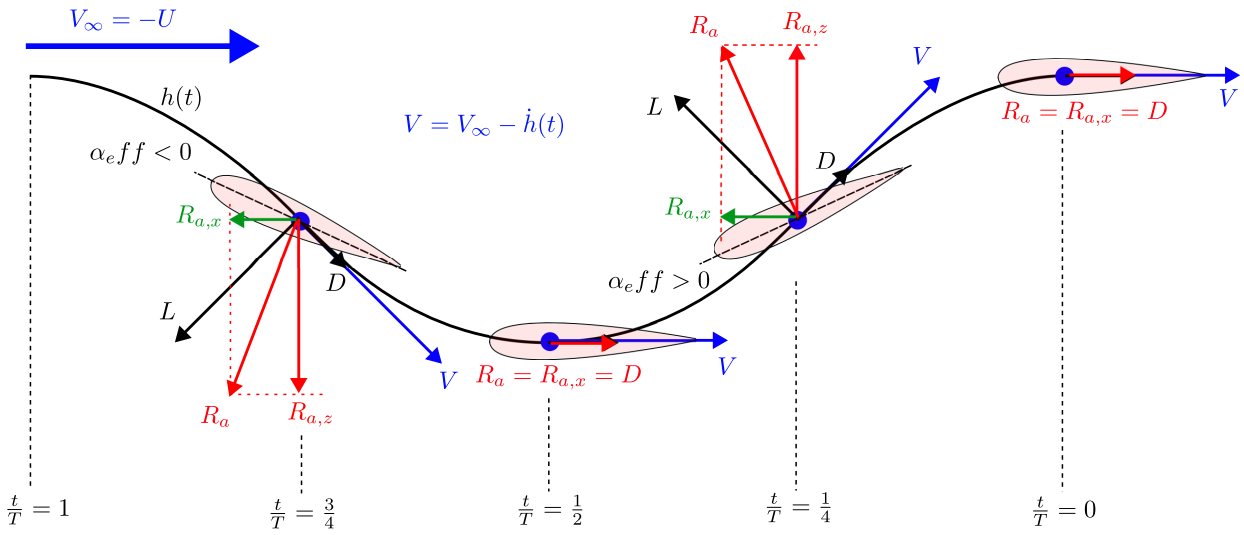

(a) Propulsive airfoil ($\bar{C_L} = 0$)

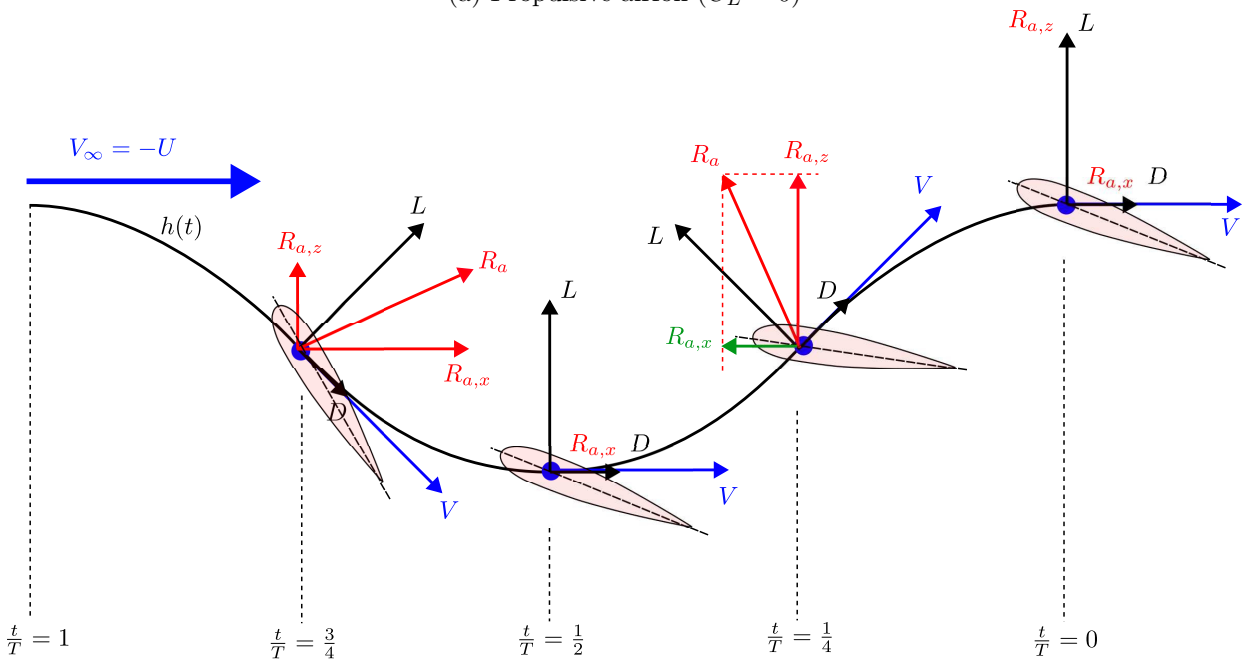

(b) Drag reduction airfoil ($\bar{C_L} > 0$)

Figure 2.15: Plunging airfoil vs drag reduction

Dividing the above expression by T gives the mean specific power of the rigid aircraft

$$\mathcal{P}^{\mathcal{R}} = (1-\eta_T)\mathcal{P}_S^R - \eta_T \mathcal{P}_{EH}^R \tag{2.21}$$

Following the same way the mean specific power of the flexible aircraft is given as:

$$\mathcal{P}^{\mathcal{F}} = (1-\eta_T)\eta_S^F \mathcal{P}_S^R - \eta_T \eta_{EH}^F \mathcal{P}_{EH}^R \tag{2.22}$$

where η_S^F has been introduced as the mission performance degradation or improvement factor. If greater than 1, the flexible aircraft will require more power to maintain the same flight state. Similarly, η_{EH}^F has been introduced as the energy harvesting performance improvement factor. If greater than 1, the flexible aircraft will harvest more energy than the rigid one. Let us now consider the RC glider (SXBC) mentioned at the beginning of this chapter. Its specific power in mission flight is assumed to be $\mathcal{P}_S^R = 10\ W/kg$ and its average specific power harvested in the thermal presented earlier is $\mathcal{P}_{EH}^R = 10 W/kg$. From now on, let us imagine that some analysis has shown that if the glider is flexible, its mean specific power harvested is now $\mathcal{P}_{EH}^R = 11 W/kg$, so $\eta_{EH}^F = 1.1$ (10 % improvement). From now on, the question to be asked is, if the flexible aircraft degrades the flight mission performance, how much time do we need to devote to the energy harvesting strategy η_T in order to equal the rigid aircraft's total mean specific power? In other words, for a given η_T, what is the minimum degradation factor that is acceptable in order not to be less performant than the rigid aircraft? The figure 2.16 shows the time required to achieve the same performance as the rigid aircraft for different energy harvesting improvement factors. As shown, the problem is very sensitive

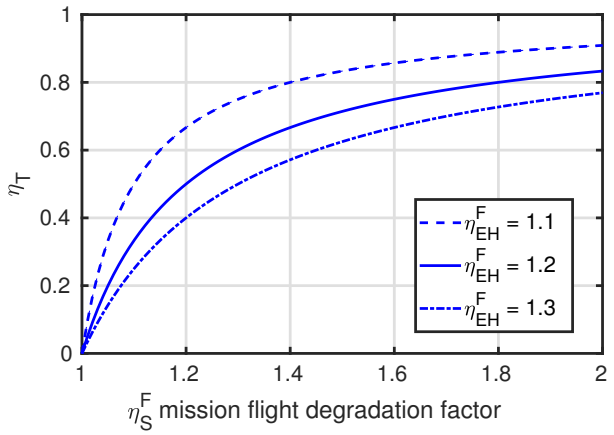

Figure 2.16: The need of studying the mission flight condition

to mission performance degradation. Thus, there is an important need to have a numerical framework capable of predicting the impact of flexibility on the flight performance of an aircraft mission. Typically, UAVs have 2 main flight mission conditions, which are steady level flight and steady level turn for target monitoring and tracking. These are 2 steady configurations from a flight mechanics perspective. Therefore, the numerical framework must be able to trim a UAV for a given flight condition. Ideally, if the software can directly provide the propeller shaft power instead of the trimmed thrust, this would save a lot of time for the user and avoid offline post-analysis on a dedicated propeller model. Finally, it is very important to note that the analysis of the flight mission performance is the second step of the complete analysis. If there is no benefit to flexibility from the outset, it can be omitted. However, we felt that having a numerical tool that meets all the above requirements was a safe approach.

2.7 Numerical framework: ASWING

In the light of the previous sections, there is a need for a numerical framework that proposes different functions. ASWING(Drela 1999) has been chosen as it offers all the functions previously presented and more. Also, since it is written in FORTRAN, the code is expected to be very efficient, which makes it even more attractive. Other solutions have been proposed in the literature. The table 2.2 suggests a comparison between the available functions of each. Note that only the most cited solutions are compared. Among them is Openaerostruct, developed at the University of Michigan (Jasa et al. 2018, Chauhan and Martins 2019), FNSA (Fast Nonlinear Static Aeroelasticity) developed at Airbus and ISAE-SUPAERO (Chandre Vila et al. Chandre Vila et al.-2022-2023) and finally a no-name framework developed at Delft University (Werter and De Breuker 2016). The latter have been compared with each other as they are derived from very close theories, namely potential methods extended with viscous loops for aerodynamics and Euler-Bernoulli/Timoshenko beam theory for structural modelling. They are also considered to be the best candidates for use in optimisation work due to their very close low computational time cost. From the table 2.2 ASWING offers more features than its modern alternatives, thus widening its range of applications. Its main disadvantage is that it is not coupled to the OPENMDAO planform. However, it is in early development at ISAE-SUPAERO. The second major drawback is that ASWING is licensed, but free for academic use. The software is provided in a non-compiled version so that the user can modify it if necessary. As the code cannot be published, ASWING lacks the consequences of an open source community. The con-

clusion is quite clear, ASWING [1] proposes much more features and so its choice for this thesis work. Now, ASWING does have some drawbacks that need to be mentioned. In fact Before using it, a literature review was carried out on the use of ASWING in the literature. This work was carried out in 2020 and a total of 196 references were cited Drela, while 220 were cited in 2023. As the reader can imagine, the 200 papers were not read in full. Instead, a quick literature search was carried out using carefully chosen keywords. The main aim was to find papers that mentioned the use or evaluation of ASWING against experimental or higher fidelity data. Figure 2.17 shows the citation history of ASWING until 2020, where 3 categories have been created: cited as an existing tool (blue), used as a pre-design or analysis tool (yellow) and evaluated or benchmarked (orange). From the results, only 30 papers mention the use of ASWING, while only 6 present evaluations González et al., Warwick et al., Jones, Colas et al., Love et al., Variyar et al.. Looking at the latter, only 2 aeroelasticity characteristics were evaluated, the flutter speed prediction and the response to a gust. Furthermore, the geometries studied in these papers (high aspect ratio) were not really stressful for the theoretical model. This lack of evaluation has probably led to the limited use of ASWING, despite the many interesting features it proposes. Consequently, there is a need to evaluate ASWING on the basis of experimental data.
When considering ASWING in the case of this thesis, only a few features need to be evaluated, but I thought that the community could benefit from evaluating all the features. Consequently, the next 4 chapters are dedicated to the experimental evaluation and modification of ASWING using experimental data and model gathered from the literature. The evaluation work has been divided into 4 parts, first the pure aerodynamic model is evaluated and modified, then the one of the propeller and structure. In the fourth part, all 3 models are combined and evaluated together. In this way it was easier to find experimental data and also to better isolate what could cause problems in each model in order to implement appropriate modifications.

2.8 Conclusions

In this chapter the 3 main energy harvesting strategies have been introduced. Their study in the case of flexible aircraft or UAV poses different numerical needs, which are summarised here.

- ***Static Soaring:*** In order to correctly assess the issues arising from the thesis in the static soaring strategy, a numerical framework with the following characteristics must be used. First, it must be able to model flexible UAVs or aircraft. Then it must be able to correctly predict their performances and the effect of the structure on them. Speed polars, torsional divergence and flutter speed must be calculable. Linear stability and controllability as well as aileron/flap effectiveness analysis must be considered. Finally, for all of the above requirements, the predictions must be qualitative, as must the computational time required to investigate a wide range of stiffness parameters.
- ***Dynamic Soaring:*** All in all, this topic can be summarised as a multi-objective optimal path planning problem. Therefore, in order to assess the performance improvement of flexibility in this type of strategy, a numerical framework is needed. The latter must be able to model the mentionned atmospheric phenomena and the flight dynamics of flexible aircraft. Time marching simulations must be performed relatively quickly in order to converge to an optimal trajectory. The framework must also be able to provide the aeroelastic divergence speed, as this will define a constraint for the various optimisation algorithms. Finally, it must provide a control toolbox to implement an autopilot capable of following the computed trajectories. We will see in the next chapters that even the most efficient aeroelastic framework is too slow to solve the optimal trajectory problem. A methodology is proposed to overcome this problem.
- ***Gust Soaring:*** The framework must be able to correctly capture unsteady aerodynamics, including gusts, turbulence and small thermals modelling. Finally, it must be possible to perform time marching computations with an attractive computational time in order to investigate the largest range of structural parameters as possible.
- ***Common analysis methodology:*** The numerical framework must be able to predict the effect of flexibility on the flight performance of an aircraft mission. Typically, UAVs have 2 main flight mission conditions, which are steady level flight and steady level turn for target surveillance. These are 2 stable configurations from a flight mechanics point of view. Therefore, the numerical framework must be able to trim a UAV for a given flight condition. Ideally, if the software could

[1] We would like to mention Sharpy from Emperial College as a new open solution, proposing various features. However, it seems that there are less than those of ASWING. We also discover this tool in the last year of the PhD programme. As it is based on Open Source solution, it could be a serious competitor in the future and we will look forward to further litterature review of its use and evaluation.

Table 2.2: ASWING features comparison with modern most citeauthord aeroelastic framework (A,S,AE,O) : Aerodynamic, Structure, Aeroelastic and Other features

		ASWING	Openaerostruct	FNSA	Delft
	Reference papers	[14], [15]	[29], [7]	[6] [5]	[41]
A	Non linear planform	✓	✓	✓	✓
	3D Aerodynamic	✓	✓	✓	✓
	Steady wake interaction	✓	NC	✗	NC
	Propeller jet/wing interaction	✓	✗	✗	✗
	Fuselage modeling Volume effect	✓	✗	✓	✗
	Unsteady aerodynamic	✓	✗	✗ : QS	✓
	Drag predictions	✓	✓	✓	✗
	Flap/Ailerons effects	✓	✗	✗	✗
	Steady-stall	✓	✗	✓	✗
S	Non-linear delfection	✓	✗	✗	✓
	6-DOF	✓	✓	✓	✓
	Structural damping (unsteady)	✓	✗	✗	✗
	Tension/elastic axis decoupling	✓	✗	✗	✓
	Ponctual and concentrated mass effect	✓	✗	✗	✓
	Wing box	✓ with [8]	✓	✗	✓
AE	Steady deflection	✓	✓	✓	✓
	Gust response	✓	✗	✓	✓
	Torsional divergence	✓	✓	✓	✓
	Structure failure	✓	✓	✗	✓
	Ailerons reversal	✓	✗	✗	✗
	Flutter analysis	✓	✗	✗	✓
	Whirl flutter analysis	✓	✗	✗	✗
	Limit cycle oscillations	✓	✗	✗	✗
O	Embeded control toolbox	✓ [28]	✗	✗	✗
	Open MDAO coupling	✗ In progress	✓	✗ In progress	✗
	Opensource	✓	✓	✗ Airbus	✓

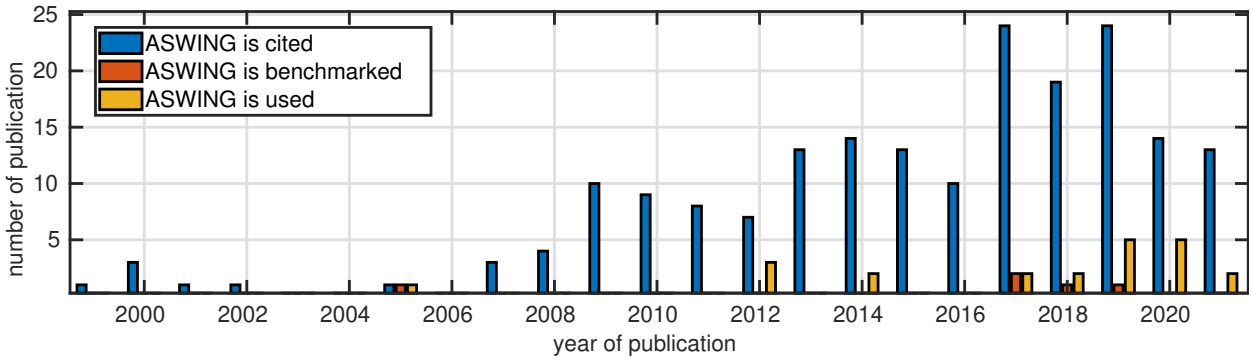

Figure 2.17: ASWING citation history, blue bars : mentioned as an existing tool; yellow : used as a tool ; orange : used and validated against experimental or higher fidelity CFD data

directly provide the propeller shaft power instead of the trimmed thrust, this would save the user a lot of time by avoiding offline post-analysis on a dedicated propeller model.

ASWING was chosen due to the large number of functions required. It offers all the functions needed to correctly assess the subject and more. Compared to other solutions found in the literature, ASWING remains the best choice. However, after a literature review of its use, the need for an experimental evaluation became apparent. The latter is essential to ensure that the conclusions drawn from the energy harvesting analysis are based on accurate predictions. Experimental evaluations and modifications of ASWING are therefore presented in the next 4 chapters. It should be noted that more features have been evaluated than needed for this thesis.

Bibliography

[1] Bencatel, R., Kabamba, P., and Girard, A. (2014). Perpetual dynamic soaring in linear wind shear. *Journal of Guidance, Control, and Dynamics*, 37(5):1712–1716. 52

[2] Bonnin, V., Bénard, E., Moschetta, J.-M., and Toomer, C. (2015). Energy-harvesting mechanisms for uav flight by dynamic soaring. *International Journal of Micro Air Vehicles*, 7(3):213–229. 52

[3] Bronz, M., Gavrilovic, N., Drouin, A., Hattenberger, G., and Moschetta, J.-M. (2021a). Flight testing of dynamic soaring part-1: Leeward inclined circle trajectory. In *AIAA Scitech 2021 Forum*, page 1527. 52

[4] Bronz, M., Gavrilovic, N., Drouin, A., Hattenberger, G., and Moschetta, J.-M. (2021b). Flight testing of dynamic soaring part-2: open-field inclined circle trajectory. In *AIAA AVIATION 2021 FORUM*, page 2803. 52

[5] Chandre-Vila, O., Boin, J.-P., Barriety, B., Nivet, Y., Morlier, J., and Gourdain, N. (2023). Fast Nonlinear Static Aeroelasticity Method for High-Aspect-Ratio Wings at Different Mach Regimes. *Journal of Aircraft*, pages 1–21. 56, 58

[6] Chandre Vila, O., Nivet, Y., Morlier, J., and Gourdain, N. (2022). Fast Method For Dynamic Fluid-Structure Interactions Considering Unsteady Aerodynamics. In *AIAA SCITECH 2022 Forum*, San Diego, CA & Virtual. American Institute of Aeronautics and Astronautics. 56, 58

[7] Chauhan, S. S. and Martins, J. R. R. A. (2019). Low-Fidelity Aerostructural Optimization of Aircraft Wings with a Simplified Wingbox Model Using OpenAeroStruct. In Rodrigues, H., Herskovits, J., Mota Soares, C., Araújo, A., Guedes, J., Folgado, J., Moleiro, F., and Madeira, J. F. A., editors, *EngOpt 2018 Proceedings of the 6th International Conference on Engineering Optimization*, pages 418–431. Springer International Publishing, Cham. 56, 58

[8] Colas, D., Roberts, N. H., and Suryakumar, V. S. (2018a). HALE Multidisciplinary Design Optimization Part I: Solar-Powered Single and Multiple-Boom Aircraft. In *2018 Aviation Technology, Integration, and Operations Conference*, Atlanta, Georgia. American Institute of Aeronautics and Astronautics. 58

[9] Colas, D., Roberts, N. H., and Suryakumar, V. S. (2018b). HALE Multidisciplinary Design Optimization Part I: Solar-Powered Single and Multiple-Boom Aircraft. In *2018 Aviation Technology, Integration, and Operations Conference*, Atlanta, Georgia. American Institute of Aeronautics and Astronautics. 57

[10] Cutler, M., McLain, T., Beard, R., and Capozzi, B. (2010). Energy harvesting and mission effectiveness for small unmanned aircraft. In *AIAA guidance, navigation, and control conference*, page 8037. 52

[11] de Saint-Exupéry, A. (2020). *Vol de nuit*. epubli. 52

[12] Deittert, M., Richards, A., Toomer, C. A., and Pipe, A. (2009). Engineless unmanned aerial vehicle propulsion by dynamic soaring. *Journal of guidance, control, and dynamics*, 32(5):1446–1457. 52

[13] Drela, M. (1999). Integrated simulation model for preliminary aerodynamic, structural, and control-law design of aircraft. In *40th Structures, structural dynamics, and materials conference and exhibit*, page 1394. 56, 57

[14] Drela, M. (2008). ASWING 5.81 Technical Description — Unsteady Extension. page 42. 58

[15] Drela, M. (2009). ASWING 5.86 Technical Description — Steady Formulation. page 57. 58

[16] Floryan, D., Van Buren, T., Rowley, C. W., and Smits, A. J. (2017). Scaling the propulsive performance of heaving and pitching foils. *Journal of Fluid Mechanics*, 822:386–397. 54

[17] Floryan, D., Van Buren, T., and Smits, A. J. (2018). Efficient cruising for swimming and flying animals is dictated by fluid drag. *Proceedings of the National Academy of Sciences*, 115(32):8116–8118. 54

[18] Floryan, D., Van Buren, T., and Smits, A. J. (2019). Large-amplitude oscillations of foils for efficient propulsion. *Physical Review Fluids*, 4(9):093102. 54

[19] Gao, X.-Z., Hou, Z.-X., Guo, Z., and Chen, X.-Q. (2015). Energy extraction from wind shear: reviews of dynamic soaring. *Proceedings of the Institution of Mechanical Engineers, Part G: Journal of Aerospace Engineering*, 229(12):2336–2348. 52

[20] Gavrilovic, N. (2018). *Endurance improvement of mini UAVs through energy harvesting from atmospheric gusts*. PhD thesis, Toulouse, ISAE. 42, 54

[21] Gavrilovic, N., Bénard, E., Pastor, P., and Moschetta, J.-M. (2017). Performance improvement of small uavs through energy-harvesting within atmospheric gusts. In *AIAA Atmospheric Flight Mechanics Conference*, page 1630. 54

[22] Gavrilovic, N., Benard, E., Pastor, P., and Moschetta, J.-M. (2018). Performance improvement of small unmanned aerial vehicles through gust energy harvesting. *Journal of Aircraft*, 55(2):741–754. 54

[23] Gavrilović, N., Bronz, M., and Moschetta, J.-M. (2020). Bioinspired energy harvesting from atmospheric phenomena for small unmanned aerial vehicles. *Journal of Guidance, Control, and Dynamics*, 43(4):685–699. 54

[24] González, O., Boschetti, P., Cárdenas, E., and Amerio, A. (2010). Static-Stability Analysis of an Unmanned Airplane as a Flexible-Body. In *AIAA Atmospheric Flight Mechanics Conference*, Toronto, Ontario, Canada. American Institute of Aeronautics and Astronautics. 57

[25] Grenestedt, J., Montella, C., and Spletzer, J. (2012). Dynamic soaring in hurricanes. *Proceedings of the ICUAS*, 12. 52

[26] Grenestedt, J. and Spletzer, J. (2010). Optimal energy extraction during dynamic jet stream soaring. In *AIAA Guidance, navigation, and control conference*, page 8036. 52

[27] Hanna, S. R. (1969). The thickness of the planetary boundary layer. *Atmospheric Environment (1967)*, 3(5):519–536. 45

[28] Jan, R., Condomines, J.-P., and Moschetta, J.-M. (2021). Fast simulation model for control law design andbenchmark of high aspect ratio flexible UAVs. 58

[29] Jasa, J. P., Hwang, J. T., and Martins, J. R. R. A. (2018). Open-source coupled aerostructural optimization using Python. *Structural and Multidisciplinary Optimization*, 57(4):1815–1827. 56, 58

[30] Jones, J. R. (2017). Development of a Very Flexible Testbed Aircraft for the Validation of Nonlinear Aeroelastic Codes. 57

[31] Lawrance, N. R. (2011). *Autonomous soaring flight for unmanned aerial vehicles*. PhD thesis. 42, 43, 46, 52

[32] Liu, D.-N., Hou, Z.-X., Guo, Z., Yang, X.-X., and Gao, X.-Z. (2017). Bio-inspired energy-harvesting mechanisms and patterns of dynamic soaring. *Bioinspiration & biomimetics*, 12(1):016014. 52

[33] Long, N., Watkins, S., Moschetta, J.-M., and Bonnin, V. (2019). Regenerative dynamic soaring trajectory augmentation over flat terrains. In *AIAA Scitech 2019 Forum*, page 0569. 52

[34] Love, M., Zink, P., Wieselmann, P., and Youngren, H. (2005). Body Freedom Flutter of High Aspect Ratio Flying Wings. In *46th AIAA/ASME/ASCE/AHS/ASC Structures, Structural Dynamics and Materials Conference*, Austin, Texas. American Institute of Aeronautics and Astronautics. 57

[35] Mears, M. (2012). Energy harvesting for unmanned air vehicle systems using dynamic soaring. In *50th AIAA Aerospace Sciences Meeting Including the New Horizons Forum and Aerospace Exposition*, page 851. 52

[36] Richardson, P. L. (2012a). High-speed dynamic soaring. *R/C Soaring Digest*, 29(4):36–49. 52

[37] Richardson, P. L. (2012b). High-speed robotic albatross: Unmanned aerial vehicle powered by dynamic soaring. *R/C Soaring Digest*, 29(6):4–18. 52

[38] Van Buren, T., Floryan, D., and Smits, A. J. (2019). Scaling and performance of simultaneously heaving and pitching foils. *AIAA Journal*, 57(9):3666–3677. 54

[39] Variyar, A., Economon, T. D., and Alonso, J. J. (2017). Design and Optimization of Unconventional Aircraft Configurations with Aeroelastic Constraints. In *55th AIAA Aerospace Sciences Meeting*, Grapevine, Texas. American Institute of Aeronautics and Astronautics. 57

[40] Warwick, S., Bras, M., Richards, J., and Suleman, A. (2019). Measurement of Aeroelastic Wing Deflections Using Modal Shapes and Strain Pattern Analysis. In *AIAA Scitech 2019 Forum*, San Diego, California. American Institute of Aeronautics and Astronautics. 57

[41] Werter, N. and De Breuker, R. (2016). A novel dynamic aeroelastic framework for aeroelastic tailoring and structural optimisation. *Composite Structures*, 158:369–386. 56, 58

[42] Zikmund, P. (2015). Wake vortex gliding. In *6th EUCASS Conference, Krakow*. 52

[43] Zikmund, P. (2017). Dynamic soaring of unmanned aerial vehicle within airliner wake vortex in climb regime. *Proceedings of the Institution of Mechanical Engineers, Part G: Journal of Aerospace Engineering*, 231(13):2479–2486. 52

Part II

The numerical framework

Chapter 3

Aeroelastic framework Part I : Aerodynamics

Abstract

This chapter presents an experimental validation and modification of the ASWING aeroelastic framework. The study focuses on the aerodynamic model. Firstly, the chapter reviews the nonlinear unsteady lift line and slender body theories. Then, modifications to the ASWING framework are proposed based on recent literature. The experimental validation is divided into two sections: steady and unsteady. The study evaluates the nonlinear steady lift line model using six single planform configurations and examines stall predictions where possible. The investigation also includes the effects of ailerons and flaps on roll and yaw performance. Additionally, steady wake interaction predictions are evaluated using two tandem configurations with particular emphasis on lift and drag up to stall. The study evaluates the slender body theory using four airship configurations to highlight a numerical anomaly with the current version of ASWING. A solution is proposed. Additionally, the unsteady lift line model is evaluated using two cases: a plunging airfoil and a wing. Particular emphasis is placed on the time average, amplitude and phase of the first harmonic, and the phase average of the lift. The investigation includes several reduced frequencies, amplitudes, and wing root angles. The paper concludes by comparing the computational time costs with higher fidelity methods. Based on this initial comparative work, ASWING appears to be an attractive, fast, and accurate aerodynamic pre-design tool.

Publications:

Materials from chapter 3 and 4 have been gathered and summarized so that a journal paper could be submitted to AIAA Journal of Aircraft with the title:

R.Jan, J-M. Moschetta and J-P. Condomines, Experimental evaluation of ASWING for preliminary design of flexible aircraft: aerodynamic model, AIAA Journal of Aircraft, 2024.

This paper will be published after the PhD manuscript would have been made public so that the complete evaluation work can be cited in the paper.

Contents

List of Symbols

Theoretical model variables and parameters

α	angle of attack
α_0	airfoil zero lift angle of attack
$d\alpha_0/d\delta F$	2D section flap zero lift angle of attack derivative
$dc_l/d\alpha = c_{l_\alpha}$	airfoil incompressible lift slope
c_m	airfoil pitch moment coefficient
$dc_m/d\delta F$	airfoil pitch moment coefficient
δ_F	control deflection
w_k, w_∞	induced velocity influence funtion
ρ	air density
Γ_k	discrete bound circulation strength
σ_k, ϑ_k	discrete source and doublet strength
λ	Plandtl-Glauert factor $\lambda = \frac{1}{\sqrt{1-M_\infty^2}}$
$[P]$	Plandtl-Glauert transformation matrix

Experimental validation parameters

c_d, C_D	steady 2D and 3D drag coefficient
c_l, C_L	steady 2D and 3D lift coefficient
$\bar{c_l}, \bar{C_L}$	time average 2D and 3D lift coefficient
$\tilde{c_l}, \tilde{C_L}$	2D and 3D lift first harmonic amplitude
ϕ_{c_l}, ϕ_{C_L}	2D and 3D lift first harmonic phase
$c_l(s)$	steady cl spanwize distribution (SBT)
k	reduced plunging frequency
A/c	reduced plunging amplitude
λ	wing taper ratio
AR	wing aspect ratio
b	wing span
C_l	rolling moment coefficient
C_n	yawing moment coefficient
G	vertical gap between tandem wings
b_f, b_b	forward and backward tandem wings span
c_f, c_b	forward and backward tandem wings chord
$\epsilon_{c_{l_\alpha}}$	error in c_l slope

Accronyms

$NLLT$	Non linear Lifting Line Theory
SBT	Slender Body Theory
VLM	Vortex Lattice Method
VPM	Vortex Particule Method
$U-\square$	Unsteady - $\square$
CFD	Computational Fluid Dynammic
UAV	Unmanned Aerial Vehicules

Résumé du chapitre en français

Ce chapitre est le premier de quatre dédiés à la validation expérimentale de l'espace numérique retenu (ASWING) pour ces travaux de thèse. Dans un soucis de rigueur méthodologique, les modèles aérodynamique, hélice et structure sont évalués séparément dans un premier temps. D'une part il est plus aisé de trouver des données expérimentales permettant de mettre en défaut chaque fonctionnalité des différents modèles couplés. D'autre part en adoptant cette stratégie, il est bien plus aisé de détecter les paramètres critiques conditionnant le domaine de validité de l'outil. Ce chapitre se concentre donc sur la validation expérimentale du modèle aérodynamique d'ASWING. Ce dernier dispose d'une implémentation non-linéaire instationnaire. Il permet la modélisation d'aéronefs avec de multiple surfaces portantes. Parmis ces dernières, deux types peuvent être modélisées. Les fuselages à symétrie locale de révolution et les ailes. De ce fait deux théories distinctes sont utilisées pour modéliser les forces aérodynamiques qu'elles génèrent, à savoir respectivement, la théorie des corps élancés et la ligne portante. Toutes deux tirant leur formalisme du début du XXe siècle, elles ont fait l'objet d'une extension non linéaire et instationnaire. Pour recouvrir les effets de viscosité, elles ont été agrémentées de fonctions semi-empiriques. Parmi les ajouts on peut notamment citer, la prise en compte de gouverne aérodynamique, le décrochage local, l'alignement du sillage en fonction des condition d'écoulement, la prise en compte des effets instationnaires locaux etc. Il est important de noter pour le lecteur qu'il n'existe pas de version détaillé des développements théoriques proposés dans les documentations techniques. De ce fait les résultats théoriques ont fait l'objet d'un développement exhaustif, avec un accent mis sur l'illustration de ce dernier pour faciliter la compréhension du modèle à un public non expert. Cette démarche est motivée par l'utilisation potentielle d'ASWING par la communauté du controle/commande non nécessairement au fait des différentes limites de ce dernier. Ce fut aussi l'opportunité de proposer des améliorations à la lumière de la littérature des 20 dernières années (age de l'outil) que l'on dénote ASWING-m. Il vient logiquement dans un second temps la validation expérimentale de l'outil et de sa version modifiée. Celle-ci est faite en deux temps. Une première partie est dédiée aux phénomènes aérodynamiques stationnaires. La ligne portantes est évaluée contre 8 cas expérimentaux issus de la littérature. Les 5 premiers étant choisis pour évaluer son schéma non linéaire. Le 6e fut retenu pour apprécier l'effet de gouvernes aérodynamiques sur les performances en roulis et lacet. Enfin les deux derniers sont des configurations en tandem visant à évaluer la prise en compte des interactions de sillage sur la portance et trainée. A noter que chacun des cas a été retenu de part sa géométrie mettant à l'épreuve le modèle (faible rapport d'allongement, grande flèche, fort dièdre etc) . La théorie des corps élancés quant à elle fait l'objet d'une validation stationnaire contre 4 modèles de dirigeable à forme ellipsoïde et rapport d'aspect variable.
L'évaluation expérimentale se poursuit dans une seconde partie se concentrant sur les effets instationnaires. Celle ci propose uniquement une mise à l'épreuve de la ligne portante. Deux bases de données bi et tri-dimensionnelles ont été utilisées pour dresser les limites du modèle. Une comparaison avec les travaux de Theodorsen (dont dérive le modèle) est proposée. Enfin le chapitre se termine avec une étude des performances en temps de calcul d'ASWING proposant une comparaison avec des outils dits de plus "haute fidélité".
Conclusions générales: A la lumière des comparaisons expérimentales, ASWING présente d'excellents résultats quelques soient les cas considérés. Le décrochage est correctement capturé, cependant, pour des angles d'attaque post décrochage la qualité des prédictions diminue drastiquement. La version ASWING-m présente de meilleures performances en particulier sur la prédiction de la trainée. La ligne portante instationnaire présente d'excellents résultats que ce soit dans le cas 2D ou 3D sur la plage habituelle de fréquence et amplitude réduite. Une baisse de performance a été identifiée pour une mise en incidence proche du décrochage, due à l'apparition d'une vorticité de bord d'attaque, non capturée par le modèle.
La théorie des corps élancés présente également d'excellents résultats malgré la non capture des effets de séparation en bout de fuselage.

Résumé (suite)

L'analyse de performance en temps de calcul montre qu'ASWING est plus rapide de 2 à 4 ordres de grandeur que des modèles de plus haute fidélité. Certains des cas présentés ayant fait l'objet d'une comparaison avec ces derniers, et aux vus des résultats il convient de reconsidérer le terme "basse fidélité" souvent employé dans la littérature concernant ASWING. En particulier sur la prédiction de grandeurs macroscopiques comme la portance, la trainée, le moment piqueur et l'effet des gouvernes aérodynamiques.
Pour finir, cette analyse a permis de converger vers des paramètres limites assurant de bonnes prédictions. Les ailes et fuselages doivent présenter un rapport d'allongement et d'aspect supérieur à 5. Les ailes doivent avoir des angles de dièdre et flèche inférieurs à 45 degrés. Il est aussi conseillé de ne pas trop abuser de la fonction de décrochage rapidement détériorée. Enfin il est recommandé de considérer des écoulements dont le nombre de Reynolds moyen est supérieur à 100 000 (typique des mini drones). Au vu des cas considérés, nous ne pouvons pas donner de recommandation sur le nombre de Mach.

3.1 Introduction

Over the last three decades, the increase in computer power has led to the growing use of fast models for pre-design and geometry optimisation of unmanned aerial vehicles (UAVs) and commercial aircraft. In the future, both will be exposed to higher levels of gusts and turbulence due to climate change, and their design will have to take these predictions into account. Therefore, it is crucial to have a proper understanding of the aeroelastic phenomenon to optimize the flight envelope while minimizing the use of raw materials. As an aircraft/UAV manufacturer, ensuring good aerodynamic performance is essential to remain competitive in a growing market. Accurately predicting such a characteristic provides a significant advantage. Fast models can be a useful starting point for exploring ideas that can later be verified with higher fidelity methods.

ASWING is a software that was first released in 1999 (Drela 1999 2009 and 2008) Specifically, ASWING can provide steady lift and drag predictions up to stall, as well as unsteady lift forecast. The software can capture the effect of ailerons and flaps, and take into account wake interference. It can also provide information on thrust and moment of propellers and their jets/swirl can be modelled so that their interactions with lifting surfaces can be captured. In terms of aeroelastic properties, the software can provide steady analysis such as torsional divergence, aileron reversal speed and wing washout. The prediction of structural deformation of wings and fuselage under steady and unsteady flow is also possible. Modal analysis can be used to predict flutter boudaries and divergence speed. The impact of nacelles, struts, structure tailoring, and propellers on the flutter speed can be investigated. Additionally, ASWING allows for the study of Limit Cycle Oscillations (LCO) as the model is fully non-linearly coupled. To provide these features, the unsteady nonlinear lifting line and slender body theory are coupled with a nonlinear extended Euler-Bernoulli beam model. Each lifting body is then connected to the others using compliant, elastic, or restrictive joints. Up to 40 lifting bodies, 10 engines, and 20 flaps can be implemented. ASWING is mainly dedicated to high aspect ratio geometries due to its formalism. This framework is used, for example, for designing High Altitude Long Endurance (HALE) UAVs.

Table 3.1 compares the main features of ASWING with other modern frameworks used in academia and industry. These include Openaerostruct, developed at the University of Michigan (Jasa et al. 2018,Chauhan and Martins 2019), FNSA (Fast Non-linear Static Aeroelasticity) developed at Airbus and ISAE-SUPAERO (Chandre Vila et al. 2022 and 2023) and finally a no-name framework developed at Delft University (Werter and De Breuker 2016). The softwares are compared as they are derived from similar theories, namely potential methods extended with viscous loops for aerodynamics and Euler-Bernoulli/Timoshenko beam theory for structural modelling. They are also considered the best candidates for use in optimization work due to their low computational cost. The main ASWING disadvantage is that it is not coupled to the OPENMDAO planform. However, it is in early development at ISAE-SUPAERO. Despite these drawbacks, ASWING is in early development at ISAE-SUPAERO. The software is provided in a non-compiled version so that the user can modify it if necessary. However, ASWING lacks the benefits of an open-source community since the code cannot be published. Therefore, despite its combined features, ASWING is not widely used by the community. In fact, as shown in figure 3.1, ASWING has been cited a little less than 200 times since 1999. Nevertheless, it is mostly cited and presented as an existing tool. Upon closer examination of all publications, it is evident that ASWING has been utilised as an analysis and pre-design tool in 30 publications. However, only 6 of these publications presented a benchmark or validation of the tool against experimental and higher fidelity CFD data (cf the work of González et al., Warwick et al., Jones, Colas et al., Love et al., Variyar et al.). All six papers evaluated the same features: flutter speed or gust load predictions. Additionally, the aircraft considered in these papers were not stress cases of the model, as they all had high aspect ratio wings. Neither the original paper nor the technical documentation includes a section dedicated to code validation. Therefore, our main contribution is to provide experimental validation of the main features proposed by ASWING. In consideration of recent literature, updates have been made to the code and evaluated. The updated model will be referred to ASWING-m. To facilitate evaluation, the work has been divided into 4 parts: 1 - aerodynamics, 2 - propellers and jets, 3 - structure, and 4 - aeroelasticity. The third motivation, following validation and modification, is to provide greater insight into the theoretical results used in the model. As stated by the author, this tool is primarily intended for individuals in the aircraft design community. But it can also be used by the control community, especially since the implementation of a modern control toolbox (Jan et al. 2021). Control engineers may not be familiar with all the theoretical advancements of ASWING and their limitations. Therefore, based on the validation results, the critical parameter limits are emphasised to ensure proper use of the tool. This chapter presents the first part of the experimental validation and modification

Table 3.1: ASWING features comparison with modern most cited aeroelastic framework (A,S,AE,O) : Aerodynamic, Structure, Aeroelastic and Other features

		ASWING	Openaerostruct	FNSA	Delft
	Reference papers	[14], [15]	[27], [5]	[4] [3]	[43]
A	Non linear planform	✓	✓	✓	✓
	3D Aerodynamic	✓	✓	✓	✓
	Steady wake interaction	✓	NC	✗	NC
	Propeller jet/wing interaction	✓	✗	✗	✗
	Fuselage modeling Volume effect	✓	✗	✓	✗
	Unsteady aerodynamic	✓	✗	✗ : QS	✓
	Drag predictions	✓	✓	✓	✗
	Flap/Ailerons effects	✓	✗	✗	✗
	Steady-stall	✓	✗	✓	✗
S	Non-linear delfection	✓	✗	✗	✓
	6-DOF	✓	✓	✓	✓
	Structural damping (unsteady)	✓	✗	✗	✗
	Tension/elastic axis decoupling	✓	✗	✗	✓
	Ponctual and concentrated mass effect	✓	✗	✗	✓
	Wing box	✓ with [10]	✓	✗	✓
AE	Steady deflection	✓	✓	✓	✓
	Gust response	✓	✗	✓	✓
	Torsional divergence	✓	✓	✓	✓
	Structure failure	✓	✓	✗	✓
	Ailerons reversal	✓	✗	✗	✗
	Flutter analysis	✓	✗	✗	✓
	Whirl flutter analysis	✓	✗	✗	✗
	Limit cycle oscillations	✓	✗	✗	✗
O	Embeded control toolbox	✓ [26]	✗	✗	✗
	Open MDAO coupling	✗ In progress	✓	✗ In progress	✗
	Opensource	✓	✓	✗ Airbus	✓

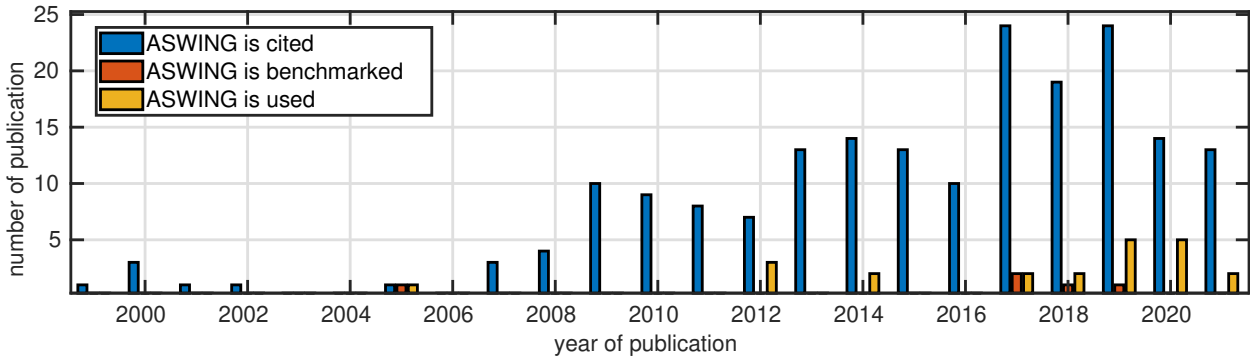

Figure 3.1: ASWING citation history, blue bars : mentioned as an existing tool; yellow : used as a tool ; orange : used and validated against experimental or higher fidelity CFD data

of ASWING. The focus is on the aerodynamic model. Firstly, the chapter recalls the nonlinear unsteady lifting line and slender body theories and introduces some modifications based on modern literature. Secondly, it proposes an experimental validation. It is important to note that no experimental campaign has been carried out. The dataset is a compilation of peer-reviewed data from journal articles, technical reports, and conference proceedings. It has been divided into two parts: I - steady and II - unsteady. The steady lift and drag predictions up to stall are presented for single and tandem layouts to evaluate the lifting line theory. Additionally, the effect of different ailerons is studdied. The slender body theory is evaluated using four airships to highlight a numerical problem that arises from its implementation. A solution is proposed. Finally, the study evaluates 2D and 3D unsteady lift predictions for a plunging airfoil and a wing. The lift time, phase average, and first harmonic amplitude and phase are presented against various reduced frequencies, amplitudes, and root angles. Thirdly, this paper presents a computational time comparison between ASWING and higher fidelity methods to highlight its advantages. The paper concludes by discussing future theoretical developments and experimental validation.

3.2 The extended unsteady slender body theory

In ASWING there are 2 types of lifting bodies: wings and fuselage. Since the aeroelastic behaviour is of interest, the aerodynamic loads must be derived in a distributed form. To start with the fuselage, only fuselages with a local cross-section having a symmetry of revolution (circular) are considered. In this case, the unsteady distributed lift on a fuselage is given by the unsteady vector form of the slender body theory.

Theorem 3.2.1 (Extented SBT)**.** *Let R(s) be the cross-section radius at the spanwise location s. Let V and a_i be the air relative speed and local inertial acceleration evaluated at the cross-section centre. The local or distributed unsteady lift applied on an infinitesimal fuselage element of length ds is given by*

$$\begin{aligned}\frac{d\vec{L}}{ds} = \vec{f_{lift}} &= 2\pi\rho V \cdot s\vec{V_\perp} R\frac{dR}{ds} - 2\pi\rho R^2 \vec{a_{i,\perp}} \\ &= 2\pi\rho V \cdot s\vec{V_\perp} R\frac{dR}{ds} - 2\pi\rho R^2(\vec{a_i} - (\vec{a_i}\cdot\vec{s})\vec{s})\end{aligned} \tag{3.1}$$

Proof. see Appendix B □

Note that $V_\perp$ and $\vec{a_{i,\perp}}$ are the components of V and a_i lying in the cross-section plane as shown in figure 3.2. The latter gives a visual insight into the aerodynamic lift direction and the effect of a positive or negative variation of R with respect to s on the steady lift. The second term in the equation 3.44 represents the unsteady components, also known as the added mass terms. It will be seen in the later section that the equation 3.44, as it is implemented numerically, can cause some instabilities. As the extended slender body theory is derived from potential methods, i.e. the inviscid assumption, ASWING recovers the viscosity effect using a semi-empirical equation. The elementary drag per unit length is then given by

$$\vec{f_{drag}} = \frac{1}{2}\rho|\vec{V}|\vec{V}2Rc_{d_f} + \frac{1}{2}\rho|V_\perp|\vec{V_\perp}2Rc_{d_p} \tag{3.2}$$

Note that in the expression 3.2 the different drag contributions do not have the same direction. In fact, as shown in the figure 3.2, the pressure drag acts in the direction of $\vec{V_\perp}$. From empirical data, the value of the pressure drag coefficient is usually between 0.4 and 1.2, depending on the nature of the flow. Skin friction drag, on the other hand, is applied in the direction of the upcoming flow $\vec{V}$. Assuming that the low velocity streamlines of the boundary layer are aligned with the free flow, so are the viscous shear stress efforts. The latter is shown in the upper right part of the figure 3.2

3.3 The extended non-linear lifting line model

3.3.1 Vectorial formulation of the unsteady Kutta-Joukowsky theorem

The unsteady aerodynamic loads on the wings are calculated using the extended nonlinear lifting line theory originally introduced by Prandtl and Glauert. The aerodynamic loads are divided into two contributions, circulatory and non-circulatory. The local unsteady circulatory lift is given by the unsteady vector form of the Kutta-Joukowsky theorem:

Theorem 3.3.1 (Unsteady Kutta-Joukowsky in its vectorial form)**.** *. Let Γ be a vortex line resulting from the vortex sheet lumping at the horseshoe boundary $r_{hv} = c/4$. The unsteady circulatory lift generated by an airfoil of chord c into a flow of velocity $V(r_{hv})$ is given by*

$$\begin{aligned}\vec{f}_{lift,\Gamma} &= \rho\frac{\partial\Gamma}{\partial t}c_\beta + \rho\Gamma(\vec{V}\times\vec{s}) \\ &= \rho c\frac{\partial\Gamma}{\partial t}\frac{(\vec{V}\times\vec{s})}{|V_\perp|} + \rho\Gamma(\vec{V}\times\vec{s})\end{aligned} \tag{3.3}$$

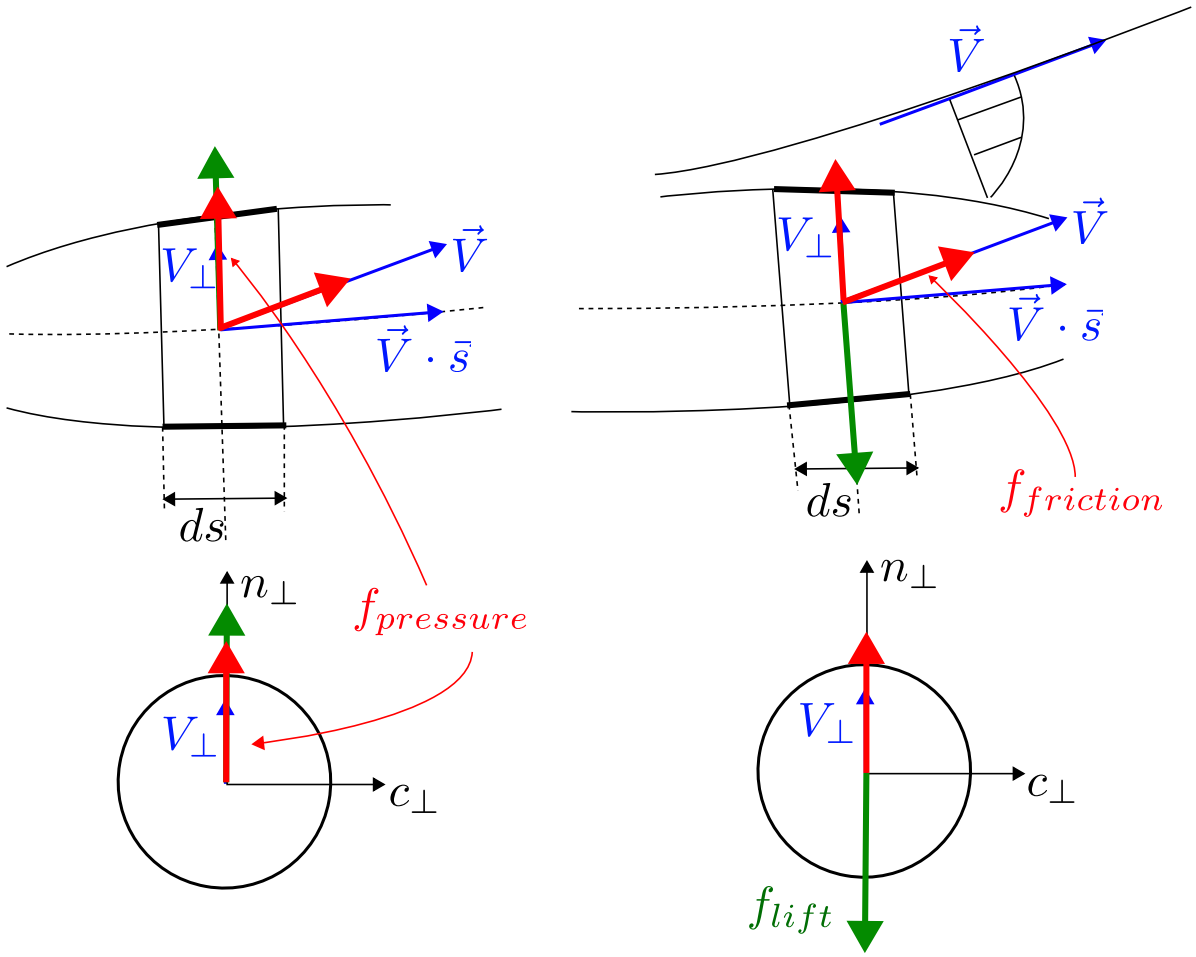

Figure 3.2: Slender Body Theory : lift and drag directions. The drag is split into 2 components : 1 - the pressure drag is always aligned with $V_\perp$ and 2 - the skin friction drag aligned with the upcoming velocity V.

Proof. see Appendix C □

Note that c_β in equation 3.3 denotes the wind-aligned projected chord. In fact, as shown in figure 3.4 (a) and (b), the unsteady Kutta-Joukowsky theorem is integrated along the wake. Or the latter is wind-aligned in the ASWING model. The pressure integration must be performed over a corrected airfoil of length c_β (see Appendix C for more details). In the equation 3.3 Γ is unknown and distributed along the span. As will be seen in the velocity influence section, it is represented by a finite Fourier transform where the coefficients are unknown. Therefore, an appropriate set of constraints must be established to calculate them. Non-circulatory lift, i.e. source/sink lift, also known as an added mass effect, is provided by an approximation of Theodorsen's theory.

Theorem 3.3.2 (Theodorsen : apparant mass terms)**.** *The unsteady lift and momentum due to a source/sink distribution ensuring the impermeability condition over the entire airfoil is given by*

$$\vec{f_{am}} = \frac{\pi}{4}c^2\left[\vec{V}\times(\vec{\Omega}+\vec{\omega_i})\cdot\vec{n} - \vec{a_{c/2}}\cdot\vec{n}\right]\cdot\vec{n} \tag{3.4}$$

$$\begin{aligned}\vec{m_{am}} = &\\ &-\frac{\pi}{4}c^2\frac{c}{4}\left[\vec{V}\times(\vec{\Omega}+\vec{\omega_i})\cdot\vec{n} + \frac{c}{8}(\alpha_0+\dot{\omega_i})\cdot\vec{s}\right]\cdot\vec{s}\\ &+\Delta\vec{r_{c/2}}\times\vec{f_{am}}\end{aligned} \tag{3.5}$$

Proof. see (Theodore Theodorsen 1935). It is important to note that the equations 3.4 and 3.5 are a vectorial formulation of Theodorsen's theory. Moreover, they do not exactly reproduce the results proposed in 1935. In fact, the airfoil is assumed to pitch and plunge around the mid chord, which is more conservative. □

3.3.2 Modelling drag

As the lifting line and Theodorsen are inviscid theories, viscosity effects are recovered using 2D airfoil polars. In consequence, the distributed drag generated over a wing is locally given by :

$$\begin{aligned}\frac{d\vec{D}}{ds} = \vec{f_{drag}} = &\frac{1}{2}\rho|\vec{V}|\vec{V}\bar{c}c_{df} + \frac{1}{2}\rho|\vec{V_\perp}|\vec{V_\perp}\bar{c}c_{dp}\\ &+2\rho\frac{\vec{V_\perp}}{|\vec{V_\perp}|}(\vec{V}\cdot n)^2{}_{cp}\end{aligned} \tag{3.6}$$

In equation 3.6 the first term is the skin friction drag contribution, aligned with the free stream velocity (figure 3.3-a). As in slender body theory, the streamlines in the boundary layer are assumed to be aligned with the upcoming free stream, as shown in figure 3.3 (b). The second term implies that the pressure drag contribution lies in the cross-sectional plane (as the lift) (figure 3.3-a). Finally, the third term appears only at stall and is also in the cross-section plane. Note that c_{df} and cd_p can be obtained from higher fidelity methods or experimental data for any airfoil used on a wing. However, in the equation 3.6 the latter are considered to be constant. This simplification was made because lift-induced drag is usually more important than skin friction/pressure drag. This assertion is true for high Reynolds number flow, but in the case of mini UAV design (low Reynolds number flight), errors in the prediction of drag should be observed.

3.3.3 Aerodynamic moment

The distributed aerodynamic moment applied to a lifting surface is the sum of the lift and airfoil pitch moment coefficient contributions. Note that drag has been omitted because it is mostly chord-wise (the moment arm is small). Furthermore, its amplitude is usually much smaller than that of the lift.

$$\vec{m}_{\text{lift}} = \Delta\vec{r}_{hv}\times\vec{f}_{\text{lift}} + \frac{1}{2}\rho\left|\vec{V}_\perp\right|^2\bar{c}^2c_m\hat{s} \tag{3.7}$$

with the pitching moment coefficient and its flap-induced shift given as

$$c_m = \left(c_{m_0} + \frac{dc_m}{d\delta_{F_1}}\delta_{F_1} + \frac{dc_m}{d\delta_{F_2}}\delta_{F_2}\dots\right)\frac{1}{\sqrt{1-M_\perp^2}} \tag{3.8}$$

The linear shift of the pitching moment is valid for reasonable flap deflections as illustrated in Appendix C.The Prandtl-Glauert factor uses the local perpendicular Mach number $M_\perp = \left|\vec{V}_\perp\right|/V_{\text{sound}}$ to take into account the compressibility effects.

3.3.4 Extented Kutta-Joukowsky condition

The extended Kutta condition serves several purposes in ASWING. Firstly, it imposes physical constraints on the circulation Fourier coefficients in order to build a good constraint system of equations. Secondly, it recovers the 2D airfoil properties such as the linear lift slope cl_α, the camber line α_0 and the effect of flaps. Thirdly, it recovers the unsteady effect using a lag term that brings reasonnable consistency with Theordorsen's circulatory lift.

To do this, for each circulation Fourier coefficient, a flow tangency condition is imposed on the airfoil at each "control point" location. In other words, the local

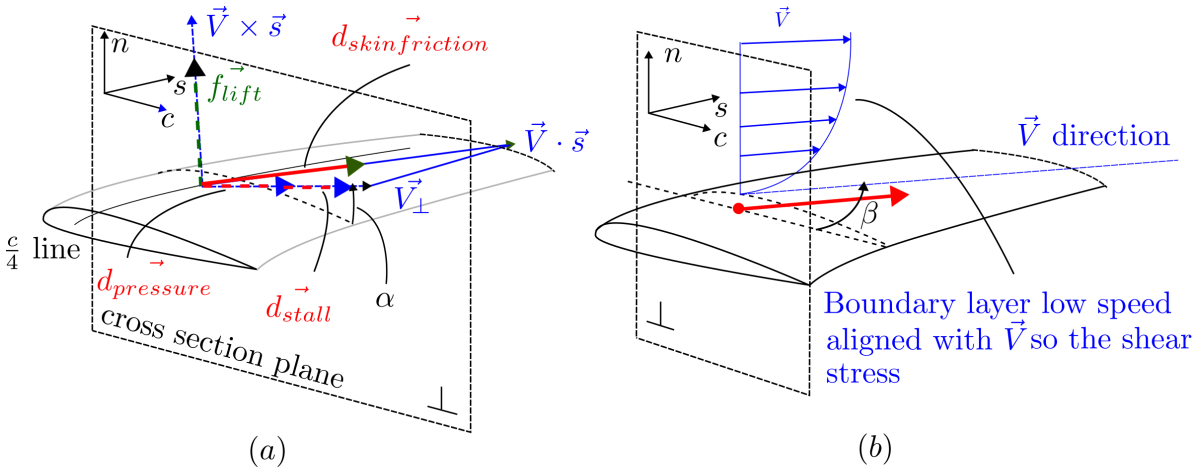

Figure 3.3: ASWING lifting line forces directions
(a) 3D directions of lift and drag contributions
(b) zoom on the boundary profile low-speed profile

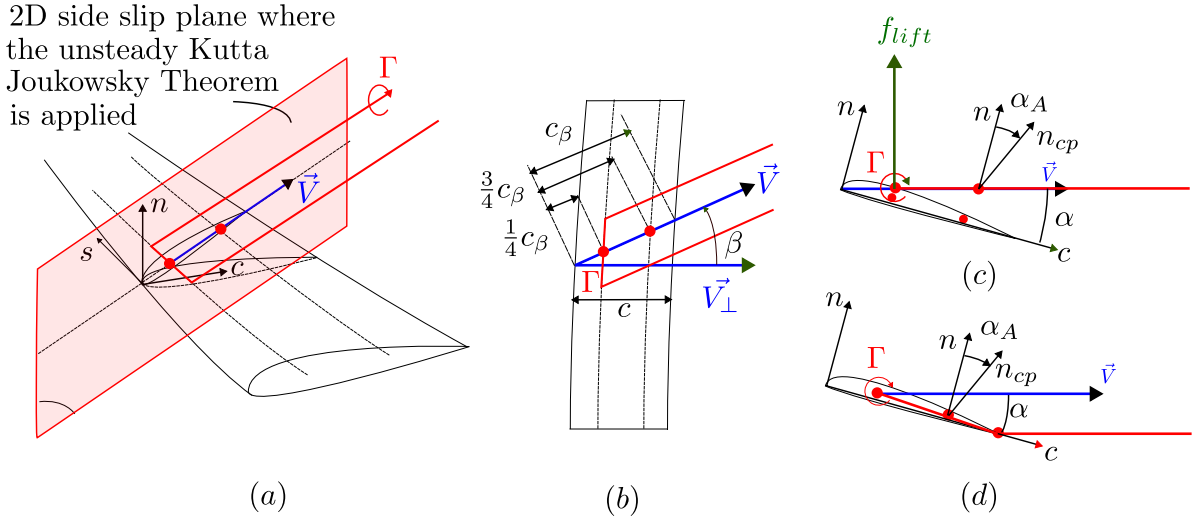

Figure 3.4: ASWING horseshoe representation
(a) 2D Kutta Joukowski plane
(b) top view with corrected chord c_β
(c) ASWING wake straight shedding
(d) Modern literature horseshoe representation

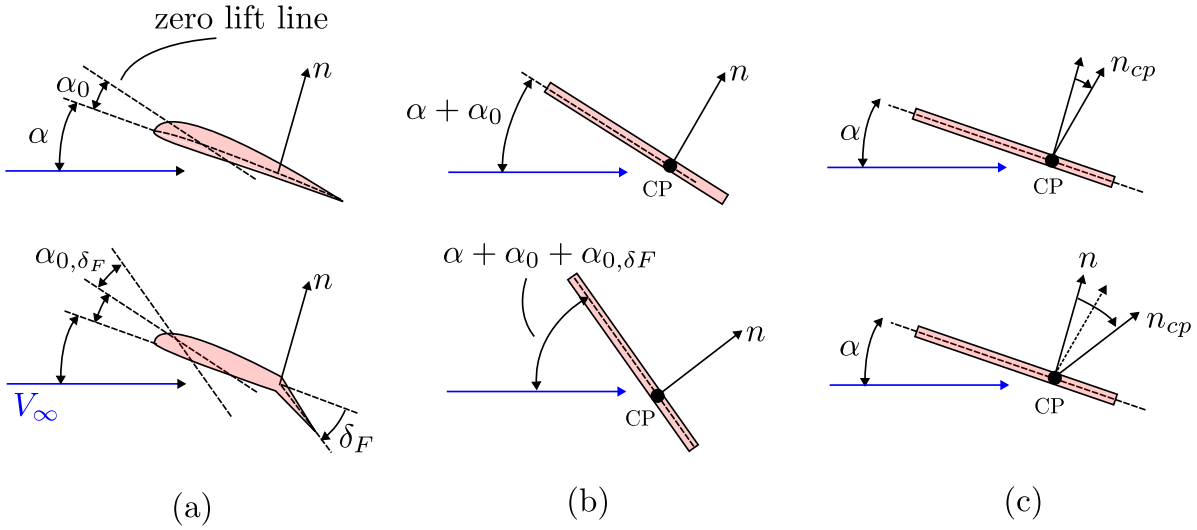

Figure 3.5: Recovering airfoil camber line (first line) and flap deflection effect (second line):

velocity evaluated at this point must be parallel/tangent to the surface of the airfoil, as shown in figure 3.4(d). However, because of the ASWING formalism, the Kutta-Joukowsky condition has been modified. First, as shown in figure 3.4 (c), the wake is shed directly from the centre of pressure (quarter chord) and no longer from the trailing edge. As the control point must be placed on the vortex sheet, it is no longer part of the wing geometry. Secondly, as the wake is wind-aligned, the position of the centre of pressure and control point varies with the upcoming freestream direction. Criticism of this horseshoe representation has been made in (Chreim 2019). Stability issue and a lack of 'physical' meaning as the wake is not shed from the trailing edge have been reported. However, in our validation work, we did not observe such instabilities related to the wake representation. Furthermore, although the second argument is valid, at high aspect ratios the difference in wake position between the two representations is negligible. The ASWING representation has the advantage of having a direct vectorial solution for the vortex-induced velocities, while the second requires the computation of the contribution of a vortex ring and a horseshoe vortex, which increases the computational time. The horseshoe boundary or centre of pressure and the control point are placed at a distance of $\frac{1}{4}c_\beta$ and $(\frac{1}{4}+h)c_\beta$ respectively along the wind-aligned unit vector $\vec{\xi} = \frac{\vec{V_\infty}}{|\vec{V_\infty}|}$ from the leading edge of the wing. The meaning of h will be derived in the next lines. If $\vec{r_{cp}}$ is given as the local position of the control point. The flow tangency condition is written as follows.

$$\vec{V}(\vec{r_{cp}}) \cdot \vec{n_{cp}} = 0 \tag{3.9}$$

where $\vec{V}(\vec{r_{cp}})$ is the air relative velocity evaluated at the control point. The latter depends on the body motion, the velocity induced by the horseshoe vortices, the sources, the doublets, the engine jet and the gust. The position of the control point is wisely chosen in order to recover the linear incompressible lift airfoil slope $c_{l,\alpha}$. In fact, if the position of the control point is defined as :

$$\vec{r}_{cp} = \vec{r}_{hv} + \frac{h\bar{c}}{|\vec{\xi} \times \hat{s}|}\vec{\xi} = hc_\beta\hat{\xi} = \frac{1}{4\pi}\frac{dc_l}{d\alpha}c_\beta\vec{\xi} \tag{3.10}$$

when the Kutta condition is solved to compute the circulation and combined with the lift theorem, the latter is given by

$$f_{lift} = \frac{1}{2}\rho c l_\alpha \alpha_{eff} V_\infty^2$$

recovering the airfoil lift slope on the local lift. 2 other airfoil properties can be recovered by modifying the flow tangency condition. Indeed, let us introduce the zero lift angle of attack and its linear shift induced by the deflected flap defined as

$$\alpha_A = \alpha_0 + \frac{dc_l}{d\delta_{F_1}}\frac{d\alpha}{dc_l}\delta_{F_1} + \frac{dc_l}{d\delta_{F_2}}\frac{d\alpha}{dc_l}\delta_{F_2} + \dots \tag{3.11}$$

where α_0 is the zero lift angle of attack of the airfoil, $\frac{dc_l}{d\delta_{F_1}}\frac{d\alpha}{dc_l}$ is the linear shift slope induced by a flap placed on the airfoil. The linearity of the shift as for the pitch momentum is valid for reasonable small flap deflections as shown in Appendix C. It is possible to consider more than 1 flap per airfoil, but this is very unlikely to be used on a UAV.

As shown in the figure 3.5 these airfoil parameters can be recovered by tilting the normal vector of the flow tangency condition by the angle α_A. This tilting is the only way to achieve compatibility with the structural model as the structure cannot be virtually deformed to match the airfoil properties as shown in the second line of figure 3.5. The flow tangency condition is then

rewritten as

$$\vec{V}(\vec{r_{cp}}(c_{l_\alpha})) \cdot \vec{n_{cp}}\left(\alpha_0, d\alpha/d\delta_{F_1}\right) = 0 \tag{3.12}$$

The airfoil local stall is caught through the use of the lift slope decambering function in the flow tangency condition

$$\begin{aligned}&\vec{V}(\vec{r_{cp}}(c_{l_\alpha})) \cdot \vec{n_{cp}}\left(\alpha_0, d\alpha/\delta_{F_1}\right)\\ &- \frac{V_\perp}{4\pi h} K_{\mathrm{s}} f_{\mathrm{stall}}\left(c_l, cl_{min}, cl_{max}\right) = 0\end{aligned} \tag{3.13}$$

with $c_l = \frac{2\Gamma}{cV_\perp}$ the 2D lift coefficient and $f_{\mathrm{stall}}\left(c_l, , cl_{min}, cl_{max}\right)$ the stall activation function defined as

$$f_{\mathrm{stall}}\left(c_\ell\right) = \Delta c_\ell \log \frac{1 + \exp\left[\left(c_\ell - c_{\ell\max}\right)/\Delta c_\ell\right]}{1 + \exp\left[\left(c_{\ell\min} - c_\ell\right)/\Delta c_\ell\right]}$$

Note that $K_S = 40$ and $\Delta c_l = 0.05$ have been empirically chosen to match pre-stall usual behaviour. Finally, a 2D unsteady approximation of the wake is used leading to the final modification of the flow tangency condition.

$$\begin{aligned}&\vec{V}(\vec{r_{cp}}(c_{l_\alpha})) \cdot \vec{n_{cp}}\left(\alpha_0, \frac{d\alpha}{d\delta_{F_1}}\right)\\ &- \frac{V_\perp}{4\pi h} K_{\mathrm{s}} f_{\mathrm{stall}}\left(c_l, , cl_{min}, cl_{max}\right)\\ &- \frac{b}{V_\perp}\frac{\partial\Gamma}{\partial t} = 0\end{aligned} \tag{3.14}$$

This lag term is claimed by the author [14] to be the best temporal fit possible to the Theodoren theory. Indeed when the full aerodynamic model is translated into the frequency domain, it is possible to build a lift coefficient transfer function defined as

$$C_{\mathrm{ASWING}}\left(k\right) = \left(F + iG\right)_{\mathrm{ASWING}} = \frac{1 + 2ik}{1 + 4ik} \tag{3.15}$$

which is graphically compared to the Theodorsen circulatory lift function in figure 3.6. ASWING lag function seems to be weak to reproduce the Theodorsen's for reduced frequency between 0 and 1. This range is of particular interest in the experimental validation sections.

3.3.5 Velocity influence of lifting bodies

As it has been seen, the air relative speed is needed to compute the lift and drag in both LLT and SBT. As described earlier the latter is the summation of different contributions, as follow

$$\vec{V}(\vec{r}) = \vec{V_\infty} - \vec{\Omega} \times \vec{r} + \vec{V_{ind}}(\vec{r}) + \vec{V_{gust}}(\vec{r}) \tag{3.16}$$

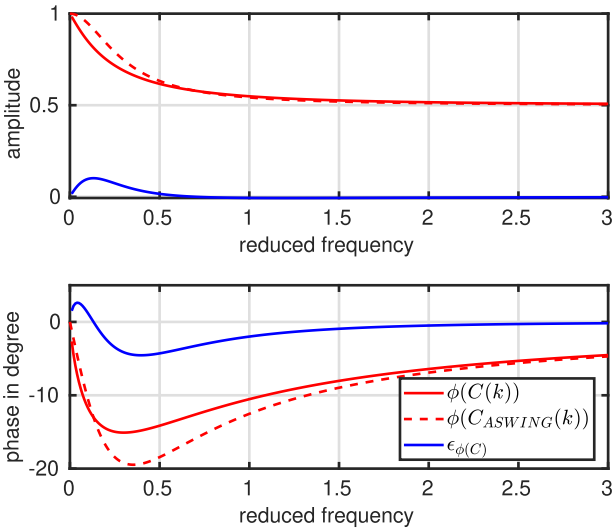

Figure 3.6: Modulus and phase comparison of Theordorsen and ASWING lag function

In this section, the velocities induced by the singularities used in the SBT and LLT ie doublets, sources, and vortices are derived.

Plandtl Glauert Transformation

The singularities induced velocities are computed in the Prandtl Glauert space through the use of the following transformation (PGT)

$$\begin{aligned}\overline{\overline{P}} &= \begin{bmatrix} \cdots\vec{\xi}\cdots \\ \cdots\hat{\eta}\cdots \\ \cdots\hat{\zeta}\cdots \end{bmatrix}\\ &= \begin{bmatrix} \frac{1}{\lambda}\cos\alpha\cos\beta & -\frac{1}{\lambda}\sin\beta & \frac{1}{\lambda}\sin\alpha\cos\beta \\ \cos\alpha\sin\beta & \cos\beta & \sin\alpha\sin\beta \\ -\sin\alpha & 0 & \cos\alpha \end{bmatrix}\end{aligned} \tag{3.17}$$

where α, β, and λ are the angle of attack, side slip angle, and compressibility stretching factor. The PGT has mainly 2 purposes. Firstly to provide a direct vectorial solution of the horseshoe vortices induced velocity. The second is to take into account the compressibility effect using the stretching factor λ

Vortex influence function

Let us consider an aircraft having N_w wings (lifting surfaces) and its j^{th} wing. Its circulation spanwise distribution is given by the Fourier series

$$\begin{aligned}\Gamma_j(s) &= \sum_{k=1}^{K_j} A_{k,j} sin(k\ acos(s/s_{max}))\\ &= \sum_{k=1}^{K_j} A_{k,j} sin(k\theta)\end{aligned} \tag{3.18}$$

where $A_{k,j}$ are the Fourier coefficients associated with the j^{th} wing, K_j is the number of coefficients, s is the wing spanwise coordinate, and s_{max} its maximum value (usually close to the wing half span). Equation

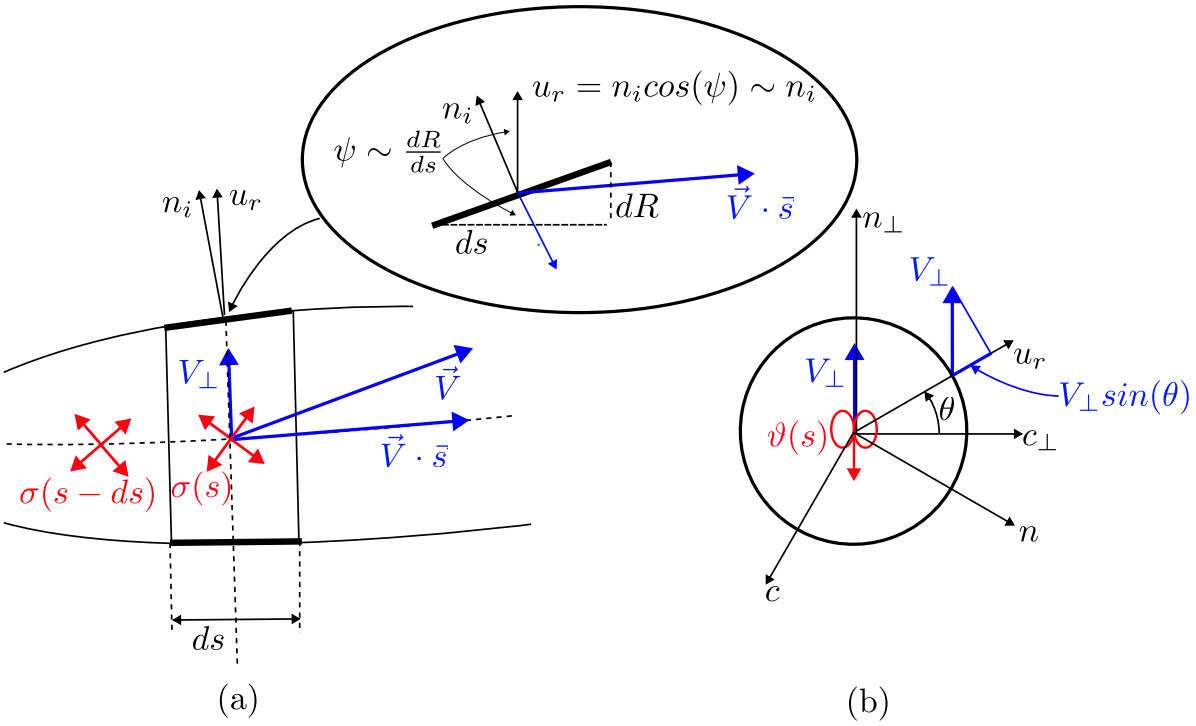

Figure 3.7: Slender Body Theory: Flow field modelling with source/sink and doublet distribution, 2D simplification of the problem.

3.18 is very convenient as it is continuous in s. As a consequence, it can be directly used in equation 3.3 to compute the local lift. $\frac{\partial \Gamma(s)}{\partial t}$ is numerically computed using a first order backward difference. Let us consider now that the j^{th} wing has been discretized in I_j structural nodes. The wing wake is represented by a discrete horseshoe system associated with the structural mesh. Each discrete horseshoe has a circulation of strength $\Gamma_j(s_{a,i})$

$$\begin{aligned}\Gamma_j(s_{a,i}) &= \Gamma_j(\theta_{a,i}) \\ &= \sum_{k=1}^{K_j} A_{k,j} sin(k\ arcos(s_{a,i}/s_{max})) \\ &= \sum_{k=1}^{K_j} A_{k,j} sin(k\theta_{a,i})\end{aligned} \tag{3.19}$$

where $s_{a,i} = \frac{1}{2}(s_{i+1} - s_i)$ is the spanwize averaged position of the discrete circulation segment. The velocity induced by the i^{th} horseshoe is given by the Biot Savart's law

$$\begin{aligned}V_{\Gamma_{j,i}}(\vec{r}) =& [P]^T \left[\sum_{k=1}^{K_j} A_{k,j} sin(k\theta_{a,i})\right] \\ & \frac{1}{4\pi} \oint_{\Gamma_{j,i}} \frac{\vec{\delta}_i(\vec{r}) \times d\vec{l}_i}{\delta_i(\vec{r})^3}\end{aligned} \tag{3.20}$$

In the above equation, the integrand has a vectorial solution that can be found in equation (6.33) of (Drela 2014). The latter can be desingularized when the i^{th} horseshoe legs cross the position of a point where the local velocity must be computed. The denominator of the integrand is then replaced by $(\delta_i^2 + \epsilon_i)^{3/2}$ with $\epsilon_i = c_{a,i}/4$. The velocity induced by the j^{th} wing horseshoe system is then given by summing the contribution of each horseshoe vortices.

$$\begin{aligned}V_{\Gamma_{j,i}}(\vec{r}) = [P]^T & \sum_{i=1}^{I_j - 1} \left[\sum_{k=1}^{K_j} A_{k,j} sin(k\theta_{a,i})\right] \\ & \frac{1}{4\pi} \oint_{\Gamma_{j,i}} \frac{\vec{\delta}_i(\vec{r}) \times d\vec{l}_i}{\delta_i(\vec{r})^3}\end{aligned} \tag{3.21}$$

The latter equation is not very convenient to compute the $A_{k,j}$ coefficients using the Kutta condition. By noticing that the latter does not depend on structural index i they can be set outside of the i summation. The velocity induced by the j^{th} wing can be rewritten as follows

$$\begin{aligned}V_{\Gamma_{j,i}}(\vec{r}) =& \sum_{k=1}^{K_j} A_{k,j} \vec{v_{k,j}}(\vec{r}) \\ =& \sum_{k=1}^{K_j} A_{k,j} \\ & \left[[P]^T \sum_{i=1}^{I_j - 1} sin(k\theta_{a,i}) \frac{1}{4\pi} \oint_{\Gamma_{j,i}} \frac{\vec{\delta}_i(\vec{r}) \times d\vec{l}_i}{\delta_i(\vec{r})^3}\right]\end{aligned} \tag{3.22}$$

where $\vec{v_{k,j}}$ can be interpretated as the velocity induced by the k^{th} Fourrier coefficient of the j^th wing

circulation function. The total velocity induced by the N_w lifting surfaces is then given by

$$V_\Gamma(\vec{r}) = \sum_{j=1}^{N_w} V_{\Gamma_j}(\vec{r}) = \sum_{j=1}^{N_w}\sum_{k=1}^{K_j} A_{k,j}\vec{v_{k,j}} \tag{3.23}$$

which now defines a solvable set of equations when integrated into the Kutta condition. The Kutta condition must be applied $K = \sum_{j=1}^{N_w} K_j$ times, corresponding to the number of Fourier coefficients to be computed. Describing the circulation distribution as a finite Fourier transform instead of a piecewise one drastically reduces the number of unknowns in the system. It also allows the aerodynamic model to be decoupled from the structural model. As the discrete horseshoe system is related to the structural one, the wake would be particularly refined despite the small number of Fourier coefficients.

Volume influence function

The velocity induced by the sources and doublets distributions used (cf figure 3.7) in the slender body theory is given by.

$$\vec{V_\sigma}(\vec{r}) = V_\infty[P]^T \left(\frac{1}{4\pi} \sum_{k=1}^{N_\sigma} \frac{\sigma_k \vec{\delta_k}(\vec{r})}{(\vec{\delta_k}^2 + \epsilon_k^2)^{3/2}} \right) \tag{3.24}$$

where N_σ is the number discrete sources used in the SBT and δ_k the relative position vector to the k^{th} source. σ_k is the strength of the sources placed at the position $\vec{r_k}$ To avoid any numerical divergence, each source has an associated desingularizing core $\epsilon_k = R(r_k)/2$. Similarly, the flow field induced by a doublet distribution is given by

$$\vec{V_\vartheta}(\vec{r}) = V_\infty[P]^T \left(\frac{1}{4\pi} \sum_{k=1}^{N_\vartheta} \frac{\vec{\vartheta_k}\delta_k^2 - 3(\vec{\vartheta_k}\cdot\vec{\delta_k})\cdot\vec{\delta_k}}{(\vec{\delta_k}^2 + \epsilon_k^2)^{3/2}} \right) \tag{3.25}$$

In practice $N_\vartheta = N_\sigma$ so equations 3.24 and 3.25 can be merged. Appendix A gives an insight into the role of sources and doublets in the slender body theory and how their strengths σ_k and ϑ_k are computed. Induced velocity functions allow us to recover the close interaction between lifting bodies and take into the 3D effects on the aerodynamic forces (wake downwash). In consequence, the total induced velocity can be defined using equation 3.25, 3.24, and 3.23 as follows

$$\vec{V_{ind}}(\vec{r}) = V_\Gamma(\vec{r}) + \vec{V_\sigma}(\vec{r}) + \vec{V_\vartheta}(\vec{r}) \tag{3.26}$$

Modelling Ground Effects:
During take-off and landing, an aircraft flies quite close to the ground, where strong aerodynamic effects such as an increase in lift and a reduction in drag can be observed (Recant. 1939). The ground acts as a solid surface where the impermeability condition must be respected. As a consequence, the flow field around the aircraft is drastically modified if it is close enough to the ground. In ASWNG, the ground is considered as an infinite flat oriented plane. In order to ensure the impermeability condition over the entire ground plane, a system of symmetric vorticity, source and doublet is created, whose intensity is equal in absolute value to maintain the same number of variables in the system. Figure 3.8 shows how such a system is constructed for a solid ground. The predictions of the ground effects are evaluated in the following sections [1].

3.4 ASWING aerodynamic model improvements

This section describes the various improvements made to the ASWING model. From now on the modified model will be called ASWING-m. The most important aerodynamic improvements are described below:

1 - Improvements in drag prediction: The ASWING source code has been modified to allow the polar to vary with angle of attack and Reynolds number. A polar lookup table for each airfoil used on the wing is provided to ASWING. Then, during the time marching or steady state computation, the lookup table is interrogated at each spanwise location based on the local angle of attack and Reynolds number. Note that no convergence problems are expected as the variation of the polar is convex with α. The Watchdogs routines have been coded so that if the Reynolds number is outside the boundary set of the lookup table, the polars are stops at the bounds to avoid their divergence. This is of particular interest for elliptical wings where the local chord is zero at the tip, so the Reynolds number is. The wing drag equation is then rewritten as follows

$$\begin{aligned}\frac{d\vec{D}}{ds} &= \frac{1}{2}\rho|\vec{V}|\vec{V}\bar{c}c_{df}(\alpha, Re) + \frac{1}{2}\rho|\vec{V_\perp}|\vec{V_\perp}\bar{c}c_{dp}(\alpha, Re) \\ &\quad + 2\rho\frac{\vec{V_\perp}}{|\vec{V_\perp}|}(\vec{V}\cdot n)^2{}_{cp}\end{aligned} \tag{3.27}$$

2 - Pre-stall viscous de-cambering: During the validation analysis, we observed that ASWING does not accurately capture the lift for a high angle of attack, especially at a low Reynolds number. This discrepancy is mainly due to the linear lift assumption. Since cl_α is assumed to be constant, it can introduce

[1] A second type of ground exists in ASWING (free-surface) but is not presented here

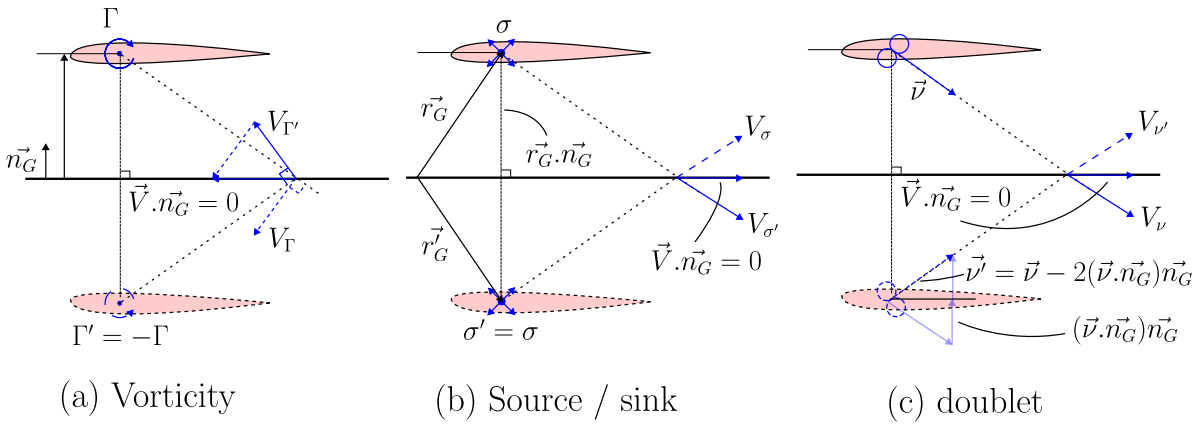

(a) Vorticity (b) Source / sink (c) doublet

Figure 3.8: Ground effect modelling in ASWING

errors in the lift predictions, depending on the quality of the linear regression of the lift polar. Consequently, we have implemented a vicious loop to calculate a new "decambered" lift slope at a high angle of attack based on the XFOIL viscous polar provided to ASWING-m. We also added a dependence on the Reynolds number to more accurately capture the variation of airfoil lift across the flight envelope.

3 - Airfoil parameter dependence on Reynolds number:

Some of the airfoil parameters vary with the Reynolds number, such as the *cl* linear slope. Among them, cl_{min}, cl_{max}, α_0, $d\alpha_0/d\delta F$ and $dc_m/d\delta F$ can vary quite significantly as illustrated in Appendix C. As a result, the source code was modified. At each Newton iteration during the time marching calculation, the Reynolds number is calculated at each spanwise location. The airfoil parameters are changed accordingly using pre-computed single-entry lookup tables. This brings a degree of convenience to any aircraft analysis on its flight envelope.

4 - Shift of stall limits due to flap deflection:

This change is motivated by the analysis presented in Appendix C. For a positive deflection, cl_{max} and cl_{min} are positively shifted as follows

$$\begin{aligned} cl_{min}(\delta_F) &= cl_{min} + cl_\alpha \frac{d\alpha_0}{d\delta_F}\delta_F \\ cl_{max}(\delta_F) &= cl_{max} + cl_\alpha \frac{d\alpha_0}{d\delta_F}\delta_F \end{aligned} \tag{3.28}$$

This modification should provide more accuracy for wing washout and flap effectiveness analysis. Unfortunately, no experimental data were found to evaluate this modification. Improvements 1 to 3 are evaluated against ASWING in the following sections.

3.5 Numerical mesh convergence, aliasing and stability analysis

The convergence of the numerical scheme for 3D lift prediction was evaluated against the Prandlt theoretical solution for 3 different angles of attack. The wing considered was elliptical. As shown in figure 3.9, all configurations converge quite quickly to their respective theoretical solutions. Therefore, discretising a wing with 20 to 40 circulation variables (or Fourier coefficients) seems to be a reasonable choice. The study of the lift convergence is sufficient to infer the drag and pitch moments. In fact, both depend on the flow field formed by the horseshoe vortex system. The aerodynamic moment also depends on the lift. Since the lift is given by the circulation distribution, when the latter has numerically converged, so will the induced flow field and thus the drag and the aerodynamic pitching moment.

During the later analysis, instabilities were observed for the elliptical wing. As the chord tends to zero towards the wing tip, so does the singularizing core of the horseshoe vortex. As the structural model is discretised by a cosine clustering function, the distance between the control point and the legs of the horseshoe becomes smaller and smaller towards the wing tip. This results in a singular calculation of the velocity. However, this is not actually a problem, as the solution converged for a much smaller number of nodes than the one where this phenomenon is observed (40 against 400).

Finally, aliasing effects were observed on the post-processed data from the ASWING output files. This artefact is illustrated in figure 3.10 (a). This problem originates in the writing of the output files. In fact, in the ASWING source code, it is possible to assign a certain number of decimal places to each characteris-

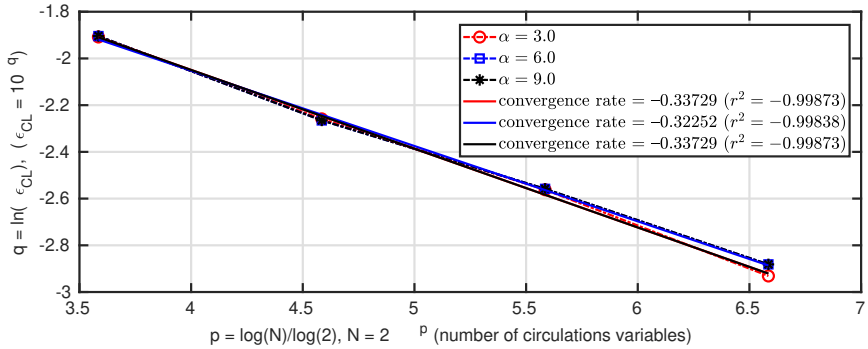

Figure 3.9: CASE # 1: Numerical scheme relative convergence to theoretical Prandlt's solution (inviscid case)

tic output value. Therefore, after identification, the spatial quantities are returned with 2 decimal places. This problem can be solved by a simple modification of the source code (see figure 3.10-b). Note that this problem is accentuated for particularly refined meshes, as the cosine clustering function tends to produce a very fine mesh towards the wing tip.

3.6 Experimental validation

This section presents an experimental/CFD[2] validation of ASWING. An important focus is placed on the steady aerodynamics. Through the use of 6 cases, single planforms have been selected to stress the non-linear lifting line model. Case number 1 is an academic rectangular planform where C_L and C_D predictions up to stall have been investigated. Case number 2 is a 45° swept-back wing, chosen mainly to evaluate the vector formulation of drag and lift. Cases 3 and 4 are chord-varying swept and unswept wings. The fifth case is a 45° dihedral angle wing chosen to virtually reproduce a highly deflected wing. The effects of aileron deflection are then investigated on a straight wing (6th case). Rolling and yawing moments induced by deflected ailerons are studied. Thirdly, 2 tandem cases are presented. Both were chosen to test the ability of the ASWING to consider wake interactions. Two cases were necessary to evaluate both the lift and drag of each planform up to stall. Note that for each case we have tried to find a platform with the lowest aspect ratio possible. In the next section, the reader will have a complete detail of each case experimental/CFD bench and its ASWING equivalent parameters. The slender body theory is evaluated with 4 different airship cases. Note that the latter have been chosen more to highlight a numerical problem arising from the ASWING model than to validate the slender body theory. The second part is entirely dedicated to 2D and 3D unsteady aerodynamics. Each steady and unsteady case and its purpose are summarised in the tables 3.2 and 3.3.

[2]higher fidelity CFD : URANS, LES, etc

3.6.1 Steady non-linear lifting line validation

CASE 1: Straight Wing

The first case chosen is a straight wing tested and presented in the work of (Applin 1995). The experiments were carried out in Langley's 14 by 22-foot subsonic wind tunnel. The wing model was mounted vertically on a six-component strain gauge balance. The wing span is 116 inches (2.95m) and the chord is 39.37 inches (1.0m). The airfoil selected was a NACA0012. The wing was deliberately made rigid to avoid any aeroelastic phenomena. The boundary layer transition was forced by the use of strips located on the upper and lower surfaces. Their position (assumed to be the same as the transition) was 2 inches from the leading edge (0.05c). Pressure measurements were taken on the upper and lower surfaces at 10 spanwise locations. However, the pressure distribution was not integrated chordwise or spanwise, so the Webplot digitiser had to be used to obtain the local lift and drag coefficient distribution. The spanwise location of the pressure measurements is shown in figure 3.11. The ASWING airfoil parameters were calculated using XFOIL 6.99. As the boundary layer transition was forced, the XFOIL Nt parameter was adjusted to match the level of turbulence in the wind tunnel. When calculating the polar we ensured that the position of the transition was close to 5% of the chord as in the experiments. The airfoil parameters in the ASWING formalism were then: $cd_f = 0$, $cd_p = 0.01$, $cl_\alpha = 6.26 \sim 2\pi$, $\alpha_0 = 0$, $cl_{min} = -1.5$ and $cl_{max} = 1.5$. Note that cd_f is equal to 0. As the wing is straight and there is no side slip angle, pressure and skin friction drag will act in the same direction, we can consider $cd_f = 0$ without being conservative. Based on the mesh convergence analysis

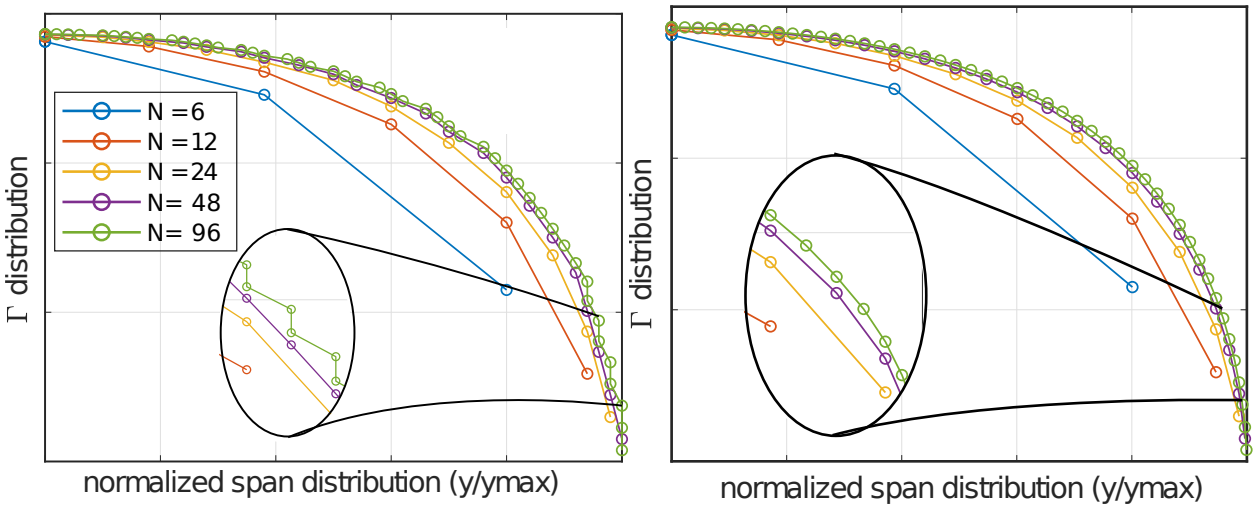

(a) 2 digits

(b) 4 digits

Figure 3.10: CASE # 1: Aliasing effects on the Γ distribution due to floating point number of digits in ASWING outputs file (default value: 2 for coordinates variables).

Table 3.2: Lifting Line and Slender Body Theories steady validation cases and their purpose

CASE	Geometry	Exp data	Evaluation type
1	Straight wing	[1]	Baseline case (CL and CD up to stall)
2	45° swept back	[24]	Non linear scheme drag formalism evaluation (CL and CD)
3	Elliptical wing	[37]	Chord varying planform (CL and CD)
4	Crescent wing	[37]	Non linear scheme evaluation
5	45° dihedral wing	CFD	Non linear scheme evaluation (CL and CD) highly deflected wing approximation
6	Straight wing	[22], [23]	Rolling and Yawing momentum induced by various ailerons
7	Tandem 1 (Straight wing)	[19], [19]	Wake interaction (CL and CD)
8	Tandem 2 (Straight wing)	[6]	Wake interaction (CL up to stall)
9 A-E	5 Swept forward, and backward wing	[31], [38]	lift loading distribution, center of pressure spanwise location
10	Straight wing with, winglet and tip sails	[32]	effect of tip devices on, lift and drag
11	Swept back wing with, Whitcomb winglet	[25] [2]	discussion on transonic flight, limits of ASWING
12 A-B	Rectangular wing with plain and slotted flaps	[34]	ground effects on lift and drag, of a rectangular wing with flaps
13 A-D	Airships / fuselages	[40]	Slender Body Theory validation lift and pressure distribution on 4 airships
14	45 degrees swept back wing with fuselage	[30]	Wing body interference: local and total lift effect with and without body

Table 3.3: Lifting Line Theory, unsteady validation cases and their purpose

CASE	Geometry	Exp data	Evaluation type
2D	Plunging airfoil	[8]	Comparison with Theordorsen on - Time average of CL - CL first harmonic amplitude and phase - Phase average Purpose : identify the limits of both theories imposed by the leading edge vortices developement
3D	Plunging wing	[7]	Comparison with Theordorsen on - Time average of CL - CL first harmonic amplitude and phase Purpose : same as in the 2D case but also highlight the benefit of ASWING against Theodorsen in the 3D case

performed in the previous section, 40 nodes were used for the circulation distribution.

Figure 3.11 (a) and (b) show the total C_L and C_D predictions of ASWING 5-96 and the author's modified version, i.e. ASWING-m. A linear regression of C_L was performed on the linear domain. According to the slope errors, both versions show excellent agreement with the experimental data. Pre-stall is even captured. ASWING-m shows advantages in drag prediction, especially at high angles of attack. As predicted, the error in the drag prediction of ASWING is mainly determined by the constancy of the drag polar. When its variation with the angle of attack is taken into account, improvements are observed.

CASE 2 : 45° swept back wing

A second test case has been chosen to evaluate the lift and drag prediction of a highly swept wing. Note that a 45° sweep is very unlikely to be found in reality (for mini UAVs), so it is considered an extreme case. Experimental data come from J. WEBER, Dr.rer.nat. and G. G. BREBNER, M.A-1958 The tests were carried out in the No 2 11.5 by 8.5 ft Royal Aircraft Establishment wind tunnel. Three wing models were investigated, but only one case is presented here. The wing span is 98 inches (2.48 m). The chord is 20 inches (0.50 m) constant along the span up to 0.9b, then the wing tip has a curved leading edge and a straight trailing edge. Figure 3.12 shows the geometry. The airfoil was the RAE 101 (equivalent to NACA0012). Neither the turbulence level nor the location of the boundary layer transition were specified. Pressure measurements were taken on both the top and bottom sides of various spanwise locations (8 in total). The report provides spanwise and chordwise integration of the C_L and C_D values. Wall corrections have been applied to the data so there is no raw data. The angle of incidence range is 0 to 10°. The wind speed was set to 163 ft/s (41.4528m/s) for an equivalent Reynolds number of 1.68E6. The case was numerically reproduced using the following parameters: $c_{l,\alpha} = 6.28$, $\alpha_0 = 0°$ and $cd_p = 7.5.10^{-4}$, $cd_f = 3.0.10^{-3}$. As in the first case, 40 circulation nodes were used. Figure 3.12 (a) and (b) highlights the lift and drag predictions of ASWING and ASWING-m. Again, the proposed modification seems to have better performance, especially at high angles of attack for drag. According to the figure 3.12 (a) the second case shows for the first time the advantage of a viscous loop correction on the 2D c_l slope. The ASWING-m data agrees better with the experiment at high angles of attack. Despite these improvements, both versions show good agreement with the experimental data.

CASE 3 & 4: Quasi elliptical and crescent wing:

The aim of this validation process was to evaluate different chord and swept varying platforms. Consequently, experiments were chosen from the work of van Dam et al. (1991). Both wings were tested in NASA Langley's 7 x 10-foot high-speed wind tunnel. The first wing was a quasi-elliptical planform with an unswept quarter chord line as shown in figure 3.13. The second has a variable sweep angle as shown in figure 3.14. Both wings have an aspect ratio of 6 with a root chord and span of 8 inches (0.20 m) and 48 inches (1.22 m) respectively. The wings also have the same airfoil as the NASA NLF(1)-0416 with a maximum thickness of 16%. The models were mounted on a 6-component strain gauge

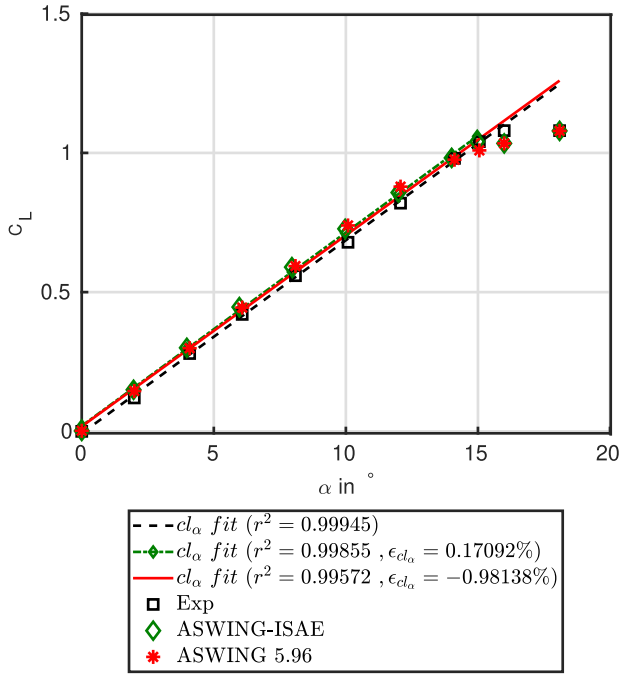

(a) C_L

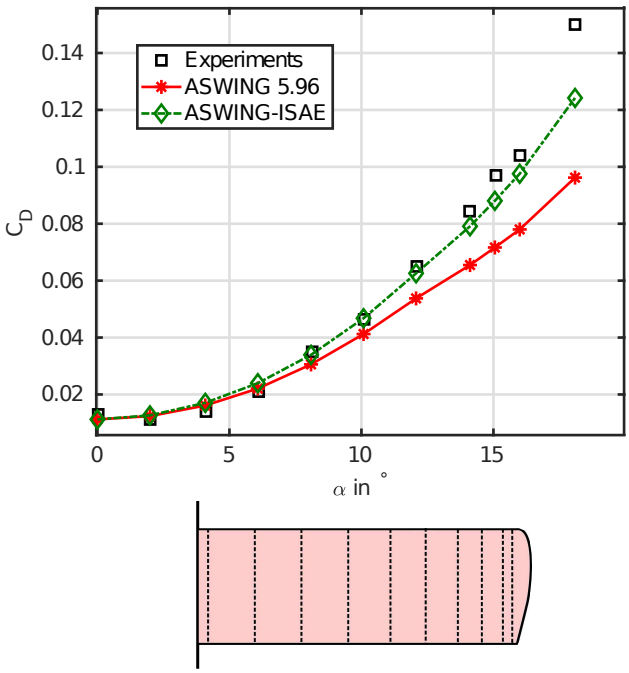

(b) C_D

Figure 3.11: CASE # 1 : Straight wing C_L and C_D predictions versus experimental from [1]. Improvement of C_L and C_D brought by a viscous loop and a quadratic varying 2D drag coefficient.

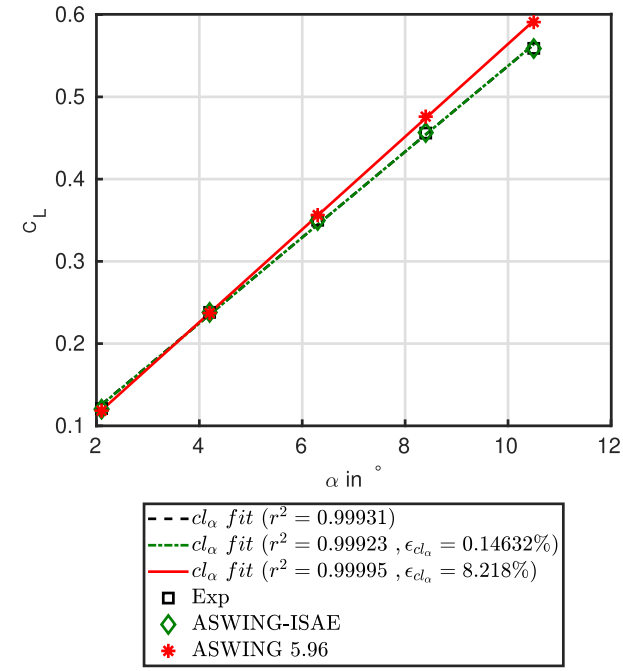

(b) C_L

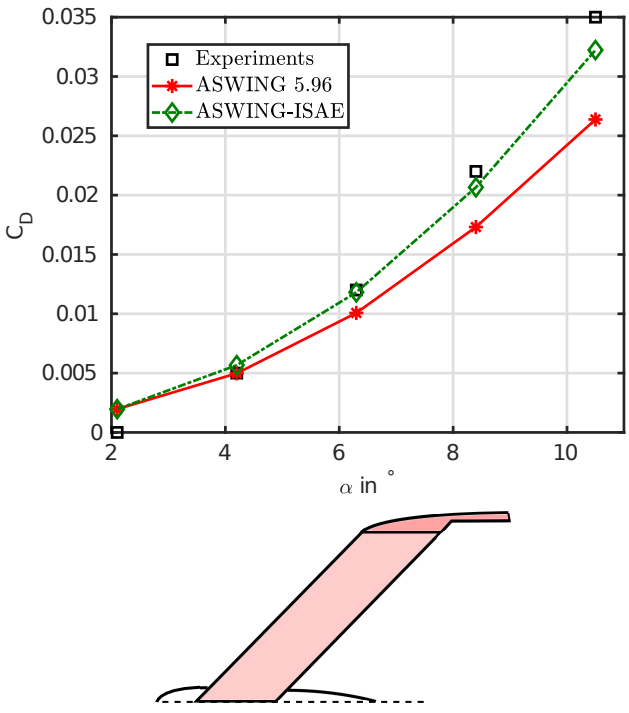

(b) C_D

Figure 3.12: CASE # 2 : 45° swept back wing C_L and C_D predictions versus experimental from J. WEBER, Dr.rer.nat. and G. G. BREBNER, M.A-1958. Improvement of C_L and C_D brought by a viscous loop and a quadratic varying 2D drag coefficient.

balance supported by a straight string. The latter was chosen to match the maximum balance to the maximum expected load. The measurement accuracy was reported to be approximately 0.1% of full scale for normal force (lift) and 0.3% for axial force (drag). The accuracy of the angle of incidence was reported to be less than 0.01°. Finally, the uncertainty in the lift and drag coefficients was 9.10^{-4} and 3.10^{-4} respectively. The latter makes this experimental set highly reliable. The boundary layer transition was forced by the use of a 0.12-inch (0.3 cm) strip line placed on the top and bottom surfaces of the wing. A constant chordwise position was chosen to be 0.075c from the leading edge. Numerically, the geometries of the cases were reproduced using *equations (2) and (3)* of the van Dam et al. report (1991). As the boundary layer transition was reported at 0 angle of attack, XFOIL was used with N_t chosen to match the turbulence level of the configuration. The same number of circulation nodes was used as in the previous cases. Figures 3.13 (a) and 3.14 (a) show the lift predictions in the linear range of ASWING and ASWING-m. Again, the second seems to be more accurate, especially at high angles of attack. Both linear slope errors remain excellent. Figures 3.13 (b) and 3.14 (b) show the improvement obtained by taking into account the angle of attack dependence of the drag polar. The improved accuracy is not so obvious for the third case, but it is for the fourth. Note that if information about the transition of the boundary layer is provided when ASWING is mixed with XFOIL, it can predict the drag of a wing quite well.

CASE 5: Straight Wing with 45° Dihedral Angle

The last non-linear stress test for the lifting line is a straight wing with a dihedral angle of 45°. Again, as the second case, it is very unlikely to be seen, so it is considered a boundary case. This time no experimental data is available, so this is the first of a few high-fidelity CFD cases presented as stress tests. StarCCM+ was used to calculate the lift and drag coefficients of the wing. The aspect ratio of the wing was 5 with a NACA0012 airfoil. The Reynolds number was set to 100,000 (typical range for mini-UAVs). A structural grid mesh with a symmetry plan was used. The boundary layer was also discretised. For moderate angles of attack, a steady-state solver was sufficient to calculate the lift and drag coefficients. However, for angles of attack greater than 10° an unsteady solver had to be used due to the unsteady behaviour of the boundary layer. The C_L and C_D are computed along the z- and x-axis in STARCCM, while in ASWING they are computed along the planform normal and the chordwise vector. In order to respect the StarCCM+ formalism, the lift distribution has been integrated into ASWING and the lift coefficient has been calculated along the z-axis. The figures 3.15 (a) and (b) show the lift and drag predictions. Note that in figure 3.15 (a) we use the term "uncorrected LLT" to denote the previous comments on how the lift coefficient is calculated in ASWING. For the sake of clarity, only the lift prediction of the ASWING-m version is plotted. Again, excellent agreement is observed for the linear slope. With regard to drag, the better performance of ASWING-m in predicting drag is highlighted.

CASE 6: Effect of ailerons on rolling and yawing moment coefficients

As seen in the theoretical section, ASWING can take into account the effect of different ailerons or flaps on the lift and drag distribution. A lift asymmetry induced by deflected ailerons has 2 main effects, inducing rolling and yawing moments. To evaluate this feature, the experimental data of HEALD and STROTHER 1929 and 1930 have been used. In their work, they evaluated the rolling and yawing moments induced by the anti-symmetric deflection of different ailerons. The wing was straight with an aspect ratio of 6, again a very good stress test for the lifting line model. The airfoil was the ClarkY. The test was carried out in the 10ft Bureau of Standards wind tunnel. Rolling moments were measured using a balance connected to the wing tip by a stiff wire at the quarter chord line. The yawing moments were measured using the same type of balance but connected to the tail of the fuselage. The moment coefficients were then calculated at the wing root on the quarter chord line. The accuracy of the measurements is given in the author's work and is excellent (about 1%). Various ailerons with different span and chord lengths were tested. Figure 3.16 (a) shows the different configurations (lower span variation, upper chord variation). The flap deflection range was 0 to 40° with an interval of 4°. The author also specified that the slots created by the deflected ailerons were filled with wax to ensure a certain smoothness of the geometry. In total, 3 wing incidences were tested, but we will present only 2 for the sake of this document readability.

Numerically, the ClarkY airfoil polars and flap derivatives were calculated in XFOIL and summarised in the table 3.4. Note that convergence failure was observed at high flap deflections in XFOIL, the range had to be reduced to calculate the flap derivatives. As ASWING can natively provide the roll and yaw moment coefficients, the bench was easily reproduced without the airframe. Again, 40 circulation point circulation variables were sufficient to obtain satisfactory results.

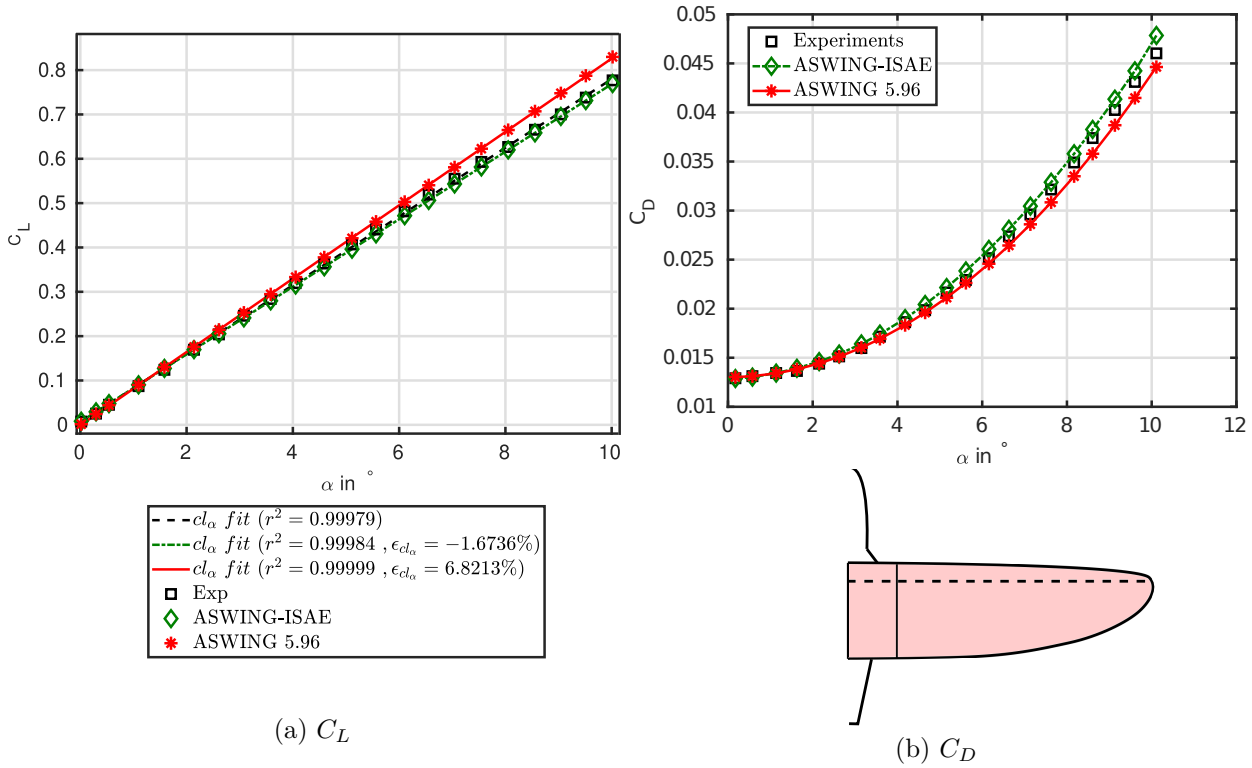

(a) C_L (b) C_D

Figure 3.13: CASE # 3 : Quasi-Eliptical wing C_L and C_D predictions versus experimental from van Dam et al. 1991). Improvement of C_L and C_D brought by a viscous loop and a quadratic varying 2D drag coefficient.

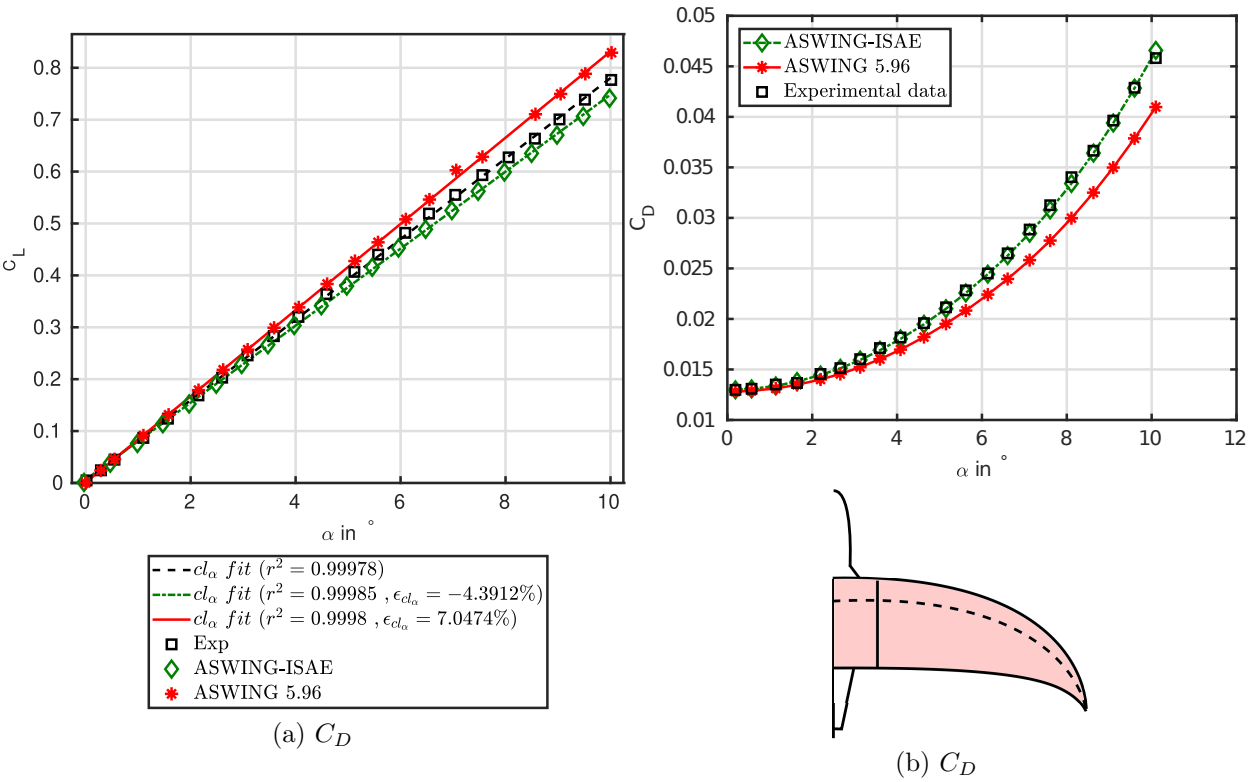

(a) C_D (b) C_D

Figure 3.14: CASE # 4 : Crescent wing C_L and C_D predictions versus experimental from van Dam et al. 1991. Improvement of C_L and C_D brought by a viscous loop and a quadratic varying 2D drag coefficient.

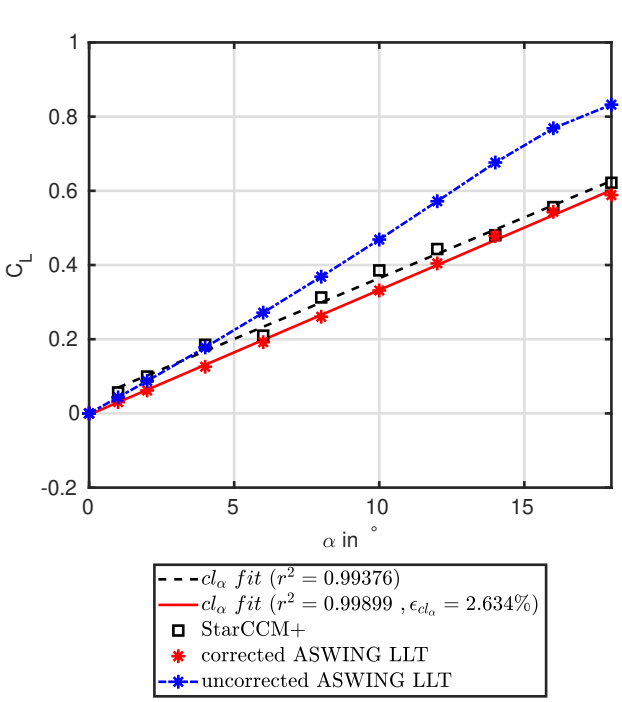

(b) C_L

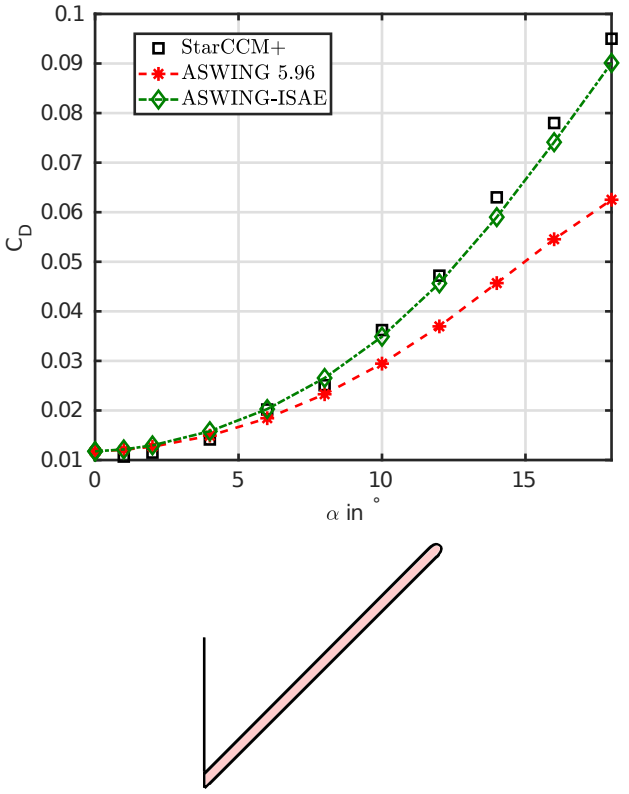

(b) C_D

Figure 3.15: CASE # 5 : Straight Wing with 45° dihedral angle C_L and C_D predictions

Figure 3.16(a)-(d) shows the ASWING predictions of the rolling and yawing moment coefficients for different aileron configurations and the level flight condition ($\alpha = 4°$). HEALD and STROTHER reported that there were 2 linear behaviours, from $\delta_F = 0°$ to $\delta_F = 20°$ and above. In the first, we compared the linear slopes. ASWING shows excellent agreement with experiments for the rolling moment coefficient as shown in figure 3.16(a) and (b), regardless of the aileron configuration. The average slope error is 4.4 %. The same conclusions cannot be drawn for the yawing moment coefficient predictions (figures 3.16(c) and (d)) where the slope error is above 50%. The yaw moment induced by a deflected aileron is mostly drag-related. Or ASWING assumes a symmetrical shift of the viscous/pressure drag polars when a flap is deflected negatively or positively. In reality, this is not the case. This can be easily seen in XFOIL. The asymmetry of the viscous/pressure drag is not taken into account, whereas the lift-induced one is. As a result, ASWING misses a large contribution to the yawing moment. The same tests were carried out but in the post-stall condition ($\alpha = 16°$). These are interesting to show the limits of the ASWING. Based on figures 3.17 (a) to (b), the framework is no longer able to predict the rolling moment coefficients even for moderate flap deflections. The average pitch error increases to 20%, which is unacceptable. For the yaw moment (figures 3.17 c and d) the same remarks are made as for the level flight case.

Finally, the last remarks are made for high-deflected ailerons (above 20°). Emphasis is placed on the level flight configuration and the predictions of the rolling moment coefficients. ASWING seems to capture the slope damping due to the local stall, but not enough. A first suggestion would be that the geometry becomes extremely sharp at high flap deflection, regardless of the hinge position. At a lower angle of attack, the airflow would be more likely to detach, which is not captured by ASWING. In conclusion, ASWING correctly predicts the rolling moment coefficient induced by the ailerons for moderate deflections and when the wing is in its linear lift range. It can also predict an induced yawing moment, but not accurately.

CASE 7 and 8: Multiple lifting surfaces, tandem aircraft

As seen in the theoretical sections, ASWING can take into account the wake interactions between multiple lifting surfaces. In this section, 2 different sets of data from the literature have been used. The C_L predictions of each lifting surface in the linear and pre-stall range have been evaluated. Total C_L vs C_D predictions were also evaluated. CASE 7 is based on experimental data from the work of (Feistel et al., 1981) and compared to high fidelity and potential

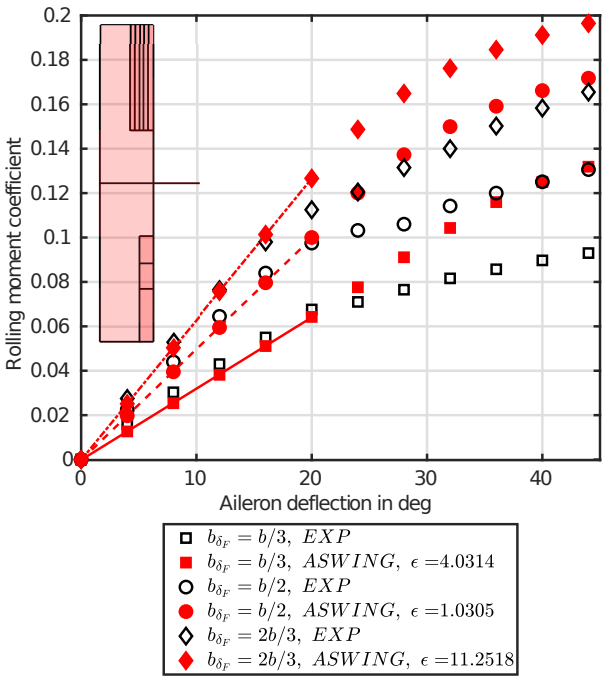

(a) $C_l(\delta_F)$, span varying

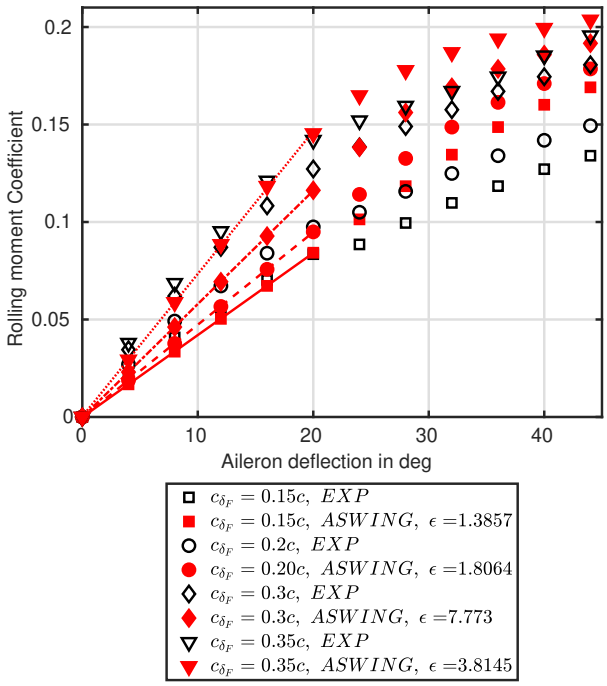

(b) $C_l(\delta_F)$, chord varying

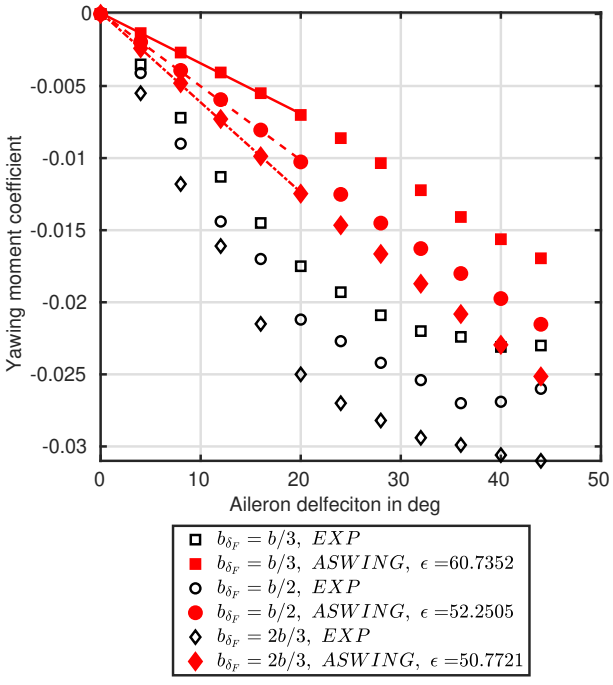

(c) $C_n(\delta_F)$, span varying

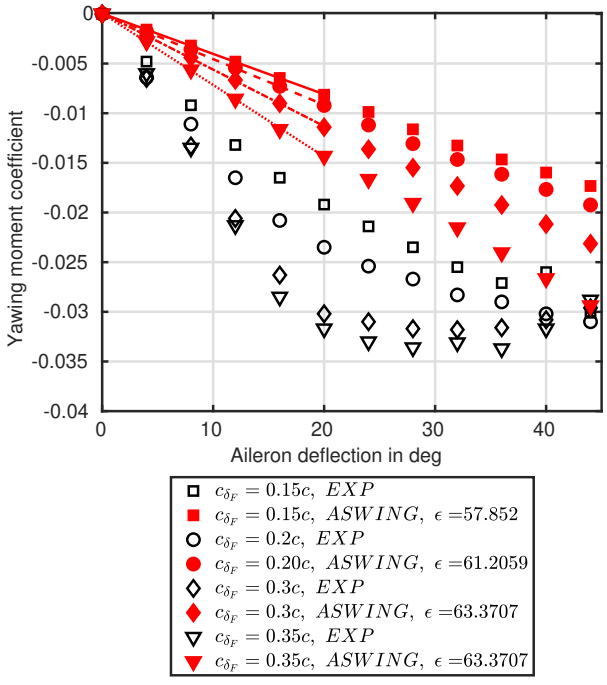

(d) $C_n(\delta_F)$, chord varying

Figure 3.16: CASE # 6: Effect of various deflected ailerons on the rolling and yawing moment coefficients. ASWING prediction against experimental data (HEALD and STROTHER, 1929). Level flight condition (un-stalled $\alpha = 4°$)

Table 3.4: ClarkY wing parameters (Re = 3E5)

Ailerons chord	0.15c	0.20c	0.25c	0.30c	0.35c
$dc_l/d\delta F$	-0.039	-0.045	-0.055	-0.061	-0.71
cl_α			5.77		
α_0			$-3.77°$		
ϑ			$4°$		

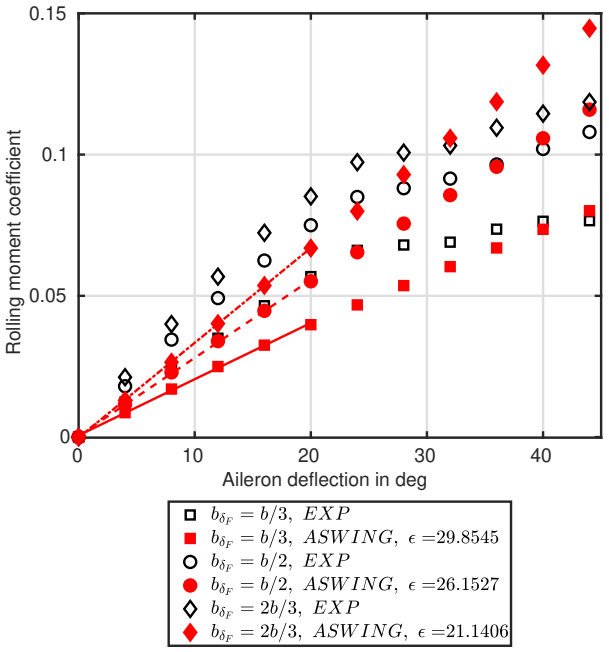

(a) $C_l(\delta_F)$, span varying

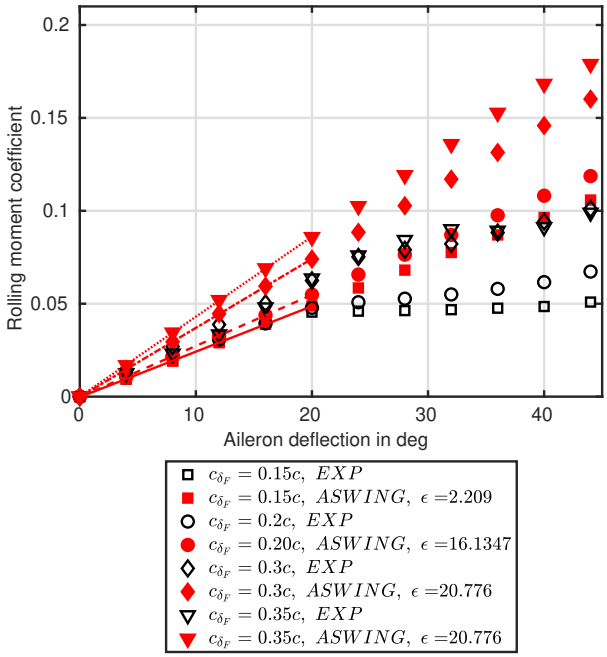

(b) $C_l(\delta_F)$, chord varying

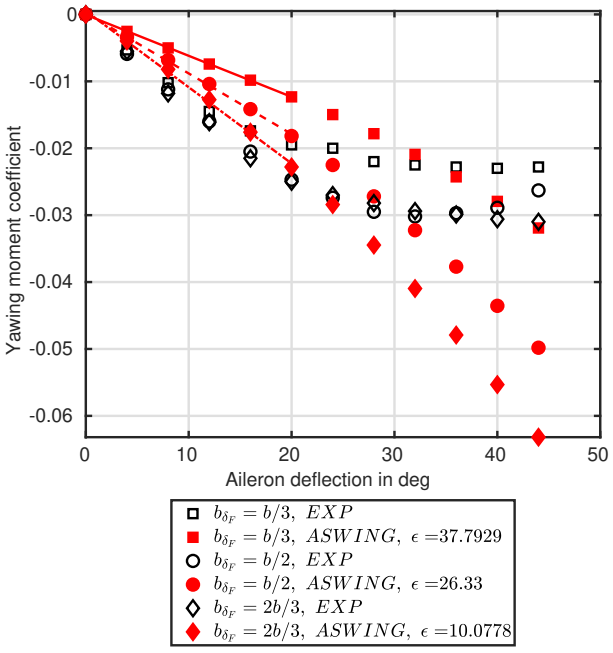

(c) $C_n(\delta_F)$, span varying

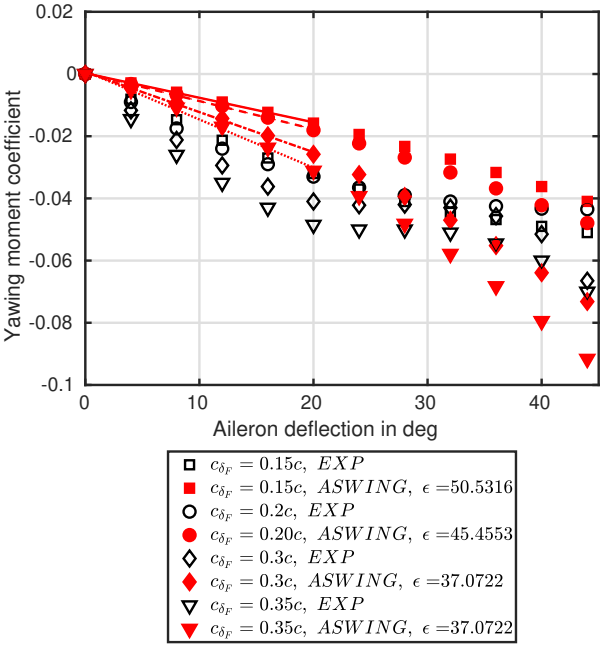

(b) $C_n(\delta_F)$, chord varying

Figure 3.17: CASE # 6: Effect of various deflected ailerons on the rolling and yawing moment coefficients. ASWING prediction against experimental data from HEALD and STROTHER 1930. Level flight condition (post-stall $\alpha = 16°$)

methods of (Cheng and Wang, 2018). CASE 8 is a high-fidelity CFD (RANS) case presented in the latter author's paper.
In case 7, the experiments were performed in the 7 x 10 ft wind tunnel at the Ames Research Center. The tandem configuration consists of 2 rectangular blades: one forward and one aft. Both were constructed based on the GA(W)-2 airfoil section and had the same aspect ratio, which is 6. The forward wing span and chord were $b_f = 1.29m$ (4.24ft) and $c_f = 0.22$ (0.71ft) respectively, while the rear wing span and chord were $b_b = 1.83m$ (6.0ft) and $c_b = 0.305m$ (1.0ft). In their work, the authors studied the influence of geometric parameters on the overall tandem performance. Among them, the vertical and horizontal gaps could be modified. In this paper, only the worst-case scenario is presented, where the wake interaction was the strongest. So the vertical gap was chosen to be positive from the front to the rear wing with a value of $G = 0.5c_f$. Similarly, the horizontal gap was chosen to be $1.63c$. The reader can get an overview of the geometry in figure 3.18. The tests were carried out at a Reynolds number of 1.6E6 and the angle of attack varied from -2 to 20°. Two balances were placed on each wing to measure each wing C_L and C_D.
In the 8th case, the geometry was slightly different as the wing spans were almost the same. The forward wing span is 2.1805 m, while the rear wing span is 2.0424 m. They have the same chord and airfoil, which is 0.129m and NACA4309. The horizontal and vertical distances are set to 0.89m and -0.101m. Note that a square section airframe is modelled with a length of 1.25m and a section size of 0.129 by 0.129m. The geometry is shown in figure 3.19. The flight speed is set to 30m/s for an equivalent Reynolds number of 265000. RANS calculations were performed in the linear and pre-stall domains. The latter was performed using a structured grid solving the 3D Navier-Stokes equations using the finite volume method and the SST $k-\omega$ turbulence model. The author provided the C_L of each lifting surface and the total lift. Note that the drag was not presented. The author also presented the previous set with and without the influence of the airframe.

Numerically, the same comments are made for both cases. The airframe influence was neglected on ASWING because it cannot model non-circular airframes. Furthermore, the exact dimensions of the latter have not been given. For each platform, 40 circulation nodes were selected using a cosine clustering function. Note that Cheng and Wang (2018) uses a slightly different clustering function for case 7. As the wingspans are not equal, i.e. the front wing is shorter, they suggested using a dual cosine clustering function on the rear wing. This, in fact, recovers more accurately the effect of the forward wing wake, as the circulation mesh on the rear wing is more refined where the wake gradient is important. In ASWING it is not possible to implement such clustering functions. However, it will be seen that this is not necessarily a problem.

In both cases, the predictions of ASWING-m are not presented. Instead, a comparison of ASWING predictions with other authors' potential methods and high-fidelity methods is proposed. In the linear domain, the slopes of the lift coefficients were calculated using linear regression. The results for case 7 are shown in figure 3.18(a)-(d). As with the single planform, the ASWING C_L predictions (Figures 3.18a-c) are in excellent agreement with the experiments. Note that the ASWING slopes errors are less than 8%. They are also equivalent to the results obtained by Cheng and Wang (2018).It is interesting to note that for C_L predictions, the high-fidelity CFD results are almost comparable to those of the LLT. Regarding the drag predictions (Figure 3.18-d), the ASWING predictions are in good agreement at a high angle of attack and become weaker around zero lift.

Regarding the 8th case, again the C_L predictions (cf. Figures 3.19 a to c) are in excellent agreement with the CFD data. Note that Cheng and Wang's LLT error seems to be more important than ASWING. This could be due to the airfoil polar calculations. ASWING and Cheng and Wang's work is based on the same physics and assumptions. It is therefore very unlikely that ASWING is better than the author's work. Note that ASWING captures the pre-stall effect on both tandem wings, while [6]'s LLT doesn't.

In summary, we can conclude that ASWING can correctly predict the lift and drag of tandem configurations. Despite ASWING's horseshoe representation, which is straight and shed from the horseshoe boundary and not from the trailing edge of the airfoil, it has no or little effect on the wake interaction. Finally, the dual cosine clustering for the circulation mesh does not seem to have a major impact on the quality of the predictions. The last two examples conclude the section dedicated to the steady lift and drag predictions of the ASWING lifting line model and its proposed improvements.

CASE 9 A-E : Lift distribution and centre of pressure location

So far, the main problem that could be attributed to the previous cases is that they do not present local lift predictions, which is actually mandatory for a flexible aircraft framework. In fact, they have all presented total lift coefficient predictions. Despite for

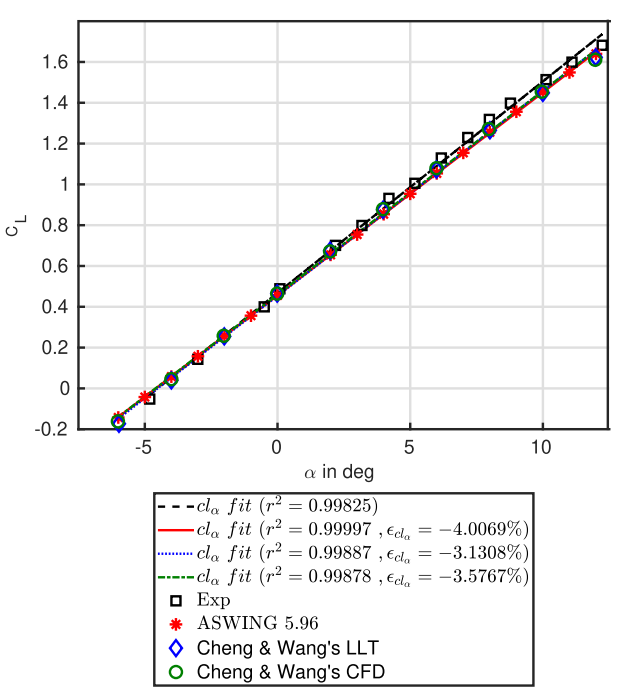

(a) Total C_L

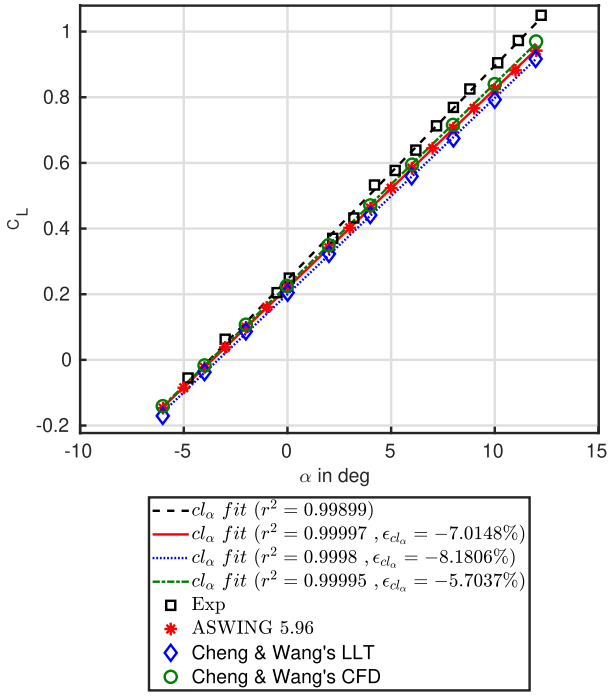

(b) Backward wing C_L

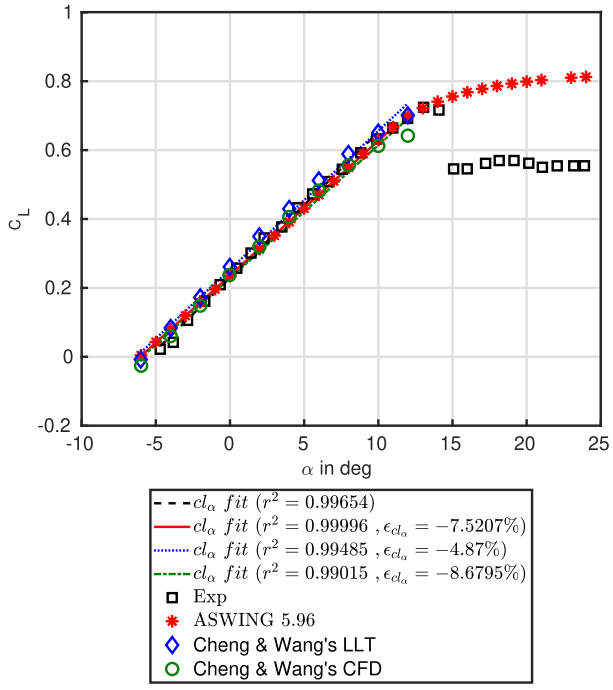

(c) Forward wing C_L

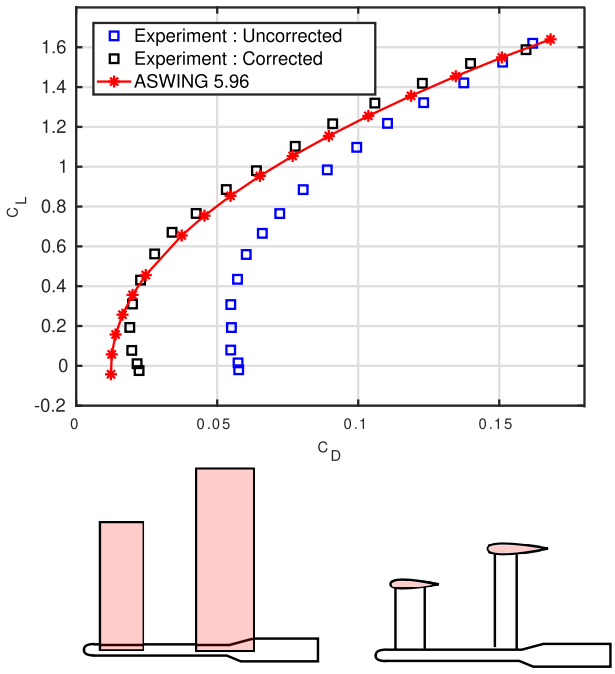

(d) Total C_L versus C_D

Figure 3.18: CASE 7 : Tandem #1, total, backward and forward wing C_L and C_D predictions versus experimental and CFD data from Feistel et al. (1981)and Cheng and Wang (2018))

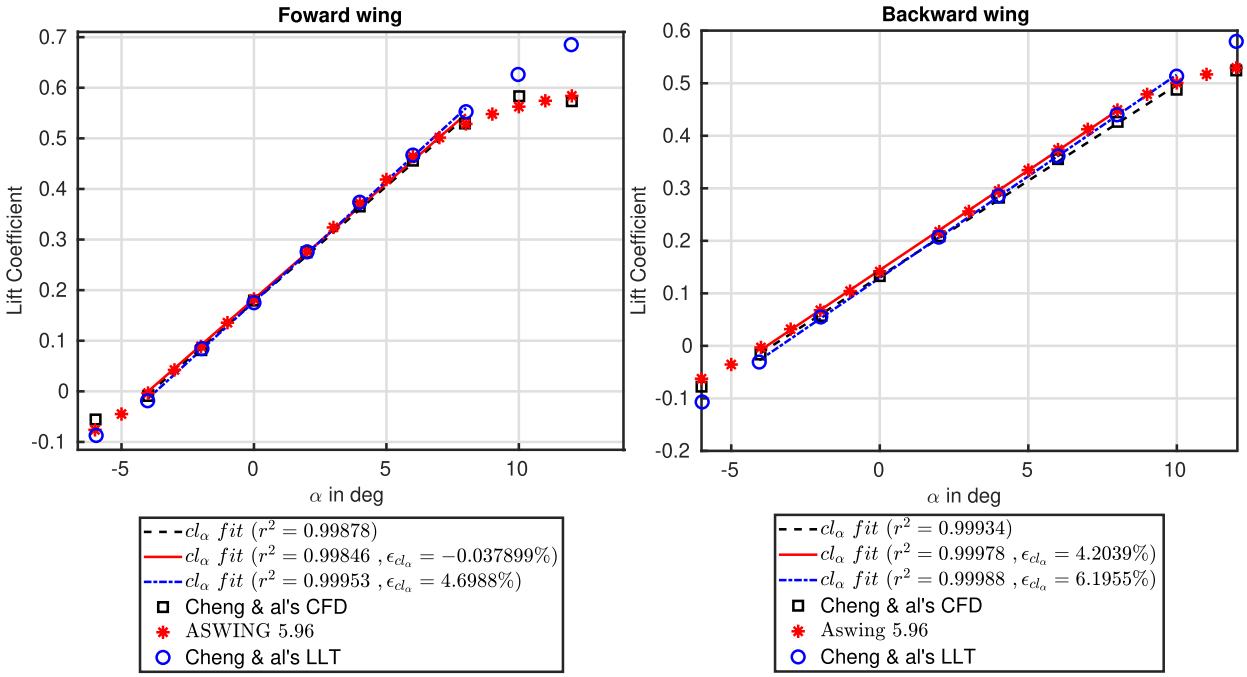

(a) Forward wing C_L

(b) Backward wing C_L

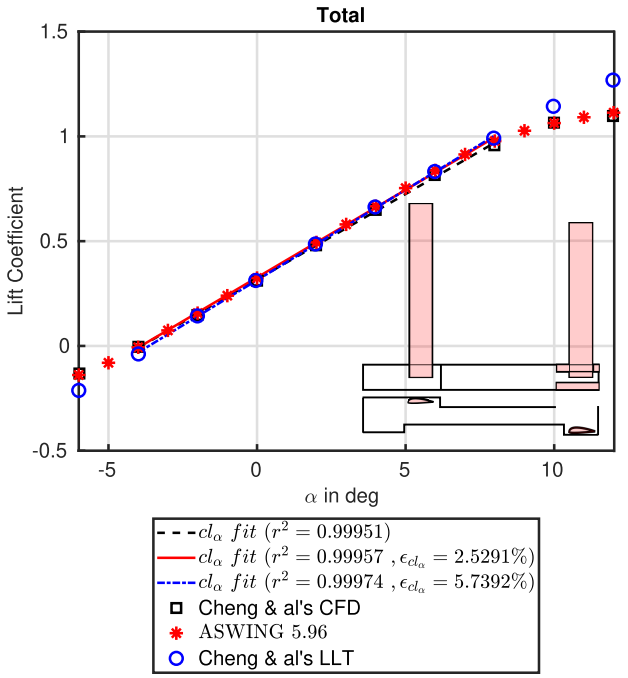

(c) Total C_L

Figure 3.19: CASE 8 : Tandem #2, total and backward wing C_L predictions vs higher fidelity data from Cheng and Wang (2018)

different lift distributions, the total lift coefficient can be the same. Therefore in this section 5 swept forward and backward wing lift distributions and loading predictions are compared with experimental data.

Experimental bench: The work of McCormack and Stevens Jr (1947) and VanDorn and DeYoung (1947) has been used. Five swept forward and backward wings were tested. The root and tip airfoils were NACA0015 and NACA23009 respectively. The wing dihedral angle was kept at 0 degrees. The twist in the chord plane of the wing was approximately 0.25 degrees. The main geometric parameters are summarised in the table 3.5. Note that the sweep angle is defined from the quarter chord line, with a negative angle defining a forward sweep angle. The wing was mounted on a faired string attached to a 3-strut support system. The tests were carried out in the AMES 40 x 80 ft wind tunnel at a Reynolds number of 9E6. Pressure sensors were placed at various spanwise and chordwise locations. The results were integrated and presented as local lift coefficients.

Numerical bench: The benches were easily reproduced in ASWING. Due to the high Reynolds number, XFOIL analysis of NACA0015 and 23009 was not performed. The airfoil lift slope and zero lift angle of attack were set to 2π and $0°$. During the simulations, a drop in the lift coefficient distribution at the wing root was observed. For some reason, this drop increases with the sweep angle regardless of its sign. No explanation has yet been found. In order to get rid of this problem, the circulation mesh was voluntarily refined. Thus, 200 instead of 40 circulation piece-wise variables were used for the simulations.

Results: The ASWING predictions are compared with the experimental data of McCormack and Stevens Jr (1947) in figure 3.20. Irrespective of the sweep angle, ASWING is able to correctly predict the lift distribution of low aspect ratio swept wings. It can also provide qualitative predictions of the spanwise location of the wing centre of pressure. For example, it can be seen that the centre of pressure tends to move towards the wing root at negative sweep angles and towards the wing tip at positive sweep angles. From a structural point of view, this would result in a lower root bending moment. Note that VanDorn and DeYoung (1947) have proposed a comparison between a lifting line model and a vortex grid model. Both have similar performance in predicting lift distributions. Therefore, it is clearly reasonable to use the lifting line theory for wings with these aspect ratio.

CASE 10 Wingtip and Tip Sails:

An interesting feature of ASWING is that it can model multiple lifting surfaces. Thus, experimental data from Miklosovic (2008) has been used to assess the predictions of the effects of wingtip devices. In their work they have tested various wingtip devices, from tip extensions to tip sails with different cant angles. The devices tested in this thesis are shown in figure 3.21 (a). These were chosen as they are the only ones for which lift and drag measurements have been provided. Miklosovic also provided the airfoil polars as they also compared their results with the Vortex Lattice predictions. Therefore, for the sake of readability, the numerical bench is not described here. Figure 3.21 (b) shows the lift predictions of ASWING 5-96 against the experimental data. Linear slopes have been calculated on the apparent linear region. As can be seen, ASWING does a is capturing well the increase in the linear lift slope due to a blended wingtip. Note that the lift measurements of the wingtip configuration have not been provided. For the other cases, which are planar wings, the prediction errors are quite consistent with the previous cases presented earlier in the chapter. Figure 3.21 (c) shows a comparison of the ASWING drag predictions with experimental measurements. For the planar wings, the drag predictions are in good agreement with the experiments. It captures well the increase in zero lift drag coefficient for the extended tip configuration due to the increased wetted area. However, ASWING is not able to provide good predictions for the tip sails. In fact, during the simulations, some local lift divergences were observed at the connection between the tip sails and the wing. ASWING is not able to trigger the circulation continuity at the wing tip because of the 3 wing tips, so it does not manage the close interactions in this specific case. Thus, in this example, ASWING can capture the effect of the continuous wingtip, but not of the tip sails.

CASE 11: Discussion of transonic flight: KC-130 with Whitcomb winglets

The analysis of the single planform concludes with a discussion of transonic flight. ASWING is clearly not designed for this flow regime. However, it can provide interesting results on the effect of wingtip devices on the lift and drag predictions of a first-generation jet aircraft. To illustrate this, experimental data from Jacobs et al. (1977) has been used. They have tested different wingtip devices on a small-scale Boeing KC-135. In total we present 4 different configurations, the wing alone, the wing with a tip planar extension, the wing with an upper winglet and the wing with the Whitcomb winglet. The details of the geometry can be found in Appendix D of this chapter. We will not go into too much detail about the parameters used here, as we only want to show the tendency. Of course, reasonable values have been chosen as MSES

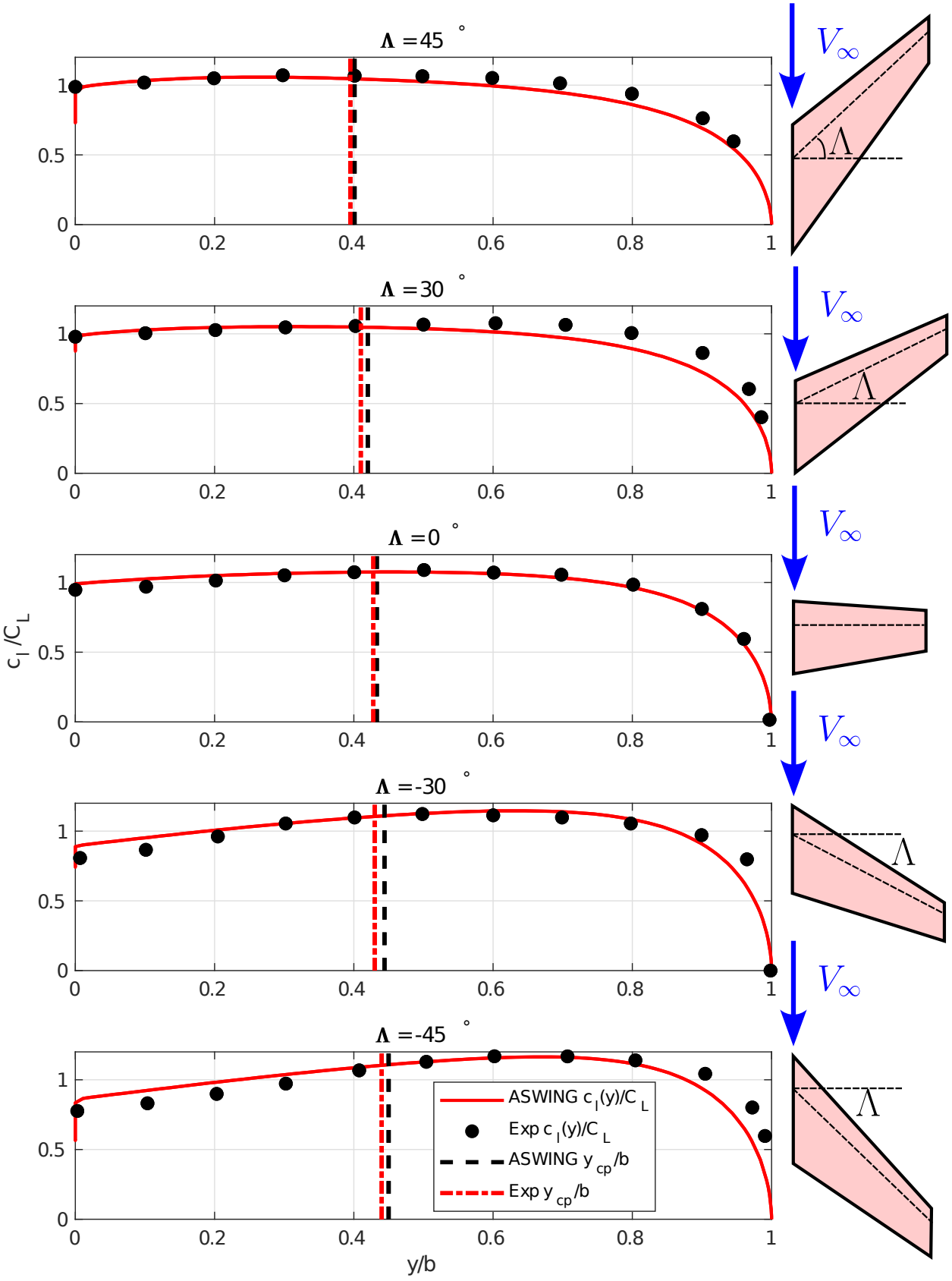

Figure 3.20: CASE # 9 A-E: lift coefficient and centre of pressure location predictions for 5 swept forward and backward wing. Comparison with experiments from McCormack and Stevens Jr (1947)

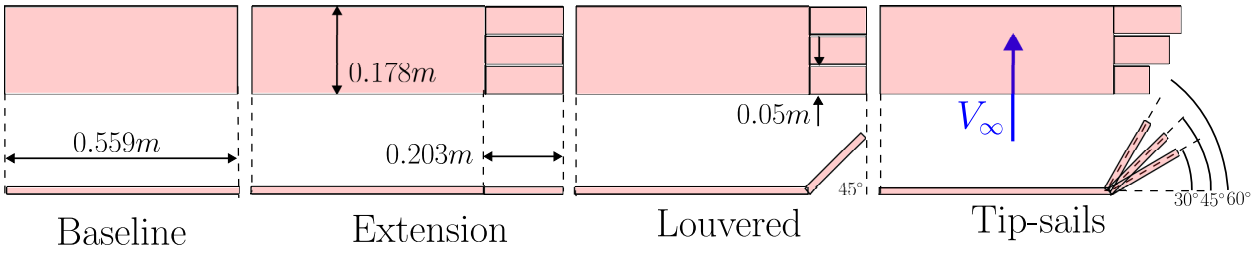

(a) cases geometry parameters

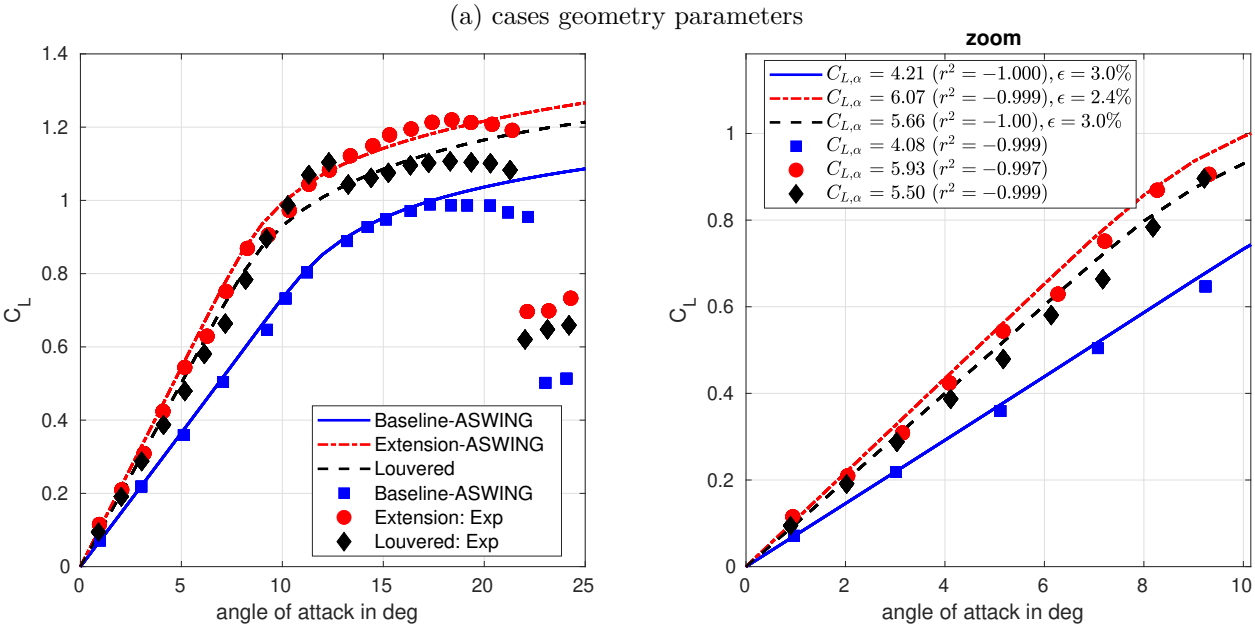

(b) Lift predictions up to stall and lift slope comparison

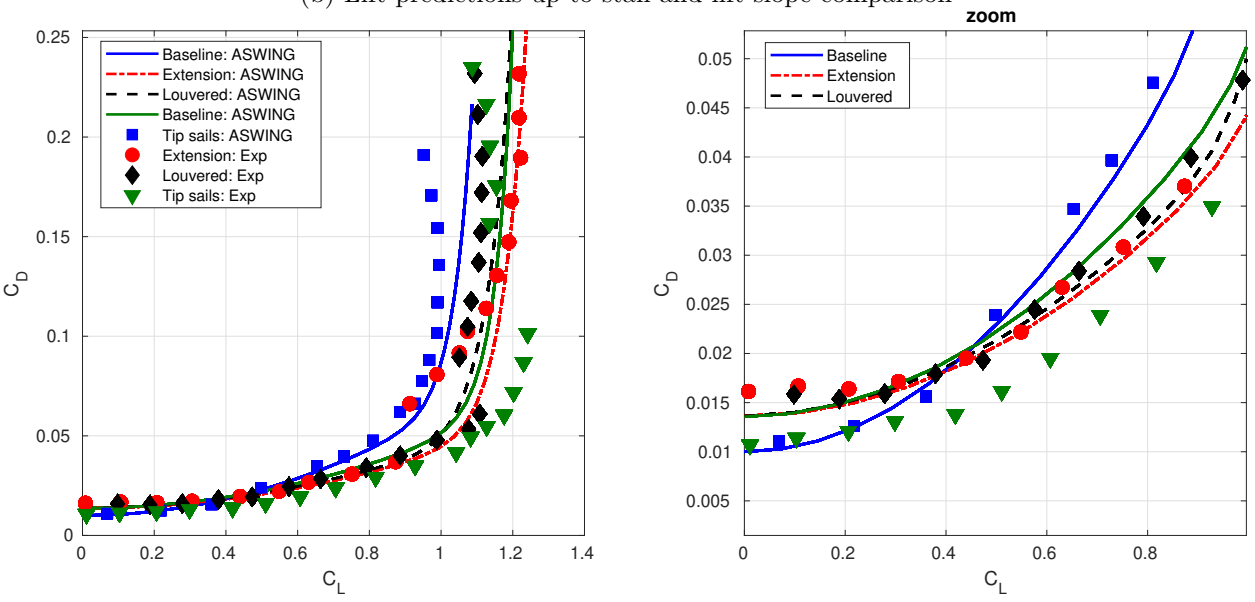

(c) drag predictions with zoom (right)

Figure 3.21: CASE # 10: Lift and drag predictions of configurations with bent winglet and tip sails. Comparison with experimental data from (Miklosovic, 2008)

CASE	Λ ($in°$)	b (in m)	AR	c_R (in m)	c_T (in m)
9-A	-45	9.87	3.12	4.69	1.76
9-B	-30	11.09 m	4.69	3.46	1.40
9-C	0	9.31 m	4.66	2.65	1.44
9-D	30	10.99 m	4.84	3.23	1.42
9-E	45	10.23 m	3.84	4.07	1.70

Table 3.5: Swept forward and backward wings parameters ($\Lambda < 0$: swept forward)

was used to compute the airfoils polars. The figures 3.22 (a) and (b) show the lift predictions against the experimental data. The linear slopes have been calculated again. While the agreement is quite good at Mach number 0.7 (figure 3.22-a), the ASWING loses its way at higher Mach numbers. Although the Prandtl-Glauert correction factor is activated, the ASWING does not capture the Mach number effect on the lift slope well. Figures 3.22 (c) and (d) show the drag versus lift coefficient predictions and as expected, ASWING does not correctly capture the drag, especially at high lift coefficients. At higher Mach numbers the discrepancies are even worse. However, it does correctly capture the tendencies introduced by the use of winglets, which is a reduction in drag. Very small reductions, such as the one reported, have been observed in cruise conditions. A good improvement to ASWING would therefore be to make the airfoil parameters a function of Mach number and angle of attack. In fact, in transonic flight, the wave shock seems to have a large influence on the airfoil drag. The wave shock itself creates drag (momentum defect) and also has an effect on the boundary layer thickness and separation as shown in Appendix D, which drastically increases the profile drag (pressure and friction). Consequently, MSES could be used to generate transonic airfoil polars at different Mach numbers, which would be implemented as a bi-polynomial function in ASWING. Improvements in lift and drag predictions should be observed. Note that the Plandtl-Glauert correction factor should be disabled as the compressibility effects will be embedded in the polynomial functions.

12 A-B: Ground effect on a rectangular wing with various flaps:

As presented in the theoretical section, ASWING can model two types of ground surfaces, solid and free. In this subsection, the experimental data of Recant (1939) have been used to evaluate the ASWING ground predictions on the lift and drag. This will highlight when the ground effects are strong. In their work, they tested several wings, a rectangular one and a tapered one with different flap configurations (plain and slotted). Similar comments have been made about the wing planform, so only the rectangular one is presented here. However, two configurations are shown, the wing without flaps and with slotted flaps. This choice has been made mainly to highlight the weakness of ASWING in predicting the ground effect on wings with slotted flaps.

Expeirmental bench:

The tests were carried out in the NACA 7 x 10 foot wind tunnel. The wing model was a rectangular wing with an aspect ratio of 6, a span of 60 inches (1.524 m) and a chord of 10 inches (0.254 m). The airfoil was a NACA23012 as shown in figure 3.23 (a). For the slotted flap version, the hinge axis was placed at 0.82 of the wing chord from the leading edge with a fixed flap down angle of 40 degrees. The wing was anchored to a balance at on the quarter chord line at the root. The altitude was then changed according to this position. For both configurations (no flap and slotted flap), drag and lift measurements were made at an effective Reynolds number of 900,000 over a range of angles of attack from -6 to 16 degrees. Several altitudes were tested, but due to the age and lack of clarity of the plots, only three are presented here. The height is given as the ratio of the chord h/c, where h is the height of the wing.

Numerical Bench:

Unfortunately, Recant's paper does not give any information about the location of the wing transition or the level of turbulence in the wind tunnel. However, these experiments were part of a larger project where 2D experimental lift and drag measurements were made. Therefore, in this case, XFOIL was not used to obtain the aerodynamic profile parameters of ASWING. Instead, the experimental measurements provided by Wenzinger and Harris (1939) have been used to obtain the lift slope, zero lift drag and angle of attack of both configurations. A linear interpolation was used to obtain the 2D lift slope. For the wing without flaps the airfoil parameters are $c_{l,\alpha} = 6.0$, $c_{d,0} = 0.01$ and $\alpha_0 = -1.0°$ while for the slotted version they are $c_{l,\alpha} = 7.44$, $c_{d,0} = 0.04$ and $\alpha_0 = -12.5°$. Note that the lift plot for plain wing has been plotted with a shift of zero lift angle of attack at the origin, so the ASWING prediction results have also been shifted accordingly. As the slotted flap deflection was the same along the test, in ASWING the airfoil parameters were simply modified instead of implementing

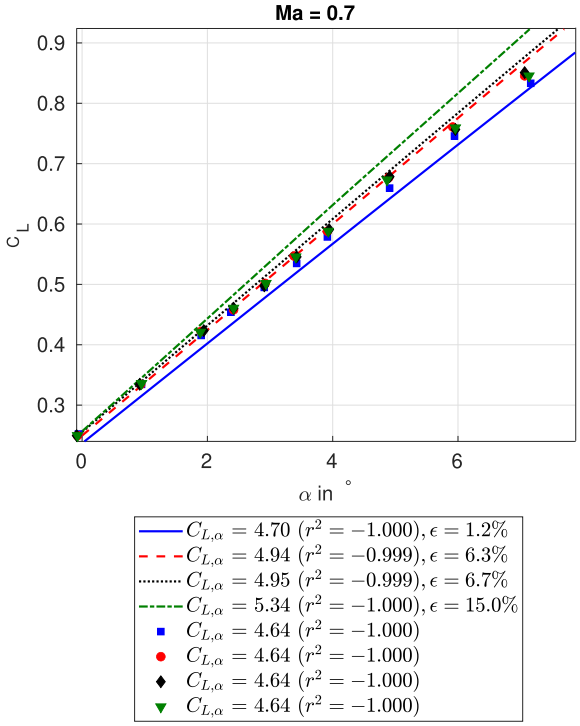

(a) Lift predictions Ma = 0.7

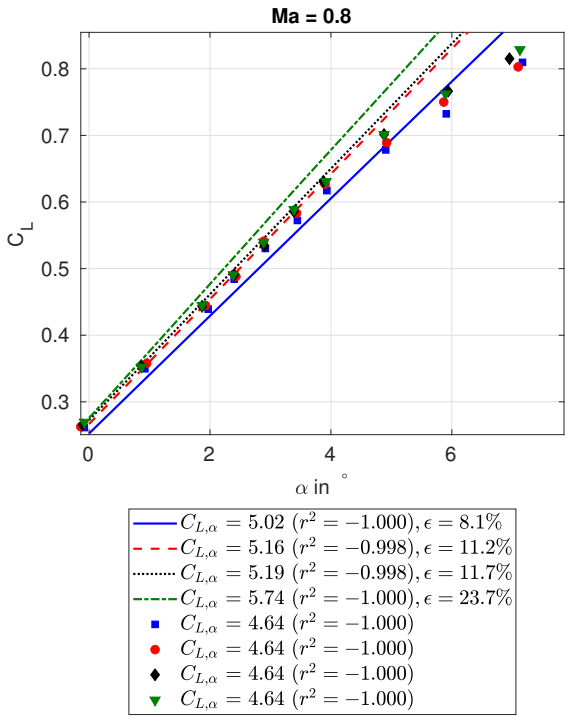

(b) Lift predictions Ma = 0.8

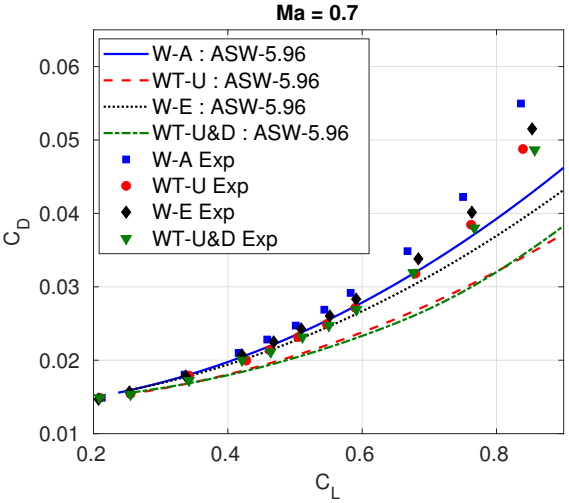

(c) Drag predictions Ma = 0.7

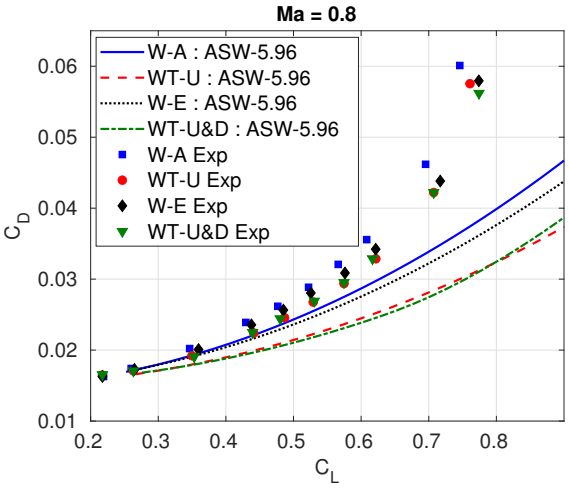

(d) Drag predictions Ma = 0.8

Figure 3.22: Lift and drag predictions of the KC-135 wing with various wingtip devices. W-A : Wing Alone, WT-U : Wingtip up only: W-E : Wing Extension, WT-U&D Wingtip Up and Down. Experimental data from Jacobs et al. (1977) part of the program Barber and Selegan (1982)

the flap derivative.

Results:

Figures 3.23 (a) to (d) show a comparison between the ASWING lift and drag predictions and the experiments for both configurations. For the wing without flaps, ASWING provides excellent agreement with the experiments for the lift slope increase due to the close proximity to the ground. The error of the lift slope prediction is less than 5 %. For the drag predictions, the results are in reasonable agreement with the experiments, the reduction of the lift-induced drag is well captured for positive lift coefficients. For high lift coefficients, the predictions start to show discrepancies. Note that when the wing was quite close to the ground the ASWING post-stall drag model was divergent, once deactivated the prediction results became better. This should be taken into account when investigating ground effects.

For the wing with slotted flaps, the ASWING predictions are not satisfactory for both drag and lift. It seems that the ground effect on the slotted flap physics is dominant compared to the ground effect on the wake vorticity. The former is not captured by the ASWING theoretical model, hence the observed discrepancies.

In conclusion, ASWING can predict well the effect of ground proximity on lift and drag as long as the aircraft is not in a high lift configuration. For example, in a dynamic soaring trajectory, where the altitude can easily be low in order to capture the maximum strength of the wind gradient, the effect of the ground on the aerodynamic performance can be captured. It is important to note that the ground effects dissipate after 2 to 3 chord lengths, which is already a very critical altitude for a UAV. Therefore, their overall effect on a dynamic soaring cycle may be negligible.

3.6.2 The Slender Body Theory validation

This section looks at the accuracy of ASWING in predicting the lift distribution on a slender body such as a fuselage or an airship (Zeppelin). The steady part in the equation 3.44 actually derives from the work of Von Karman (1930) and we should invoke the experimental benchmark done to status on the accuracy of ASWING. However, looking at the source code and the technical documentation, only the radius distribution of the slender body needs to be provided. Its variation with the spanwize coordinate $\frac{dR}{ds}$ is computed internally by a first-order backward difference. Or the latter is quite sensitive to numerical noise and diverges rapidly as the mesh is refined, leading to a very noisy distribution. Or both the lift and the source-induced velocity depend on the spatial variation of the cross-section radius. Figures 3.24 (a), (b) and (c) illustrate such problem of predicting the lift distribution with this method. Three different airships with different aspect ratios ($AR = \frac{L}{2R}$) have been used as the divergence of the numerical discretisation seems to be related to the steepness of $\frac{dR}{ds}$. The same problem is observed for the pressure distribution induced by sources for an axial flow ($\alpha = 0°$). Normally, the circular distribution of the fuselage cross-section is derived from ellipsoid functions which are differentiable in s. Consequently, by implementing a small modification so that the $\frac{dR}{ds}$ distribution is provided instead of computed, large improvements can be observed (cf. blue lines in figure3.24 a-d). Note that the problem could be solved on ASWING (unmodified) with a coarser mesh for which the backward difference is more stable. Or a coarser mesh could lead to undesired numerical errors in other physical quantities justifying the change.

From figure 3.24 (a)-(d) some conclusions can be drawn as the experimental data are shown (adapted from Von Karman and Upson and Klikoff' works). Only the modified version of the ASWING results are considered. From figures 3.24 (a) to (c) the lift predictions are in good agreement with the experiments from 0 to 80 % of the airship length. After ($x > 0.8L$) the lift, i.e. the pressure, is overestimated in absolute value by the slender body theory. The pitching mmoment of the fuselage is then slightly over-predicted. This discrepancy is due to the low-speed profile of the boundary layer, which reduces the pressure on the upper half disc of the fuselage. The slender body theory appears to be sensitive to this as the error increases for airships with lower aspect ratios where a thicker boundary layer is expected. A wall transpiration or displacement model could be used to correct this effect. This would result in a virtual thicker fuselage tail whose cross-section would vary more slowly than the real geometry, resulting in less lift produced. Overall, ASWING gives a good prediction of the lift distribution even at moderate angles of attack. From 3.24 (d) the source contribution to the pressure prediction is in excellent agreement with experimental data provided by Von Karman (1930). Note that ASWING cannot return the pressure due to the source distribution from the axisymmetry simplification made in the theoretical development (Appendix A). However, it can calculate the source-induced velocity field. Consequently, by judiciously placing numerical sensors on the fuselage surface, the velocity field can be recovered. Thus, by using the steady state Bernouilli equation, the dynamic pressure can be recovered and compared with the 1933 experiments so that the previous comment can be drawn.

Limitation of the Slender Body Theory:

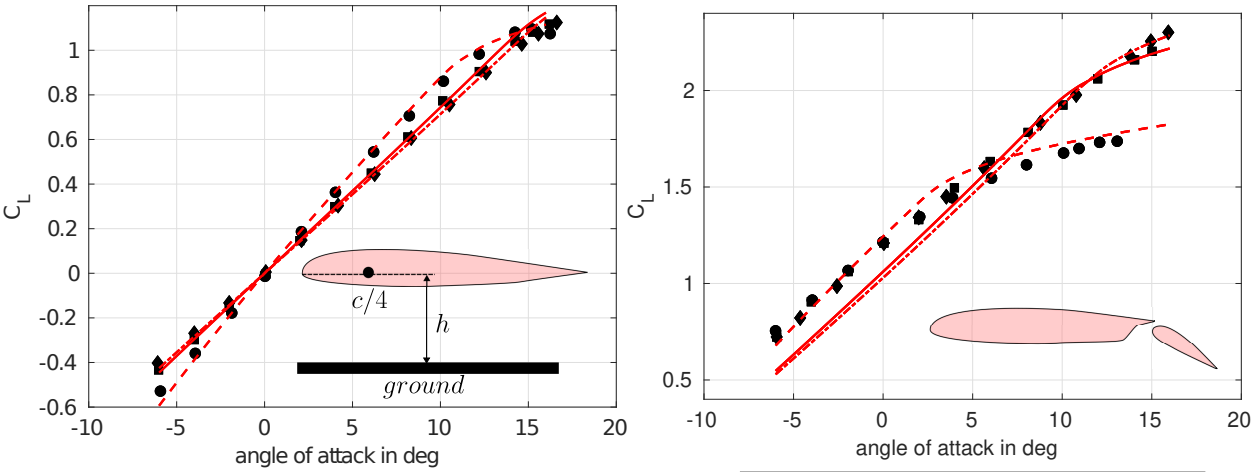

(a) no flap, lift prediction

(b) slotted flap, lift prediction

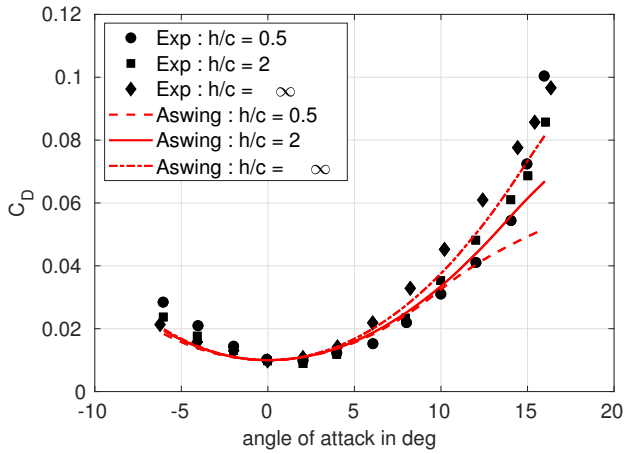

(c) no flap, drag prediction

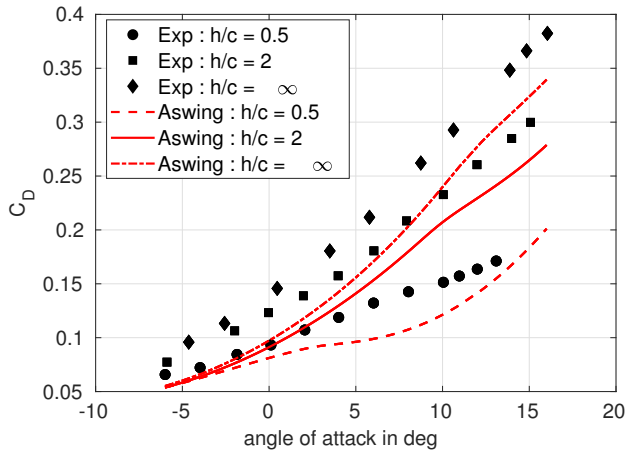

(d) slotted flap, drag prediction

Figure 3.23: CASE # 12 A-B: Ground effects on lift and drag predictions on a rectangular wing with no flaps and slotted one. Experimental data adapted from Recant (1939)

From the previous observations and based on the literature, the limitation of the slender body theory for a good use of ASWING can be drawn. The commented cases are high angle of attack configurations. The ASWING SBT is not able to capture the fuselage rear tail pressure but is still accurate. The limits of the LLT SBT combined are therefore imposed by the wing stall limits of the aircraft. Note that we do not recommend the use of a fuselage with an aspect ratio of less than 6.

3.6.3 Steady wing-fuselage interference

The lifting line and slender body theories have been evaluated separately. They both show good agreement with the experiments. In this section, the interferences between the wing and fuselage are assessed. Indeed, when a wing is anchored to a fuselage, its lift distribution is no longer the same and is slightly distorted. First of all, the fuselage changes the flow field because of the cross component of the upcoming flow denoted as $V_\infty sin\alpha$. This can be easily modelled through a doublet in which strength ϑ is computed to ensure the impermeability condition on the fuselage cross section (cf figure 3.25-a). The flow field induced by the doublet tends to increase the angle of attack seen by the wing. So as observed by Martina-1956, a wing connected to a fuselage produces more local lift than the wing alone at the same angle of attack. The second effect brought by the fuselage is the interaction between the wing wake and the body. The latter drastically impacts the aircraft wake vorticity especially at the wing root. A counter root vortex is generated that is not captured by the lifting line alone. Those counter vortices are known to trap the jet exhaust gas, favourable to contrail formations. From a singular method point of view, this counter vortex can be modelled using the Theorem of the circle (cf chapter 3 of Milne-Thomson-1973) where a set of image vortices are created to ensure the impermeability condition on the fuselage cross-section. This method can be applied to no circular cross section using conformal mapping (cf chapter 5 of Milne-Thomson-1973) but it is out of the scope of this thesis.
ASWING only models the doublet distribution mentioned above, and so does not capture the wake vorticity change. To evaluate ASWING on this feature the experimental work of Martina-1956 has been used.

Experimental bench :
A 45-degree swept wing of aspect and taper ratio 8.05 and 0.45 was placed into a wind tunnel. The wing was attached to a fuselage whose shape is described in figure 3.25 (b). A balance was fixed to the fuselage for total lift measurement, while pressure sensor lines, were placed at various spanwise locations (see figure 3.25 (b)). The wind tunnel speed was 70m/s for an equivalent Mach number of 0.2. Reynolds's number was 4 million. Local lift measurements were performed at 4 different angles of attack but only 3 are presented here (only the one on the linear range). The total lift was measured on a wider range of angle of attack from 0 to 30 degrees. Two configurations were tested, with and without the body. The wing root twist was also changed in the author's work, but this is not presented here.

Numerical bench:
In ASWING, three files have been created, the wing only, the wing + body and the wing + infinite body configurations. The third one has been created to highlight a problem described in the results section. The airfoil (NACA63A0012) polars have been generated by XFOIL at the equivalent wind tunnel condition.

Results:
Figures 3.25 (a) to (c) present the comparison between the ASWING predictions and the experimental measurements of Martina for the lift distribution. The results are pretty clear, ASWING does not capture the wing body interference. Actually, almost nothing happens when the fuselage is added. The configuration with the infinite fuselage was also tested, and the lift prediction is exactly the same as if the fuselage is not there. Figure 3.25 (e) particularly highlights this observation for the total lift (green and blue lines are the same). After looking at the source code, it seems that in the induced velocity subroutine, the doublet strength is set to zero, if there is no variation of the fuselage cross section (cf aic.f in subroutine AICVL, the command line: IF(ARAD.EQ.0.0 .AND. DRAD .EQ.0.0)). When this error is corrected, the doublet strength is computed. Results are not presented here, as some instabilities issues (not solved yet) have been witnessed.
In consequence, ASWING should be able to capture the local lift increase due to the fuselage but is not because of encoding issues. Moreover, ASWING is definitively not able to capture the counter root vortex generated by the fuselage and the associated carry-over lift. Discrepancies in the aircraft lift-induced drag predictions are to be expected. By implementing the theorem of the circle of Milne-Thomson, this problem could be solved.

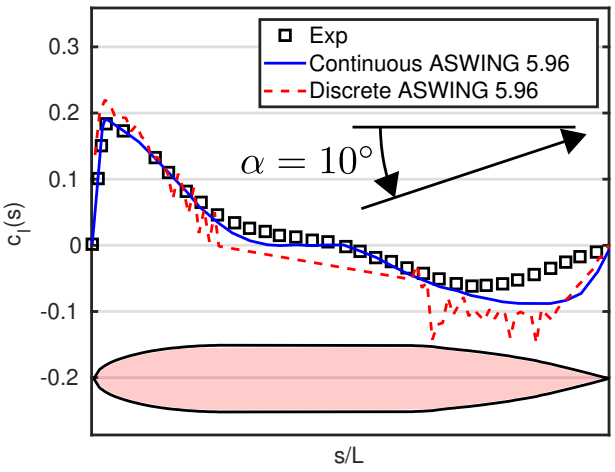

(a) Airship R-33 ($\frac{A}{R} = 16$) c_l distribution for uniaxial flow $\alpha = 10°$
(Data : ARC, R&M N 801)

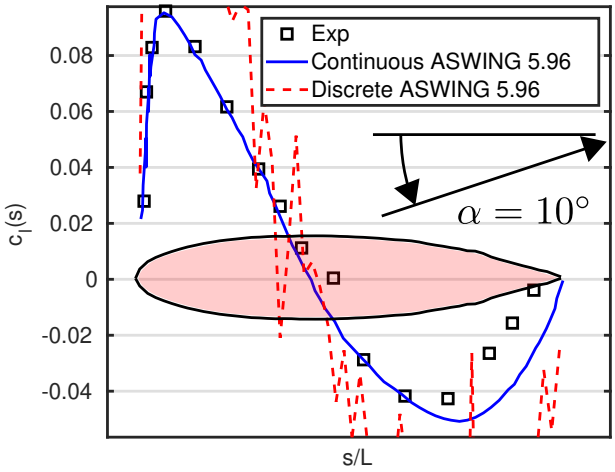

(b) Airship R-101 ($\frac{A}{R} = 11$) c_l distribution for uniaxial flow $\alpha = 10°$
(Data : ARC, R&M N 1169)

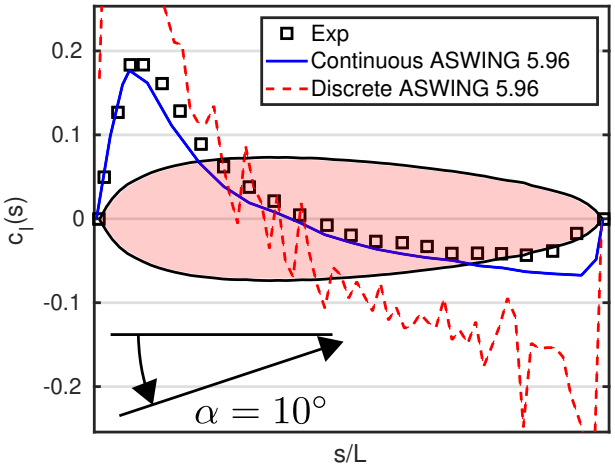

(c) Airship RS-1 ($\frac{A}{R} = 6$) c_l distribution for uniaxial flow $\alpha = 10°$
(Data : TDF Mc Cook Field)

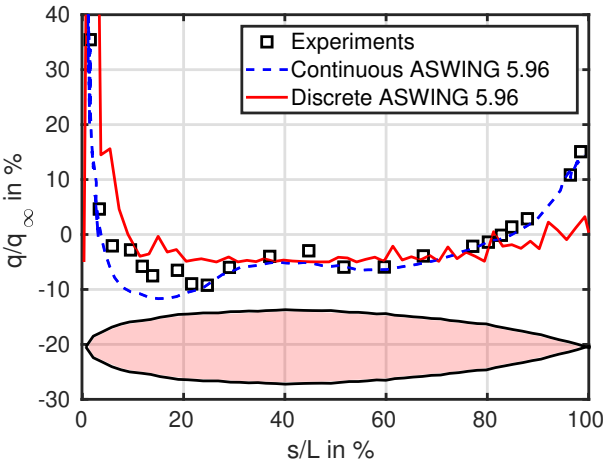

(d) $\sigma(s)$ contribution to $q(s)$ on the airship R-101

Figure 3.24: CASE # 13 A-D: Lift and dynamic pressure distribution ASWING predictions on different airship against experimental data from Von Karman (1930)

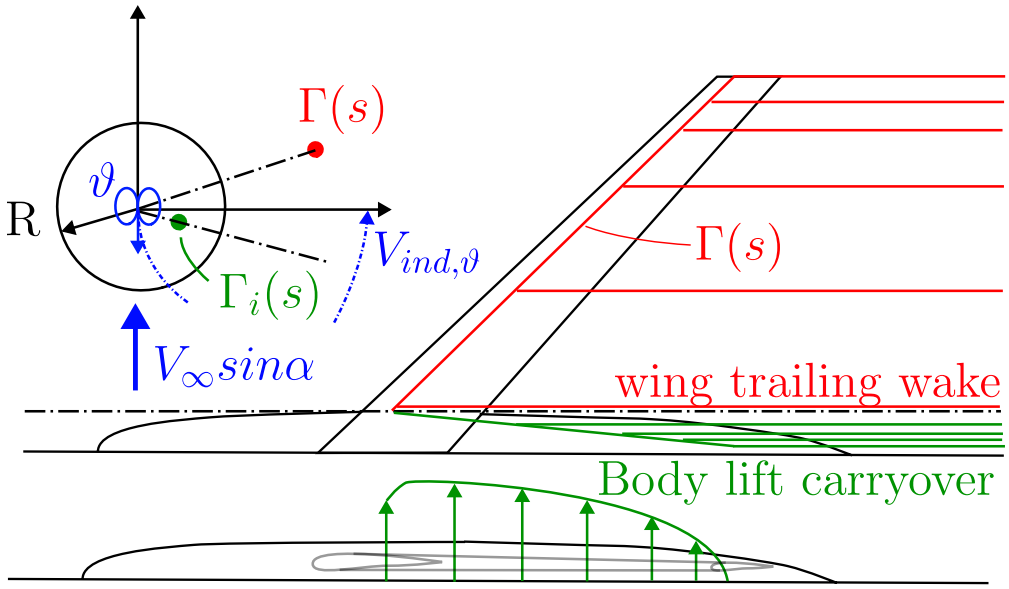

(a) Modeling wing fuselage interference using singularities. A doublet is used to ensure impermeability on the fuselage cross section due to the upcoming cross flow component $V_\infty sin\alpha$. If a vortex line $\Gamma(s)$ is present in the cross plane, a imaginary vortex $\Gamma_i(s)$ is lumped into the fuselage. The latter ensures impermeability conditioin on the cross section. ASWING only use the doublet distribution. The fuselage lift carryover is computed by integrating the Kutta Joukowsky theorem along the (green) lifting line.

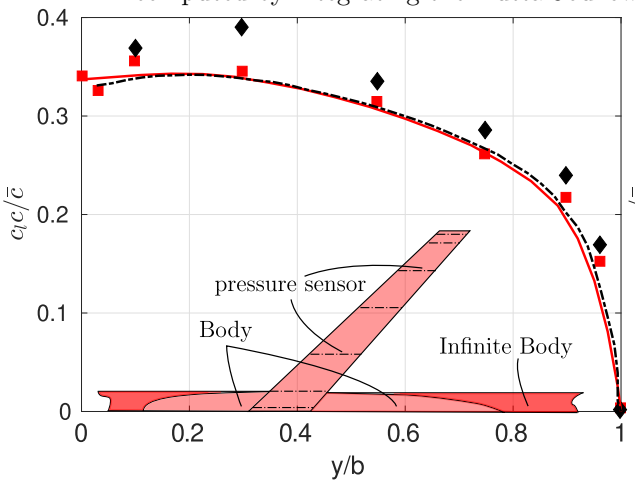

(b) lift distribution at $\alpha = 4.7°$

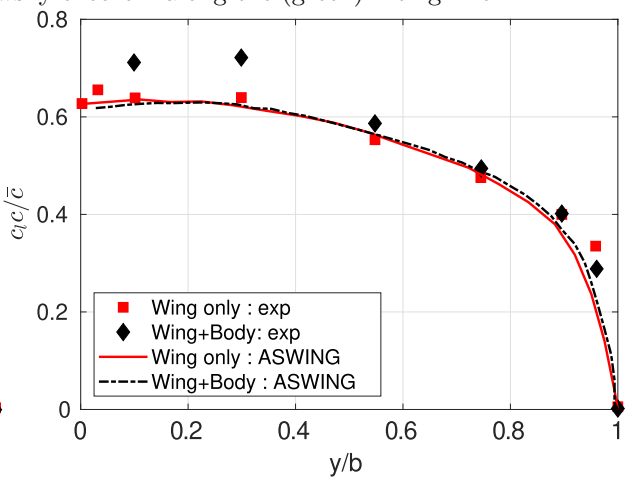

(c) lift distribution at $\alpha = 8.8°$

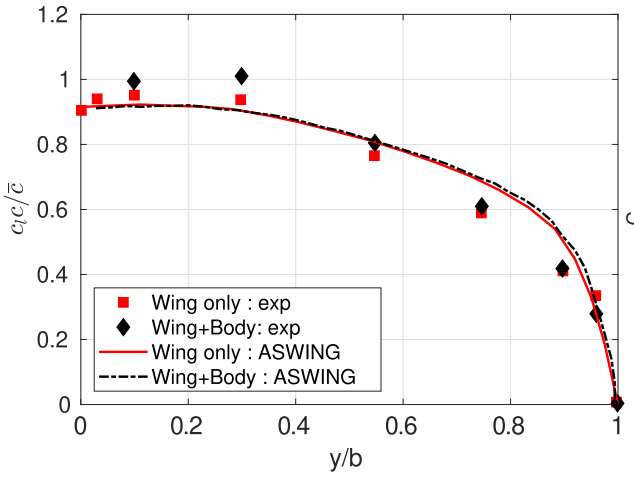

(d) lift distribution at $\alpha = 12.9°$

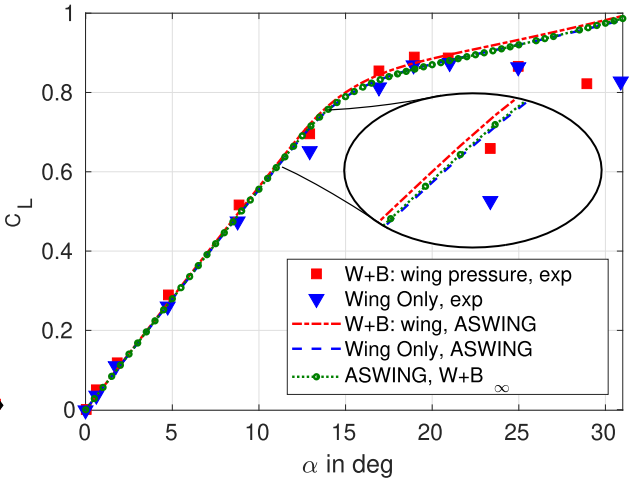

(e) Total lift, configuration comparison

Figure 3.25: CASE # 14: Wing body interference illustration and comparison with experiments. ASWING predictions against data from Martina-1956

3.6.4 Unsteady aerodynamics validation

3.6.4.1 2D unsteady aerodynamic

To benchmark the ASWING unsteady lift coefficient prediction, the experimental data set presented by Chiereghin et al. (2017b) was used.

Experimental bench: As reported by Chiereghin et al. in sections A and B, the experiments were performed at Re = 20 000 in a closed loop free surface water tunnel with a working section of 0.381X0.508X1.530 metres. The blade was mounted vertically on a linear motion mechanism. The wing profile and chord are a NACA0012 and $c = 0.0627$ m respectively. It has been designed voluntarily to avoid any structural influence, i.e. it can be considered rigid. To avoid any wing tip vortices and to restore a 2D case, 2 plates have been attached to the root and tip. Both act as symmetry planes, effectively extending the wing span to infinity. Only the plunging motion was studied and followed a sinusoidal function with a reported accuracy of less than 2%. The static wing incidence could be modified, in total 4 different angles of attack were studied ($\alpha \in [0,\ 5,\ 9,\ 15]$) for linear range pre- and post-stall behaviour studies. Transient c_l measurements were made using a balance attached to the diving mechanism. Inertial terms were subtracted from the data set to obtain the 2D c_l first harmonic, denoted $\tilde{c_l}$, via a Fast Fourier Transform (FFT). The time-averaged 2D $\bar{c_l}$ is also provided. Finally, some Particle Image Velocimetry (PIV) analyses were performed at half-span locations to provide physical insight into the change in the time-averaged lift coefficient. In total, 12 reduced frequencies k and 4 different reduced amplitudes $\frac{a}{c}$ were studied for each wing incidence angle α. In our study, we have decided not to study the highest angle of attack set $\alpha = 15°$ as it corresponds to a post-stall condition. In fact, from the continuous results on the prediction accuracy of the ASWING near and after stall, it is not possible to predict such behaviour as it is not able to capture the drop in lift after stall or the hysteresis phenomenon. Chiereghin et al.'s data set (2017b) is the most modern we have found in the literature. This data is also particularly interesting as it examines a range of reduced frequencies up to 1, where the error of the ASWING 2D unsteady lift function to Theodorsen's is the most important (cf. Fig. 3.6). We will finish the analysis by calling Theodore Theodorsen's results (1935) for higher reduced frequencies as both functions tend to be equivalent.

Numerical Methodology: In practice, it is not possible to achieve a perfect 2D case in ASWING. We first tried to increase the span until the 3D effects were negligible, but after a few tests, we noticed a small error in the theoretical function (Eq 3.29). Therefore, to avoid the accumulation of prediction errors, we decided to compare the experimental data with the theoretical ASWING function augmented with additional mass terms implemented in MATLAB:

$$c_{l,ASW}(t) = \left(c_{l_\alpha} kj C_{ASW}(k) - \pi k^2\right) \frac{A}{c} e^{j2\pi ft} + c_{l_\alpha}\alpha \tag{3.29}$$

where $C_{ASW}(k)$ is the 67th equation of [14]. Unsteady lift coefficient $c_{l,ASW}(t)$ is evaluated against Theordorsen's:

$$c_{l,Theodorsen}(t) = \left(2\pi kj C_{Theordosen}(k) - \pi k^2\right) \frac{A}{c} e^{j2\pi ft} + 2\pi\alpha \tag{3.30}$$

Note that the equations 3.29 and 3.30 are only valid for plunging motion. Both second terms in parentheses account for the added mass term. The term in brackets in both equations represents the first harmonic of the signal. Its amplitude $\tilde{c_l}$ and decay ϕ_{c_l} can be calculated directly if $C_{ASW}(k)$ and $C_{Theodorsen}(k)$ are known. The time averaged lift coefficient $\bar{c_l}$ is simply $c_{l_\alpha}\alpha$ and $2\pi\alpha$ in 3.29 and 3.30. Finally, in both equations ϕ_{c_l} does not depend on the reduced amplitude, so the results for the phase lags are only a function of the reduced frequency.

Results and comparison with Theodosen theory:

The first harmonic $\tilde{c_l}$ predictions are shown in figures 3.26(a) , 3.27(a) and 3.28(a). When the wing has no root incidence ($\alpha = 0°$), both Theodorsen and ASWING $\tilde{c_l}$ are in excellent agreement with the experiments. Note that despite the error between Theodorsen's lag function and ASWING, the difference in prediction is not so obvious. At $\alpha = 5°$ (Figure 3.27 (a)) the agreement is still good over the whole reduced frequency and amplitude range. However, near the stall angle of attack ($\alpha = 9°$) both functions become weaker but still reasonably accurate. Near the stall, the flow around the airfoil is more likely to be detached, especially at low reduced frequencies. Or in this region the circulation terms in the equations 3.30 and 3.29 dominate and are derived from an attached flow assumption. This phenomenon is particularly emphasised at high reduced amplitudes as shown in figure 3.28(a). After $k = 0.6$ the apparent/added mass terms become dominant and"the forces depend more on the pressure field of the airfoil and less on the flow separation" as claimed by the author. As a result, both theories become accurate again at high reduced frequencies.

There is less comment on the predictions of the phase lag ϕ_{c_l}. Both the Theodorsen and ASWING theories show good agreement regardless of the angle of

incidence of the airfoil, as shown in figures 3.26(b), 3.27(b) and 3.28(b). The small discrepancies at lower reduced frequencies are explained by the author as a lack of accuracy of the balance as the perturbation lift is very small. Overall, it is quite difficult to judge which theory performs best for phase lag prediction, so we will consider them equivalent in this frequency range.

Time average displacement due to Leading Edge Vortices (LEV): The analysis could stop there and conclude that both ASWING and Theodorsen have similar performance in predicting reasonably well the amplitude of the first harmonic of lift and the displacement up to the wing stall. However, when looking at the time average of lift as a function of reduced amplitudes, frequencies and angle of attack as shown in figure 3.33(a). There is an unsteady frequency phenomenon which leads to a positive or negative offset in the time average lift which is not captured by either the ASWING or Theodorsen formalism.

Phase average results: According to the shape of the phase average lift (Figure 3.29 (a)-(f)), the LEVs have a higher bandwidth than the pluning frequency. Neither ASWING nor Theordorsen functions can predict them. For aeroelasticity analysis, this would not necessarily be a problem as they would excite higher frequency modes which are usually less dominant in the transient response of the structure. In reality, the biggest problem caused by leading-edge vortices is the positive or negative offset in the time average lift. In the case of a flutter analysis, this would lead to an over- or under-estimation of the lift, i.e. the flutter boundary. Figure 3.29(b), (c), (e) and (f) show modified theories that assume the time average lift offsets are known. Under this strong assumption, ASWING is able to correctly predict the peak-to-peak amplitude. We consider this hypothesis to be too strong and stick to the conclusion that for low Reynolds number flow at high angle of attack and Stouhal number, ASWING and Theodorsen are more likely to underpredict the peak-to-peak lift amplitude and the time average lift.

3.6.4.2 3D unsteady

The unsteady 3D aerodynamics has been studied using the experimental data from Chiereghin et al. (2017a).

Experimental bench: The experimental bench is the same as in the 2D case except that the end plate has been removed. Enough space was left between the water tunnel wall and the wing tip to ensure the development of tip vortices and to correctly capture the 3D effects. Note that the aspect ratio of the wing is 5, which makes this set a stress test for the lifting line. The author's paper presents the time average, first harmonic amplitude and phase lag of the lift. 3D PIV analyses are also provided for physical insight into the 3D leading edge vortex development. Finally, phase average lift analysis was not performed. The same angle of attack reduced amplitudes and frequencies were investigated.

Numerical Methodology: Despite the 2D case, this time it is not possible to implement a theoretical function in MATLAB for the variation of the lift. Consequently, offline simulations were not possible and each case has to be run under ASWING. A slight modification of the code has to be made in order to be able to prescribe a plunging motion. Mesh and time convergence have been studied and we have used 40 circulation nodes and a time step $Te = T/40$, where T is the equivalent period of the reduced frequency to be studied. To save computational time, we ran the simulations over a single period. Instead of performing an FFT analysis, the time average was obtained by calculating the mean value of the signal, the peak-to-peak value was obtained by spotting the minimum/maximum values, and the phase lag was obtained by spotting the temporal position of the first maximum peak. This has been compared with a multi-period FFT analysis (10) and similar results have been observed. This holds as long as the march step is small enough, which is our choice. In the post-processing, we have highlighted that the phase lag does not vary with the reduced amplitude, so as in the 2D case, it is presented as varying only with the reduced frequency.

Results: The time averaged lift coefficient predictions are shown in figure 3.33(b). Offset is still present at moderate to pre-stall angles of attack, but as reported by the author, the leading edge vortices have been damped by the 3D effects. The induced velocity tends to reduce the effective angle of attack, delaying the appearance of LEVs. 3D cases appear to be less sensitive to Leading Edge Vortices for the same range of parameters. However, we do not recommend using it for near-stall configurations and high Strouhal number unsteady flows as the offset is still quite large. The first harmonic amplitude function of the reduced amplitude, frequency and angle of attack are shown in figures 3.30, 3.31 and 3.32 (a). Comparisons are made with Theodorsen's 2D function. For high reduced amplitudes (0.3, 0.5) ASWING agrees better with experimental data than Theordorsen, especially at high reduced frequency. When the angle of attack reaches 9°, the conclusion is no longer straightforward. Especially at a moderately reduced frequency (0.3 to 0.6) ASWING seems to underestimate the peak-to-peak amplitude of the lift. Note that by mak-

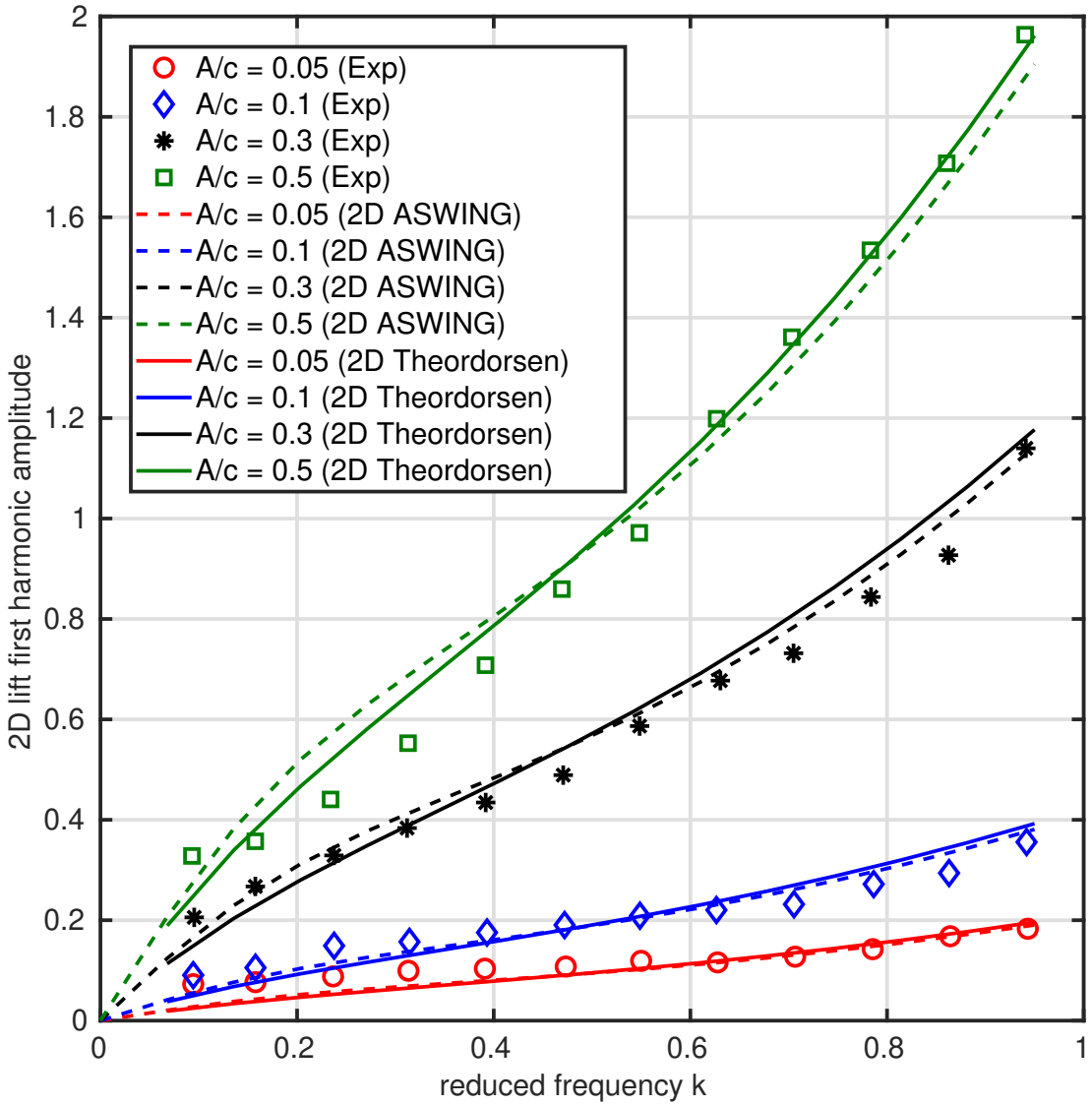

(a) $\tilde{c_l}$ first harmonic amplitude

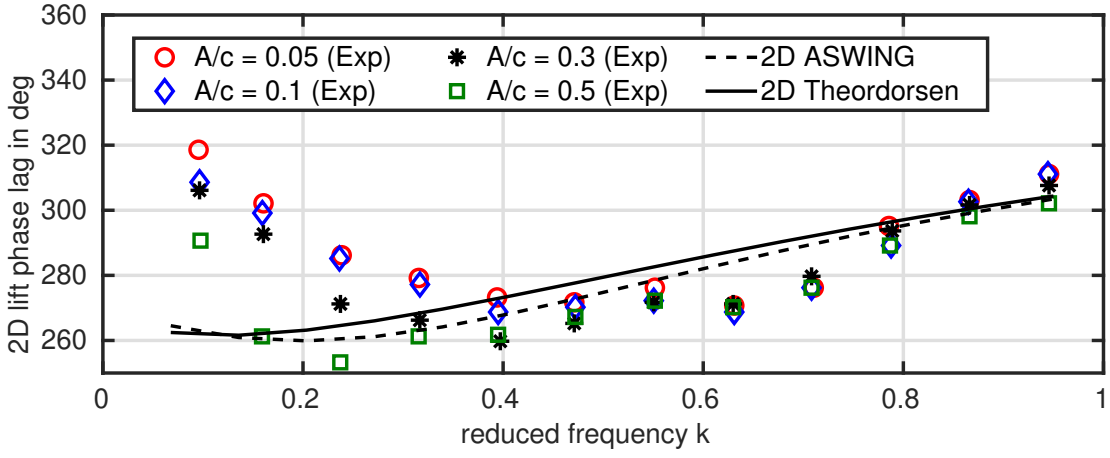

(b) ϕ_{c_l} phase lag

Figure 3.26: 2D lift coefficient first harmonic amplitude and phase lag at $\alpha = 0°$, effect of the reduced amplitude and frequency. ASWING prediction comparison with experiments (Chiereghin et al. 2017b)

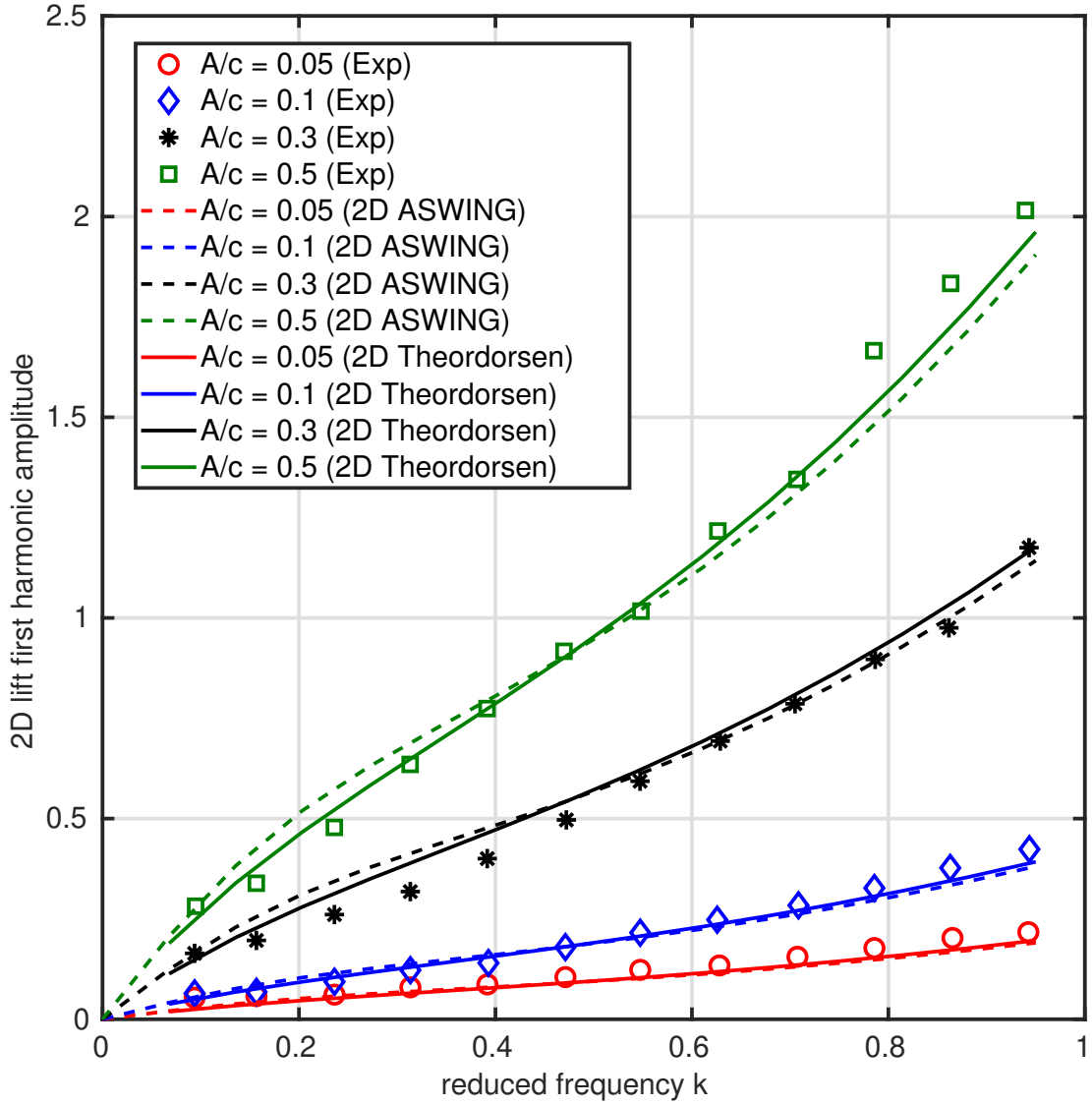

(a) $\tilde{c_l}$ first harmonic amplitude

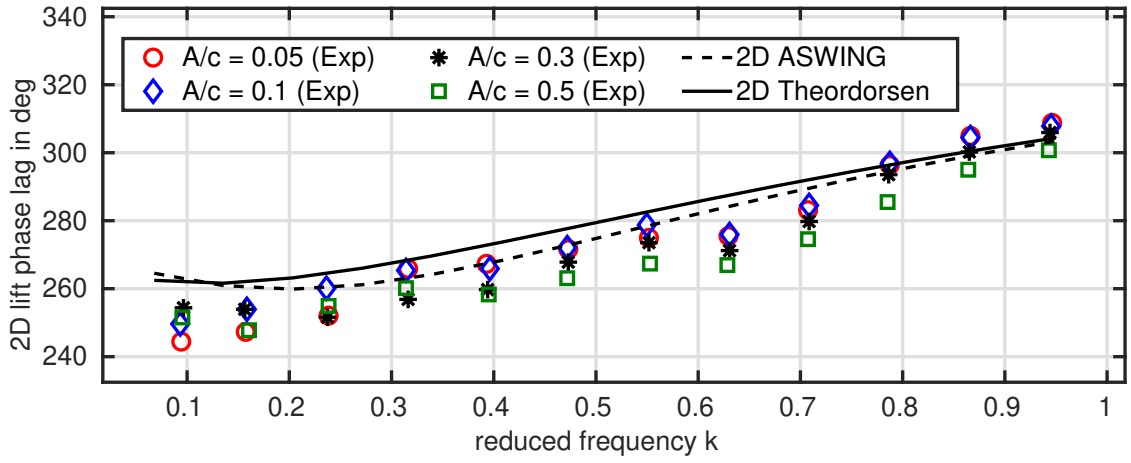

(b) ϕ_{c_l} phase lag

Figure 3.27: 2D lift coefficient first harmonic amplitude and phase lag at $\alpha = 5°$, effect of the reduced amplitude and frequency. ASWING prediction comparison with experiments (Chiereghin et al. 2017b)

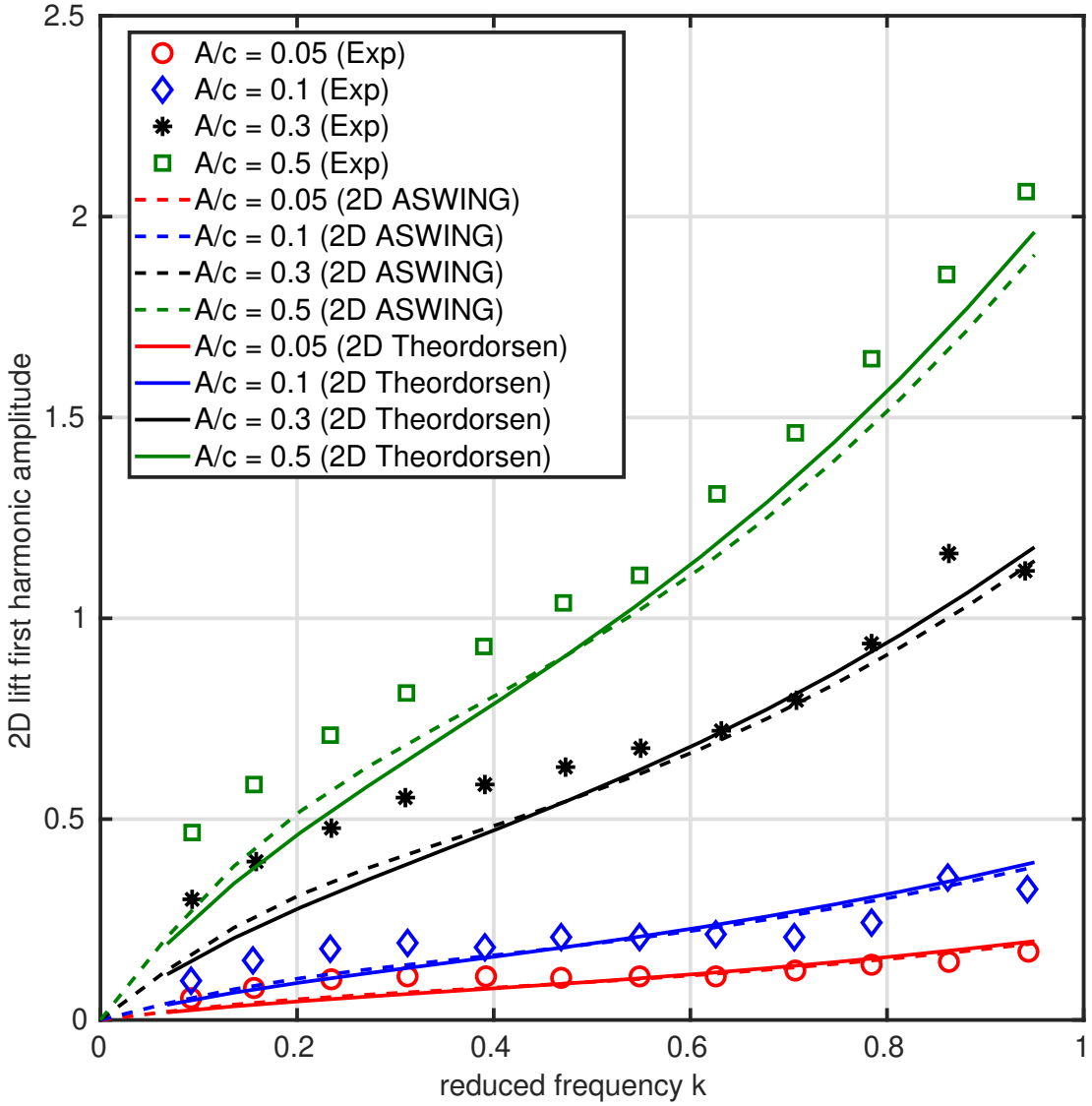

(a) $\tilde{c_l}$ first harmonic amplitude

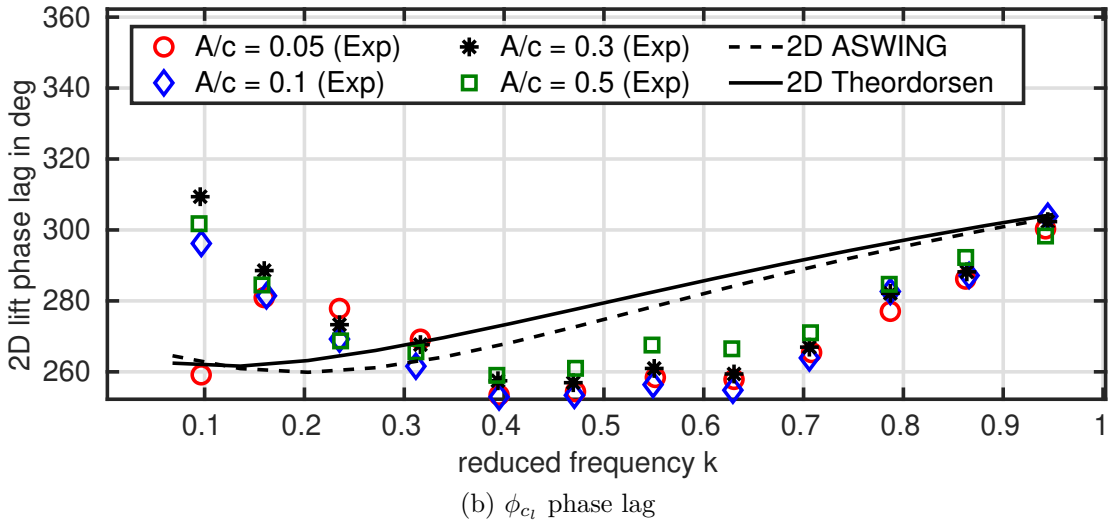

(b) ϕ_{c_l} phase lag

Figure 3.28: 2D lift coefficient first harmonic amplitude and phase lag at $\alpha = 9°$, effect of the reduced amplitude and frequency. ASWING prediction comparison with experiments (Chiereghin et al. 2017b)

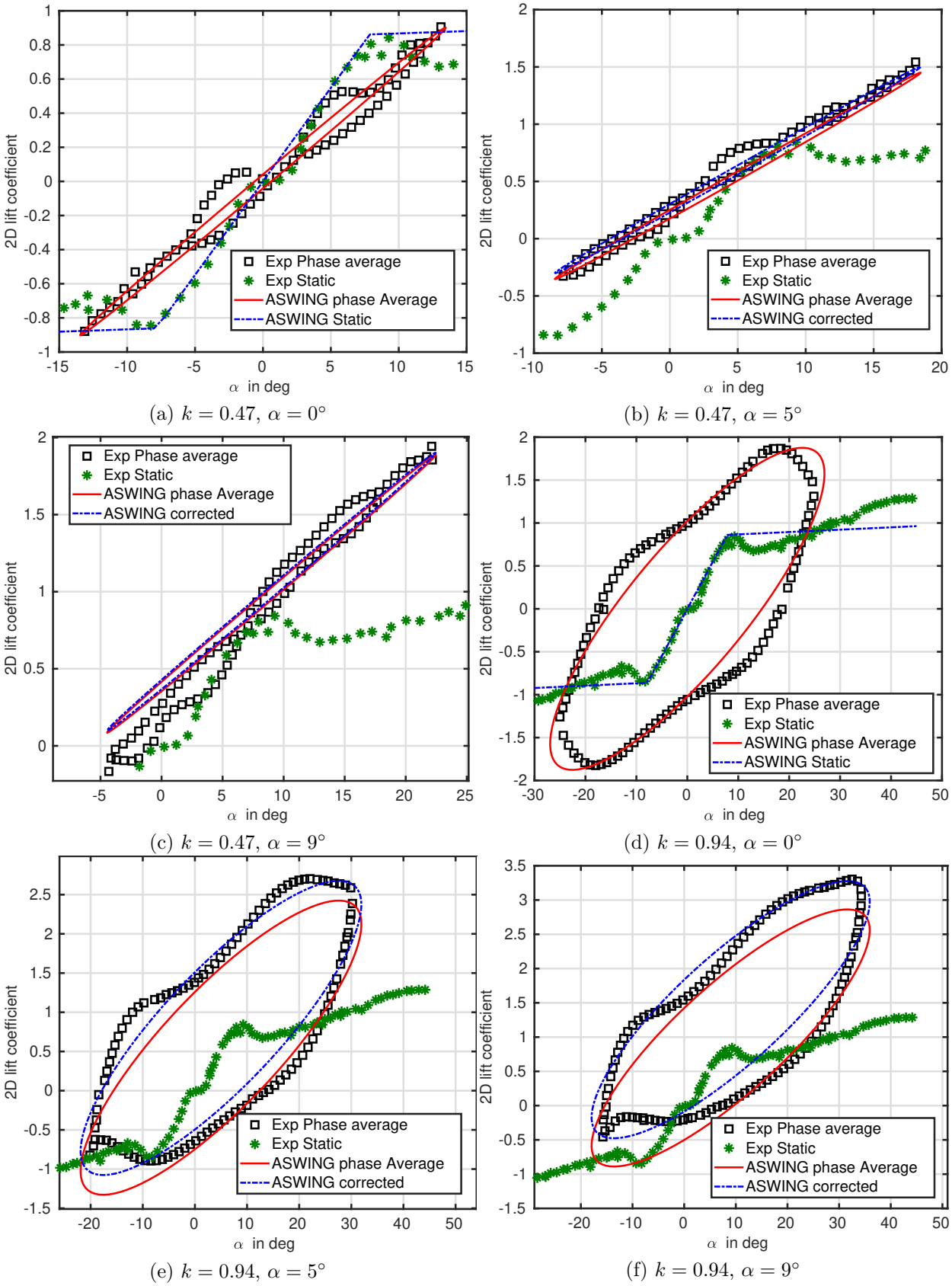

(a) $k = 0.47$, $\alpha = 0°$

(b) $k = 0.47$, $\alpha = 5°$

(c) $k = 0.47$, $\alpha = 9°$

(d) $k = 0.94$, $\alpha = 0°$

(e) $k = 0.94$, $\alpha = 5°$

(f) $k = 0.94$, $\alpha = 9°$

Figure 3.29: Phase lag average for 2 reduced frequencies and 3 angles of attack. ASWING predictions versus experiments (Chiereghin et al. 2017b). Comparison with a corrected function taking into account the time average experimental data.

ing a small correction to the 2D Theodorsen function using a 3D corrected lift slope, we obtain similar results to ASWING. However, the latter remains more interesting as it provides information on the aerodynamic spanwise force distribution, which is essential for aeroelasticity analysis. The phase lag predictions are shown in figures 3.30, 3.31 and 3.32 (b). The conclusion remains the same, at small Stouhal numbers (i.e. small k and $\frac{a}{c}$) discrepancies are due to sensor resolution. Otherwise, both ASWING and Theodorsen show good agreement with experimental data, whatever the angle of attack.

Recommendations: From the 2D and 3D validation cases we can draw conclusions about the prediction quality of ASWING. It shows excellent agreement with experiments for a range of Strouhal numbers when the wing incidence is in the non-stall region. Near stall ASWING still provides interesting results, but the results have to be interpreted carefully.

3.7 Computational performance

To evaluate the computational cost of ASWNG, the work of Fernandez-Escudero et al. (2019) has been used (with more details *in chapter 4* of the PhD manuscript of ESCUDERO). Theodorsen computation times against higher fidelity solutions were provided by the author. The tests were performed on the same single-core machine. The processor used was an Intel i7-3970K with an assumed clock speed of 3.8 GHz. All simulations were performed in 2D configurations over 10 pitch/plunge cycles. A comparison with the ASWING performance is proposed in the table 3.6. The programming language is also given for each case. The ASWING tests were carried out on a single core of an Intel Core i57360U with a fixed clock speed of 2.8GHz (lower than the i7-3970K). For medium to high fidelity codes (UVLM, Euler NLFD, Euler DTS, URANS NLFD), mesh and time step convergence studies were performed and reported by the author. Despite this tab sums up the computational cost for the 2D case, we have studied the 3D case of the previous section and implemented the flexible dynamics of the wing. Forty structure nodes and 40 circulations variables were sufficient to obtain a good mesh convergence. The time step used in the previous section was also sufficient. Given the table, ASWING is very attractive as it is very efficient. There is a difference of 2 to 3 orders of magnitude with the 2D unsteady vortex lattice method, which cannot model leading edge vortices but only a non-linear free wake. In other words, if the objective is only to study the effect of unsteady aerodynamics on the whole aircraft structure or vice versa, and we stay within the assumptions of ASWING, the latter is an excellent solution to perform heavy parametric studies such as multi-disciplinary analysis and optimisations.

3.8 Conclusions

In this chapter, an experimental evaluation of the ASWING aerodynamic model has been carried out. The various results are summarised as follows:

- ASWING can correctly capture the total lift and drag coefficients of various single planform geometries up to the early stall. The linear lift coefficients are in good agreement with the experiments.
- The drag prediction can be slightly improved when 2D airfoil polars are considered in a viscous loop, taking into account the quadratic variation of 2D viscous and pressure drag coefficients with lift. The quality of the predictions is strongly dependent on the airfoil polars. Important knowledge of the flow and experimental conditions is essential to obtain results equivalent to those presented. For real flight conditions, some discrepancies must be expected.
- ASWING can correctly capture the rolling moments induced by different ailerons on a straight wing for moderate flap deflections (up to 20 degrees). For larger deflections, ASWING detects a tendency but overestimates the rolling moment. When the wing is in a post-stall condition, the predictions are no longer accurate. In linear and post-stall conditions, ASWING underestimates the yaw moment generated by the ailerons, mainly because it cannot capture the increase in viscous and pressure asymmetric drag generated by sharp geometries.
- ASWING can capture the wake interactions between multiple lifting surfaces. In particular, it correctly predicts the loss of lift of a downstream surface due to a strong wake downwash. It also provides good predictions of the stall of each surface.
- The lift distribution prediction has been investigated on various swept forward and backward wings. The ASWING predictions are in good agreement with the experiments. It captures well the effect of the sweep angle on the spanwise displacement of the aerodynamic centre of the wing.

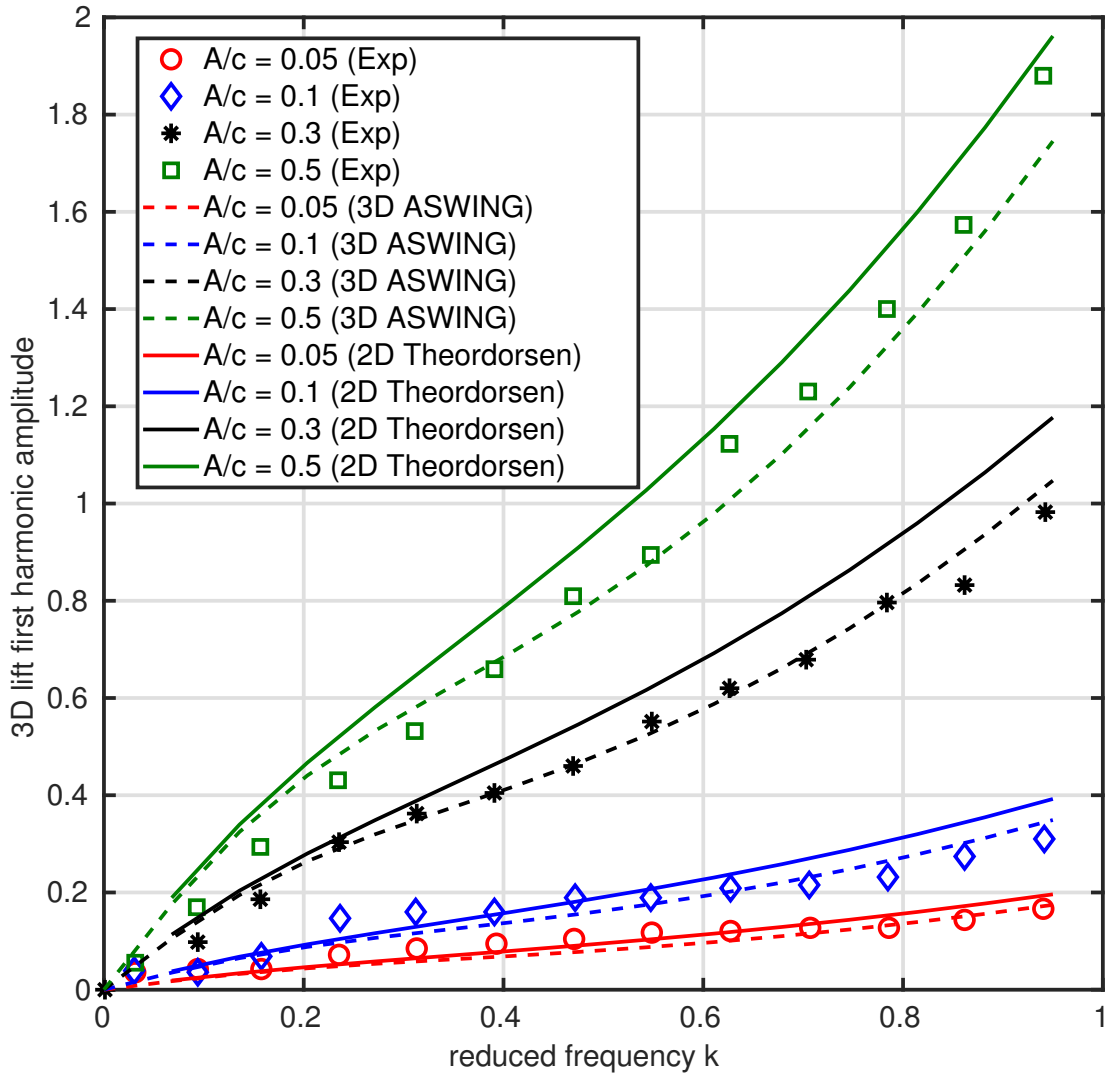

(a) $\tilde{C_L}$ first harmonic amplitude

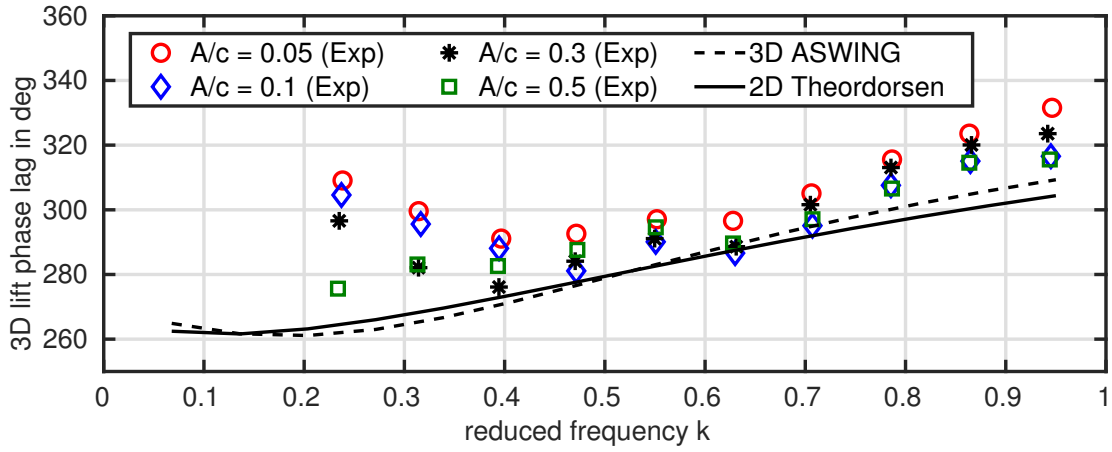

(b) ϕ_{C_L} phase lag

Figure 3.30: 3D lift coefficient first harmonic amplitude and phase lag at $\alpha = 0°$, effect of the reduced amplitude and frequency. ASWING prediction comparison with experiments from Chiereghin et al. (2017a)

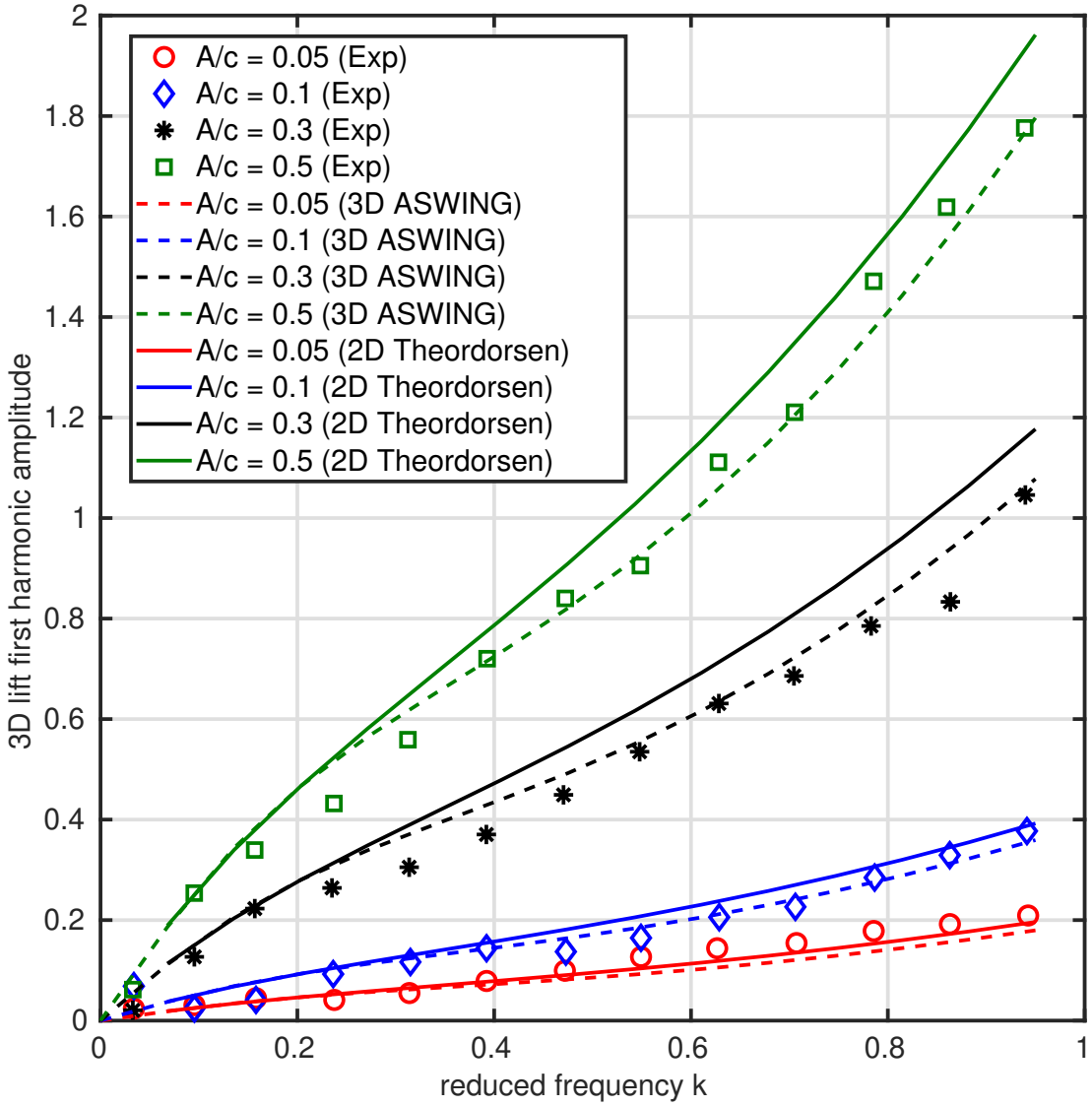

(a) $\tilde{C_L}$ first harmonic amplitude

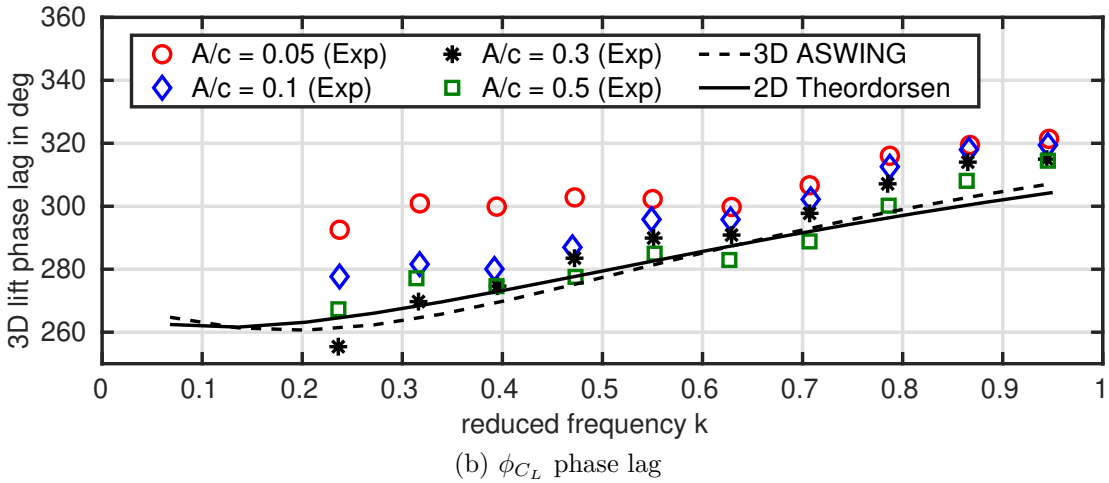

(b) ϕ_{C_L} phase lag

Figure 3.31: 3D lift coefficient first harmonic amplitude and phase lag at $\alpha = 5°$, effect of the reduced amplitude and frequency. ASWING prediction comparison with experiments from Chiereghin et al. (2017a)

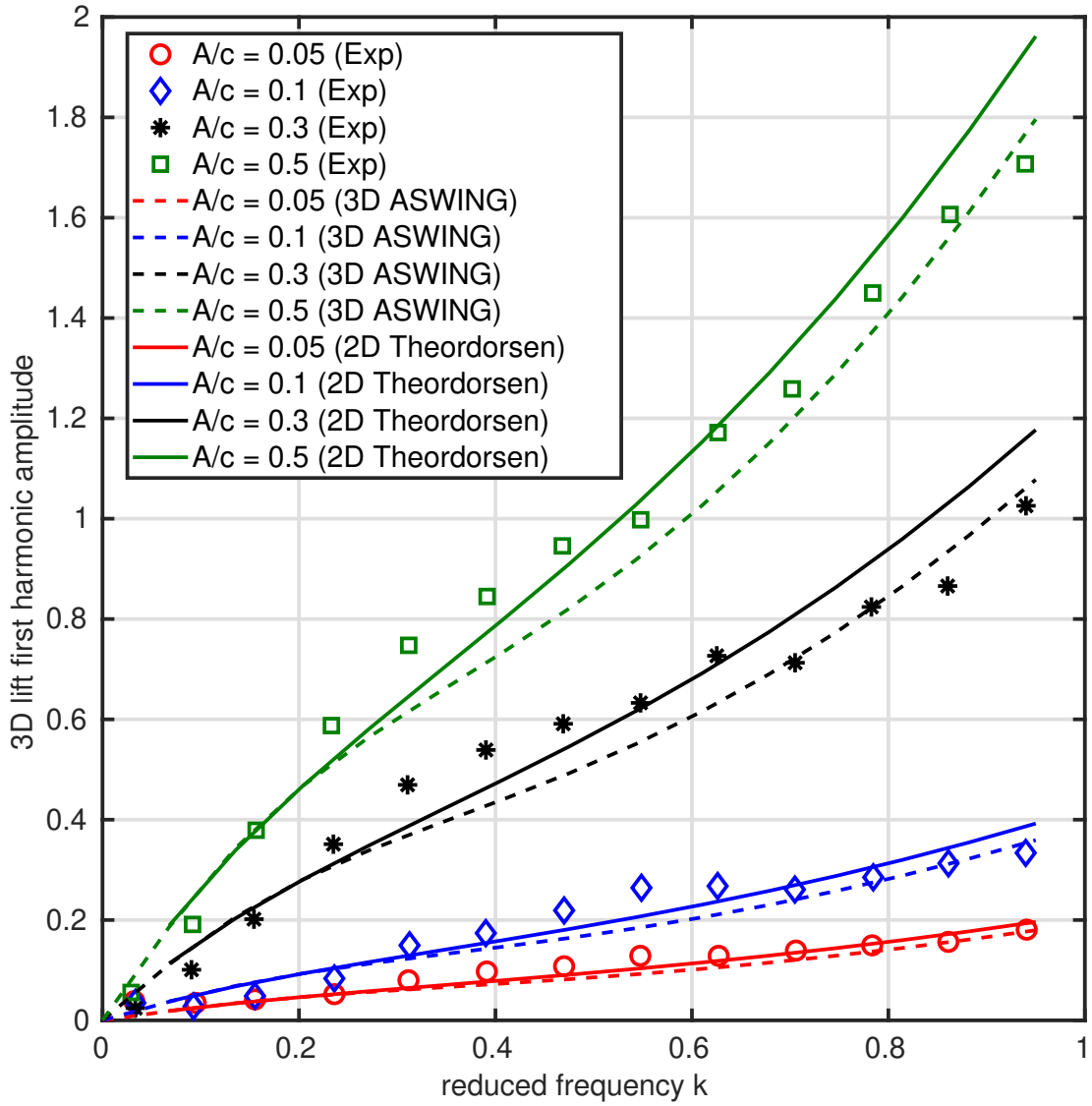

(a) $\tilde{C_L}$ first harmonic amplitude

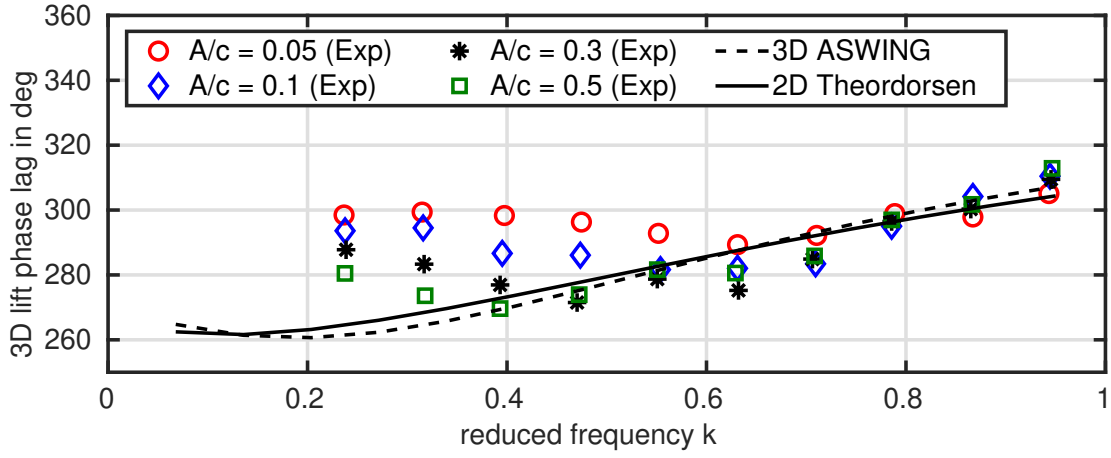

(b) ϕ_{C_L} phase lag

Figure 3.32: 3D lift coefficient first harmonic amplitude and phase lag at $\alpha = 9°$, effect of the reduced amplitude and frequency. ASWING prediction comparison with experiments from Chiereghin et al. (2017a)

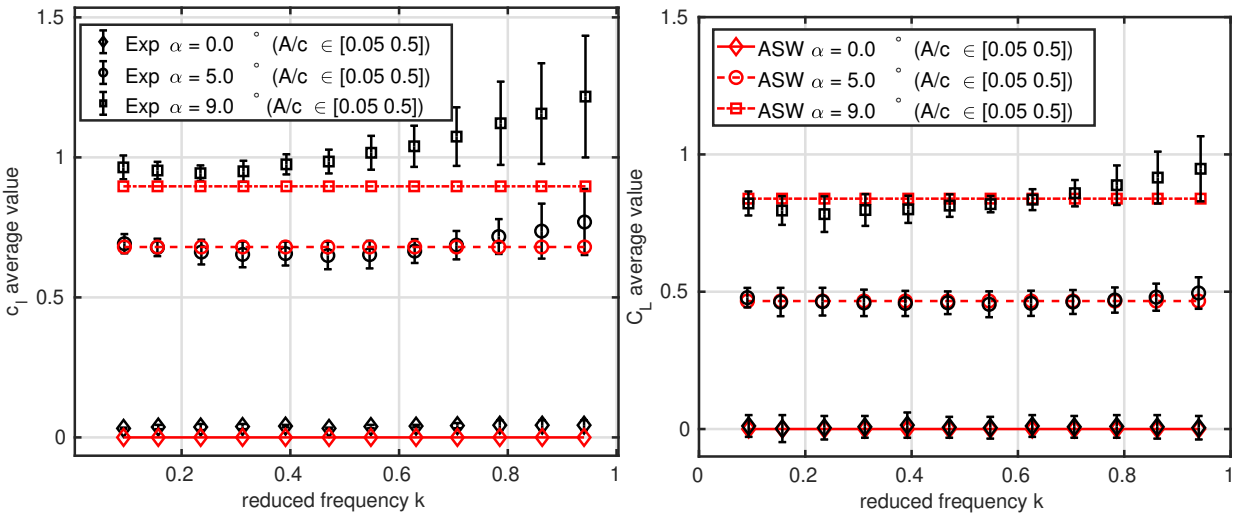

(a) 2D (b) 3D

Figure 3.33: Leading Edge Vortices effect on the time average 2D and 3D lift coefficient versus ASWING predictions. Comparison with experimental data from Chiereghin et al. 2017b and 2017a

Table 3.6: Computational time comparison with higher fidelity methods adapted from the work of Fernandez-Escudero et al. (2019)

Method	Language	Computational time (in s)
Theodorsen 2D	Matlab	30
ASWING 2D	Matlab	30
ASWING 3D	Fortran 77	60
UVLM (2D)	C++	2.7E3 ∼45 min
Euler NLFD (2D)	C++	2.1E5 ∼ 6 h
Euler DTS (2D)	C++	2.8E5 ∼ 6h
URANS NLFD (2D)	C++	8.6E5 ∼ 1 day

- The effect of wingtip devices on lift-induced drag is well captured as long as the wingtip is a single lifting surface. When tip sails are considered, ASWING shows significant discrepancies with experiments. Otherwise, it captures well the order of magnitude of the drag reduction in cruise conditions.
- Transonic flow has been studied. Thanks to the Prandtl-Glauert compressibility correction factor, the lift slope of a commercial airliner wing is reasonably well captured. For drag, ASWING is weak and does not capture the strong dependence on the Mach number. However, the source code could be modified to account for transonic airfoil polars as a polynomial function of lift coefficient and Mach number. The use of MSES is recommended as it provides a decomposition of the drag into pressure and viscous contributions which is consistent with the ASWING formalism.
- The ground effects on lift and drag can be captured for a wing with no slotted flaps deployed. The increase in lift slope and decrease in drag are well predicted for altitudes up to half the wing chord from the ground. For configurations with slotted flaps, the effects of the ground on the flap physics are dominant and are of course not captured by ASWING. Therefore, this function must be used with caution.
- Thanks to the slender body theory, the lift distribution on the fuselage with a circular cross-section is well captured, except near the tail where flow separation usually occurs. As a result, ASWING overestimates the pitch-up moment induced by the fuselage. The slender body theory gives excellent results for flow deflection.
- ASWING should be able to capture the local lift increase due to the fuselage but is not because of encoding issues. Moreover, ASWING is definitively not able to capture the counter root vortex generated by the fuselage and the associated carry-over lift. Discrepancies in the aircraft lift-induced drag predictions are to be expected. By implementing the theorem of the circle of Milne-Thomson, this problem could be solved.
- 2D unsteady aerodynamics have been studied. For a plunging wing, ASWING performs similarly to Theodorsen's theory, regardless of the reduced frequency and amplitude considered. Both capture well the pick-to-pick amplitude and the phase lag of the lift. However, when the airfoil has a significant incidence and faces a high reduced frequency or amplitude, leading-edge vortices appear. The latter, appearing on only one descending phase (down), modifies the mean value of the lift, which is not captured by ASWING or Theodorsen theory, as they are boundary layer phenomena.
- For 3D unsteady aerodynamics, the same remark can be made as for the 2D case. However, ASWING seems to capture the peak-to-peak amplitude of lift better than Theodorsen theory because it captures the 3D lift effects. This change is attenuated at higher reduced frequencies and amplitudes as the added mass terms dominate.
- In terms of computational time, ASWING is 2-4 orders of magnitude faster than higher fidelity models, and in terms of prediction quality, ASWING can clearly compete with them for macroscopic physical variables predictions (lift, drag, pitching moment etc).

This work has allowed us to converge on bounded parameters that ensure good predictions. The wings and fuselage must have an aspect ratio greater than 5. The wings must have a dihedral and sweep angle of less than 45 degrees. It is also recommended not to abuse the use of the stall function, as it will deteriorate quickly. Finally, it is recommended to consider flows with an average Reynolds number higher than 100 000 (typical for mini UAVs). In its current version, care must be taken with the predictions made in the transonic condition. Under this perspective, several modifications of the ASWING source code could be considered and are summarised as follows

- Close lifting surface interactions can be improved to more accurately model wing/body interactions. The theorem of the circle and conformal mapping could be adapted to the ASWING formalism.
- Transonic airfoil polars could be integrated as bi-polynomial functions of local lift coefficient and freestream Mach number to provide more accurate lift and drag predictions, thus extending the range of ASWING to transonic flight.
- An axisymmetric boundary layer model could be implemented in the slender body theory to capture the flow separation at the tail. For example, a wall transpiration model could be used to reasonably increase the computational cost. It would give better predictions of fuselage drag and pitch-up torque.
- The slender body theory could be extended to non-axisymetric bodies in order to model double bubble fuselages such as the one of Aurora D8. Again the theorem of circle and conformal mapping could be used to solve it.

- A prescribed helicoidal wake could be integrated, extending and allowing the study of flexible rotor blades.

As far as the funding is concerned, ASWING answers all the numerical aerodynamic needs of the thesis and even more. It is perfectly suited to multidisciplinary analysis. In the next chapter, the propeller model is studied and coupled with the aerodynamic model to provide more analysis capabilities.

Appendix A: Unsteady vectorial formulation of the slender body theory

This section aims to provide some theoretical insight into how aerodynamic unsteady forces are derived in Drela's work (2008 and 2009). The latter considers only a fusleage with symmetry of revolution, i.e. a circular cross-section. From the unsteady Bernoulli equation, we know that the local pressure in the flow field can be expressed as a function of the local dynamic pressure and the time variation of the velocity potential, as long as they are known. The aerodynamic forces acting on a fuselage are calculated by integrating the normal pressure contributions. Note that the aerodynamic model is coupled to a structural model. In other words, the geometry of a fuselage can vary with loads. Consequently, the slender body theory must be derived in a distributed form.

The unsteady slender body theory is derived from 2 main assumptions:

- The cross-sectional area varies slowly with the spanwise coordinate s, implying that the flow is mostly 2D.
- The slender body theory assumes that the incoming flow of velocity V at each disc centre is constant over the cross-section.

Consider a slice of a fuselage of length ds immersed in a fluid of velocity V. The geometry imposes an impermeability, i.e. a flow tangency condition, on the elementary surface. Let us denote by $V_\perp$ the component of the local velocity lying in the cross-sectional plane (c, n), expressed as $\vec{V_\perp} = \vec{V} - \vec{V} \cdot \vec{s}$ and shown in figure 3.7. Note that $\vec{V} \cdot \vec{s}$ is the projected axial velocity. For convenience, we now define a new local cross-section frame $(c_\perp, s, n_\perp)$ such that the cross-section velocity $\vec{V_\perp}$ is aligned with $n_\perp$, i.e. $\vec{V_\perp} = V_\perp \vec{n_\perp}$. To ensure tightness we use 2 types of singularities. A source of strength $\sigma(s)$ to ensure the tightness of the projected normal velocity component of the axial velocity $\vec{V} \cdot \vec{s}$. In fact, the normal vector n_i is not orthogonal to the axis. This is due to a change in the cross-section radius. As a consequence, the axial velocity must be distributed radially outwards or inwards as shown in figure 3.7. Not that the correction has to be radially directed, as the source choice.

The velocity potential of a source of strength $\sigma(s)$ is given as follows

$$\varphi_\sigma(s, c, n) = \sigma(s) \frac{ln(\sqrt{c^2 + n^2})}{2\pi} \tag{3.31}$$

As the previous expression is not convenient we will prefer the cylindric coordinate

$$\varphi_\sigma(s, \theta, r) = \sigma(s) \frac{ln(r)}{2\pi} \tag{3.32}$$

The velocity field due to a source placed at the centre of the cross-sectional disk is then given in the cylindric coordinates:

$$\vec{V_\sigma}(s, \theta, r) = \begin{pmatrix} \frac{\partial \varphi_\sigma}{\partial s} \\ \frac{\partial \varphi_\sigma}{\partial r} \\ \frac{\partial \varphi_\sigma}{\partial r} \frac{\partial \varphi_\sigma}{\partial \theta} \end{pmatrix} = \begin{pmatrix} \frac{\partial \sigma}{\partial s} \frac{ln(r)}{2\pi} \\ \sigma(s) \frac{1}{2\pi r} \\ 0 \end{pmatrix}_{(s, u_r, u_\theta)} \tag{3.33}$$

Now consider the small element of the cylinder and its normal vector $\vec{n_i}$. Let us define ψ as the angle between $\vec{n_i}$ and the cross-sectional plane (c, n) as shown in the figure 3.7. Due to the asymmetry of the problem, we will apply the single-point tightness condition. For the small angle approximation, ψ is equal to $\frac{dR}{ds}$, where R is the cross-section radius. The flow impermeability is then applied against $\vec{n_i}$ and at R as follows

$$(\vec{V} \cdot \vec{s}) \cdot \vec{n_i} + \frac{\partial \phi}{\partial r}(R) \cdot \vec{s} = 0$$

When projected

$$-\vec{V} \cdot \vec{s} \sin(\psi) + \frac{\partial \phi}{\partial r}(R) \cos(\psi) = \frac{dR}{ds} \vec{V} \cdot \vec{s} + \frac{\partial \phi}{\partial r}(R)$$

Comes the source strength ensuring partial impermeability

$$\sigma(s) = 2\pi R \frac{dR}{ds} \vec{V} \cdot \vec{s} \tag{3.34}$$

The latter development shows that the source term does not contribute to the lift, but it provides better accuracy in the near flow modelling and captures the thickness of the fuselage. The impermeability of the flow at the cylinder surface is not fully taken into account as the cross-section velocity term $V_\perp$ is not yet cancelled. Let us then consider a new singular element called the doublet of strength $\vartheta(s)$ with velocity potential expressed as

$$\phi_\vartheta(r, \theta, s) = \vartheta(s) \frac{sin(\theta)}{2\pi r} \tag{3.35}$$

The resulting velocity field is expressed as :

$$\vec{V_\vartheta}(s, \theta, r) = \begin{pmatrix} \frac{\partial \varphi_\vartheta}{\partial s} \\ \frac{\partial \varphi_\vartheta}{\partial r} \\ \frac{\partial \varphi_\vartheta}{\partial r} \frac{\partial \varphi_\sigma}{\partial \theta} \end{pmatrix} = \begin{pmatrix} \frac{\partial \vartheta}{\partial s} \frac{sin(\theta)}{2\pi r} \\ -\vartheta(s) \frac{sin(\theta)}{2\pi r^2} \\ -\vartheta(s) \frac{cos(\theta)}{2\pi r^2} \end{pmatrix}_{(s, u_r, u_\theta)} \tag{3.36}$$

Considering without loss of generality (under small angle assumption ie slender body) that $u_r = cos(\psi) n_i \sim n_i$. The impermeability condition can be applied

against u_r at $r = R$ such that

$$\forall\theta\ V_\perp(s)\cdot\vec{u_r} - \vartheta(s)\frac{sin(\theta)}{2\pi R^2} = 0$$

or as $V_\perp(s)\cdot\vec{u_r} = V_\perp(s)sin(\theta)$ (as illustrated on figure 3.7), the impermeability condition becomes independent of θ and the doublet strength is finally given by

$$\vartheta(s) = 2\pi V_\perp(s)R^2 \tag{3.37}$$

Now as we have expressed the sources and doublet strength in function of the local geometry. We can use the incompressible unsteady Bernoulli equation to compute the unsteady lift applied on the section of the fuselage.

$$\rho\frac{\partial\phi}{\partial t} + \frac{1}{2}\rho\nabla\phi\cdot\nabla\phi + p = p_\infty$$

where $\nabla\phi$ is the flow field velocity expressed as the gradient of the total potential. In the cylindrical coordinate system, it is expressed as

$$\begin{aligned}\nabla\phi &= \begin{pmatrix} V\cdot\vec{s} + \frac{\partial\varphi}{\partial s} \\ V_\perp\sin\theta + \frac{\partial\varphi}{\partial r} \\ V_\perp\cos\theta + \frac{\partial\varphi}{\partial r}\frac{\partial\varphi}{\partial\theta}\end{pmatrix} \\ &= \begin{pmatrix} V\cdot\vec{s} + \frac{\partial\varphi}{\partial s} \\ 0 \\ V_\perp\cos\theta + \frac{\partial\varphi}{\partial r}\frac{\partial\varphi}{\partial\theta}\end{pmatrix}\end{aligned}$$

where the second term in the vector is equal to zero as imposed by the impermeability condition. Note that φ denotes the perturbation potential induced by the source and the doublet. For a seek of clarity we will use the notation $(\varphi_s\varphi_r\varphi_\theta)$ as φ partial derivatives.Developing the scalar product comes the local dynamic pressure as follows

$$\begin{aligned}\frac{1}{2}\rho\nabla\phi\cdot\nabla\phi &= (V\cdot s + \varphi_s)^2 + (V_\perp\cos\theta + \varphi_\theta)^2 \\ &= (V\cdot s)^2 + 2\varphi_s V_s \\ &\quad + (V_\perp\cos\theta)^2 + 2V_\perp\cos\theta\varphi_\theta + \varphi_\theta^2 + \varphi_s^2\end{aligned} \tag{3.38}$$

This equation is already quite untrackable but it provides good insights that are used in the next development. The total pressure force on the elementary slice of the fuselage is given by

$$\begin{aligned}\frac{d\vec{L}}{ds} &= -\int_{\mathcal{C}} p(R,\theta)\vec{n_i}(R,\theta)dl \\ &= -\int_0^{2\pi} p(R,\theta)\vec{u_r}(R,\theta)Rd\theta\end{aligned} \tag{3.39}$$

From now we can invoke the asymmetry property. First of all the normal vector is impair in $\theta+\pi$ ie $\vec{u_r}(\theta+\pi) = -\vec{u_r}(\theta)$. In other words, if some component of the local pressure is invariant spatially or respects the property $y(\theta+\pi) = y(\theta)$, their effects cancel each other. When we inspect the element of 3.38 Every square component can be neglected and it comes

$$\frac{1}{2}\rho\nabla\phi\cdot\nabla\phi \mathrel{\mathring{=}} 2\varphi_s V_s + 2V_\perp\cos\theta\varphi_\theta \tag{3.40}$$

Note that in the equation above, we have used the $\mathring{=}$ notation to specify that only components that do not vanish with the imparity are conserved. Finally noting thanks to equation 3.36 and 3.33 the last term in equation 3.40 is proportional to $\cos\theta^2$ respects the parity property. The dynamic pressure is then simplified with no conservatism as

$$\frac{1}{2}\rho\nabla\phi\cdot\nabla\phi \mathrel{\mathring{=}} 2\varphi_s V\cdot s = 2\frac{\partial\vartheta(s)}{\partial s}\frac{sin(\theta)}{2\pi R}V\cdot s \tag{3.41}$$

By inspection of the temporal variation of the potential function comes the same type of simplification

$$\frac{\partial\phi}{\partial t} = \frac{\partial\varphi}{\partial t} \mathrel{\mathring{=}} \frac{\partial\vartheta(s)}{\partial t}\frac{sin(\theta)}{2\pi r} \tag{3.42}$$

As a consequence the simplified expression of the local pressure located in (s, R, θ)

$$-p(\theta,R) \mathrel{\mathring{=}} 2\frac{\partial\vartheta(s)}{\partial s}\frac{sin(\theta)}{2\pi R}V\cdot s + \frac{\partial\vartheta(s)}{\partial t}\frac{sin(\theta)}{2\pi R} \tag{3.43}$$

Now denoting that $n(\theta) = cos(\theta)c_\perp + sin(\theta)n_\perp$ After integration, it comes

$$\frac{d\vec{L}}{ds} = \left(\frac{\partial\vartheta(s)}{\partial s}V\cdot s + \frac{1}{2}\frac{\partial\vartheta(s)}{\partial t})\right)$$

Deriving the doubet strength against t and s using its definition 3.37 it comes

$$\begin{aligned}\frac{d\vec{L}}{ds} &= 2\pi\rho V\cdot sV_\perp R\frac{dR}{ds}\vec{n_\perp} - \rho 2\pi\frac{\partial V_\perp}{\partial t}R^2\vec{n_\perp} \\ &= 2\pi\rho V\cdot sV_\perp R\frac{dR}{ds}\vec{n_\perp} - \rho 2\pi a_{i,\perp}R^2\vec{n_\perp}\end{aligned}$$

Denoting that $\vec{n_\perp} = \frac{\vec{V_\perp}}{V_\perp} = \frac{\vec{a_\perp}}{a_\perp}$ it comes the final expression of the elementary lift.

$$\begin{aligned}\frac{d\vec{L}}{ds} &= 2\pi\rho V\cdot s\vec{V_\perp}R\frac{dR}{ds} - \rho 2\pi\vec{a_{i,\perp}}R^2 \\ &= 2\pi\rho V\cdot s\vec{V_\perp}R\frac{dR}{ds} - \rho 2\pi(\vec{a_i} - (\vec{a_i}\cdot\vec{s})\vec{s})R^2\end{aligned} \tag{3.44}$$

3.44 is the combination of Eq (68) and (86) of the Drela's technical document. This equation highlights the different properties of the lift. First of all, it does not depend on the source strength but only on that of the doublets. Secondly, the lift and added mass forces (unsteady part of the lift equation) will point towards the same/opposite direction of the cross-section projection of the local velocity ie acceleration. Indeed in the steady case, the direction of lift is $\frac{dR}{ds}$ sign dependant as depicted in figure 3.2.

Appendix B: The vectorial formulation of the unsteady Kutta Jukowski theorem

Let us consider a thin vortex sheet S made of an airfoil and wake vortex sheets S_a and S_w such that $S = S_a \cup S_w$. At any point P on S let V^+ and V^- be the upper and lower velocities as depicted in the figure 3.34. We define the jump operator $\Delta\square$ of any variable $\square$ as the difference $\square^+ - \square^-$. The vortex sheet distribution $\gamma_a(\xi)$ results in a tangential velocity jump equal to the local strength

$$\gamma_a(\xi) = V^+ - V^- = \Delta V \tag{3.45}$$

The local vortex sheet is oriented in the spanwise direction such that

$$\vec{\gamma(\xi)} = \vec{\eta} \times \Delta\vec{V}(\xi) = \Delta V \vec{s} \tag{3.46}$$

where $\vec{\eta}$ and $\vec{s}$ are respectively the vortex sheet normal and spanwise unit vectors. From incompressible and irrotational condition the 2D flow can be modeled by a potential function $\phi(\xi, \eta)$ such that

$$\vec{V} = \nabla\phi = \begin{pmatrix} \frac{\partial\phi}{\partial\xi} \\ \frac{\partial\phi}{\partial\eta} \end{pmatrix} \tag{3.47}$$

One can define any closed curve $\mathcal{C}$ that connects the upper and lower side of the sheet in P (cf figure 3.34). The circulation Γ is then defined as

$$\Gamma = \oint_{\mathcal{C}} \vec{V} \cdot d\vec{\xi} = \oint_{\mathcal{C}} \nabla\vec{\phi} \cdot d\vec{\xi} \tag{3.48}$$

Note that equation 3.48 can be separated as follow

$$\Gamma = \oint_{\mathcal{C}^+} \nabla\vec{\phi}^+ \cdot d\vec{\xi} - \oint_{\mathcal{C}^-} \nabla\vec{\phi}^- \cdot d\vec{\xi} \tag{3.49}$$

with $d\vec{\xi}$ always tangent to the vortex sheet. If we evaluate this integral on the vortex sheet, the velocity is tangent to s, in consequence, $\nabla\phi = \begin{pmatrix} \frac{\partial\phi}{\partial\xi} \\ 0 \end{pmatrix}$ Equation 3.49 simplifies then to

$$\Gamma = \oint_{\mathcal{C}^+} \frac{\partial\phi^+}{\partial\xi} \cdot d\vec{\xi} - \oint_{\mathcal{C}^-} \frac{\partial\phi^-}{\partial\xi} \cdot d\vec{\xi} \tag{3.50}$$

That is finally given as

$$\Gamma = \oint_{\mathcal{C}^+} \partial\phi^+ - \oint_{\mathcal{C}^-} \partial\phi^- = \phi^+ - \phi^- = \Delta\phi \tag{3.51}$$

From the equation 3.51 comes the vorticity strength distribution as follows.

$$\vec{\gamma} = \vec{n} \times \Delta\vec{V} = \vec{n} \times \vec{\nabla}\Delta\phi = \vec{n} \times \vec{\nabla}\Gamma \tag{3.52}$$

Now from the unsteady Bernoulli equation, the local pressure jump on the airfoil vorticity sheet can be computed

$$\frac{\partial\phi^+}{\partial t} + \frac{1}{2}V^{+,2} + \frac{p^+}{\rho} = \frac{\partial\phi^-}{\partial t} + \frac{1}{2}V^{-,2} + \frac{p^-}{\rho}$$

rearranged in

$$\frac{\partial\Delta\phi}{\partial t} + \frac{1}{2}\Delta(V^2) = -\frac{\Delta p}{\rho} \tag{3.53}$$

The dynamic pressure jump in 3.53 can be expressed as follows

$$\frac{1}{2}\Delta(V^2) = \frac{1}{2}(V^+ - V^-) \cdot (V^+ + V^-) = \Delta\vec{V} \cdot \vec{\bar{V}}$$

Using equation 3.46 combined with 3.52 The previous equation can be simplified to

$$\frac{1}{2}\Delta(V^2) = \vec{\eta} \cdot (\vec{\bar{V}} \times \vec{\gamma})$$

The local pressure jump is finally expressed using expression 3.51:

$$-\Delta p(\xi) = \rho\left(\frac{\partial\Gamma}{\partial t} + \vec{\eta} \cdot (\vec{\bar{V}} \times \vec{\gamma})\right) \tag{3.54}$$

Now in ASWING,the vortex sheet S_a is lumped into a vortex line of strength Γ at the quarter chord location as described in figure 3.34. Also, the wake vortex sheet is now considered as a straight prescribed wake of strength Γ_w. From the Kutta condition at the trailing edge ie zero pressure jump $\Gamma_w = \Gamma$. As the wake is by definition force free only the pressure forces over the airfoil have to be integrated. As $\gamma(\xi)$ distribution has been lumped its strength can be expressed as $\gamma(\xi) = \frac{\Gamma}{c_\beta}$. The contribution of circulation variables to the lift is then given by

$$\begin{aligned} \vec{f}_{lift,\Gamma} &= \int_0^{c_\beta} \Delta p d\xi \vec{\eta} = \rho\frac{\partial\Gamma}{\partial t}c_\beta\vec{\eta} + \rho\Gamma(\vec{\bar{V}} \times \vec{s}) \\ &= \rho\frac{\partial\Gamma}{\partial t}c_\beta\frac{\Gamma(\vec{\bar{V}} \times \vec{s})}{|V|} + \rho\Gamma(\vec{\bar{V}} \times \vec{s}) \end{aligned} \tag{3.55}$$

One has denoted c_β instead of the local chord c. The reason is that in the ASWING model, the wake is wind-aligned. It means that it does not necessarily lie in the cross-section place (c,n) as described in figure 3.4(a). Or, as the unsteady vectorial Kutta-Joukowsky theorem is 2D it must be integrated into the plane where the horseshoe legs of the wake. The local chord must be changed in consequence. By denoting $V_\perp$ as the projected velocity vector into the cross-section plane (c, n), we can identify thanks to figure 3.4(b) that

$$\frac{c_\beta}{c} = \frac{|V|}{|V_\perp|}$$

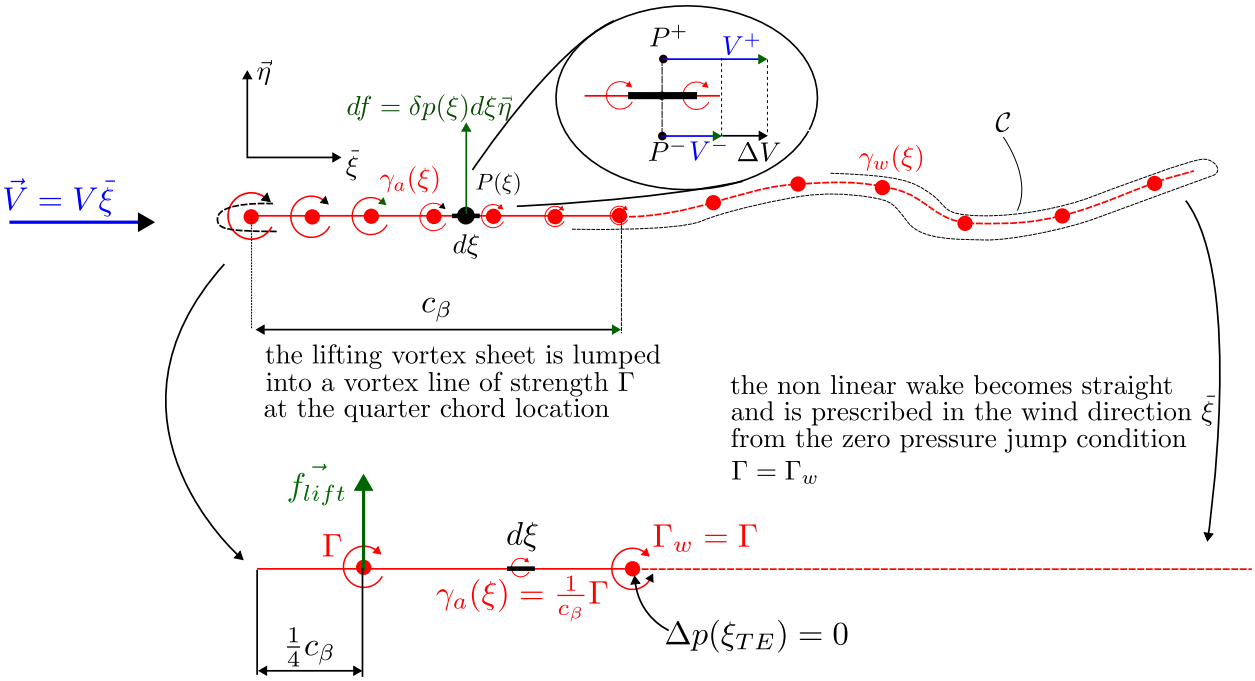

Figure 3.34: Kutta-Joukowsky theorem illustration of the vortex sheet lumping and simplification

Using it in equation 3.55 leads to the final expression of the unsteady circulatory lift.

$$\vec{f}_{lift,\Gamma} = \rho c \frac{\partial \Gamma}{\partial t} \frac{(\vec{V} \times \vec{s})}{|V_\perp|} + \rho \Gamma (\vec{V} \times \vec{s}) \qquad (3.56)$$

Equation 3.3 is finally consistent with equations (38) of Drela (2008). In light of the equation we can notice that despite the Kutta Joukowski theorem has been derived into a 2D plane that does not necessarily lie into the cross-section one, the lift forces lie into it as depicted in figure 3.3(a) Note that we have denoted the lift induced by the circulation variable Γ.

Appendix C: XFOIL analysis of the effect of the Reynolds number and a deflected flap on the ASWING parameters

An XFOIL analysis of NACA4415 is presented in figure 3.35. Figure 3.35 (a) highlights the variation of the lift stall and zero lift angle with angle of attack. Figure 3.35 (b) depicts the lift stall shifting with a flap deflection. Figures 3.35 (c) and (d) highlight the flap derivatives linearity with flap deflection angle and their variation with the Reynolds number.

Appendix D : Boeing KC-135 geometry and MSES airfoil analysis:

The figure 3.36 presents 4 MSES (Drela and Giles 1987 and 1993) KC-130-A airfoil analysis at 2 lift coefficients. The effect of the Mach number and lift coefficient on the appearance of the shock can be clearly identified. Also, the effect of the shock position on the boundary layer thickness and thus friction drag is also illustrated. There is a huge dependency of the drag coefficient with the Ma number and lift coefficient at transonic flow thus the discrepancies identified in the transonic cases presented earlier in the chapter. Figure 3.37 presents all the geometric parameters and airfoil of the KC-130 to reproduce the aircraft in ASWING.

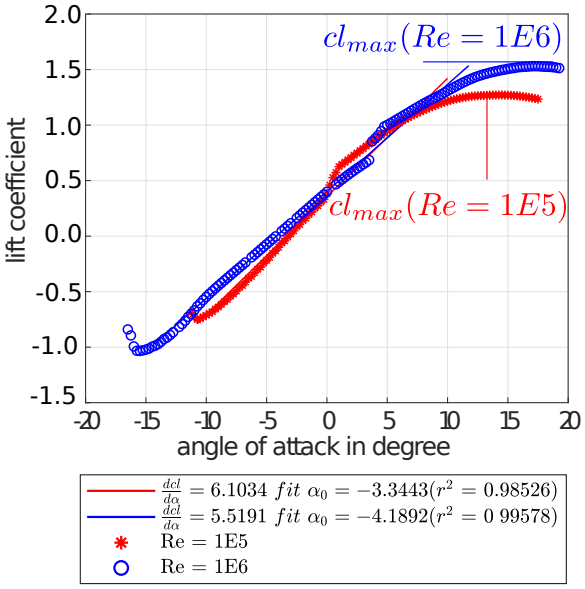

(a) *Re* effect on cl_α cl_{min}, cl_{max}, α_0

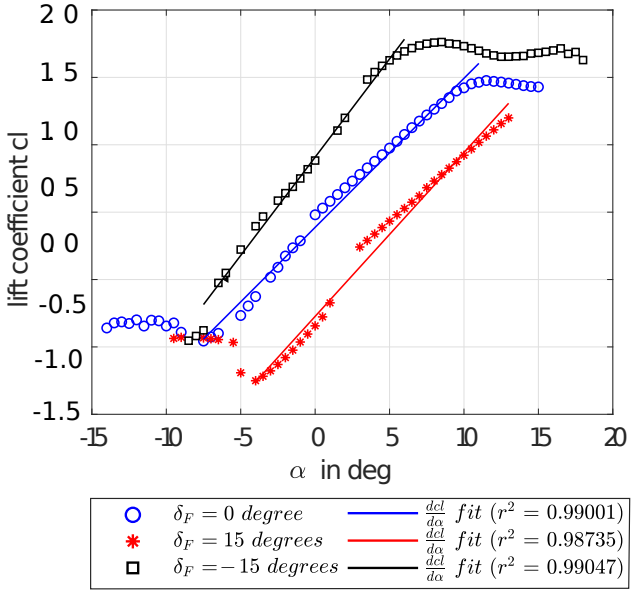

(b) Effect of a deflected flap on cl_α, α_0, cl_{min} and cl_{max}

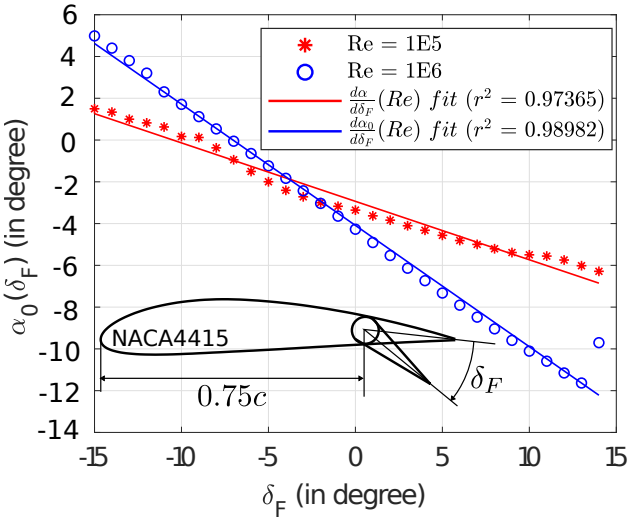

(c) *Re* effect on the $\frac{d\alpha_0}{d\delta_F}$ slope

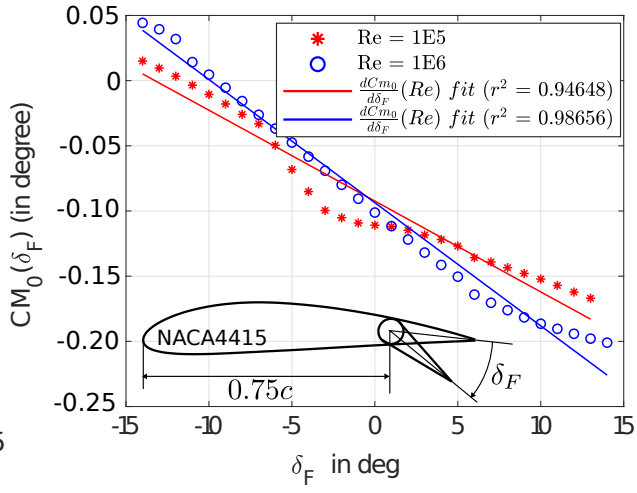

(d) *Re* effect on the $\frac{dCM_0}{d\delta_F}$ slope

Figure 3.35: Effect of Reynolds number and flap deflection on ASWING airfoil derivatives. Illustration on the NACA4415

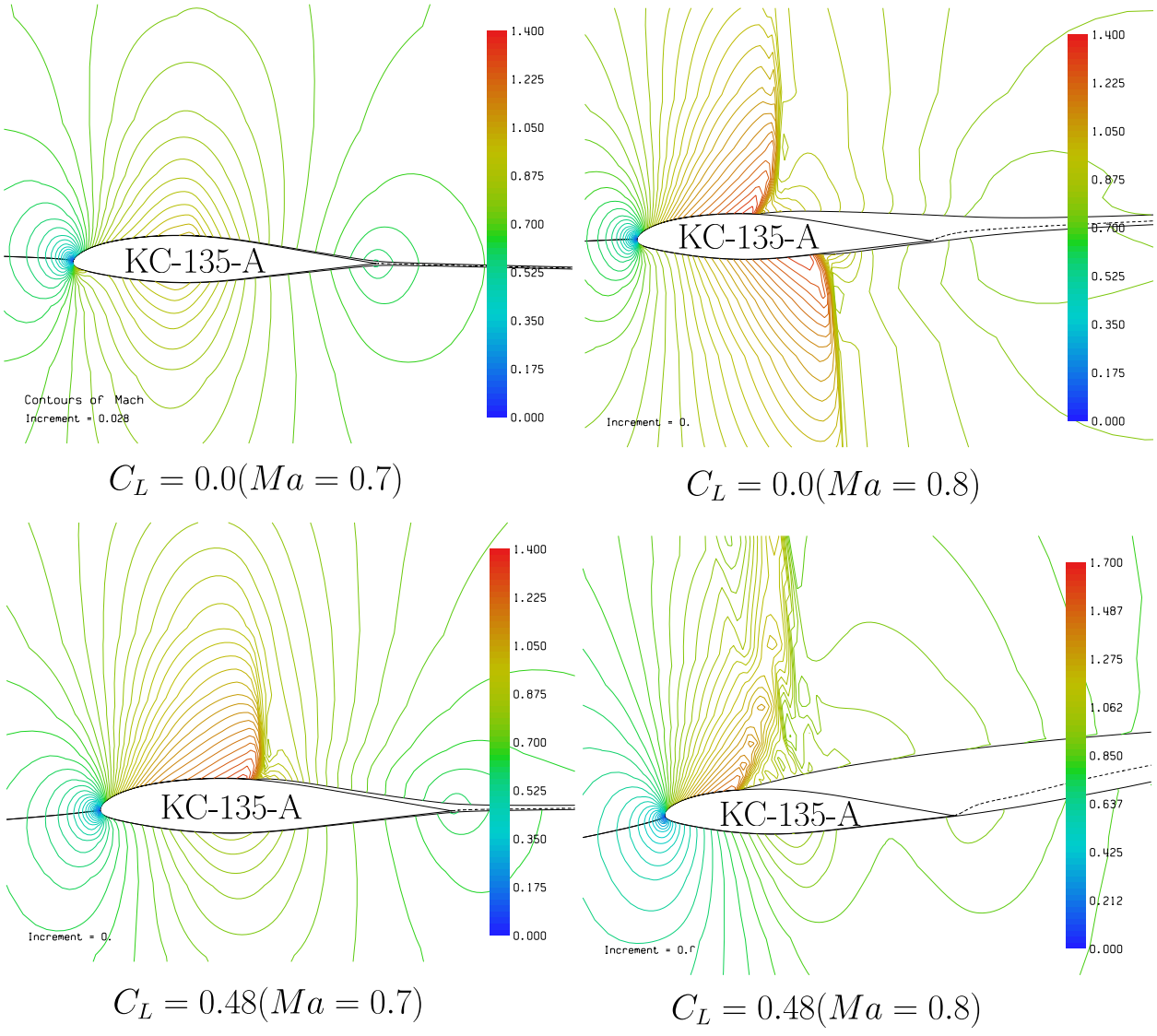

$C_L = 0.0(Ma = 0.7)$ $C_L = 0.0(Ma = 0.8)$

$C_L = 0.48(Ma = 0.7)$ $C_L = 0.48(Ma = 0.8)$

Figure 3.36: Appendix-D:Boeing KC-135 geometry and airfoils

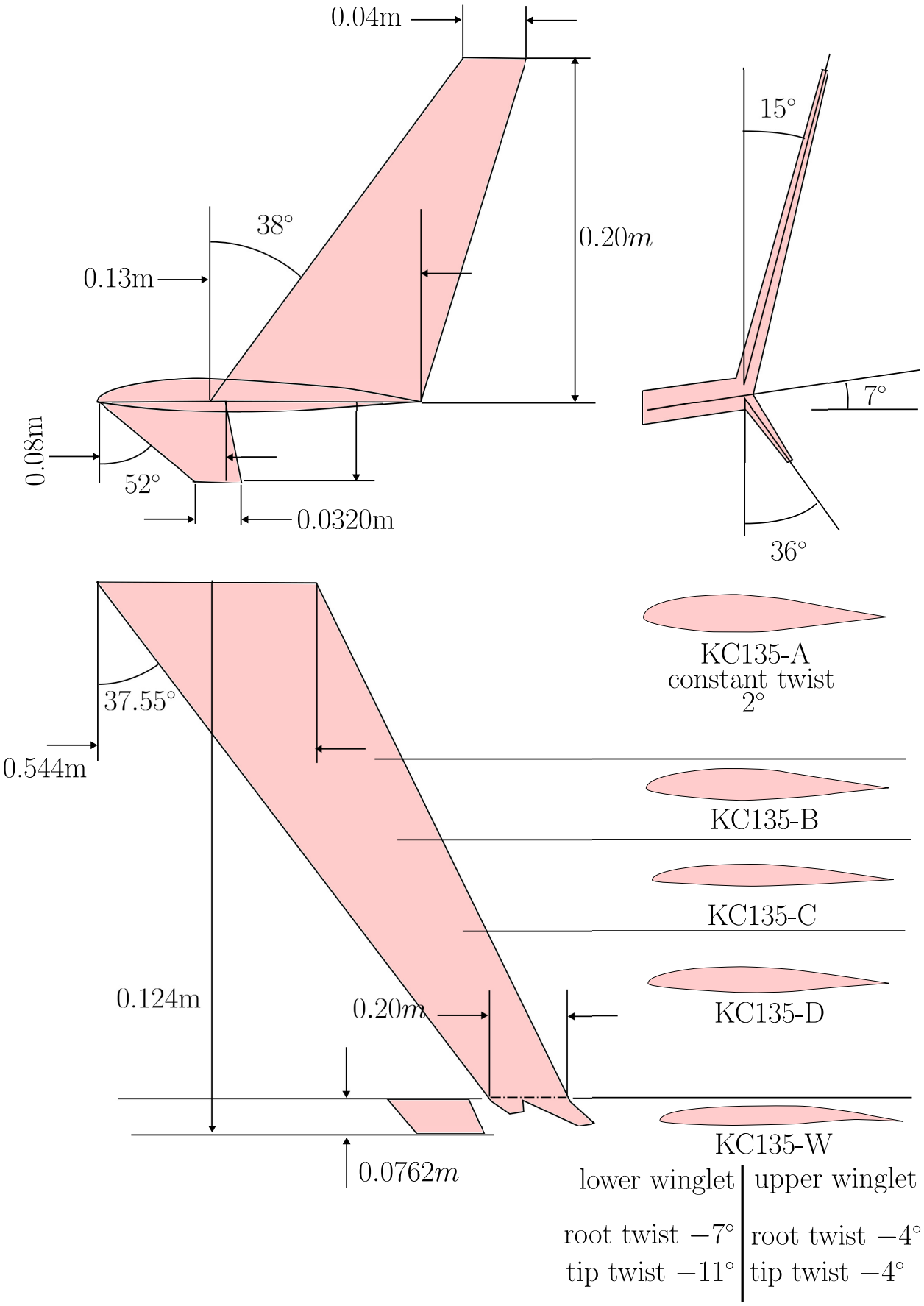

Figure 3.37: Appendix-D: Boeing KC-135 geometry and airfoils

Bibliography

[1] Applin, Z. T. (1995). Pressure Distributions From Subsonic Tests of a NACA 0012 Semispan Wing Model. NASA Technical Memorandum 110148, NASA, Langley Research Center, Hampton, Virginia. 13, 81, 82, 84

[2] Barber, M. R. and Selegan, D. (1982). Kc-135 winglet program overview. *KC-135 Winglet Program Rev.* 13, 82, 97

[3] Chandre-Vila, O., Boin, J.-P., Barriety, B., Nivet, Y., Morlier, J., and Gourdain, N. (2023). Fast Nonlinear Static Aeroelasticity Method for High-Aspect-Ratio Wings at Different Mach Regimes. *Journal of Aircraft*, pages 1–21. 70, 71

[4] Chandre Vila, O., Nivet, Y., Morlier, J., and Gourdain, N. (2022). Fast Method For Dynamic Fluid-Structure Interactions Considering Unsteady Aerodynamics. In *AIAA SCITECH 2022 Forum*, San Diego, CA & Virtual. American Institute of Aeronautics and Astronautics. 70, 71

[5] Chauhan, S. S. and Martins, J. R. R. A. (2019). Low-Fidelity Aerostructural Optimization of Aircraft Wings with a Simplified Wingbox Model Using OpenAeroStruct. In Rodrigues, H., Herskovits, J., Mota Soares, C., Araújo, A., Guedes, J., Folgado, J., Moleiro, F., and Madeira, J. F. A., editors, *EngOpt 2018 Proceedings of the 6th International Conference on Engineering Optimization*, pages 418–431. Springer International Publishing, Cham. 70, 71

[6] Cheng, H. and Wang, H. (2018). Prediction of Lift Coefficient for Tandem Wing Configuration or Multiple-Lifting-Surface System Using Prandtl's Lifting-Line Theory. *International Journal of Aerospace Engineering*, 2018:1–15. 13, 82, 90, 91, 92

[7] Chiereghin, N., Cleaver, D., and Gursul, I. (2017a). Unsteady Force and Flow Measurements for Plunging Finite Wings. In *47th AIAA Fluid Dynamics Conference*, Denver, Colorado. American Institute of Aeronautics and Astronautics. 14, 83, 104, 110, 111, 112, 113

[8] Chiereghin, N., Cleaver, D., and Gursul, I. (2017b). Unsteady Measurements for a Periodically Plunging Airfoil. In *55th AIAA Aerospace Sciences Meeting*, Grapevine, Texas. American Institute of Aeronautics and Astronautics. 13, 14, 83, 103, 105, 106, 107, 108, 113

[9] Chreim, J. R. (2019). *Development of a propeller Lifting-Line tool for analysis and design.* Mestrado em Engenharia Mecânica de Energia de Fluidos, Universidade de São Paulo, São Paulo. 76

[10] Colas, D., Roberts, N. H., and Suryakumar, V. S. (2018a). HALE Multidisciplinary Design Optimization Part I: Solar-Powered Single and Multiple-Boom Aircraft. In *2018 Aviation Technology, Integration, and Operations Conference*, Atlanta, Georgia. American Institute of Aeronautics and Astronautics. 71

[11] Colas, D., Roberts, N. H., and Suryakumar, V. S. (2018b). HALE Multidisciplinary Design Optimization Part I: Solar-Powered Single and Multiple-Boom Aircraft. In *2018 Aviation Technology, Integration, and Operations Conference*, Atlanta, Georgia. American Institute of Aeronautics and Astronautics. 70

[12] Drela, M. (1993). Design and optimization method for multi-element airfoils. In *Aerospace Design Conference*, page 969. 120

[13] Drela, M. (1999). Integrated simulation model for preliminary aerodynamic, structural, and control-law design of aircraft. In *40th Structures, Structural Dynamics, and Materials Conference and Exhibit*, St. Louis,MO,U.S.A. American Institute of Aeronautics and Astronautics. 70

[14] Drela, M. (2008). ASWING 5.81 Technical Description — Unsteady Extension. page 42. 70, 71, 77, 103, 116, 119

[15] Drela, M. (2009). ASWING 5.86 Technical Description — Steady Formulation. page 57. 70, 71, 116, 117

[16] Drela, M. (2014). *Flight vehicle aerodynamics.* MIT press. 78

[17] Drela, M. and Giles, M. B. (1987). Viscous-inviscid analysis of transonic and low reynolds number airfoils. *AIAA journal*, 25(10):1347–1355. 120

[18] ESCUDERO, C. F. (2021). *Contrôle passif des instabilités aéroélastiques des ailes d'avion par ajout d'oscillateurs non linéaires.* PhD thesis, Université de Toulouse, ISAE-SUPAERO, Polytechnique Montréal, Toulouse/Montréal. 109

[19] Feistel, T. W., Corsiglia, V. R., and Levin, D. B. (1981). Wind-Tunnel Measurements of Wing-Canard Interference and a Comparison with Various Theories. *SAE Transactions*, 90:2026–2039. Publisher: SAE International. 13, 82, 87, 91

[20] Fernandez-Escudero, C., Gagnon, M., Laurendeau, E., Prothin, S., Michon, G., and Ross, A. (2019). Comparison of low, medium and high fidelity numerical methods for unsteady aerodynamics and nonlinear aeroelasticity. *Journal of Fluids and Structures*, 91:102744. 19, 109, 113

[21] González, O., Boschetti, P., Cárdenas, E., and Amerio, A. (2010). Static-Stability Analysis of an Unmanned Airplane as a Flexible-Body. In *AIAA Atmospheric Flight Mechanics Conference*, Toronto, Ontario, Canada. American Institute of Aeronautics and Astronautics. 70

[22] HEALD, R. and STROTHER, D. (1929). Report No. 298. Effect of variation of chord and span of ailerons on rolling and yawing moments in level flight. *Journal of the Franklin Institute*, 207(5):715–716. 13, 82, 85, 87, 88

[23] HEALD, R. and STROTHER, D. (1930). Report No. 343. Effect of variation of chord and span of ailerons on rolling and yawing moments at several angles of pitch. *Journal of the Franklin Institute*, 210(1):126–127. 13, 82, 85, 89

[24] J. WEBER, Dr.rer.nat. and G. G. BREBNER, M.A (1958). Low,Speed Tests on 45.deg Swept.back Wings PART I. PRESSURE MEASUREMENTS ON WINGS OF ASPECT RATIO 5. AERONAUTICAL RESEARCH COUNCIL REPORTS AND MEMORANDA 2882, LONDON" HER MAJESTY'S STATIONERY OFFICE. 13, 82, 83, 84

[25] Jacobs, P. F., Flechner, S. G., and Montoya, L. C. (1977). Effect of winglets on a first-generation jet transport wing. 1: Longitudinal aerodynamic characteristics of a semispan model at subsonic speeds. Technical report. 13, 82, 93, 97

[26] Jan, R., Condomines, J.-P., and Moschetta, J.-M. (2021). Fast simulation model for control law design andbenchmark of high aspect ratio flexible UAVs. 70, 71

[27] Jasa, J. P., Hwang, J. T., and Martins, J. R. R. A. (2018). Open-source coupled aerostructural optimization using Python. *Structural and Multidisciplinary Optimization*, 57(4):1815–1827. 70, 71

[28] Jones, J. (2017). *Development of a very flexible testbed aircraft for the validation of nonlinear aeroelastic codes*. PhD thesis. 70

[29] Love, M., Zink, P., Wieselmann, P., and Youngren, H. (2005). Body Freedom Flutter of High Aspect Ratio Flying Wings. In *46th AIAA/ASME/ASCE/AHS/ASC Structures, Structural Dynamics and Materials Conference*, Austin, Texas. American Institute of Aeronautics and Astronautics. 70

[30] Martina, A. P. (1956). The interference effects of a body on the spanwise load distributions of two 45 degree sweptback wings of aspect ratio 8.02 from low-speed tests. Technical report. 13, 82, 100, 102

[31] McCormack, G. and Stevens Jr, V. I. (1947). An investigation of the low speed stability and control characteristics of swept-forward and swept-back wings in the ames 40-by 80-foot wind tunnel. Technical report, NATIONAL AERONAUTICS AND SPACE ADMINISTRATION MOFFETT FIELD CA AMES RESEARCH 13, 82, 93, 94

[32] Miklosovic, D. S. (2008). Analytic and experimental investigation of dihedral configurations of three-winglet planforms. 13, 82, 93, 95

[33] Milne-Thomson, L. M. (1973). *Theoretical aerodynamics*. Courier Corporation. 100, 114

[34] Recant, I. G. (1939). Wind-tunnel investigation of ground effect on wings with flaps. Technical report. 13, 79, 82, 96, 99

[35] Theodore Theodorsen (1935). Report No. 496, general theory of aerodynamic instability and the mechanism of flutter. *Journal of the Franklin Institute*, 219(6):766–767. 74, 103

[36] Upson, R. H. and Klikoff, W. (1933). Application of practical hydrodynamics to airship design. NACA Technical Report 405, NACA. 98

[37] van Dam, C. P., Vijgen, P. M. H. W., and Holmes, B. J. (1991). Experimental investigation on the effect of crescent planform on lift and drag. *Journal of Aircraft*, 28(11):713–720. 13, 82, 83, 85, 86

[38] VanDorn, N. H. and DeYoung, J. (1947). A comparison of three theoretical methods of calculating span load distribution on swept wings. Technical report. 82, 93

[39] Variyar, A., Economon, T. D., and Alonso, J. J. (2017). Design and Optimization of Unconventional Aircraft Configurations with Aeroelastic Constraints. In *55th AIAA Aerospace Sciences Meeting*, Grapevine, Texas. American Institute of Aeronautics and Astronautics. 70

[40] Von Karman, T. (1930). Calculation of pressure distribution on airship hulls. NACA Technical Memorandus 574. 13, 82, 98, 101

[41] Warwick, S., Bras, M., Richards, J., and Suleman, A. (2019). Measurement of Aeroelastic Wing Deflections Using Modal Shapes and Strain Pattern Analysis. In *AIAA Scitech 2019 Forum*, San Diego, California. American Institute of Aeronautics and Astronautics. 70

[42] Wenzinger, C. J. and Harris, T. A. (1939). Wind-tunnel investigation of an naca 23021 airfoil with various arrangements of slotted flaps. Technical report, US Government Printing Office. 96

[43] Werter, N. and De Breuker, R. (2016). A novel dynamic aeroelastic framework for aeroelastic tailoring and structural optimisation. *Composite Structures*, 158:369–386. 70, 71

Chapter 4

Aeroelastic framework Part II : Propeller and jet

Abstract

This chapter is the second part of an experimental evaluation and modification of an aeroelastic framework (ASWING). In this chapter, the propeller model is investigated. First, the theoretical models are briefly presented by referring to the fundamental work in the literature on which ASWING is based. The second part of the paper is dedicated to the experimental validation of the model. The ASWING predictions of propeller thrust and efficiency are evaluated against several propellers from the modern literature. In the light of the results, a modification of the model is proposed to increase its accuracy. Secondly, the non-axial flow condition is presented where the normal force, yaw moment and thrust predictions are investigated. Thirdly, experimental data are used to evaluate the jet and swirl velocity field prediction in static and advanced flow conditions. Finally, the ability of ASWING to predict the interactions and their consequences between a propeller jet and a lifting surface is presented. With the exception of the normal and yaw moment predictions, ASWING shows good agreement with the experimental data.

Publications:

Materials from chapter 3 and 4 have been gathered and summarized so that a journal paper could be submitted to AIAA Journal of Aircraft with the title:

R.Jan, J-M. Moschetta and J-P. Condomines, Experimental evaluation of ASWING for preliminary design of flexible aircraft: aerodynamic model, AIAA Journal of Aircraft, 2024.

This paper will be published after the PhD manuscript would have been made public so that the complete evaluation work can be cited in the paper.

Contents

List of symbols and acronyms

Symbols

$A_1 = \pi R_e^2$	Actuator disk section
$V_{xe} = V_e$	engine air relative axial velocity
V_{sw}	swirl velocity
ΔV_e	downstream velocity increment
F_e	engine thrust
M_e	engine momentum
$\mathcal{P}_e$	Engine shaft power
$\mathcal{P}_v$	Power losses due to viscous effects
$\mathcal{P}_{sw}$	Power losses due to swirl velocity
$\mathcal{E}_{sw}$	Kinematic Energy losses due to swirl velocity
$\lambda = V_e/\Omega_e R_e$	advance ratio
$\mu = cos(\alpha_p)\lambda$	axial advance ratio
Ω_e	Engine shaft rotation rate
B	Propeller number of blades
$R_e = D/2$	Propeller radius
c_d	local 2D drag coefficient
W	radial air relative velocity
$dL, \tilde{dL}$	elementary lift and pertubated lift
$dD, \tilde{dD}$	elementary lift and pertubated drag
$dS, \tilde{dS}$	elementary lift and pertubated side force
$dT, \tilde{dT}$	elementary lift and pertubated thrust
$W, \tilde{W}$	local air relative and pertubated speed
$\phi, \tilde{\phi}$	local flow angle and pertubated flow angle
v	transverse velocity pertubation
ω	pitch rate pertubation
F_v	Normal force induced by v
M_v	Yaw moment induced by v
F_ω	Normal force induced by ω
M_ω	Yaw moment induced by ω
C_0, C_1, C_2, C_3	approximated radial blade integrand
S_0, S_1, S_2, S_3	approximated radial blade integrand
α_P	propeller pitch angle
V_∞	upcoming freestream velocity
$\mathcal{L}_{\tilde{W},\tilde{\phi}}(\lambda, \alpha_P)$	P-factor logical validity map
$C_T = F_e/(\rho n^2 D^4)$	thrust coefficient
$C_P = P_e/(\rho n^3 D^5)$	power coefficient
$C_N = F_v/(\rho n^2 D^4)$	normal force coefficient
$C_n = M_v/(\rho n^2 D^5)$	yaw moment coefficient
η	propeller efficiency
$n = \Omega_e/R_e$	propeller rate
C_L/C_D	wing lift over drag ratio

Acronyms

UVLM/UVPM	Unsteady Vortex Lattice/Vortons Method
LES	Large Eddy Simulation
UAV	Unmanned Aerial Vehicule
EADT	Extended Actuator Disk Theory
VTOL	Vertical Take Off and Landing
FEZ	Flow Establishement Zone
EFZ	Established Flow Zone

Résumé du chapitre en français

Ce chapitre se concentre sur la deuxième partie du travail de validation expérimentale et de modification d'ASWING. Celle ci est dédiée au modèle d'hélice. En premier lieu ce chapitre semble éloigné du champs d'application de la thèse, cependant avoir un outil capable de prédire correctement le transfert entre poussée et puissance axiale transmise à une hélice s'avère être un atout majeur lorsque l'on considère l'étude de stratégies d'extraction d'énergie. En effet la puissance axiale est une métrique de performance bien plus pertinente que la poussée moteur puisque leur transfert n'étant pas linéaire, il convient de s'assurer de sa bonne qualité de prédiction. Il est important de noter que le modèle hélice d'ASWING propose des fonctionnalités relativement éloignées du sujet principal de thèse, cependant une revue complète est tout de même proposée car elle pourrait bénéficier à la communauté. À la lumière des comparaisons effectuées, certaines modifications sont proposées. Le modèle hélice d'ASWING consiste en la composition de 3 formulations distinctes. Le premier modèle, reposant sur une extension de la théorie de Froude (théorie de quantité de mouvement), vise à prodiguer le transfert entre la puissance axiale et la poussée moteur générée par une hélice. Sur ce dernier nous proposons une revue de la littérature remontant à la fin du 19e siècle justifiant les différentes approximations et résultats employés. Via l'utilisation d'une base de donnée expérimentale, la qualité de prédiction du modèle est étudiée sur un ensemble d'hélice destinées à des mini drones. Il est montré que via une modification très simple, la précision du modèle peut être significativement améliorée. Une deuxième partie se concentre sur le modèle instationnaire de l'hélice nommée P-factor. Ce dernier vise en premier lieu à permettre l'étude des phénomènes de flottement par effet de précession, via l'étude de l'impact de légères perturbations en tangage et vitesse transverse de l'axe de l'hélice. Or ici, une mise à l'épreuve du modèle à été effectuée dans le cadre d'un écoulement amont non axial. L'idée étant de voir si le modèle peut prédire les efforts et moments générés par l'hélice dans ces conditions. Par la suite, le modèle du jet d'hélice est évalué pour des conditions statiques et en écoulement. Les vitesses axiales et azimutales évaluées à différentes positions radiales, le long du jet sont présentées. A la lumière des résultats une modification est proposée pour prendre en compte les effets du nez d'encastrement de l'hélice ne générant pas de poussée. Pour finir les modèles de Froude et jet sont combinés avec la ligne portante d'ASWING et évalués contre différentes données de la littérature scientifique. En particulier l'impact d'une hélice sur la distribution en portance d'une aile immergée dans son jet ainsi que sa position verticale et latérale sur le rapport de finesse de la surface portante sont discutées.

Conclusions générales: Modulo la modification proposée sur la théorie de Froude, ASWING est en mesure de fournir correctement le transfert entre puissance axiale et poussée moteur. Cependant la qualité de ses prédictions dépend du jeu de données qui a été utilisé pour construire la fonction polynomiale utilisée dans la modification du modèle. La théorie de Froude donne aussi de correctes prédictions en poussée d'une hélice immergée dans un écoulement non axiale, ce jusqu'à un angle d'incidence de 60°. En revanche la partie instationnaire du modèle hélice (P-factor) n'est pas en mesure de capturer les efforts et couples non axiaux générés dans ce genre de situation. Par la suite l'étude du modèle de jet a montré une bonne prédiction de la vitesse axiale et azimutale sur différents types d'hélices dans des conditions statiques et en écoulement. En revanche, ASWING ne peut pas prendre en compte l'effet du cône d'encastrement de l'hélice ne générant pas de poussée. La modification proposée améliore légèrement la qualité du modèle. Lorsqu'une surface portante est placée dans le jet d'une hélice, l'effet de ce dernier est correctement capturé sur la distribution en portance. Et ce quelque soit le sens de rotation de l'hélice. De plus ASWING est en mesure de capturer l'effet de la position horizontale de l'hélice sur les performances aérodynamiques de l'aile. Cependant l'effet de la position verticale ne peut être capturé. En effet ces dernières font intervenir 2 phénomènes distincts. Le premier étant lié à l'effet de la vorticité du jet prise en compte par le modèle de ligne portante d'ASWING. Tandis que le second est lié à une accélération de l'écoulement sur l'intrados ou l'extrados de l'aile, non capturé. Ceci étant dit, à la lumières des résultats, le modèle d'hélice d'ASWING peut être utilisé dans le cadre de l'étude de stratégies d'extractions d'energie, ou l'objectif de ces dernières est de minimiser la puissance moteur investie au cours du vol.

4.1 Introduction

With the rise of computer power over the past 50 years, more sophisticated propeller modelling techniques are used against the historical Froude's momentum theory (Actuator disk theory). From unsteady/steady vortex lattice/vortons methods (UVLM/UVPM) to large eddy simulation (LES), they can provide very sophisticated insights into fluid mechanisms. For example, recently they allowed the acoustic and aerodynamic optimization of turbo propellers and Unmanned Aerial Vehicles (UAV) Li Volsi et al. (2022). Moreover LES and URANS provided more insight into the effect of rugosity on UAV propeller efficiency. However, when it comes to flight mechanics, such a high level of accuracy is not necessary to provide reasonable results and insights. Thus the extended actuator disk theory (EADT) is still used in modern applications to provide first-order insight into different types of applications. When the EADT is coupled to a wake and P-factor model, the field of application becomes wider. The latest version of ASWING (5.96) provides such a model (Drela, 1999, 2008 and 2009). Thus this chapter is the second part of an evaluation sequel work of ASWING. This paper is only dedicated to the propeller model. The first part of this chapter aims to provide a historical review of the theoretical model based on literature by recalling the milestone papers that led to the current model. Also, the conservative assumptions made by the author will be highlighted and discussed when needed. In the second part of this paper, an experimental evaluation of the model is presented. In particular a comparison between the static and dynamic thrust prediction and experiments using (Deters et al. 2014a, 2014 and 2014b)'s works. The effects of blade number, advance ratio λ, and Reynolds number R_e (or rotation rate Ω) are investigated. Then the P-factor model is evaluated against Leng et al. 2019, 2020 data. Normal force, yaw moments, and thrust due to non-axial flow are compared to the Leng et al.'s nonlinear model. This case is mainly chosen to draw the boundary limits of the P-factor model. Then, the jets axial and swirl velocity predictions of 3 different propellers in static and dynamic conditions are presented against Deters et al. Deters's experiments (2014 and 2015). Velocities are evaluated at different radial and streamwise positions. In light of the results, a new jet model taking into account the effect of the propeller hub is presented and compared. Finally, the capacity of ASWING to predict the interaction between a propeller jet and a lifting surface is investigated. In particular, the effect on the wing lift distribution at several angles of attack and rotation directions. Also, the effect of the vertical and spanwise position of a propeller on a downstream wing lift/drag ratio is presented. The latter cases are studied using the data of Veldhuis 1996, 2004, and 2005.

4.2 Theoretical model

4.2.1 Summary

Extended Actuator Disk Theory:
The ASWING extended actuator disk model is used to compute the steady aerodynamic thrust and torque of a propeller. Two main extensions to the initial Rankine-Froude Rankine (1865) and Froude (1889) airscrew theory are implemented. First of all, viscous losses can be considered with an approximation of the power losses due to drag through a constant term as follows

$$\mathcal{P}_v \sim \frac{1}{2}\rho \left(V_e^2 + \Omega_e^2 R_e^2\right)^{1/2} \left(V_e^2 + 3\Omega_e^2 R_e^2\right) \left(C_D A\right)_e \tag{4.1}$$

where V_e is the upcoming freestream velocity or air-relative speed at the engine shaft. Ω_e, R_e and $\left(C_D A\right)_e$ are respectively the engine rotation rate, radius and total effective blade area. Those last 3 parameters are user-defined. Note that $\left(C_D A\right)_e$ is reported by the author (Drela 2009) to vary only with the propeller blade number B as

$$\left(C_D A\right)_e = B R_e c(0.8R_e) c_d(0.8R_e) \tag{4.2}$$

Thus a single set $(c(0.8R_e),\ c_d(0.8R_e))$ can define different propellers having 2, 3, 4 etc blades. This feature is discussed in the evaluation section. Equation 4.1 brings conservatism as it gives an approximation of the viscous loss and not the exact solution to the blade element theory drag integrand. Moreover, $\left(C_D A\right)_e$ is assumed not to vary with neither the blade local Reynolds number (or rotation rate Ω) nor the advance ratio λ. Those approximations are discussed in the evaluation section. The axial momentum theory is then extended by taking into account the swirl losses due to propeller tip vorticity. This extension was early presented after Froude-Rankine by Betz Betz (1920) based on the assumption of angular momentum constancy along the propeller blade. However, in ASWING the swirl losses are approximated by an "empirical" term as follows:

$$\mathcal{P}_{sw} = \frac{1}{2} 5 \lambda^2 \Delta V_e F_e \tag{4.3}$$

with F_e the engine thrust, λ the advance ratio and ΔV_e the flow increment speed at the propeller position. We have not found yet this formulation in the literature except in the author's work (Drela 2009). Glauert(*chapter 1*) presented the general momentum

theory where a similar simplification is made but locally on the blade. Thus "5 λ^2" term in equation 4.3 could be interpretated as an approximation of Glauert (*chapter 3*) power loss integrand. That being said, the extended actuator disk theory is then normally applied leading to a solvable power cubic equation in ΔV_e given as :

$$\begin{aligned}\mathcal{P}_e &= \mathcal{P}_T + \mathcal{P}_v + \mathcal{P}_{sw} \\ &= \left[V_e + (1+5\lambda^2)\frac{\Delta V_e}{2}\right]\left(V_e + \frac{\Delta V_e}{2}\right)\Delta V_e \\ &+ P_v - P_e\end{aligned} \quad (4.4)$$

When the above equation is solved the thrust can be computed as follows

$$F_e = \rho\pi R_e^2\left(V_e + \frac{1}{2}\Delta V_e\right)\Delta V_e = F_e(P_e, \rho, V_e) \quad (4.5)$$

Finally the propeller torque is obtained by a power balance that is

$$M_e = M_e(P_e, \Omega_e) = -\frac{P_e}{\Omega_e} \quad (4.6)$$

A watchdog function is applied to respect the Betz limit Prandtl and Betz in windmill conditions. The latter being computed, the propeller thrust and torque can be obtained. The general momentum theory supposes the propeller to be mass and inertia less, in ASWING those properties are recovered by implementing a constant mass and angular momentum. Their expressions are not necessary for the next development (please refer to equations 94, 95, 113, 117 of Drela (2009) for more details).

P-factor model :
The EADT is extended with a P-factor model. The latter is there only to provide perturbated flow consequences on the propeller forces and moments. Coupled with a structural model, it can provide insight into whirl flutter. This model considers 2 types of perturbations, a uniform transverse velocity v, and shaft pitch rate ω depicted in figure 4.10. Their directions are not necessarily aligned with the engine frame axis. P-factors are computed from a simplification of the blade element theory. First of all, the local blade drag is neglected as well as the local blade aerodynamic pitch moment. Then the flow is assumed to have no slipstream angle and finally the P-factor is computed against a small perturbation assumption (ie small angles). Overall, the P-factor model returns perturbated forces and moments proportional to the transfer velocity and pitch rate perturbations. Please refer to section 14 of Drela (2008) for more details about the theoretical development. It is difficult to evaluate this model except in a whirl flutter analysis which needs a structural model (treated in the aeroelastic part of this sequel work). However, we thought that it could be interesting to see how far can go the p-factor model in non-axial flow condtion. Especially on the normal forces and yawing moments prediction in high-pitch configuration (Vertical take-off and landing configuration, VTOL). Thus only the forces and moments due to a uniform transverse velocity are briefly recalled. Let us consider that the propeller has a pitch angle α_p with the upcoming flow such as the transverse velocity seen by the propeller disk is $v = V_\infty sin\alpha_p$. The forces and moments due to the latter are given as follows

$$F_v = \frac{1}{4}\rho R^2\left[\left(c_{l,\alpha}S_0 - c_l C_0\right)V_d + 2c_l S_1 \Omega R\right]v \quad (4.7)$$

$$M_v = -\frac{1}{4}\rho R^3\left[\left(c_{l,\alpha}C_1 - c_l S_1\right)V_d + 2c_l C_2 \Omega R\right]v \quad (4.8)$$

where V_d is the airspeed at the propeller shaft provided by the EADT, $V_d = V_\infty cos\alpha_p + 0.5\Delta V_e$. Let cl_α be the propeller airfoil lift slope assumed constant and c_l the local lift coefficient evaluated at $0.75R_e$. The user defined coefficients C_0, C_1, S_0 and S_1 are aproximated radial blade integrand proposed by Drela. For their value please refers to *section 14.7* of Drela's work. Note that similar simplified models were proposed without omitting drag and pitch moment by Ribner, (1945b and 1945a)and *chapter 2 section 2.5* of Phillips (2004). When a propeller is under a non-axial flow it produces a normal force, yawing and pitching moments. The first 2 can be captured by equations 4.7 and 4.8 while the third is not. Thus in the evaluation section, the pitch moment is not presented, however, it must be kept in mind that ASWING can not predict it.

Jet wake and swirl modeling:
The extended actuator disk theory and p-factor model provide intels only on the propeller thrust and torque, but nothing about its jet. This gap is completed using jet and swirl models. Both are built to be consistent with the propeller thrust and moments. Jet modelling is still a modern topic, especially in hydrodynamic applications such as ship propeller efflux impact on scour. Wei et al. provide a historical review of "low fidelity" jet modelling techniques. From his work, it has been highlighted that the ASWING propeller jet model mainly derives from the Albertson et al. early work despite more recent propositions (Hong et al., Lam et al.). ASWING use also the Albertson et al.'s axial jet formulation to model the propeller swirl. This seems to be a real novelty as swirl effects are generally neglected as reported by Hong et al.. This simplification was made for hydrodynamic applications and is too conservative for aerodynamic ones, as the jet can spread a lifting surface. Both jet and swirl are thus necessary as they will significantly modify the lift distribution. That being said, the model consists of dividing the flow into two distinct zones,

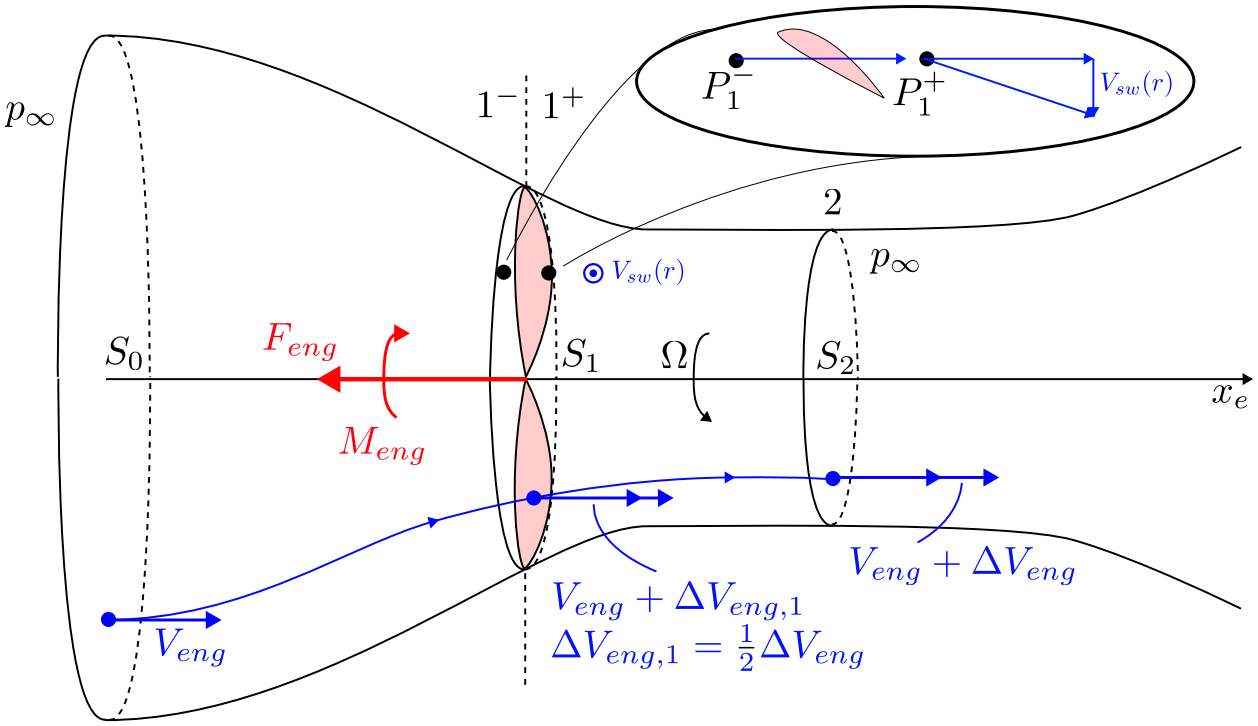

Figure 4.1: Extented actuator disk theory illustration

that are the Flow Establishment one (FEZ) and the Established Flow Zone (EFZ) as depicted in figure 4.2. Their boundaries are efflux dependent. They spread and contract linearly along the streamwise direction. Those zones are used to catch the viscous shear stress between the high and low-speed layers. The jet and swirl velocity are built as radial and streamwise coordinates functions. Their parameters are computed to be consistent with the mass flow and angular momentum conservation along the jet line. Finally, an important feature of the ASWING model, is that the jet is wind and not shaft-aligned. The jet is shed by the upcoming flow. This latter property is mainly true for high advance ratio flow. Note that the propeller hub effects are not modelled. This is discussed against a small change of the model in the evaluation section. Overall, only the propeller radius, rotation speed, and $(C_D A)_e$ are needed to model completely the jet and swirl. For more details about the jet model please refer to *section 3.4.4* of Drela (2009).

4.2.2 P-factor model for whirl flutter analysis:

In this section, the theoretical development of the ASWING p-factor model is proposed with a specific interest in detailing a bit more some of the assumptions and simplification made in the Drela's work. Thus the idea is to derive the blade element theory under simplifying assumption, to investigate how any perturbation seen by the shaft of the propeller has an effect on the overall forces and torques generated. No matter the perturbation at the shaft (gust, shaft bending/torsion, non-axial flow) it will always results in a perturbation in the local air relative speed $W = \sqrt{\Omega^2 r^2 + Vd^2}$ and the local flow angle $\phi = atan(Vd/\Omega r)$. V_d in the previous expressions is the propeller axial velocity defined from the EADT as $Vd = V_e + 0.5\Delta V_e$. The quantities W, ϕ and V_d are depicted in figure 4.3 (a) A tilde notation is adopted for the perturbed state of any variable and d for its elementary radial variation. In the ASWING p-factor model, only the lift is considered, this simplification is discussed in the evaluation section. Let us now consider that lift applied on a blade element of length dr and chord c(r) defined as

$$\begin{aligned} dL &= \frac{1}{2}\rho W(r)^2 c_l(r) c(r) dr \\ &= \frac{1}{2}\rho W^2 c_{l,\alpha}(\beta - \phi_{eff} + \alpha_0) c(r) dr \end{aligned} \tag{4.9}$$

Where c_l is the local lift coefficient embedding the 3D effect (swirl), the local geometric twist β and the local airfoil curvature α_0 (not shown in figure 4.3 -a). Now concidering a pertubation in W and ϕ denoted as $\tilde{W}$ and $\tilde{\phi}$ it comes

$$dL + d\tilde{L} = \frac{1}{2}\rho(W + \tilde{W})^2 (c_l(r) + \tilde{c_l}(r)) c(r) dr$$

Noting that the pertubated lift coefficient $\tilde{c_l}$ is given by the linear lift coefficient slope $c_{l,\alpha}$ times the pertubation angle of attack $\tilde{\alpha} = \tilde{\phi}$ Introducing into (1) it

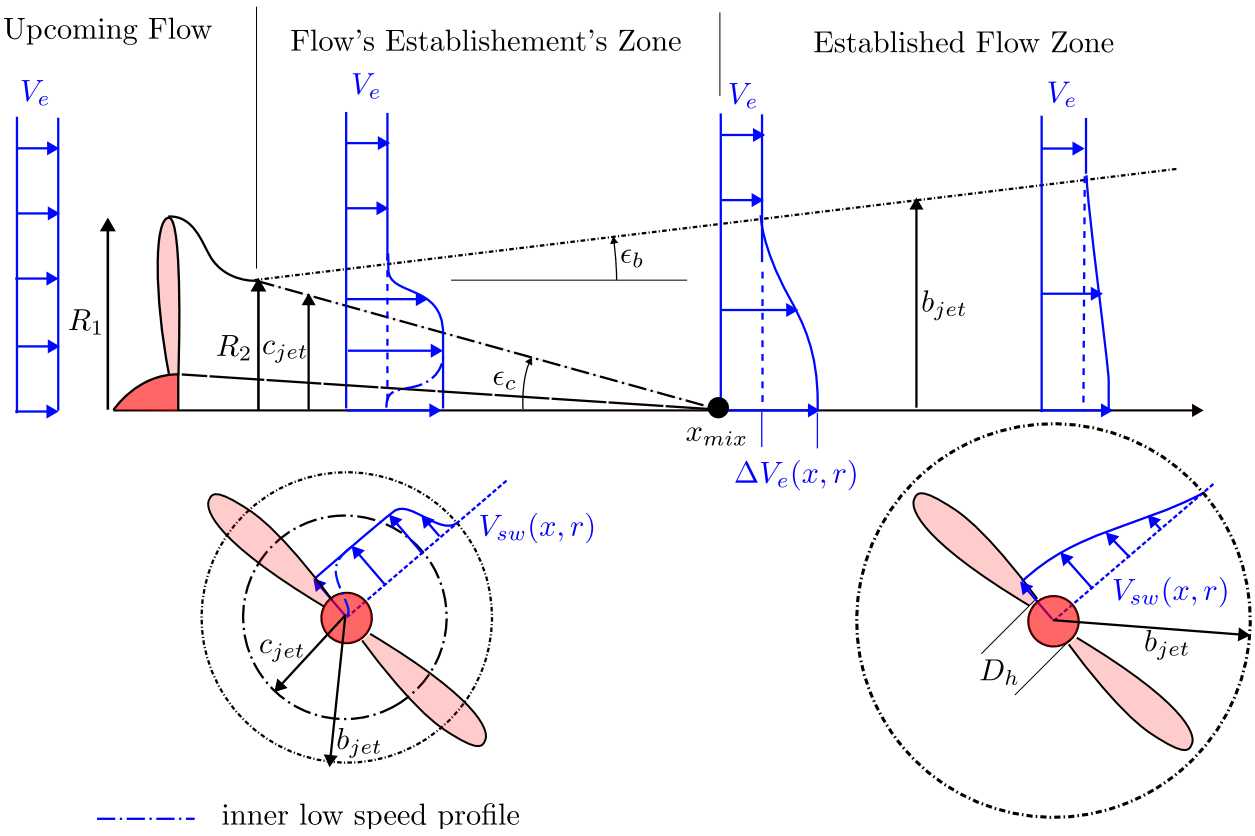

Figure 4.2: Jet axial and swirl velocity components used by Alderson & al and Drela with a proposed modification, an inner low speedcore is implemented to take into account the hub

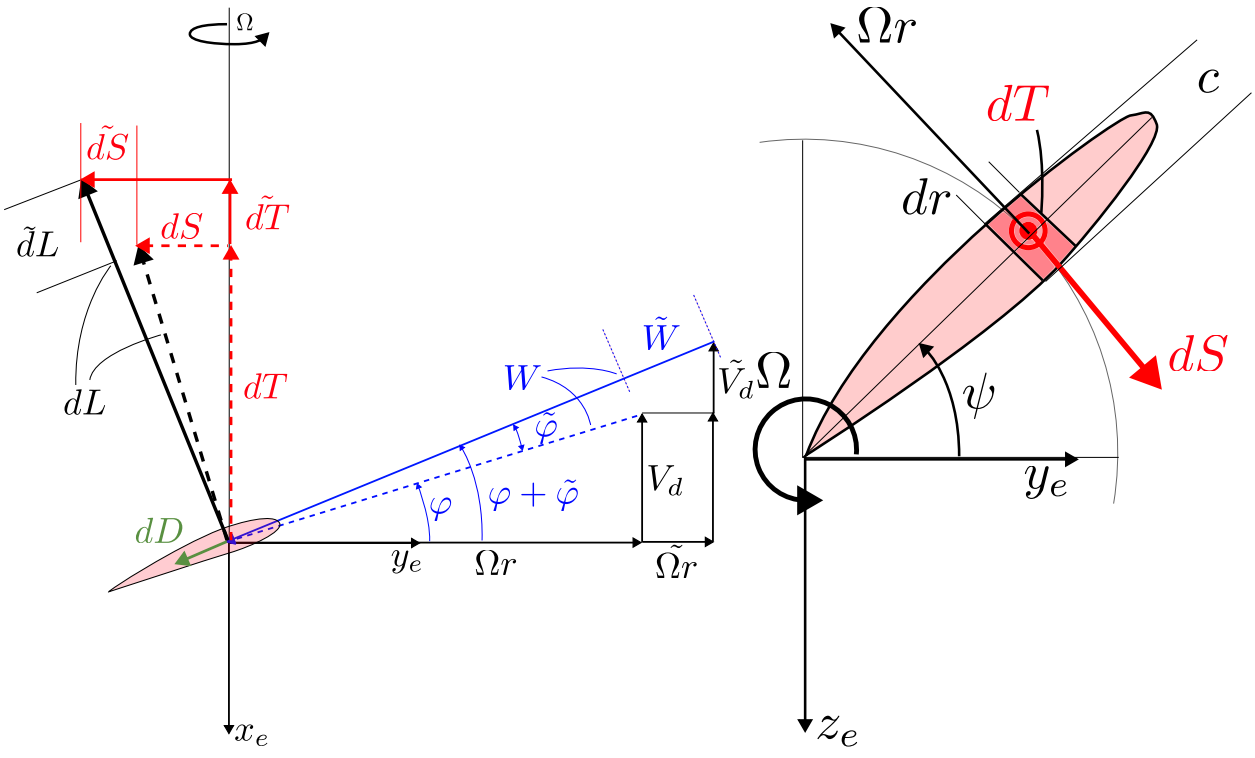

(a) Side view (b) Top view

Figure 4.3: Elementary thrust and side force generated by a blade element. Illustration of the different perturbations

comes :

$$dL + d\tilde{L} = \frac{1}{2}\rho(W + \tilde{W})^2(c_l(r) + c_{l,\alpha}\tilde{\varphi}(r))c(r)dr$$

Developping the above expression and assuming small pertubations ($\tilde{W}W \ll 1$ and $\tilde{\phi}\phi \ll 1$), second order terms can be neglected

$$dL + d\tilde{L} = \frac{1}{2}\rho W^2 c_l(r)c(r)dr + \frac{1}{2}\rho\left(c_{l,\alpha}\tilde{W}^2 + 2W\tilde{W}c_l\right)cdr$$

In the above expression dL can be identified using equation 4.9 leading to the perturbed lift expression

$$d\tilde{L} = \frac{1}{2}\rho\left(c_{l,\alpha}\tilde{\phi}W^2 + 2W\tilde{W}c_l\right)cdr \tag{4.10}$$

Now let us consider, the elementary thrust and side force produced by a blade element. Those are given by convention by,

$$dT = dL\cos(\phi) \tag{4.11}$$

and

$$dS = dL\sin\phi \tag{4.12}$$

Now in the perturbation case, the thrust and side forces are given:

$$dT + d\tilde{T} = (dL + d\tilde{L})\cos(\phi + \tilde{\phi})$$

$$dS + d\tilde{S} = (dL + dL)\sin(\phi + \tilde{\phi})$$

Invoking small angle variation ($\tilde{\phi}/\phi \ll 1$), neglecting second-order terms, and using simplified trigonometric relations on $\cos(\phi + \tilde{\phi})$ and $\sin(\phi + \tilde{\phi})$ that are

$$\cos(\phi + \tilde{\phi}) \sim \cos(\phi) - \sin(\phi)\tilde{\phi}$$

$$\sin\left(\phi + \tilde{\phi}\right) \sim \cos\phi\tilde{\phi} + \sin\phi$$

the previous equations can be re-written as:

$$dT + dT = (dL + d\tilde{L})\left[\cos\phi - \sin\phi\tilde{\phi}\right]$$

Identifying the expression of dT (equation 4.11), the perturbed thrust can be isolated and expressed as:

$$d\tilde{T} = -dL\sin\phi\tilde{\phi} + d\tilde{L}\cos\phi \tag{4.13}$$

Following the same for dS it leads to,

$$dS + d\tilde{S} = (dL + dL)[\cos\phi\tilde{\phi} + \sin\phi]$$

and

$$d\tilde{S} = dL\cos\phi\tilde{\phi} + d\tilde{L}\sin\phi \tag{4.14}$$

Using expression of dL and $d\tilde{L}$ (equations 4.9 and 4.10) into equations 4.13 and 4.14 lead to

$$d\tilde{T} = \frac{1}{2}\rho\left[W^2\left(-c_{l,\alpha}\cos\phi - c_l\sin\phi\right)\tilde{\phi} + 2W\tilde{W}c_l\cos\phi\right]cdr \tag{4.15}$$

$$d\tilde{S} = \frac{1}{2}\rho\left[W^2\left(-c_{l,\alpha}\sin\phi + c_l\cos\phi\right)\tilde{\phi} + 2W\tilde{W}c_l\sin\phi\right]cdr \tag{4.16}$$

$\tilde{\phi}$ and $\tilde{W}$ in equations 4.15 and 4.16 remains unknows. They must be expressed in function of the exogenous disturbances. In ASWING only perturbation in transverse velocity v and shaft pitch rate ω are considered. As depicted in figure 4.4-(a), a transverse velocity v assumed uniform over the propeller disk induced a change in the local azimuthal speed as follows

$$\Omega r \to \Omega r + \partial\Omega r = \Omega r + v\cos\psi$$

where ψ is the azimuthal angle depicted in figure 4.4-(a). Thus $\tilde{\phi}$ and $\tilde{W}$ can be defined as partial derivatives in Ωr as follow

$$\tilde{W_v} = \frac{\partial W}{\partial\Omega r}\partial\Omega r = \frac{\partial\sqrt{V_d^2 + (\Omega r)^2}}{\partial\Omega r}\partial\Omega r = \frac{v\Omega r\cos\psi}{W} \tag{4.17}$$

$$\tilde{\phi_v} = \frac{\partial\phi}{\partial\Omega r}\partial\Omega r = \frac{\partial atan(Vd/\Omega r)}{\partial\Omega r}\partial\Omega r = \frac{-vV_d\cos\psi}{W^2} \tag{4.18}$$

A perturbation in the shaft pitch rate ω could occur if the latter or the wing where the propeller is attached is flexible. A pitch rate perturbation will induce a change in the local axial velocity as depicted in figure 4.4-(b). For small pitch range pertubation only effect on the axis can be considered. Thus the axial velocity is perturbed as follow

$$V_d \to V_d + \partial V_d = V_d + \omega r cos\psi$$

where $rcos\psi$ is the projected pitch arm as depicted on figure 4.4-(b). As for transverse velocity analysis $\tilde{\phi}$ and $\tilde{W}$ can be expressed as partial derivative with respect to V_d.

$$\tilde{W_\omega} = \frac{\partial W}{\partial V_d}\partial V_d = \frac{\partial\sqrt{V_d^2 + (\Omega r)^2}}{\partial V_d}\partial V_d = \frac{-\omega V_d\cos\psi}{W} \tag{4.19}$$

$$\tilde{\phi_\omega} = \frac{\partial\phi}{\partial V_d}\partial V_d \quad \text{t} = \frac{\partial atan(Vd/\Omega r)}{\partial V_d}\partial V_d = \frac{-\omega r^2\Omega\cos\psi}{W^2} \tag{4.20}$$

Being derived equations 4.17, 4.18,4.19, 4.20 can be injected in the elementary thrust and side force equa-

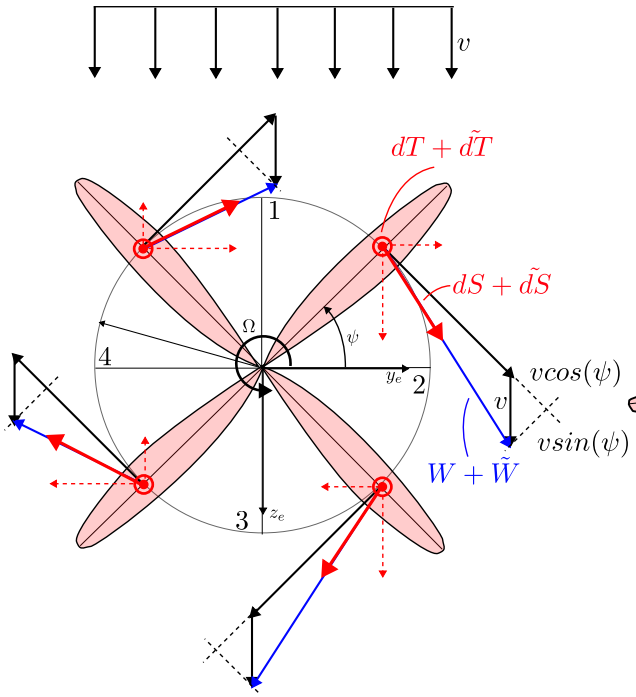

(a) A perturbation in transverse velocity v only induced a perturbation in tangential speed $\tilde{\Omega r} = vcos(\psi)$

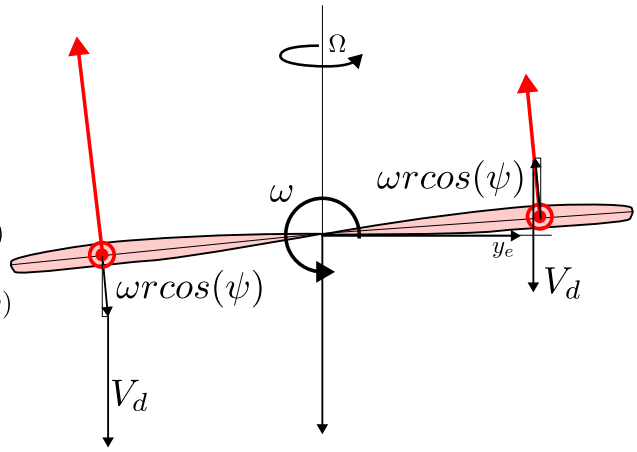

(b)Perturbation in pitch rate ω only induces a axial velocity perturbation $\tilde{V_d} = \omega rcos(\psi)$

Figure 4.4: Effect of perturbation in transverse velocity (a) and pitch rate (b), illustration of the assumption made in the model

tions 4.15 and 4.16 leading to the contribution of v and ω to them giving

$$d\tilde{T}_v = \frac{1}{2}\rho\left[(c_{l,\alpha}cos\phi + c_l sin\phi\ )\, V_d + 2c_l cos\phi\Omega r\ \right] v cos\psi dr \tag{4.21}$$

$$d\tilde{S}_v = \frac{1}{2}\rho\left[(c_{l,\alpha}sin\phi - c_l cos\phi\ )\, V_d + 2c_l sin\phi\Omega r\ \right] v cos\psi dr \tag{4.22}$$

$$d\tilde{T}_\omega = \frac{1}{2}\rho\left[(c_{l,\alpha}cos\phi + c_l sin\phi\ )\, \Omega r + 2c_l cos\phi V_d\ \right] \omega r cos\psi dr \tag{4.23}$$

$$d\tilde{S}_\omega = \frac{1}{2}\rho\left[(c_{l,\alpha}sin\phi - c_l cos\phi\ )\, \Omega r + 2c_l sin\phi V_d\ \text{t}\right] \omega r cos\psi dr \tag{4.24}$$

The dependency with the azimuthal angle can be removed by integrating the above equations over ψ. This can be in practice done if the perturbations v and ω are considered steady over a blade complete rotation. Said differently the propeller rotation speed (frequency) is assumed much greater than the bandwidth of the perturbations. If whirl flutter analysis is considered, the first 2 structural modes of the propeller shaft or the wing where it is attached, are responsible for pitching and transverse velocity. If their frequencies are much lower than the propeller rotation speed then the proposed simplification is reasonable. Before averaging it is useful to pay attention to the parity in ψ of the projected forces and moments. Let us define the pertubation frame $(x_E,\ y_v,\ z_v)$ such that $\vec{v} = v\vec{y_v}$ or $\vec{\omega} = \omega\vec{y_v}$. y_v and z_v lie into the (y_e, z_e) propeller plane. The change of frame is mandatory as the direction of the perturbation is necessarily aligned with y_E or z_E (engine frame propeller plane vectors). That being said let's consider the first time the forces generated by $d\tilde{T}$ and $d\tilde{S}$. $d\tilde{T}$ points towards x_e so is not projected, it contains a single term $cos\psi$ so will be null when averaged. The perturbated thrust does not generate any force. The elementary perturbed side force $d\vec{\tilde{S}}$ points towards the azimutal direction so must projected against y_v and z_v. When projected $d\vec{\tilde{S}}.\vec{y_v}$ contains $cos^2(\psi)$ so won't be null when averaged while $d\vec{\tilde{S}}.\vec{z_v}$ will be as it contains a $cos\psi sin\psi$ term. Thus only the side force will generate forces and will point towards the same direction as the pertubations. The same analysis must be made for moments. Let us consider the moment arm expressed in the perturbation frame $\vec{r} = r(0\ sin\psi\ cos\psi)^T$. Inspecting the cross product $\vec{r}\times d\vec{\tilde{T}}$ and $\vec{r}\times d\vec{\tilde{S}}$ 2 types of terms in ψ are identified that are $cos\psi sin\psi$ (zero when averged) and $cos^2\psi$ (non zero). It turns out that only the elementary thrust generates a zon zero moment pointing in the same direction as the perturbation. The previous comments drastically simplify the analysis. Let $d\tilde{F}$ and $d\tilde{M}$ be the elementary forces and moments. The total force and moment due to exogenous perturbations is computed by averaging the elementary forces over the azimuthal angle and integrating them over each blade as follows

$$F = \frac{1}{2\pi}\int_0^{R_e}\int_0^{2\pi} d\tilde{F}\ \ and\ \ M = \frac{1}{2\pi}\int_0^{R_e}\int_0^{2\pi} d\tilde{M}$$

The resulting forces and moments due to the transverse velocity or pitch rate are finally given as follows

$$F_v = \frac{1}{4}\rho R^2\left[(c_{l,\alpha}S_0 - c_l C_0)\, V_d + 2c_l S_1 \Omega R\right] v \tag{4.25}$$

$$M_v = -\frac{1}{4}\rho R^3\left[(c_{l,\alpha}C_1 - c_l S_1)\, V_d + 2c_l C_2 \Omega R\right] v \tag{4.26}$$

$$F_\omega = \frac{1}{4}\rho R^3\left[(c_{l,\alpha}S_2 - c_l C_2)\, \Omega R + 2c_l S_1 V_d\right] \omega \tag{4.27}$$

$$M_\omega = \frac{1}{4}\rho R^4\left[(c_{l,\alpha}C_3 + c_l S_3)\, V_d + 2c_l C_2 V_d\right] \omega \tag{4.28}$$

where C_k and S_k $(k \in [0\ 3])$ are simplified blade radial integrand involving products of the type $r^k cos(\phi)$ and $r^k sin(\phi)$. Their simplified equations are given in *equations 256-263 of section 14.7* of Drela's script and are not recalled here. Equations can be then projected in the engine frame leading to the unsteady force and torque of the propeller

$$\vec{F_e} = \begin{pmatrix} -F_e \\ F_v v_y + sign(\Omega) F_\omega \omega_y \\ F_v v_Z + sign(\Omega) F_\omega \omega_Z \end{pmatrix} \tag{4.29}$$

and

$$\vec{M_e} = \begin{pmatrix} -M_e \\ sign(\Omega) M_v v_y + M_\omega \omega_y \\ sign(\Omega) M_v v_Z + M_\omega \omega_Z \end{pmatrix} \tag{4.30}$$

4.3 Experimental validation

4.3.1 Propeller thrust and torque predictions

To evaluate the extended actuator disk theory, the experimental data of Deters et al. and 2014 were used. The propeller performance measurements were performed in the 28 by 40-foot UICC open return wind tunnel. The turbulence intensity was reported to be lower than 0.1% at all operating conditions. The propeller thrust measurements were done using a T shape mechanism pendulum balance constrained by a load cell (cf figure 4.5-a). 2 types of cells were used according to each propeller size to exploit the full range of the balance and ensure better accuracy. Torque measurements were fulfilled using a reaction torque

sensor (RTS). Overall the C_T and C_P measurements errors were reported to be lower than 1%. Each propeller rotation speed (in RPM) was actively controlled using laser feedback. Two types of wind-tunnel corrections were applied, fairings and wind tunnel walls were captured using source distribution terms. For more details refer to *chapter 2* of Deters. Dozens of propellers have been tested in static and advanced flow conditions, in this paper, only 4 of them have been retained for thrust/torque and slipstream predictions. The DA4022 propeller in its 2, 3, and 4 blades version (9 inches) has been chosen mainly to stress out the Drela hypothesis that the "total effective blade drag area" term C_DA (equation 4.2) can vary linearly with the number of blades B. Specific data were also chosen to evaluate its sensitivity to the rotation rate Ω (ie Reynolds number) and advance ratio λ. Numerically, ASWING EADT has been fed with Deters et al. C_P measurements as the main idea of this evaluation is to show if for a given C_P the model provides a reasonable C_T prediction or vice et versa. As the C_P measurements are obtained by a power balance with the torque coefficient C_Q (equation 4.6), its prediction quality is not necessary to be studied. Figures 4.10 (a) and (b) present the C_T static prediction against the rotation speed. C_DA values used for the simulations are specified. Figure 4.10 (b) depicts the non-conservation of the C_T prediction error from the 2-blade version to the 4 one. C_DA values have been computed using a reverse formulation of the EADT from the experimental value of C_P and C_T. Figure 4.7-(a) gives the C_DA/B values against the rotation speed. As it can be seen, the C_DA/B curves are not exactly equal, and the mean error between the 2 blades (reference case) and the 3 and 4 versions are respectively 16 % and 22%. However, the latter does not impact as much the C_T predictions. Indeed the velocity increment ΔV_e needed to compute the thrust in the EADT is a cubic root of the power balance equation 4.4, while the thrust (equation 4.5) is a square function in ΔV_e. Thus the error due to C_DA mismatch is drastically damped leading to the witnessed small error offset from the 2 to 4 blades versions. The same conclusion can be drawn on the Reynolds number (ie rotation speed) dependency as the variation is about the same from the minimum to the maximum rotation rate. Thus considering, that the total effective blade drag area does not vary with the rotation speed and is proportional to the blade number is quite reasonable. A similar conclusion can not be drawn about the dependency with the advance ratio λ. Indeed as depicted in figure 4.7-(b) which presents the reverse value of C_DA based on the experimental C_T and C_P values in advance flow condition, the variation with the advance ratio are much more pronounced leading to higher predictions error, as depicted on figure 4.8(a) to (d). The plots present the C_T predictions for different C_DA constant values. Those are the extremum case. A trade-off could be found to minimize the error however it would be case-dependent and difficulty trackable. Instead according to the shape of C_DA variation with the advance ratio, a cost-less modification is proposed, by considering CDA as a second-order polynomial function in λ as follows:

$$C_DA(\lambda) = A_2\lambda^2 + A_1\lambda + A_0 \tag{4.31}$$

where the polynomial coefficients can be computed from experimental data, CFD, or other propeller codes such as QPROP for example. When implemented, the C_T predictions become better as depicted in figure 4.8(a)-(d) where the polynomial coefficients have been specified. The interest of the method is particularly highlighted by figures 4.8 (b) and (d) for the efficiency predictions. To verify the consistency of the method, the 4-blades case has been treated and the predictions are presented in figure 4.16 in the appendix of this paper. Similar results are witnessed. Criticisms must be made on this modification. The latter is mainly dependent on the quality of the input data. Here the C_DA polynomial functions were computed based on experimental data, so the good results. The methodology will recover correctly the data that are provided. If higher fidelity CFD tools are used to compute the propeller C_DA polynomial function, prediction errors are expected then but equivalent to that of the higher fidelity method.

4.3.2 Thrust, normal force and yaw moment due to a axial flow

To evaluate the capacity of the ASWING P-factor model to predict normal forces and yaw moment due to a non-axial flow, the data from Leng Yuchen were used. The measurement was performed in 2019 in ISAE low Reynolds number wind tunnel SaBRe. The turbulence was reported to be lower than 0.1%. The propeller-motion assembly was supported by a rotating strut installed from the test section ceiling. The strut could rotate giving the propeller a pitch angle from 0 to 90° as depicted in figure 4.5 (b). A 5 component balance was used to measure the normal force, yaw, and pitch moments. The test bench has been validated against similar data from the literature on a Graupner E-prop. The bench was reported as qualitative. The author provided in Leng et al. (2019 and 2020) the thrust, torque, normal force, yaw, and pitch moments coefficient. The latter was given as a function of the propeller pitch angle α_p and advance ratio λ_∞. Note that the ASWING P-factor model can not predict the pitch moment due to non-axial flow.

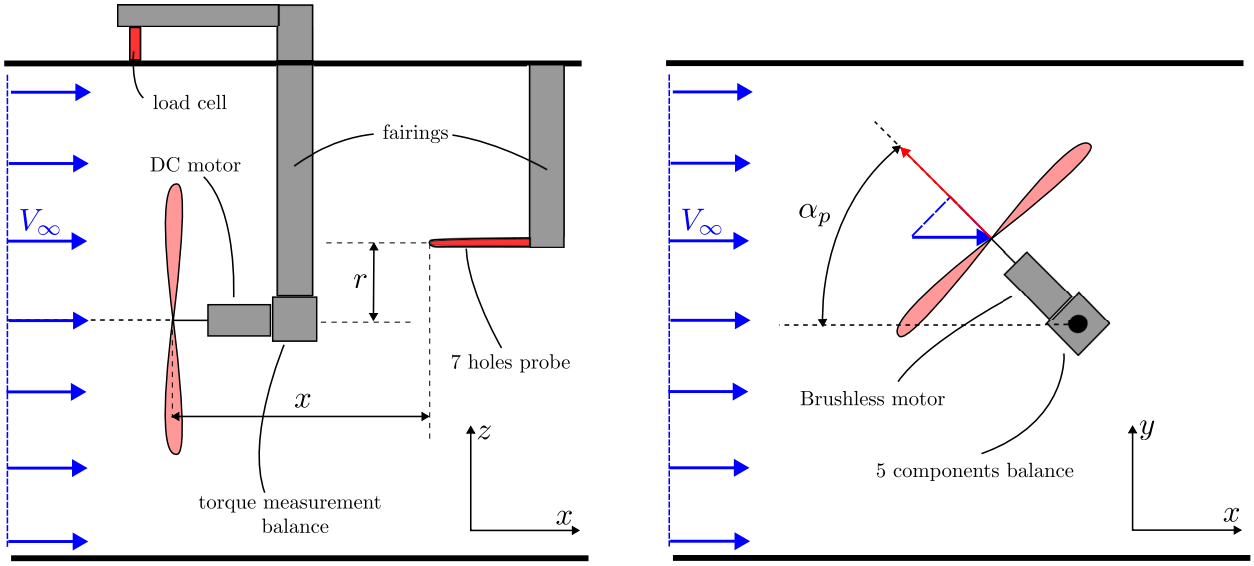

(a) Deters et al's bench (b) Leng et al's bench

Figure 4.5: Experimental benches of [3] [17]

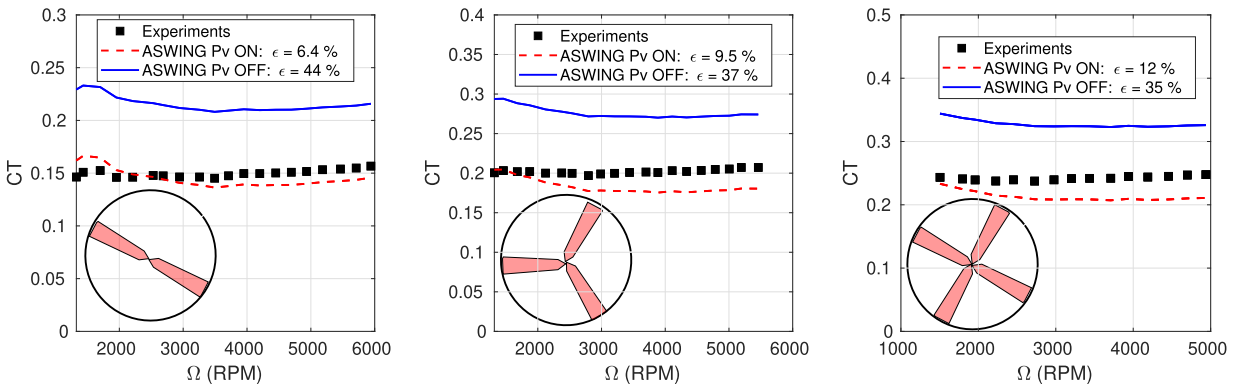

(a) 2 Blades ($C_DA = 1.6\ 10^{-4}m^2$) (b) 3 Blades ($C_DA = 2.4\ 10^{-4}m^2$) (c) 4 Blades ($C_DA = 3.2\ 10^{-4}m^2$)

Figure 4.6: Static thrust coefficient ASWING prediction for the DA4022 propellers, comparison between the 2, 3 and 4 blades versions. ϵ is the mean error between predictions and experiments

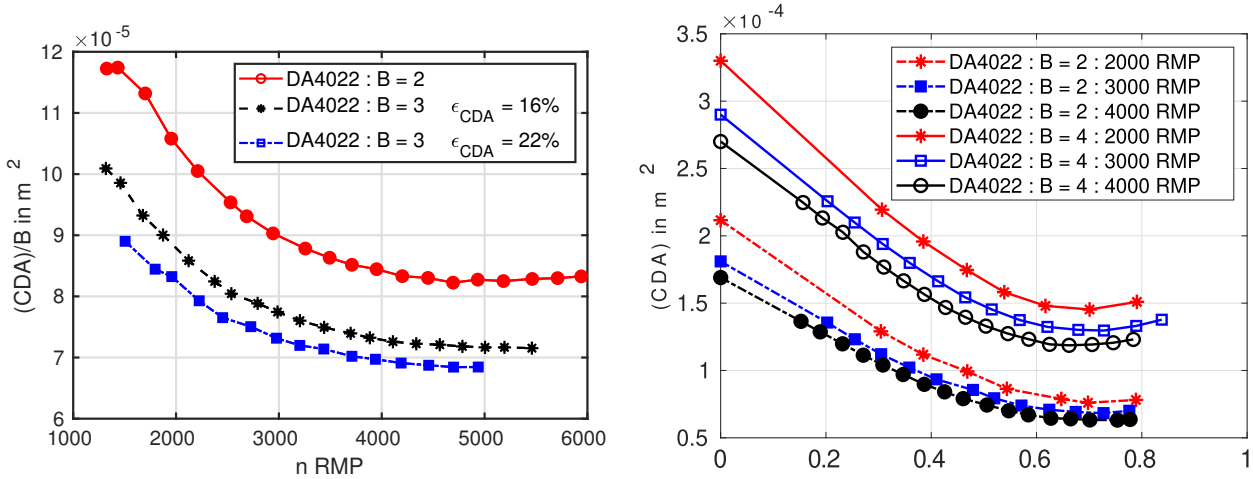

(a) $\frac{CDA(\Omega)}{B}$ (static condition) (b) $CDA(\lambda, \Omega, B)$

Figure 4.7: C_DA reverse computation from experimental data in static and advance flow condition. Effect of B, Ω and λ. ϵ_{CDA} is the mean error between C_DA value of the 2 blades version and the other one

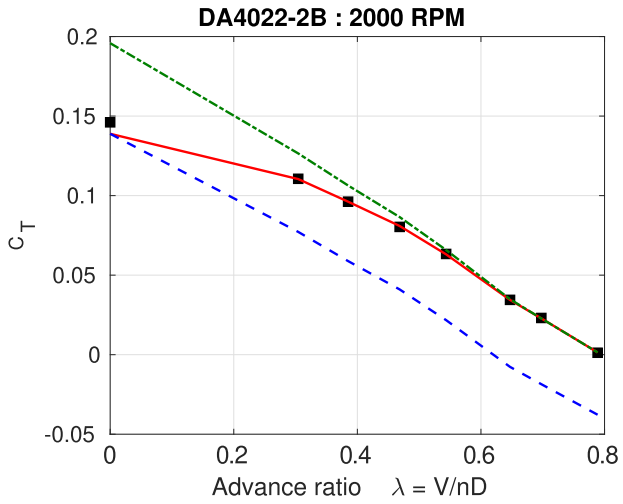

(a) C_T at 2000 RPM

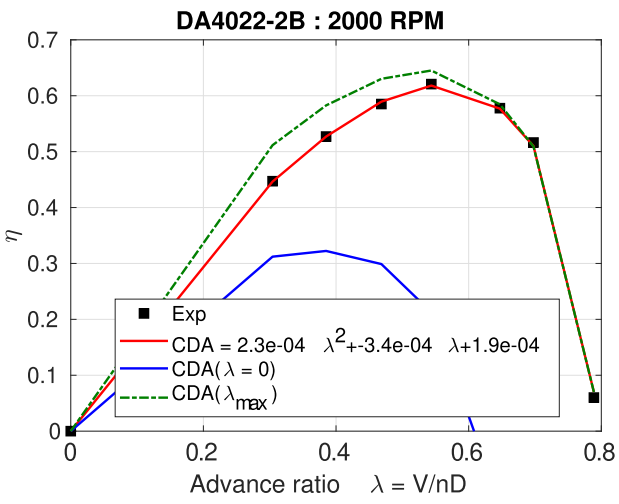

(b) η at 2000 RPM

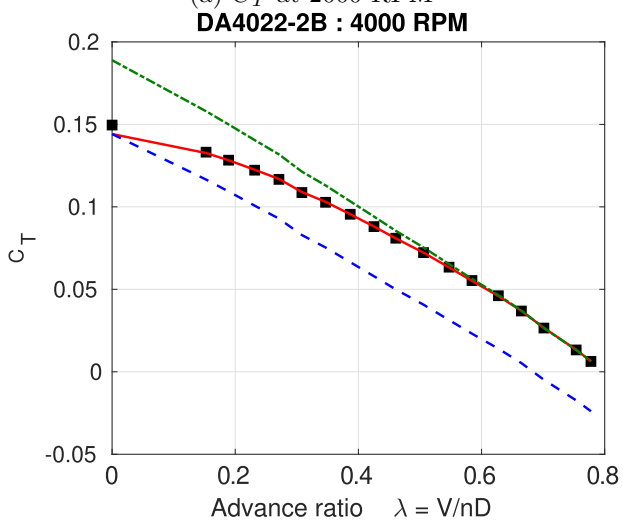

(c) C_T at 4000 RPM

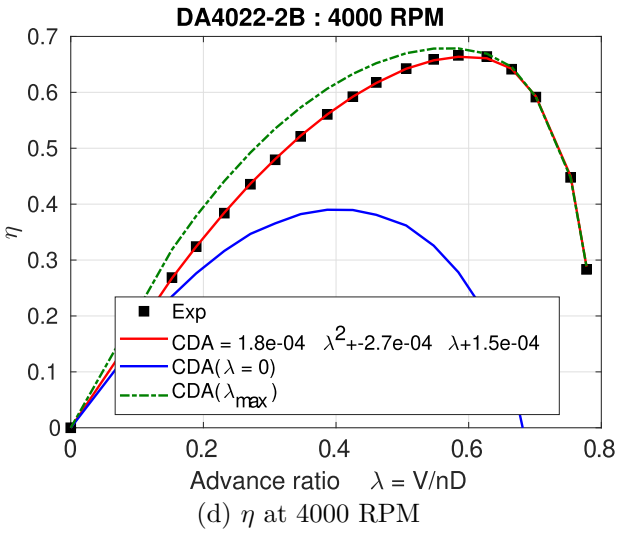

(d) η at 4000 RPM

Figure 4.8: Advance flow : C_T and η ASWING predictions for the DA4022-2B, comparison with rotation speed. Performance improvement with $C_D A$ defined as a polynomial function of the advance ratio λ. The value λ_{max} corresponds to $C_T(\lambda_{max} = 0/0$

Thus only the normal force, yaw moment, and thrust coefficients (C_N, C_n, C_T) predictions are presented. A NACA propeller was used with a linear blade pitch varying. The geometry is provided in *Appendix A* of Leng Yuchen's script. The blade tip pitch angle and airfoil are respectively 20° and NACA0012. The propeller size ($R_e = 0.85m$) was chosen as a tradeoff between minimal wall interactions and 3D printing quality.

Figure 4.9 (a)-(c) presents the normal forces, yawing moments, and thrust coefficients ASWING predictions. The latter are compared to Leng et al.'s experimental data and non-linear model. The coefficients are given against the propeller pitch angle α_p (cf figure 4.5-b) for different advance conditions ($\lambda \in [0.2,\ 0.45,\ 0.7,\ 1.0]$). As expected from the small angle assumption of the model, ASWING is not able to predict the yawing and normal force coefficient accurately, on $\lambda = 0.2$ seems to show interesting agreements at low pitch angle but is still far beyond Leng et al.'s non-linear model accuracy. This is consistent with Leng Yuchen's *chapter 2* observations on lower advance-ratio and pitch angle on a close linear model. Moreover, as the blade drag contributions are not taken into account, the model loses the track after a pitch angle superior to 45° when the drag contributions become dominant. From this comparison and the data of Leng Yuchen (*chapter 3*), a validity map in α_p and λ could be built and is depicted in figure 4.10. The dark grey represents the set of parameters where the P-factor model is considered satisfying. Despite those latter bad predictions, this model remains interesting for whirl flutter analysis that is presented in the aeroelastic part of this sequel work. Here the objective was to build and identify the boundaries of the p-factor model for flight mechanics analysis.

As Leng et al. provided C_T and C_P measurements in the function of the pitch angle α_p and advance ratio λ, the EADT could be benchmarked against Leng et al.'s non-linear model in non-axial flow condition. To do so a quadratic $C_D A$ in μ was used where μ is the shaft advance ratio defined as $\mu = \lambda cos\alpha_p$. The polynomial coefficients are provided in figure 4.9-(c) legend. It turns out that the ASWING modified EADT model shows excellent agreements with experiments until 60° no matter λ. After that, Leng et al.'s non-linear model becomes better.

4.3.3 Propeller slipstream measurements

The jet slipstream predictions are evaluated against Deters et al. and Deters (2014 *chapter 8*) experimental work. The same bench (figure 4.5-a) as depicted in the thrust prediction section was used. A 7 hole probe has been used to measure the axial and swirl velocities. Its position could vary vertically and horizontally (cf figure 4.5-a). According to Deters et al., measurements on the complete propeller disk were not necessary from the axisymmetry property of the flow. Each measurement slice was spaced by 45 cm. The maximum streamwise and radial coordinates of the probe to the propeller centre were respectively 3.0 and 1.5 propeller diameter. Each probe hole was connected to a series of MKS pressure transducers giving an accuracy of 0.06 m/s and 0.9° for axial velocity and angle of attack. The measurement errors were reported as small enough to be not plotted in the author's publication. The data have been digitalized using webplotdigitalizer. Several propellers at different rotation rates and advance flow have been used to evaluate the jet model. In this paper, the GWS APC and DA4002 results are presented. Their geometries are depicted in figure 4.17 in the appendix of this paper. Axial and swirl velocity predictions are presented in static and advanced flow conditions. For the static one, the engine jet model was reproduced in MATLAB while in advanced flow conditions, a numerical bench was set up in ASWING. Axial velocities and angle of attack were provided by the numerical sensors at each streamwise and radial position. The swirl velocity was reconstructed using the local angle of attack or side slip angle measurements combined with the axial velocities.

That being said, the figures 4.11 (a) and (b) present the static axial and swirl velocity predictions against Deters et al. experimental data on the GWS propeller. A single rotation rate ($\Omega = 5000RPM$) is presented. Five normalized streamwise locations are presented ($\frac{x}{D} \in [0.125,\ 0.5,\ 1.0,\ 3.0]$). For the axial velocity, a general trend can be observed, ASWING is weak near the propeller plane ($\frac{x}{D} < 0.5$) to show good agreements while satisfying one is witnessed after. Similar observations are done on the swirl predictions (figure 4.11 -b). Those discrepancies are mainly due to the propeller hub which does not accelerate the fluid, thus a low-speed region is observed for small radial positions. In consequence a modification has been proposed to take into account those effects. A low-speed region has been implemented as depicted in figure 4.2. Its diameter tends to reduce linearly with the streamwise distance until the mixing point. The velocity profile is constructed to be consistent with the other regions. This modification is denoted as ASWING-m. From figure 4.11 (a), the modification improves a bit the axial and swirl velocities predictions at $\frac{x}{D} = 0.125$. The benefit tends to lower for greater spanwise locations. Another propeller (APC at 9000 RPM) was used to robustify the analysis. Predictions results are presented in figures 4.18 (a)

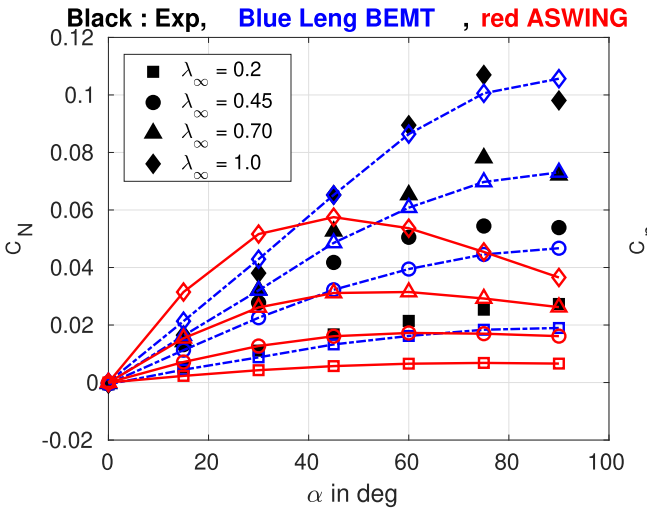

(a) Normal force coefficient C_N

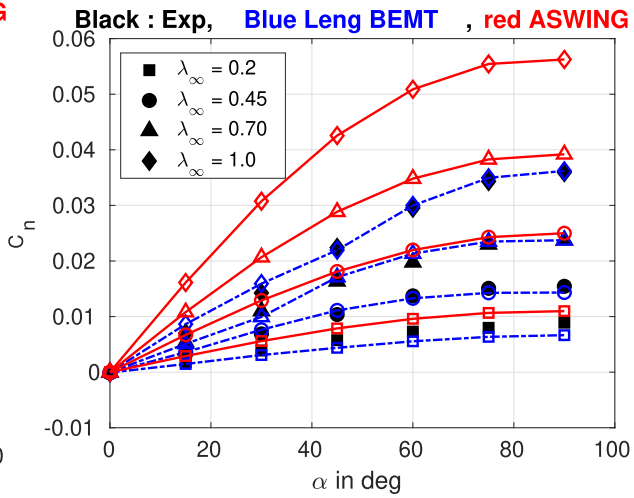

(b) Yaw moment coefficient C_n

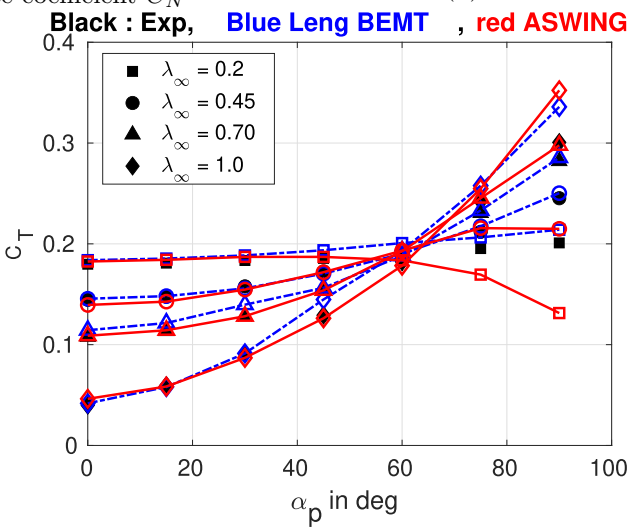

(c) Thrust coefficient C_T
with $C_D A(\mu) = 0.0019\mu^2 - 0.0026\mu + 0.0006$

Figure 4.9: Normal force, Yaw moment and thrust coefficient ASWING's predictions comparison with experiments from Leng et al..

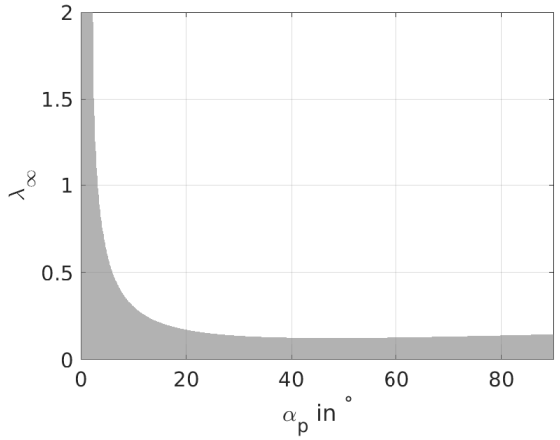

Figure 4.10: $\mathcal{L}_{\tilde{W},\tilde{\phi}}(\alpha_P, \lambda_\infty)$ small pertubation validity map

and (b). This case contradicts the previous observations, especially on the swirl predictions near the propeller blade. Indeed the ASWING unmodified version shows better agreements with experiments. For axial velocity, ASWING-m remains better. Also using 2 propellers as static validation case are of interest to highlight the difference in velocity profile because of each propeller geometry. This change is not captured by ASWING nor its modified version. However, they both capture quite well the jet spreading and the ZEF and EFZ boundaries.

Figure 4.12(a) and (b) presents predictions in advance flow condition ($\lambda = 0.52$) on the GWS propeller at a rotation speed of 5000 RPM. A large low-speed profile ($r/R < 0.25$) is not captured by both models. Also a negative swirl velocity zone (cf 4.12-b) is observed for streamwise location ($x/D = 0.125$ and $x/D = 0.5$) and is not captured. For downstream locations, ASWING-m shows better agreements. Again by studying another propeller (DA4002 at 5000RPM and $\lambda = 0.64$), depicted in figure 4.19 in Appendix, contradicting results are observed. Indeed, ASWING shows better performances than ASWING-m no matter the streamwise location on the swirl velocity predictions. For axial velocity, ASWING-m remains better. In light of the results, both ASWING jet models show reasonable agreements with experiments for axial and swirl velocities predictions for $\frac{x}{D} >= 0.5$. Lower performances are reported for swirl computations on both models. Better performances are witnessed on ASWING-m only for axial velocity predictions. Finally, prediction errors must be commented on. A swirl velocity will induce a local change in the angle of attack. Local lift varies linearly (in unstalled region) with the angle of attack while it does quadratically with the axial velocity. As the swirl velocity induces a change in the local angle of attack, its prediction error is weightless in comparison to the axial velocity. Predictive performances can be considered equivalent.

4.3.4 Propeller slipstream/lifting surface interaction

In this last evaluation section, the capacity of ASWING to predict the interactions between a propeller jet and a wing is investigated. To do so, the experimental data of 2 benches were used from the work of Veldhuis (*chapter 5*), Veldhuis (1996 and 2004). The first one named PROWIM had the purpose of highlighting the effect of a propeller jet on the lift distribution while the second (APROPOS) aimed at providing insight into the propeller spanwise and vertical position effect and the lift/drag ratio of the wing. No matter the bench, the tests were performed in the 1.8 X 1.25 m Delft University Low Turbulence Tunnel. The wind speed was 50m/s for both benches. The level of turbulence was 0.025%. The same wing was used on PROWIM and APROPOS that was straight with a smoothed tip as depicted in figure 4.13. The wing chord and half span were 0.24 and 0.64m (AR = 5.3) and the airfoil was a NACA642-A015. Strips were placed on the intrados and extrados to force the boundary layer transition at 30 % of the chord. Several monitoring devices were used but only are of interest in this paper, a 6-degree of freedom balance to measure the total lift and drag coefficient and 20 pressure tape rows to measure the local lift coefficient. The latter were wisely placed to refine the pressure measurement near the propeller axis (cf figure 4.13-a).

Numerically, the first bench was reproduced without the airframe where the propeller is connected. Its spanwise, streamwise, and vertical coordinates are respectively $x_p = -0.23m$, $y_p = 0.3m$, and $z_p = 0.0m$. The airfoil polars were computed in XFOIL at the given Reynolds number condition (800 000) and the n_{crit} was adjusted to ensure the transition of the boundary layer around 30% of the chord. The NACA642-A015 lift linear slope is then $c_{l,\alpha} = 5.72$. The maximum lift coefficient and zero lift angle of attack are respectively $c_{l,max} = 1.2$ and $\alpha_0 = 0.0°$ while the profile drag coefficient was set to $c_d = 0.0635$. The propeller was turning at the same rate in both benches ie $\Omega = 500 rad/s$. The latter was not provided by the author but has been computed from the propeller tip Reynolds number and the advance ratio. The propeller blade drag area was set to $(C_D A) = 4.4874e-04\ m^2$. The propeller thrust coefficient and advance ratio of the PROWIM bench were set to $C_T = 0.168$ and $\lambda = 0.85$ while the APROPOS were $C_T = 0.120$ and $\lambda = 0.92$. From those values, the shaft power was computed to match the latter values and injected in ASWING avoiding

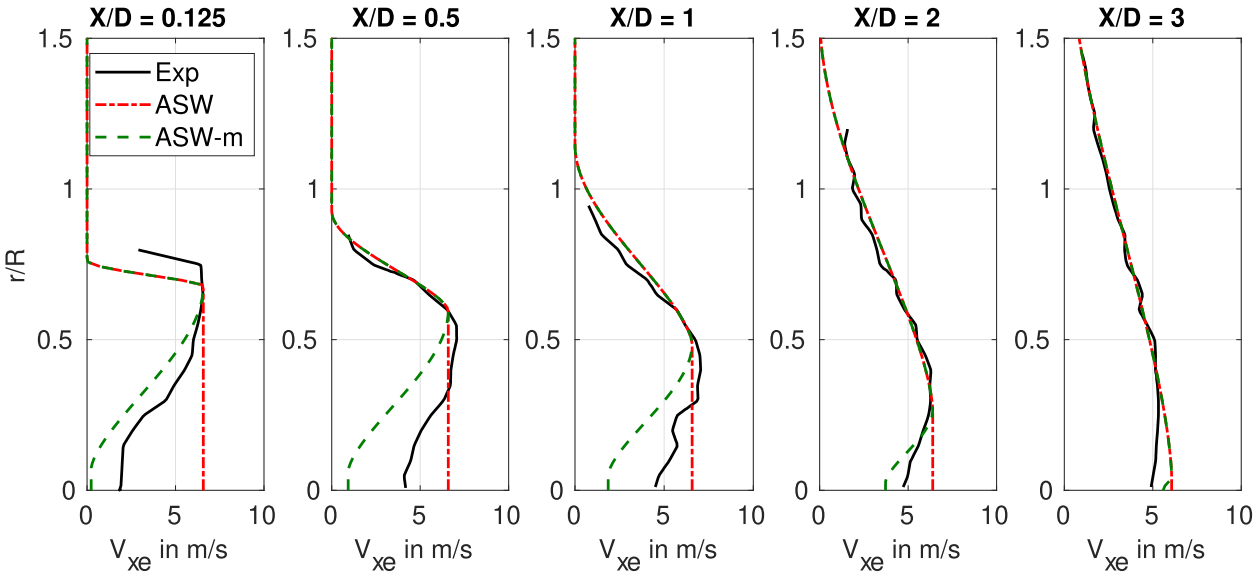

(a)Axial velocity

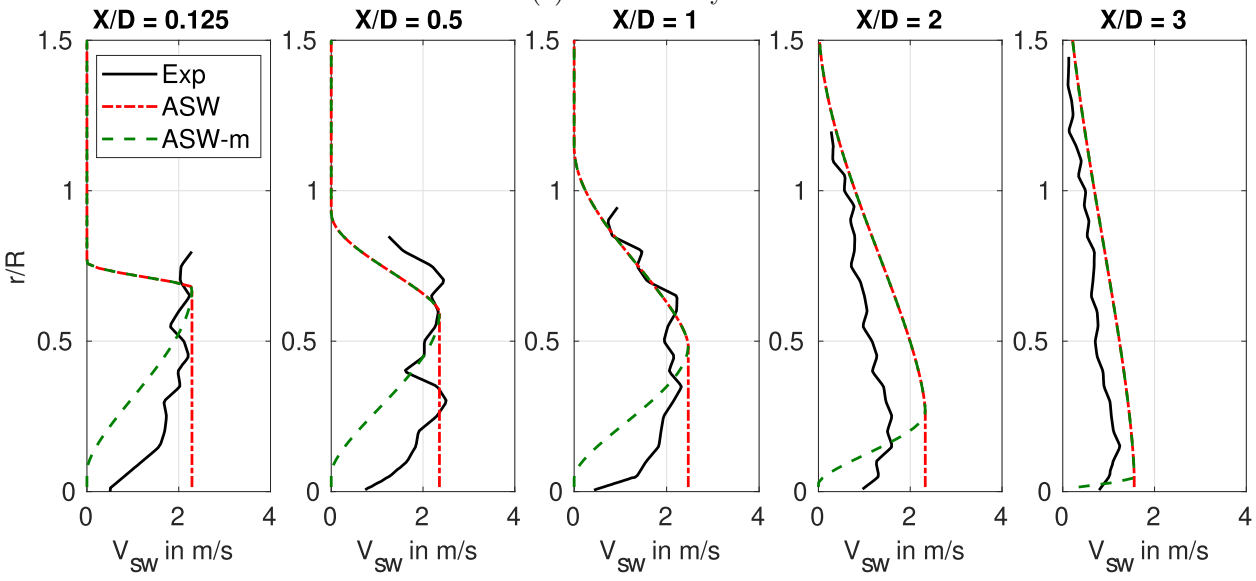

(b) Swirl velocity

Figure 4.11: Static GWS (5000 RPM) axial and swirl velocities evaluated at different streamwise location $\frac{x}{D}$ and different radial position $\frac{r}{R}$ (y-axis). Comparison of ASWING 5.96 and ASWING-m predictions with experimental data from Deters et al. (2015)

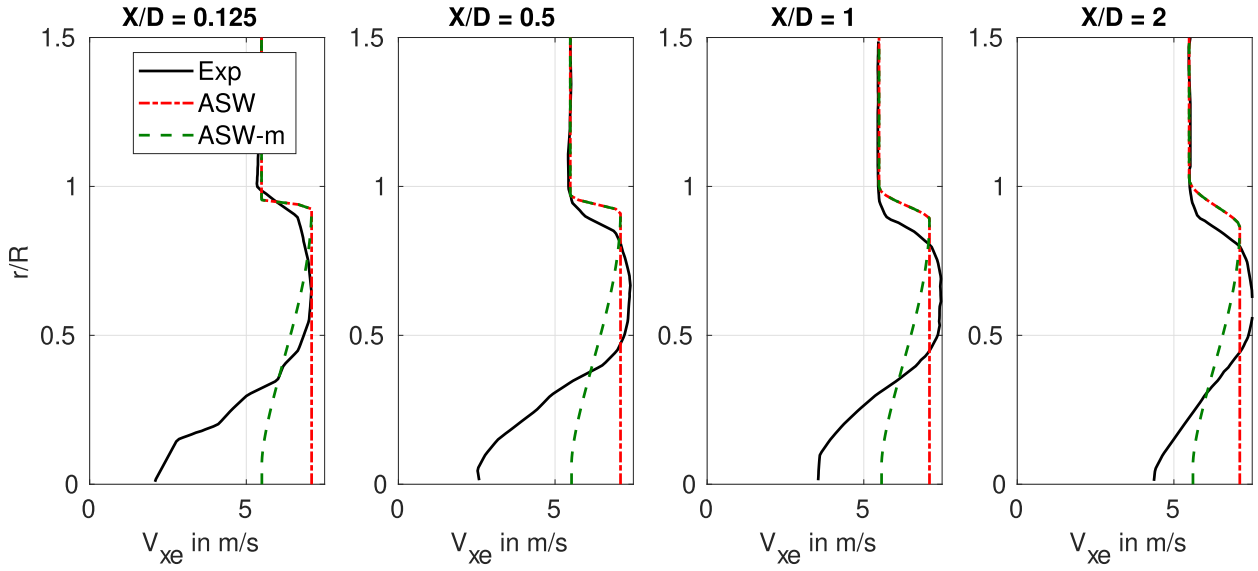

(a)Axial velocity

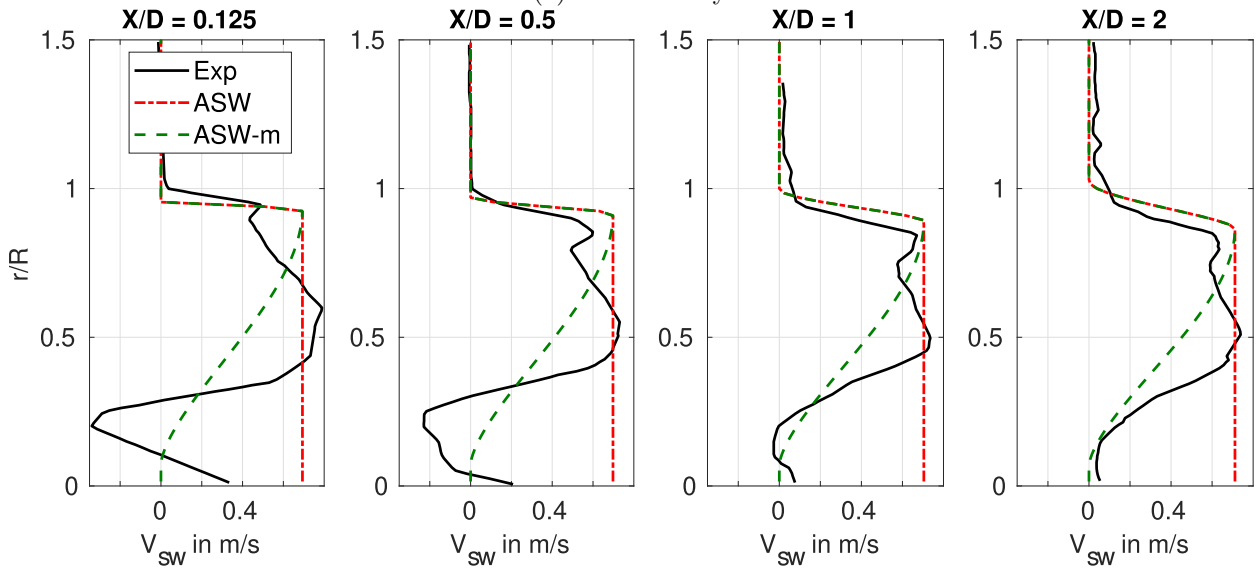

(b) Swirl velocity

Figure 4.12: Advanced flow GWS (5000 RPM), $\lambda = 0.52$, axial and swirl velocities evaluated at different streamwise location $\frac{x}{D}$ and different radial position $\frac{r}{R}$ (y-axis). Comparison of ASWING 5.96 and ASWING-m predictions with experimental data from Deters et al. (2015)

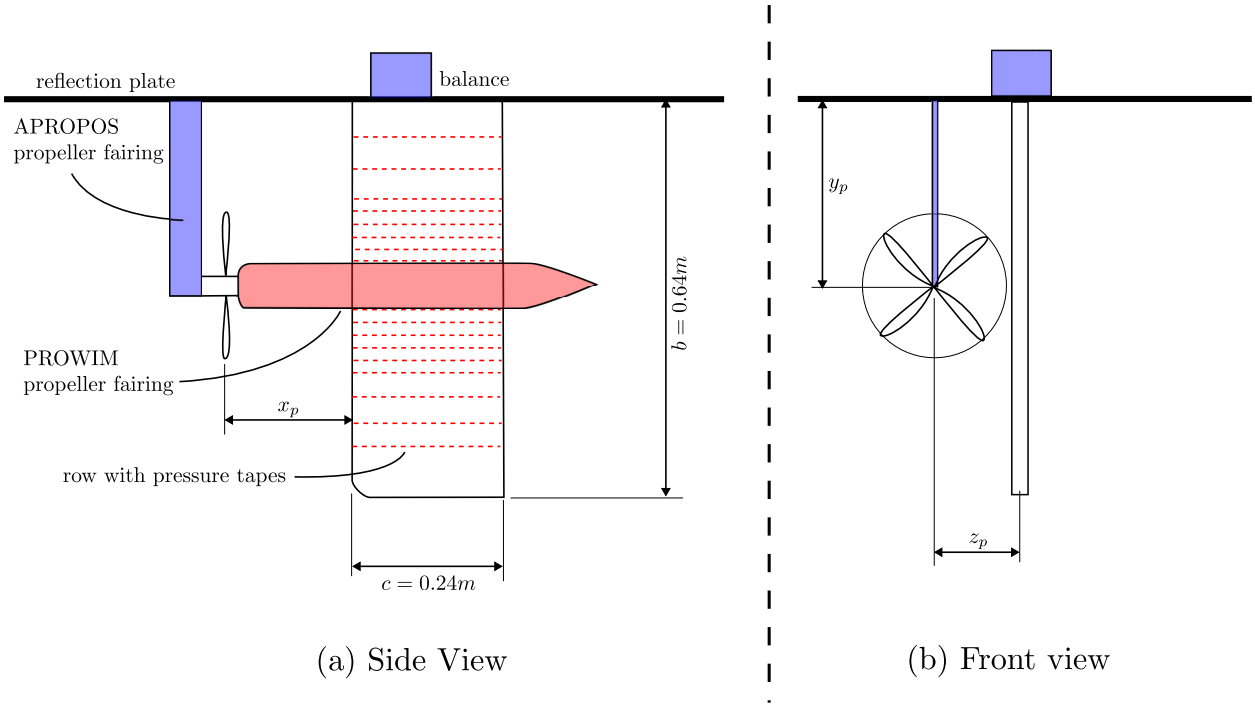

Figure 4.13: Veldhuis PROWIM and APROPOS experimental benches

accumulating errors from the EADT.

Figure 4.14 depicts the ASWING predictions for the first bench (PROWIM). Three different angles of attack were evaluated ie $\alpha = 0,\ 4,\ 10°$ and 2 rotation directions (ClockWise and Counter-ClockWise, CW and CCW). For the data used in the figure 4.14 ASWING is compared to the work of Goates who implemented a different propeller jet model and a less sophisticated lifting line one. From figure 4.14, ASWING predicts in good agreement with experiments the lift distribution for $\alpha = 0.0°$ and $\alpha = 4.0°$. Moreover, it performs better than Goates's model. At $\alpha = 10°$, both models seem weak to predict the lift distribution near the propeller axis. ASWING shows better lift predictions than Goates's model outside the propeller disk but it is out of this article's scope. Finally from figure 4.14 (b) where the rotation direction is inverted (Counter-ClockWise), the same remark can be made on the accuracy of ASWING at a low angle of attack. In both figures, some discontinuities can be witnessed in the ASWING lift distribution. This is not due to a coarse mesh but to the inversion of the swirl velocity direction at the propeller axis, inducing a sudden change in the angle of attack. The discontinuity around the propeller disk boundary is due to the steepness of the jet velocities profile as illustrated for example in the figures 4.12(a) and (b).

The figures 4.15 (a) and (b) depict the ASWING predictions of the impact of the propeller spanwise and vertical position (y_p and z_p) on the lift over drag ratio. 2 angles of attack were tested ie $\alpha = 1.05°$ and $\alpha = 4.2°$. In both positions, 5 vertical positions were tested and for each of them, 13 spanwise locations were chosen. The propeller spanwise location could not start from 0.0 because of physical constraints with the wind tunnel walls. In figure 4.15 (a) and (b) the black markers indicate experimental data while the red one indicates ASWING predictions. Marker type indicates the vertical position of the propeller. Also in blue is displayed the lift drag ratio value if the propeller is off (ASWING only). The same conclusions can be drawn from both figures. ASWING is not capable of capturing the effect of the vertical position on the lift-drag ratio. This comes from the ASWING lifting line model. The lift and drag are computed based on the air relative velocity computed at the quarter chord location. This implies a vertical uniform flow. Or as reported by Veldhuis 2005 (in *section 5.5.2*) the increase in lift drag ratio when the propeller axis is placed above the wing is due to an increasing speed on the wing leeward ie a loss of pressure leading to a rise in the lift. The effect is the opposite when the propeller axis is placed below the wing. Figure 4.15 (a) and (b) do highlight a capture of the vertical position, however, it does originate in the above physical insight. The propeller jet and swirl regardless of the rotation direction drastically modify the lift distribution leading to greater lift-induced drag than if the propeller was off. When the propeller is moved vertically, the axial and swirl velocities decrease with the vertical position modifying less in consequence the lift distribution and thus the induced drag. That being said when only the neutral vertical position ($z = 0$)

is considered, ASWING captures well the effect of the propeller spanwise position on the lift drag ratio ie an increase with it towards the wing tip. When the propeller direction is clockwise the swirl velocity tends to oppose the wing tip vortices reducing the lift-induced drag of the wing. When the propeller turns in a counterclockwise direction (not shown), Veldhuis (2005) witnessed a decrease of performance. Similar conclusions were drawn from ASWING analysis.

Final remarks must be made on the capture of the slipstream deviation due to the jet wing interaction. Veldhuis provided in his work a wake survey of the PROWIM bench for clockwise rotation. He identified a slipstream deformation. The propeller jet disk was split by the wing in 2 half disks, the upper one shifted toward the wing root and the lower down in the opposite way. The shift length was around 20% of the propeller radius. This phenomenon was also witnessed and investigated experimentally in static flow conditions by Deters et al., [3] (*chapter 8*), Leng et al., [17] (*chapter 4 and appendix D*). In the case of the PROWIM the non-zero lift outside the propeller disk in 4.12(a) at $\alpha = 0°$ indicates a non-zero circulation ie vorticity. Thus the resulting velocity field from the horseshoe systems of the wing tends to spread the propeller jets. However, it is quite difficult to quantify the half-disk shift. Moreover, if other lifting surfaces are placed more downstream it is very unlikely to catch correctly the effect of the spread jet on the lift distribution. So it is not recommended to use ASWING for such applications.

4.4 Conclusions

This chapter has presented an experimental evaluation of the ASWING propeller model. Some of the assumptions of the extended actuator disk theory (EADT) have been discussed and some modifications have been proposed. Here is a summary of the different findings:

- When extended, the EADT shows good agreements with experiments on several propellers in static and advanced flow conditions. ASWING can directly provide the propeller shaft power needed to trim an aircraft in a given situation (steady level or banked flight).
- The p-factor model mainly used for whirl flutter analysis is not able to predict normal force and yawing moments due to a non-axial flow because of its small perturbation assumption. A logical map in advance ratio and pitch angle has been provided where the model is expected to behave reasonably well. However, the use of ASWING for V-TOL configuration (high pitch) is not yet recommended.
- Contrary to the normal and yaw moments, the modified EADT shows good agreements with experiments for thrust coefficient predictions in non-axial flow conditions up to $\alpha_p = 60°$. ASWING will capture in consequence the effect of small side slip and angle of attack on the propeller performances.
- Then the jet and swirl model and its modification proposed show good agreements with experimental data on several propellers in advance and static flow conditions. The predictions become better when the flow is evaluated at a downstream distance greater than half the propeller diameter.
- Finally, propeller jet wing interactions have been presented. ASWING is capable of capturing the effect of a propeller jet on the wing lift distribution no matter the rotation direction. Plus it can capture the effect of the spanwise location of the propeller on the wing lift drag ratio. However, it can not be for the vertical position influence as it involves a fluid mechanism not captured by ASWING (different upcoming speeds on leeward and windward sections).

Bibliography

[1] Albertson, M. L., Dai, Y. B., Jensen, R. A., and Rouse, H. (1950). Diffusion of Submerged Jets. *Transactions of the American Society of Civil Engineers*, 115(1):639–664. 133

[2] Betz, A. (1920). Zeitschr f Flugtechnik u Motorl. 132

[3] Deters, R. (2014). *Performance and slipstream characteristics of small-scale propellers at low Reynolds numbers*. PhD thesis, Graduate College of the University of Illinois. 14, 15, 132, 138, 139, 140, 142, 148, 153, 154

[4] Deters, R. W., Ananda, G. K., and Selig, M. S. (2015). Slipstream Measurements of Small-Scale Propellers at Low Reynolds Numbers. In *33rd AIAA Applied Aerodynamics Conference*, Dallas, TX. American Institute of Aeronautics and Astronautics. 15, 132, 142, 145, 146, 148

[5] Deters, R. W., Ananda Krishnan, G. K., and Selig, M. S. (2014a). Reynolds Number Effects on the Performance of Small-Scale Propellers. In *32nd AIAA Applied Aerodynamics Conference*, Atlanta, GA. American Institute of Aeronautics and Astronautics. 132, 138, 139

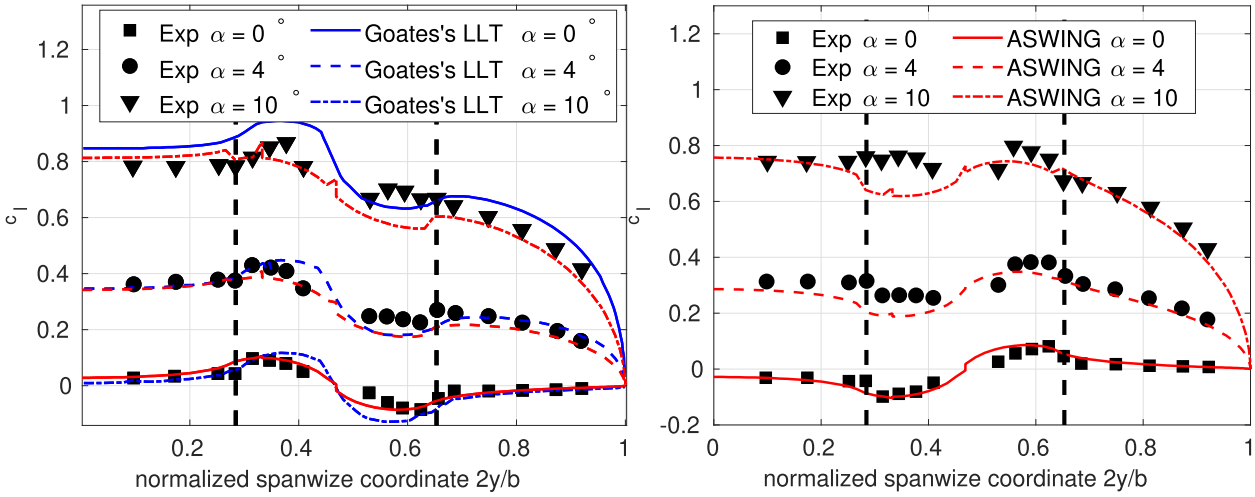

(a) clockwise (b) counter-clockwise

Figure 4.14: Jet wing interaction, effect on the lift distribution, comparison with Goates's jet and non-linear lifting line theory model. Experimental data from PROWIM bench of Veldhuis

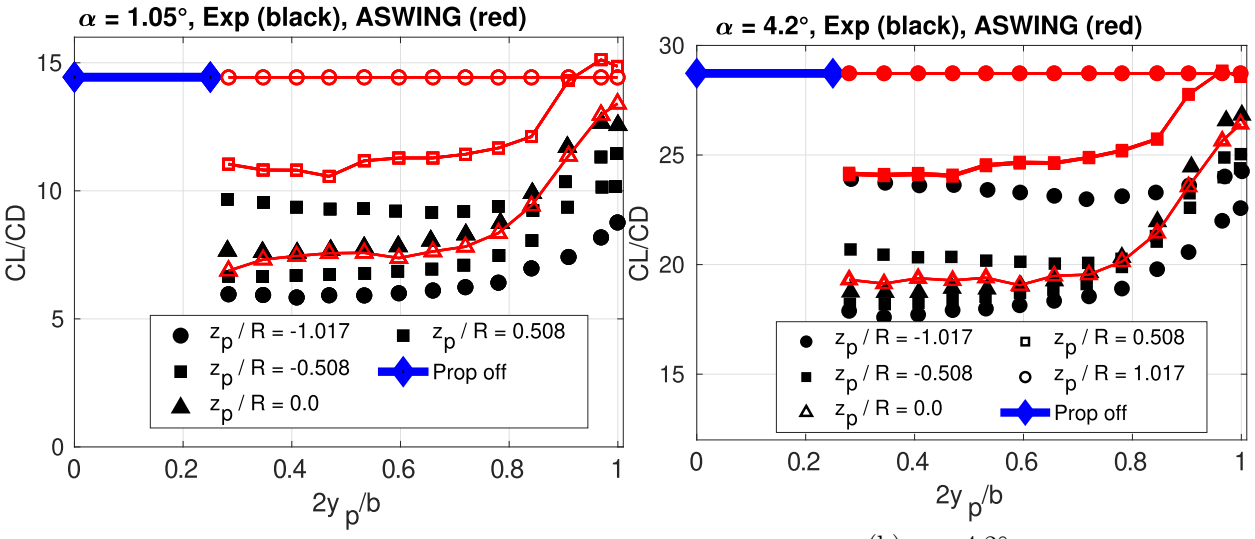

(a) $\alpha = 1.05°$ (b) $\alpha = 4.2°$

Figure 4.15: Effect of the spanwise and vertical position of the propeller on CL/CD ratio. Aswing prediction versus Veldhuis's experiments (bench APROPOS)

[6] Deters, R. W., Ananda Krishnan, G. K., and Selig, M. S. (2014b). Reynolds Number Effects on the Performance of Small-Scale Propellers. In *32nd AIAA Applied Aerodynamics Conference*, Atlanta, GA. American Institute of Aeronautics and Astronautics. 132

[7] Drela, M. (1999). Integrated simulation model for preliminary aerodynamic, structural, and control-law design of aircraft. In *40th Structures, Structural Dynamics, and Materials Conference and Exhibit*, St. Louis,MO,U.S.A. American Institute of Aeronautics and Astronautics. 132

[8] Drela, M. (2008). ASWING 5.81 Technical Description — Unsteady Extension. page 42. 132, 133, 138

[9] Drela, M. (2009). ASWING 5.86 Technical Description — Steady Formulation. page 57. 132, 133, 134, 139

[10] Froude, W. (1889). Ibidem Vol 30 p 390 1889. 132

[11] Glauert, H. (1935). *AIRPLANE PROPELLERS*, volume IV of *Aerodynamic Theory*. New-York, springer edition. 132, 133

[12] Goates, J. T. (2018). Development of an Improved Low-Order Model for Propeller-Wing Interactions. 15, 147, 149

[13] Hong, J.-H., Yeh, P.-H., and Chiew, Y.-M. (2020). Prediction of Mean Axial Velocity of a Free Turbulent Propeller Jet. *Journal of Hydraulic Engineering*, 146(3):04019070. 133

[14] Lam, W., Hamil, G., Song, Y., Robinson, D., and Raghunathan, S. (2011). A review of the equations used to predict the velocity distribution within a ship's propeller jet. *Ocean Engineering*, 38(1):1–10. 133

[15] Leng, Y., Bronz, M., Jardin, T., and Moschetta, J.-M. (2020). Slipstream Deformation of a Propeller-Wing Combination Applied for Convertible UAVs in Hover Condition. *Unmanned Systems*, 08(04):295–308. Publisher: World Scientific Publishing Co. 148

[16] Leng, Y., Yoo, H., Jardin, T., Bronz, M., and Moschetta, J.-M. (2019). Aerodynamic Modeling of Propeller Forces and Moments at High Angle of Incidence. In *AIAA Scitech 2019 Forum*, San Diego, California. American Institute of Aeronautics and Astronautics. 14, 132, 139, 142, 143

[17] Leng Yuchen (2020). *Aerodynamic design of long endurance convertible UAV*. PhD thesis, Université de Toulouse, ISAE-SUPAERO, Toulouse. 14, 132, 139, 140, 142, 148

[18] Li Volsi, P., Gomez-Ariza, D., Gojon, R., Jardin, T., and Moschetta, J.-M. (2022). Aeroacoustic optimization of MAV rotors. *International Journal of Micro Air Vehicles*, 14:175682932110708. 132

[19] Phillips, W. F. (2004). *Mechanics of flight*. Wiley, New York. 133

[20] Prandtl, L. and Betz, A., editors (2009). *Ergebnisse der Aerodynamischen Versuchsanstalt zu Göttingen - IV. Lieferung*, volume 7 of *Göttinger Klassiker der Strömungmechanik*. Göttingen University Press, Göttingen. 133

[21] Rankine, W. (1865). Transactions Institute of Naval Architects. Technical Report 6. 132

[22] Ribner, H. S. (1945a). Propeller in Yaw. NACA Technical Report 820. 133

[23] Ribner, R. (1945b). Formulas for propellers in Yaw and chats of the side force derivative. Technical Report 819. 133

[24] Veldhuis, L. (1996). Analysis of propeller slipstream effects on a trailing wing. 132, 144

[25] Veldhuis, L. L. M. (2004). Review of Propeller-Wing Aerodynamic Interference. 132, 144, 148

[26] Veldhuis, L. L. M. (2005). *Propeller wing aerodynamic interference*. s.n., S.l. OCLC: 840392156. 15, 132, 144, 147, 148, 149

[27] Wei, M., Chiew, Y.-M., and Cheng, N.-S. (2020). Recent advances in understanding propeller jet flow and its impact on scour. *Physics of Fluids*, 32(10):101303. 133

4.5 Appendix - A : Complementary data, and propellers geometries

This appendix presents additional experimental comparison with ASWING predictions. Figures 4.16 (a) to (d) present extra validation of the extended actuator disk theory one DA4022 propeller at 2 different rotation speeds. Figures 4.17 (a) to (d) present the the propellers geometries. Figures 4.18 (a) and (b) present an additional validation of the jet and swirl models in static condition on the APC propeller at 9000RPM. Finally 4.19 (a) and (b) highlight the same validation but in advance flow condition.

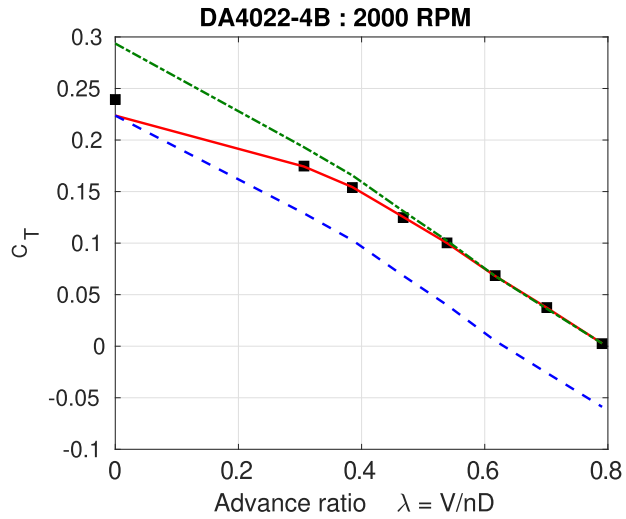

(a) C_T at 2000 RPM

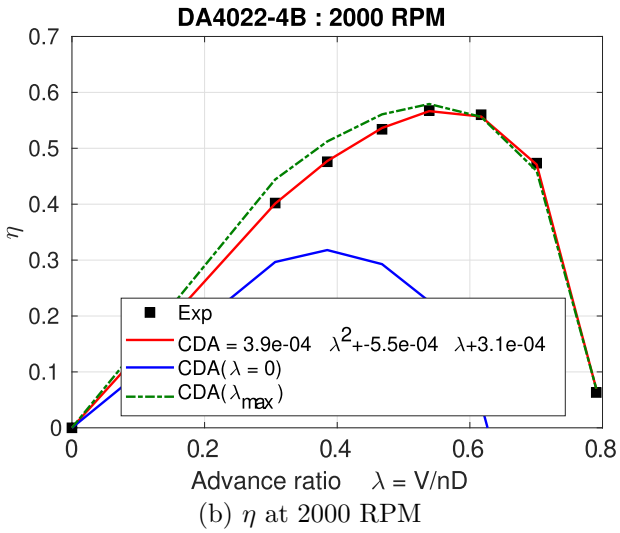

(b) η at 2000 RPM

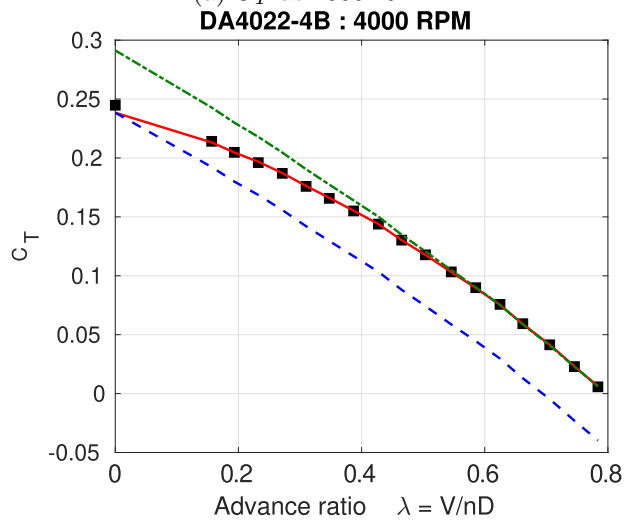

(c) C_T at 4000 RPM

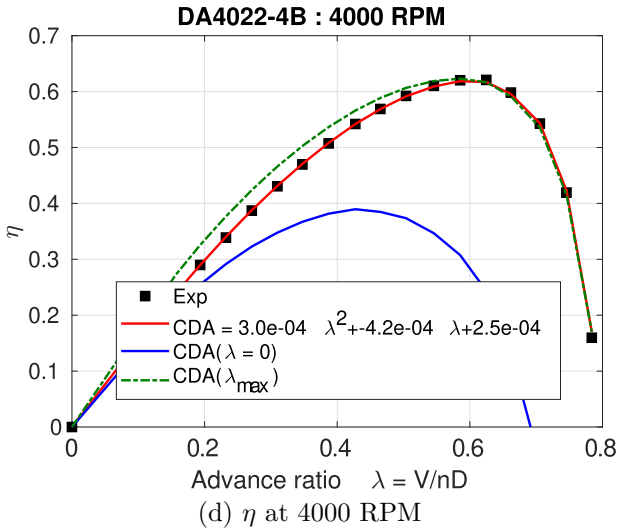

(d) η at 4000 RPM

Figure 4.16: Advance flow : C_T and η ASWING predictions for the DA4022-4B, comparison with rotation speed.

(a) GWS 5X4.3

(b) APC Sport 4.2X2

(c) DA4002 9 in

(d) DA4022 9 in

Figure 4.17: Propellers used for thrust, power, axial jet and swirl predictions

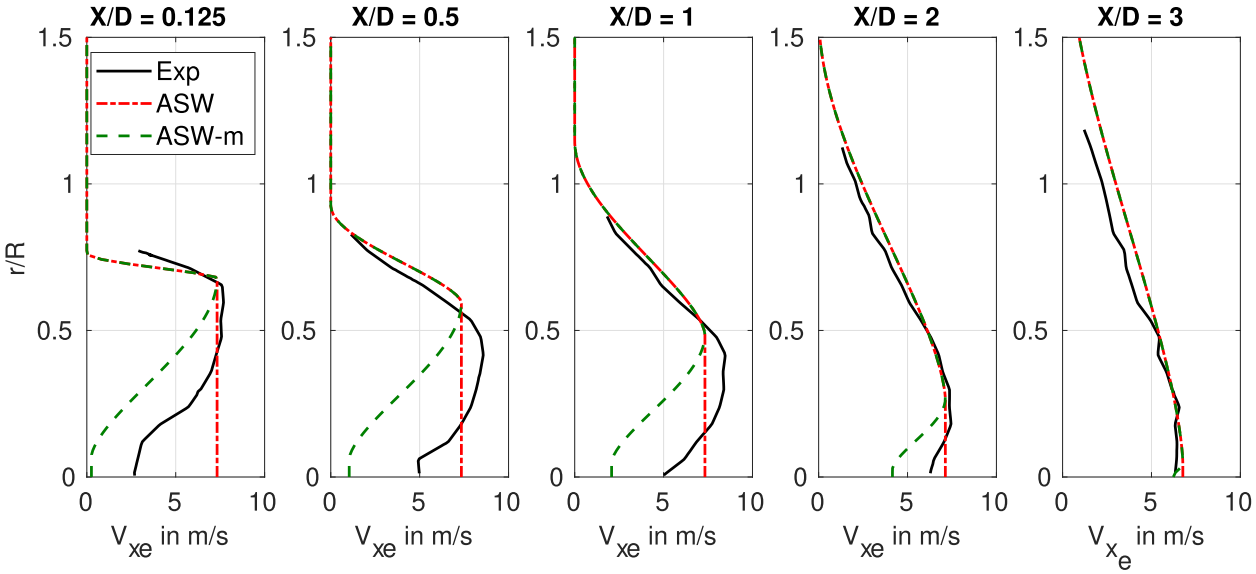

(a)Axial velocity

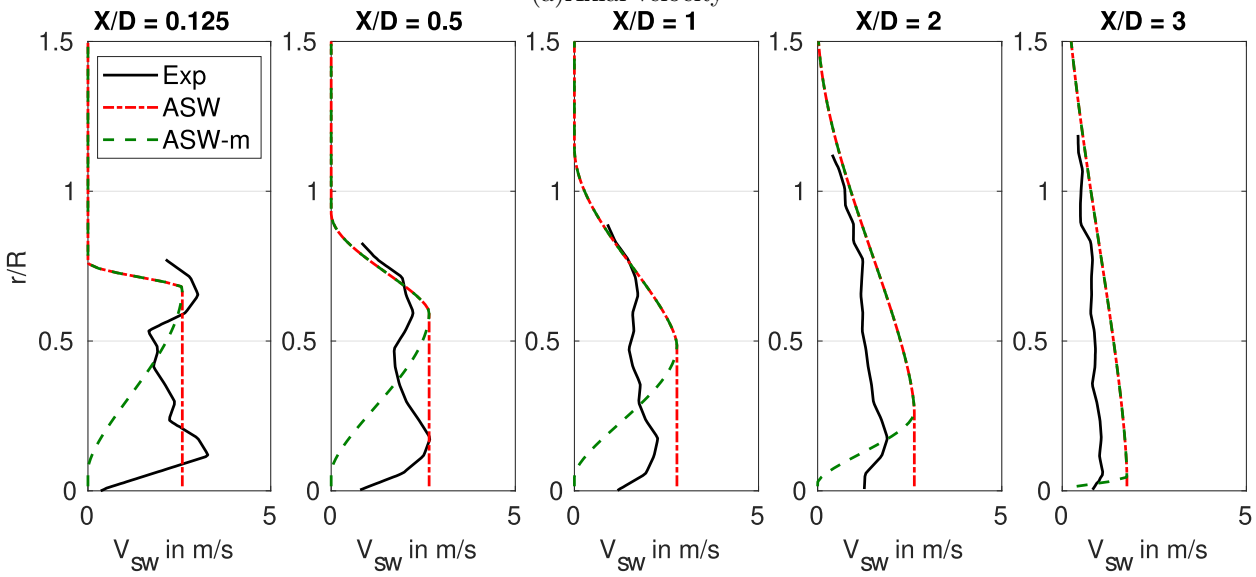

(b) Swirl velocity

Figure 4.18: Static APC (9000 RPM) axial and swirl velocities evaluated at different streamwise location $\frac{x}{D}$ and different radial position $\frac{r}{R}$ (y-axis). Comparison of ASWING 5.96 and ASWING-m predictions with experimental data from Deters

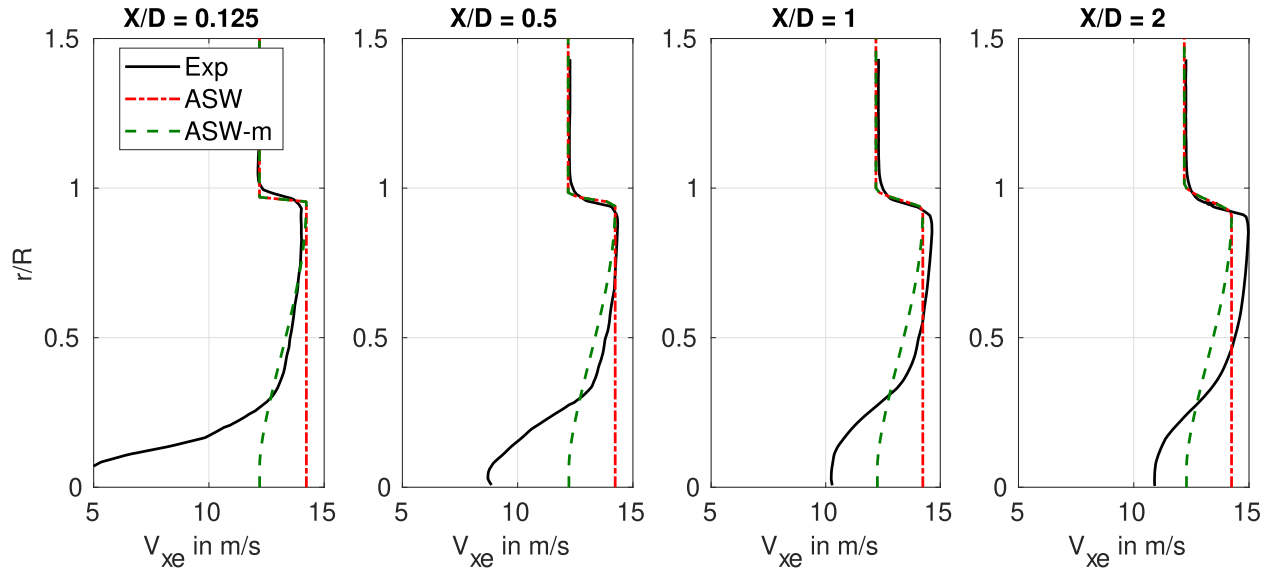

(a)Axial velocity

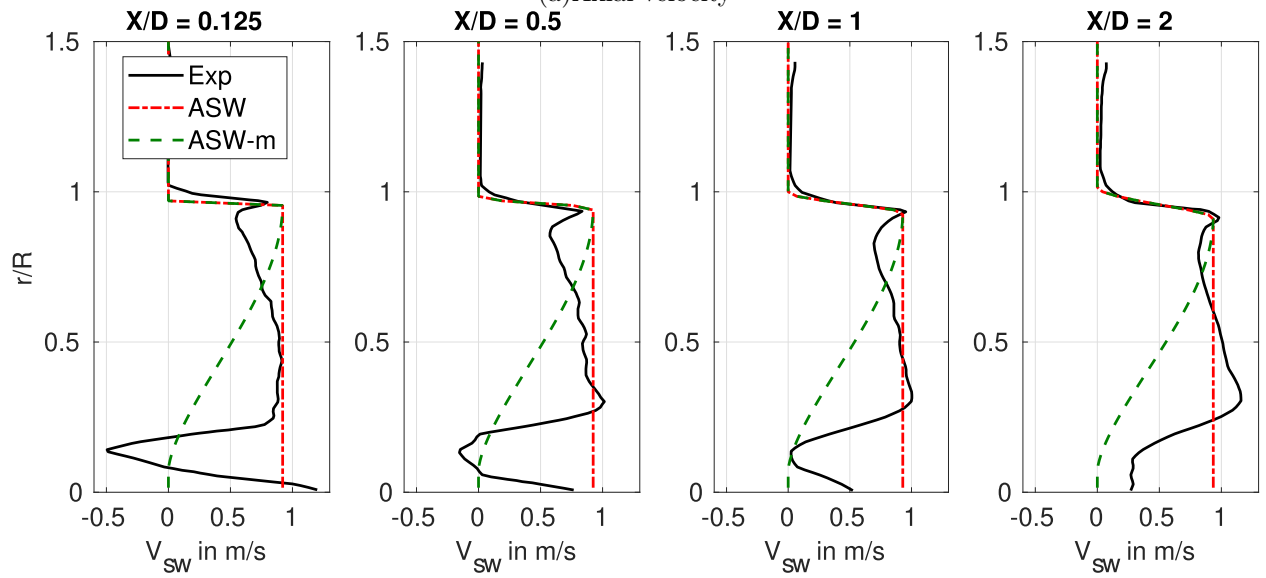

(b) Swirl velocity

Figure 4.19: Advanced flow DA4002 (5000RPM),$\lambda = 0.64$, axial and swirl velocities evaluated at different streamwise location $\frac{x}{D}$ and different radial position $\frac{r}{R}$ (y-axis). Comparison of ASWING 5.96 and ASWING-m predictions with experimental data from Deters

Chapter 5

Aeroelastic framework Part III : Structure

Abstract

This chapter presents an experimental validation of the ASWING structural model. In the first section, the models are recalled and detailed. Secondly, the numerical scheme convergence and the computational time for tip deflections and modal response predictions are provided. Thirdly, experimental validations are presented. Large tip deflection on helicopter blades and moderate to low aspect ratio wings are presented These cases are chosen to highlight both stiffness coupling and aspect ratio limitation. Finally, the modal responses of each case are compared with experiments found within the literature. This chapter also assesses the impact of concentrated masses, such as nacelles or tanks, on a wing modal response. Specifically, it analyses the effects of their position along the chord and span of the wing. Overall, ASWING provides excellent agreements with experiments for tip deflection, twist and modal response for beams with an aspect ratio greater than 6. And so no matter the composite layout, that can involve various bending coupling terms. ASWING captures also well the spanwise and chordwise position effect of the nacelle on the modal response of a wing. Finally, those predictions are provided in less than 0.1 (deflection) and 2.0 seconds (modal response) on modern laptops.

Publications:

Materials from this chapter have been gathered and summarized so that a journal paper could be submitted to AIAA Journal of Aircraft with the title:

R.Jan, J-M. Moschetta and J-P. Condomines, Experimental evaluation of ASWING for preliminary design of flexible aircraft: structural model, AIAA Journal of Aircraft, 2024.

This paper will be published after the PhD manuscript would have been made public so that the complete evaluation work can be cited in the paper.

Contents

Nomenclature

Geometrical parameters

$\square_E$		Earth frame subscript
$\square_b$		Body frame subscript
$\square_l$		Local frame subscript
$\vec{R_E} = (X_E,\ Y_E,\ Z_E)^T$	m	Body frame location relative to the earth frame
$\vec{\Theta} = (\Phi,\ \Theta,\ \Psi)^T$	rad	Body frame orientation relative to the earth frame
$\vec{U} = (U_x,\ U_y,\ U_z)^T$	m/s	Body frame speed relative to the earth frame
$\vec{\Omega} = (\Omega_x,\ \Omega_y,\ \Omega_z)^T$	rad/s	Body frame rotation rate relative to the earth frame
$\vec{a_0} = (a_{0,x},\ a_{0,y},\ a_{0,z})^T$	m/s^2	Body frame absolute acceleration relative to the earth frame
$\vec{\alpha_0} = (\alpha_{0,x},\ \alpha_{0,y},\ \alpha_{0,z})^T$	rad/s^2	Body frame angular acceleration relative to the earth frame
$(X,\ Y,\ Z)^T$		Earth frame axis
$[T_E]$		Body to earth frame transformation matrix
$[C_E]$		(x, y, z) projection to x, Y_1, Z axis
$(x,\ y,\ z)^T$		Body frame axis
$(c,\ s,\ n)^T$		Local frame axis
$\vec{\theta} = (\varphi,\ \vartheta,\ \psi)^T$	rad	local frame orientation relative to body frame
$\vec{r} = (r_x,\ r_y,\ r_z)^T$	m	local frame position relative to the body frame
$[T]$		body to local frame transformation matrix
$\vec{u} = (u_x,\ u_y,\ u_z)^T$	m/s	local frame velocity relative to the body frame
$\vec{\omega} = (\omega_x,\ \omega_y,\ \omega_z)^T$	m/s	local frame rotation rate relative to the body frame
$[C]$		(x, y, z) projection to x, s, z_1 axis
$\vec{r_p} = (r_x,\ r_y,\ r_z)^T$	m	arbitrary point position relative to the body frame
$\vec{a_p} = (a_x,\ a_y,\ a_z)^T$	m/s^2	absolute acceleration of a point p
$\Delta\vec{r}_p = (c_p,\ s_p,\ n_p)^T$	m	arbitrary point relative positon to the body frame
$(\kappa_c,\ \kappa_s, \kappa_n)$	$1/m$	local beam curvature
$(\kappa_{c,0},\ \kappa_{s,0}, \kappa_{n,0})$	$1/m$	local unloaded beam curvature
$[\mathcal{K}]$	$1/m$	local curvature tensor
$[K]$		local beam curvature definition matrix
$[K_0]$		local unloaded beam curvature definition matrix
$ds,\ ds_0$	m	loaded and unloaded beam elementary length
$(\gamma_c,\ \epsilon_s, \gamma_n)$		shear and extensional strain

Forces and moments parameters

$\vec{F} = (F_c,\ F_s,\ F_n)^T$	N	Interior beam forces expressed in the local frame
$\vec{M} = (M_c,\ M_s,\ M_n)^T$	Nm	Interior beam moments about the csn frame
$\vec{M} = (M_{c'},\ M_{s'},\ M_{n'})^T$	Nm	Shifted interior beam moments
$\vec{f}$	N/m	distributed forces
$\vec{m}$	N/m^2	distributed moments
$\Delta\vec{F}$	N	pontual loads
$\Delta\vec{M}$	N/m	pontual moments

Structural parameters

μ	kg/m	Isection mass per length
$[\iota]$	kgm	inertia tensor/lenght
$c_{cg},\ n_{cg}$	m	local center of gravity sectional positon
$c_{TA},\ n_{TA}$	m	tension axis sectional position
$c_{EA},\ n_{EA}$	m	Elastic axis
$\mathcal{H}$	kgm^2s^{-1}	Point mass angular momentum
J_E	kgm^2	Engine shaft moment of inertia
Ω_E	rad/s	Engine rotation rate
$(EI_{cc},\ EI_{nn},\ EI_{cn})$	Nm^2	Bending stifnesses
$(GJ,\ EI_{cs},\ EI_{sn})$	Nm^2	torsion and bending torsion coupling stiffnesses
$(GK_c,\ EA,\ GK_n)$	Nm^2	shear and extensional stiffnesses
$(t_\gamma,\ t_\epsilon)$	s	structural damping time

Résumé du chapitre en français

Ce chapitre est dédié à la présentation de la troisième partie du travail de validation expérimentale d'ASWING. L'accent est mis ici sur le modèle structure. Suivant la même construction que les chapitres précédent, le document commence avec un rappel théorique et historique du modèle. Un intérêt particulier est porté sur les différentes fonctionnalités proposées par ce dernier. On notera par exemple, la prise en compte de large amplitude, de section à propriétés élastiques non uniformes, d'un amortissement structurel interne. Le modèle permet également le placement arbitraire des axes élastique, de tension et de gravité. Des masses ponctuelles ou concentriques peuvent être fixés sur les structures pour modéliser des réservoirs externes ou nacelles. Enfin une description des différents types d'interconnexion entre les éléments constituant un aéronefs sont décrits. Comme par exemple l'utilisation de haubans élastiques, de joints rigides ou permissifs. Ces derniers sont particulièrement intéressants pour la modélisation de saumons à charnières élastiques ou l'étude du battement d'ailes d'oiseaux. Il est important de noter que contrairement aux deux chapitres précédents, aucune modification n'a été apportée au modèle structure d'ASWING. Ceci étant dit, le chapitre se poursuit avec l'étude du schéma numérique. Les taux de convergence du maillage pour le calcul de déformés statiques et réponse modale sont calculés et comparés au temps de calcul nécessaire pour chaque cas visant à trouver le meilleur compromis entre temps de calcul et précision numérique. Vient ensuite, la validation expérimentale basée sur l'utilisation de données issues de la littérature scientifique. Un jeu de pales d'hélicoptères a été utilisé pour apprécier la qualité de prédictions des déformations non linéaires. Différents agencements de fibres sont étudiés faisant intervenir différents termes de couplage en raideur. Les réponses modales des ces pales sont aussi présentées. Par la suite l'évaluation est complétée via l'utilisation d'un jeu de données mettant plus en défaut le modèle. Trois ailes distinctes d'allongement faibles ont été utilisées. De la même manière, les déformations statiques et réponses modales sont présentées. Sur ce cas test, les prédictions d'ASWING ont été comparées à un modèle de plus haute fidélité issu de la littérature. Pour finir une dernière comparaison est introduite. Dans celle ci l'effet de la position latérale et longitudinale de réservoir ou nacelle sur la réponse modale d'une aile de faible allongement est présentée.

Conclusions générales:

Sur des structures de fort allongement, ASWING capture parfaitement les déformations non linéaire dûes à une masse ponctuelle en bout de pale/aile. Quelques soient les termes de couplage en raideur présents, les prédictions sont de très bonne qualité. De plus il est montré que, le fait de négliger certains termes dans la matrice de raideurs (couplage extension/extension) ne semble pas posé de problème sur l'ensemble des composites étudiés. De la même manière les prédictions des réponse modales sont excellentes et ce pour les 5 premiers modes structuraux.

Le second banc de tests (aile de faible allongement) est plus intéressant pour mettre en évidence les limites du modèle structure. Les prédictions des déformés statiques sont très mauvaises quelque soit le degré de liberté et composite considéré. En revanche les prédictions en réponse modale restent encourageantes. Enfin le dernier banc utilisé permet de montrer qu'ASWING capture correctement l'effet de la position latérale et horizontale d'une nacelle sur la réponse modale de faible allongement. A la lumière de ces cas tests, nous pensions pourvoir dresser les limites d'usage d'ASWING cependant nous verrons dans le chapitre suivant, lorsque les modèles structure et aérodynamique sont couplés, ASWING peut tout de même fournir d'excellentes prédictions sur des ailes de faibles allongements.

5.1 Introduction

In order to reduce commercial aircraft fuel burn, the major work related to conceptual design tends to show that higher aspect ratio and lighter wing are ininevitable. Thus highly flexible structures are expected, with large deflections in cruise conditions. The latter will be more likely subject to flutter and their modal response is expected to be very close to the aircraft flight dynamics [1, 29, 5]. With the large deflection comes the problem of flutter onset [40, 41, 23]. It becomes mandatory now to predict the latter phenomena directly during the pre-design loop to ensure a feasible and flyable architecture. Then without loss of generality on the previous comments, new types of architectures are studied such as joined, C, blended and strut wings, distributed and rear-mounted propulsion etc [21, 38, 45, 7, 10, 46]. They all rise new aeroelastic problems, and simple structural models are no longer enough to assess those types. Also floating wingtips are more and more studied as passive gust alleviation devices and rolling performance improvement solutions [25, 27, 26, 9]. Having a structural model capable of capturing their effects is a real asset for the analysis of this type of application.

In light of the previous comments, one-dimensional non-linear beam models remain prevalent in aeronautics [39, 44, 22, 6, 48]. These models hold interest owing to their ability to produce fast analysis with a reasonable level of accuracy. When fast aerodynamic models such as lifting-line or vortex lattice methods are combined with them, a wide range of aeroelastic phenomena can be studied. SharpY (del Carre et al.-2019) , UMNAST (Su and Cesnik-2010), Openaerostruct (Chauhan and Martins-2019) and Aswing (Drela-1999) are framework proposing the coupling of such models. The latter (Aswing) is of interest in this chapter. This software was first introduced in the 1990s by Drela (1990, 1999) as part of Deadalus project and has been then improved in the 2000s(Drela-2008, 2009). The major problem is that ASWING has been evaluated only 6 times [24, 49, 28, 11, 34, 47]. All the 6 articles have evaluated the same features, i.e. flutter speed or gust load predictions. Furthermore, the aircraft considered in these papers were not stress cases of the model as they all had very high aspect ratio wings. In consequence, we have performed a complete experimental evaluation of the model and its various features in 4 main steps. The three main models that are aerodynamics, structure and propellers have been evaluated separately as it is easier to find experimental data from the literature. Also, it is more convenient to do so in order to highlight the critical parameters of each one of them. Then they were gathered together so that the aeroelastic features could be evaluated. This chapter presents the ASWING structural model evaluation . The latter derives from a nonlinear, unsteady extension of the classical Euler-Bernoulli beam theory. The ASWING structural model is a multi-beam code mainly adapted from Minguet's works (1989). This code can predict the non-linear deflections (large amplitudes) and modal responses of very flexible structures. Beams can be cantilevered to non-inertial frames, connected by constrained or compliant joints. The section properties (stiffness and mass) are spanwise varying. Elastic, tensile, and centre of gravity position can be arbitrarily defined. The unsteady formulation of the Minguet's model is extended with viscous structural damping, adapted from the work of Banks and Wang (1987, 1991). Internal forces and moments are computed based on the strains and curvatures changes, with coupling terms on bending and torsion. Finally, the discrete model captures pure load discontinuities (point masses, engine thrust, struts) through the use of zero-length intervals.

The chapter is built as follows. In section II, the theoretical model is recalled and voluntary illustrated. As ASWING is a multidisciplinary tool that can be used by the control, aerodynamic and structural design community, our effort is to provide an extended understanding of the models than in the technical documentation ([16, 17] where they have been summarized. In section III, The numerical scheme convergence and computational time are assessed to provide the reader with the optimal mesh refinement and computational performances on a modern laptop. Then in section IV, the experimental evaluation of the model with a focus on non-linear large deflections, modal responses and the effect of concentrated masses (nacelle, tank) on them (modal response only). The test cases have been chosen from high to moderate-low aspect ratios in order to clearly identify the limits of the model. Moreover, test cases have been multiplied as some of them are presenting different composite layouts. The latter are used to assess the simplification made in the model (stiffness matrix reduction). Finally, when it was possible, the predictions have been compared to other models from the literature. The experimental data set is based on the work of Minguet (1990b,1990a) for large deflection and modal response of high aspect ratio helicopter blade (CASE A). For moderate aspect ratio, the recent Pazy wing bench of Avin et al.-2022 is also discussed as an intermediate stress test (CASE B). The work of Dunn and Dugundji (1992) has been used for the large deflection and modal response of low aspect ratio rectangular wing (CASE C). Regarding the tank or engine position

effect on the modal response of a straight wing, the work of Runyan and Sewall (1948) has been chosen (CASE D). All the different parameters used in the simulations have been summarised and translated into the metric systems in the appendix of this chapter.

5.2 Structural model

This section proposes to derive the structural model of ASWING. First, useful coordinate systems are introduced with their relative position, velocity, acceleration, etc. Secondly, the inertial acceleration of any point of the structure is derived to be used in the following sections. Thirdly, beam curvature and strains are detailed so that the internal forces and moments introduced in the force equilibrium section can be derived. Fifthly, distributed and punctual inertial and gravitational loads are derived. Finally, the section concludes with comments on beam connections and discretisation of the problem.

5.2.1 Useful coordinate systems

The ASWING structural model differs from the classical Euler-Bernoulli theory in that the beams are cantilevered on non-inertial frames. In fact, the model has to describe the steady-state and transient structural behaviour of aircraft elements that may be in non-uniform accelerated motion in space. Consequently, to derive the model accurately, 3 frames are required.

Inertial Frame (Earth)

This frame, cantilevered to any point on the Earth's surface, is inertial. Assuming a flat Earth, it is used to provide the position $\vec{R_E}$, orientation $\vec{\Theta}$, velocity $\vec{U}$, rotation rate $\vec{\Omega}$, inertial and angular acceleration $\vec{a_0}$ and $\vec{\alpha_0}$ of the rigid body frame, i.e. the aircraft. The inertial frame axes are denoted as $(X,\ Y,\ Z)$ as shown in the figure 5.1. $\vec{\Theta} = (\Phi,\ \Theta,\ \Psi)^T$ defines the rotation sequence to obtain the body frame orientation according to the sequence shown in figure 5.2. The body to earth axis transformation matrix is given as follow:

$$[T_E] = \begin{bmatrix} \cos\Psi & \sin\Psi & 0 \\ -\sin\Psi & \cos\Psi & 0 \\ 0 & 0 & 1 \end{bmatrix} \begin{bmatrix} \cos\Theta & 0 & \sin\Theta \\ 0 & 1 & 0 \\ -\sin\Theta & 0 & \cos\Theta \end{bmatrix} \begin{bmatrix} 1 & 0 & 0 \\ 0 & \cos\Phi & \sin\Phi \\ 0 & -\sin\Phi & \cos\Phi \end{bmatrix} \tag{5.1}$$

The above equation translates the transformation sequence of figure 5.2, but from right to left. Note that $\vec{R_E}$ in the Earth frame is expressed as $\vec{R_E} = (X_E,\ Y_E,\ Z_E)^T_E$, hile the velocity vector is expressed in the body frame as $\vec{U} = (U_x,\ U_y,\ U_z)^T_b$. The time variation of the position vector is then given by

$$\frac{d\vec{R_E}}{dt} = [T_E]\vec{U_b} \tag{5.2}$$

From the equation above the absolute acceleration expressed in the earth frame can be expressed as

$$\vec{a_0} = \frac{d\vec{U}}{dt} + \vec{\Omega} \times \vec{U} \tag{5.3}$$

The orientation vector $\vec{\Theta}$ is not expressed in the body nor the earth frame as
$\vec{\Theta} = (\Phi\vec{x},\ \Theta\vec{Y}1,\ \Psi\vec{Z})^T$ while the rotation rate vector $\vec{\Omega}$ is expressed in the body frame $(\Omega_x,\ \Omega_y,\ \Omega_z)^T_b$. The relation between $\vec{\Omega}$ and $\vec{\theta}$ is given by projecting the vectors $\vec{x}$, $\vec{y}$ and $\vec{z}$ on x, $Y1$ and Z as follow

$$\frac{d\vec{\Theta}}{dt} = \begin{bmatrix} -1 & \sin\Phi\tan\Theta & -\cos\Phi\tan\Theta \\ 0 & \cos\Phi & \sin\Phi \\ 0 & \sin\Phi/\cos\Theta & -\cos\Phi/\cos\Theta \end{bmatrix} \vec{\Omega} = [C_E]\vec{\Omega} \tag{5.4}$$

where $[C_E]$ is the projection matrix. The latter is invertable. From $\vec{\Omega}$ can be derived the angular acceleration $\vec{\alpha_0}$ as follow :

$$\vec{\alpha_0} = \frac{d\vec{\Omega}}{dt} \tag{5.5}$$

This frame is attached to the aircraft (see figure 5.1, x points to the tail, y to the right wing and z is constructed to ensure a normal frame (right hand rule). The direction of the body frame axis is provided by the transformation sequence derived in the equation 5.1. Most of the physical variables are derived in this frame. The latter is really useful for evaluating global aerodynamic parameters such as infinite relative airspeed, angle of attack and side slip angle. At least one of the aircraft elements is cantilevered from the body frame, although the use of a rigid pylon (distant cantilevering) may be considered.

Local frame $(c,\ s,\ n)^T$

This frame is placed along the reference line and is very useful to derive the aerodynamic and structural loads and moments. In ASWING its origin can be placed anywhere along the chord line. However, in the next development it is assumed to be fixed at the leading edge of each wing section.

I - Classical Euler-Bernoulli beam theory (CEB)	**II - Extended CEB [37]**	**III - ASWING 5.96**
1750	1989	2008
- small deflection - uniform beam - no torsion -flat straight beam (zero curvature) - small torsion - tension and center of gravity axis at the mid chord	- **Improvements of I:** + large deflection (non linear) §5.2.3 & §5.2.5 + bending torsion coupling §5.2.5 + shear and extensional stress §5.2.5 + elastic axis at the mid chord + rotating beam + coupled to a blade element theory	- **Improvements of II:** + Non inertial cantilevering §5.2.1 & §5.2.3 + non uniform beam §5.2.5 + Multi-beams code §5.2.7 + structural damping (Kelvin-Voigt damping)§5.2.5 + zero length interval §5.2.8 + aerodynamic damping (added mass term, Theodorsen) [16] + ponctual mass loads §5.2.6 +arbitrary location of the tension, elastic and center of gravity axis §5.2.5 §5.2.6 + coupled to a non linear unsteady lifting line model [16]
continuous solution	discrete solution	discrete solution §5.2.8

Table 5.1: Evolution of the classical Euler-Bernoulli beam theory to the ASWING structural model. References to the sections are displayed where the improvements are detailed

The c-axis is aligned with the chord line pointing downstream, the s-axis is tangent to the reference line and the n-axis is constructed using the right hand rule. As for the body frame, the local axes are rotated from the body axis according to the sequence shown in figure 5.3. The transformation matrix is given by

$$[T] = \begin{bmatrix} \cos\vartheta & 0 & -\sin\vartheta \\ 0 & 1 & 0 \\ \sin\vartheta & 0 & \cos\vartheta \end{bmatrix} \begin{bmatrix} \cos\psi & \sin\psi & 0 \\ -\sin\psi & \cos\psi & 0 \\ 0 & 0 & 1 \end{bmatrix} \begin{bmatrix} 1 & 0 & 0 \\ 0 & \cos\varphi & \sin\varphi \\ 0 & -\sin\varphi & \cos\varphi \end{bmatrix} \tag{5.6}$$

where $\vec{\theta} = (\varphi\ \vartheta\ \psi)^T$ are the local frame rotation angles. The latter vary with the reference line coordinate s. The position of the local frame origin is given by $\vec{r}(s)$ expressed in the body frame. In the unsteady formulation of the structural model, the local frame may have a relative velocity and orientation rate expressed in the body frame, denoted by $\vec{u}(s)$ and $\vec{\omega}$.The position and velocity $\vec{r}(s)$ and $\vec{u}(s)$ are related as follows

$$\vec{u}(s) = \frac{d\vec{r}(s)}{dt} \tag{5.7}$$

Relation between $\vec{\omega}$ and $\dot{\vec{\theta}}$ is not as trivial. Indeed $\vec{\theta}$ defines the rotation rate around x, s and z_1. The last 2 are not part of the body frame. When x, y, z components of $\vec{\omega}$ are projected against $\vec{x}$, $\vec{s}$ and $\vec{z_1}$ it comes :

$$\begin{aligned} \dot{\vec{\theta}} &= [C]\vec{\omega} \\ &= \begin{bmatrix} 1 & \cos\varphi\tan\psi & \sin\varphi\tan\psi \\ 0 & \cos\varphi/\cos\psi & \sin\varphi/\cos\psi \\ 0 & -\sin\varphi & \cos\varphi \end{bmatrix} \begin{pmatrix} \omega_x \\ \omega_y \\ \omega_z \end{pmatrix} \end{aligned} \tag{5.8}$$

where $[C]$ is the $\vec{x}$, $\vec{y}$ and $\vec{z}$ to $\vec{x}$, $\vec{s}$ and $\vec{z_1}$ projection matrix As it will be seen in the next section, $\vec{\omega}$ is more convenient than $\dot{\vec{\theta}}$ to derive the intertial acceleration of any point attached to the local frame.

5.2.2 Inertial acceleration

In order to calculate the inertial and gravitational loads derived in the following sections, the absolute acceleration [1] of a point rigidly attached to the local frame origin is required. To do this, an acceleration composition is used. First, the absolute acceleration of the local frame origin is given below. Terms of interest are indicated by brackets.

$$\vec{a}\,(\vec{r}) = \vec{a}_o + \underbrace{\dot{\vec{u}} + \vec{\alpha}_o \times \vec{r} + \overbrace{\vec{\Omega} \times \left(\vec{\Omega} \times \vec{r}\right)}^{\text{centrifugal acceleration}}}_{\text{swinging acceleration}} + \underbrace{2\vec{\Omega} \times \vec{u}}_{\text{Coriolis}} \tag{5.9}$$

The blue terms in the equation in 5.9 highlight the unsteady terms. From the previous equation one can derive the absolute acceleration of any point "rigidly" connected to the csn frame by a pylon. By denoting $\vec{r_p}$ the position of the point so that

$$\vec{r_p} = \vec{r(s)} + \delta\vec{r_p} = \vec{r(s)} + \begin{pmatrix} c_p \\ s_p \\ n_p \end{pmatrix}_{c,s,n}$$

Considering that (c, s, n) has a relative [2] rotation rate $\vec{\omega}$, the relative [3] change of the offset vector is due only to this rotation and is given by

$$\vec{u_p} = \frac{d}{dt}\Delta\vec{r_p} = \vec{\omega} \times \Delta\vec{r_p}$$

Finally, the absolute acceleration of point p is

$$\begin{aligned} \vec{a}\,(\vec{r_p}) = \vec{a}_p = \vec{a}(\vec{r}) &+ \left(\vec{\alpha}_o + \dot{\vec{\omega}}\right) \times \Delta\vec{r_p} \\ &+ \vec{\Omega} \times \left(\vec{\Omega} \times \Delta\vec{r_p}\right) + \vec{\omega_i} \times (\vec{\omega} \times \Delta\vec{r_p}) \\ &+ 2\vec{\Omega} \times (\vec{\omega} \times \Delta\vec{r_p}) \end{aligned} \tag{5.10}$$

5.2.3 Beam curvatures and strains

As will be explained in more detail in the next section, when any load (distributed or point) is applied to a beam, it experiences a change in its geometry. In this section, curvature and strains are introduced as they will be used to calculate internal forces and moments.

Curvature

When the local frame is moved along the reference line from a spanwise location s to $s + ds$, the (c, s, n) axes undergo a small rotation. Figure 5.4 shows a simplified case. The s and n axes undergo a small rotation of an angle $d\theta$ around the c axis. The latter angle is related to the curvature κ_c as follows: $d\theta = \kappa_c ds$. Note that $\frac{1}{\kappa_c}$ can be interpreted as the radius of curvature of the beam at the spanwise point s. A circle with its centre at the intersection of $n(s)$ and $n(s + ds)$ with the latter radius of curvature is perfectly tangent to the vectors $s(s)$ and $s(s + ds)$. Figure 5.4 shows the 2D case. In the 3D case the illustration is not so simple. As a result, when the local frame is moved along the reference line, it can undergo a small rotation as

[1] The absolute acceleration denotes the acceleration relative to the inertial frame.

[2] relative to the body frame

[3] relative to the csn frame

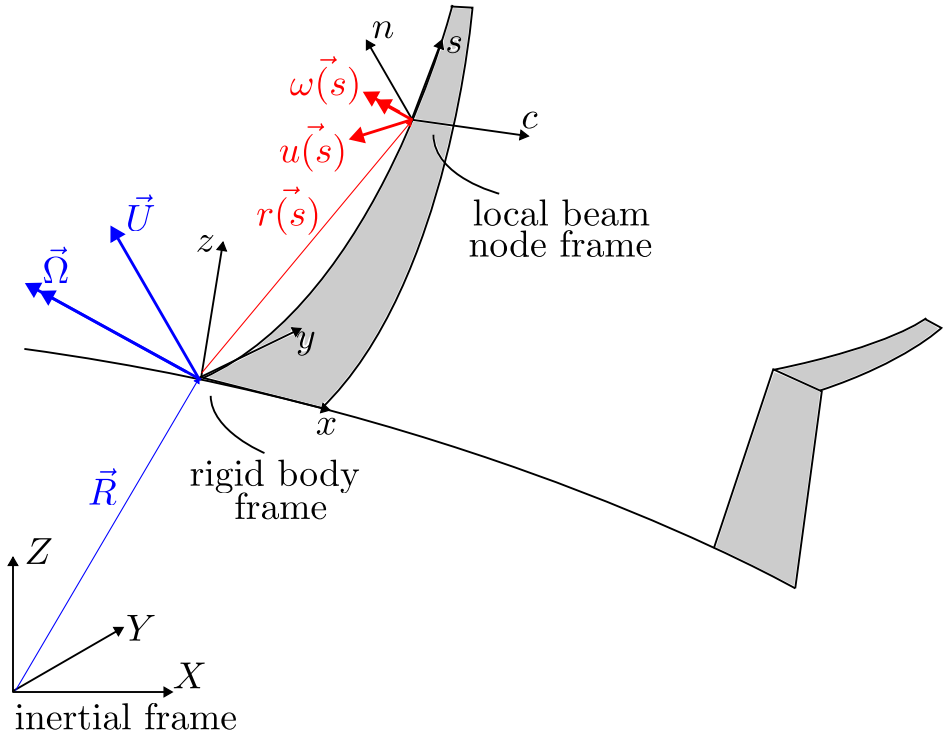

Figure 5.1: Structural model useful frames

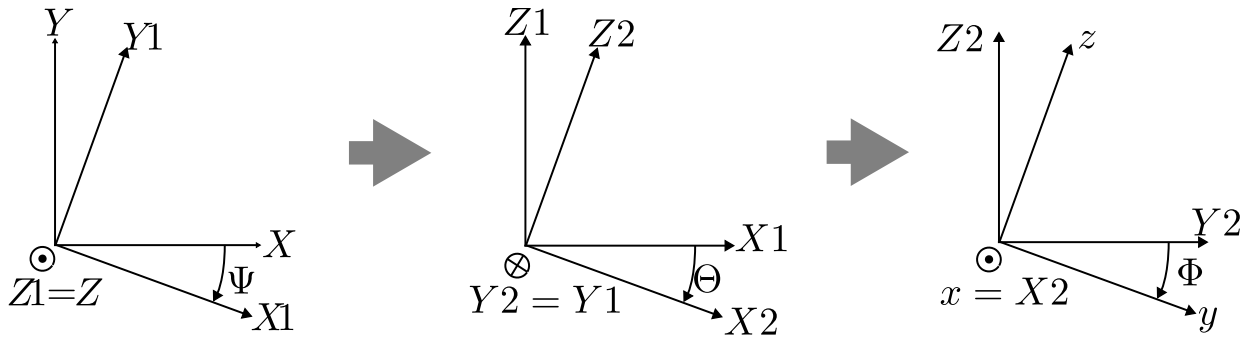

Figure 5.2: Earth to body frame transformation sequence

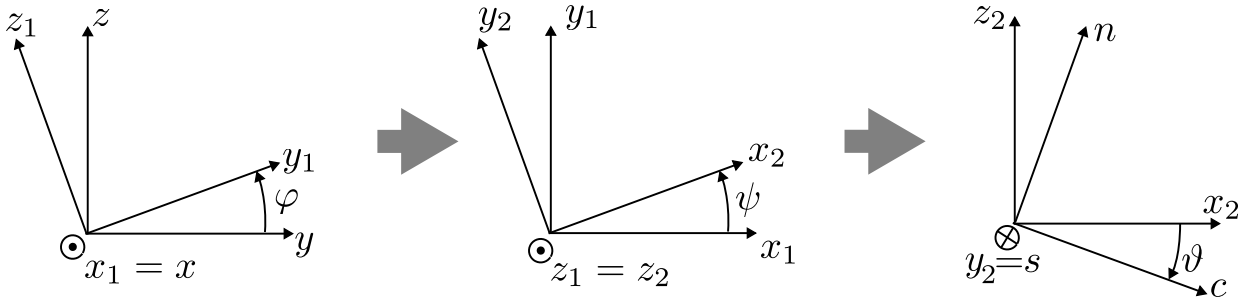

Figure 5.3: Body to local frame transformation sequence

follows:

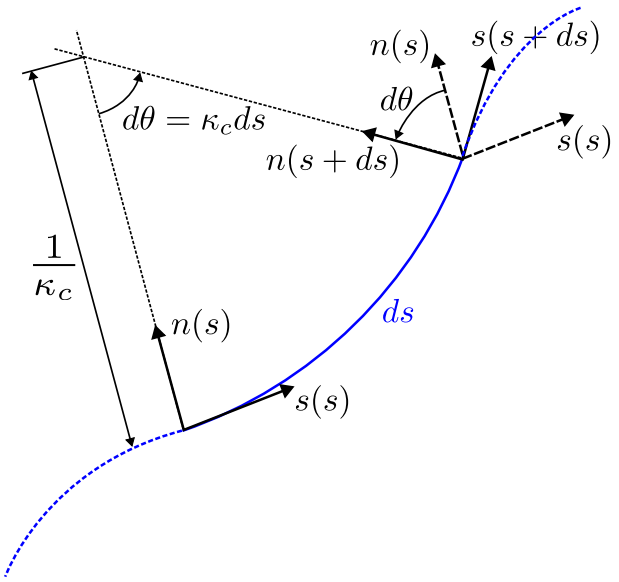

Figure 5.4: Beam local curvature, simplified case for illustration

$$\begin{pmatrix} c(s) \\ s(s) \\ n(s) \end{pmatrix} = [T(s)] \begin{pmatrix} x \\ y \\ z \end{pmatrix}$$
$$\begin{pmatrix} c(s+ds) \\ s(s+ds) \\ n(s+ds) \end{pmatrix} = \left[T(s) + \frac{d[T]}{ds} ds \right] \begin{pmatrix} x \\ y \\ z \end{pmatrix} \tag{5.11}$$

The small elementary transformation in equation 5.11 is linked to the curvature as follow :

$$\frac{d[T]}{ds} = -[\mathcal{K}][T] = \begin{pmatrix} 0 & -\kappa_n & \kappa_s \\ \kappa_n & 0 & -\kappa_c \\ -\kappa_s & \kappa_c & 0 \end{pmatrix} [T(s)] \tag{5.12}$$

where $[\mathcal{K}]$ is the local curvature tensor. Using a mix of the scalar and vectorial product, the curvature c, s, n component can be obtained from equation 5.12 as follow:

$$\begin{pmatrix} \kappa_c \\ \kappa_s \\ \kappa_n \end{pmatrix} = \begin{bmatrix} \cos\psi\cos\vartheta & 0 & -\sin\vartheta \\ -sin\psi & 1 & 0 \\ \cos\psi\sin\vartheta & 0 & \cos\vartheta \end{bmatrix} \begin{pmatrix} d\varphi/ds \\ d\vartheta/ds \\ d\psi/ds \end{pmatrix}$$
$$= [K] \begin{pmatrix} d\varphi/ds \\ d\vartheta/ds \\ d\psi/ds \end{pmatrix} \tag{5.13}$$

where $[K]$ is the curvature definition matrix. Two types of beam curvature are of interest in the next sections, the loaded and the unloaded, denoted as $(\kappa_c, \kappa_s, \kappa_n)$ and $(\kappa_{c,0}, \kappa_{s,0}, \kappa_{n,0})$. The latter is obtained with the equation 5.13 and is given as

$$\begin{pmatrix} \kappa_{c,0} \\ \kappa_{s,0} \\ \kappa_{n,0} \end{pmatrix} = [K_0] \begin{pmatrix} d\varphi_0/ds \\ d\vartheta_0/ds \\ d\psi_0/ds \end{pmatrix} \tag{5.14}$$

where $[K_0]$ is the unloaded curvature definition matrix.The unloaded curvature is of particular interest for modelling non-flat beams. Another quantity of interest to derive the internal forces and moments is the rate of curvature. The latter is given by deriving the equation 5.13 with respect to time. From now on the notations $\vec{\theta} = (\varphi, \vartheta, \psi)^T$ and $\vec{\theta_0} = (\varphi_0, \vartheta_0, \psi_0)^T$ are used.

$$\begin{pmatrix} \dot{\kappa}_c \\ \dot{\kappa}_s \\ \dot{\kappa}_n \end{pmatrix} = [K] \frac{d\dot{\vartheta}}{ds} + [\dot{K}] \frac{d\vec{\theta}}{ds} \tag{5.15}$$

with $[\dot{K}]$ is given as follow

$$\dot{K}] = \frac{\partial[K]}{\partial\varphi}\dot{\varphi} + \frac{\partial[K]}{\partial\vartheta}\dot{\vartheta} + \frac{\partial[K]}{\partial\psi}\dot{\psi}$$
$$= [K]_\varphi\dot{\varphi} + [K]_\vartheta\dot{\vartheta} + [K]_\psi\dot{\psi}$$

Multiplying by $\frac{d\vec{\theta}}{ds}$ it comes:

$$\dot{[K]}\frac{d\vec{\theta}}{ds} = \left([K]_\varphi\dot{\varphi} + [K]_\vartheta\dot{\vartheta} + [K]_\psi\dot{\psi}\right)\frac{d\vec{\theta}}{ds}$$
$$= \frac{d[K]}{ds}\vec{\theta}$$

Using it in the equation 5.16 gives the final expression of the curvature rate

$$\begin{pmatrix} \dot{\kappa}_c \\ \dot{\kappa}_s \\ \dot{\kappa}_n \end{pmatrix} = [K] \frac{d\dot{\vartheta}}{ds} + \frac{d[K]}{ds}\vec{\theta} \tag{5.16}$$

Tension and shear strains: As explained earlier, the curvature provides information about how the local frame axes are rotated. Another useful piece of information is the displacement of the frame origin along the reference line. When the beam is unloaded, the position of the local frame at the spanwise location $s + ds$ is given by

$$\vec{r}(s+ds) = \vec{r}(s) + [T(s)]^T ds_0 \begin{pmatrix} 0 \\ 1 \\ 0 \end{pmatrix}_{c,s,n}$$
$$= \vec{r}(s) + \frac{d\vec{r}}{ds} ds \tag{5.17}$$

where $d_{s,0}$ denotes the unloaded element length. Now, supposing that the beam is locally subject to shear and extensional stress, the *csn* origin is shifted as

follows

$$\begin{aligned}\vec{r}(s+ds) &= \vec{r}(s) + [T(s)]^T ds_0 \begin{pmatrix} \gamma_c \\ \epsilon_s + 1 \\ \gamma_n \end{pmatrix}_{c,s,n} \\ &= \vec{r}(s) + \frac{d\vec{r}}{ds} ds\end{aligned} \tag{5.18}$$

The difference between the loaded and unloaded csn origin shift is shown in the figure 5.5. It is important to note that the strains have no dimensions, the shift induced by them is proportional to ds. The equation 5.18 can be inverted to obtain the relation between the strains and the variation of the local position vector with respect to the spanwise location.

$$\begin{pmatrix} \gamma_c \\ \epsilon_s + 1 \\ \gamma_n \end{pmatrix}_{c,s,n} = [T(s)] \frac{d\vec{r}}{ds_0} \tag{5.19}$$

As for the curvature, the strain rates will be useful. Deriving equation 5.19 with respect to time leads to

$$\begin{pmatrix} \dot{\gamma}_c \\ \dot{\epsilon}_s \\ \dot{\gamma}_n \end{pmatrix}_{c,s,n} = [T(s)] \frac{d\dot{\vec{r}}}{ds_0} + [\dot{T}(s)] \frac{d\vec{r}}{ds_0} \tag{5.20}$$

The transformation matrix rate $[\dot{T}(s)]$ is actually related to $\vec{\omega}(s)$ with $[\dot{T}(s)] = -T(s)[\omega(s)]$ [4]. Based on that the stains rates are related to the local frame origin speed, position and rotation rates as follows

$$\begin{pmatrix} \dot{\gamma}_c \\ \dot{\epsilon}_s \\ \dot{\gamma}_n \end{pmatrix}_{c,s,n} = [T(s)] \left(\frac{d\vec{u}}{ds_0} - \vec{\omega}(s) \times \frac{d\vec{r}}{ds_0} \right) \tag{5.21}$$

5.2.4 Forces and moment equilibrium

Let us consider a beam element of length ds, (cf figure 5.6). Applying the Newton's principle comes :

$$\begin{aligned} -\vec{F(s)} + \vec{F}(s+ds) + \vec{f}ds + \Delta\vec{F}\delta(1) = 0 \\ d\vec{F(s)} + \vec{f}ds + \Delta\vec{F}\delta(1) = 0 \end{aligned} \tag{5.22}$$

where $\vec{F(s)}$ denotes the internal beam force, $\vec{f}$ are the distributed forces (lift and drag) and $\Delta\vec{F}$ the point loads (engine, struts, point mass, joints). In this chapter only the point mass and the distributed inertia and gravity loads are derived, as they will be derived later. The others (lift, drag, engine) are described in [16, 17]. The moment equilibrium around the left element is given by :

$$\begin{aligned} &-\vec{M(s)} + \vec{M}(s+ds) + \vec{m}ds + \Delta\vec{M}\delta(1) \\ &+ [T]^T \begin{pmatrix} 0 \\ ds \\ 0 \end{pmatrix}_l \times \vec{F}(s+ds) = 0 \\ &d\vec{M}(s) + \vec{m}ds + \Delta\vec{M}\delta(1) \\ &+ [T]^T \begin{pmatrix} 0 \\ ds \\ 0 \end{pmatrix}_l \times \vec{F}(s+ds) = 0 \end{aligned} \tag{5.23}$$

Note that the moments induced by the distributed loads f are already included in the distributed moments m.

5.2.5 Internal forces and moments in non uniform beams

From the expressions of strain and curvature expressed in the local frame (c, s, n), the internal forces can be derived. In fact, the shear and extensional strains and the bending/torsional curvature provide information on how the length of the fibres changes in the beam element. Firstly, ASWING differs from the classical Euler-Bernoulli or its non-linear extension (Minguet) in that it takes into account the stiffness properties of non-uniform sections. Figure 5.7 shows what motivated this change. Wings are made of different materials, the shell can be made of carbon fibre with specific tailoring, balsa, aluminium foam, etc. The main and secondary spars can be made of plywood, aluminium, plywood covered with carbon fibre, etc. The latter have different Young's and Coulomb's moduli. Consequently, in the next development the E and G moduli will be considered as varying with the section coordinates (c, n). The next development will be divided into different parts where each strain and curvature contribution to forces and moments will be considered.

Forces and moments due to extensional strains: Assuming that the section does not wrap, the extensional strain $\epsilon_s(s)$ does not vary in the section plane (c,n) and is considered to be uniform. When a beam element fibre is stretched to length $ds + \epsilon(s)ds$, the elementary extensional force due to $\epsilon_s(s)$ is given by

$$\vec{df}_{\epsilon_s} = E(c,n)\epsilon_s dcdn\vec{s}$$

where $dcdn$ is a small cross-sectional element area. Since the beam element Young's modulus E is not uniform along the section, the extensional stress is also not uniform as shown in the figure 5.8. Since a wing section does not have the shape of a plate, the strain stress is not uniform, but also does not occur along the entire chord depending on the section

[4] $[\omega(s)]$ must not be confused with $\vec{\omega}(s)$, $[\omega(s)]$ is the rotation rate tensor

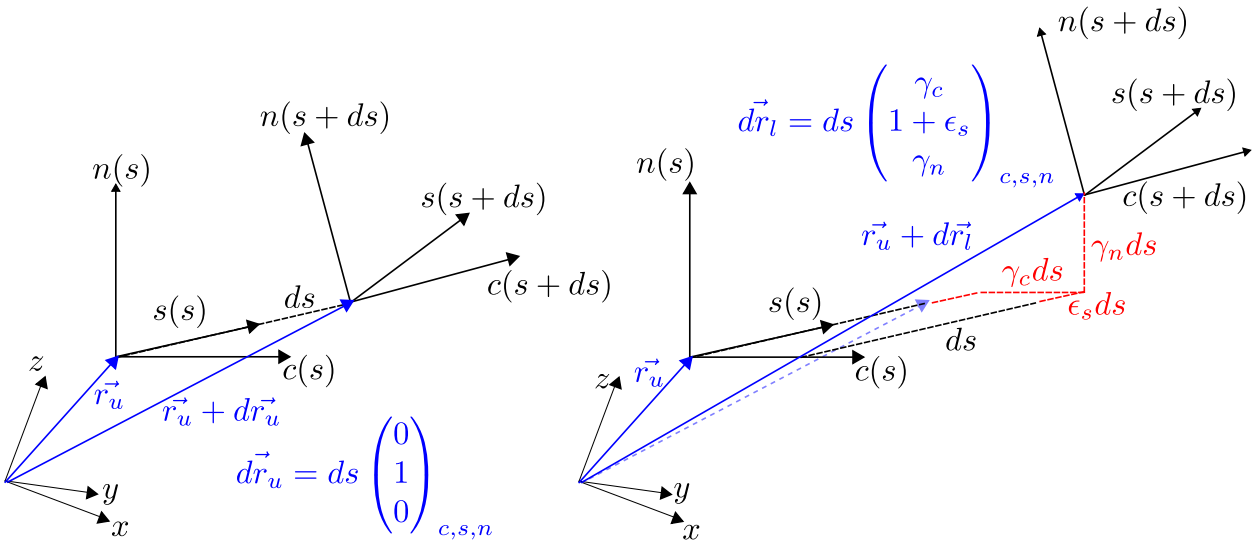

(a) unloaded beam, csn frame origin displacement (b) loaded

Figure 5.5: extensional and shear strains illustration

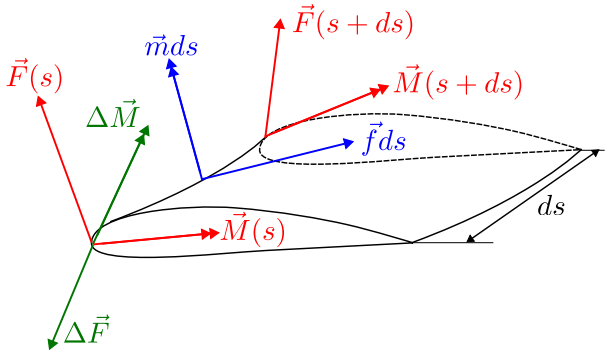

Figure 5.6: Forces and moments equilibrium on a beam element

layer considered, as shown on the right side of the figure. This non-uniformity leads to the lumping of the extensional stress around the tension axis of the coordinate (c_{TA}, n_{TA}). The latter is not necessarily at the centre of the chord and half the thickness as in classical Euler-Bernoulli theory. Overall, the internal stress due to an extensional strain is given by integrating the elementary stress over the section

$$F_{s,\epsilon_s} = \epsilon_s \iint E(c,n)\vec{s}dcdn = EA\epsilon_s \tag{5.24}$$

EA must not be confused with the Young modulus E multiplied by the cross-section area. Another proposition of this model is to add structural damping and assume the extensional stress varies proportionally with the strain rate as follows

$$F_{s,\epsilon_s} = \epsilon_s \iint E(c,n)\vec{s}dcdn = EA(\epsilon_s + t_\epsilon \dot{\epsilon}_s) \tag{5.25}$$

where t_ϵ is the extensional damping time. The added term (in blue) is known as the Kelvin-Voigt damping factor (Banks and Wang 1987,1991). Also EA must not be confused with the Young modulus E multiplied by the cross-section area A. As highlighted above, another proposition of this model is to add structural damping and assume the extensional stress varies proportionally with the strain rate. For the sake of clarity, the latter expression will be considered in its steady state form for the next development. The unsteady terms will be reintroduced in the final strain/curvature force/moment relations. From the above equation, the position of the tension axis (tension barycentre) can be derived as follows

$$\begin{aligned} c_{TA} &= \frac{\iint cE(c,n)\vec{s}dcdn}{\iint E(c,n)\vec{s}dcdn} = \frac{\iint cE(c,n)\vec{s}dcdn}{EA} \\ n_{TA} &= \frac{\iint nE(c,n)\vec{s}dcdn}{EA} \end{aligned} \tag{5.26}$$

From equations 5.25 and 5.26, the moments due to F_{s,ϵ_s} at the c, s, n origin can is given as:

$$\begin{aligned} \begin{pmatrix} M_{c,\epsilon_s} \\ 0 \\ M_{n,\epsilon_s} \end{pmatrix} &= \begin{pmatrix} M_{c',\epsilon_s} \\ 0 \\ M_{n',\epsilon_s} \end{pmatrix} + \begin{pmatrix} c_{TA} \\ 0 \\ n_T A \end{pmatrix} \times \begin{pmatrix} 0 \\ F_{s,\epsilon_s} \\ 0 \end{pmatrix} \\ \begin{pmatrix} M_{c,\epsilon_s} \\ 0 \\ M_{n,\epsilon_s} \end{pmatrix} &= \begin{bmatrix} 0 & -n_{TA} & 0 \\ 0 & 0 & 0 \\ 0 & c_{TA} & 0 \end{bmatrix} \begin{pmatrix} \gamma_c \\ \epsilon_s \\ \gamma_n \end{pmatrix} \end{aligned} \tag{5.27}$$

where c' and n' are vectors associated with the stress axis as shown in the figure 5.8.

Forces and moments due to c and n shear strains:

The same analysis as above is not possible for c and

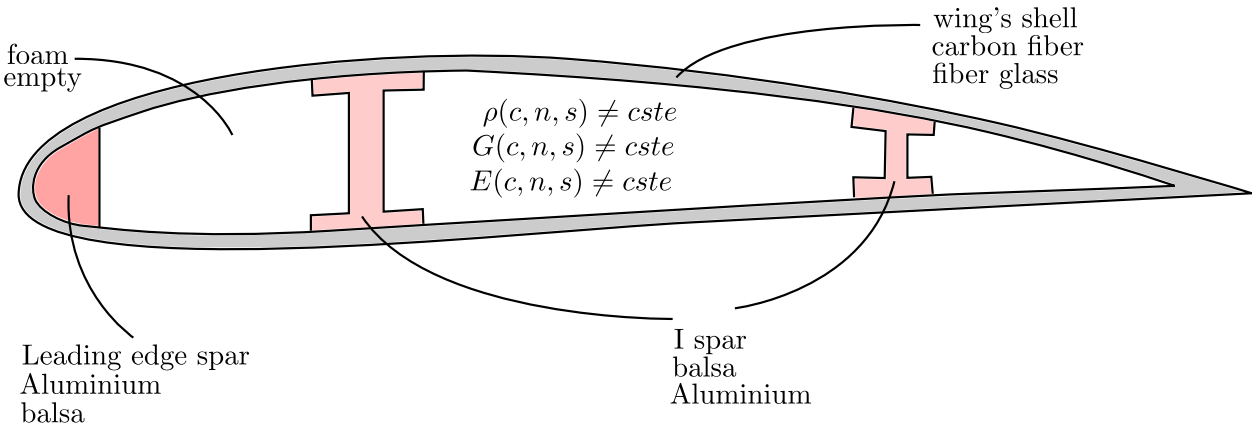

(a) - Non-uniformity of the section material properties

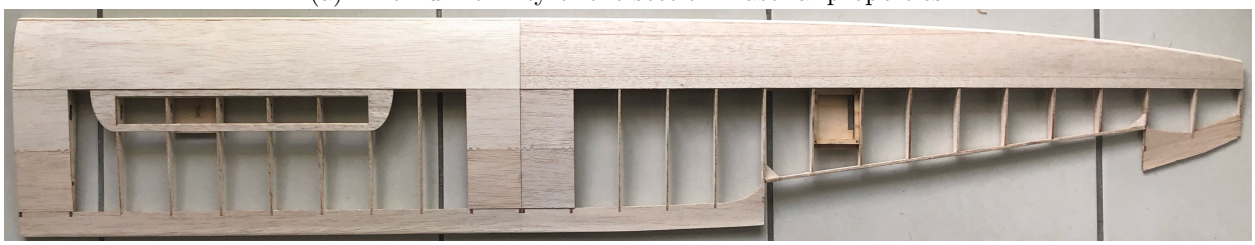

(b) - RC glidder balsa wing example

Figure 5.7: Non-uniformity of the section material properties

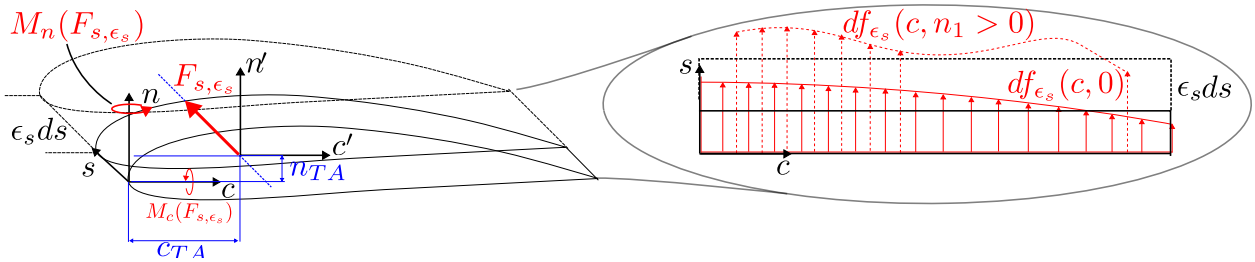

Figure 5.8: Non uniform extensional load distribution, lumping on the tension axis

n shear stresses. The shear stiffness of the section is still considered non-uniform and so are the induced shear stresses. The c-shear stresses can be grouped on a horizontal elastic line with an offset from the c-axis marked n_{EA} as shown in figure 5.9. In the same way the n-shear stresses are lumped on a vertical elastic line having an offset with the n-axis noted as c_{EA}. The intersection of the elastic lines defines the elastic axis of the section. The c and n-shear stresses are given as below

$$\begin{pmatrix} F_{c,\gamma} \\ F_{s,\gamma} \\ F_{n,\gamma} \end{pmatrix} = \begin{bmatrix} GK_c & 0 & 0 \\ 0 & 0 & 0 \\ 0 & 0 & GK_n \end{bmatrix} \begin{pmatrix} \gamma_c \\ 0 \\ \gamma_n \end{pmatrix} \tag{5.28}$$

where GK_c and GK_n are the c and n shear stiffnesses respectively. Note that neither the shear stiffness nor the elastic axis coordinate (c_{EA},n_{EA}) integral expressions (such as Eq 5.25 and 5.26) exist. They can be obtained using shear flow analysis codes such as Co-Blade. As for the extensional stress, the shear stress is also assumed to vary proportionally to the shear strain rate. The unsteady terms will be recalled later and are avoided for now. Note that the zero off-diagonal terms in the equations 5.29 emphasise the hypothesis that there are no cross-coupling terms between stresses and strains. In practice, this is not a conservative assumption, as bending stiffnesses are mostly dominant in wings. Nevertheless, the moments at the *csn* frame origin due to c and n strains are given by :

$$\begin{pmatrix} F_{c,\gamma} \\ F_{s,\gamma} \\ F_{n,\gamma} \end{pmatrix} = \begin{bmatrix} GK_c & 0 & 0 \\ 0 & 0 & 0 \\ 0 & 0 & GK_n \end{bmatrix} \begin{pmatrix} \gamma_c + t_\gamma \dot{\gamma_c} \\ 0 \\ \gamma_n + t_\gamma \dot{\gamma_n} \end{pmatrix} \tag{5.29}$$

The unsteady terms will be recalled later and are avoided for now. Note that the zero off-diagonal terms in the equations 5.28 emphasise the hypothesis that there are no cross-coupling terms between stresses and strains. In practice, this is not a conservative assumption, as bending stiffnesses are mostly dominant in wings. Nevertheless, the moments at the *csn* frame origin due to c and n strains are given by :

$$\begin{pmatrix} M_{c,\gamma} \\ M_{s,\gamma} \\ M_{n,\gamma} \end{pmatrix} = \begin{pmatrix} 0 \\ M_{s',\gamma} \\ 0 \end{pmatrix} + \begin{pmatrix} c_{EA} \\ 0 \\ n_E A \end{pmatrix} \times \begin{pmatrix} F_{c,\gamma} \\ 0 \\ F_{n,\gamma} \end{pmatrix}$$
$$\begin{pmatrix} 0 \\ M_{s,\gamma} \\ 0 \end{pmatrix} = \begin{bmatrix} 0 & 0 & 0 \\ n_{EA} & 0 & -c_{EA} \\ 0 & 0 & 0 \end{bmatrix} \begin{pmatrix} \gamma_c \\ \epsilon_s \\ \gamma_n \end{pmatrix} \tag{5.30}$$

The forces and moments due to shear and extensional strains remain those due to bending and torsional curvatures.

Forces and moments due to c and n curvatures: Before deriving the force and moment expressions, another proposed feature must be highlighted. The ASWING structural model can consider a non-flat/straight beam. Geometrically, this means that the unloaded beam can have a non-zero curvature. Figure 5.10 (a) and (b) shows the previous idea and compares it with the classical non-linear Euler-Bernoulli theory. It is said that when a beam is bent or twisted it experiences a change in its curvature. This causes a change in the length of the fibre. For example, in figure 5.10 (b), the inner side of the elements sees its fibres "contracted" and the outer side "extended". These notions of extension/contraction are relative to the way the user has defined the elementary unloaded length ds. This can be seen in the figure 5.10 (a) where the element ds has been defined at the leading edge of the wing, whereas in classical theory it was defined at the mid-chord. This has no effect on the loads and moments. The position of the local frame can be arbitrary as long as it is in the cross section. As mentioned above, a change in curvature induces a local change in fibre length, i.e. strain. The latter is therefore not uniform across the section. The induced strain is calculated relative to the element length ds. In the ASWING structural model it is calculated relative to the unloaded curvature. Only the case for the n-curvature is derived, as the other one follows the same principle. The local strain induced by the n-curvature is given by

$$\begin{aligned} \epsilon_{s,\kappa_n}(c) &= \frac{\left(\frac{1}{\kappa_n} d\theta + c\right) - \left(\frac{1}{\kappa_{n,0}} d\theta_0 + c\right)}{\frac{1}{\kappa_{n,0}} d\theta_0} \\ &= c(\kappa_n - \kappa_{n,0}) \end{aligned} \tag{5.31}$$

with $\left(\frac{1}{\kappa_n} d\theta + c\right)$ and $\left(\frac{1}{\kappa_{n,0}} d\theta_0 + c\right)$ denotes the loaded and unloaded arc length at the chordwise location c (cf figure 5.10-a). In the same way the extensional strain due to the c-curvature is given by

$$\epsilon_{s,\kappa_c} = -n(\kappa_c - \kappa_{c,0}) \tag{5.32}$$

where the minus sign is related to the axis definition. From the induced strain the local extension stress is given as:

$$df_{s,\kappa} = E(c,s)\left(c(\kappa_n - \kappa_{n,0}) - n(\kappa_c - \kappa_{c,0})\right) dcdn$$

The above expression highlights a peculiarity of a non-uniform beam. As the Young's modulus varies across the section, this will result in a asymmetric load distribution about the mid chord, as it should be in classical Euler-Bernoulli theory. This is highlighted in figure 5.11-(b). Because of the asymmetry property, the extensional loads cancel each other out but produce a bending moment. If the Young's modulus is not uniform, a non-zero extension load is possible (see figure 5.11-a). This is emphasised by the following integration of the elementary extension loads over the

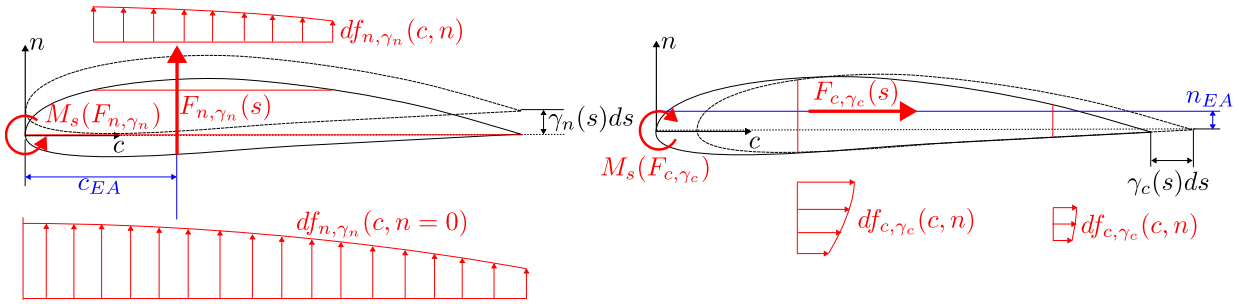

Figure 5.9: Non uniform c ans n shear loads due to c and n strains. Lumping on the c-shear and s-shear elastic lines

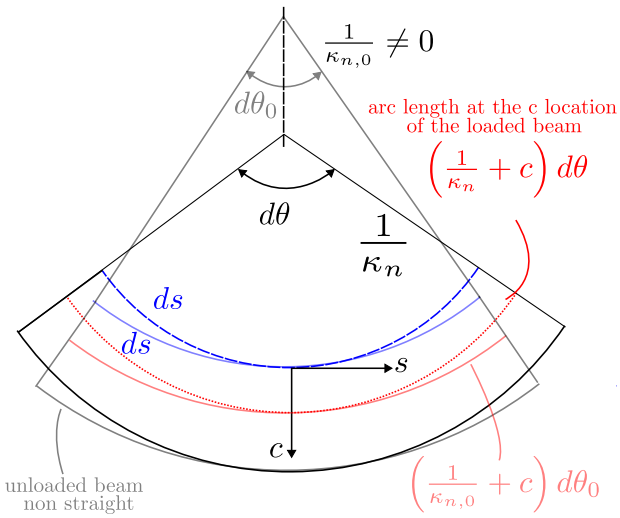

(a) ASWING : the unloaded beam can have a non-zero curvature

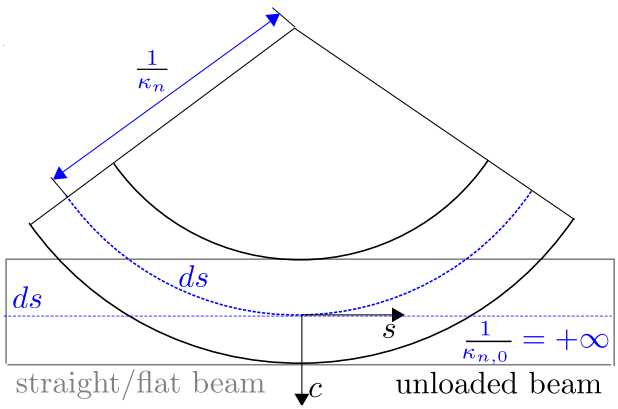

(b) Non-linear Euler Bernoulli beam theory : flat and straight beam

Figure 5.10: ASWING vs classical Euler-Bernoulli beam theory: zero curvature

section

$$F_{s,\kappa} = \iint E(c,s)\,(c(\kappa_n - \kappa_{n,0}) - n(\kappa_c - \kappa_{c,0})\,)\,dcdn$$

The curvature being uniform across the section the above equation is rewritten

$$F_{s,\kappa} = (\kappa_n - \kappa_{n,0}) \iint cE(c,s)dcdn - (\kappa_c - \kappa_{c,0}) \iint nE(c,s)dcdn$$

The first and second terms can be rewritten identifying the tension axis chordwise and normal coordinate.

$$\begin{aligned} F_{s,\kappa} &= (\kappa_n - \kappa_{n,0})c_{TA}EA - n_{TA}(\kappa_c - \kappa_{c,0})EA \\ \begin{pmatrix} 0 \\ F_{s,\kappa} \\ 0 \end{pmatrix} &= \begin{bmatrix} 0 & 0 & 0 \\ -n_{TA}EA & 0 & c_{TA}EA \\ 0 & 0 & 0 \end{bmatrix} \begin{pmatrix} \kappa_c - \kappa_{c,0} + t_\epsilon \dot{\kappa}_c \\ 0 \\ \kappa_n - \kappa_{n,0} + t_\epsilon \dot{\kappa}_n \end{pmatrix} \end{aligned} \tag{5.33}$$

In the same way the torsion (s-curvature) change induces a non-uniform c and n shear stress load distribution, when integrated across the section the loads induced are given as

$$\begin{pmatrix} F_{c,\kappa_s} \\ 0 \\ F_{n,\kappa_s} \end{pmatrix} = \begin{bmatrix} 0 & GK_c n_{EA} & 0 \\ 0 & 0 & 0 \\ 0 & -GK_n c_{EA} & 0 \end{bmatrix} \begin{pmatrix} 0 \\ \kappa_s - \kappa_{s,0} + t_\gamma \dot{\kappa}_s \\ 0 \end{pmatrix} \tag{5.34}$$

As for the strain loads, the unsteady structural damping terms have been added to the above equations. From equations 5.25, 5.29, 5.33 and 5.34 the final form of the load strain/curvature relation is given

$$\begin{aligned} \begin{pmatrix} F_c \\ F_s \\ F_n \end{pmatrix} &= \begin{bmatrix} GK_c & 0 & 0 \\ 0 & EA & 0 \\ 0 & 0 & GK_n \end{bmatrix} \begin{bmatrix} 0 & GK_c n_{EA} & 0 \\ -EAn_{EA} & 0 & EAc_{EA} \\ 0 & -GK_c c_{EA} & 0 \end{bmatrix} \begin{pmatrix} \gamma_c + t_\gamma \dot{\gamma}_c \\ \epsilon_s + t_\epsilon \dot{\epsilon}_s \\ \gamma_n + t_\gamma \dot{\gamma}_n \\ \kappa_c - \kappa_{c,0} + t_\epsilon \dot{\kappa}_c \\ \kappa_s - \kappa_{s,0} + t_\gamma \dot{\kappa}_s \\ \kappa_n - \kappa_{n,0} + t_\epsilon \dot{\kappa}_n \end{pmatrix} \\ &= [\mathcal{E}_{F,\gamma}\ \mathcal{E}_{F,\kappa}] \begin{pmatrix} \gamma_c + t_\gamma \dot{\gamma}_c \\ \epsilon_s + t_\epsilon \dot{\epsilon}_s \\ \gamma_n + t_\gamma \dot{\gamma}_n \\ \kappa_c - \kappa_{c,0} + t_\epsilon \dot{\kappa}_c \\ \kappa_s - \kappa_{s,0} + t_\gamma \dot{\kappa}_s \\ \kappa_n - \kappa_{n,0} + t_\epsilon \dot{\kappa}_n \end{pmatrix} \end{aligned} \tag{5.35}$$

where $[\mathcal{E}_{F,\gamma}]$ and $[\mathcal{E}_{F,\kappa}]$ are the load/strain and load-/curvature stiffness matrices respectively which parameters can identified from the previous developement. The moments induced by a change in curvature must be derived. It is interesting to note that the load induced by the c and n shear strains does not induce a moment about s' because of the uniformity of the strains. The same observation is made for the load induced by the extensional strain, but for the c' and n' axes. The moments about these axes are then derived. A change in the s-curvature induces unevenly distributed c and n loads, the moments due to the latter are then given along each axis as follows

$$\begin{pmatrix} M_{c',\kappa_s} \\ M_{s',\kappa_s} \\ M_{n',\kappa_s} \end{pmatrix} = \begin{bmatrix} 0 & E_{cs} & 0 \\ E_{cs} & GJ & E_{sn} \\ 0 & E_{sn} & 0 \end{bmatrix} \begin{pmatrix} 0 \\ \kappa_s - \kappa_{s,0} + t_\gamma \dot{\kappa}_s \\ 0 \end{pmatrix} \tag{5.36}$$

where GJ is the torsional stiffness, E_{sn} and E_{cs} are the torsional bending coupling terms. Shear flow codes must be used to obtain their values[5]. In the case of aircraft, GJ and E_{cs} are of most interest. For the bending stiffness, real values can be derived. First of all, as the moments are calculated along c', s', a small change of variable is required. The elementary loads due to a change in curvature c and n are given by

$$df_{s,\kappa} = E(c,s)\,((c - c_{TA})(\kappa_n - \kappa_{n,0}) - (n - n_{TA})(\kappa_c - \kappa_{c,0}))\,dcdn$$

[5] For shell wings, torsional stiffness formulae exist and are recalled in Drela (2008)
$GJ = 4GA_{sh}^2 t_{sh}/S_{sh}$ with A_{sh}, S_{sh} and t_{sh} being the enclosed area, perimeter and wall thickness of the shell respectively

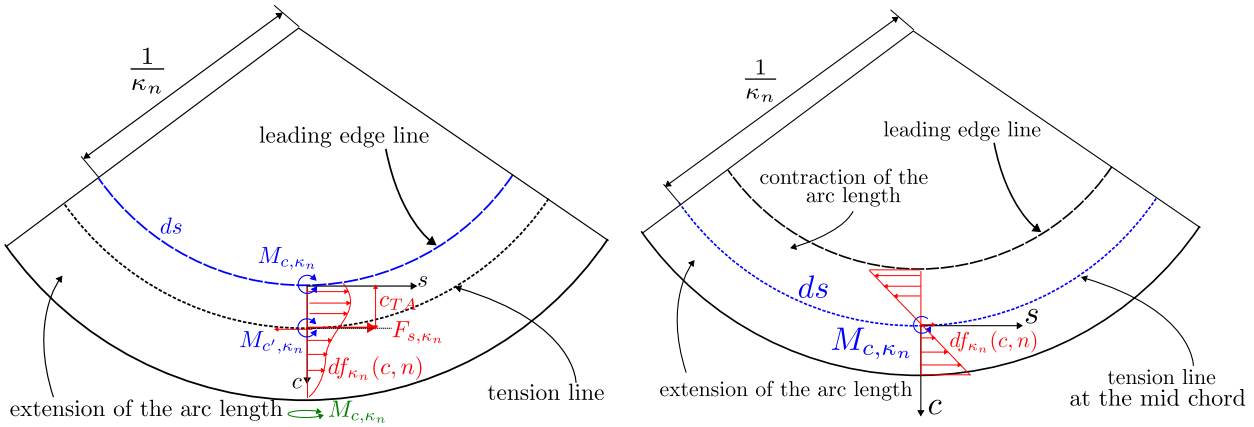

(a) ASWING (b) Non-linear Euler Bernoulli beam theory

Figure 5.11: ASWING vs classical Euler Bernoulli beam theory: loads distribution

where $(c-c_{TA})$ and $(n-n_{TA})$ are the distances relative to the tension axis. Note that the above equation implies that the element length ds must be defined along the tension axis to be consistent with previous developments. The elementary moments induced at c' and s' are then given as

$$\begin{aligned} dm_{s,\kappa} &= E(c,n)\begin{pmatrix} c-c_{TA} \\ 0 \\ n-n_{TA} \end{pmatrix} \times \begin{pmatrix} 0 \\ df_{s,\kappa} \\ 0 \end{pmatrix} dcdn \\ &= E(c,n)\begin{pmatrix} (n-n_{TA})^2(\kappa_c-\kappa_{c,0}) \\ 0 \\ (n-n_{TA})(c-c_{TA})(\kappa_c-\kappa_{c,0}) \\ +(n-n_{TA})(c-c_{TA})(\kappa_n-\kappa_{n,0}) \\ 0 \\ +(c-c_{TA})^2(\kappa_n-\kappa_{n,0}) \end{pmatrix} dcdn \end{aligned}$$

When integrated over the section comes the following matrix form

$$\begin{pmatrix} M_{c',\kappa_s} \\ M_{s',\kappa_s} \\ M_{n',\kappa_s} \end{pmatrix} = \begin{bmatrix} EI_{cc} & 0 & EI_{cn} \\ 0 & 0 & 0 \\ EI_{nc} & 0 & EI_{nn} \end{bmatrix} \begin{pmatrix} \kappa_c-\kappa_{c,0}+t_\epsilon\dot{\kappa}_c \\ 0 \\ \kappa_n-\kappa_{n,0}+t_\epsilon\dot{\kappa}_n \end{pmatrix}$$

with

$$\begin{aligned} EI_{cc} &= \iint E(c,s)(n-n_{TA})^2 dcdn \\ EI_{nn} &= \iint E(c,s)(c-c_{TA})^2 dcdn \\ EI_{cn} &= EI_{nc} \\ &= \iint E(c,s)(c-c_{TA})(n-n_{TA}) dcdn \end{aligned} \tag{5.37}$$

Combine to moment induced by the s curvature comes the final moment-curvature relation

$$\begin{aligned} \begin{pmatrix} M_{c'} \\ M_{s'} \\ M_{n'} \end{pmatrix} &= \begin{bmatrix} EI_{cc} & EI_{cs} & EI_{cn} \\ EI_{sc} & GJ & EI_{sn} \\ EI_{nc} & EI_{ns} & EI_{nn} \end{bmatrix} \begin{pmatrix} \kappa_c-\kappa_{c,0}+t_\epsilon\dot{\kappa}_c \\ \kappa_s-\kappa_{s,0}+t_\gamma\dot{\kappa}_s \\ \kappa_n-\kappa_{n,0}+t_\epsilon\dot{\kappa}_n \end{pmatrix} \\ &= [E(s)] \begin{pmatrix} \kappa_c-\kappa_{c,0}+t_\epsilon\dot{\kappa}_c \\ \kappa_s-\kappa_{s,0}+t_\gamma\dot{\kappa}_s \\ \kappa_n-\kappa_{n,0}+t_\epsilon\dot{\kappa}_n \end{pmatrix} \end{aligned} \tag{5.38}$$

The equation 5.38 is not consistent with the moment equilibrium equation 5.23 as the moments must be computed along the c,s,n axis. However, the latter has a very interesting feature in the sense that it can be inverted as

$$\begin{pmatrix} \kappa_c-\kappa_{c,0}+t_\epsilon\dot{\kappa}_c \\ \kappa_s-\kappa_{s,0}+t_\gamma\dot{\kappa}_s \\ \kappa_n-\kappa_{n,0}+t_\epsilon\dot{\kappa}_n \end{pmatrix} = [E]^{-1} \begin{pmatrix} M_{c'} \\ M_{s'} \\ M_{n'} \end{pmatrix} \tag{5.39}$$

From the previous equation can be derived the strain/-moment relation

$$\begin{aligned} \begin{pmatrix} \gamma_c+t_\gamma\dot{\gamma}_c \\ \epsilon_s+t_\epsilon\dot{\epsilon}_s \\ \gamma_n+t_\gamma\dot{\gamma}_n \end{pmatrix} &= [\mathcal{E}_{F,\gamma}]^{-1} \begin{pmatrix} F_c \\ F_s \\ F_n \end{pmatrix} \\ &\quad - [\mathcal{E}_{F,\kappa}][E]^{-1} \begin{pmatrix} M_{c'} \\ M_{s'} \\ M_{n'} \end{pmatrix} \end{aligned} \tag{5.40}$$

The equations 5.39 and 5.40 are of particular interest as they allow the restriction of some of the beam degrees of freedom. Analytically it is equivalent to imposing coefficients of the stiffness matrices $[E]$ and $[\mathcal{E}_{F,\gamma}]$ to ∞. However, this is not numerically possible if the equations 5.35 and 5.38 are implemented in this way. The inverse relationship is preferred because the coefficients of $[E]^{-1}$ and $[\mathcal{E}_{F,\gamma}]^{-1}$ can be set

to zero to restrict the beam degrees of freedom. If some of the stiffness coefficients are unknown, they are automatically set to ∞. This allows the user to completely ignore the structural dynamics if required. As a result, ASWING can also be used as a pure rigid aerodynamic pre-design tool if required.

5.2.6 Distributed/ponctual inertial and gravity loads

So far, the beam has been considered to be mass and inertial free. However, each beam element in motion generates inertial loads and moments and is subject to gravity. A feature proposed by the ASWING structural model is to arbitrarily set the location of the sectional centre of gravity. In fact, the materials used to construct the wing may have different volumetric masses for isoelastic properties (E,G) or vice versa. Consequently, the elastic, tensile and centre of gravity axes are not necessarily in the same place. Nevertheless, let us consider a concentrated mass/length that is lumped at the centre of mass location and rigidly attached to the local frame. The position relative to the *csn* frame (shown in figure 5.12) is given by

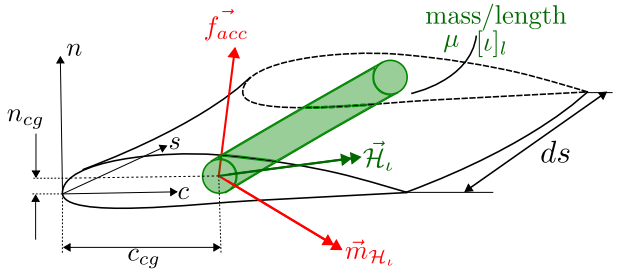

Figure 5.12: Distributed inertial and gravity loads, vector directions are arbitrary

$$\Delta\vec{r}_{cg} = \begin{pmatrix} c_{cg} \\ 0 \\ n_{cg} \end{pmatrix}_l$$

The inertial loads of the lumped mass are given by its acceleration relative to the inertial (earth) frame. Summed to the gravity effect comes the inertial and gravity loads of the mass/length

$$\vec{f}_{\text{acc}} = \mu\left(\vec{g} - \vec{a}_{cg}\right) \tag{5.41}$$

with

$$\begin{aligned} \mu &= \iint \rho(c,s)dcdn, \\ c_{cg} &= \frac{\iint \rho(c,s)cdcdn}{\mu}, \\ n_{cg} &= \frac{\iint \rho(c,s)ndcdn}{\mu} \end{aligned}$$

where $\mu(s)$ is the local mass/length. The latter can vary along the span. $\vec{a}_{cg}$ is computed using equation 5.9 with $\Delta\vec{r_p} = \Delta\vec{r_{cg}}$. The lumped mass is "concentrated" ie not punctual, in consequence, a local inertia/length tensor is introduced and denoted as $[\iota(s)]_l$. The mass/length can vary along the reference line and is expressed in the local frame as follow

$$[\iota]_l = \begin{bmatrix} \iota_{cc} & 0 & 0 \\ 0 & \iota_{ss} & 0 \\ 0 & 0 & \iota_{nn} \end{bmatrix}_l + \frac{ds^2}{12}\begin{bmatrix} \mu & 0 & 0 \\ 0 & 0 & 0 \\ 0 & 0 & \mu \end{bmatrix}_l$$

with

$$\begin{aligned} \iota_{cc} &= \iint \rho(c,s)(n-n_{cg})^2 dcdn, \\ \iota_{nn} &= \iint \rho(c,s)(c-c_{cg})^2 dcdn, \\ \iota_{ss} &= \iota_{cc} + \iota_{nn} \end{aligned}$$

This concentrated mass, being rigidly attached to the body frame, its rotation rate relative to the inertial frame is given by summing the relative rotation rate of the body and local frame $\vec{\Omega}$ and $\vec{\omega}$. The mass has in consequence an angular momentum because of its non-zero inertia tensor

$$\vec{\mathcal{H}}_{\iota,b} = [T]^T[\iota]_l[T]\left(\vec{\Omega} + \vec{\omega}\right)_b$$

The transformation matrix $[T]$ and its inverse are used to express the rotation rate in the local frame as the inertia/length tensor. The inverse transformation $[T]^T$ is used to provide the angular momentum/length in the body frame. The torque induced by the angular momentum is given by its derivation with respect to time

$$\begin{aligned} \vec{m}_{\mathcal{H}_\iota} =& -\frac{d\left([T]^T[\iota][T]\right)}{dt}\left(\vec{\Omega} + \vec{\omega}\right)_b \\ & - [T]^T[\iota]_l[T]\frac{d\left(\vec{\Omega} + \vec{\omega}\right)_b}{dt} \\ =& -\frac{d\vec{\mathcal{H}}_{\iota,b}}{dt} = -[T]^T[\iota][T]\left(\vec{\alpha}_o + \vec{\dot{\omega}}\right) \\ & - \left(\vec{\Omega} + \vec{\omega}\right) \times \left\{[T]^T[\iota][T]\left(\vec{\Omega} + \vec{\omega}\right)\right\} \end{aligned}$$

The distributed inertia and gravity moments about the *csn* origin are given by summing the angular momentum and the inertia/gravity loads moment as follows

$$\begin{aligned} \vec{m}_{\text{acc}} =& \Delta\vec{r}_{cg} \times \vec{f}_{\text{acc}} + \vec{m}_{\mathcal{H}_\iota} \\ \vec{m}_{\text{acc}} =& \Delta\vec{r}_{cg} \times \vec{f}_{\text{acc}} - [T]^T[\iota][T]\left(\vec{\alpha}_o + \vec{\dot{\omega}}\right) \\ & - \left(\vec{\Omega} + \vec{\omega}\right) \times \underbrace{\left\{[T]^T[\iota][T]\left(\vec{\Omega} + \vec{\omega}\right)\right\}}_{\mathcal{H}_{\iota,b}} \end{aligned} \tag{5.42}$$

Ponctual mass inertia and gravity loads

The second type of mass being considered in the model

are punctual masses. They are used to reproduce the effect of a nacelle, sensors, actuators etc. They can generate 3 types of loads, engine thrust and torque, drag, inertia and gravity loads. Only the third and last one will be derived. First of all the engine torque doesn't catch the inertia effect of a rotating shaft/propeller. The engine rotation rate vector is recalled and denoted $\vec{\Omega_{Ee}} = \Omega_E \vec{x_E}$. The shaft inertia is denoted as J_E. The angular momentum of the rotating shaft is given in the engine frame

$$\mathcal{H}_{p,e} = \Omega_E J_E \vec{x_E}$$

The latter is illustrated on the figure 5.13. Considering the rotation speed constant its torque is given by

$$\Delta\vec{M}_{E,e} = \frac{d\Omega e}{dt} J_E \vec{x_E} + \Omega_E J_E \frac{d\vec{x_e}}{dt} = \Omega_E J_E \frac{d\vec{x_e}}{dt}$$

Thus the torque induced by the angular momentum does not depend on the angular acceleration. The previous line illustrated the idea, and now a more general case will derive. From now one, $\mathcal{H}_{p,l}$ is denoting the point mass angular momentum expressed in the local frame as follows

$$\mathcal{H}_{p,b} = [T]^T [T_0] \begin{pmatrix} H_{x_p,0} \\ H_{y_p,0} \\ H_{z_p,0} \end{pmatrix}$$

where $[T_0]$ is the unloaded transformation matrix evaluated at the spanwise location where the point mass is attached. That being said, the torque induced by the angular momentum is given in the body frame.

$$\Delta\vec{M}_{\mathcal{H}_p} = -(\vec{\Omega} + \vec{\omega}) \times \vec{\mathcal{H}}_{p,b}$$

Now let us consider that the point mass is rigidly attached to the local frame having a relative position to it

$$\Delta\vec{r_{p,b}} = [T]^T \Delta\vec{r_{p_b}} = [T]^T [T_0] \left(x_0,\ y_0,\ z_0\right)^T$$

The inertia and gravity loads of the punctual mass are given

$$\Delta\vec{F}_b = m_p(\vec{g} - \vec{a_p}) \tag{5.43}$$

where m_p is the pontual mass, and a_p the acceleration relative to the inertial frame computed using equation 5.9. From the equation 5.43, the point mass moment about the csn origin and expressed in the body frame is given as follows

$$\Delta\vec{M}_{\mathrm{p,b}} = \Delta\vec{r}_{p,b} \times \Delta\vec{F}_{\mathrm{p}} - \left(\vec{\Omega} + \vec{\omega}\right) \times \vec{H}_{p,b} \tag{5.44}$$

5.2.7 Beams connections

Another interesting feature proposed by the ASWING structural model is the implementation of multiple beam objects. The beams are connected to each other using "restrictive" or "spring/compliant" joints. They are inherently massless and can be virtually connected to distant beams with a rigid pylon. Restrictive joints ensure that the compliant connection and orientation between the beams is maintained throughout the simulation. Each joint has 12 variables associated with it, i.e. position, orientation, forces and moments. Elastic hinges are used to allow a degree of freedom between the beams. Note that Willis et al. (2007) used an unpublished modification of the code to prescribe motion between beams. Their work showed that they could reproduce the behaviour of a flapping bird in ASWING. The figures 5.14 (a) and (b) show the geometry they used at 2 different snapshots. It can clearly be seen that the orientation of the hinge axis has been specified. This feature will be presented in the aeroelastic part of this evaluation. Figure 5.14 (c) shows the use of elastic struts on the MIT Daedalus human prototype (Drela 1990 and 1988). Finally, figure 5.14 (d) shows the most common beam connection with the MICADO prototype Krengel et al. (2019).

5.2.8 Discretization of the problem

The equations 5.7, 5.8, 5.22, 5.23, 5.39 and 5.40 form a set of 18 non-linear differential equations with 18 unknowns, namely ($\vec{r}$, $\vec{\theta}$, $\vec{u}$, $\vec{\omega}$, $\vec{F}$, $\vec{M}$). The latter are continuous functions in s, but no analytical solution to the above set of equations has yet been found in the literature. Therefore, the problem has to be discretised. For the sake of clarity, a single beam is considered. Also, the distributed and point loads/moments are considered as prescribed (i.e. not a function of the state vector). The beam is discretised into N_b nodes using a cosine clustering function. This refines the beam tip and root where high curvature/deflection is expected. However, it results in a finite element problem with $Nb \times 18$ unknowns and the same number of non-linear differential equations. Note that during the discretisation process all non-linear differential equations are pre-multiplied by the small element length ds. This effectively allows a zero length interval, as the latter is no longer the denominator of any $\frac{d}{ds}$ term, which would otherwise lead to numerical divergence. Thus the punctual forces/moments are captured as a pure discontinuity as shown in figure 5.15. Unlike the aerodynamic model, it is not necessary to impose $Nb \times 18$ constraints to have a well-posed system of equations. The boundary conditions are simple: two free forces/moments are imposed at the beam tip, plus

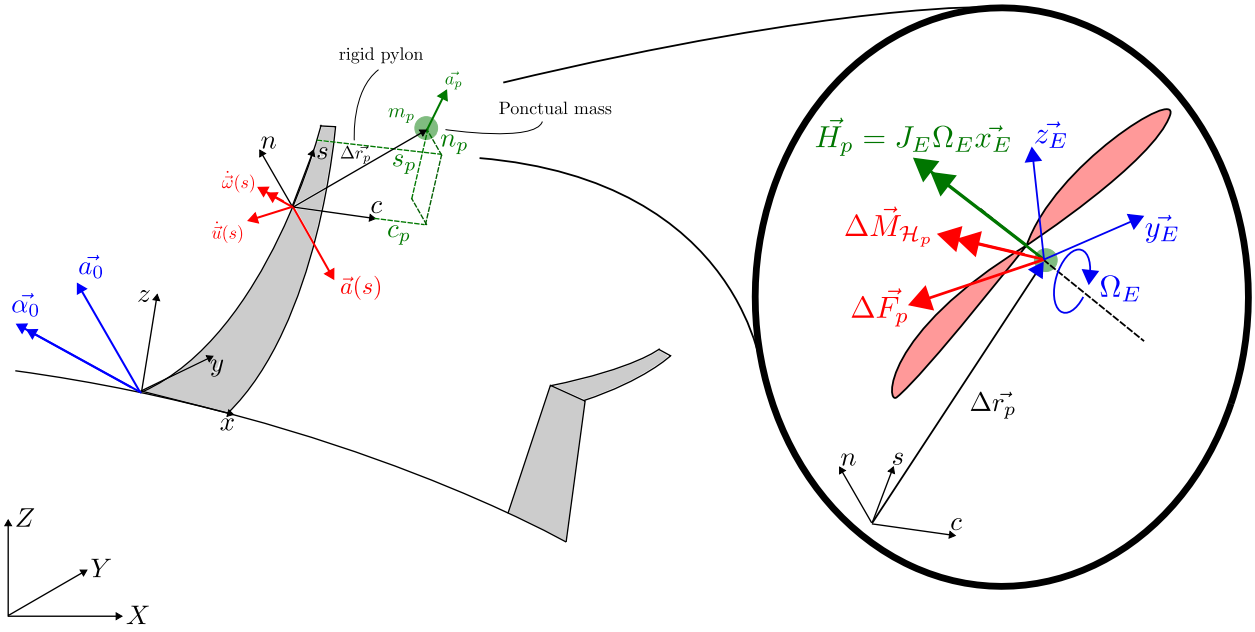

Figure 5.13: Ponctual mass rigidly connected to the local frame (left). Angular momentum of an engine (right), directions of the vectors are arbitrary

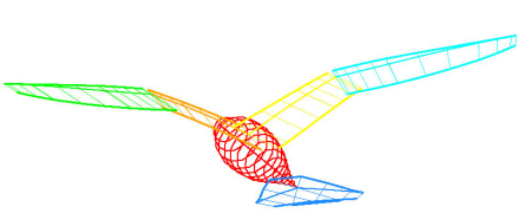

(a) Flapping bird, snapshot 1 Willis et al.

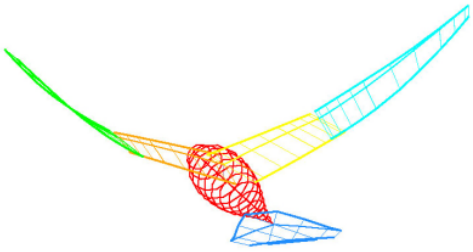

(b) Flapping bird, snapshot 2 Willis et al.

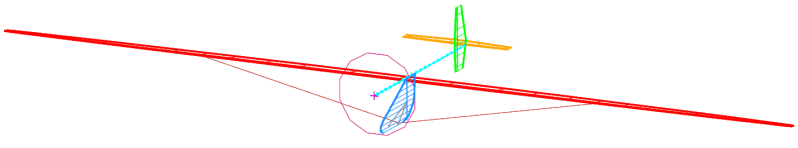

(c) MIT Daedalus (strusts connections) Drela

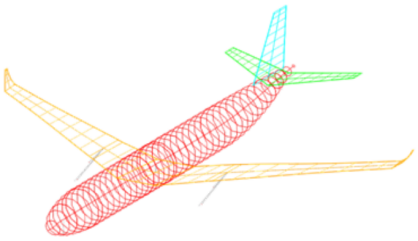

(d) MICADO design Krengel et al.

Figure 5.14: Examples of geometries implementable in ASWING

ground or joint constraints on position, local velocity, orientation and rate of rotation. The latter are illustrated in the figure 5.15.

5.2.9 Structural failure analysis

ASWING offers an embedded function for structural failure analysis. In fact, maximum strains and torsional shear stress distributions can be calculated and reported. The latter can be compared with the maximum strains of the wing material to conclude whether the structure would fail under the specified applied load. The maximum extensional shear stress is expressed in ASWING as

$$\epsilon_{s,max}(s) = |c_{sh}\kappa_n| + |n_{sh}\kappa_c| + |F_s/EA| \quad (5.45)$$

where c_{sh} and n_{sh} are the relative coordinates to the stress axis of any point on the wing surface. The above equation can be considered conservative by its positive definition. In fact, materials may have different maximum strains in compression and extension. Or parts of the wing are very likely to work in compression, such as the lee side of the wing. This small limitation can be overcome as $(M'_c,\ M'_s,\ M'_n)$ and (F_c, F_s, F_n) distributions are also provided by ASWING for post-treatment. Using the curvature load relations 5.39 and 5.40 the curvature can be used to recover the induced strains. This would provide information on which materials in the section are under compression or extension and whether it is close to failure. As the latter may have different maximum extension/-compression strains, the use of this technique would provide a better insight into which specific element of the section should be reinforced.

5.3 Numerical scheme convergence and time computation

Three different types of numerical analysis are possible in ASWING: modal/frequency, steady state and time marching. The latter do not use the same solver. Firstly, linear modal analysis involves an analysis of the linearised Jacobian matrix of the system. As its size can increase rapidly with mesh refinement, the eigenvalue problem cannot be solved by direct methods. Instead, an Arnoldi iteration method is used to compute the first modes of the system using the ARPACK library from Lehoucq et al. (1998). The steady and transient structural behaviour is computed using a Newton descent algorithm whose main computational complexity comes from the inversion of the steady/transient Jacobian matrix of the following nonlinear constrained system below

$$r(\dot{x}, x, u) = 0 \quad (5.46)$$

where r is the set of ordinary nonlinear differential equations of the system, x is the system discrete state vector, and u is the exogenous input vector. The latter inversion solver follows a specific pattern, so the complexity is not in n^3. Thus ASWING uses 2 solvers so, 2 mesh convergence comparisons have been performed. For the Newton descent algorithm, 3 steady deflections were chosen as the convergence criterion, while for the Arnoldi iteration, the first 4 beam modes were chosen. In both cases, the number of structural nodes was multiplied by 2 from one case to the other. For each case the computation time was reported. Figures 5.16(a)-(c) show the degree of convergence of each variable considered in each solver analysis. Figure (c) particularly highlights the difference in computational complexity of the different solvers. Overall, 40 nodes per beam provide acceptable results for a reasonable computational time.

5.4 Experimental Validation

This section aims to provide a partial validation of the features of the ASWING structural model. These include the nonlinear static deflections and the modal response predictions. Four sets of experiments were used. Minguet (1989, 1990a and 1990b) present high deflections and modal response of helicopter blades. The latter is considered as a baseline set as the aspect ratio of the sample is quite high (AR = 20). The evaluation is refined by slowly reducing the test cases aspect ratio. To this end, the Pazy Wing of Avin et al. (2022) is employed, with a wing aspect ratio of 5.5. A "boundary" case is then used to highlight the structural model limits in terms of aspect ratio. To do this, data from Dunn and Dugundji (1992 and 1992) are used, again evaluating static deflections and modal response predictions for a wing with aspect ratio 4. Finally, a final "boundary" case is used to study the effect of concentrated mass on the modal response of a straight wing (AR of 6). The latter case from Runyan and Sewall (1948) does not provide static deflection data.

5.4.1 CASE A : Static deflection and modal response of high aspect ratio helicopter blades

CASE A : experimental bench:
In this work, the static tip deflections of 4 different

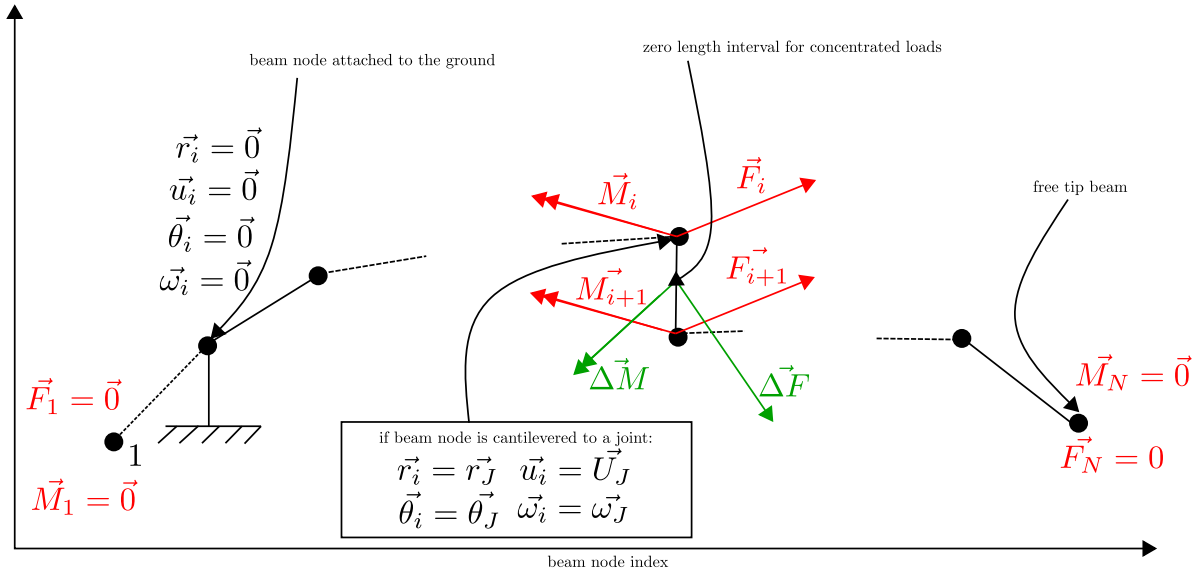

Figure 5.15: Concentrated load on zero length interval captured as perfect discontinuity. Beam constraints imposed at free tip joint and ground attachment

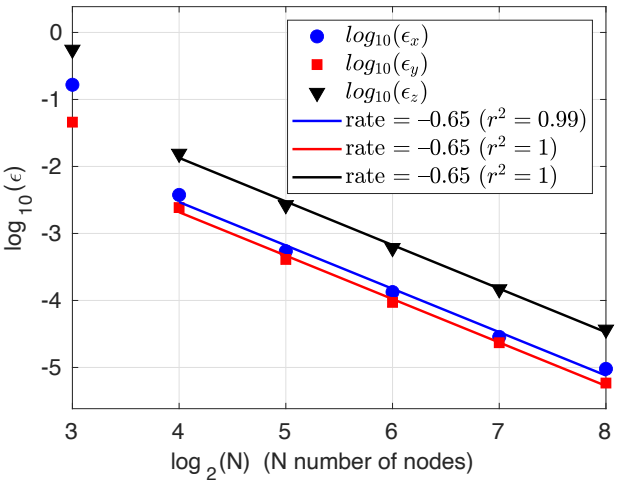

(a) Numerical scheme convergence rate for 3D deflection prediction

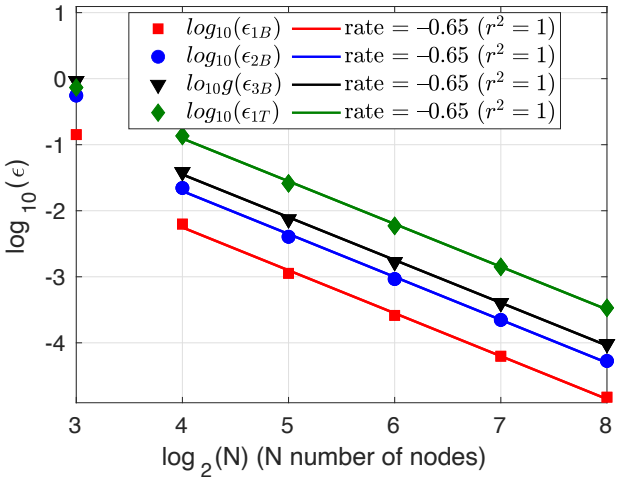

(b) Numerical scheme convergence rate for the prediction of the first 4 modes

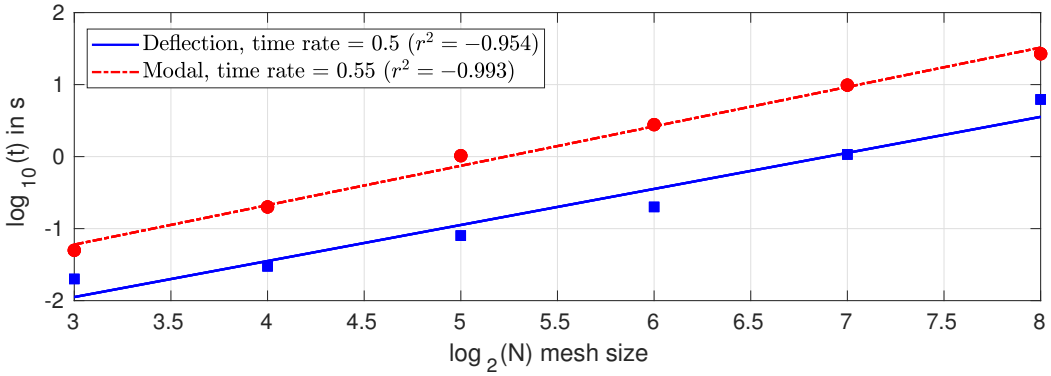

(c) Computational time versus mesh size, comparison between modal analysis and static deflection computation

Figure 5.16: Structural model numerical scheme performances

blades were investigated for various tip loads. Their modal response up to the 5th mode was also evaluated. An experimental bench was set up for this purpose (see figure 5.17). Each blade was rigidly cantilevered from an aluminium clamping device. The blade length and chord were 0.55m and 0.03 m respectively, for an aspect ratio of approximately 20. The stiffness and mass properties of each blade are given in tables 5.6, 5.7 and 5.8. For static deflection, the tests consisted of attaching a mass to the tip of the blade on the half chord axis. The mass varied from 0 to 0.5 kg, with increments of 0.1 kg for high deflections and 0.05 kg for low deflections. A millimetre ruler was used to measure the tip deflections. As the blades were initially horizontally cantilevered and quite flexible, they bent under their own weight.Minguet provided relative data (difference between loaded and unloaded beams). Finally, the clamping system could be rotated against the spanwise axis at 3 different angles, i.e. $\theta = (-45°, 0°, 45°)$, allowing the effect of stiffness coupling terms on the measurements to be captured. For the modal analysis, each blade was in the configuration $\theta = 0°$ and unloaded. An electromagnetic shaker was attached to the blade near the root (50mm from the root) but slightly off the half-chord axis to excite the torsional mode. A strain gauge was attached at the same location and connected to a digital oscilloscope. The shaker was controlled by a frequency generator, which was also the first input to the oscilloscope. By looping the strain gauge signal, they could see when the beam was in resonance (Lissajou figures). In total, up to 5 modes could be precisely identified.

CASE A : numerical analysis: The numerical analysis was split into two parts. Firstly, the tip deflections were studied by replicating the bench and applying tip loads through puntual masses derived from the theoretical section. Numerical sensors were located at the trailing and leading edge, in the same positions as the experiments. Subsequently, unloaded and loaded deflections were measured. A separate ASWING file was produced for each blade configuration, using the parameters retrieved from tables 5.6, 5.7, and 5.8. To ensure numerical convergence, 40 structural nodes were clustered according to a cosine function. The blade was geometrically twisted by θ to model the clamping system rotation. Note that during the crafting process, one of the blades became naturally twisted ($[45/0]_{3a}$). This was taken into account during the ASWING analysis. For the modal analysis, the point mass and root twist were eliminated, and the non-linear equations were solved using the OPER menu to produce a steady-state solution. Next, a modal analysis was conducted on the Jacobian matrix of the linearized system in the MODE menu. The first five modes were computed quickly thanks to the Arnoldi algorithm that is implemented natively. Again, based on mesh convergence analysis, 40 structural nodes were utilized to execute all modal analyses.

CASE A : Results: The analysis begins with comments on static deflection predictions. Four laminates were selected overall to evaluate a specific feature of the structural model.

The first laminate examined, $[0/90]_{3s}$, serves as a baseline case with only c and s bending stiffness coefficients (EI_{cc}, GJ). From the non-coupling property of its stiffness matrix, only one blade root inclination was necessary ($\theta = 45°$). The non-zero inclination was primarily used to measure x deflections (in the plane bending). Figures 5.18 (a) and (b) depict the (x, y, z) relative predictions against experimental data. In both cases, ASWING accurately captured the non-linear deflections for high tip loads. Furthermore, the x deflection was in excellent agreement with the experimental results when the wing was twisted.

The purpose of the second laminate ($[20/-70/-70/20]_{2a}$) is to investigate whether omitting certain stiffness matrix coefficients, as done in the theoretical development, could lead to problems. In such a scenario, the layout exhibits a coupling between an extension in the s direction and a chordwise torsion (E_{25}). Since no bending coupling terms are present, the situation is regarded as symmetrical and only two root twists were taken into consideration ($\theta = 0°$, $\theta = 45°$). The graphs in Figures 5.21 (a) and (b) illustrate the predicted relative deflections in the x, y, and z directions. Notably, the prediction for the z direction is highly accurate when compared to the experimental data. It is worth noting that despite the omission of the E_{25} coefficient in the numerical model, the prediction errors are similar to those of the initial layout.

The third laminate ($[45/0]_{3s}$) was selected to introduce the bending coupling term, specifically the chordwise and spanwise bending coupling terms. To clearly observe its impact, three angles of rotation at the roots were evaluated ($\theta = -45°$, $\theta = 0°$, $\theta = 45°$). The numerical predictions are shown in figure 5.20 (a) to (c). It is noteworthy that when the wing is flat, the x deflection is non-zero. If the non-zero root angle is taken into account, the latter change is not symmetrical because of bending torsion coupling. This characteristic is effectively modelled by ASWING. Although the y deflection is slightly weaker, it is still in good agreement. In terms of aerodynamics, spanwise deflection (y) has less of an impact than deflection in the z or x directions.

The fourth case ($[45/0]_{3a}$) shares similarities with the first, except for a twisted tip resulting from the

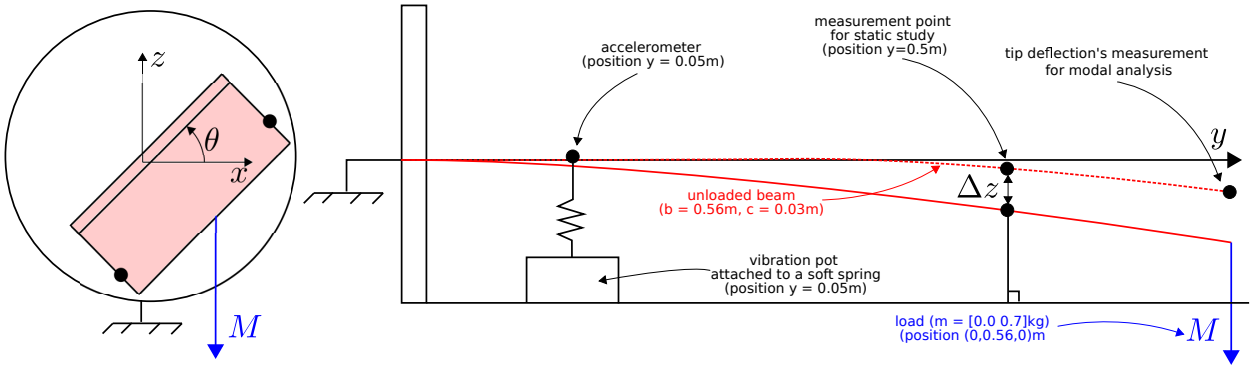

Figure 5.17: CASE A: experimental bench description

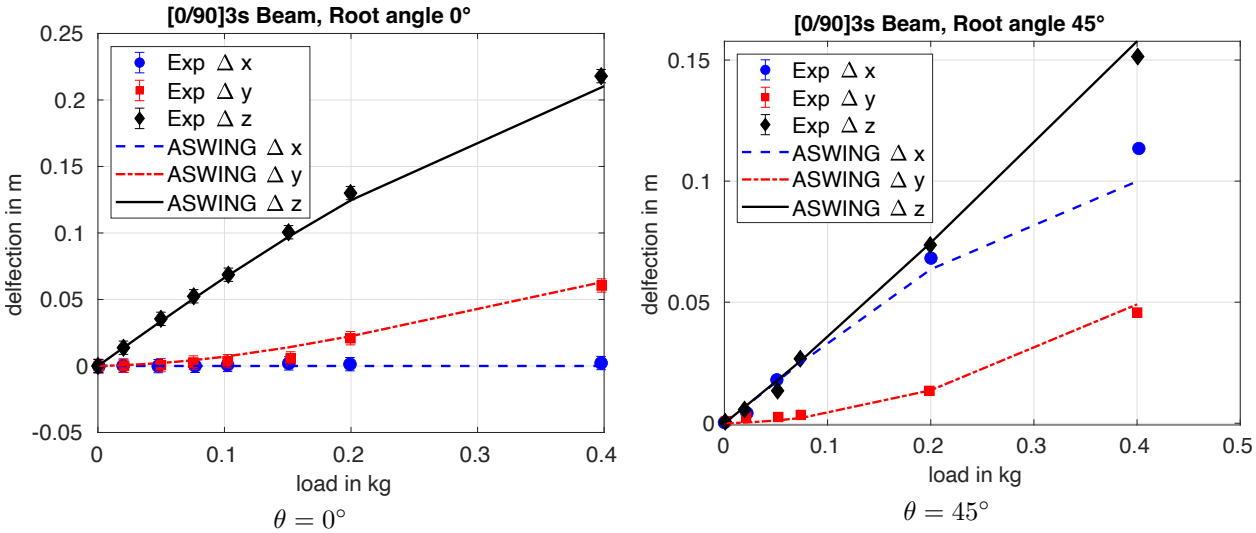

$\theta = 0°$ $\theta = 45°$

Figure 5.18: CASE A, layout : $[0/90]3s$ $(\Delta_x, \Delta_y, \Delta_z)$ predictions against experiments from Minguet 1989

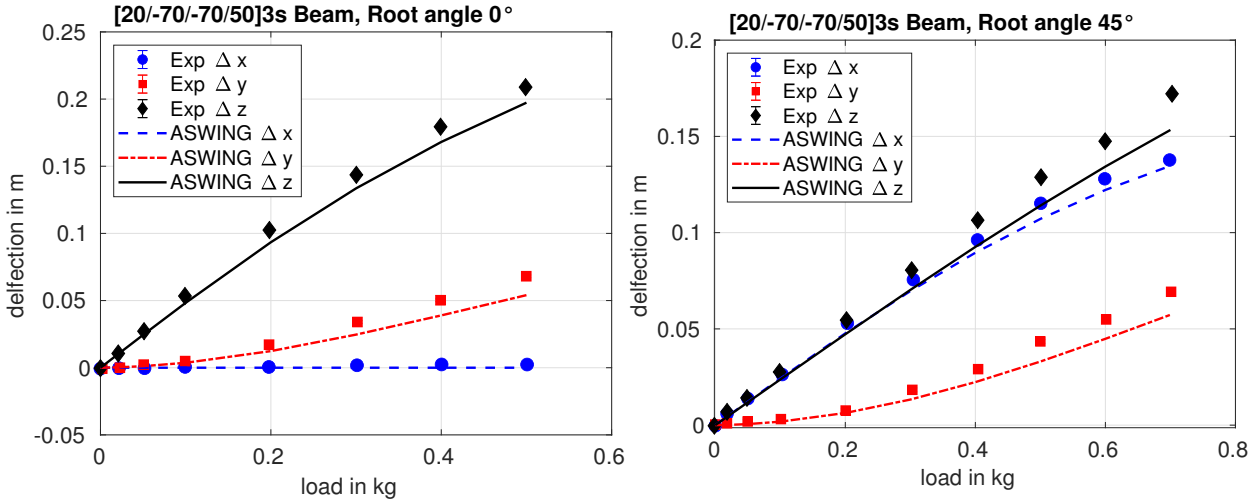

(a) $\theta = 0°$ (b) $\theta = 45°$

Figure 5.19: CASE A, layout : $[20/\text{-}70/\text{-}70/20]2a$, tip $(\Delta_x, \Delta_y, \Delta_z)$ predictions against experiments from Minguet 1989

crafting process. Figure 5.21 (a) and (b) illustrate the satisfactory agreements with experiments of every tip displacement component.

Modal analysis was conducted on three laminates that have been previously introduced, namely ($[0/90]_{3s}$, $[45/0]_{3s}$ and $[20/-70]_{2a}$). The fourth case was selected to highlight the potential issue arising with highly flexible blades. The ASWING predictions, along with their discrepancies against experimental

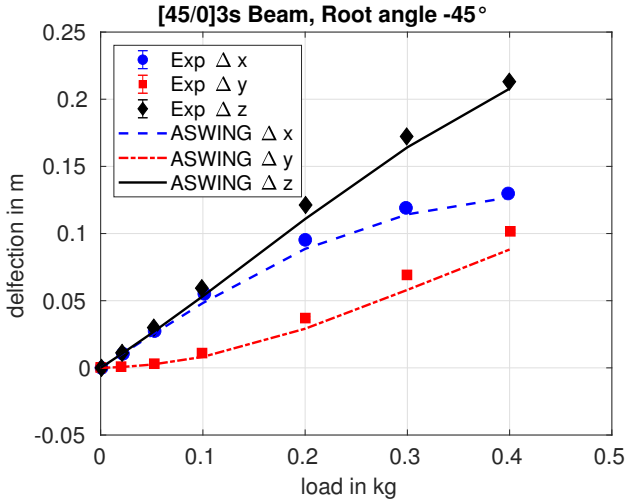

(a) $\theta = -45°$

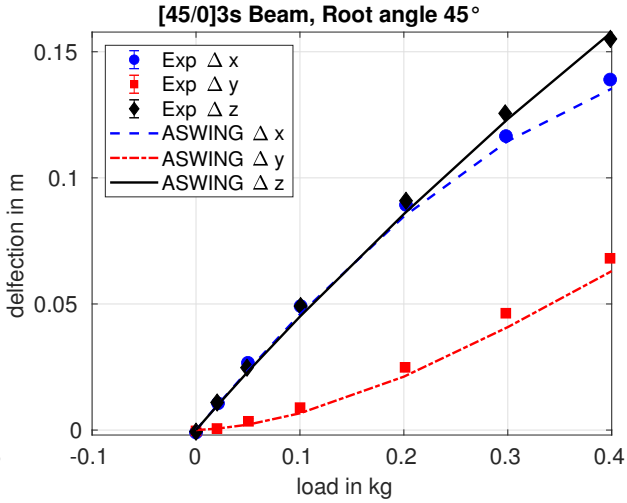

(b) $\theta = 45°$

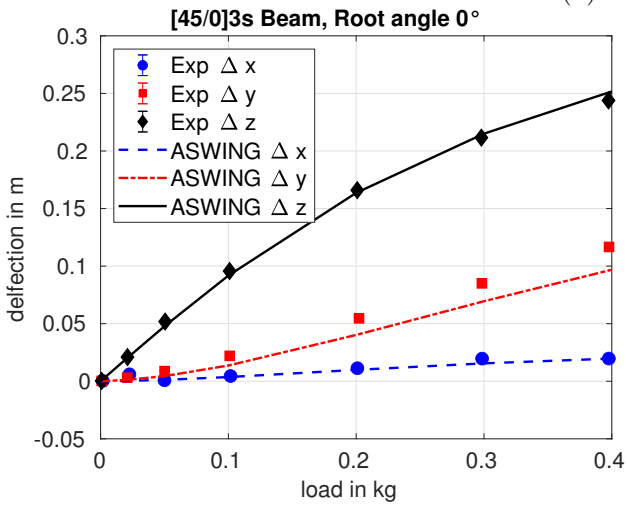

(c) $\theta = 0°$

Figure 5.20: CASE A, layout : [45/0]3s, tip $(\Delta_x, \Delta_y, \Delta_z)$ predictions against experiments from Minguet 1989

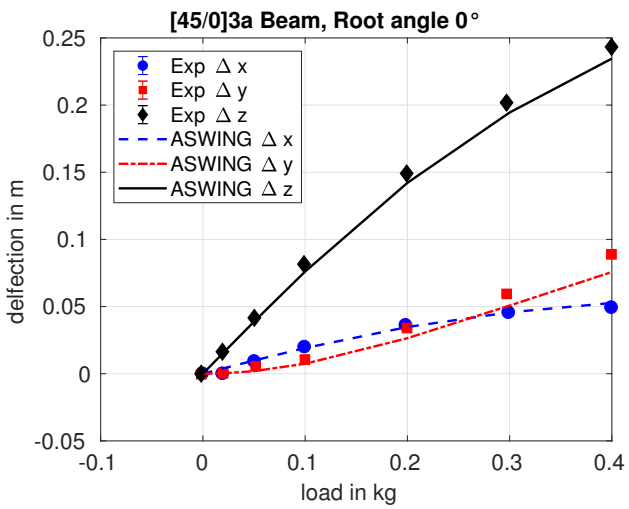

(a) $\theta = 0°$

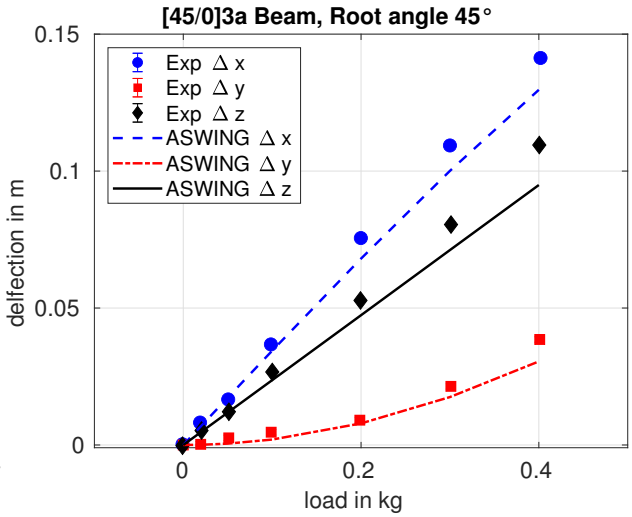

(b) $\theta = 45°$

Figure 5.21: CASE A, layout : [45/0]3a $(\Delta_x, \Delta_y, \Delta_z)$ predictions againts experiments from Minguet 1989

data, have been presented in table 5.2. The last two rows of the table showcase a highly flexible blade, with tests performed in face down and up configurations. A huge asymmetrical effect on the wing tip deflection has been witnessed by the author. And at the light of the first torsion mode column, this asymmetry has an impact on rising the ASWING prediction error from one configuration to another. The author reported that this asymmetry was mainly due to manufacturing limits, as the blade was extremely thin in comparison to the others. Moreover, this case is very stressful and is impossible to witness in reality as it is too flexible and would break under any aerodynamic loads. Nevertheless, commentary can be provided for the first three laminates. Firstly, the forecasts align excellently with the experiments. The highest forecast error is below 10% and has an average of 7% for the first three bending modes. While slightly inferior for the torsion, it is still reasonable. Note that ASWING accurately captures the impact of a coupling term that affects the first torsion mode, resulting in improved decoupling between the first bending and torsion modes. Since these modes are typically associated with flutter, using the $[45/0]_{3s}$ and $[20/-70]_{2a}$ laminate should lead to a greater flutter robustness, despite having the same bending stiffness properties as the $[0/90]_{3s}$ laminate.

Based on the initial outcomes, ASWING demonstrated good modal and deflection prediction performances for different composite layouts of helicopter blades. Nevertheless, this specific dataset does not sufficiently test the efficacy of the structural model mainly due to the high aspect ratio of the blade. However, the said attribute has been preserved since it exhibited intriguing characteristics that were absent in situations with lower aspect ratios. Two of the measurements taken were the 3D non-linear large deflections and high-frequency modes. The following sections will present the validation analysis using two moderate to low aspect ratio wings.

5.4.2 CASE B : Static deflection and modal response on a moderate aspect ratio wing:

The previous cases pose no real stress on the theoretical model as they only present a high aspect ratio. The assessment is therefore refined to a lower one, in order to more accurately capture the limits. To this end, the Pazy Wing of Avin et al. (2022) is employed, with a wing aspect ratio of 5.5. For further information on the wing's design, please refer to Avin et al.'s articles.

CASE B: experimental Setup:

The wing is clamped. To prevent torsion to be involved, a mass is positioned on the mid chord wing tip for tip deflection measurements as shown in Figure 5.22-a. The structure is constructed from a flat aluminium plate covered with a shell. As the elastic axis is approximately located at 44% of the chord, placing the mass at mid chord is improbable to involve torsion. For tip torsion measurements, the mass is again located at the tip, but with a chordwise offset (see figure 5.22-d). The offset is fixed at 0.08m from the leading edge of the wing tip. The tip mass is adjusted to achieve a 50% span tip deflection, regardless of the configuration. The tip deflections are measured at the mid-chord, while the tip torsion is calculated from the differential vertical and lateral position of the leading and trailing edges. Deflection tests have been conducted both with and without the skin (see figures 5.22 a and b). Additionally, ground vibration tests have been carried out in both vertical and horizontal positions, which are denoted as undeformed and deformed configurations.

CASE B : numerical Bench:

The Pazy wing has been replicated in ASWING using stiffness, mass, and inertia per unit length data provided by Riso and Cesnik (2023). Tip masses have been attached at the given positions with three sensors placed at the leading, trailing, and mid-chord edges. The implementation consists of forty structural nodes, guaranteeing converged forecasts. For the purpose of modal analysis, two files were generated: one for the Pazy wing in the vertical position (un-deformed) and another for the wing in the horizontal position (deformed on its own weight).

CASE B : results:

Figures 5.22 (a) to (f) display the deflection predictions for the "bending" bench (mass at mid-chord) and "torsion" bench (mass forward of the leading edge). The comparison between ASWING predictions and UM/NAST results from Riso and Cesnik-2023 shows a high level of agreement. The presented error in predictions is solely for ASWING. Remarkably, the tip deflection follows experimental measurements with predictions errors lower than 10%, even at large deflections, irrespective of whether the skin is on or off. In terms of the tip twist, ASWING achieves excellent agreement with experimental measurements when the wing skin is off, with prediction errors below 10% for large deflections. When the skin is attached, both UM/NAST and ASWING show poor predictions at high deflections. According to Riso and Cesnik, this behaviour is due to challenges in modelling the wing skin behaviour during stretching and could partly result from measurement errors (estimated at up to 1.2 degrees for twist angle). The ASWING, UM/NAST and SHARPY predictions of the pazy wing modes are compared with the ground vibration tests of Avin et al. in the table 7.2. The first 3 out-of-plane (OOP)

Layup	Type	w_{tip}, mm	1B, Hz	2B, Hz	3B, Hz	1T, Hz	1F, Hz
$[0/90]_{3s}$	***Exp***	20	5.7	34	98	62	
	ASW	1.2E-2	5.74	36	101	78	
	ϵ_1	40%	0.75 %	6.02 %	3.4 %	16%	
$[45/0]_{3s}$	***Exp***	18	4.3	28	78	135	
	ASW	17	4.75	29.81	83.7	95.0	
	ϵ_1	5.5 %	10 %	6.46 %	7.38 %	29 %	
$[20/-70]_{2a}$	***Exp***	12	5.8	36	103	166	
	ASW	11	5.86	36.8	103	187	
	ϵ_1	7.5 %	2.2 %	4.2 %	0 %	12 %	
$[45/0]_{s,u}$	***Exp***	137	1.4	8.0	20	68	10
	ASW	210	1.4	8.14	21.8	59	7.6
	ϵ_1	53 %	0 %	1.75 %	9 %	13 %	24 %
$[45/0]_{s,d}$	***Exp***	202	1.4	8.2	20	57	6.5
	ASW	210	1.4	8.14	218	59	7.6
	ϵ_1	3.9 %	0 %	0.7 %	9 %	3.3 %	16 %

Table 5.2: CASE A : helicopter blades modal analysis against experiments (Minguet 1989)

measurements are well captured by ASWING with a prediction error of less than 10% in each case. The first torsional mode is also well captured. Finally, the In Plane (IP) mode is not well captured with a prediction error greater than 200%. This is not really consistent with the Minguet bench results. Errors in the in plane stiffness or inertia estimation could explain such discrepancies. Also from an aeroelastic point of view, such a mode is poorly energetic due to the large difference between the chordwise and normal stiffnesses. Furthermore, the aerodynamic loads are very unlikely to excite an in-plane mode. Consequently, the discrepancies in the predictions for these modes are not that important. Finally, according to the predictions of the other model (UM/NAST and Sharpy), ASWING presents similar results.
Overall, for moderate aspect ratios, the ASWING predictions are still in good agreement with the experiments. At high deflections the twist predictions start to show weakness, but the results are still reasonable. The evaluation is then pushed further to really capture the limits of the model in terms of aspect ratio.

5.4.3 CASE C : static deflection and modal response of low aspect ratio wings : boundary case

In order to clearly identify the limits of the model, the aspect ratio of the test cases needs to be lowered again. This last case is adapted from the work of Landsberger (1983), Landsberger and Dugundji, (1985), Dunn (1992) and Dunn and Dugundji (1992) where several aeroelastic experimental analyses have been carried out.

CASE C : experimental setup:
The wing is made of a flat 6-ply composite plate with polystyrene fairings glued to it to reproduce a NACA0012 shape. A total of 3 wings have been built with 3 different composite layouts with different stiffness couplings. The latter was adapted to the ASWING formalism and derived in the tab 5.9. The aspect ratio of each wing was 4, making them excellent stress cases for the ASWING structural model. Each wing was cantilevered on an aluminium clamping device as shown in figure 5.23. For static quantification, 2 rulers were placed very close to the leading and trailing edges of the wing tip. Their accuracy was about 0.1 mm. A force was applied to the wing tip at the half chord line using a mass pulley system. A moment was applied around the half chord line using 2 mass pulley systems connected to the leading and trailing edges. Both have opposite directions and equal masses. The force was increased in steps of 100g while the moment was increased by 20g. As far as the modal analysis is concerned, this test bench differs from the previous one. In fact, since the latter was mainly dedicated to flutter measurements, the modal analysis was carried out in the wind tunnel to check if the structure had been damaged from one run to the next. To do this, they used bending and torsion strain gauges connected to a digital oscilloscope to record the transient response of the structure. An impulse force was then applied between each run using a rod at the tip of the blade, away from the torsional axis. The impulse, which had a large bandwidth, exited the wing first natural modes. Through a Fast Fourier Transform

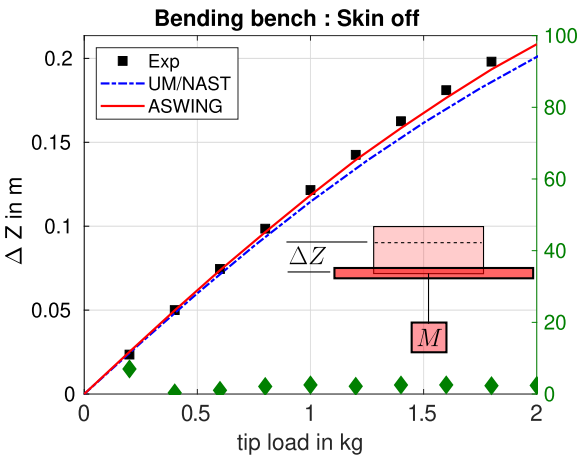

(a) Tip deflection (Skin off, bending bench)

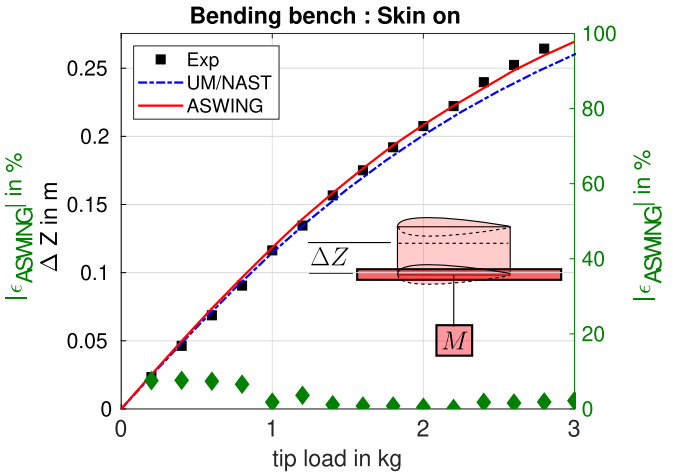

(b) Tip deflection (Skin on, bending bench)

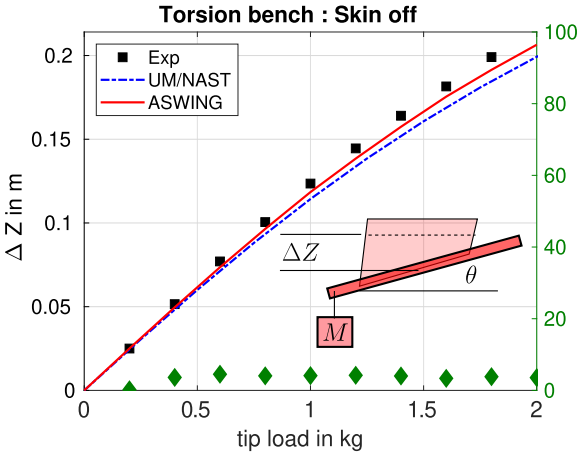

(c) Tip deflection (Skin off, torsion bench)

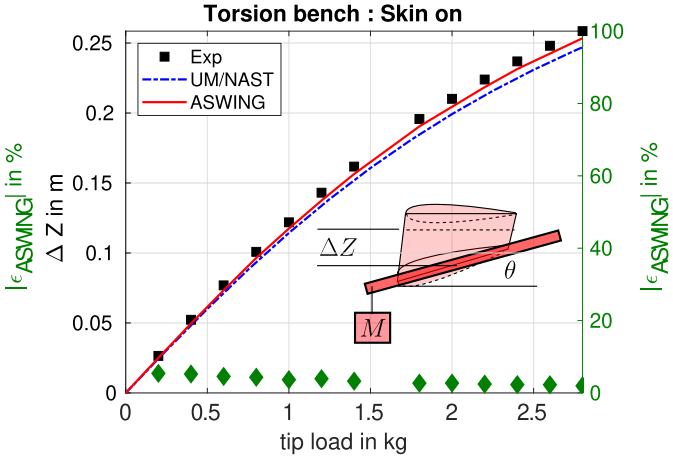

(d) Tip deflection (Skin on, torsion bench)

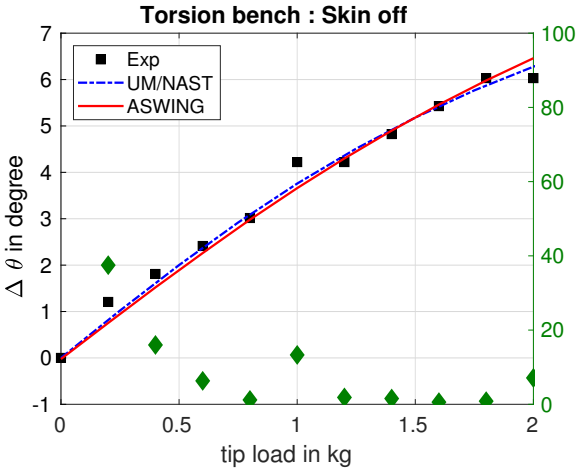

(e) Tip twist (Skin off, torsion bench)

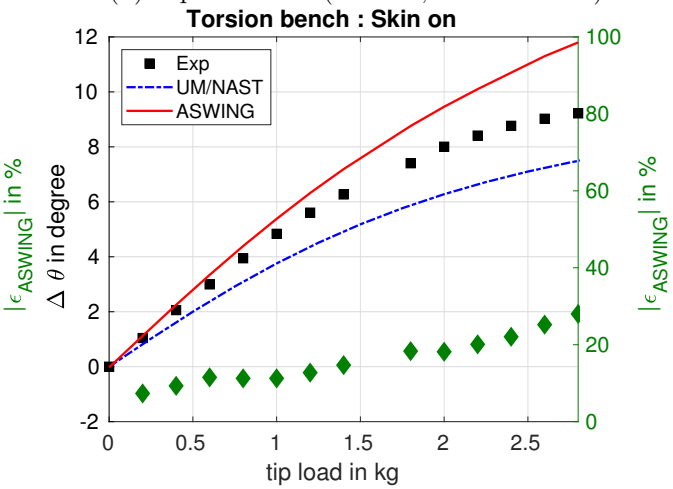

(f) Tip twist (Skin on, torsion bench)

Figure 5.22: CASE B : Pazy wing static deflection and twist. ASWING predictions against UM/NAST (Riso and Cesnik-2023) and experimental data (Avin et al.-2022)

		Modes in (Hz)				
Configuration	**Data**	**OOP1**	**OOP2**	**T1**	**IP1**	**OOP3**
Undeformed	**Exp**	4.26	28.5	42.0	60.7	81.5
	ASWING	4.59	29.1	43.4	128	81.4
	ϵ_A	7.2 %	2.1 %	3.3 %	+200 %	speed -0.1 %
	UM/NAST	4.19	28.5	41.9	83.1	105.89
	ϵ_U	-1.6 %	-0.02 %	-0.1 %	1.7 %	73 %
Deformed	**Exp**	4.39	29.8	41.0	N/A	82.5
	ASWING	4.67	29.2	43.2	116	81.4
	ϵ_A	11 %	-2 %	3.84 %	NC	-1.9 %
	UM/NAST	4.19	28.5	41.6	100.1	83.03
	ϵ_U	-4.6 %	-4.4 %	1.4 %	NC	NC
	SHARPY	4.69	30.87	43.71	NC	88.19
	ϵ_S	6.8 %	3.7 %	6.6 %	NC	6.9 %

Table 5.3: CASE B : Pazy wing modal response in undeformed and deformed condition. ASWING, UM/NAST (Riso and Cesnik-2023), Sharpy (Goizueta et al.-2022) predictions against experimental data (Avin et al.-2022)

analysis of the transient response, the 3 first natural mode frequencies were calculated and reported in the author's paper. Only the 2 first bending modes and 1 torsional mode could be calculated due to the typology of the bench. In fact, high frequency modes are very difficult to extract using this method and so their contribution to the transient response was probably lost in the measurement noise.

CASE C : numerical bench: In spite of the helicopter blade bench, it was not possible to reproduce exactly the configuration in ASWING for the deflection measurements. In fact, since the wing is mounted vertically in this case, it is not possible to apply horizontal punctual forces. In ASWING, the wing is mounted horizontally and its inertial properties have been eliminated. For force measurements, a point mass was placed at the wing tip on the half chord line. For momentum predictions, the mass was attached to the trailing edge of the wing. Note that in both cases it is possible to implement a negative mass so that negative moments and forces can be implemented. In terms of modal analysis, the wing could be cantilevered vertically, so the same procedure as in the previous section was used with the same numerical parameters and conclusion on mesh convergence.

Results: Figure 5.24 (a) to (d) show the deflection and torsion predictions of ASWING against the experimental data. Contrary to the previous case, the agreement is not satisfactory, although the framework captures the tendency for a bending-torsion coupling. ASWING seems to be a bit weak for tip deflection (Figure 5.24 (a)). This highlights the limitations of structural model for wings/beams with an aspect ratio less than 4. Below, 3D finite element models should be considered, such as the predictions of Dunn shown in figure 5.24. Note that the development of such a modification in ASWING would be pointless if it will still coupled to the lift line model. In fact, although the lifting line performance is expected to decrease rapidly as the aspect ratio squeezes. Consequently, a modification of the structural model would imply the use of a new aerodynamic one, such as the unsteady vortex/particle or lattice methods. The reader can take a look at the work of Drela et al. (2019) who has proposed such a solution.
The conclusion about the modal response of the cases is less severe. the frequency predictions are still reasonable. This could be explained by the small excitation configuration where the 3D shear stress coupling is expected to dominate. Obviously there is a decrease in prediction performance. Despite the poor tip and twist deflection predictions in this case, we will see in the aeroelastic part of this evaluation work that ASWING shows interesting results in this case and that the conclusion about the boundary limit of the model is not as sharp as the one above.

5.4.4 CASE D : Effect of a concentrated mass on the modal response of a straight wing

As seen in the theoretical section, it is possible to take into account the effect of point masses attached to any beam by means of a rigid pylon. This feature is of particular interest when analysing the effect of a nacelle or wing tip tank on the aeroelastic response of the whole aircraft. To evaluate this feature, the experimental database provided by Runyan and Sewall (1948) has been used. In this note the author provided an experimental analysis of the effect of the spanwise and chordwise position of concentrated weights on the

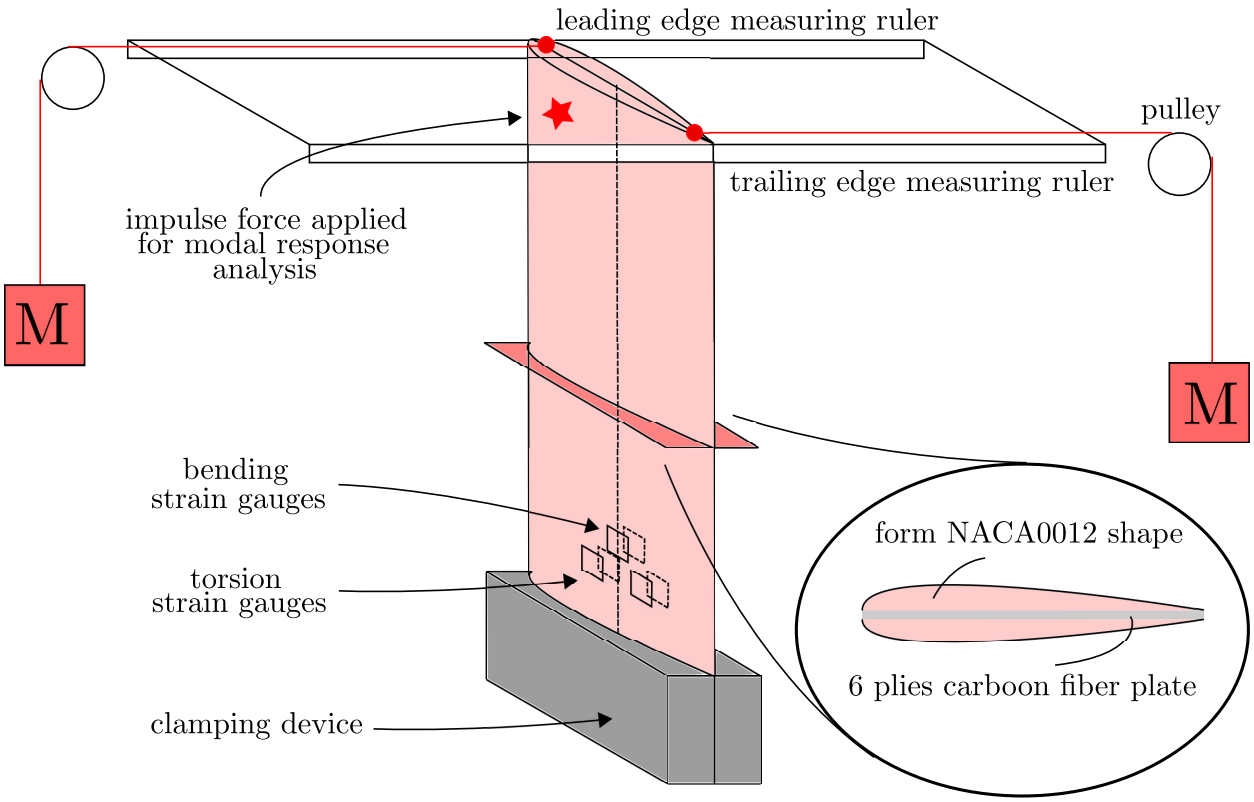

Figure 5.23: CASE C: low aspect ratio wing, static deflection and modal response experimental bench Dunn

Layup	Type	1B (in Hz)	2B (in Hz)	1T (in Hz)
	Exp	4.0	27.1	21.4
	ASWING	4.5	28.2	25.9
$[0_3/90]_s$	ϵ_1	12.5%	4.0 %	16.6 %
	P.E Dunn	4.3	27.2	24.6
	ϵ_2	7.5 %	0.4 %	15 %
	Exp	3.6	22.7	27.1
	ASWING	3.9	23.5	26.7
$[+15_2/0_2]_s$	ϵ_1	8.3 %	3.5 %	-1.5 %
	P.E Dunn	4.5	23.5	28.6
	ϵ_1	8.3%	3.5 %	5.5 %
	Exp	3.6	24.5	27.4
	ASWING	3.7	22.5	26.5
$[-15_2/0_2]_s$	ϵ_1	2.8%	-8.2 %	-3.3 %
	P.E Dunn	3.6	24.1	27.8
	ϵ_2	11.1 %	-1.6 %	1.5 %

Table 5.4: CASE C : NACA0012 straight wing modal analysis Dunn (1992)

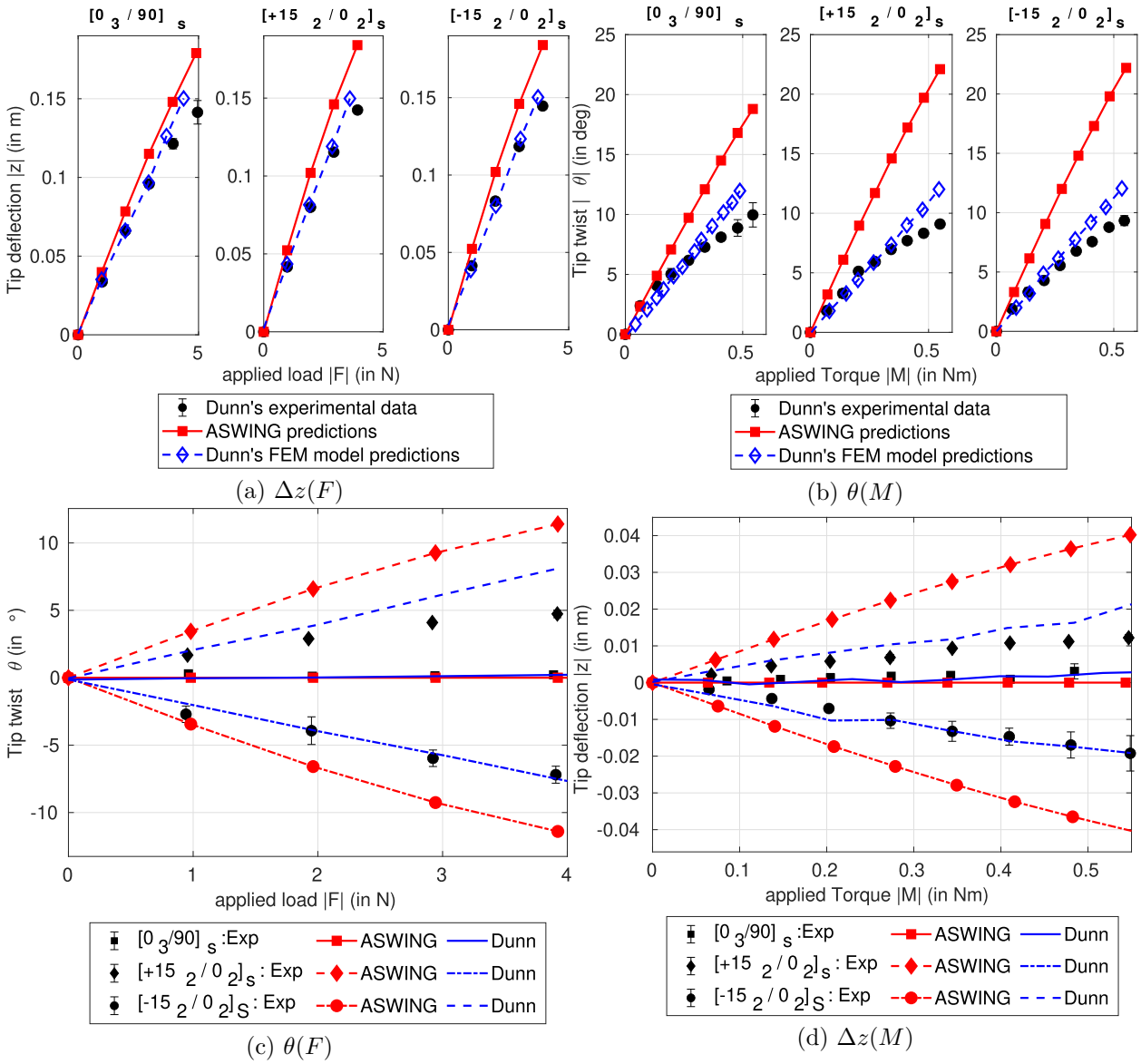

(a) $\Delta z(F)$ (b) $\theta(M)$

(c) $\theta(F)$ (d) $\Delta z(M)$

Figure 5.24: CASE C: NACA0012 wing static tip deflection and twist against tip forces and moments : ASWING and Dunn's model comparison with experimental data (Dunn -1992)

modal response and flutter speed.

CASE D : experimental setup: The tests were carried out in Langley's 4 x 5 ft flutter research wind tunnel. The modal response was performed in a non-flow condition in the wind tunnel. A straight wing was mounted vertically from the top of the section as shown in figure 5.25. The wing half aspect ratio was 6, providing a good stress test for the Euler-Bernoulli model. The geometrical and structural parameters of the wing are given in the author's work and have been translated into the ASWING formalism and metric system in tab 5.11. The bending and torsional stiffness were determined experimentally from the static deflection curves of the wing in bending and torsion. Vibrations were recorded using strain gauges attached to the wing as shown in figure 5.25. The strain gages were connected to a bridge/amplifier cascade system to reduce measurement noise. Frequencies were recorded on an oscillograph. A total of 100 runs were carried out to ensure that the wing was not structurally damaged from one run to the next, and modal response measurements were taken before and after each run. Based on the results, the author reported that the wing did not suffer any damage throughout the experiment. This was mainly due to the use of wires connected to the wing tip to prevent high deflections when the wing went into flutter. A total of 7 weights with different characteristics were tested, but the 7th will be of particular interest as it varies in span and chord. For ease of reading, weights I-VI have been given the *weights 7a-f* of the technical note Runyan and Sewall (1948). These weights have very close mass properties (constant) as shown in the tab 5.10. Their index indicates a change in chordwise position. The latter is given as the distance to the elastic axis, denoted as d_W, as shown in figure 5.25(b)

CASE D : numerical setup: In view of the ASWING formalism, it is not possible to model a concentrated mass, since it has a non-zero inertia tensor. For this purpose, a potential mass dipole was used, equidistant from the centre of gravity of the concentrated mass at a distance r_W (see figure 5.25-b). The point mass was half the concentrated mass. The distance r_w, i.e. the radius of gyration, is calculated to recover the concentrated mass inertia. Its numerical values are given in the tab 5.10. As the weights were designed to have a minimum aerodynamic pressure (symmetrical and slender), we believe that the use of a mass dipole was the best option to virtually recover the behaviour of a concentrated mass. Once this was decided and implemented, the modal analysis was carried out using the same numerical protocol described in the previous sections.

CASE D : Results: The figures 5.26 (a) and (b) show an illustrative comparison between experiments and ASWING predictions of the effect of the span size position of a concentrated mass on the first bending and torsion mode frequency. The more the weight is placed towards the wing tip, the lower these mode frequencies will be. The table 5.5 summarises the 3 first mode predictions and the effect of each weight spanwise coordinate. The results are presented in this way because the results are quite untraceable on a graph, regardless of the mode considered. For the first mode, ASWING captures well the effect of the spanwise position on its frequency. The latter tends to decrease linearly as the weight moves towards the wing tip. The chordwise position (weight index) has no effect. For the second bending mode, ASWING again captures the weight position effect with slightly less accuracy than for the first mode. The mode decreases from 0 to 40% of the half span, then increases between 40 and 70% and finally decreases to the wing tip. Throughout the wing, the second bending mode remains lower than in the configuration where the weight is placed at the wing root. Finally, the torsional mode prediction captures a "tendency" of the weight effect, which is a decrease with weight location. However, the prediction errors are larger than for the previous modes. Despite the low aspect ratio of this case, ASWING is able to capture the effect of concentrated weights on its modal response reasonably well.

5.5 Conclusion:

An experimental evaluation of the ASWING structural model was presented in this chapter. The focus was on static deflections, modal response and the effect of concentrated weights on these. The experimental cases were chosen to be as stressful as possible. In the light of the results, the following findings can be summarised

- The mesh convergence study for tip deflection and modal response predictions shows that only 40 structural nodes clustered by a cosine function are sufficient to provide converged results. Using this, the computation times on a modern laptop for a single tip deflection and modal analysis are 0.250 s and 2.0 s respectively. When both near-point analyses are performed, the computation time drops to 0.100 and 1.0 seconds, respectively.
- ASWING shows excellent agreement with experiments for high aspect ratio beams. In particular, the non-linear 3D high deflections are well captured. The modal predictions of the first 5

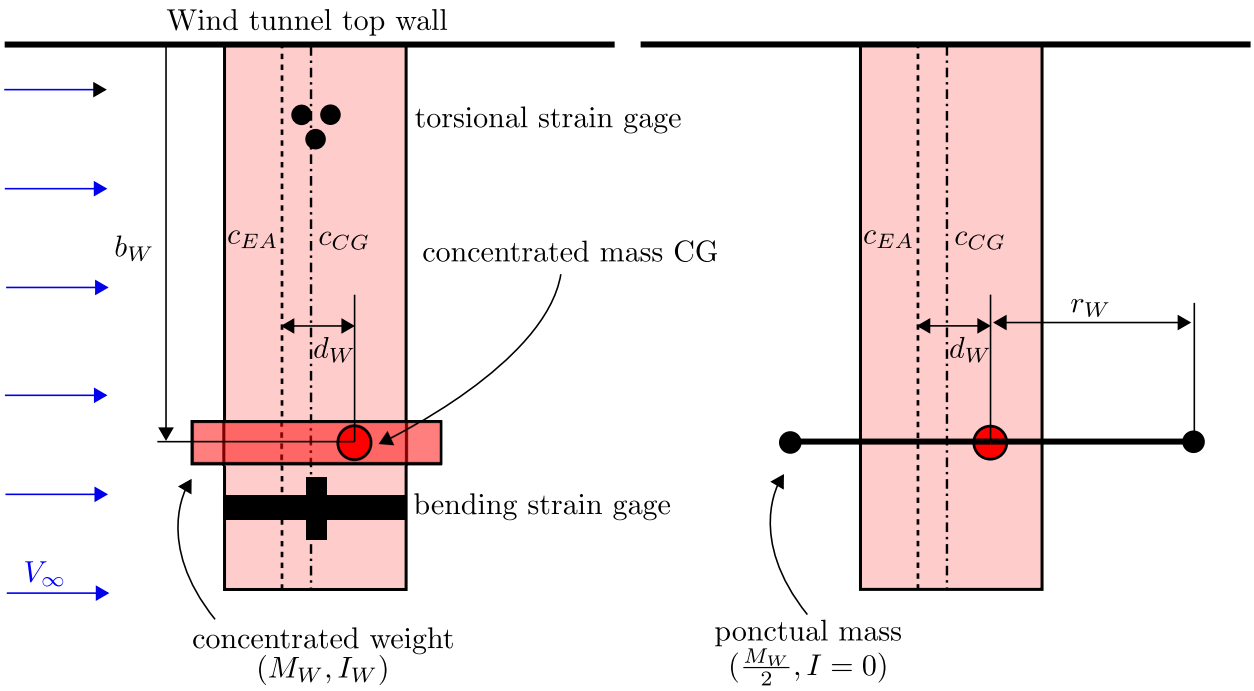

(a) NACA16010 Experimental bench

(b) ASWING's concentrated mass ponctual mass dipole modeling

Figure 5.25: CASE D: concentrated mass effect bench Runyan and Sewall (1948)

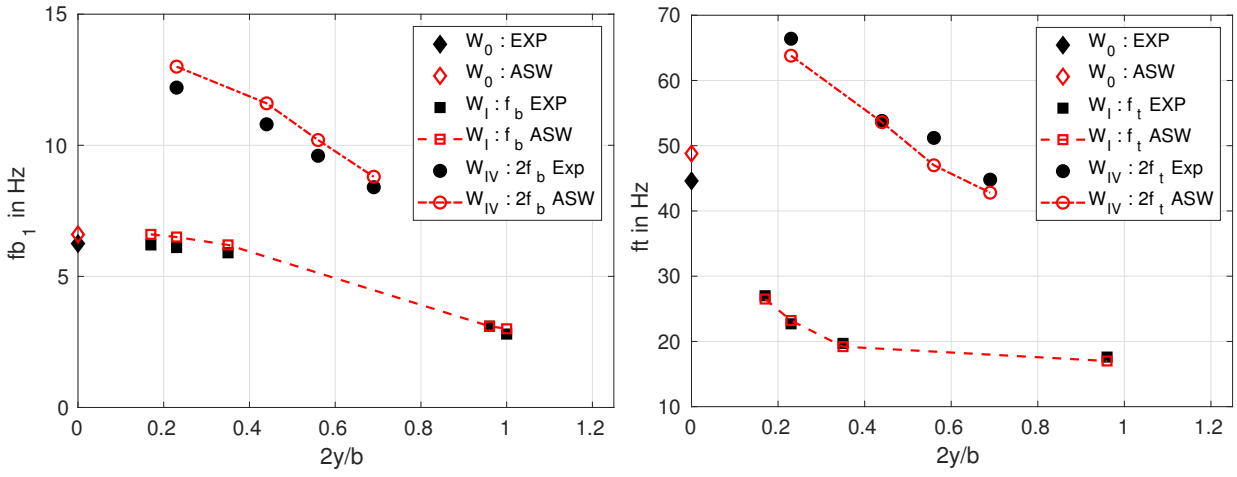

(a) first bending mode

(b) first torsion

Figure 5.26: CASE D : Concentrated weight effect on the first bending and torsion modes. ASWING predictions versus experiments of Runyan and Sewall (1948).

modes are also good. Neglecting some of the extensional/bending terms shows no effect on the tip deflection predictions and modal response.

- The Pazy wing bench has been used to stress ASWING for moderate aspect ratio. The latter still shows good agreement with experiments for tip deflection, while for torsion it starts to get weaker at high deflections. The mode frequency predictions are in excellent agreement with the experiments. Overall, ASWING can still be used for this type of layout.

- Three low aspect ratio cases have shown the weakness of the model in predicting tip deflections. The use of a strong tip loads seems to involve effects that are not captured by ASWING. As the aerodynamic loads are much more scattered along the beam, fewer discrepancies are expected. Tip pontual load benches could not be well adapted for aeroelasticity evaluation.

- ASWING can also capture well the effect of concentrated weights in spanwise and chordwise positions on the modal response of a wing. This last feature is of particular interest when it comes to study the tank or nacelle position effect on the flutter response of a wing.

Note that structural viscous damping has not been evaluated. This has been done by Banks and Wang (1987) but for a small pinch time marching response. An experimental campaign should be considered to evaluate this last feature. Also, with the advent of modern sensors, modal shape response measurements should be considered and compared with the ASWING predictions.

N_W	**ew**	**y/b**	$fb1_{exp}$ **(Hz)**	$fb1_{ASW}$ **(Hz)**	ϵ **(%)**	$fb2_{exp}$	$fb2_{ASW}$	ϵ	ft_{exp}	ft_{ASW}	ϵ
0	0	0	6.25	6.6	5.9	35.8	40.54	13.2	44.6	48.8	9.59
I	-0.818	0.17	6.2	6.6	5.9	36	36.5	1.4	27	26.5	-1.6
		0.23	6.1	6.5	6.7	35	34.6	-1.3	22.7	23.2	2.0
		0.35	5.9	6.2	5.0	NC	31.5		19.7	19.2	-2.45
		0.96	3.1	3.1	0	31.7	33.3	5.0	17.6	17	-3.4
		1	2.8	3.0	7	29.8	31.3	5.0	NC	16.8	
II	-0.578	0.23	6.1	6.5	6.2	25.6	28	9.5	33.6	38	13
		0.44	2.3	5.8	9.6	25.0	21.6	-13.6	28	33	17
III	-0.360	0.23	6.2	6.5	5.7	26.7	27.6	3.5	34.5	32.9	-4.6
		0.44	5.4	5.8	8.0	22.5	22.2	-1.2	27	28.8	4.8
		0.58	4.6	5.0	8.0	29.4	30.4	3.6	23.1	21.8	-5.8
IV	-0.140	0.23	6.1	6.5	6.8	24.5	29.3	19.7	33.2	31.9	-4.0
		0.44	5.4	5.8	7.4	23.2	24.3	4.8	26.1	26.8	2.5
		0.56	4.8	5.1	7.0	27.4	28.6	4.5	25.6	23.5	-8.4
		0.69	4.2	4.4	4.9	34.2	39.1	14.1	22.4	21.4	-3.9
V	0.034	0.23	6.3	6.5	3.6	26.7	29.6	10.8	37.4	31.6	-15.4
		0.44	5.6	5.8	4.4	29.4	25.6	-12.8	29.1	25.2	-13.5
		0.60	4.7	4.9	4.3	30	30.2	0.8	25.3	23.1	-8.5
		0.72	4.0	4.2	3.6	35.6	37.7	5.7	30.0	21.9	-26.9
		0.83	3.6	3.6	0.0	34.6	38.5	11.4	22.7	21.1	-7.2
VI	0.5	0.23	6.2	6.5	4.9	38.3	33.8	NC	36.8	26.7	-27.6
		0.33	6	6.3	4.5	35.3	31.0	-12.1	34.6	22.9	-33.7
		0.5	5.25	5.82	11	31.7	28.3	-10	26.2	22.2	-15.2
		0.83	4.4	4.5	3.7	34.2	34.9	2.1	21.5	21.5	0

Table 5.5: CASE D : NACA16010 straight wing modal analysis (NC : reported as Not Clear) Runyan and Sewall (1948).
Effect of concentrated weights spanwise and chordwise position on the modal response
$\epsilon_{\bar{fb}_1} = 5.6 \pm 2.5\%$, $\epsilon_{\bar{fb}_2} = 7.5 \pm 5.3\%$, $\epsilon_{\bar{ft}} = 10.5 \pm 9\%$

Bibliography

[1] Afonso, F., Vale, J., Oliveira, É., Lau, F., and Suleman, A. (2017). A review on non-linear aeroelasticity of high aspect-ratio wings. *Progress in Aerospace Sciences*, 89:40–57. 160

[2] Avin, O., Raveh, D. E., Drachinsky, A., Ben-Shmuel, Y., and Tur, M. (2022). Experimental aeroelastic benchmark of a very flexible wing. *AIAA Journal*, 60(3):1745–1768. 16, 19, 160, 176, 181, 183, 184

[3] Banks, H. T. and Inman, D. J. (1991). On Damping Mechanisms in Beams. *Journal of Applied Mechanics*, 58(3):716–723. 160, 167

[4] Banks, H. T. and Wang, Y. (1987). Parameters identification techniques for the estimation of damping in flexible structure experiments. volume TP6 of *Descision and Control Conference*, Los Angeles. Descision and Control Conference. 160, 167, 189

[5] Cesnik, C. E., Palacios, R., and Reichenbach, E. Y. (2014). Reexamined structural design procedures for very flexible aircraft. *Journal of Aircraft*, 51(5):1580–1591. 160

[6] Chambon, A., Sanches, L., Prothin, S., Eloy, C., and Michon, G. (2022). Structural dynamics of flexible rotor blades to study aeroelastic phenomena. In *AIAA AVIATION 2022 Forum*, Chicago, IL & Virtual. American Institute of Aeronautics and Astronautics. 160

[7] Chau, T. and Zingg, D. W. (2022). Aerodynamic design optimization of a transonic strut-braced-wing regional aircraft. *Journal of Aircraft*, 59(1):253–271. 160

[8] Chauhan, S. S. and Martins, J. R. (2019). Low-fidelity aerostructural optimization of aircraft wings with a simplified wingbox model using openaerostruct. In *EngOpt 2018 Proceedings of the 6th International Conference on Engineering Optimization*, pages 418–431. Springer. 160

[9] Cheung, R. C., Rezgui, D., Cooper, J. E., and Wilson, T. (2020). Testing of folding wingtip for gust load alleviation of flexible high-aspect-ratio wing. *Journal of Aircraft*, 57(5):876–888. 160

[10] Clarke, M. A., Erhard, R. M., Smart, J. T., and Alonso, J. (2021). Aerodynamic optimization of wing-mounted propeller configurations for distributed electric propulsion architectures. In *AIAA Aviation 2021 Forum*, page 2471. 160

[11] Colas, D., Roberts, N. H., and Suryakumar, V. S. (2018). HALE Multidisciplinary Design Optimization Part I: Solar-Powered Single and Multiple-Boom Aircraft. In *2018 Aviation Technology, Integration, and Operations Conference*, Atlanta, Georgia. American Institute of Aeronautics and Astronautics. 160

[12] del Carre, A., Muñoz-Simón, A., Goizueta, N., and Palacios, R. (2019). Sharpy: A dynamic aeroelastic simulation toolbox for very flexible aircraft and wind turbines. *Journal of Open Source Software*, 4(44):1885. 160

[13] Drela, M. (1988). Low-Reynolds-number airfoil design for the M.I.T. Daedalus prototype- A case study. *Journal of Aircraft*, 25(8):724–732. 174

[14] Drela, M. (1990). Method for simultaneous wing aerodynamic and structural load prediction. *Journal of Aircraft*, 27(8):692–699. 160, 174, 175

[15] Drela, M. (1999). Integrated simulation model for preliminary aerodynamic, structural, and control-law design of aircraft. In *40th Structures, Structural Dynamics, and Materials Conference and Exhibit*, St. Louis,MO,U.S.A. American Institute of Aeronautics and Astronautics. 160

[16] Drela, M. (2008). ASWING 5.81 Technical Description — Unsteady Extension. page 42. 160, 162, 166, 171

[17] Drela, M. (2009). ASWING 5.86 Technical Description — Steady Formulation. page 57. 160, 166

[18] Drela, M., Galbraith, M., Haimes, R., Allmaras, S. R., and Darmofal, D. (2019). Hybrid Shell Model for Aeroelastic Modeling. In *AIAA Scitech 2019 Forum*, San Diego, California. American Institute of Aeronautics and Astronautics. 184

[19] Dunn, P. (1992). *NONLINEAR STALL FLUTTER of WINGS with BENDING-TORSION COUPLING*. PhD thesis, MIT, Boston, MA. 16, 19, 20, 176, 182, 184, 185, 186, 193, 194

[20] Dunn, P. and Dugundji, J. (1992). Nonlinear stall flutter and divergence analysis of cantilevered graphite/epoxy wings. *AIAA Journal*, 30(1):153–162. 160, 176, 182

[21] Gallman, J. W., Smith, S. C., and Kroo, I. M. (1993). Optimization of joined-wing aircraft. *Journal of Aircraft*, 30(6):897–905. 160

[22] Gilbert, C., Armstrong, B., Johansson, O., Squibb, C., and Philen, M. (2023). Control of a Flapping Plate Shape with Fluidic Flexible Matrix Composites. In *AIAA SCITECH 2023 Forum*,

National Harbor, MD & Online. American Institute of Aeronautics and Astronautics. 160

[23] Goizueta, N., Wynn, A., Palacios, R., Drachinsky, A., and Raveh, D. E. (2022). Flutter predictions for very flexible wing wind tunnel test. *Journal of Aircraft*, 59(4):1082–1097. 19, 160, 184

[24] González, O., Boschetti, P., Cárdenas, E., and Amerio, A. (2010). Static-Stability Analysis of an Unmanned Airplane as a Flexible-Body. In *AIAA Atmospheric Flight Mechanics Conference*, Toronto, Ontario, Canada. American Institute of Aeronautics and Astronautics. 160

[25] Gu, H., Healy, F., Rezgui, D., and Cooper, J. (2023). Sizing of high-aspect-ratio wings with folding wingtips. *Journal of Aircraft*, 60(2):461–475. 160

[26] Healy, F., Cheung, R., Rezgui, D., Cooper, J., Wilson, T., and Castrichini, A. (2023a). Experimental and numerical nonlinear stability analysis of wings incorporating flared folding wingtips. *Journal of Aircraft*, pages 1–15. 160

[27] Healy, F., Courcy, J. D., Gu, H., Rezgui, D., Cooper, J., Wilson, T., and Castrichini, A. (2023b). On the dynamic behavior of wings incorporating floating wingtip fuel tanks. *Journal of Aircraft*, pages 1–16. 160

[28] Jones, J. (2017). *Development of a very flexible testbed aircraft for the validation of nonlinear aeroelastic codes*. PhD thesis. 160

[29] Jonsson, E., Riso, C., Lupp, C. A., Cesnik, C. E., Martins, J. R., and Epureanu, B. I. (2019). Flutter and post-flutter constraints in aircraft design optimization. *Progress in Aerospace Sciences*, 109:100537. 160

[30] Krengel, M. D., Hepperle, M., and Huebner, A. (2019). Aeroservoelastic Wing Sizing Using a Physics-Based Approach in Conceptual Aircraft Design. In *AIAA Aviation 2019 Forum*, Dallas, Texas. American Institute of Aeronautics and Astronautics. 174, 175

[31] Landsberger, B. J. (1983). AEROELASTIC PROPERTIES OF STRAIGHT AND FORWARD SWEPT GRAPHITE/EPOXY WINGS. 182

[32] Landsberger, B. J. and Dugundji, J. (1985). Experimental aeroelastic behavior of unswept and forward-swept cantilever graphite/epoxy wings. *Journal of Aircraft*, 22(8):679–686. 182

[33] Lehoucq, R. B., Sorensen, D. C., and Yang, C. (1998). *ARPACK Users' Guide: Solution of Large-Scale Eigenvalue Problems with Implicitly Restarted Arnoldi Methods*. Society for Industrial and Applied Mathematics. 176

[34] Love, M., Zink, P., Wieselmann, P., and Youngren, H. (2005). Body Freedom Flutter of High Aspect Ratio Flying Wings. In *46th AIAA/ASME/ASCE/AHS/ASC Structures, Structural Dynamics and Materials Conference*, Austin, Texas. American Institute of Aeronautics and Astronautics. 160

[35] Minguet, P. and Dugundji, J. (1990a). Experiments and analysis for composite blades under large deflections. I - Static behavior. *AIAA Journal*, 28(9):1573–1579. 160, 176

[36] Minguet, P. and Dugundji, J. (1990b). Experiments and analysis for composite blades under large deflections. II - Dynamic behavior. *AIAA Journal*, 28(9):1580–1588. 160, 176

[37] Minguet, P. J. (1989). *Static and Dynamic Behavior of Composite Helicopter Rotor Blades under Large Deflections*. PhD thesis, MIT, Boston, MA. 16, 19, 160, 162, 176, 178, 179, 180, 182, 193, 194

[38] Ning, S. A. and Kroo, I. (2010). Multidisciplinary considerations in the design of wings and wing tip devices. *Journal of aircraft*, 47(2):534–543. 160

[39] Otsuka, K. and Makihara, K. (2019). Absolute Nodal Coordinate Beam Element for Modeling Flexible and Deployable Aerospace Structures. *AIAA Journal*, 57(3):1343–1346. 160

[40] Patil, M. J., Hodges, D. H., and Cesnik, C. E. (2001a). Limit-cycle oscillations in high-aspect-ratio wings. *Journal of fluids and structures*, 15(1):107–132. 160

[41] Patil, M. J., Hodges, D. H., and Cesnik, C. E. (2001b). Nonlinear aeroelasticity and flight dynamics of high-altitude long-endurance aircraft. *Journal of Aircraft*, 38(1):88–94. 160

[42] Riso, C. and Cesnik, C. E. (2023). Impact of low-order modeling on aeroelastic predictions for very flexible wings. *Journal of Aircraft*, 60(3):662–687. 16, 19, 181, 183, 184

[43] Runyan, H. L. and Sewall, J. L. (1948). Experimental investigation of the effects of concentrated weights on flutter characteristics of a straight cantilever wing. NACA Technical Note 1594, NACA, Langley Memorial Aeronautical Laboratory, Langley Field. 16, 19, 20, 161, 176, 184, 187, 188, 190, 193, 195

[44] Sinha, A. (2021). Free Vibration of an Euler–Bernoulli Beam with Arbitrary Nonuniformities and Discontinuities. *AIAA Journal*, 59(11):4805–4808. 160

[45] Su, W. and Cesnik, C. E. (2010). Nonlinear aeroelasticity of a very flexible blended-wing-body aircraft. *Journal of Aircraft*, 47(5):1539–1553. 160

[46] Uranga, A., Drela, M., Greitzer, E. M., Hall, D. K., Titchener, N. A., Lieu, M. K., Siu, N. M., Casses, C., Huang, A. C., Gatlin, G. M., et al. (2017). Boundary layer ingestion benefit of the d8 transport aircraft. *AIAA journal*, 55(11):3693–3708. 160

[47] Variyar, A., Economon, T. D., and Alonso, J. J. (2017). Design and Optimization of Unconventional Aircraft Configurations with Aeroelastic Constraints. In *55th AIAA Aerospace Sciences Meeting*, Grapevine, Texas. American Institute of Aeronautics and Astronautics. 160

[48] Wang, X. and Xia, P. (2022). Novel Modeling and Vibration Analysis Method on a Helicopter Drive Train System. *AIAA Journal*, 60(7):4288–4301. 160

[49] Warwick, S., Bras, M., Richards, J., and Suleman, A. (2019). Measurement of Aeroelastic Wing Deflections Using Modal Shapes and Strain Pattern Analysis. In *AIAA Scitech 2019 Forum*, San Diego, California. American Institute of Aeronautics and Astronautics. 160

[50] Willis, D., Israeli, E., Persson, P.-O., Drela, M., Peraire, J., Swartz, S., and Breuer, K. (2007). A Computational Framework for Fluid Structure Interaction in Biologically Inspired Flapping Flight. In *25th AIAA Applied Aerodynamics Conference*, Miami, Florida. American Institute of Aeronautics and Astronautics. 174, 175

Appendix

The tables 5.6-5.8 provides the helicopter blades properties. The properties of the first 4 laminates can be found in the table 5.1 p 100 while the fifth in Table 5.2(a) p 124 of Minguet (1989) The table 5.9 provides the properties of the laminates of CASE C. Data from *Appendix B page 175* of Dunn's PhD script (1992) were used and translated to the Euler-Bernoulli formalism. Mass/length and inertia/length were not provided and so were deducted from the material properties given in *Appendix A page 173-174* of Dunn's work (1992) The tables 5.10 and 5.11 provide the wing and weight properties of CASE D .The weights values are taken from *Table I page 8* and the wing ones are given on *page 4* of Runyan and Sewall (1948)'s technical report. Data is translated from the imperial to the metric system.

Laminate	GKc	EA	GKn	E_{12}	E_{25}
Unit	N	N	N	N	Nm
$[0/90]_{3s}$	2.6E5	3.7E6	2.9E5		
$[45/0]_{3s}$	2.6E5	4.0E6	5.5E5	2.7E5	
$[20/-70/-70/20]_{2a}$	1.1E6	3.9E6	1.210E5		5.22E2
$[45/0]_{3a}$	8.7E5	3.7E6	2.2E6		2.26E2
$[45/0]_s$	2.7E5	1.3E6	1.0E5	9E4	

Table 5.6: CASE A: helicopter blades: properties 1/3 Minguet (1989)

Laminate	$EIcc$	GJ	$EIcs$	E_{45}
Unit	Nm^2	Nm^2	Nm^2	Nm^2
$[0/90]_{3s}$	7.07E-1	1.83E-1	2.76E2	
$[45/0]_{3s}$	5.22E-1	3.68E-1	2.98E2	1.02E-1
$[20/-70/-70/20]_{2a}$	9.83E-1	1.18	2.9E2	
$[45/0]_{3a}$	5.55E-1	8.54E-1	2.79E2	
$[45/0]_s$	1.43E-2	1.95E-2	9.9E1	6.32E-1

Table 5.7: CASE A: helicopter blades: properties 2/3

Laminate	mg	$mgIcc$	$mgInn$	ϑ
Unit	kg/m	kgm	kgm	degrees
$[0/90]_{3s}$	7.95E-2	1.31E-8	5.3E-6	0
$[45/0]_{3s}$	6.97E-2	1.25E-8	5.22E-6	0
$[20/-70/-70/20]_{2a}$	9.10E-2	2.79E-8	6.82E-6	0
$[45/0]_{3a}$	6.92E-2	1.22E-8	5.19E-6	65
$[45/0]_s$	2.38E-2	6.22E-10	1.91E-6	0

Table 5.8: CASE A: helicopter blades: properties 3/3

Parameters	**Units**	$[0_3/90]_s$	$[+15_2/0]_s$	$[+15_2/0]_s$
EI_{cc}	N	1.4163	1.2947	1.2947
EI_{nn}	N	$1.8499\ 10^4$	$2.2775\ 10^4$	$2.2775\ 10^4$
EI_{cn}	N	0.0023	0.0021	0.0021
EI_{cs}	N	0	0.5151	-0.5151
GJ	N	1.2	1.2	1.4
EA	N	$1.132\ 10^7$	$1.3944\ 10^7$	$1.3944\ 10^7$
μg	kg/m	0.2310	0.2310	0.2310
μgi_{cc}	kgm	$9.2385\ 10^{-7}$	$9.2385\ 10^{-7}$	$9.2385\ 10^{-7}$
μgi_{nn}	kgm	$3.4623\ 10^{-4}$	$3.4623\ 10^{-4}$	$3.4623\ 10^{-4}$
c	m	0.140	0.140	0.140
b	m	0.558	0.558	0.558
AR	m	4	4	4
c_{EA}	m	0.5	0.5	0.5
c_{TA}	m	0.4	0.4	0.4

Table 5.9: CASE C: NACA0012 wing stiffness and geometry parameters Dunn (1992)

Parameters	M_W	d_w	$I_{W,EA}$	I_W	r_W
Unit	kg	m	kgm^2	kgm^2	m
I	1.4475	-0.0831	0.0185	0.0085	0.0766
II	1.4696	-0.0587	0.0124	0.0073	0.0707
III	1.4838	-0.0366	0.0089	0.0069	0.0680
IV	1.4933	-0.0142	0.0067	0.0064	0.0657
V	1.5059	0.0035	0.008	0.0068	0.0670
VI	1.4475	0.0508	0.0099	0.0061	0.0650

Table 5.10: CASE D: NACA16010 wing concentrated weights properties Runyan and Sewall (1948)

Parameters	c	b	AR	λ	μI_{cc}	EI_{cc}	GJ	c_{CG}	c_{EA}
Unit	m	m			kgm	kgm^2	kgm^2	m	m
Value	0.2032	1.2193	6	1	7.8E-3	41.17	20.25	0.0923	0.088

Table 5.11: CASE D: NACA16010 wing geometry and structural properties Runyan and Sewall (1948)

Chapter 6

Aeroelastic framework Part IV : Aeroelasticity

Abstract

This chapter deals with the fourth and last part of the experimental evaluation and modification of ASWING. It focuses on the aeroelastic features of the software. Experimental data from the literature have been gathered to evaluate the good prediction of deflections and twists under steady flow and their effect on aerodynamic control surfaces effectiveness. Based on that last case, modifications of the code are proposed to provide better flap/aileron rolling performance predictions. Then, the predictions of torsional and flutter divergence are discussed. The impact of different parameters such as the angle of attack and the position of a nacelle on the latter are discussed. Whirl flutter on a propeller/wing configuration closes the part on dynamic phenomena. The chapter continues with a discussion on the response of a flexible aircraft to a vertical gust and the post-flutter limit cycle oscillations. Finally, the impact of folding wingtip devices on gust alleviation and rolling performances is discussed.

Publications:

Materials from this chapter have been gathered and summarized so that a journal paper could be submitted to AIAA Journal of Aircraft with the title:

R.Jan, J-M. Moschetta and J-P. Condomines, Experimental evaluation of ASWING for preliminary design of flexible aircraft: aeroelastic model, AIAA Journal of Aircraft, 2024.

This paper will be published after the PhD manuscript would have been published so that the complete evaluation work can be cited in the paper.

Contents

Nomenclature

b	m	wing span
c	m	chord
cl_α		2D linear lift coefficient slope
$V,\ V_\infty$	m/s	Freestream velocity
AR		Aspect Ratio
$\lambda = \frac{c_t}{c_r}$		taper ratio
$(cl_{min},\ (cl_{max})$		minimum and maximal 2D lift coefficient
C_L		3D lift coefficient
C_M		3D pitching moment coefficient
α	*rad or degree*	angle of attack
$\frac{\partial C_l}{\partial \delta_F}$		Rolling moment induced by δ_F
$\frac{\partial pb/2V}{\partial \delta_F}$		helix angle induced by δ_F
$\frac{\partial c_m}{\partial \delta_F}$		linear pitching moment shift due to δ_F
$\frac{\partial \alpha_0}{\partial \delta_F}$		linear zero lift angle of attack shift due to δ_F
EI_{cc}	Nm^2	linear bending stiffness about c-axis
GJ	Nm^2	linear torsional stiffness
EI_{nn}	Nm^2	linear bending stiffness about n-axis
EI_{cn}	Nm^2	linear bending cross-stiffness
EI_{cs}	Nm^2	linear n-bending/torsion coupling stiffness
EA	N	linar extension stiffness
GK_n	N	linear n-shear stiffness
(c_{EA}, n_{EA})	m	elastic axis local position in the csn frame
(c_{TA}, n_{TA})	m	tension axis local position in the csn frame
(c_{CG}, n_{CG})	m	center of gravity axis position in the csn frame
M_W	kg	concentrated weight mass
I_W	kgm^2	concentrated weight inertia
r_W	m	concentrated weight equivalent radius of gyration
d_W	m	concentrated weight cg distance to the elastic axis
m	kg/m	linear mass
I_{cc}	kgm	linear inertia about c-axis
I_{nn}	kgm	linear inertia about n-axis
(c_{CG}, n_{CG})	m	center of gravity local position in the csn frame
ΔV	m/s	relative speed to the flutter one (positive above)
T_e	s	time marching sampling time
$\Delta R_y,\ \Delta\theta$	*m and rad*	relative tip position and twist
Λ	*degree*	folding wingtip hinge angle
V_g	m/s	vertical gust speed
$\theta_R\ \theta_L$	*degree*	Right and Left folding wingtip angle
ϕ	*degree*	bank angle

Résumé du chapitre en français

Dans ce chapitre nous abordons la dernière partie de ce travail de validation expérimentale d'ASWING. Celle ci se concentre sur les fonctionnalités d'analyses de phénomènes aéroélastiques. Ici aucun rappel théorique n'est fourni, le document se concentre sur la présentation de cas experimentaux retenus. L'évaluation commence par la présentation de phénomènes aéroélastiques stationnaires. Les déformées et gauchissements sous écoulement d'une aile de faible allongement sont présentés. Trois cas sont étudiés présentant différents termes de couplage en raideur. Par la suite, l'étude de l'efficacité de gouvernes aérodynamiques et leur vitesse d'inversion sur une aile trapézoidale de faible alongement est présentée. Par la suite les phénomène dits dynamiques sont étudiées. Le même jeu de donnée que pour les déformées sous écoulement est utilsée pour évaluer la bonne prédictions des vitesses de flottement et de divergence en torsion. L'effet de l'angle d'attaque sur leur apparitions prématurées est aussi discuté. Les différents travaux de littérature ayant fait état d'une validation d'ASWING de ce genre sont également rappelés pour consolider la démarche. Par la suite un autre jeu de données est utilisé pour mettre en avant l'impact de la position latérale et longitudinale d'une nacelle ou d'un réservoir externe sur l'apparition prématurée ou retardée du flottement. Un dernier cas de mise en flottement est discuté. En particulier ici, le phénomène de mise en flottement par effet de précession. Une aile de faible allongement munie d'un ensemble nacelle/hélice à son extrémité est utilisée pour apprécier la bonne qualité de prédiction d'ASWING de la vitesse de mise en flottement. Le lecture se poursuit avec une présentation des phénomènes aéroélastiques instationnaires. A savoir la réponse d'une structure à une rafale de vent verticale. Jusqu'à présent, n'ayant pas réussi à trouver de données expérimentales, une étude effectuée sur un aéronef commercial type 737 est présentée. Par la suite le banc sur les déformées statiques est une dernière fois réutilisé pour l'étude d'oscillations de cycle limites (LCO). Ces dernières étant nombreuses et tirant leur causes de différents phénomènes physiques, il est question ici, de l'effet des efforts structuraux non-linéaires apportant une légère marge de stabilité à la divergence en flottement. Ce dernier cas conclut l'évaluation des fonctionnalités aéroélastiques d'ASWING. Le document est complété par l'étude de saumons à charnières libres ou élastiques. Deux études expérimentales ont été utilisées pour apprécier les performances d'ASWING sur la prédiction des effets de ces dispositifs sur la réponse d'une aile à une rafale verticale et sur ses performances en roulis.

Conclusions générales:

En premier lieu nous pensions au vu des résultats de validation sur le modèle structure (Part III), qu'ASWING présenterait de faible performances sur des géométries de faibles allongement. Or ce fut tout l'inverse, quelques soient les cas présentés dans ce document, ASWING présente de très bonnes performances de prédictions, hormis sur la prédictions de l'effet de l'angle d'incidence sur la mise en flottement et les oscillations de cycle limites. De même ASWING semble capturer correctement l'effet de saumons à charnières élastiques ou libres sur les performances de mécanique du vol d'un aéronef. En ce sens et à la lumière des résultats obtenus, ASWING s'avère être un excellent outil de pré-dimmensionnement et d'analyse d'aéronef flexible avec ou sans les modifications présentées dans les 4 derniers chapitres. Son choix est donc adapté pour ces travaux de thèse.

6.1 Introduction

With the increasing need for aircraft to minimize their carbon footprint, the first vector of aerodynamic performance improvements is the increase of the wingspan. Indeed, this tends to reduce the vorticity of the wing tips inducing the lift-induced drag (accounting for the biggest contribution to drag). Or a higher aspect ratio geometry is generally more flexible, thus raising new issues. Those aircraft are therefore much more likely to encounter aeroelastic phenomena in their flight envelope. Among them, torsional divergences and flutter, reduction of the aerodynamic control surfaces effectiveness up to the reversal behaviour can be mentionned. In addition, the position of a nacelle or an external tank on a wing can drastically change its aeroelastic response. In the same way, a rotating propeller, or an inertial defect of a rotating machine (engine, turbofan etc) can lead to a premature flutter of the structure. All these phenomena are of first order from an aeronautical safety point of view and define the upper bound of the aircraft flight envelope. They are generally defined by critical speeds (flutter, divergence and control reversal speed). In this sense, having a rapid diagnostic and analysis tool that allows the accurate prediction of these phenomena is essential in the modern aircraft design chain. The recent Aura Aero crash (BEA report n C-2022-06-A) caused by flutter during a high load factor manoeuvre, unfortunately, recalls the need for such predesign tool.
Other aeroelastic phenomena of interest can be mentioned, such as deformation and twist under steady flow, which provide interesting insight on the aerodynamic performance of a wing once deformed at different flight conditions. The local modification of the twist can also give information on the stall and the ailerons unusability (washout). Again from an aeronautical safety point of view, the intensity of turbulence and gusts encountered during flights is likely to increase due to climate change. In this sense, having a tool that can predict the aeroelastic response of an aircraft to a gust or turbulence is a real asset. In particular, the root bending moment time response is often of interest in terms of structural failure forecast. Moreover some more fundamental phenomena can be of interest, such as post-flutter limit cycle oscillations. Another issue arise by airline companies is the use of folding wingtip to reduce airport taxes rising with the aircraft span. It turns out that those devices can bring benefits to the behaviour of the aircraft in flight Castrichini et al. (2016 and 2017), Cheung et al. (2017, 2018, 2020 and 2022) and Healy et al. (2022c, 2022b, 2022d and 2022a). Having a tool allowing the fast study of those devices is also of interest to an aircraft manufacturer.
ASWING integrates and proposes the study of all the phenomena mentioned above. As a consequence, this chapter is the fourth and last part of an experimental evaluation work of ASWING. This one focuses on the evaluation of the prediction quality of the aeroelastic phenomena mentioned earlier.

6.2 Experimental evaluation

This section presents the evaluation of the aeroelastic features and the folding wingtip devices of ASWING. It focuses first on aeroelasticity phenomena. The steady phenomena are addressed first with the wing deflection and twist as well as ailerons/flap effectiveness under steady flow. Then comes the phenomena involving the dynamics of the structure, namely flutter, torsional divergence, whirl flutter, the impact of the angle of attack and the position of a nacelle on those. The aeroelastic part ends with the unsteady phenomena prediction evaluation namely, the response to a gust and the post-flutter limit cycle oscillations. In a second time, the folding wing tip devices are studied, in particular their impact on the rolling performance of a wing and their ability to effectively alleviate a gust. As for the previous evaluation part, the experimental cases have been chosen as stressful as possible for the theoretical model. Most of the cases present then low aspect ratio wings.

6.2.1 Steady : tip deflection and twist

The first feature to be evaluated is the steady tip deflection and twist predictions. The latters are of interest in the design of an aircraft as they provide relevant intel. For example, capturing them correctly can give an insight on their consequences on aerodynamic performances such as lift-to-drag ratio. The total lift stall being of interest to define the flight envelope lower bound can be predicted. Secondly, it is possible for a given flight speed and angle of attack to evaluate the maximum extensional and shear strains locally on the structure implied by the aerodynamic loads. Fibres strain computation can provide insight into when structural failure will occur. Sometimes before the flutter and divergence phenomenon. Finally lifting surface washout can be investigated with this feature. The local stall can be computed and structural modification can be implemented to optimize its appearance and spanwise position so that, the local section where the control surfaces are (flap, ailerons) do not stall first. To evaluate this feature, two experimental benches have been used that are a low and moderate aspect ratio

straight wing. The work of Dunn 1992 (presented to the community in Dunn and Dugundji 1992) has been used for the low aspect ratio wing. Note that the experimental bench presented in the latter is used to evaluate other features which are: flutter and divergence speed, flutter boundaries and limit cycle oscillations. For the moderate aspect ratio, a more modern data set from Avin et al. (2022) has been used.

Experimental bench # A-1:(low aspect ratio)
The wing is made of a flat 6-plies composite plate with styrofoam fairings glued to it, to reproduce a NACA0012 shape. In total 3 wings were built with 3 different composite layouts involving different stiffness coupling. The latter has been adapted to the ASWING formalism and derived in Table 6.7. Each wing aspect ratio was 4 making them excellent stress cases for the ASWING model. Each wing was cantilevered to a rotating aluminium clamping device as depicted in figure 6.1. The latter playing also the role of a plane of symmetry. It was reported by the author that the foam pieces were contributing a lot to the torsion stiffness, the elastic and tension axis was reported to lie on the 0.4 and 0.35 chord lines. The tests were performed in the MIT Department of Aeronautics and Astronautics Acoustics open throat 1.5 by 2.3 meters wind tunnel. The speed range was varying from 0 to 30 m/s. The level of turbulence in the wind tunnel was not reported. For each wing, the tip deflections and twist measurements were captured for 4 different angles of attack ($\alpha = 1,\ 5,\ 10,\ and\ 15°$) on the speed range until divergence or flutter occurs. Near those phenomena, experimental data was reported to become difficult to track. Higher error bars appear in consequence on the further plots. Among the composite layouts, an uncouple one ($[0_3/90]_S$)[1] was presented as a baseline case while 2 others were presenting positive and negative torsion/bending coupling ($[+15_2/0_2]_S$ and $[-15_2/0_2]_S$).

Numerical bench # A-1: (low aspect ratio)
In ASWING, each bench has been reproduced with the laminates properties of table 6.7. As the wing was anchored vertically to a symmetry plane, the ground flag for the solid surface was activated (see *section 4.5* of Drela-2009). Two numerical sensors were placed at the wing tip, at the leading and trailing edge. Both were capturing the tip deflection. The geometric tip twist was directly provided by ASWING OPER Menu. Forty circulations and 40 structural node variables clustered with a cosine function were enough to ensure converged predictions. An XFOIL analysis of the NACA0012 at the corresponding Reynolds number has been fulfilled leading to the retain parameters $c_{l,\alpha} = 5.73$, $c_{l,min} = -1.1$ and $c_{l,max} = 1.1$. The drag polar were neglected as assumed to have a very small impact on the structural deformations.

Results # A-1: (low aspect ratio)
Figure 6.2 (a) to (f) present a comparison between ASWING predictions and Dunn and Dugundji's experimental data (1992 and 1992) for each laminate considered in his work. The same x and y axis scales have been used for all the figures to clearly highlight the benefit or not of the layouts.
For the $[0_3/90]_S$ layout, (figure 6.2 a and b) ASWING seems to capture quite well the tip deflection and twist for moderate speed. Near maximum ones, it tends to underestimate the twist. Moreover, at high angle of attack ($\alpha = 10°$ and $15°$), the tip deflections are overestimated no matter the speed. ASWING has an embedded stall function (see *section 5.7* Drela-2009 documentation), however, it only damps the linear lift slope after the stall occurs. It can not catch the lift drop and slightly overestimates it so the discrepancies on the tip deflections.
For the $[+15_2/0_2]_S$ layout (figure 6.2 c and d), the predictions are in excellent agreement with experiments no matter the speed or the angle of attack. ASWING clearly captures the effects and benefits of a positive bending torsion coupling stiffness. The structure tends to reduce the tip angle of attack. This in effect will lead the wing tip to stall much later reducing the ASWING prediction discrepancies.
For the $[-15_2/0_2]_S$ layout (figure 6.2 e and f), because of the negative bending torsion coupling stiffness, the structure tends to rise the wing tip angle of attack as depicted on figure 6.2 (f), this local stall occurs very quickly even at low root angle of attack. ASWING looses rapidly the track with experiments but clearly capture the tendency imposed by the composite tailoring.
Overall, ASWING shows good agreements with Dunn's steady tip deflections and twist measurements (1992). It becomes weaker at high angle of attack $\alpha = 15°$ (post-stall). More importantly, it captures well the structure tailoring impact which is mandatory in the case of an aircraft design. Last comments must be made on those results. The maximum tip deflection witnessed was around 0.3m ie 55% of the wing span. This can be nearly considered as high deflections. Or in the structural part of this evaluation work (Part III), huge discrepancies were witnessed for static tip load deflections. For the maximum applied mass, the tip deflection was not exceeding 30% or the span. It seems from the aero-elastic evaluation that the tip load test is very

[1]This notations means that the composite beam is made of sandwich of different fibers with various orientation. Their orientation are defined relatively to the spanwise axis.

conservative. In reality, the aerodynamic lift being quasi elliptically distributed along the span, induced structural loads much more smoothly scattered. The structural model is thus less sensitive to high tip load leading to less discrepancies. In consequence, tip load deflection tests are not the most appropriate for aero-elastic code separate evaluation as they overestimate the real loads that could be applied on a wing.

Experimental bench # B-1: (moderate aspect ratio)
The steady tip and twist deflection is refined with the experimental bench of Avin et al. (2022) denoted as Pazy. The wing is straight with an aspect ratio of 5.5. The structure is made of a flat aluminium plate. The latter is wrapped with a series of plastic ribs and and shell to recover the shape of a NACA0018. The wing was placed in the Technion low-speed wind tunnel. Tip displacement and twist were measured at various speed and angle of attack. For more details on the measurement devices please refer to the author's work.
Numerical bench # B-1: (moderate aspect ratio)
The Pazy wing bench was reproduced in ASWING using the structural parameters provided by Riso and Cesnik (2023). A numerical sensor was placed at the tip of the wing around the mid-chord.
Results # B-1: (moderate aspect ratio)
Figures 6.3 (a) to (d) present the ASWING prediction against Avin et al.'s experimental measurements. Figures 6.3 (a) and (b) present the tip displacement and twist against airspeed for a root angle of attack of $\alpha = 5°$ while figure 6.3 (c) and (d) present the tip displacement and twist against airspeed for a root angle of attack of $\alpha = 7°$. For tip deflection, ASWING shows good agreement with the experiment until large amplitude. For $\alpha = 5°$ predictions are weaker. For tip twist, the prediction errors vary quite a lot mostly due to the difficulty of Avin et al. to measure it. Nevertheless, predictions are satisfactory. Finally, the ASWING predictions have been compared to the ones of UM/NAST provided by Riso and Cesnik (2023). As it can be seen similar results are obtained. The UM/NAST more sophisticated structural model does not show any better performances than ASWING except at very large amplitude when $\alpha = 5°$. In conclusion, ASWING is able to capture correclty the steady aeroelastic behaviour of the Pazy wing

6.2.2 Steady : ailerons effectiveness and reversal speed

Aerodynamic control surfaces (ailerons, flaps etc) can be implemented in ASWING. The latter, when deflected modify the lift and pitch moment locally, deforming, in consequence, the structure. This change in the wing or aircraft shape can drastically impact the flap/aileron effectiveness up to a point where reverse behaviour is witnessed. The latter is mentioned in the literature as reversal speed. An inverse behaviour is not necessarily dangerous a priori as long as its appearance is known. However, usually, the reversal speed is very close to aeroelastic divergence phenomenom such as flutter and divergence. For a pilot, all those 3 phenomena set an upper bound limit to the flight envelope not to be exceeded. In consequence, the experimental study of Cole (1951) has been used to evaluate ASWING on this feature. The authors investigated the rolling moments and free rolling rate due to aileron deflection for various speed and flap geometries.

Experimental bench # C:
Investigations were done on 2 different wings : a straight and swept back wing. In this work, only the straight wing will be considered as reported as the worst case. The tests were performed in the F.K Kirsten wind tunnel with an 8 by 12 feet (2.4 by 3.7 meters) test section. The wing considered was straight and tapered. Its span, taper ratio and aspect ratio were respectivelly $b = 4ft$ (1.2m), $\lambda = 0.45$, $AR = 8$. The airfoil section was a NACA 63A012. The wing geometry is depicted in figure 6.9. Several ailerons size were tested. The hinge position was always fixed at 70% of the chord from the leading edge. However, the flap spanwise length could vary in the next interval 0.2, 0.4, 0.6, 0.8 and 0.95 the half span.During the tests, 2 mounts were considered.
Mount 1: the wing is attached to a balance and cannot roll. For several wind speeds the flaps were deflected and the roll moment C_l was measured with a balance and reported. Results were presented as the roll moment induced by a deflected flap $\frac{\partial C_l}{\partial \delta F}$.
Mount 2: The wing was free to roll. Over the same speed range, the rolling rate has been measured for every flap configuration. The author presented the results as the helix angle induced by a flap deflection $\frac{\partial pb/2V}{\partial \delta F}$ against the dynamic pressure q_∞. The helix angle is represented on the right side of the figure 6.9. Note that p is the wing rolling rate. The latter data is presented in this way as it has been reported by the authors to vary linearly with the dynamic pressure. It is also much more convenient for prediction comparisons. Finally, the authors experienced flutter earlier for configuration with

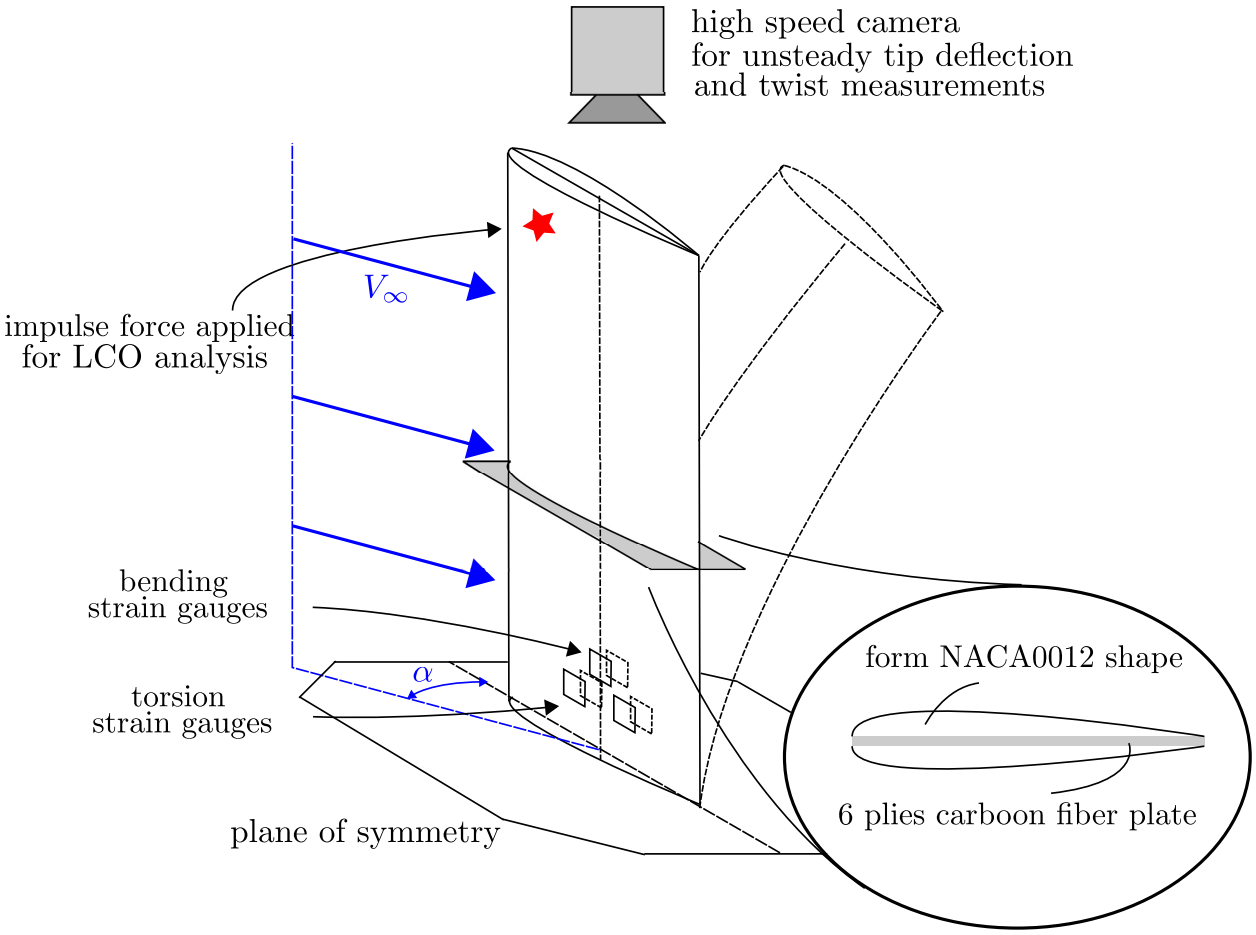

Figure 6.1: Steady tip deflection and twist, flutter and divergence speed, limit cycle oscillations Dunn's experimental bench (1992)

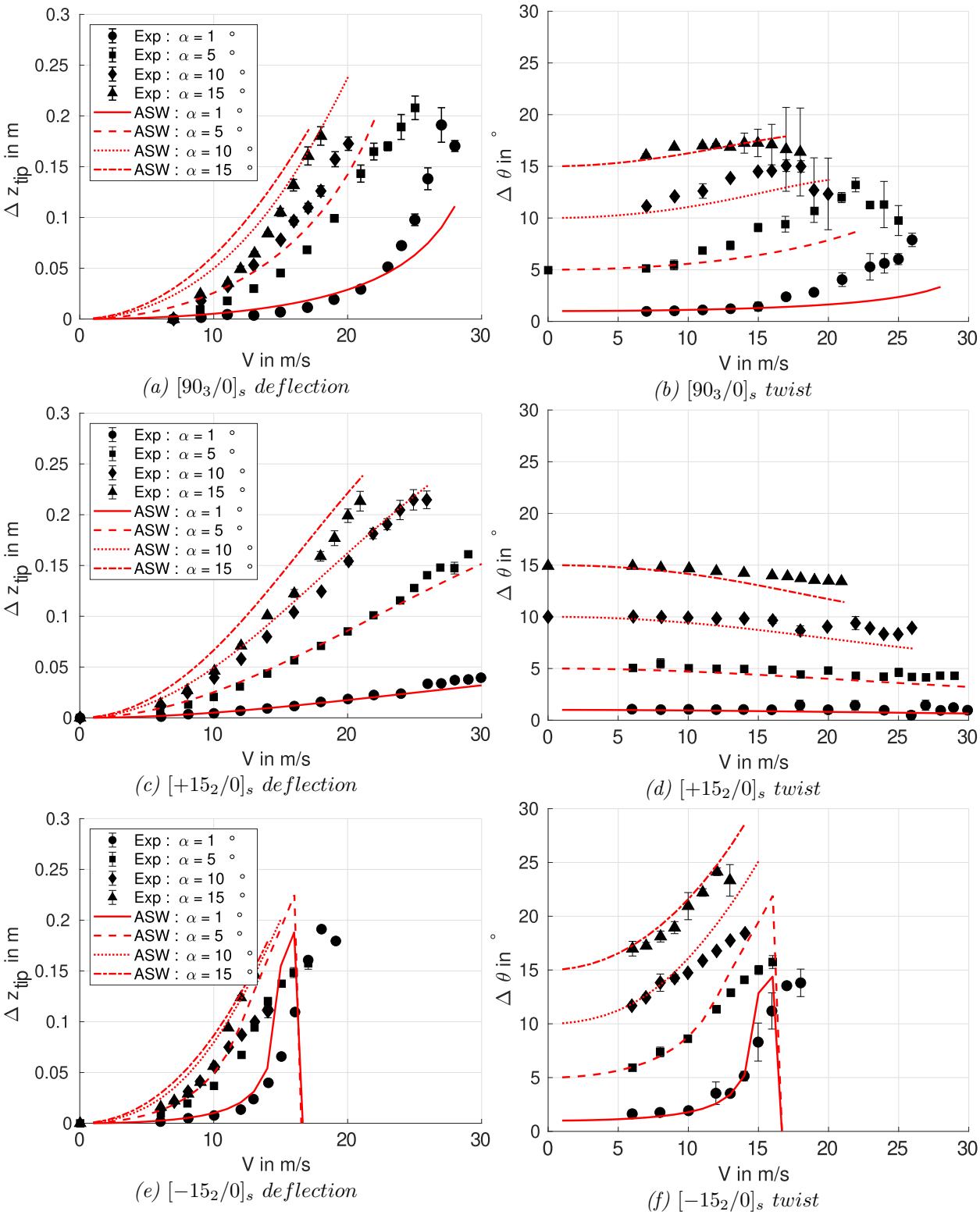

(a) $[90_3/0]_s$ *deflection*

(b) $[90_3/0]_s$ *twist*

(c) $[+15_2/0]_s$ *deflection*

(d) $[+15_2/0]_s$ *twist*

(e) $[-15_2/0]_s$ *deflection*

(f) $[-15_2/0]_s$ *twist*

Figure 6.2: Time average tip deflection and twist in function of the flight speed and angle of attack. ASWING 5.96 predictions comparison with experimental data Dunn (1992)

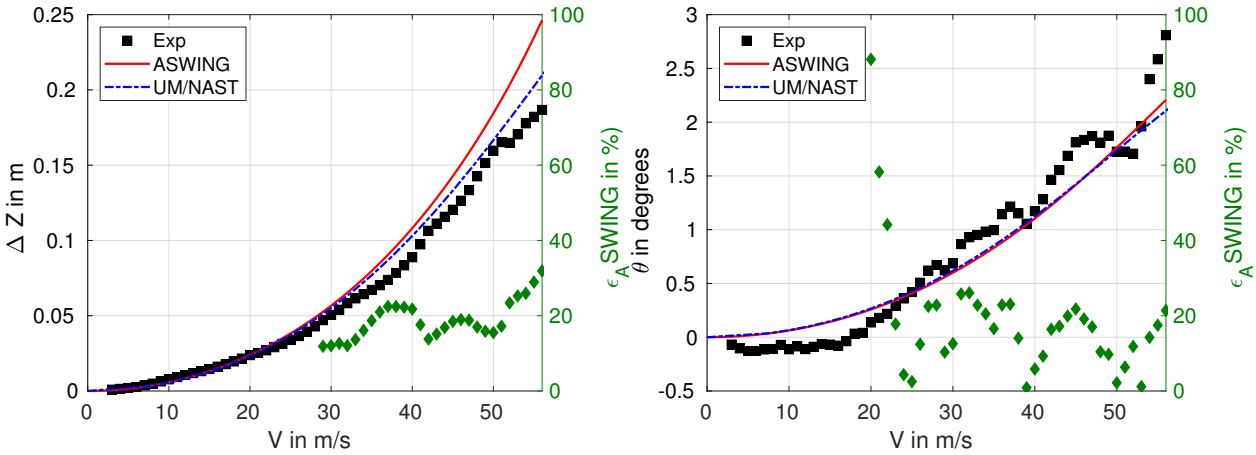

(a) $\alpha = 5°$ *tip delfection*

(b) $\alpha = 5°$ *tip twist*

(c) $\alpha = 7°$ *tip delfection*

(d) $\alpha = 7°$ *tip twist*

Figure 6.3: Pazy wing : tip deflection and twist at various angle of attack. ASWING and UM/NAST (Riso and Cesnik-2023) UMNAST predictions comparison with experiments Avin et al.-2022

larger flaps so the number of measurements decreases with the flap length increasing.

Numerical bench # C:
Numerically, the NACA63A012 2D polars were computed with XFOIL. As the speed in the experiments were varying, the analysis was performed over the equivalent range of Reynolds number (Re = 300-600E3). Then $\alpha_0 = 0.0°$, $cl_\alpha = 5.66$, $\partial c_l/\partial \delta F = 0.0581$, $\partial c_{m,0}/\partial \delta F = -0.0107$ were used. A benefit of this evaluation case is to introduce an ASWING modification. An inner function has been implemented to take into account the Reynolds number effect on the flap and airfoil polars directly in the loop. At each chordwize location, a local Reynolds number is computed, then the flap derivatives is interpolated accordingly thanks to a lookup table. The latter provides the variation of flap derivatives with the Reynolds number. Here only 2 points have been used. For elliptical wings, where the Reynolds can reach 0 towards the tip, the flap derivatives is clipped to lower value of the look-up table. This modification is denoted as ASWING-m. This change was motivated by the important variation of $\partial c_l/\partial \delta F$ and $\partial c_{m,0}/\partial \delta F$ on the speed range ie (16% and 5%). Note that for ASWING 5.96 constant values taken at the highest Reynolds number were used as the main objective was to find the reversal speed. ASWING-m was fed with the polars computed from the XFOIL analysis. The torsional and bending stiffness of the wing varies cubically with the spanwise coordinate so they can not be provided here. Please refer to *figure 10* of Cole (1951) for their values. Unfortunately, the mass and inertia distribution were not provided in the document so rolling accelerations could not be compared with the experimental data.
Results # C:
ASWING 5.96 and ASWING-m predictions for $\frac{\partial Cl}{\partial \delta F}$ are presented against experimental measurements on the figure 6.5(a). The advantage of taking into account the variation of the aerodynamic parameters with the Reynolds number is clearly highlighted by the green lines. Predictions tend to be equivalent with the dynamic pressure rising. For the sake of clarity, only ASWING-m $\frac{\partial pb/2V}{\partial \delta F}$ predictions are presented on figure 6.5(b). Linear slopes were computed and compared to the experiment's. ASWING-m shows good agreement with the experiments no matter the size of the ailerons, with a mean slope error below 8%. Note that ASWING 5.96 was not that far with a 12% error. The reversal speed can be identified from the helix angle plots when the latter crosses the 0.0 y-axes. Prediction errors were in the same range as the slope's. Note that the modification is not a breakthrough improvement, but it does bring comfort of use, avoiding computing aerodynamic parameters for each condition that has be investigated. The aerodynamic polars must be generated only once on the first-guess flight envelope (large enough). Thus ASWING 5.96 ASWING-m can be used to predict the flaps effectiveness and their reversal speed.

6.2.3 Dynamic: flutter and divergence Speed

This section introduces the evaluations of the first dynamic aeroelastic phenomena. First, a clarification must be made between flutter divergence and "regular " divergence also known as torsional divergence. The first involves the structural stiffness and inertia while the second is only the stiffness. The aerodynamic loads vary quadratically with the flight speed, there is a moment when the latter is too important to be stabilized by the structure alone. The main difference between flutter and torsional divergence is the structural behaviour. One has an exponential harmonic response (flutter) while the second an exponential only (divergence). The harmonic response is mainly due to the inertia loads of the structure. Numerically, flutter and divergence speed are usually computed through modal analysis. A flutter response involves a complex mode with a positive real part while the divergence implies a strictly positive real mode. Flutter and divergence phenomena are very dangerous are they necessarily lead to structure failure, which can be delayed by active control devices and optimal structure tailoring. Flutter and divergence speed constitute an upper bound of the aircraft flight envelope and must not be exceeded at all costs. Knowing their value is thus mandatory during the predesign process. To evaluate ASWING flutter and divergence predictions, experimental data from Dunn (1992 and 1992) have been used.

Experimental bench # A-2:
The same bench as in the steady tip deflections and twist is used. Strain gauges were fixed to the wing (cf figure 6.1) and connected to a numerical oscilloscope mainly to report the flutter and structural modes frequencies. The speed was incrementally increased until the flutter appeared and was reported.

Numerical bench # A-2:
The same numerical benches were used. The flutter and divergence speed analysis were conducted in 2 steps. First, a steady analysis at each flight speed must be performed in the OPER menu, so that the Jacobian matrix could be further analysed. Please refer to *section 13* of Drela (2008) for more details. Then in the MODE menu, the modal analysis were

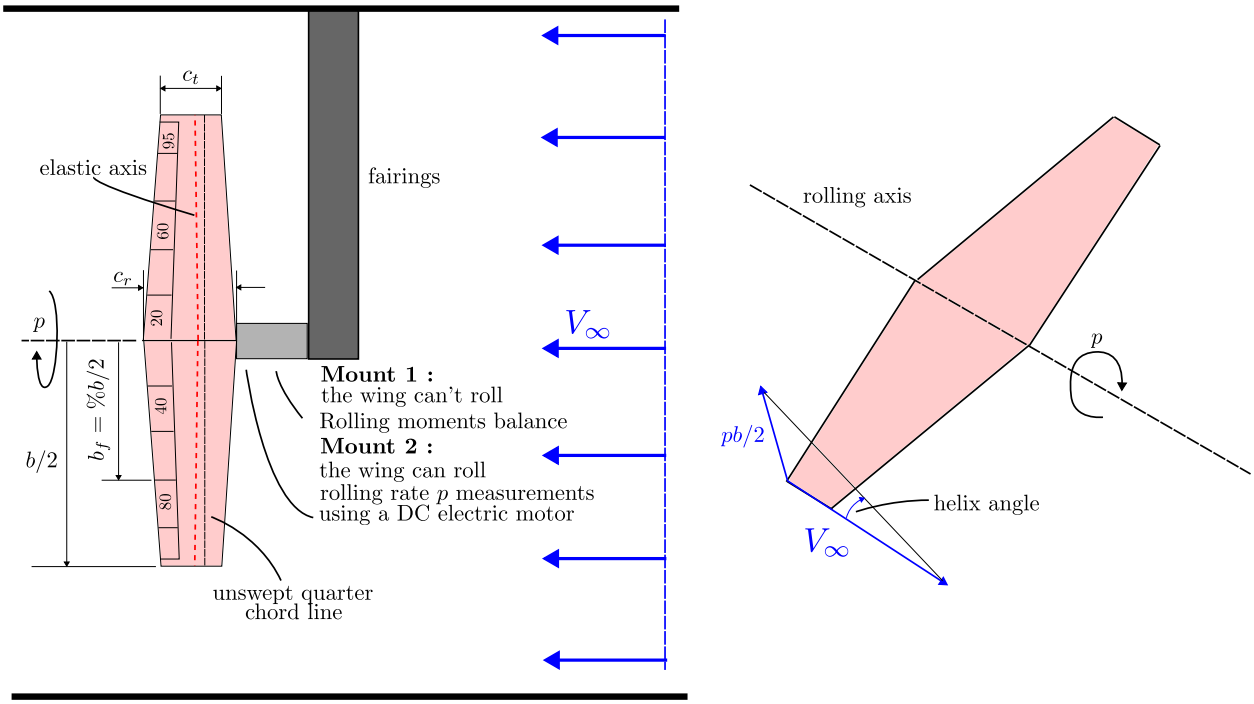

Figure 6.4: Experimental bench of Cole (1951)

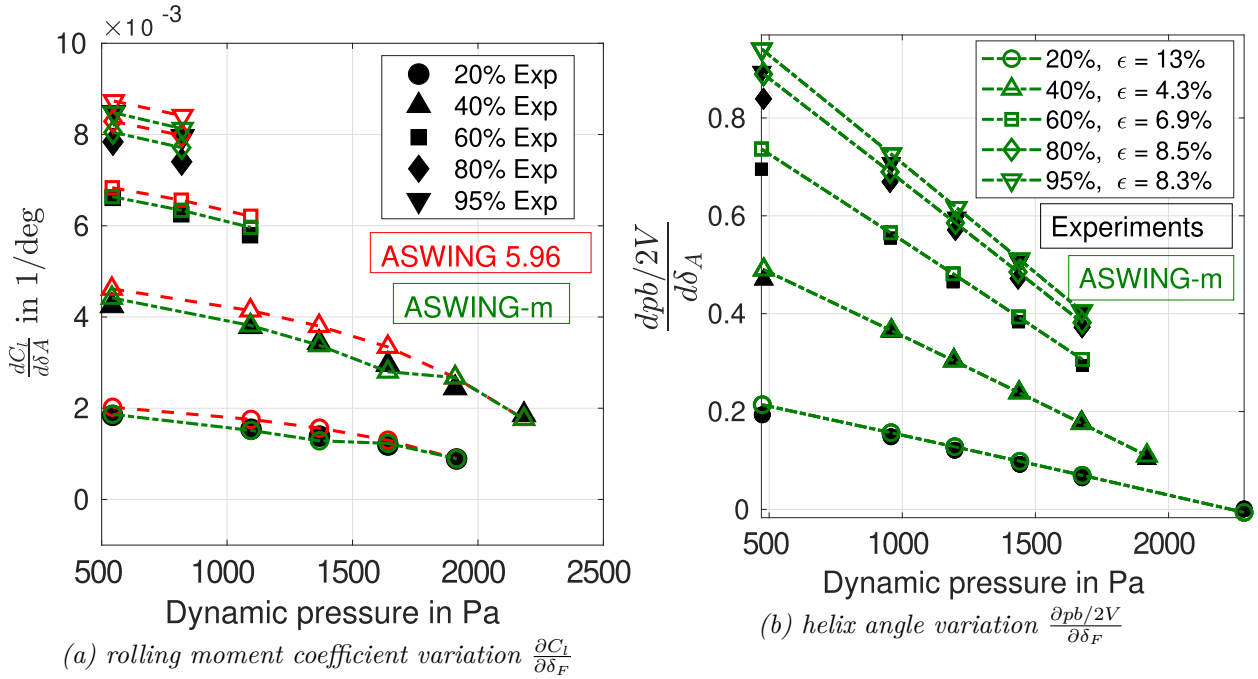

(a) rolling moment coefficient variation $\frac{\partial C_l}{\partial \delta_F}$ *(b) helix angle variation* $\frac{\partial pb/2V}{\partial \delta_F}$

Figure 6.5: Ailerons effectiveness and reversal speed predictions. Comparison with experiments from Cole (1951)

performed in order to spot the flutter and divergence modes. A first analysis was performed to have a coarse idea of the flutter and divergence speed. Secondly, the speed range was refined to precisely spot the desired intels.

Results # A-2: Each laminates modal analysis are presented in figure 6.5. The unstability zone has been highlighted in red. On each row, the analysis presents the modes in the complex plane, the damping factor and the frequency of the first mode in function of the flight speed.
The laminate $[0_3/90]_S$ is characterized by very close divergence and flutter speeds as highlighted by the middle figure 6.5-(a). The flutter response is dominated by the first torsional mode. From the frequency plot, no coalescence is clearly identified. The divergence comes from the first bending mode.
The laminate $[+15_2/0_2]_S$ clearly shows the benefit of a positive torsion/bending coupling. The flutter speed is still characterized by the first torsion mode but slightly delayed (10% higher) as depicted in figure 6.5-(b). The divergence speed occurs at a much higher speed around 100 m/s (3 times the flutter speed). From the complex plane damping plots, the torsion mode tends to be a "pure" divergence mode until its damping coefficients reach -1 becoming a real unstable mode.
The laminate $[-15_2/0_2]_S$, as expected shows the drawbacks of a negative bending coupling term. Divergence speed occurs before the flutter speed. It was difficult as for Dunn to clearly identify the nature of each mode, so the change in the figure 6.5-(b) legend. Note that the first mode was the first to lead to divergence while the third is leading to flutter later.

Experimentally it was reported by Dunn that the divergence speed of the $[+15_2/0_2]_S$ could not be detected as it was over the wind tunnel maximum speed (50 m/s). Also as $[-15_2/0_2]_S$ was reported to be extremely unstable after the divergence speed occured, the flutter speed could not be evaluated. The nature of each divergence was reported based on video recording and observation. The ASWING predictions against experimental data were reported in Table 6.1 and 6.2. A comparison with Dunn's high-order finite element model is also presented. Overall ASWING shows excellent agreements with the experiments and better performances than Dunn's model except for the flutter frequency of the $[0_3/90]_S$ laminate. Despite the low aspect ratio of the wing considered, ASWING provides excellent results regarding the flutter and torsional divergence prediction.

Other work from the literature : Work from the literature can be invoked to robustify the conclusion on the flutter speed prediction capacity of ASWING. Variyar et al. for example did an evaluation against low aspect ratio configurations with a high sweep angle (Goland and Agard) showing similar predictions performances. Love et al. compared the ASWING and NASTRAN ("higher" fidelity) modal response and flutter speed predictions of a high aspect ratio flying wing. Again good performances were witnessed. Colas et al. presented a comparison between ASWING and NASTRAN of the flutter speed and frequency at different flying altitudes on a HALE aircraft (High Altitude Long Endurance). Excellent prediction performances were witnessed on the high-aspect configuration.

6.2.4 Dynamic: flutter boundaries

Dunn and Dugundji also studied the impact of wing incidence on wing flutter appearance. Figure 6.7 shows the variation of the flutter or divergence speed with the angle of attack. The predictions of ASWING and Dunn's model are compared to the experimental data of the same author. Note that the ASWING predictions did not all converge especially on the $[0_3/90]_S$ and $[-15_2/0_2]_S$ laminates. Indeed, a bounce was identified of the flutter modes against the imaginary axis probably due to a stiffening of the structure in the ASWING structural model for high amplitude deflections. Obviously, that stiffening is not consistent with the experimental observations. As we have seen, the layout $[+15_2/0_2]_S$ tends to delay high amplitudes of deflection, so the same phenomena have not been witnessed, and the flutter speed could be computed on the considered angle of attack range. On the three layouts considered, for low angle of attack, ASWING captures well the flutter speed decrease and has similar predictions quality as Dunn and Dugundji's model. For the $[0_3/90]_S$, ASWING and Dunn and Dugundji's finite element model present similar predictions and can be considered as consistent with experiments until $\alpha = 10°$ which is the stall angle of attack. After that value, both models are weak to predict the flutter. Thus for the flutter boundaries analysis, higher aspect ratio geometries are recommended in light of the non-satisfying results.

As Dunn and Dugundji's bench is quite stressful for the theoretical model (low aspect ratio), The Pazy wing bench from Drachinsky et al. (2022) has been used to see if ASWING is able to capture the flutter boundaries of a moderate aspect ratio wing. Regarding the bench, a rectangular straight wing of an aspect ratio 5.5 has been placed in the Technion low Reynolds number wind tunnel. It was mounted vertically (denoted as unload case) and horizontally with a plane of symmetry (loaded case). The angle of attack of

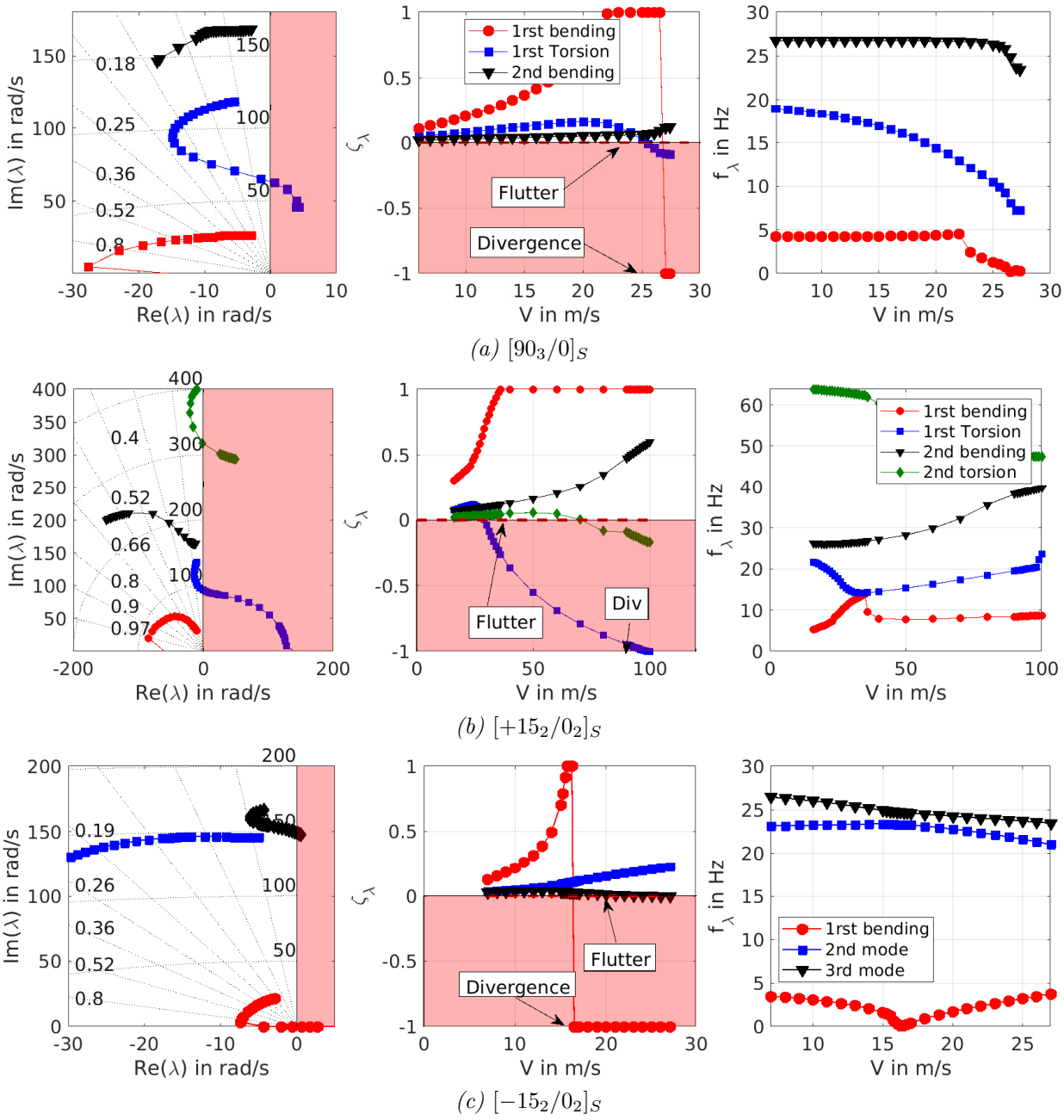

Figure 6.6: Modal analysis of Dunn and Dugundji's layouts. Flutter and divergence speed, modal coalescence identification

Layup	$V_{f,exp}$	$V_{f,theo}$	$V_{f,ASW}$	ϵ_1 in %	ϵ_2 in %	**Remark**
$[0_3/90]_S$	26.5	28.27	25.5	+6.7	-3.8	N.T.R
$[+15_2/0_2]_S$	29.0	26.9	29	-7.2	0.0	N.T.R
$[-15_2/0_2]_S$	NR	35.0	25	NC	NC	**Divergence**
Layup	$f_{f,exp}$	$f_{f,theo}$	$f_{f,ASW}$	ϵ_1	ϵ_2	**Remark**
$[0_3/90]_S$	12	11.9	9.89	-0.83	-17.58	N.T.R
$[+15_2/0_2]_S$	15.0	11.6	14.89	-22.6	-0.73	N.T.R
$[-15_2/0_2]_S$	NR	13.3	23.7	NC	NC	**Divergence**

Table 6.1: Flutter speed and frequency measurements, modal analysis comparison between Dunn's results and ASWING 5.96. (N.R = not reached, N.C = not computed, N.T.R = nothing to report)

Layup	Experiments	ASWING	ϵ in %
$[0_3/90]_S$	28.20 m/s	27.0 m/s	-4.2
$[+15_2/0_2]_S$	∞ N.R m/s	96	NC
$[15_2/0_2]_S$	18.04 m/s	16.5 m/s	-8.5366

Table 6.2: Torsional divergence speed predictions of the NACA0012 wing (N.R = not reached, N.C = not computed). Comparisons with Dunn's experiments

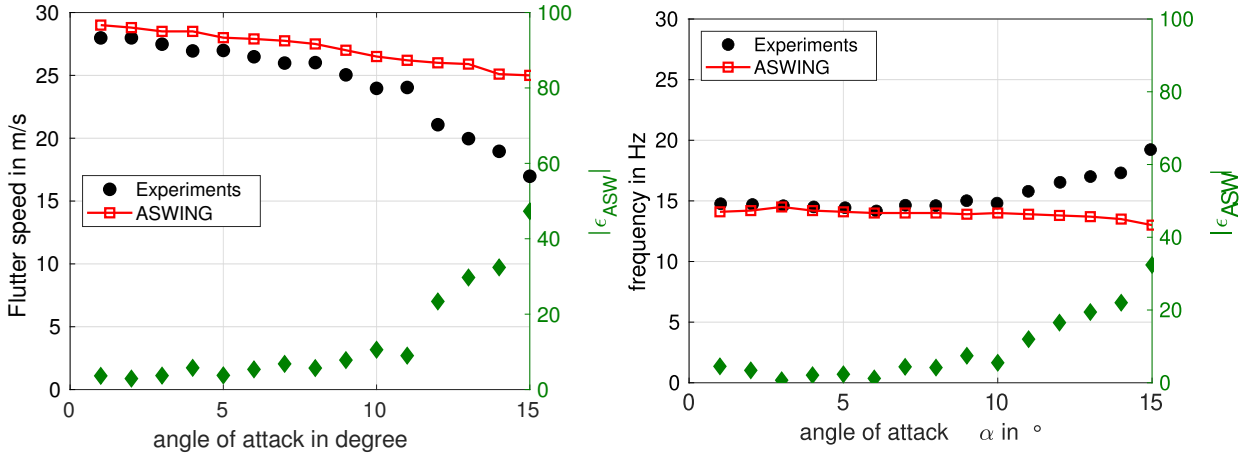

(a) flutter speed

(b) flutter frequency

Figure 6.7: Flutter boundaries of the $[+15_2/0_2]_s$ layout. ASWING predictions against experimental data of Dunn and Dugundji-1992

the wing was fixed at various values, then the wind tunnel speed varied until flutter was reached. The tests were testing sweep up and down of the speed to detect the flutter zone of the Pazy wing and so at each angle of attack. The flutter zone is highlighted in figure 6.8 (a) by the green colour. For more details about the bench, the reader is invited to take a deeper look at Drachinsky et al.'s work. In consequence, the bench was reproduced numerically with ease. The Pazy wing equivalent beam model parameters can be found in the work of Riso and Cesnik (2023). Figure 6.8 (a) presents the ASWING flutter and divergence speed prediction against the experimental data from Drachinsky et al.. From it, ASWING captures well the flutter boundaries no matter the angle of attack of the wing. Table 6.3 presents a more detailed analysis of those results, and compares the ASWING predictions with the one of UM/NAST performed by Riso and Cesnik (2023). From it, ASWING has the same prediction difference as UM/NAST despite its less sophisticated beam model. The aspect ratio of the wing is high enough to make the Euler-Bernoulli beam model of ASWING relevant in this case. The same conclusion can be drawn from table 7.1 for the flutter frequency. No matter the case the ASWING prediction errors are below 7%. The unloaded case flutter and divergence speed predictions are compared to the work of Riso and Cesnik (2023) where the reference data is denoted as SOL 145. Again ASWING shows good agreement with the higher fidelity data with a prediction error below 6% (very close to UM/NAST performances).

For the Pazy wing, ASWING shows good predictions of the flutter speed and frequency as well as the divergence. However Drachinsky et al. specified that the Pazy wing once entered a flutter regime was not diverging and was even going to a stable state after the speed raised enough. Or from the ASWING modal analysis depicted in figure 6.8 (b), the Pazy wing is supposed to diverge between the flutter boundaries as the flutter mode damping ratio is negative. To make sure that ASWING is able to capture this self-oscillatory behaviour (Limit cycle Oscillations), a complete time marching computation of the wing has to be performed. The initial speed of the wing was set up in the flutter boundary, then a small impulsive perturbation was applied (flap deflection). The simulations were run over a significant amount of flutter period to make sure the wing is really in LCO behaviour. Figures 6.8 (c) and (d) present those simulations for $\alpha = 3°$ and $\alpha = 5°$. From them, ASWING predicts that the Pazy wing is indeed in a limit cycle oscillation behaviour between the flutter boundaries and so on each angle of attack. This statement must be clarified. Indeed Drachinsky et al. observed that depending on if the speed was going up or down, the Pazy wing was leaving the LCO regime at a different speed than the one predicted by the modal analysis.

In other words, ASWING predicts well the lower flutter boundary if the speed is going up and caputure well the upper one if it's slowing down. However if the speed is going up, the Pazy wing leaves its LCO regime later than the modal prediction predictions. It means that the LCO involves a non-linear phenomenon that is not captured by ASWING. Our first guess would be the leading edge vortices that can appear in plunging and pitching motion as reported by (Chiereghin et al. 2017). The leading edge vortices can take some time to vanish and represent a source of exogenous input keeping the overall system self exited for a while until the structural and linear aerodynamic damping effects become stronger.

6.2.5 Dynamic: Effect of a Nacelle/-tank's relative position on the flutter speed

Nacelle and tanks can be modelled in ASWING using point masses or slender bodies. They can be rigidly attached to a wing with a pylon. The position and mass properties of a tank or nacelle can have a huge impact on the modal and aeroelastic response of a wing. To evaluate this, the experimental data provided by Runyan and Sewall-1948 were used. Note that this work has already been used in the structural part of this sequel evaluation work (Part III)

Experimental bench # D: The tests were performed in the Langley 4 by 5-foot (1.2 by 1.5 meters) flutter research wind tunnel. The modal response was performed in no flow condition but in the wind tunnel. A straight wing was vertically mounted from the top of the section as shown in figure 6.9. The wing-half aspect ratio was 6 making a good stress test for the ASWING model. The wing geometrical and structural parameters were given in the author's work and have been translated into the ASWING formalism and metric system in tab 6.9. The bending and torsional stiffness were determined experimentally from the static deflection curves of the wing in bending and torsion. Vibrations were recorded thanks to strain gages placed on the wing as depicted in figure 6.9. The gages were connected to a system of bridges/amplifiers cascade to reduce the measurement noise. The frequency report was made on an oscillograph. In total 100 runs have been performed, to be sure that the wing did not get any structural damage from one run to another, a modal response measurement was performed before and after each one of them. In light of the results, the author reported that the wing did not witness any damage during the entire experiment. This was mainly due to the use of wires connected to the wing tip to prevent any high deflections when the wing entered into a flutter. In total 7 weights with different properties were tested but one will have a closer interest in the 7th as its spanwise and chordwise position varies. For a better reading experience, one has denoted weights I-VI the weights 7a-f of the technical note. Those weights have very close mass properties (constant) as depicted in table 6.8. Their index mostly indicates a change in chordwise position. The latter is given as a distance to the elastic axis denoted as d_W as depicted in figure 6.9(b)

Numerical bench # D: In light of the ASWING formalism it is not possible to model a concentrated weight as this one has a non-zero inertia tensor. To do so, one has used a potential mass dipole equally spaced from the concentrated mass centre of gravity by a distance r_W (cf figure 6.9(b)). The punctual mass was half the concentrated's. The distance r_w ie radius of gyration is computed to recover the concentrated mass's inertia. Their numerical values are given in the table 5.10. As the weights were crafted to have a minimum aerodynamic print (symmetrical and slender), I think that using a mass dipole was the best option to virtually recover the behaviour of a concentrated mass. Being said and implemented, the modal analysis were performed following the same numerical protocol described in the previous sections.

Results # D:

In light of the various cases considered here, damping coefficients variation with the flight speed as presented in figure 6.5 will not be presented for the sake of clarity. Instead, the flutter speed and frequency of each case have been summed up in Table 6.6 where ASWING predictions errors are presented. The flutter speed predictions are in good agreement with experiments with a mean error of 6.9 % and a standard deviation of 5 % . The flutter frequency predictions however are not as good with a mean error of 11.6% and a standard deviation of 10%. The most important intel provided by Table 6.6 is that ASWING captures well the spanwise and chordwise position effect of a concentrated mass on the flutter appearance. Indeed weights that are placed forward from the elastic axis tend to delay the flutter appearance. When the weights are laterally placed between 1/3 and 2/3 of the span, the flutter speed increases no matter the chordwise location. Both observations were captured by ASWING. Capturing the nacelle position effect on the flutter appearance is mandatory in modern applications. Especially with the rise of boundary layer ingestion devices whose some can be placed near the trailing edge of a wing (distributed propulsion). ASWING could be used to estimate more precisely the performances of those when integrated as they will impact the flutter appearance.

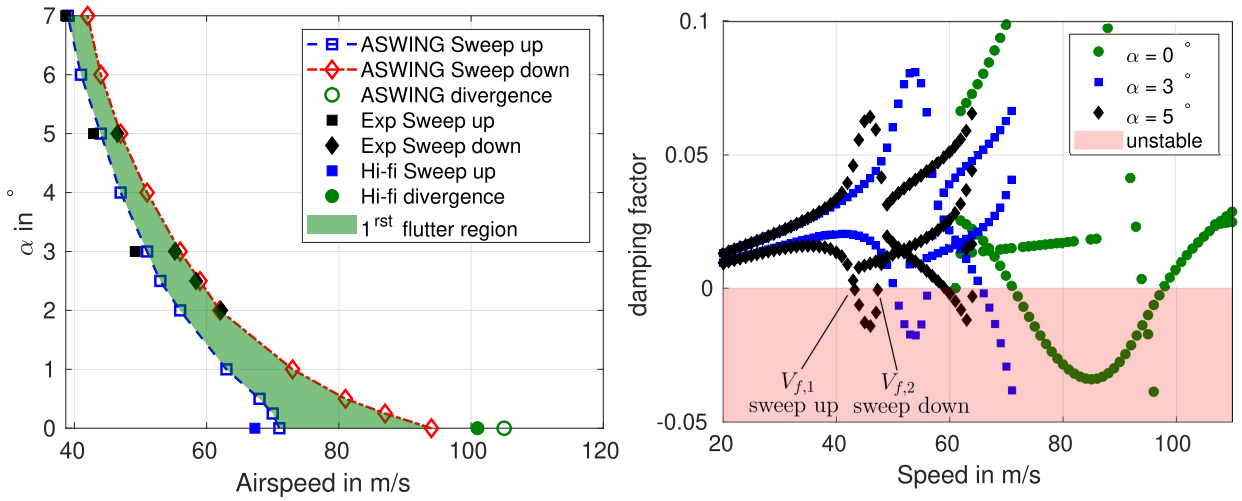

(a) flutter boundaries

(b) damping ratio

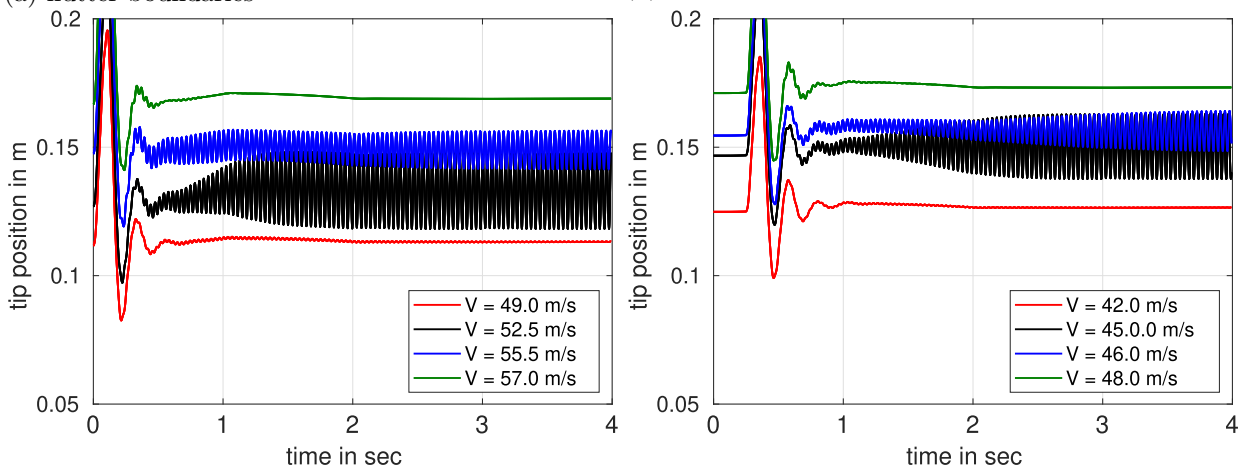

(c) LCO at $\alpha = 3°$

(d) LCO at $\alpha = 5°$

Figure 6.8: Pazy wing : flutter boundaries ASWING predictions againts experiments Drachinsky et al.-2022

Flutter onset						
α (in deg)	Sweep type	Exp.	UM/NAST	ϵ_U (%)	ASWING	ϵ_A (%)
3	Up	49,00	48,24	-1,55	51	4,08
5	Up	43,00	41,44	-3,62	44	2,32
7	Up	38,00	37,19	-2,14	39	2,63
3	Down	55,00	56,37	2,50	56	1,81
5	Down	48,00	47,23	-1,60	47	-2,08

Table 6.3: Pazy wing : flutter boundaries (1/2), ASWING and UM/NAST (Riso and Cesnik-2023). Comparisons with experiments (Drachinsky et al.-2022)

Flutter frequency					
AoA	Sweep type	Exp.	UM/NAST	Diff (%)	ASWING
3	Up	30,00	31,91	6,37	30,69
5	Up	29,90	31,10	4,01	30,16
7	Up	29,40	30,53	3,84	30,25
3	Down	28,20	27,77	-1,51	28,01
5	Down	26,70	27,76	3,98	28,3

Table 6.4: Pazy wing : flutter boundaries (2/2), ASWING and UM/NAST (Riso and Cesnik-2023). Comparisons with experiments (Drachinsky et al.-2022)

Unloaded flutter speed						
Quantity	Unit	SOL 145	UM/NAST	Diff (%)	ASWING	Diff (%)
Flutter speed	m/s	67,30	72,40	7,58	71	5,49
Flutter frequency	Hz	34,72	34,72	0,00	33,2	-4,38
Divergence speed	m/s	100,97	98,32	-2,62	105	3,99

Table 6.5: Pazy wing : unloaded flutter and divergence, ASWING and UM/NAST (Riso and Cesnik-2023). Comparisons with higher fidelity methods (Riso and Cesnik-2023)

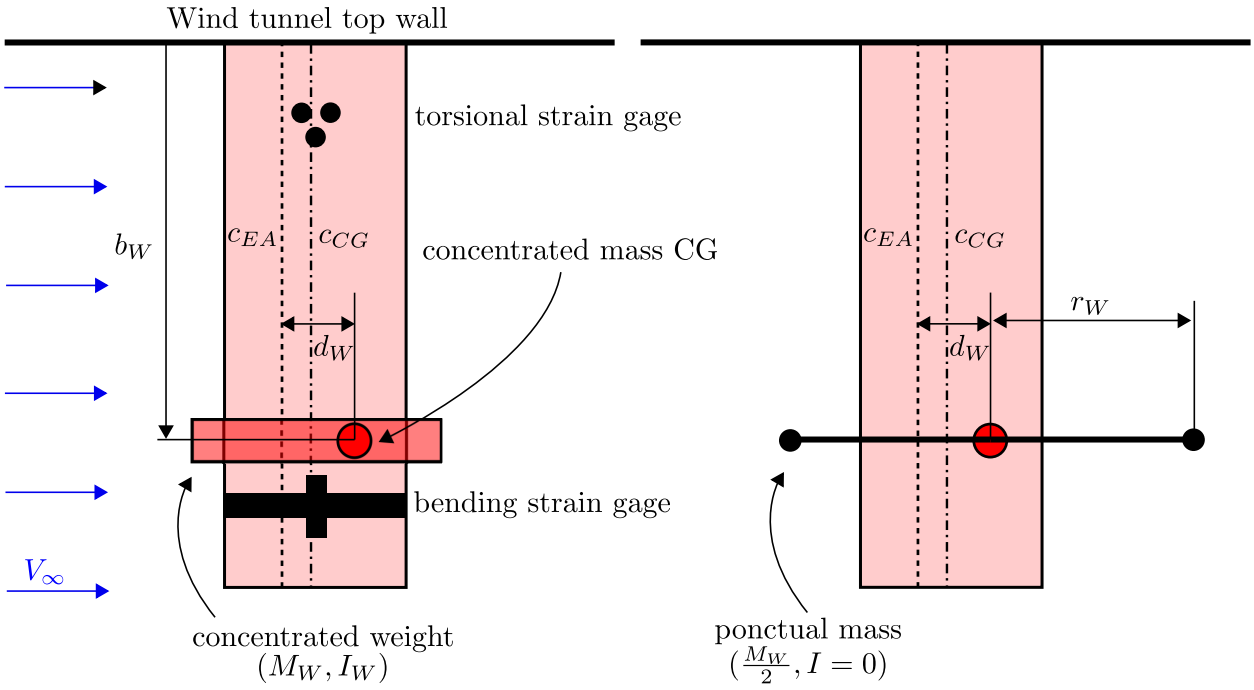

(a) NACA16010 Experimental bench

(b) ASWING's concentrated mass ponctual mass dipole modeling

Figure 6.9: Concentrated mass effect bench Runyan and Sewall (1948)

N_W	e_w	y/b	$V_{f,exp}$ **(m/s)**	$V_{f,ASW}$ **(m/s)**	ϵ_{V_f} **(%)**	$f_{f,exp}$ **(Hz)**	$f_{f,ASW}$ **(Hz)**	ϵ_{f_f} **(%)**
0	0	0	101.7	102	0.25	22.1	24.476	10.75
I	-0.818	0.17	98.6	98	-0.54	19.1	20.0	4.78
		0.23	98.8	100	1.26	17.4	18.2	4.76
		0.35	116.5	131.5	12.9	26.8	29.6037	10.4478
		0.63	160	140	-12.5	T-DIV	T-DIV	N.C
		0.94	112.2	127	3.9	T-DIV	T-DIV	N.C
I	-0.578	0.23	99.1	106	6.9	18.54	20.1	8.41
		0.44	112.776	127	12.6	24.5	T-DIV	N.C
III	-0.360	0.23	99.4	100	0.64	19.6	20.294	3.6
		0.44	105.5	126	19.4	16.5	16.1	-2.42
		0.58	111.9	137	22	14	15.6	11.42
IV	-0.140	0.23	97.5	97	-0.6	20	21.09	5.5
		0.44	96.9	102.5	5.7	17.6	18.27	3.8
		0.56	100.9	108.5	7.5	15.3	16.6	8.6
		0.69	104.6	115	10	13.2	14.9	13.2
V	0.034	0.23	95.1	93	-2.2	23.33	21.4	-8.3
		0.44	86.9	86	-1.0	17.6	19.3	9.7
		0.60	90.1	90	-0.9	14.5	16.8	15.4
		0.72	90.1	96	6.6	13	14.9	14.2
		0.83	95.7	103.5	8.1	11.4	12.9	13.3
VI	0.5	0.23	84.7	87.5	3.2	19.1	21.6	13.2
		0.33	76.8	75	-2.3	17.1	20.0	16.5
		0.5	69.8	62.5	-10.4	14.3	18.3	28.2
		0.83	74.9	68.5	-8.6	12	16.4	36.7

Table 6.6: Effect of a nacelle/tank position on the flutter speed and frequency.
ASWING 5.96 prediction against Runyan and Sewall's experimental data.$\bar{\epsilon_{V_f}} = 6.9\%$, $\bar{\epsilon_{f_f}} = 11.6\%$

6.2.6 Dynamic: whirl flutter

In this section, whirl flutter speed ASWING prediction is discussed. This phenomenon is different from classical flutter, as it is not produced by the wing but by a propeller fixed on the structure. When a propeller faces a non-axial flow because of any perturbation (gust, change in its shaft orientation etc) normal force and yawing moment are generated. If the latter is strong enough, it can deform the wing geometry. With the flight speed rising, there is a moment when the wing structure can no longer be stable and the flutter occurs. The term "whirl" is used, as when the phenomenon happens, the propeller canopy has a diverging whirl trajectory. . Tiltrotor aircraft (like in figure 6.10) are very subject to this type of phenomenon.

The most recent experimental work done on the

Figure 6.10: XV-15 (picture source : NASA)

topic has been proposed by Kambampati (2016 and 2017) and Costa (2015) Unfortunately, in their work, the authors did not provide all the necessary parameters needed to reproduce numerically the different benches. However, they have provided a comparison of their numerical model with experimental data. Or the latter model derived from a less sophisticated but similar model as the one of ASWING. Indeed the structure model was a linear Euler Bernoulli beam theory where only chordwise and beamwise bending, and torsion are considered. It was coupled to a linear lifting line theory. Finally, to capture the perturbed loads generated by the propeller, a p-factor model was implemented. The latter differs from the ASWING model just by taking into account the drag contributions. Or for small perturbations, the latter is negligible and has been removed from the ASWING model. Considering ASWING p-factor model (*section 14* of Drela-2008) is similar to Kambampati's one. Thus in light of the previous comments, ASWING is expected to behave the same as Kambampati coupled models. The reader is nevertheless invited to read carefully the next lines. Thus Kambampati proposed in his work a comparison between its model and the experimental measurements. No matter the different benches tested, its model was able to predict correctly the damping ratio evolution with speed of the in the plane and out of the plane bending modes aswell as the torsion mode. It could also predict the whirl flutter speed with a good level of accuracy (below 10%). So far it is reasonnable to think that ASWING will provide the same forecast, however real comparison are planned in the future to really status.

6.2.7 Unsteady: Gust Reponse

During my literature review, no experimental work has been founded **yet** on the gust response of a flexible low-aspect wing. Thus to evaluate the ASWING capacity to predict the gust response, the work of Krengel et al. is invoked. The authors performed a comparison between ASWING and "higher fidelity" CFD data on a Boeing 737-like geometry (named MICADO). The simulations were performed at Ma $= 0.83$ ($k \approx 0.5$) with a gust having a wavelength of 100m with a turn-off pitch controller. They have provided in their work the total lift and moment prediction time marching simulations for a rigid and flexible aircraft. Their conclusions were that in both cases, ASWING catures well the maximum lift peak seen by the wing during the gust encounter (prediction error lower than 10%). The transient response is excellent on the rigid aircraft while it's a bit weaker on the flexible one. From an aircraft design point of view, the maximum lift peak is the most important quantity to be predicted. For the maximum pitching moment, the ASWING predictions are still in good agreement but not as good as the lift (prediction error between (10-20%). Also, the ASWING simulations were reported to be delayed in comparison to the higher fidelity one. The work of Krengel et al. is the only one that could be invoked. However, care must be taken on their conclusions, as they have compared the ASWING simulations to higher fidelity for wich the accuracy is not known. Thus, wind tunnel campagn should be considered to rigouralsy assess the ASWING accuracy for gust analysis.

6.2.8 Unsteady: Limit cycle oscillations (LCO)

This section deals with limit cycle oscillations and how ASWING can capture them. Originally introduced by Henri Poincaré in the early 20th century the LCO

can have different origins in aeroelastic problems. A modal analysis as we have seen earlier is based on the linearization of the system over an equilibrium point. In the case of aero-elasticity, flutter and torsional divergence define instabilities. But most of the time, the non-linear effects are neglected in the analysis and tend to provide a small stability robustness to the system. In the case of a flutter for example, when the critical speed is reached and slightly overcome, if the system is excited it will tend to diverge but will be damped by the non-linear effect leading to a self exited oscillatory system. The more the speed is increased, the higher will be the oscillations amplitudes until the real (non-linear) divergence occurs. In the aeroelasticity problem, there are different types of non-linear terms that can lead to limit cycle oscillations. The most famous one being the non-linear structural and inertial loads ;and the dynamic stall. Other phenomena leading to LCO can be mentionned like leading edge vortices whose bandwidth can excite aeroelastic modes leading to a self excited oscillatory response. Note that the latter can happen in the stability range of the system. As ASWING is not able to capture the dynamic stall and the leading edge vortices, only non-linear structural load effects will be studied here. To do so Dunn experimental data (1992 and 1992) are used one last time.

Experimental bench # A-3:
The same bench as for the flutter boundaries section was used. The tip deflection and twist peak-to-peak amplitude were provided by two types of measuring devices that are a high-speed camera and strain gages reading. The latter were converted from empirical formulae so important error measurements were reported. During the tests, the speed was set very close to the flutter speed and incrementally increased by $\Delta V = 1.0m/s$. A small stick pinch was applied on the wing to excite its structure (as depicted in figure 6.1. Dunn reported that the LCO response was extremely sensitive to the pinch intensity so great care is taken in the comment of the results. Overall they performed LCO measurements on each wing at different angles of attack. As we have seen in the previous section that ASWING is weak to predict the flutter speed when the angle of attack is increasing only the cases at $\alpha = 1.0°$ are considered. Finally, during our analysis I did not manage to get LCO on the $[-15_2/0_2]_s$ laminate, in consequence only the $[90_3/0]_S$ and $[+15_2/0_2]_S$ laminates are considered in this work.

Numerical bench # A-3:
To numerically capture the LCOs, a time marching computation was mandatory. It was not possible to implement the stick punch so a flap was used and impulsively deflected at $t = 0.1s$ as depicted in figure 6.11 (a). A 1° flap deflection was enough to excite the structure and reach the LCO. The time marching period Te was chosen based on a Shannon criterium on the third bending mode ($Te \approx 0.001s$). Forty structural nodes and pointwise circulation variables were enough to get a reasonable mesh convergence (please refer to the chapter 3 and 5 for more details). The tip deflections and twists measurements were performed using 2 numerical sensors placed at the wing tip on mid chord line. To obtain the LCO peak-to-peak amplitude, the self oscillatory response has to be established. Figure 6.11 (a) is depicted as the vertical displacement relative to the steady position temporal evolution. Three distinct phases can be highlighted that are the linear exponential response (red), the non-linear damping effect or LCO establishment (grey) and the established LCO (white). The peak-to-peak measurements were performed in this last zone.

Results # A-3:
For the $[0_3/90]_S$ layout, the LCO results are presented in figures 6.11 (b) and (c). Figure (b) present the phase average plot of the tip vertical displacement versus the tip twist variations and so for different relative speed ΔV. The latter is defined as the relative speed from the flutter one computed in the linear modal analysis. The phase average plot is provided mostly to have better insight into the flutter type and the higher frequency mode effect. For example from the shape of the plot (squeezed ellipsoïde), the effect of the second bending mode whose frequency is 2.5 times bigger than the torsional mode is clearly identified. Then the curve thickness has not been voluntarily increased, but it actually highlights the effect of higher frequency modes retained by the Shannon criterium. From the elliptic shape, it is clear that the first torsional mode dominates the limit cycle oscillations as reported by Dunn and Dugundji. Figure 6.11 is more of interest as it provides the ASWING and Dunn's non-linear model predictions of the peak-to-peak tip deflections and twists. The finite element model introduce in Dunn's work seems to provide better predictions at $\Delta V = 1.0m/S$ while ASWING performed finer at $\Delta V = 2.0m/S$. However, it is not possible to say that both show good agreement with experiments.

For the $[+15_2/0_2]_S$ layout the flutter response is much different. Indeed from the phase average shape in figure 6.12 (a), the coalescence of the first torsion and bending modes is clearly highlighted. Note that the coalescence was also predicted by the linear modal analysis in figure 6.6 (b) (frequency plot). Then the effect of the second bending mode can be identified (small loop shape). Also as for the previous laminate, the effect of the higher frequency mode is lumped in the thickness of each plot. From the shape of the phase average plot, we can also see that the first torsion and bending modes are out of phase. Regarding peak-to-peak amplitude, Dunn's non-linear predictions are not presented as they were not clear to us. For more detail please refer to *figure 30 up and down*

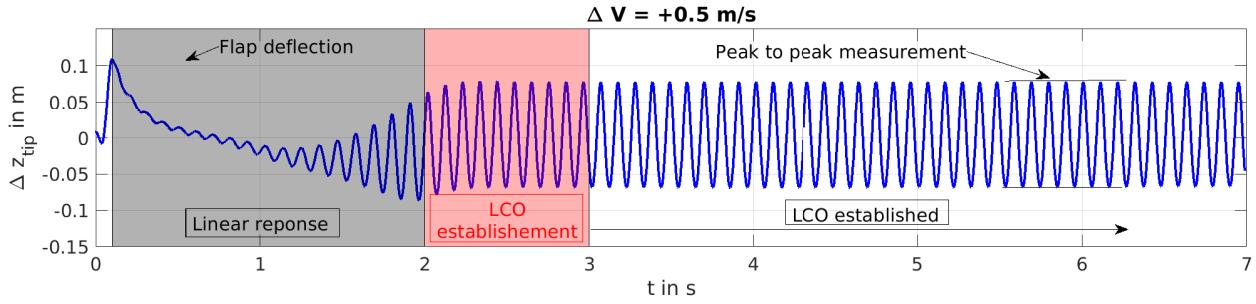

(a) Limit cycle oscillations establishment example

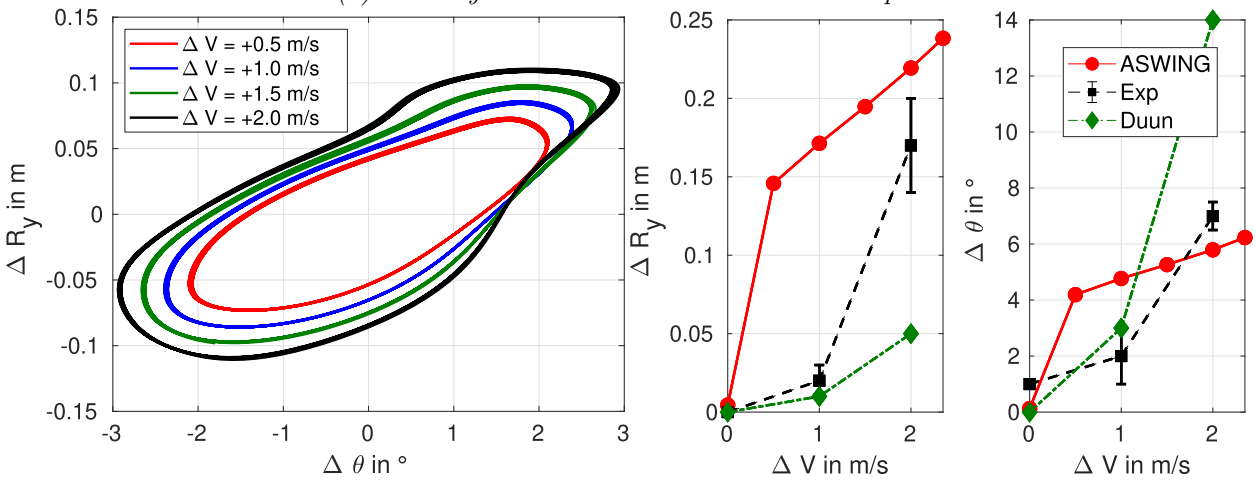

(b) Phase average evolution with flight speed above the flutter speed. LCO are established

(c) Peak to peak LCO amplitude variation with flight speed.

Figure 6.11: Limit cycle oscillations ASWING analysis : Layout $[0_3/90]_S$. Comparison with experiments of Dunn

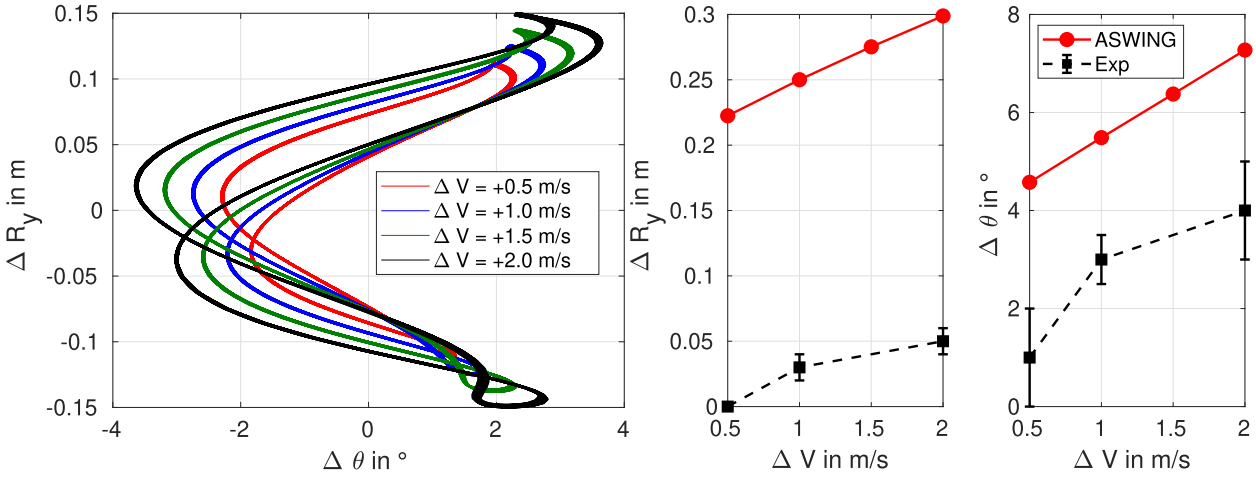

(a) Phase average evolution with flight speed above the flutter speed. LCO are established

(b) Peak to peak LCO amplitude variation with flight speed.

Figure 6.12: Limit cycle oscillations ASWING analysis : Layout $[+15_2/0_2]_S$. Comparison with experiments of Dunn

of his PhD script. Thus figure 6.12 (b) presents the ASWING peak-to-peak predictions of the tip deflection and twist against experiments. Here there is no doubt, ASWING is not able to catch correctly the amplitudes no matter the relative speed. In light of the previous results, it is clear that ASWING does not provide satisfying results regarding limit cycle oscillations. It can however capture the main tendency and which modes are dominating the LCO responses. The prediction discrepancies can come from the low aspect ratio geometry considered in this section. Thus investigations are still necessary to appreciate more precisely the capacity of ASWING to predict such phenomena. Note that during the pre-design of an aircraft, the flutter or divergence speed define an upper bound to the flight envelope not to be exceeded. So LCOs that are related to flutter and divergence are very unlikely to be encountered in real flight. Usually, aircraft manufacturers do not prioritise their studies.

6.3 Folding wing tip devices

This last section is dedicated to folding wingtip devices. Those are treated in the aeroelastic part of this evaluation work as their behaviours are very close to a flexible structure. Wing Tip Devices (WTD) is a recent topic whose studies are mostly motivated by the reduction of commercial aircraft span as the airport taxes increase with it. The impact of such mechanisms on aircraft performances has been recently experimentally studied by Castrichini et al. (2016 2017), Cheung et al. (2017, 2018, 2020 and 2022) and Healy et al. (2022c,2022b, 2022d and 2022a). Folding wingtip devices can reduced the root bending moment when a gust is encountered. They reduced temporally the wing-span reduced the moment arm. Also they improve the rolling performances. By reducing the wingspan, they reduce the wing rolling damping phenomena. Thus Wings with folding wingtip can perform higher rolling rate. In this section,

6.3.1 Effect of stiff, sprung and free folding wing tip on the gust response

In this section, the experimental observations of Cheung et al. (2018) on the effect of folding wingtip on the gust load alleviation are discussed against ASWING capacity. The word "observations" is use with care as the articles Cheung et al. (2017 and 2018) has published do not provide enough information about the experimental bench to be reproduced numerically. Here, the main objective was to spot if ASWING can capture similar observations as the authors. The second one was to show the community that ASWING can model such devices.

Experimental bench # E:
Two swept backward wings were placed in front of the open-jet wind tunnel at the University of Bristol. The wings span and chord were respectively 0.7 m and 0.3m. They were anchored to a plane of symmetry at the root. A balance was used to measure the total lift and root bending moment coefficient (C_L and C_l). The wing profile was a NACA0015 and was rigidly crafted to isolate strictly the behaviour of the wing tip devices. Finally, the wing tip position was chosen so that they account for a third of the exposed area. The hinge angle Λ were 10 and 30 degrees, Λ was also the wing sweep angle as depicted in figure 6.13. The biggest problem arise by Cheung et al.'s paper is that the author did not provide the wing tip mass and inertia. Despite the gust response introduced later is extremely sensitive to those parameters. We have chosen an estimated value in consequence but we prefer to compare observations instead of measurements. As only the latter are discussed, neither the sensors precision nor the wind tunnel level of turbulence are recalled here. In total 3 hinge stiffness were tested and provided corresponding to *Free*, *Sprung* and *Stiff* folding wingtip. Two gust vanes (cf right side of figure 6.13) were placed at the wind tunnel throat exit. The gust response was performed at a flight speed of 20m/s. Measurements of the lift and rolling moment coefficient were performed as well as folding angle measurements θ (cf figure 6.13). The upper and lower bounds in each variable change were reported against the different angles of attack.
Numerical bench # E:
The two benches were reproduced with ease in ASWING, except that the full wing was modelled. A numerical sensor at the wing tip was used to measure the wingtip folding angle. A mass dipole was used to reproduce the expected mass and inertia of the wing tip. The folding wingtip device and the wing were connected using a joint whose hinge axis and stiffness were specified. To reproduce the cosine gust, the inner ASWING gust program was used. The time marching sampling time was chosen to be 100 times lower than the gust duration. Steady analyses were also performed to investigate the wing tip aerodynamic stability on the full range of angle attack considered.
Observations # E:
First of all, during the steady analysis, the wingtip devices showed aerodynamic stability. In a sense that the aerodynamic loads are compensating the wingtip weight leading it to reach a stable folding angle. An so no matter the hinge angle or stiffness.

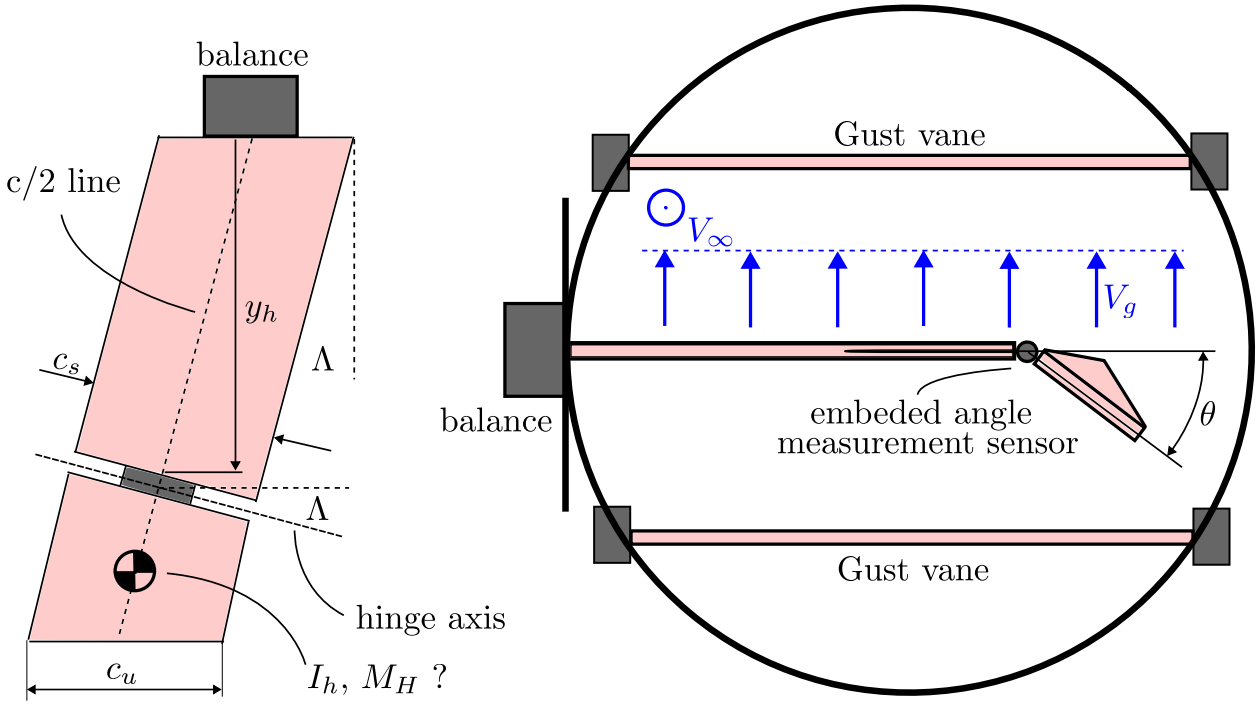

Figure 6.13: Testing of a hinged wingtip device for gust load alleviation: Cheung et al.'s bench (2017 and 2018). The gap between the wingtip and the folding devices is important leading to important pressure leaks.

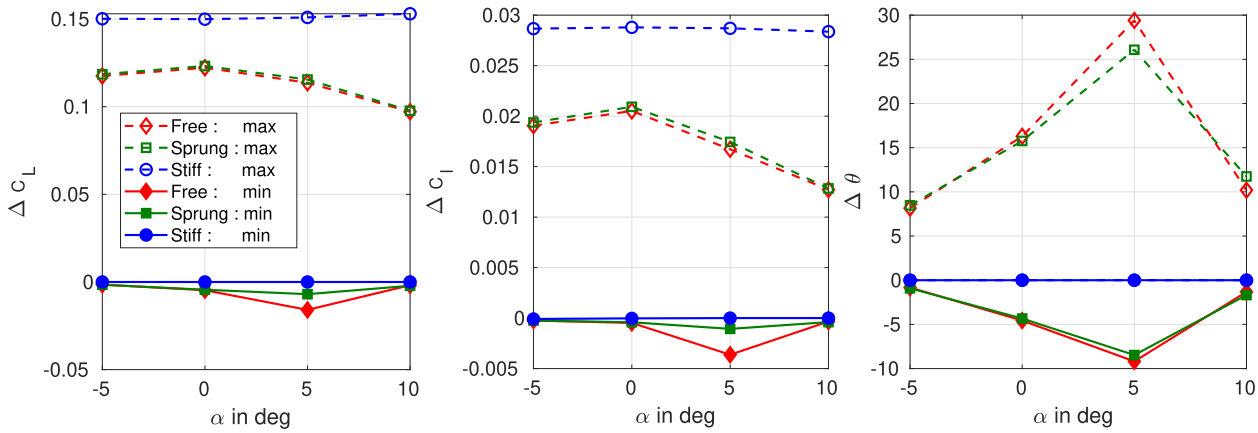

(a) ΔC_L (b) ΔC_l (c) $\Delta\theta$

Figure 6.14: ASWING, lift, root bending moment, and fold angle peak to peak variations prediction. Response to a cosine gust of length 7m and amplitude 0.75m/s. $\Lambda = 10°$ hinge angle. Comparison between free, sprung and stiff wingtip.

The folding angle was logically increasing with the angle of attack. The same observations have been reported in the work of Cheung et al.. Secondly, figures 6.14 (a) to (c) are depicting respectively the upper and lower bound of the lift, rolling moment and folding angle during a gust encounter, on the $\Lambda = 10°$ configuration. The figures 6.15 (a) to (c) do the same for the $\Lambda = 30°$ set-up. In both configurations a significant root bending moment (rolling moment) reduction was reported on the *Free* and *Sprung* stiffness settings. They also reported that the *Free* one was outperforming slightly its stiffer version. Also, greater folding wingtip angles upper and lower were witnessed on the $\Lambda = 10°$ configuration, also observed in the ASWING simulations. In both setups, a reduction in lift coefficient during the gust encounter was reported. Overall it seems that ASWING captures well the tendency imposed by the use of folding wingtip devices on the gust response of the wing. The effect of the hinge axis angle and stiffness are also well highlighted.

6.3.2 Dynamic: Effect of folding wing tip on the rolling performances of a straight wing

I propose in this section to use the experimental data provided in [17] where Healy et al. studied the impact of different configurations of folding wingtip on the rolling performances of a straight wing. This time all the necessary parameters to ensure qualitative numerical analysis were provided.

Experimental bench # F:

A rectangular wing of aspect ratio AR = 15 ($b = 1.0m$ and $c = 0.067m$) was connected to a rolling rig as depicted in figure 6.16. An electromechanical brake could hold the wing while the ailerons are deflected. The latter spans from the wing root to $b_F = 0.364$ with a width of 25% the wing chord. Two wingtip configurations were tested. A 10 and 30-degree hinge angle Λ (cf right side of the figure 6.16). The hinge axis was connected on the mid chord line at $b_H = 0.364m$. The wing airfoil was a NACA0015. In total 4 configurations were tested : *Removed* (no wing tip devices, $b = 0.788m$), *Fixed*, *Free10* and *Free30* [2]. The hinge mechanism was manufactured to be friction less. Also, the wing was designed and voluntarily re-enforced to avoid any effect from the structure. The different configurations parameters were provided by the author and reported in *Table 4* of Healy et al.'s article. Finally, the tests have been performed in the university of Bristol 7 by 5 foot low-speed closed return wind tunnel. Foour wind speed ($V = 15,\ 20,\ 25,\ and\ 30\ m/s$) and three flap deflection ($\delta_F = 7,\ 14,\ and\ 21°$) were tested. No information on the turbulence level was provided in Healy et al.'s article .

Numerical bench # F:

Wing tip devices can be modelled in ASWING using joints. Their hinge axis can be specified with ease. Thus four lifting surfaces have been implemented to model the *Removed*, *Fixed*, *Free10* and *Free30* configurations. XFOIL has been used to compute the NACA0015 polars for each speed and flap deflection. A mass dipole system was used in order to reproduce the wing and folding wingtip masses and moments of inertia. The radius of gyration of the dipole was computed to find the masses positions that will recover each element's inertia.

Results # F:

Healy et al. performed in a first-time anchored tests. The wing was set horizontally into the wind tunnel, and the roll was prevented. Ailerons were deflected and each wingtip folding angle was measured (cf figure 6.16). Note that the tests were also performed with the wing upside down for the *Free10* configuration to eventually identify the manufacturing default. Figure 6.17 depicts the ASWING folding angles prediction against experimental data. Two markers were used for the *Free10* configuration accounting for top and upside-down tests. ASWING predicts quite well the left and right folding angles on the *Free30* configuration, especially at high speed. For the *Free10* version, the predictions are a bit weaker but still in good agreement with the experiments. Thus ASWING can correctly capture the effect of deflected ailerons on the steady behaviour of folding wing tip devices no matter their hinge angle and the flight speed.

In a second time, Healy et al. performed rolling performance measurements. Two main quantities were provided in their work that are the mean rolling rate $\bar{p}$ and the peak-to-peak roll rate amplitude Δp. Figures 6.18 (a) to (c) present the mean roll rate ASWING predictions against Healy et al.'s experimental data for 3 different ailerons deflections. The results are presented against the flight speed. The predictions for the *Removed* and *Fixed* are in good agreement with the experiments which are consistent with what we have found in the aerodynamic part of this evaluation work (Part I). Even if the ASWING predictions are a bit weaker for the *Free10* and *Free30* configurations, the software correctly catches the major information. The *Free30* configuration provides better rolling performances than the *Free10* one on the complete flight speed and ailerons deflections range considered in the experiments.

Finally, because of the inertia of the wingtip devices, during the tests, when the wing was rolling the latter were also rotating around their hinge axis because of the centrifugal loads. Thus their local angle of attack was varying through time inducing an oscillation

[2] 10 and 30 are the hinge axis angle relative to the wing cross section

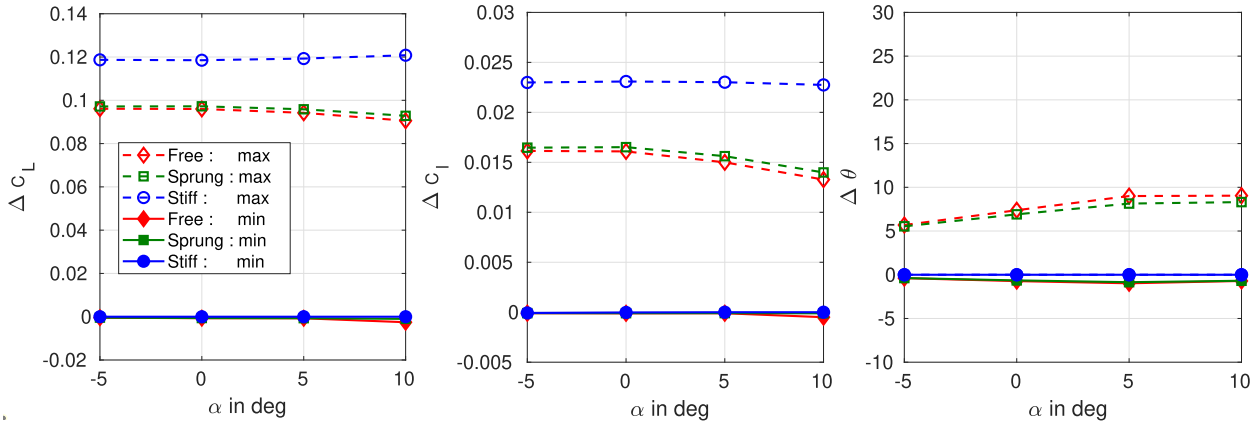

(a) ΔC_L (b) ΔC_l (c) $\Delta\theta$

Figure 6.15: ASWING, lift, root bending moment, and fold angle peak to peak variations prediction. Reponse to a cosine gust of length 7m and amplitude 0.75m/s $\Lambda = 30°$ hinge angle. Comparison between free, sprung and stiff wingtip.

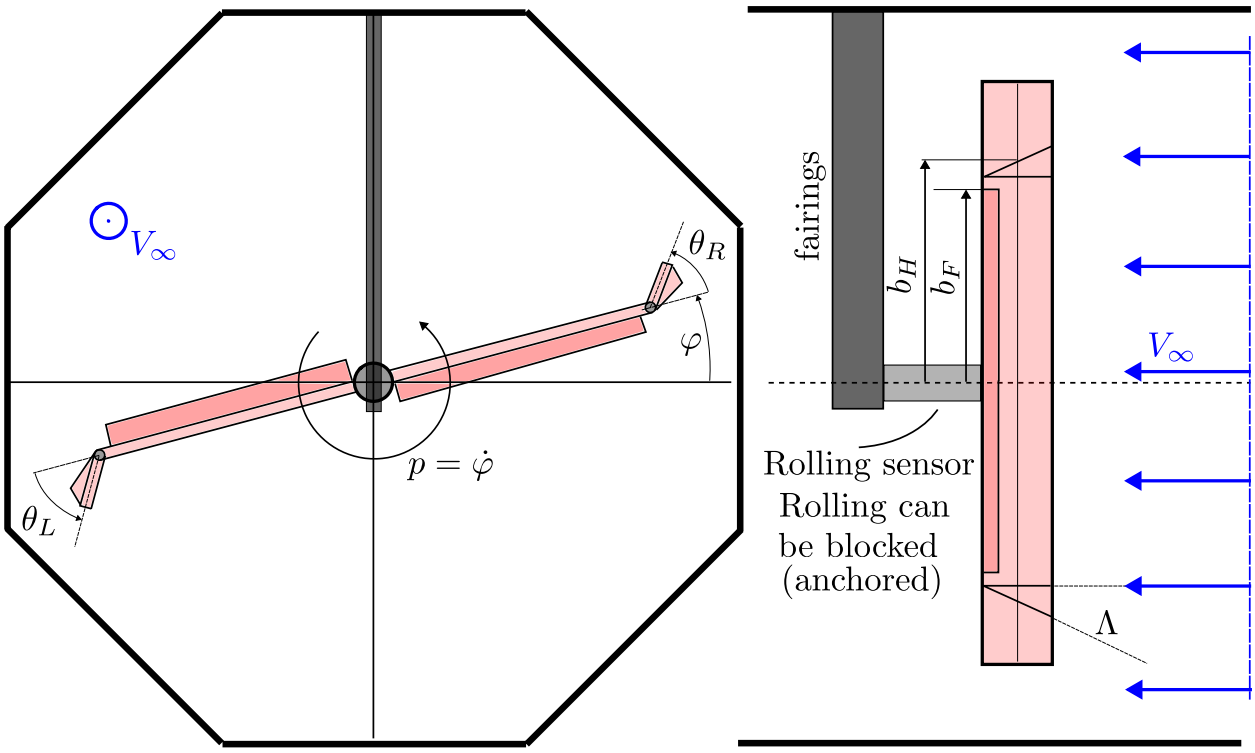

Figure 6.16: Effect of folding wingtip on rolling performances of a wing. Experimental bench adapted from Healy et al.

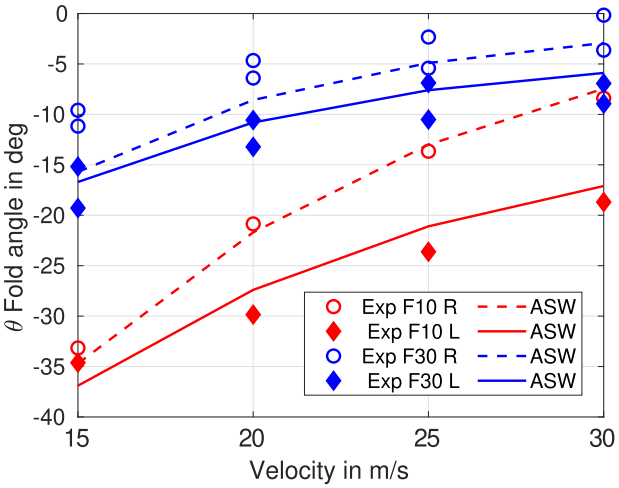

Figure 6.17: Effect of folding wingtip on rolling performances of a wing. Experimental bench adapted from Healy et al.

over the mean value of the roll rate. Healy et al. provided the peak-to-peak amplitude of the rolling rate and its variation with flight speed and the ailerons deflections. The figures 6.19 (a) and (b) depict the previously mentioned quantities and the equivalent ASWING predictions. For the *Free10* configuration, only experimental data were provided for $\delta_F = 14°$ against the speed range. For an aileron deflection of 21° the measurements were performed at a single speed ie $V = 20m/s$ (square full markers on figure 6.19-a). ASWING shows excellent agreement with experiments, especially at high speed. At $V = 20m/s$ ASWING loses the track and provides non-satisfying predictions. The same type of remarks can be drawn from figure 6.19-(b) for the *Free30* configuration. The lack of precision at low speed could come from the low Reynolds number flight where I have faced a lot of difficulties to make XFOIL converge so that to obtain the ailerons ASWING derivatives. With the flight speed increasing the problem vanished so the better predictions.

6.4 Conclusions

In this chapter, the last part of the ASWING experimental evaluation has been presented. This part focuses on the analysis of aeroelastic phenomena. Here no theoretical reminder has been provided, the document focused on the presentation of selected experimental cases. The evaluation started with the presentation of steady aeroelastic phenomena. Deflections and twist under steady flow on a low aspect ratio wing have been presented. Three cases were studied with different stiffness coupling terms. Then, the study of the effectiveness of aerodynamic control surfaces and the reversal speed on a trapezoidal wing of low aspect ratio has been presented. Then dynamic phenomena were discussed. The same data set as for the steady deflection and twist has been used to evaluate the good prediction of the flutter and torsional divergence speed. The effect of the angle of attack on their appearance was also discussed. The various works in the literature that have reported such a validation are also recalled to consolidate the analysis. Then another set of data has been used to highlight the impact of the lateral and longitudinal position of a nacelle or an external tank on the early or delayed appearance of flutter or torsional divergence of a straight wing. A final case of flutter was discussed. In particular here, the phenomenon of flutter by precession effect or whirl flutter. A low aspect ratio wing with a nacelle/propeller anchored at its tip has been used to appreciate the good quality of ASWING prediction of the flutter speed. The chapter continued with a presentation of the unsteady aeroelastic phenomena. Namely the response of a structure to a vertical wind gust. Here we have failed to find experimental data, a study carried out on a commercial aircraft type 737 has been recalled. Then the steady deflection bench has been used one last time for the study of limit cycle oscillations. The LCOs being numerous and having various causes from different physical phenomena, it was question here of the effect of the non-linear structural loads bringing a light stability margin to flutter. This last case concluded the evaluation of the aeroelastic features of ASWING. However, this chapter has been completed by the study of folding wingtip devices with elastic hinge axis. Two experimental studies were used to assess the performance of ASWING on the prediction of the effects of these devices on the response of a wing to a vertical gust and on its rolling performance.
The different findings can be summarized as follow

- Despite bad results in the chapter dedicated to the structural model (Chapter 5), ASWING captures well the steady tip deflection and twist of low aspect ratio wings. The aerodynamic loads are distributed along the span reaching zero towards the tip. The tip pontual mass bench in the structural evaluation part involves much more important stress at the beam tip. Cross sectional shear stresses are very likey to be involved. Thus from this analysis, tip ponctual masses bench seem to not be appropriate for aeroelastic representative cases. Three different wing tailoring have been used, with various bending torsion coupling terms. All of them shows good agreements with experiments, except the case with a negative bending torsion coupling term. This feature is very important as the wing geometry of a high aspect ratio UAV is very likely to deform, spe-

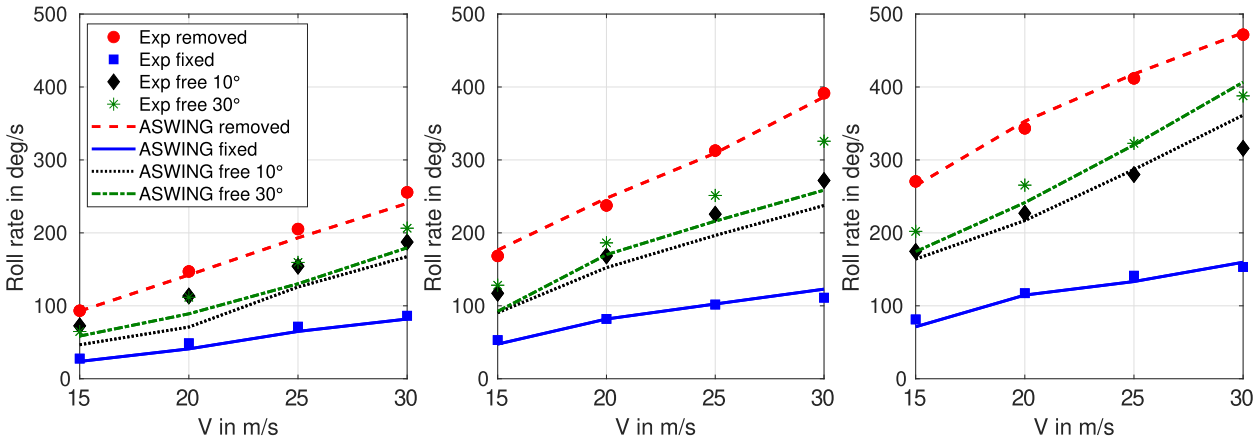

(a) $\delta_F = 7°$ (b) $\delta_F = 14°$ (c) $\delta_F = 21°$

Figure 6.18: Rolling performances of Healy et al.'s straight wing with fixed, removed and 2 free folding wing tip devices

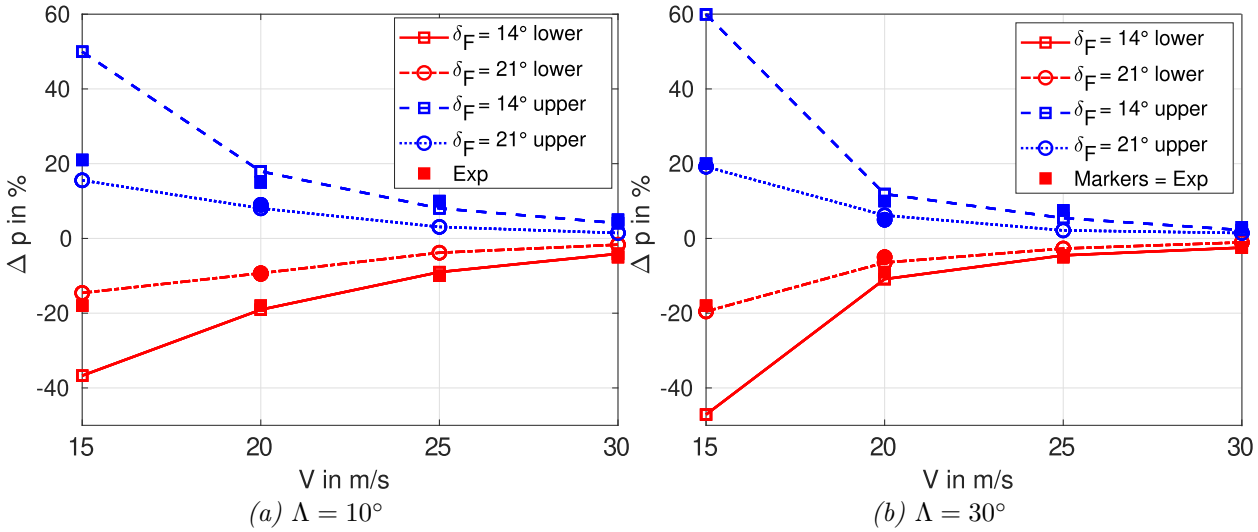

(a) $\Lambda = 10°$ (b) $\Lambda = 30°$

Figure 6.19: Rolling peak to peak variation of Healy et al.'s straight wing with for various hinge angle Λ and ailerons deflections δ_F. Comparison with experiments

cialy in thermal soaring when high load factor turn are involved. Aerodynamic performances are thus expected to vary.

- The loss of ailerons or flap effectiveness up to the reversal behaviour is correctly predicted. However, it has been shown that it can be slightly improved by taking into account the flap derivatives variation with the Reynolds number. This feature will be of particular interest in chapter 8, where the loss of effectiveness can impact energy harvesting performances in dynamic soaring.

- The flutter speed and frequency of low aspect ratio wings is correclty captured. Also on 3 different composite layouts, ASWING predict the nature of the divergence (torsional, or coalescence of 2 strcutral modes).

- When a nacelle or tank is anchored to a wing, the effect of its chordwise and spanwise loaction on the flutter speed, nature and frequency is well captured.

- From the litterature, it is reasonnable to think that ASWING predicts correctly the whirl flutter speed of a tiltrotor configuration. However, we invite the reader to remain carefull, as this feature has not been evaluated. Conclusions were made on litterature work involving close or similar theoretical models.

- A study of litterature has been invoked to asses the gust response predictions quality of a wing. The latter are in good agreement specificaly to compute the lift and moments peak values, which are critical parameters for structure design. However, care must be taken for gust analysis. Indeed, the unsteady aerodynamic loads are decomposed into 2 contributions in ASWING, the circulatory and added mass loads. A gust is a sudden change through time and space of the surrounding wind speed and so the air-relative one. This change is perfectly captured by the circulatory formulation but not by the added mass term. Indeed the later is function of the inertial acceleration of the cross section mostly. The added mass terms being mostly dominant at high reduced frequencies, care must be taken when a gust is modeled to not involve such ones. Thus we recommand to study gust whose size involve reduced frequency lower than 0.2-0.5. In the next chapter care is taken to remain below it.

- Post-flutter limit cycle oscillations due to nonlinear stiffening can be studied in ASWING. However the predictions show important errors with experimental measurements. Note that even higher fidelity models which have been compared, do not show better results. Also LCO is a very fundamental topic and an aircraft is very unlikely to fly in condition involving such phenomena as they are out of the safety flight enveloppe.

- Folding wingtip devices can be studied using ASWING. In this chapter, their effects on gust alleviation and rolling performances improvements have been studied and confirmed. Care must be taken on the presented results, as not all the mandatory data necessary to build the numerical bench have been provided by the author of the experimental work. However ASWING captures well the major effects brought by folding wingtip devices.

In light of the previous results and by invoking the 3 previous chapters, it is clear that ASWING can be used to asses the question arise by the thesis that is *Can the flexibility of a wing improve the performance of a UAV in energy harvesting strategy ?*
ASWING can be used to study all the three major strategies that are static, dynamic and gust soaring. Moreover, if a benefit is proved, the effect of the flexibility on the full flight enveloppe can be studied to make sure that on the complete mission there is a real endurance improvement. The next two chapters present in consequence how ASWING has been used to provide some answer to the question arise by the thesis.

Bibliography

[1] Avin, O., Raveh, D. E., Drachinsky, A., Ben-Shmuel, Y., and Tur, M. (2022). Experimental aeroelastic benchmark of a very flexible wing. *AIAA Journal*, 60(3):1745–1768. 16, 202, 203, 206

[2] Castrichini, A., Cooper, J. E., Wilson, T., Carrella, A., and Lemmens, Y. (2017). Nonlinear Negative Stiffness Wingtip Spring Device for Gust Loads Alleviation. *Journal of Aircraft*, 54(2):627–641. 201, 219

[3] Castrichini, A., Hodigere Siddaramaiah, V., Calderon, D. E., Cooper, J. E., Wilson, T., and Lemmens, Y. (2016). Nonlinear Folding Wing Tips for Gust Loads Alleviation. *Journal of Aircraft*, 53(5):1391–1399. 201, 219

[4] Cheung, R. C. M., Castrichini, A., Rezgui, D., Cooper, J. E., and Wilson, T. (2017). WIND TUNNEL TESTING OF FOLDING WING-TIP DEVICES FOR GUST LOADS ALLEVIATION. 16, 201, 219, 220

[5] Cheung, R. C. M., Gu, H., Healy, F., Rezgui, D., and Cooper, J. E. (2022). LATERAL GUST BEHAVIOUR OF AIRCRAFT INCORPORATING FLARED FOLDING WINGTIPS. *ICAS*. 201, 219

[6] Cheung, R. C. M., Rezgui, D., Cooper, J. E., and Wilson, T. (2018). Testing of a Hinged Wingtip Device for Gust Loads Alleviation. *Journal of Aircraft*, 55(5):2050–2067. 16, 201, 219, 220, 221

[7] Cheung, R. C. M., Rezgui, D., Cooper, J. E., and Wilson, T. (2020). Testing of Folding Wingtip for Gust Load Alleviation of Flexible High-Aspect-Ratio Wing. *Journal of Aircraft*, 57(5):876–888. 201, 219

[8] Chiereghin, N., Cleaver, D., and Gursul, I. (2017). Unsteady Measurements for a Periodically Plunging Airfoil. In *55th AIAA Aerospace Sciences Meeting*, Grapevine, Texas. American Institute of Aeronautics and Astronautics. 212

[9] Colas, D., Roberts, N. H., and Suryakumar, V. S. (2018). HALE Multidisciplinary Design Optimization Part I: Solar-Powered Single and Multiple-Boom Aircraft. In *2018 Aviation Technology, Integration, and Operations Conference*, Atlanta, Georgia. American Institute of Aeronautics and Astronautics. 209

[10] Cole, H. A. (1951). EXPERIMENTAL INVESTIGATION OF ROLUNG P E RF OR MANCE OF STRAIGHT AND SWEPTBAC K FLEXIBLE WINGS WITH VARIOUS AI LERONS. *NACA Technical Note*, (2563):46. 16, 203, 207, 208

[11] Costa, G. J. (2015). *Design, Fabrication, test, and evluation of small-scale tiltrotor whirl flutter wind tunnel models*. Master of Science thesis, Pensylvania State University. 216

[12] Drachinsky, A., Avin, O., Raveh, D. E., Ben-Shmuel, Y., and Tur, M. (2022). Flutter tests of the pazy wing. *AIAA Journal*, 60(9):5414–5421. 16, 20, 209, 211, 213

[13] Drela, M. (2008). ASWING 5.81 Technical Description — Unsteady Extension. page 42. 207, 216

[14] Drela, M. (2009). ASWING 5.86 Technical Description — Steady Formulation. page 57. 202

[15] Dunn, P. (1992). *NONLINEAR STALL FLUTTER of WINGS with BENDING-TORSION COUPLING*. PhD thesis, MIT, Boston, MA. 16, 20, 202, 204, 205, 207, 209, 210, 211, 217, 218, 227, 228

[16] Dunn, P. and Dugundji, J. (1992). Nonlinear stall flutter and divergence analysis of cantilevered graphite/epoxy wings. *AIAA Journal*, 30(1):153–162. 16, 202, 207, 209, 210, 211, 217

[17] Healy, F., Cheung, R., Neofet, T., Lowenberg, M., Rezgui, D., Cooper, J., Castrichini, A., and Wilson, T. (2022a). Folding Wingtips for Improved Roll Performance. *Journal of Aircraft*, 59(1):15–28. 17, 201, 219, 221, 222, 223, 224

[18] Healy, F., Cheung, R., Rezgui, D., and Cooper, J. (2022b). EXPERIMENTAL ANALYSIS OF THE BEHAVIOUR OF FLARED FOLDING WINGTIPS WITH SIDESLIP ANGLE. 201, 219

[19] Healy, F., Cheung, R., Rezgui, D., Cooper, J., Wilson, T., and Castrichini, A. (2022c). On the Effect of Geometric Nonlinearity on the Dynamics of Flared Folding Wingtips. *Journal of Aircraft*, pages 1–14. 201, 219

[20] Healy, F., Cheung, R. C., Rezgui, D., and Cooper, J. E. (2022d). Nonlinear Stability Analysis and Experimental Exploration of Limit Cycle Oscillations with Flared Folding Wingtips. In *AIAA SCITECH 2022 Forum*, San Diego, CA & Virtual. American Institute of Aeronautics and Astronautics. 201, 219

[21] Kambampati, S. (2016). OPTIMIZATION OF COMPOSITE TILTROTOR WINGS WITH EXTENSIONS AND WINGLETS. 216

[22] Kambampati, S. and Smith, E. C. (2017). Aeroelastic Optimization of High-Speed Tiltrotor Wings with Wing Extensions and Winglets. *Journal of Aircraft*, 54(5):1718–1727. 216

[23] Krengel, M. D., Hepperle, M., and Huebner, A. (2019). Aeroservoelastic Wing Sizing Using a Physics-Based Approach in Conceptual Aircraft Design. In *AIAA Aviation 2019 Forum*, Dallas, Texas. American Institute of Aeronautics and Astronautics. 216

[24] Love, M., Zink, P., Wieselmann, P., and Youngren, H. (2005). Body Freedom Flutter of High Aspect Ratio Flying Wings. In *46th AIAA/ASME/ASCE/AHS/ASC Structures, Structural Dynamics and Materials Conference*, Austin, Texas. American Institute of Aeronautics and Astronautics. 209

[25] Riso, C. and Cesnik, C. E. (2023). Impact of low-order modeling on aeroelastic predictions for very flexible wings. *Journal of Aircraft*, 60(3):662–687. 16, 20, 203, 206, 211, 213, 214

[26] Runyan, H. L. and Sewall, J. L. (1948). Experimental investigation of the effects of concentrated weights on flutter characteristics of a straight cantilever wing. NACA Technical Note 1594, NACA, Langley Memorial Aeronautical Laboratory, Langley Field. 16, 20, 212, 214, 215, 227, 228

[27] Variyar, A., Economon, T. D., and Alonso, J. J. (2017). Design and Optimization of Unconventional Aircraft Configurations with Aeroelastic Constraints. In *55th AIAA Aerospace Sciences Meeting*, Grapevine, Texas. American Institute of Aeronautics and Astronautics. 209

Appendix - Benches properties

The table 6.7 provides the properties of the laminates used for steady tip deflections, flutter and divergence speed and LCO predictions. Data from *Appendix B page 175* of Dunn's PhD script were used and translated to the Euler-Bernoulli formalism. Mass/length and inertia/length were not provided and so were deducted from the material properties given in *Appendix A page 173-174* of the Dunn's work The tables 6.8 and 6.9 provide the wing and weight properties used for the study of a nacelle position effect on the flutter speed of a wing. The weights properties are taken from *Table I page 8* and the wing ones are given on *page 4* of Runyan and Sewall's report. Data has been translated from the imperial to the metric system.

Parameters	Units	$[0_3/90]_s$	$[+15_2/0]_s$	$[+15_2/0]_s$
EI_{cc}	N	1.4163	1.2947	1.2947
EI_{nn}	N	1.8499 10^4	2.2775 10^4	2.2775 10^4
EI_{cn}	N	0.0023	0.0021	0.0021
EI_{cs}	N	0	0.5151	-0.5151
GJ	N	1.2	1.2	1.4
EA	N	1.132 10^7	1.3944 10^7	1.3944 10^7
μg	kg/m	0.2310	0.2310	0.2310
$\mu g i_{cc}$	kgm	9.2385 10^{-7}	9.2385 10^{-7}	9.2385 10^{-7}
$\mu g i_{nn}$	kgm	3.4623 10^{-4}	3.4623 10^{-4}	3.4623 10^{-4}
c	m	0.140	0.140	0.140
b	m	0.558	0.558	0.558
AR	m	4	4	4
c_{EA}	m	0.5	0.5	0.5
c_{TA}	m	0.4	0.4	0.4

Table 6.7: NACA0012 wing's stiffness and geometry parameters [15]

Parameters	M_W	d_w	$I_{W,EA}$	I_W	r_W
Unit	kg	m	kgm^2	kgm^2	m
I	1.4475	-0.0831	0.0185	0.0085	0.0766
II	1.4696	-0.0587	0.0124	0.0073	0.0707
III	1.4838	-0.0366	0.0089	0.0069	0.0680
IV	1.4933	-0.0142	0.0067	0.0064	0.0657
V	1.5059	0.0035	0.008	0.0068	0.0670
VI	1.4475	0.0508	0.0099	0.0061	0.0650

Table 6.8: NACA16010 wing's concentrated weights' properties Runyan and Sewall (1948)

Parameters	c	b	AR	λ	μI_{cc}	EI_{cc}	GJ	c_{CG}	c_{EA}
Unit	m	m			kgm	kgm^2	kgm^2	m	m
Value	0.2032	1.2193	6	1	7.8E-3	41.17	20.25	0.0923	0.088

Table 6.9: NACA16010 wing's geometry and structural properties Runyan and Sewall (1948)

Part III

Contribution to energy harvesting analysis

Chapter 7

Steady and unsteady thermal soaring on a flexible UAVs

Abstract

In this chapter, 3 optimisation problems are proposed in order to find the optimal set of structural parameters of a UAV wing, maximising the energy harvested in steady and unsteady thermal soaring. ASWING is firstly experimentally validated and then used as an in-the-loop analysis tool to solve the above problems. From the results and comparison, it seems that providing more flexibility to the structure is only beneficial for the dolphin kicks strategy (unsteady thermal soaring). The latter being much less used than static thermal soaring, it is not recommended to build a UAV based on the optimal set of structural parameters found as it degrades a lot the aerodynamic performances of the aircraft on its flight envelope. Also after analysing what was bringing this extra performance, we figured out that a wise control of the pitch angle of the UAV with the elevator was providing the same gain of performance and even more in some cases. For static thermal soaring, it seems that the structural set of parameters that maximise the static thermal soaring power extraction is more the translation of a non-optimised rigid geometry than a real benefit of giving deformation capacity. In other words, using structural parameters as optimisation variables in this problem is another way to optimise the UAV geometry or shape, than using regular geometric parameters such as twist and dihedral angle

Publications:
This chapter has been submitted as a journal paper to the International Journal of Micro Air Vehicles. The latter has been submitted with the title:
R.Jan, J-M. Moschetta and J-P. Condomines, Mini-UAV structure optimisation for efficient thermal soaring, International of Micro Air Vehicles, 2024.

Contents

Nomenclature

b	m	wing span
c	m	wing chord
S	m^2	UAV wetted area
m	kg	UAV mass
AR		UAV aspect ratio
u	$^\circ$	UAV control vector
δ_A	$^\circ$	aileron deflection angle
δ_E	$^\circ$	elevator deflection angle
δ_R	$^\circ$	rudder deflection angle
$(\alpha_x, \alpha_y, \alpha_z)$	$^\circ s^{-2}$	UAV angular acceleration
(a_x, a_y, a_z)	ms^{-2}	UAV acceleration
V	ms^{-1}	air speed
ϕ	$^\circ$	UAV bank angle
(U_X, U_Y, U_Z)	$^m s^{-1}$	UAV inertial speed
$(\Omega_x, \Omega_Y, \Omega_Z)$	$^\circ s^{-1}$	UAV angular rate
R_{turn}	m	Radius of turn
G_R/C_R		Glide and Climb ratio
X		Optimisation variables vector
c_{EA}	m	elastic axis chordwise position
c_{EA}	m	tension axis chordwise position
EI_{cc}	Nm^2	Bending stiffness
GJ	Nm^2	Torsional stiffness
W_z	ms^{-1}	Wind updraft speed
$W_{z,max}$	ms^{-1}	Thermal max updraft speed
R_T	m	Thermal radius
(x_T, y_T)	m	Thermal center position
$\Phi_{thermal,z}$	$m^3 s^{-1}$	Thermal flux
k		reduced frequency
c		reduced amplitude
M_n		yawing moment
M_q		pitching moment
M_p		rolling moment
C_l		rolling moment coefficient
ΔZ	m	tip relative deflection
θ	$^\circ$	tip relative twist
C_L, C_D		lift and drag coefficient
$\lambda(s)$	$^\circ$	local dihedral angle
s	m	spanwise coordinate

Résumé du chapitre en français

Ce chapitre vise à proposer une méthode d'analyse des performances d'un drone dans le cadre du vol d'ascendance thermique. Ici 2 techniques d'extraction d'energie existent. La première consiste à enrouler la thermique en virage stabilisé. Pour maximiser l'énergie extraite, la vitesse et le rayon de virage doivent être choisie de façon optimale. Pour mesurer la performance d'un drone en virage stabilisé dans une thermique, il est commun d'étudier sa polaire en virage. Cette dernière nous donne une information sur la vitesse de chute stationnaire en fonction du rayon de virage et de la vitesse relative. L'idée de ce chapitre est d'étudier l'impact de paramètres structuraux élémentaires sur les performances du vol d'ascendance. En ce sens, plusieurs problèmes d'optimisations et leur résolutions sont proposés afin de déterminer le jeu de paramètres idéal. Par la suite, la seconde stratégie à savoir l'exploitation instationnaire de thermiques est abordée. De la même manière un nouveau problème d'optimisation est proposé pour déterminer le meilleur jeu de paramètres structuraux. Les différentes solutions optimales sont comparées les unes aux autres afin de déterminer la compatibilité des stratégies entre elles. Par la suite, les différents jeux de paramètrès trouvés sont mises en perspectives avec les performances sur l'enveloppe de vol du drone, et les phénomènes aéroélastiques inhérents aux voilures très souples.

Conclusions générales:

A la lumière de cette analyse il semblerait, que des déformations elastiques importantes de la voilure principale ne soient bénéfiques que pour l'exploitation instationnaire de thermique. La variation du gauchissement de l'aile semble bénéficier à la production d'une portance supplémentaire lors de la recontre de la thermique/rafale. Cependant nous avons montré qu'une configuration rigide avec un contrôle optimale de l'angle d'incidence via l'élévateur principal procure les mêmes gains. Le gain en performance sur l'exploitation stationnaire en virage plané n'est pas significative. Il semblerait que les paramtètres structuraux ont permis de converger vers une géométrie rigide optimisée sur le plan aerodynamique. Autrement dit la version rigide utilisée pour les comparaisons n'était tout simplement pas un optimum. De ce fait lorsque cette correction est prise en compte (nouvelle géométrie rigide), les fortes déformations tendent à s'éloigner de cet optimum aérodynamique et donc dégrade la performance globale d'extraction. Les différents jeux de paramètres déterminés pour chaque problème d'optimisation ne semblent pas compatibles entre eux. Pour finir, les fortes déformations élastiques réduisent fortement les performances aérodynamiques du drone sur son enveloppe de vol. Ils favorisent également l'appariton des phénomènes aéroélastiques divergents et la perte d'efficacité des gouvernes aérodynamiques.Enfin une voilure très souple rompra sous un facteur de charge très faible. Nous verrons dans le prochain chapitre que cette remarque est importante pour le vol de gradient.

7.1 Introduction

The UAV market has seen a remarkable surge over the past two decades, largely due to the shrinking size of internal electronics. Drone manufacturers prioritize two key elements—extended flight duration and maximum payload—to stay competitive. Enhancing a UAV's range and efficiency involves various methods and technologies. By leveraging a multidisciplinary optimization tool that integrates different devices and approaches, manufacturers can craft an ideal design (Pollet et al.-2022,Bronz-2012 and Fayez et al.-2021). To mitigate payload penalties and reduce mass, using fewer materials in the aircraft's structure becomes crucial. Additionally, aerodynamic efficiency often favors high aspect ratio wing configurations, especially for long-endurance UAVs that require flexibility in their design to accommodate significant deformations.

Even after achieving optimal design, there's potential to further extend a UAV's endurance by tapping into the surrounding environment for additional energy sources. Techniques like thermal soaring hold promise in significantly expanding both the range and endurance of existing drones.

Thermal soaring has gained considerable attention as a technique to extend the endurance and range of UAVs. This method involves utilizing rising columns of warm air, known as thermals, to gain altitude and sustain flight without expending onboard power.

Researchers have explored the application of thermal soaring in UAV operations. Studies by Raymer and et al. and Anderson and et al. delve into the principles of thermals and their suitability for autonomous soaring. They emphasise the potential for improved endurance and expanded mission capabilities in UAVs through efficient exploitation of these atmospheric phenomena.

Moreover, advancements in sensor technologies and onboard systems have enhanced UAVs' ability to detect and utilise thermals effectively. Works by Qin and et al. and Pumrin and et al. discuss the integration of sophisticated algorithms and sensors to autonomously detect, track, and exploit thermals for prolonged UAV flight.

Despite its promising potential, challenges remain in optimising the utilisation of thermal soaring in various environmental conditions. Research efforts by Smith and et al. and Johnson and et al. focus on developing adaptive control strategies and modelling techniques to navigate and exploit thermals efficiently under changing atmospheric conditions.

In conclusion, thermal soaring stands as a promising technique to extend the endurance and range of UAVs, with ongoing research aiming to refine strategies, algorithms, and control systems for effective implementation in diverse operational scenarios.

The contribution of this chapter is to provide an insight on the benefits or drawbacks brought by the flexibility of a UAV on its thermal soaring performances. The chapter is built as follows. In the first section, the two different ways to harvest energy from a thermal are explained. From them, 3 optimisation problems are introduced. The latters are defined to find the best set of structural parameters that maximise the thermal soaring performances. Follow a section dedicated to the experimental validation of the numerical framework (ASWING, Drela) retained to solve the optimisation problems. Finally, the last section is dedicated to the optimisation results and a discussion on the question raised by the chapter. Comments are also provided regarding the impact of the structural parameters on the UAV flight envelope to be sure that the solutions are feasible or not.

7.2 Application example: Aeronaut Triple Thermic Neo

To present this new methodology, the Aeronaut Triple Thermic Neo is used. The latter has been chosen and bought by the author to perform numerical and further experimental analysis. It was chosen as it is relatively cheap and spare wings can be bought separately in case of a crash. The first model was crafted by the author and is depicted in figure 7.1 in flight condition. The mass, wing span, wetted area,

Figure 7.1: Application example: Aeronaut triple thermic (in flight)

and aspect ratio are respectively 2.55 meters, 0.49 m^2, 1.0 kg, and 13.5. Because of its high aspect ratio, ASWING numerical predictions of the UAV behaviour are expected to be reasonable in regard to the model's theoretical limits. In this work, freedom is taken on

the structural parameters as the idea here is to highlight what could be the benefits or drawbacks brought by a highly deformable structure. Thus the latter parameters are not specifically provided. However for the aerodynamic parameters, XFOIL Drela (1989) analysis of the wing and V-stab profiles have been performed to feed ASWING for further analysis.

The model was also picked up as its geometry fits in the Mini UAV category which is of interest in this chapter. So the Aeonaut Triple thermic seems to be a good candidate to highlight or not the benefit of the flexibility in thermal soaring.

Baseline parameters estimation:
Once crafted, wrapped and equipped, some mandatory parameters could be experimentally estimated. For example, the wings were detached from the main body to measure their mass and the centre of gravity position. Then from their knowledge, a pendulum bench was crafted to measure the moment of inertia about the spanwise axis of the wing. That being done, the wings were fixed again to the body. The aircraft's centre of gravity position about the wing trailing edge could be estimated using techniques. From its position, a similar pendulum system was crafted to compute the longitudinal moments of inertia of the aircraft. Here it was held from the tail, and nose down using a friction-less attachment. The test consists of measuring the pendulum (fuselage) small oscillations period over 5 to 10 periods. From it, the longitudinal moment of inertia about the aircraft's centre of gravity could be computed.
Real flight observations:
Some flight tests (cf figure 7.1) were performed, and interesting observations could be drawn. For example, in high banked (ie high load factor) turn, we have figured out that mainly the wing was subject to major deformations and small flutter. In high-speed level flight, we haven't witnessed any loss of elevator or rudder effectiveness, or V-Tail shape deformation. Thus in the next sections, the fuselage and V-tail are considered stiffer than the wing. And so for simplicity, all their stiffness parameters have been set to infinite. The fuselage and V-tail masses distributions are thus lumped in the total mass and moment of inertia of the aircraft.
Numerical model:
The UAV numerical model was built in a few steps. First of all XFOIL analysis of the wing and V-tail airfoils has been performed to get the aerodynamic mandatory ASWING parameters. From a visual inspection of the wing profile, the SD7037 airfoil seemed to be the best fit. For the V-Tail, a NACA0008 has been chosen. Note that in reality, the V-Tail airfoil is closer to a flat plate, however, the NACA0008 was retained as it could be easily crafted from a 3D printed mould and carbon fibre. The ailerons, rudder and elevator derivatives have been computed also using XFOIL and are summed up in Appendix B of this chapter(cf figure 7.19). Note that for the wing and V-Tail, the XFOIL analysis was performed at 2 Reynolds number to take into account the chord variation (ie Reynolds number). The Reynolds number has been picked up to be close to the stall speed of the aircraft as the lower speed region of the speed polar is of interest. Secondly, the mass and inertia of the fuselage and V-Tail were lumped into a "concentrated mass". The moment of inertia has been recovered using a punctual mass dipole. They have been equally spaced from the fuselage/Vtail centre of gravity (the distance is obtained from the radius of gyration recovering the moment of inertia). Thirdly, not so much effort was put into the estimation of the wing structure parameters as they aim at varying into a reasonable set in the following analysis. However, their spanwise distribution is assumed to be elliptical as the wing is. Finally, 1 sensor has been implemented and placed at the aircraft's centre of gravity to provide the aircraft with inertial and air-relative speed.

7.3 Steady thermal soaring:

In this section, the performances of the Aeronaut Triple Thermic Neo in static soaring are discussed. The turning polar provides information on how the glider is sinking at a given turn radius and airspeed. The glider pilot can thus wisely choose his speed and turn radius to maximise the energy extracted in a thermal of a given size for example. The turning polar is built from the speed polar that is constructed from steady banked glide trimming computations.

7.3.1 Static soaring performance metric

It is important to note that the thermal profile is not needed to assess the static soaring performances of a UAV. Indeed as the latter are considered as much wider than the aircraft size their speed profile varies spatially slowly and can be considered constant along the wing span. Thus only the speed and turning polars are enough to status on the UAV performances. In this section, the static soaring performance metrics are introduced to define optimization problems. Their goal is to find the optimal set of structural parameters that maximize the energy harvested in this specific strategy. As mentioned above, the speed and turning polars are very useful metrics of performance. The turning polar is built from the speed one. To build it,

the following trimming problem must be numerically solved

Banked glide trimming problem:

$$\begin{aligned} &\textit{find } u = (\delta_A, \delta_E, \delta_R)^T \text{such that } r(\dot{x}, x, u) = 0 \\ &\text{subject to :} \\ &(\alpha_x, \alpha_y, \alpha_z)_{body} = (0,0,0)^T \\ &a_x = a_{x,ref} = 0 \\ &V = V_{ref} \\ &\phi = \phi_{ref} \\ &\dot{U_Y} - \Omega_Z U_X = \dot{U_Y} - \Omega_Z^2 R_{turn} = 0 \end{aligned} \tag{7.1}$$

where r is the non-linear set of differential equations defining the flexible aircraft dynamics and equations of motion. The first line of constraint imposes no angular acceleration in the body frame. The second is a constant x speed (azimuthal speed). The third and fourth are the airspeed V and bank angle ϕ where the trim problem must be solved (user-defined in red). The fifth ensures that the centrifugal acceleration of the aircraft in the inertial frame is perfectly balanced with its lateral acceleration. In other words, the projected lift on the lateral axis must balance the centrifugal force. The problem seeks the set of control parameters which are the ailerons, elevator and rudder deflections that satisfy the above problem. To solve this problem ASWING uses a gradient-based method in order to find the zero of a corrected EOM system $r_{trim,problems}$ where the above constraints have been implemented as penalty functions. This formulation is used to build the turning polar of the UAV. As it has been said before, on mini UAVs because of their low Reynolds number flight, the minimal sink speed is equal to the stall speed. In consequence, the lower bound of the turning polar is defined by each stall speed at a given bank angle. Or it is quite dangerous to fly near those speeds as the aircraft becomes less and less controllable and is very likely to enter into deep stall behaviour leading to a certain crash. As the literature on the control of stalled aircraft is still young the choice of a "conservative" turning polar has been picked up. Here instead of building the turning polar from the stall speed, the "first local" stall is chosen. Indeed, before a complete stall, local sections on the wing are stalling first (generally root sections), and then the local stall spreads towards the wing tip until the latter is not able to lift the aircraft anymore. The local stall appears at a higher speed than one of the complete stall. However, in this range, the aircraft is still reasonably controllable. Finally from a numerical point of view, even if ASWING is able to capture the early stallbound of the turning polar defined by an aircraft, the way it is modelled is not that realistic. In consequence, detecting the local stall is preferred in this work to avoid the numerical discrepancy introduced by the ASWING model. Thus to build the turning polar, the banked glide trimming problem must be solved at each bank angle and local stall speed. To do so, a subroutine has been implemented to detect the first local stall. A flag is then returned by ASWING when the local stall is reached on the glide trimming problem. To have a precise idea of the local stall speed, a heuristic algorithm has been implemented to converge quickly to the desired speed. The speed accuracy has been set up to 0.05m/s. Once the convergence is reached the algorithm returns the local stall speed, and the inertial speed U and rotation rate Ω. From them, the turn radius R_{turn} can be computed as follows

$$R_{turn}(\phi) = \frac{\sqrt{U_X^2 + U_Y^2}}{\Omega_Z} \tag{7.2}$$

The turning polar is then built from the knowledge of the turn radius and the sink speed U_Z. From it, the performance of the UAV in static soaring can be evaluated. When the bank angle precision is set up to 2.5° it takes around 50 seconds to build a complete turning polars upper bound of a given UAV configuration.

7.3.2 Optimal glide ratio

The second performance metric useful in static soaring is the glide ratio. Indeed, thermals, leewaves, ridges etc are bounded in space and time, so they eventually vanish. The glide ratio gives information on how far the glider will travel from one exploitable phenomenon to another one. In consequence, the bigger it is better the range. Computing the glide ratio is mandatory to appreciate the performances of a glider in static soaring. Thus, a heuristic algorithm has been implemented in order to detect the optimal travel speed where the glide ratio is maximum. For each airspeed considered the trimmed glide problem is solved at $\phi = 0°$. The same speed precision has been used as the local stall speed detection. Once the algorithm has converged ASWING return the inertial speed and the glide ratio is given as

$$G_R = \frac{U_X}{U_Z} \tag{7.3}$$

where U_X and U_Z are the aircraft inertial speed components.

7.3.3 Optimal problem definitions : OP1 and OP2

From the previous metric of performances introduced, it is possible to set up optimisation problems. In

this work, the objective is to status if flexibility can increase the performance of a given UAV in thermal soaring. Thus in this work, the optimisation variables are the wing stiffness and tailoring parameters that are, $EIcc$ the chordwise bending stiffness, GJ the torsional stiffness, c_{ea} and c_{ta} the elastic and tension axis chordwise locations. The normal bending stiffness has been omitted as it is usually much greater than the chordwise one. Thus it has been set up to infinite (rigid). Also in order to minimise the number of variables involved in the problem, the torsion coupling terms have been omitted so far. That being said, two optimisation problems have been defined in this work. The first one consists of maximising the sinking power (defined as negative) at a given turn radius here chosen at 13m. We also tested a problem taking every turn radius sinking speed with a weighted function but similar results were found. So a single-turn radius evaluation has been chosen. The first optimisation problem has been defined as follows:

Optimisation Problem # 1 (OP1): *best sink*

$$\begin{aligned} \textbf{maximize: } & \mathcal{P}_{sink}(R=13m) \equiv U_Z(R=13m) \\ over: & X = (c_{EA}, c_{TA}, EI_{cc}, GJ) \\ \text{subject to: } & 0.15 \leq c_{EA}/c \leq 0.5 \\ & 0.15 \leq c_{TA}/c \leq 0.5 \\ & 2.5Nm^2 \leq EI_{cc} \leq 25Nm^2 \\ & 2.5Nm^2 \leq GJ \leq 25Nm^2 \end{aligned} \tag{7.4}$$

where the lower and upper bounds of each variable have been chosen to remain realistic. For a given bending or torsion stiffness it is possible to place the tension axis just by wisely placing the reinforcement part, however, it is very unlikely that the axis lies out of the boundaries defined above as the section thickness decreases rapidly towards the leading and trailing edges. Lower and upper bounds have been defined on the bending and torsion stiffness, and also on a reasonable range where those values could be achieved by using various materials, from balsa to glass and carbon fibre. For example, the balsa kit used for further experiments has a bending stiffness of 19 Nm^2 (from tip mass coarse tests).

A second optimisation problem has been defined in order to maximise the glide ratio of the UAV

Optimisation Problem # 2 (OP2): *optimal travel*

$$\begin{aligned} \textbf{maximize: } & G_R \\ over: & X = (c_{EA}, c_{TA}, EI_{cc}, GJ) \\ \text{subject to: } & 0.15 \leq c_{EA}/c \leq 0.5 \\ & 0.15 \leq c_{TA}/c \leq 0.5 \\ & 2.5Nm^2 \leq EI_{cc} \leq 25Nm^2 \\ & 2.5Nm^2 \leq GJ \leq 25Nm^2 \end{aligned} \tag{7.5}$$

The same variables and bounds have been set up so no comments are added. It is clear that optimal problems 1 and 2 should be mixed together with a weighted cost function. However, no information on how much time a UAV is spending in glide and soaring has been found yet. Without this intel, it was difficult to set up a realistic scenario. Thus separated problems have been preferred. Each optimal solution X_{OP1} and X_{OP2} are compared in a dedicated section.

7.4 Unsteady thermal soaring: the dolphin kick

As with every glider, the Aeronaut Triple Thermic has a minimum steady glide turn radius. In consequence, it can not harvest energy from a thermal having a lower one using a "static" soaring technique. However, the UAV can still benefit from smaller thermals. The idea is just to fly or glide through it and get this small upwash pump, providing a small increase in the aircraft's altitude. This technique, also known as "dolphin kick" can be used to improve slightly the UAV gliding slope by successively flying through small thermals and having those small jumps. In theory, this technique allows us to extend the gliding range of the aircraft as depicted in figure 7.2. From the size of the thermal and the gliding speed, unsteady aerodynamic is involved and so a pur unsteady analysis is mandatory to status on the performances of the aircraft. In this section, a third optimization problem is presented.

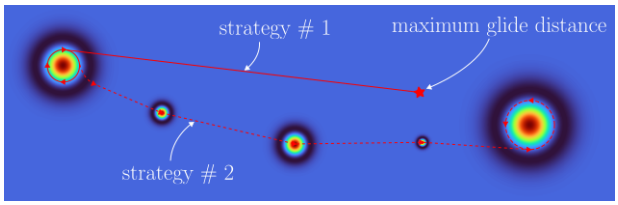

Figure 7.2: Glidding slope improvement using unsteady thermal soaring (dolphin kick)

7.4.1 Thermal model

As it has been seen, for this strategy it is not possible to rely on steady analysis. Thus the wind field must be taken into account for a complete time marching computation. Here a thermal model with sink edges is proposed with the vertical speed profile defined as :

$$\begin{aligned} W_z(x,y) &= W_{z,max} e^{-\delta r^2/R_T^2} \left(1 - \delta r^2/R_T^2\right) \\ with\ \delta r &= \sqrt{(x-x_T)^2 + (y-y_T)^2} \end{aligned} \tag{7.6}$$

This model is widely used in the literature and is implemented in the current version of ASWING so its choice. The other advantage of the latter is that the wind field function defined a zero net vertical flux. This means that the sink edge intensity are function of the inner core speed such that

$$\Phi_{thermal,z} = \iint W_z(x,y)dxdy = 0 \qquad (7.7)$$

making the thermal a balanced system. In this work, a thermal of radius $R_T = 2.5m$ with a maximum core speed of $1.0m/s$ has been chosen. The radius has been picked up in order to involve unsteady aerodynamic flow when the UAV flies through the thermal. The reduced frequency should vary around $k = 0.2$. The inner core intensity has been chosen to avoid the UAV stall during the transient response to keep the ASWING accuracy later discussed.

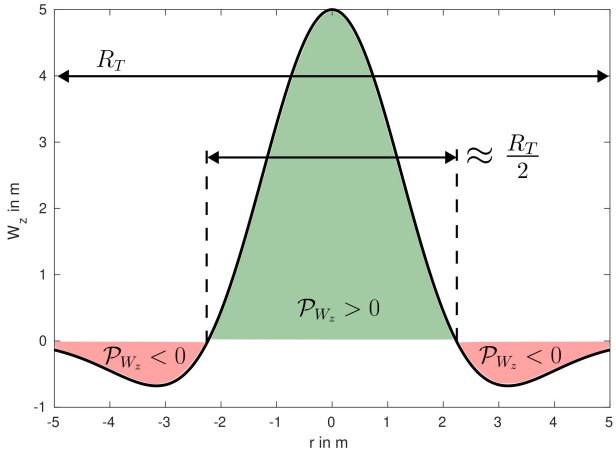

Figure 7.3: Thermal model illustration ($W_{z,max} = 5m/s$, $R_T = 5m$))

7.4.2 Corrected climbing/gliding slope

To measure, the UAV dolphin kick performances, a single fixed problem has been defined. Let H_0 be the initial altitude of the aircraft at $t = 0s$. The latter starts to glide at the optimal gliding speed from a fixed distance D_T to the thermal centre (cf figure 7.4). When the UAV glides through the thermal, a small gain of altitude is witnessed. After the UAV has entered the thermal the maximum altitude position is detected and the corrected climbing or gliding ratio is computed as follows.

$$C_R = \frac{\Delta Z}{\Delta X} = \frac{Z_{max,z,bump} - H_0}{X_{max,z,bump} - X_0} \qquad (7.8)$$

where $Z_{max,z,bump}$ is the maximum altitude reached after the thermal/gust encounter and $X_{max,z,bump}$ is its position. Fixing the thermal size, distance and

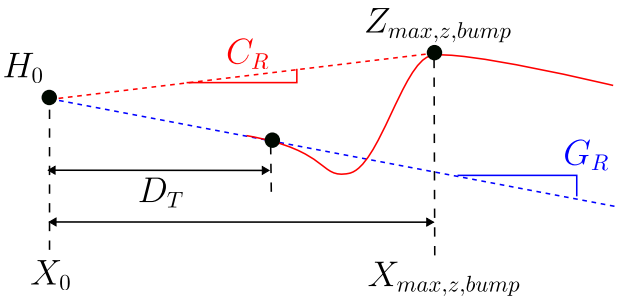

Figure 7.4: Corrected slope illustration

intensity seems more rigorous as it allows the comparison of different aircraft for the same wind field. It will capture both the change in the UAV glide slope and the bump performances. For example, a UAV could be extremely efficient during the bump and very bad for glide while a second UAV would have moderate performances in both cases but will perform better overall. In consequence, to measure the performances 2 main functions are needed to evaluate the new climb rate C_R. First, the optimal gliding speed must be computed using the function introduced in the static soaring section. Then a full unsteady time marching computation must be performed. From the simulation results, a post-process function computes the climbing rate. For all the unsteady simulations a time step of 0.01s has been chosen enough to capture the first structural modes effects. A fixed number of time steps has been fixed to 250 with the maximum bump reached around 200. Overall, 12.5 to 15s are needed to compute the "corrected" climbing rate of a given UAV configuration.

7.4.3 Optimal problem definition : OP3

From the previous section, the third optimisation problem can be defined as follows

Optimisation Problem # 3 (OP3): *best dolphin kicks*

$$\begin{aligned} \textbf{maximize: } & C_R \\ over: & X = (c_{EA}, c_{TA}, EI_{cc}, GJ) \\ \text{subject to: } & 0.15 \leq c_{EA}/c \leq 0.5 \\ & 0.15 \leq c_{TA}/c \leq 0.5 \\ & 2.5Nm^2 \leq EI_{cc} \leq 25Nm^2 \\ & 2.5Nm^2 \leq GJ \leq 25Nm^2 \end{aligned} \qquad (7.9)$$

where the same parameters bounds as OP1 and OP2 have been used and C_R is defined in equation 7.8.

7.5 Numerical framework evaluation:

The above optimisation problems raise a number of numerical needs. For steady thermal soaring, it is mandatory to capture well, the aerodynamic performances of a given flexible UAV in steady trimmed glide. Thus the numerical framework chosen that is ASWING [Drela, Drela, Drela] must be able to accurately trim a given UAV for a given speed V and bank angle ϕ. As it is difficult to find experimental data on trim conditions, to make sure that ASWING is accurate, several separate features have been evaluated. When a glider is in a steady banked turn, asymmetric lift loads are applied on the wing because of the different azimuthal speeds and dihedral angle effects (cf figure 7.5-a). This, in consequence, induces a yawing and rolling moment that must be balanced using ailerons and the rudder. This will ensure the lateral balance of the UAV. For the longitudinal one, the horizontal stab is used to compensate for the pitching moment induced by the lifting surfaces (wing, fuselage etc). Moreover, the wing wake has a strong impact on the horizontal stabiliser because of the down-wash effect (cf figure 7.5-b). The following sub-sections aim to present the experimental evaluation work performed on each critical aspect mentioned above.

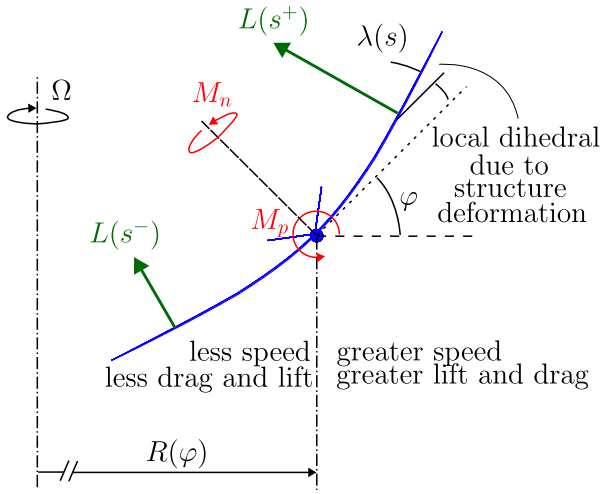

(a) Lateral trimming

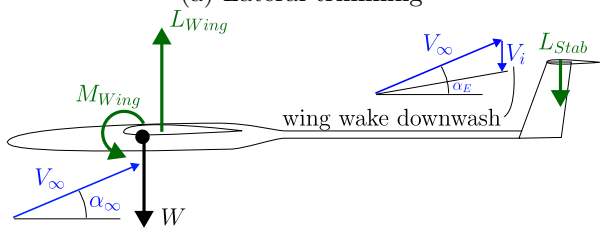

(b) Longitudinal trimming

Figure 7.5: Steady glide in turn trimming problem illustration

Lift and wake interference:

The longitudinal balance of an aircraft is affected by the wing and the horizontal stab. Thus capturing the lift they produce is important to assess the trimming problem correctly. Also, the horizontal stabiliser is downstream of the wing and thus strongly affected by the wing wake. To make sure that ASWING captures well those effects, the "higher fidelity data of Cheng and Wang have been used. A tandem aircraft was considered in their work (cf figure 7.6). This layout was chosen as tandem is strongly sensitive to wake interaction and the authors have provided the lift measurements of each lifting surface. Figures 7.6 (a) and (b) present a comparison between the ASWING lift predictions and the "higher fidelity" data. Note that no matter the lifting surfaces, the forecast is in good agreement with experiments, with a linear slope error below 5%. Thus ASWING captures well the downwash effect on the lift of the backward wing. Moreover, ASWING captures the pre-stall effect of both the lifting surfaces especially highlighted by figure 7.6 (a).

Fuselage effect on the longitudinal balance:

Another element that contributes to the longitudinal balance of the UAVs (and also to the lateral one) is the fuselage. Indeed fuselage for a positive angle of attack generates a pitching up moment that tends to fight the pitching down moment of the wing. Its effect is important to take into account as it will drastically change the amount of lift that must be generated by the elevator to trim the UAV. To do so, the experimental results of Von Karman have been used. The worst airship (fuselage) has been used (lower aspect ratio). Experimental data in comparison with the ASWING predictions are presented in figure 7.7. The local lift coefficient against the spanwise coordinate is in good agreement with the experiments except at the rear part. This discrepancy is due to the boundary layer thickness effect that is not taken into account in the ASWING model. However, if the local lift is integrated, the pitching moment induced by the fuselage is well captured by ASWING.

Ailerons effects

Ailerons are used to counter the induced roll in a steady turn because of the difference in azimuthal speed inducing an unbalanced lift distribution (cf figure 7.5-a). Thus capturing their effect is very important. To evaluate this feature, the experimental data of Heald and Strother is used. A rectangular flat wing (cf figure 7.8-a) was placed into a wind tunnel, with various ailerons configurations (spanwise and chordwise length varying). Induced rolling and yawing moment measurements were performed for various

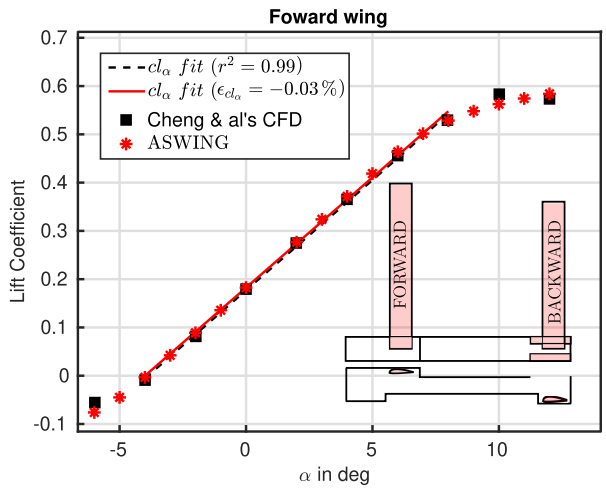

(a) Forward wing

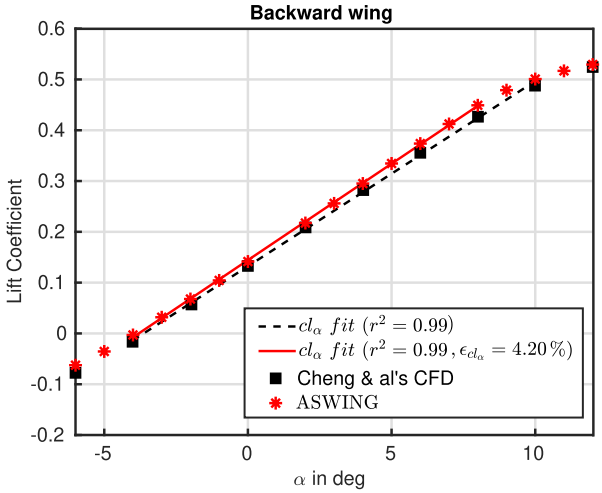

(b) Backward wing

Figure 7.6: Tandem aircraft lift coefficient predictions against higher fidelity data from Cheng and Wang

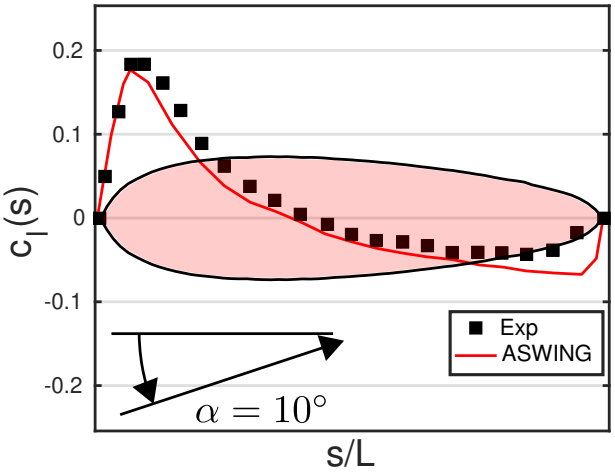

Figure 7.7: Lift distribution over a fuselage. Aswing predictions against experimental data from Von Karman

aileron deflections and angle of attack at the air-speed of the Mini-UAV category. Figure 7.8 (a) presents the comparison between the ASWING predictions and the experiments for the rolling moment. Linear slopes have been computed on what Heald and Strother called the first linear range. No matter the aileron configuration, ASWING shows excellent agreement with the experiments. For high deflection, however, the linear slope error increases. Figure 7.8 (b) present a similar comparison but for the yawing moment. This time ASWING shows bad agreements. However, the yawing moment induced by a deflected aileron is an order of magnitude smaller than the rolling moment. Thus when solving the trimming problem, the rudder effect on the yaw will be dominant. Finally, the rolling moment is a pur translation of the lift distribution over the wing, and thus the effect of the aileron on the local lift. In consequence, this evaluation comparison can be invoked for the remaining control surfaces of the UAVs, such as the rudder and the elevator. ASWING is thus able to capture accurately the primary effect of control surfaces.

Ailerons effectiveness:

When a UAV is flexible, it can be subject to aileron reversal because of local twist. The reversal behaviour is not sudden, indeed the aileron effectiveness linearly decreases with the dynamic pressure as reported by Cole. As in this chapter, the trimming problem is solved at various speeds (ie dynamic pressure), and ASWING must be able to capture well the loss of effectiveness. To do so, the experimental data of Cole have been used. Here a trapezoidal wing with various ailerons configuration (length as a % of the half span) was anchored into a wing tunnel. The structure stiffness of the wing was chosen so that the reversal behaviour appears in the wing tunnel speed range. Rolling moment measurements were performed at each airspeed tested. The comparisons with ASWING predictions are presented in figure 7.9. No matter the aileron configuration, ASWING is in good agreement with the experiments. The loss of effectiveness and the reversal behaviour are well captured. Note this phenomenon is not restricted only to ailerons but to every control surface. Thus this evaluation conclusion can be accounted for the remaining control surfaces of the UAV.

Steady deflection:

The more the radius of turn reduces, the greater the load factor is on the wing, because of the higher bank turn. Thus along the turning polar, the structure will deform modifying the aerodynamic performances of the aircraft. In particular, it will modify the shape of the wake and thus the lift-induced drag. Capturing its change is thus mandatory. To do so, the experimental data from Avin et al. have been used. The Pazy wing (moderate aspect ratio) was placed in Tennion's wind tunnel. The tip deflection and twist have been mea-

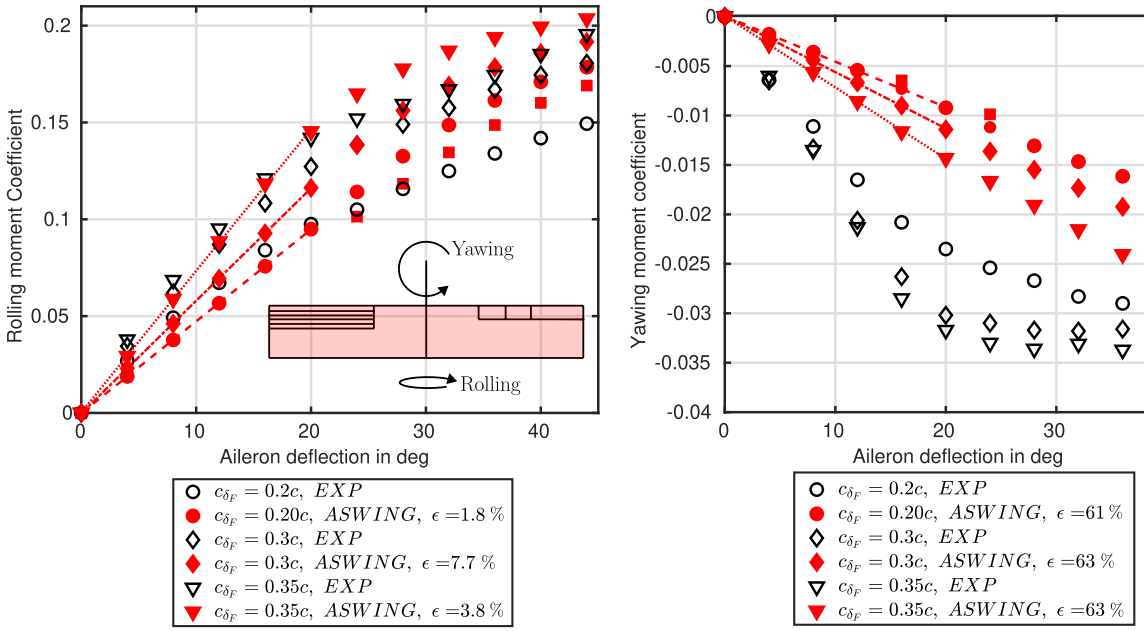

(a) Rolling moment (b) Yawing moment

Figure 7.8: Various ailerons configuration effect on the rolling and yawing moment of a straight wing. ASWING predictions against experimental data from Heald and Strother

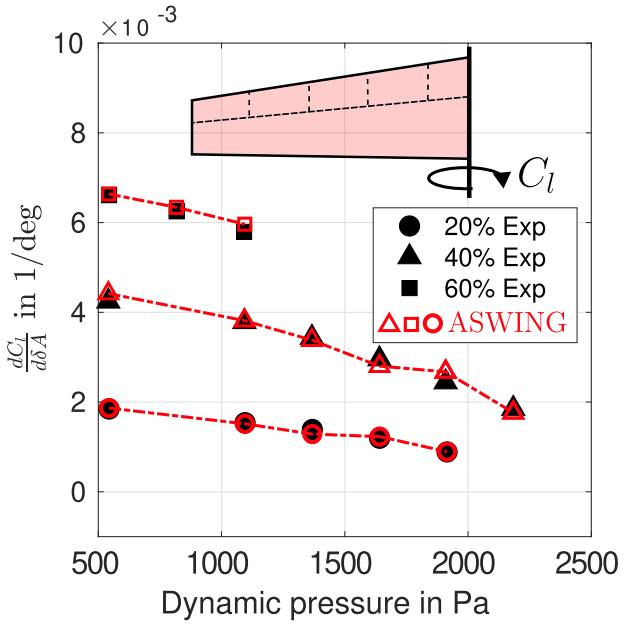

Figure 7.9: Loss of rolling effectiveness with dynamic pressure of a trapezoidal wing. ASWING predictions against experimental data from Cole. Various ailerons length (as a % of the half span)

sured at various angles of attack and speed. Figures 7.10 (a) and (b) present the ASWING predictions against the experiments. Tip deflections are in good agreement with a prediction error below 10% for large deformations. The prediction error for the twist is greater but ASWING follows well the twist trend and is satisfactory for this chapter's application.

Drag prediction of deformed shapes:
ASWING captures well the change of a wing shape due to the aerodynamic loads. Its capacity to predict the drag of deformed shapes must be assessed. To do so, 2 planforms are used. First a planar straight wing as a reference case for comparison and the same wing but with a 45° dihedral angle (here used to simulate deformed shapes). Figures 7.11 (a) and (b) present the comparison between the ASWING predictions and experimental data from Applin for the flat wing and StarCCM+ (higher fidelity) data for the second one. From the latter, even at a high angle of attack, ASWING shows good agreement with the data. The gliding performances will thus be well captured.

Unsteady aerodynamics:
For unsteady thermal soaring, the size of the thermal and the UAV speed can be such that unsteady aerodynamics can be involved. Change in the lift and phase lag can be witnessed in a given configuration. Capturing them is thus mandatory to assess correctly the third optimisation problem OP3. To do so, the experimental data of Chiereghin et al. have been used. A straight wing (low aspect ratio) has been placed into a wing tunnel. Various reduced plunging amplitudes and frequencies were tested. Also, the root wing

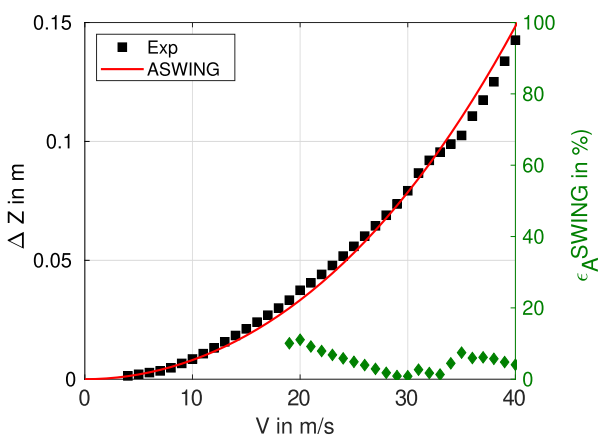

(a) Tip deflection

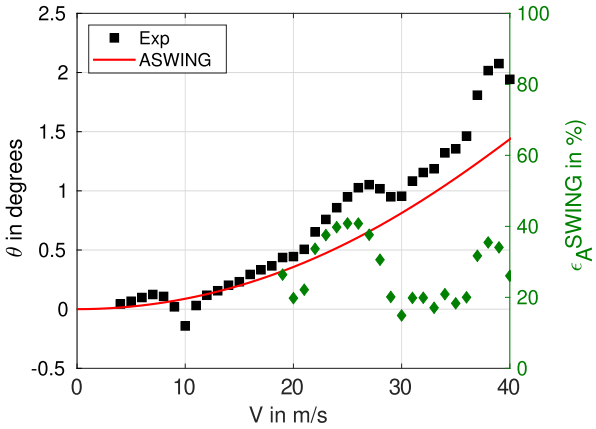

(b) Tip twist

Figure 7.10: ASWING prediction of the Pazy wing steady tip deflection and twist at $\alpha = 7°$. Comparison with experiments from Avin et al..

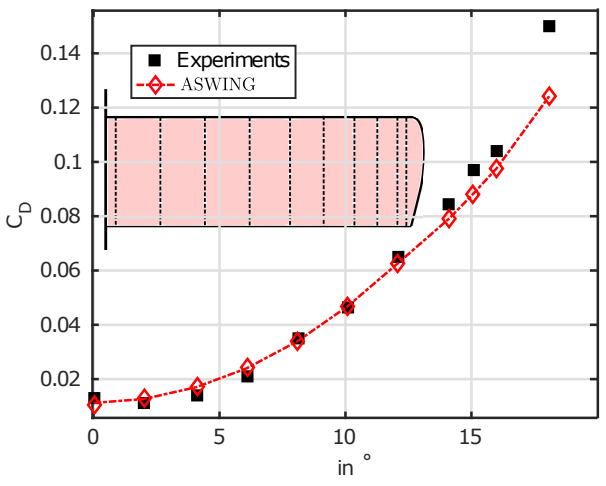

(a) Straight wing

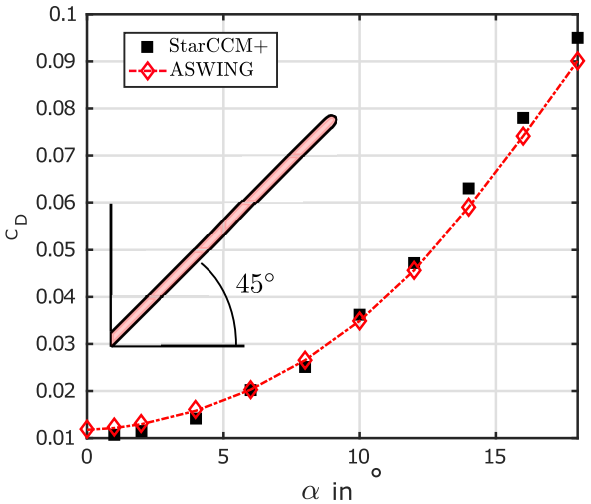

(b) 45° dihedral angle wing

Figure 7.11: ASWING drag prediction of 2 different planform. Comparison against experiments from Applin and StarCCM+ data

angle was changed. Here only the pre-stall configuration is presented ($\alpha = 9°$). Figures 7.12 (a) and (b) present the comparison with Aswing predictions. For the lift first harmonic amplitude, the forecast is in good agreement with the experiments no matter the reduced amplitudes and frequencies. For the phase lag, here the Aswing model does not vary with the reduced amplitude (please refer to Drela) so the single line on the plot. Predictions are in reasonable agreement with the experiments and are more than satisfactory for this chapter's application.

Flutter speed and aeroelasticity dynamics:

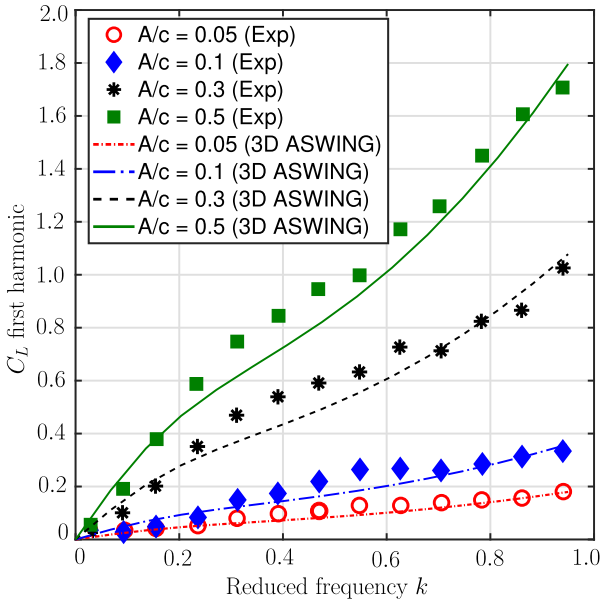

(a) Lift coefficient first harmonic amplitude

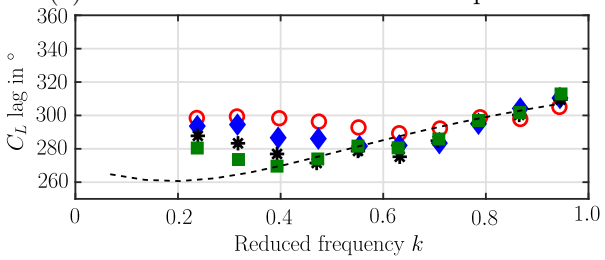

(b) Lift coefficient first harmonic phase lag

Figure 7.12: ASWING unsteady lift amplitude and phase lag of a plunging wing. ASWING predictions in comparison with experiments from Chiereghin et al.

Even if a thermal can be a time-frozen wind field, when the UAV is flying through it (unsteady thermal soaring), a transient response is witnessed. The latter can easily excite the dynamic of the UAV and especially its flexible modes. Moreover, if the glider is flying near its flutter speed, the sudden increase in speed and angle of attack can lead to a self exited behaviour. The latter would make unsteady thermal soaring unfeasible. Thus capturing the flutter speed and frequency of a flexible UAV at various angles of attack is mandatory to assess the optimisation problem OP3. The Pazy wing has been used again to evaluate ASWING's capacity to predict the above phenomena. Drachinsky et al. provided the experimental flutter analysis of the Pazy wing. The wing was placed into the Tennion's wind tunnel. At each angle of attack, different speed sweeps (up = increase, down = decrease) were performed as different self exited behaviours have been witnessed depending on the sweep sign. They provided the flutter speed and frequency at each of the test conditions. Figure 7.13 presents the ASWING predictions comparison with the experiments for the flutter speed. No matter the angle of attack, ASWING captures well the flutter boundaries, with a prediction error is below 5%. Drachinsky et al. have witnessed that the Pazy wing was not diverging between the flutter boundaries (green zone in figure 7.13) because of non-linear stabilising effect (Limit cycle oscillations). This behaviour can not be captured by the modal analysis function of ASWING as it predicts an unstable flutter mode between the boundaries. However, when a full-time marching simulation is performed, ASWING simulates the full non-linear effects and captures the limit cycle oscillations identified by Drachinsky et al.. Table 7.1 also presents the comparison of the ASWING prediction and the experiments for the flutter frequency. Again, ASWING is in excellent agreement with the experiments. In addition, the vacuum modal analysis of the Pazy wing is also compared to the ASWING predictions. Table 7.2 presents the results in comparison to the experimental measurements of Avin et al.. Modes are presented in un-deformed and deformed conditions. This simply means that the Pazy wing was anchored vertically or horizontally to the vibrating device. Overall, ASWING predicts well the first 3 out of the plane bending modes as well as the first torsion mode. Regarding the first In-the-plane bending mode, the accuracy of prediction is bad. However, this mode was reported to be difficult to measure. Also, this type is very unlikely to be excited as the in-plane bending stiffness of wings is usually an order of magnitude greater than the out-of-plane one. Also, only the drag is susceptible to excite it but its magnitude is usually much lower than the lift one that excites both the out-of-the-plane and torsion modes. The transient response of the wing is thus mostly dominated by the latter modes. In consequence, ASWING is adapted to unsteady thermal soaring analysis as it predicts well all the phenomena that are expected in such techniques.

Flutter frequency				
AoA	**Sweep type**	**Exp.**	**ASWING**	**Diff (%)**
3	Up	30,00	30,69	2,3
5	Up	29,90	30,16	2,9
7	Up	29,40	30,25	0,67
3	Down	28,20	28,01	6,0
5	Down	26,70	28,3	3,98

Table 7.1: Pazy wing : flutter boundarie, ASWING flutter frequency predictions. Comparisons with experiments from Drachinsky et al.

		Modes in (Hz)				
Configuration	**Data**	**OOP1**	**OOP2**	**T1**	**IP1**	**OOP3**
Undeformed	**Exp**	4.26	28.5	42.0	60.7	81.5
	ASWING	4.59	29.1	43.4	128	81.4
	ϵ_A	7.2 %	2.1 %	3.3 %	+200 %	-0.1 %
Deformed	**Exp**	4.39	29.8	41.0	N/A	82.5
	ASWING	4.67	29.2	43.2	116	81.4
	ϵ_A	11 %	-2 %	3.84 %	NC	-1.9 %

Table 7.2: Pazy wing modal response in undeformed and deformed condition. ASWING predictions against experimental data of Avin et al.. OOP = Out Of the Plane bending mode, T = Torsion mode and IP = In-the Plane bending mode

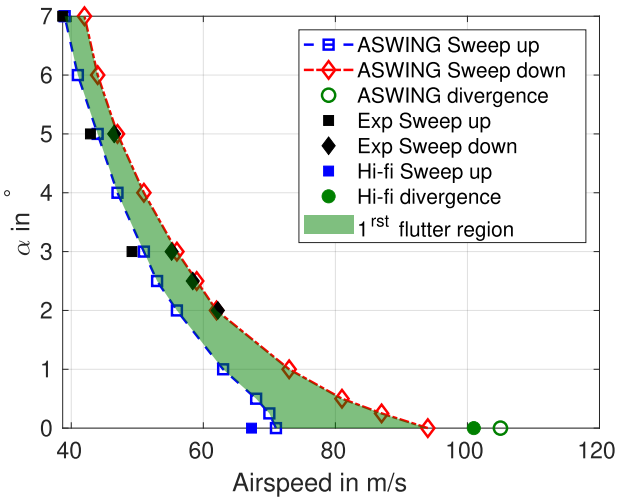

Figure 7.13: Pazy wing flutter boundaries ASWING predictions angainst experiments from Drachinsky et al.

Conf	c_{TA}/c	c_{EA}/c	EI_{cc}	GJ
OP1	0.34	0.47	2.5	7.7
OP2	0.26	0.28	24.9	4.7
OP3	0.5	0.5	4.24	2.5
rigid	0	0	∞	∞

Table 7.3: Optimization problem solutions

7.6 Optimal configuration comparison

In this section, a comparison of the optimal solutions is proposed. To solve OP1, 2 and 3 a genetic algorithm implemented in MATLAB has been used. As the same number of optimal variables were chosen, the same optimiser parameters were used. The population size was fixed to 20 with a max number of generations fixed to 50. The first optimisation problem has converged in 20 generations with a total computation time of 6 hours. The second one has converged approximately in 25 generations with a computational time of 2 hours. Finally, the last problem converged in 15 generations with a computational time of approximately 3 hours. The structural parameters of each optimal problem solution are given in the table 7.3.

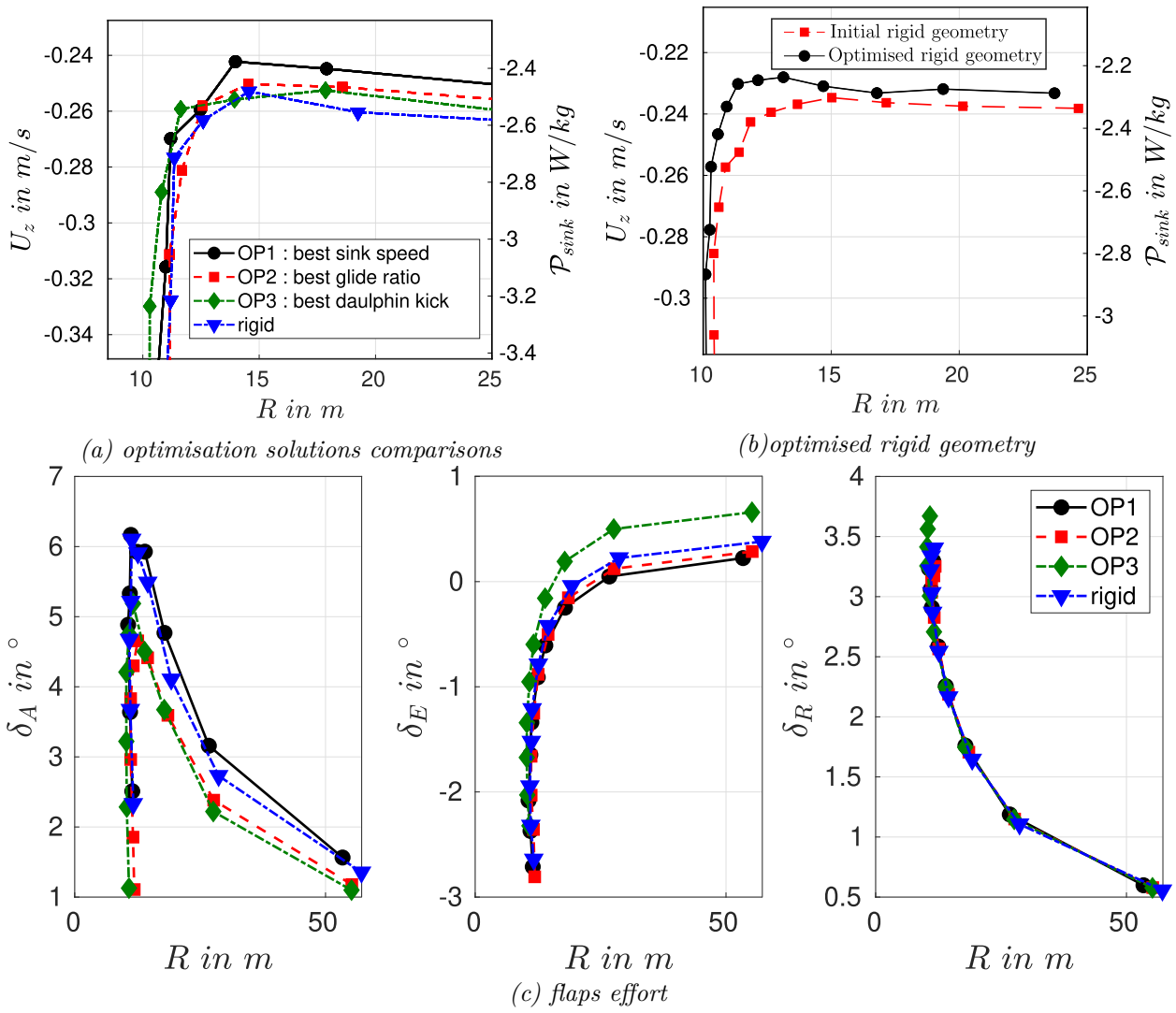

(a) optimisation solutions comparisons

(b)optimised rigid geometry

(c) flaps effort

Figure 7.14: Turning polar comparison of the optimal solutions

	G_R	Difference to rigid in %
OP1	26.42	-0.23
OP2	26.47	-0.02
OP3	26.33	-0.56
rigid	26.48	0

Table 7.4: best glide ratio comparison of the different optimal solutions

7.6.1 Static thermal soaring performances:

The first and second optimisation problems are quite disappointing as, the difference in performances between the rigid and the flexible version are not that significant. The figures 7.14 (a) to (c) present the turning polar and the control effort of each optimal solution and rigid version. Figure 7.14 (a) highlight how the OP1 solution outperformed the other one for the radius of turn above 13 meters. However the gain in performance is not that significant, a maximum of 7% of the sink speed reduction is performed at the optimisation problem turn radius definition (R=13m). Also from the control effort plots (cf figure 7.14-c), the gain in performance can be discussed. Indeed at a radius of turn of 13 meters, the aileron deflection angle of the OP1 solution is greater than the one needed on the OP2 solution (best glide). In this problem, the viscous and pressure drag increments due to deflected flap have not been taken into account. Thus the sink speed gain could be lower than as presented.
Can we really talk about the benefit of the flexibility in this case? When a look is taken a bit deeper into why this set of structural parameters has been chosen, we figure out that the rigid geometry was not optimal from an aerodynamic point of view. The optimiser has converged to this set of parameters so that when the glider is in steady banked flight, the geometry deforms and converges to a more aerodynamic efficient configuration. The lift distribution is favourably changed to reduce the lift-induced drag of the wing. Also on UAV, flying at a high bank angle while minimising the sink speed becomes very quickly limited because of the poor low Reynolds number aerodynamic performances. Thus, for the range of interesting bank angles, the load factor is quite low and so the geometry is deforming reasonably. In consequence, using structural parameters as an optimisation variable was another way to optimise a given geometry shape instead of using for example; polynomial local dihedral and twist angle functions. From a physical point of view, a rigid wing with the equivalent deformed geometry provides the same turning polar. This is highlighted by figure 7.14 (b) where the turning polar of the above configurations are presented. In consequence, the gain in performance of OP1 to rigid can not be attributed to the flexibility itself.
Regarding the OP2 problem (best glide), the results (summarised in table 7.4) are even more disappointing as no change has been witnessed from the rigid. The change is so tiny that it might be drowned in either the numerical noise or the prediction errors. So basically no conclusion can be drawn from it, and there is a chance that the optimiser has converged to an irrelevant set of structural set of parameters due to the cascade of numerical discrepancies introduced in the heuristic algorithm.
The OP1 and OP2 mostly have highlighted the limitation of the genetic optimisation approach to maximise the performances of physical systems. When there is an improvement, the set of parameters found has been shown to not have real physical meaning. Thus care must taken on the results interpretations.

7.6.2 Dolphin kicks performances discussion

The dolphin kicks performances of each optimal solution are compared in table 7.5. For the chosen thermal, every flexible solution has better performance than the rigid configuration. The OP3 solution outperforms the rigid one by 17%. Also, it is better in comparison to the OP1 by 14%. The local twist allowed by every optimal solution raises the local angle of attack and so lifts during the gust encounter. From the OP3 structural parameters, the chordwise location of the torsion and elastic axis upper bound have been reached as they maximise the torsion twist. Moreover, the torsion stiffness lower bound is reached. When the UAV encounters the thermal there is a sudden change in the aerodynamic loads. The wing bends and twists up. When the bending stiffness is too low, the deformations will lead to an increase in the local dihedral angle. The lift contribution to the vertical axis is thus reduced by the latter angle cosinus (cf figure 8.8). At the same time, the chordwise bending deformation tends to slightly increase the local angle of attack inducing the same benefit as for the torsion. The lower bound of the bending stiffness has not been reached; the optimiser has thus converged to

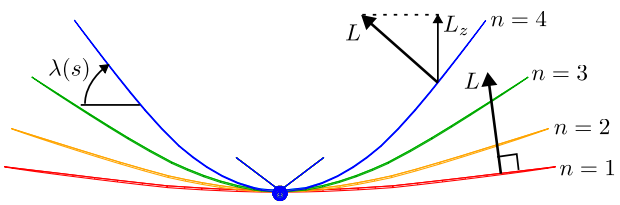

Figure 7.15: Aeronaut Triple Thermic Neo flexible change of the geometry with the load factor

a trade-off between the loss of lift mentioned earlier and the small gain in the geometric local twist. In consequence, a very flexible geometry tends to maximise the energy gain during a dauphin kick. Note that the performances found are quite consistent with the results presented by Mai (1985).
A flexible structure tends to passively increase the dolphin kick performances. Now a question arises from those observations, it seems that the positive change in the local twist tends to increase the energy harvested from the thermal. What if instead of gaining passively a local twist on the geometry, the aircraft pith angle is wisely changed? Of course, the passive property is lost but stiffer UAVs could show the same performances as the very flexible solution of OP3. This proposition is motivated by the fact that the OP3 solution is degrading a lot of the UAV flight envelope performances as described in the next section. In consequence, a sinusoidal pitching command law has been implemented on the UAV elevator. A 1.5-degree elevator deflection has been randomly chosen. The half period was chosen to fit the thermal length and the command was delayed so that the UAV pitched up when flying through the gust and then pitched down to go back to its trimmed condition after. The elevator deflection angle was so negative (up) in the thermal and positive (down) after. Overall just with this random set of command parameters, the corrected climbing rate was equal to 0.065 which is 45% better than the best OP3 value of table 7.5. The time response of the UAV altitude in both configurations is depicted in figure 7.16. It is clear that wise control of the pitching angle of the aircraft performs better than the passive behaviour of the structure deformations. It was actually demonstrated by (Gavrilovic et al.-2017-2018 and 2020) for gust soaring techniques. Also using a control law is much more convenient to recover rapidly the trimmed state of the aircraft. Indeed during the optimisation process, the post bump was not taken into account but the more the aircraft is flexible the more hazardous its response is as its flexible modes are very close to the one of the flight dynamics. A slow transfer of energy can occur, with a very low-damped response.

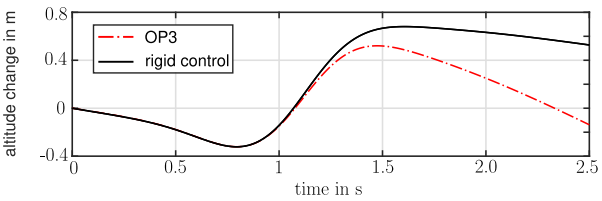

Figure 7.16: Daulphin kicks performances with and without control. Comparison with OP3 configuration

OP	C_R	Δ to rigid in %
OP1	0.0390	2.5
OP2	0.0388	+1.54
OP3	0.0445	+17 | + 14 to OP1
rigid	0.0381	0

Table 7.5: daulphin kicks comparison of the different optimal configurations

7.6.3 Aerodynamic performances

In this subsection, a comparison of the drag polars of the OP1 and OP2 is proposed. As those configurations are flexible, the drag polar is not expected to be similar to the rigid version, as the geometry deforms with the aerodynamic loads changing the performances. To build the drag polar of each version, several airspeeds and angles of attack have been tested. Then from the lift and drag coefficient and the airspeed, the drag polar could be built with a colour map that is a function of the load factor. Also during the ASWING simulations, a subroutine has been implemented to return a convergence flag to sort the data. The drag polar of the OP1 and OP2 solutions are presented in figure 7.17 (a) and (b). They highlight quite well how quickly the aerodynamic performances of the OP1 solutions degrade with the load factor rising. Indeed when the aerodynamic load increase the wing tends to bend up (figure 8.8). This has the effect of creating a local dihedral angle that reduces the projected lift contribution to the vertical axis. In other words, the wing loses lift capability. Thus to provide the same lift coefficient as a less deformed geometry, the angle of attack of the wing must be raised and so the drag increases with it. Also from figure 7.17(a), it can be seen that the stall of the wing decreases with the load factor. For example, at a load factor of 1, the maximum lift coefficient of the OP1 solutions is 1.3 while at a load factor of 2, it is close to 1.1. This loss of performance was also witnessed on the turning polar when the bank angle was reaching 60°, and the sink speed of the glider was rising quite quickly. In comparison when the structure is very stiff the change in aerodynamic performances is much different. For example, on the OP2 solution, the aerodynamic performances at a high lift coefficient do not change a lot with the load factor up to 8Gs. If other energy harvesting strategies are expected to be studied such as dynamic soaring, it is very likely that the OP1 and OP3 solutions will underperform the OP2 one.

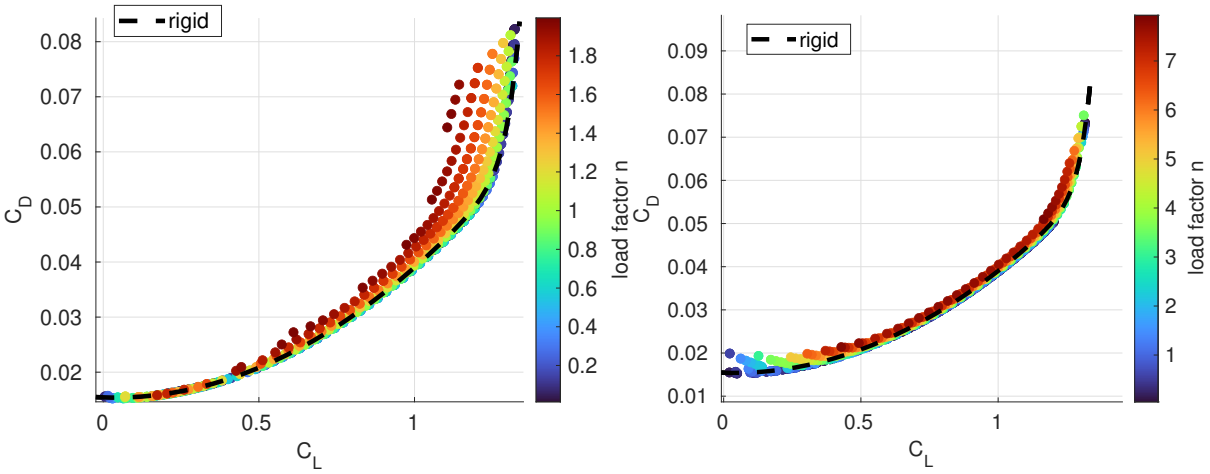

(a) OP1 : drag polars *(b) OP2 : drag polars*

Figure 7.17: drag polars comparison

7.6.4 Additionnal discussion

In the previous sections, it has been seen that some optimal structural parameters can be found to maximize some specific energy harvesting strategies such as static and unsteady thermal soaring. However, it seems that the parameters tend to not be really optimal when they are evaluated on the flight envelope of the aircraft. In this section, a discussion is proposed on what drawbacks should be brought by choosing them anyway. First, both optimal solutions OP1 and OP3 propose low bending and torsion stiffness. This leads to high deflections of the wing. The structure is more likely to break than the OP2 solutions for example. The UAV will be limited to low G manoeuvres in consequence. Secondly reducing the torsion stiffness has an effect on aero-elastic divergence phenomena. The flutter speed will appear much earlier. Also, the aileron's loss of effectiveness up to the reversal behaviour will be witnessed at a lower speed. The variability of the aircraft controllability on its rolling axis is expected to be high which is not very convenient for control law synthesis. Moreover during the time marching computation, after the gust bump, the flexible version OP3 was slowly stabilising its trajectory with an important oscillatory behaviour. It seems that after a modal analysis of this aircraft, the phugoïd mode was much less damped than the one of OP2. Finally, the UAV is expected to fly into a very gusty and turbulent environment, and having such low bending and torsion stiffness will cause a lot of fatigue on the materials composing the wing. The life expectancy should be much lower than a stiffer UAV. Active control systems could be used to alleviate those effects but they would drastically reduce the aerodynamic performances as they are usually using the control surfaces creating a lot of drag when highly deflected.

7.7 Conclusions

In this chapter, 3 optimisation problems have been proposed in order to find the optimal set of structural parameters of a UAV wing, maximising the energy harvested in thermals. ASWING has been used as an in-the-loop analysis tool to solve the above problems. The findings can be summarised as follows

- From an experimental evaluation, ASWING is adapted to the analysis of UAV performance in thermal soaring.
- It seems that providing more flexibility to the structure is only beneficial for unsteady thermal soaring. The updraft gust tends to pitch up to the local section because of the weak torsional stiffness increasing the local angle of attack and thus the lift. The latter being much less used than static thermal soaring, we do not recommend building a UAV based on the optimal set of structural parameters found as it degrades a lot the aerodynamic performances of the aircraft on its flight envelope.
- After analysing what was bringing this extra performance in dolphin kicks, we figured out that a wise control of the pitch angle of the UAV with the elevator was providing the same gain of performance and even more in some cases. In light of the drawbacks brought by the structural parameters found, it is preferable to use a stiffer UAV with active control maximising the power extracted from a thermal.
- For static thermal soaring, it seems that the structural set of parameters that maximise the static thermal soaring power extraction is more the translation of a non-optimised rigid geometry

than a real benefit of giving deformation capacity. Indeed, along the turning polar studied, the structure does not deform a lot because of the low load factor turn. The optimiser has converged to a set of parameters leading to a better geometry from an aerodynamic performance point of view. In other words, using structural parameters as optimisation variables in this problem is another way to optimise the UAV "rigid" geometry, than using regular geometric parameters such as twist and dihedral angle non-linear distribution. The latter involves many more optimisation variables, the previous problem can be seen as a more efficient way to optimise the aerodynamic performances of a rigid wing. The favourable change in performances is not due to the flexibility itself.

- The above conclusions are quite pessimistic, mostly due to the "constant mass" constraint imposed. The mass saved on a UAV must be dedicated to either its fuel or payload. If this constraint is released, the conclusion would be much more different.

Bibliography

[1] Anderson E and et al (2015) Autonomous soaring for long-endurance uavs. *Journal of Guidance, Control, and Dynamics* 38(9): 1610–1622. 235

[2] Applin ZT (1995) Pressure Distributions From Subsonic Tests of a NACA 0012 Semispan Wing Model. NASA Technical Memorandum 110148, NASA, Langley Research Center, Hampton, Virginia. 17, 242, 243

[3] Avin O, Raveh DE, Drachinsky A, Ben-Shmuel Y and Tur M (2022) Experimental aeroelastic benchmark of a very flexible wing. *AIAA Journal* 60(3): 1745–1768. 17, 20, 241, 243, 244, 245

[4] Bronz M (2012) *A contribution to the design of long endurance mini unmanned aerial vehicles*. PhD Thesis, Institut Supérieur de l'Aéronautique et de l'Espace-ISAE. 235

[5] Cheng H and Wang H (2018) Prediction of Lift Coefficient for Tandem Wing Configuration or Multiple-Lifting-Surface System Using Prandtl's Lifting-Line Theory. *International Journal of Aerospace Engineering* 2018: 1–15. DOI:10.1155/2018/3104902. URL https://www.hindawi.com/journals/ijae/2018/3104902/. 17, 240, 241

[6] Chiereghin N, Cleaver D and Gursul I (2017) Unsteady Force and Flow Measurements for Plunging Finite Wings. In: *47th AIAA Fluid Dynamics Conference*. Denver, Colorado: American Institute of Aeronautics and Astronautics. ISBN 978-1-62410-500-5. DOI:10.2514/6.2017-3127. URL https://arc.aiaa.org/doi/10.2514/6.2017-3127. 17, 242, 244

[7] Cole HA (1951) Experimental investigation of rolling performance of straight and sweptback flexible wings with various ailerons. *NACA Technical Note* (2563): 46. 17, 241, 242

[8] Drachinsky A, Avin O, Raveh DE, Ben-Shmuel Y and Tur M (2022) Flutter tests of the pazy wing. *AIAA Journal* 60(9): 5414–5421. 17, 20, 244, 245

[9] Drela M (1989) Xfoil: An analysis and design system for low reynolds number airfoils. In: *Low Reynolds Number Aerodynamics: Proceedings of the Conference Notre Dame, Indiana, USA, 5–7 June 1989*. Springer, pp. 1–12. 236

[10] Drela M (1999) Integrated simulation model for preliminary aerodynamic, structural, and control-law design of aircraft. In: *40th Structures, Structural Dynamics, and Materials Conference and Exhibit*. St. Louis,MO,U.S.A.: American Institute of Aeronautics and Astronautics. DOI:10.2514/6.1999-1394. 235, 240

[11] Drela M (2008) ASWING 5.81 Technical Description — Unsteady Extension : 42. 240, 244

[12] Drela M (2009) ASWING 5.86 Technical Description — Steady Formulation : 57. 240

[13] Fayez K, Leng Y, Jardin T, Bronz M and Moschetta JM (2021) Conceptual design for long-endurance convertible unmanned aerial system. In: *AIAA Scitech 2021 Forum*. p. 1059. 235

[14] Gavrilovic N, Bénard E, Pastor P and Moschetta JM (2017) Performance improvement of small uavs through energy-harvesting within atmospheric gusts. In: *AIAA Atmospheric Flight Mechanics Conference*. p. 1630. 248

[15] Gavrilovic N, Benard E, Pastor P and Moschetta JM (2018) Performance improvement of small unmanned aerial vehicles through gust energy harvesting. *Journal of Aircraft* 55(2): 741–754. 248

[16] Gavrilović N, Bronz M and Moschetta JM (2020) Bioinspired energy harvesting from atmospheric phenomena for small unmanned aerial vehicles. *Journal of Guidance, Control, and Dynamics* 43(4): 685–699. 248

[17] Heald R and Strother D (1929) Report No. 298. Effect of variation of chord and span of ailerons on rolling and yawing moments in level flight. *Journal of the Franklin Institute* 207(5): 715–716. DOI:10.1016/S0016-0032(29)91609-4. 17, 240, 241, 242

[18] Johnson A and et al (2021) Learning-based control for solar-powered uavs in thermal updrafts. In: *2021 IEEE Aerospace Conference*. IEEE. 235

[19] Mai H (1985) The effect of aeroelasticity upon energy retrieval of a sailplane penetrating a gust. *OSTIV Publications* 18. 248

[20] Pollet F, Delbecq S, Budinger M, Moschetta JM and Liscouët J (2022) A common framework for the design optimization of fixed-wing, multicopter and vtol uav configurations. In: *33rd Congress of the International Council of the Aeronautical Sciences*. 235

[21] Pumrin S and et al (2020) Autonomous thermal soaring for long-endurance uavs using machine learning. In: *2020 IEEE Aerospace Conference*. IEEE. 235

[22] Qin L and et al (2019) Real-time thermal soaring for solar-powered unmanned aerial vehicles. In: *2019 IEEE International Conference on Robotics and Automation (ICRA)*. IEEE. 235

[23] Raymer DP and et al (2013) Solar powered uavs for persistent stratospheric flight. In: *2013 IEEE Aerospace Conference*. IEEE. 235

[24] Smith A and et al (2018) Adaptive soaring for fixed-wing uavs in thermalling flight. In: *2018 IEEE International Conference on Robotics and Automation (ICRA)*. IEEE. 235

[25] Von Karman T (1930) Calculation of pressure distribution on airship hulls. NACA Technical Memorandus 574. URL `https://authors.library.caltech.edu/47901/1/19930094841.pdf`. 17, 240, 241

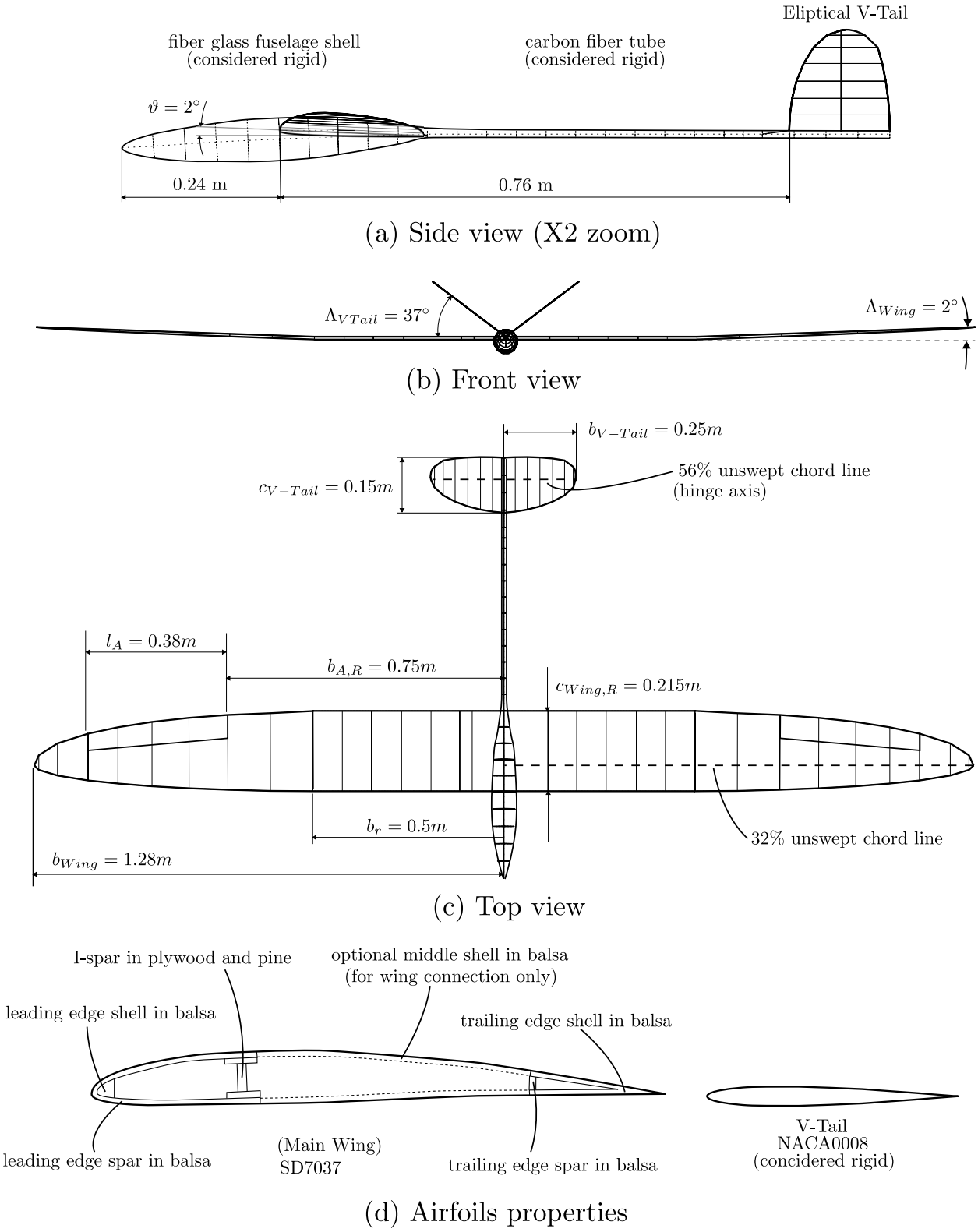

Figure 7.18: Appendix A - Aeronaut Triple Thermic main parameters and ASWING geometry

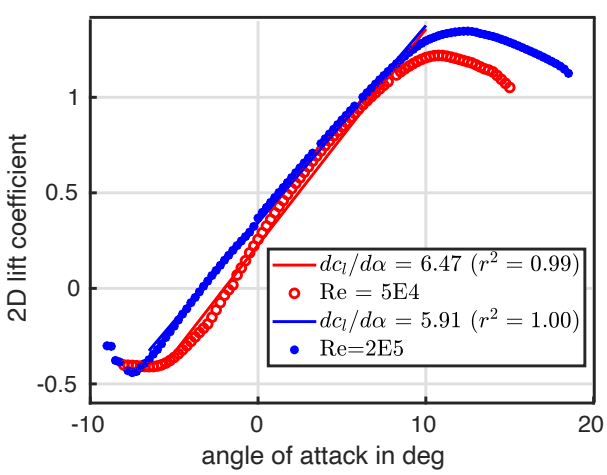

(a) SD7037 lift slope

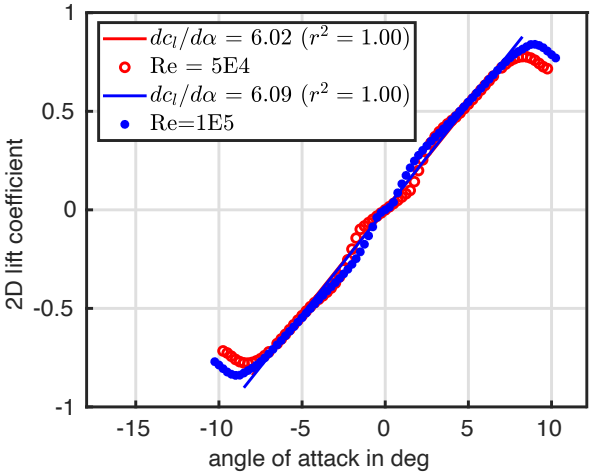

(b) NACA0008 lift slope

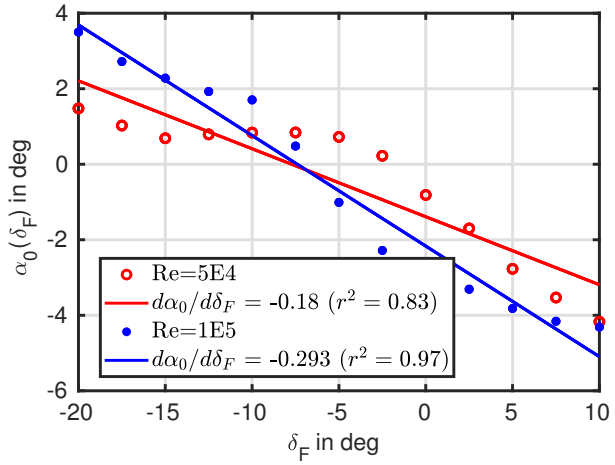

(c) SD7037 zero lift angle of attack shift

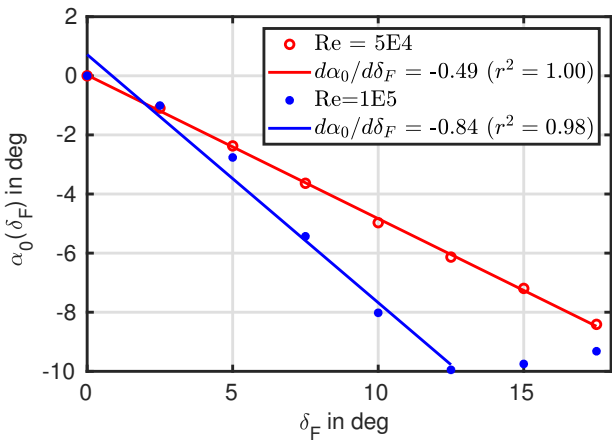

(d) NACA0008 zero lift angle of attack shift

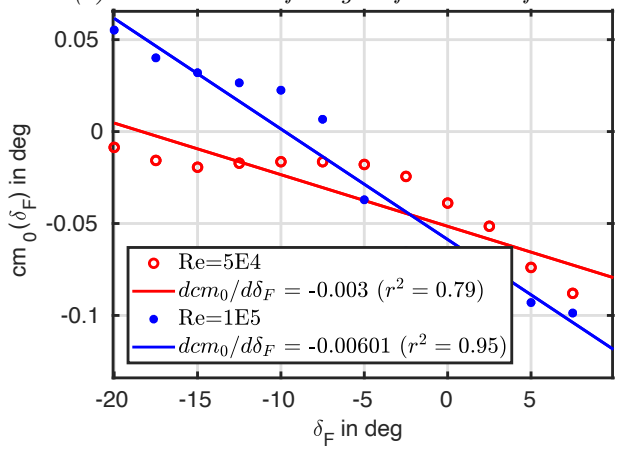

(e) SD7037 zero lift pitch moment shift

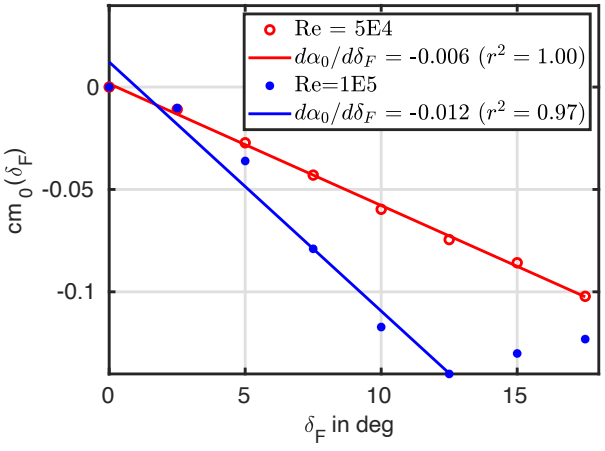

(f) NACA0008 zero lift pitch moment shift

Figure 7.19: Appendix B - Aeronaut triple thermic wing and V-tail airfoils XFOIL analysis

7.8 Appendix C - Aeronaut triple thermic neo ASWING file

```
#============
Name
Aeronaut Triple Thermic Neo Baseline
End
#============
Units
L 1.0 m
T 1.0 s
F 1.0 N
End
#============
Constant
#    g      rho_SL       V_sound
   9.81    1.285     341
End
#============
Reference
! Reference parameters for non dimensionalized paramters computation
# Sref   Cref   Bref
  0.49   0.215    2.55
#
#  Xmom   Ymom   Zmom
   -0.0   0.0    0.0
   -0.0   0.0    0.0
   -0.0   0.0    0.0
End
#============
Joint
! Non compliants joints connection between the different lifting surfaces
#  Nbeam1   Nbeam2     t1       t2
     3        1          0.0      0.0
     3        2         0.72     0.0
End
#============
Ground
! Location where the aircraft is anchored (wind tunnel configuration)
#  Nbeam   t       Kground
     3       0.087    0
End
#=====================
Weight
! A longitudinal mass dipole has been used to model the y and z moment of
! inertia (dominated by the fuselage). The x moment of inertia is dominated
! by the wing and embeded in the mass/length distribution
! positions of the ponctual masses are computed based on the radius of
! gyration to recover the moments of inertia.
#  Nbeam   t       Xp       Yp       Zp       Mg      CDA      Vol      Hx    Hy    Hz
*           1.      1.       1.       1.       9.81      1.       1.       1.    1.    1.
    3     -0.2352   -0.4910    0.0      0.0    0.240    0.0      0.0      0.0   0.0   0.0
    3      0.6630    0.6630    0.0      0.0    0.240    0.0      0.0      0.0   0.0   0.0
End
#=====================
Sensor
! The fist sensor is placed at the aircraft CG and provide the inertial speed
! (GPS) in order to build the speed and turn polars. Sensor 1 is also used to
! measure the maximum extensional strain for eventual structural failure
! analysis.
! The second sensor is used to measure the wing tip deflection and twist
# KS Nb    t       Xp       Yp       Zp      Vx      Vy      Vz       Ax      Ay      Az
*           1.      1.       1.       1  1.      1.      1.       1.      1.      1.
    1  1    0.086  0.086   0    0    1.0     0.0     0.0      0.0     0.0     1.0
    2  1    1.2765   0.0680   1.2765  0.0264    1.0   0.0     0.0      0.0     0.0     1.0
End
#============
Engine
! Disable during speed polars analysis
! Extented Actuator disk theory + jet and swirl modeling
# KPeng IEtyp Nbeam t   Xp   Yp Zp   Tx   Ty Tz   dFdPe dMdPe Rdisk Omega cdA
  1   1   3  -0.2352  -0.2352  0.  -0.0257  -1.  0.  -.1   1.0     0.01    0.0    100.   0.0
```

```
End
#==========
Beam 1
Wing
! Main geometric paramters
! Quasi elliptical wing : rectangular part from 0 to 0.5m then elliptical
! part with an unswept 0.35 chord line
! 2 degree dihedral angle between the rectangular and elliptical part
! for lateral stability
! Root chord of 0.22m
      t            x      y          z          chord      Xax       twist
*     1.           1.0    1.         1.0        1.0        0.0        2.0
         0          0         0          0     0.2200     1.0000     1.0000
    0.0578          0    0.0578          0     0.2200     1.0000     1.0000
    0.1156          0    0.1156          0     0.2200     1.0000     1.0000
    0.1733          0    0.1733          0     0.2200     1.0000     1.0000
    0.2311          0    0.2311          0     0.2200     1.0000     1.0000
    0.2889          0    0.2889          0     0.2200     1.0000     1.0000
    0.3467          0    0.3467          0     0.2200     1.0000     1.0000
    0.4044          0    0.4044          0     0.2200     1.0000     1.0000
    0.4622          0    0.4622          0     0.2200     1.0000     1.0000
    0.5200          0    0.5200          0     0.2200     1.0000     1.0000
    0.5200          0    0.5200          0     0.2150     1.0000     1.0000
    0.5825     0.0002    0.5825     0.0022     0.2143     1.0000     1.0000
    0.6445     0.0009    0.6445     0.0043     0.2121     1.0000     1.0000
    0.7057     0.0021    0.7057     0.0065     0.2084     1.0000     1.0000
    0.7656     0.0037    0.7656     0.0086     0.2034     1.0000     1.0000
    0.8239     0.0057    0.8239     0.0106     0.1969     1.0000     1.0000
    0.8801     0.0082    0.8801     0.0126     0.1891     1.0000     1.0000
    0.9338     0.0111    0.9338     0.0144     0.1800     1.0000     1.0000
    0.9847     0.0143    0.9847     0.0162     0.1697     1.0000     1.0000
    1.0324     0.0180    1.0324     0.0179     0.1582     1.0000     1.0000
    1.0766     0.0219    1.0766     0.0194     0.1456     1.0000     1.0000
    1.1170     0.0262    1.1170     0.0208     0.1321     1.0000     1.0000
    1.1533     0.0308    1.1533     0.0221     0.1176     1.0000     1.0000
    1.1854     0.0356    1.1854     0.0232     0.1023     1.0000     1.0000
    1.2128     0.0407    1.2128     0.0242     0.0864     1.0000     1.0000
    1.2355     0.0459    1.2355     0.0250     0.0698     1.0000     1.0000
    1.2534     0.0513    1.2534     0.0256     0.0528     1.0000     1.0000
    1.2662     0.0568    1.2662     0.0261     0.0354     1.0000     1.0000
    1.2740     0.0624    1.2740     0.0263     0.0178     1.0000     1.0000
    1.2765     0.0680    1.2765     0.0264          0     1.0000     1.0000
! Mass properties
! Estimated from experimental measurements
! Assumed elliptical distrbution (strong)
      t          Ccg        Ncg        mg         mgcc       mgnn
*     1.         0.4        0.0        2.3166     0.0385     0.3461
         0       0.2200     0.2200     1.0000     1.0000     1.0000
    0.0578       0.2200     0.2200     1.0000     1.0000     1.0000
    0.1156       0.2200     0.2200     1.0000     1.0000     1.0000
    0.1733       0.2200     0.2200     1.0000     1.0000     1.0000
    0.2311       0.2200     0.2200     1.0000     1.0000     1.0000
    0.2889       0.2200     0.2200     1.0000     1.0000     1.0000
    0.3467       0.2200     0.2200     1.0000     1.0000     1.0000
    0.4044       0.2200     0.2200     1.0000     1.0000     1.0000
    0.4622       0.2200     0.2200     1.0000     1.0000     1.0000
    0.5200       0.2200     0.2200     1.0000     1.0000     1.0000
    0.5200       0.2150     0.2150     0.9773     0.9773     0.9773
    0.5825       0.2143     0.2143     0.9739     0.9739     0.9739
    0.6445       0.2121     0.2121     0.9639     0.9639     0.9639
    0.7057       0.2084     0.2084     0.9474     0.9474     0.9474
    0.7656       0.2034     0.2034     0.9243     0.9243     0.9243
    0.8239       0.1969     0.1969     0.8950     0.8950     0.8950
    0.8801       0.1891     0.1891     0.8595     0.8595     0.8595
    0.9338       0.1800     0.1800     0.8181     0.8181     0.8181
    0.9847       0.1697     0.1697     0.7712     0.7712     0.7712
    1.0324       0.1582     0.1582     0.7190     0.7190     0.7190
    1.0766       0.1456     0.1456     0.6619     0.6619     0.6619
    1.1170       0.1321     0.1321     0.6003     0.6003     0.6003
    1.1533       0.1176     0.1176     0.5345     0.5345     0.5345
    1.1854       0.1023     0.1023     0.4651     0.4651     0.4651
```

```
    1.2128    0.0864    0.0864    0.3926    0.3926    0.3926
    1.2355    0.0698    0.0698    0.3173    0.3173    0.3173
    1.2534    0.0528    0.0528    0.2399    0.2399    0.2399
    1.2662    0.0354    0.0354    0.1609    0.1609    0.1609
    1.2740    0.0178    0.0178    0.0807    0.1609    0.1609
    1.2765         0         0         0    0.1609    0.1609
! Stiffness properties (other default to 0 or infinite)
       t       Cea       Cta      EIcc        GJ      EIcs        EA
*      1.      0.35      0.35        20        20       0.0       0.0
          0    0.2200    0.2200    1.0000    1.0000    1.0000    1.0000
     0.0578    0.2200    0.2200    1.0000    1.0000    1.0000    1.0000
     0.1156    0.2200    0.2200    1.0000    1.0000    1.0000    1.0000
     0.1733    0.2200    0.2200    1.0000    1.0000    1.0000    1.0000
     0.2311    0.2200    0.2200    1.0000    1.0000    1.0000    1.0000
     0.2889    0.2200    0.2200    1.0000    1.0000    1.0000    1.0000
     0.3467    0.2200    0.2200    1.0000    1.0000    1.0000    1.0000
     0.4044    0.2200    0.2200    1.0000    1.0000    1.0000    1.0000
     0.4622    0.2200    0.2200    1.0000    1.0000    1.0000    1.0000
     0.5200    0.2200    0.2200    1.0000    1.0000    1.0000    1.0000
     0.5200    0.2150    0.2150    0.9773    0.9773    0.9773    0.9773
     0.5825    0.2143    0.2143    0.9739    0.9739    0.9739    0.9739
     0.6445    0.2121    0.2121    0.9639    0.9639    0.9639    0.9639
     0.7057    0.2084    0.2084    0.9474    0.9474    0.9474    0.9474
     0.7656    0.2034    0.2034    0.9243    0.9243    0.9243    0.9243
     0.8239    0.1969    0.1969    0.8950    0.8950    0.8950    0.8950
     0.8801    0.1891    0.1891    0.8595    0.8595    0.8595    0.8595
     0.9338    0.1800    0.1800    0.8181    0.8181    0.8181    0.8181
     0.9847    0.1697    0.1697    0.7712    0.7712    0.7712    0.7712
     1.0324    0.1582    0.1582    0.7190    0.7190    0.7190    0.7190
     1.0766    0.1456    0.1456    0.6619    0.6619    0.6619    0.6619
     1.1170    0.1321    0.1321    0.6003    0.6003    0.6003    0.6003
     1.1533    0.1176    0.1176    0.5345    0.5345    0.5345    0.5345
     1.1854    0.1023    0.1023    0.4651    0.4651    0.4651    0.4651
     1.2128    0.0864    0.0864    0.3926    0.3926    0.3926    0.3926
     1.2355    0.0698    0.0698    0.3173    0.3173    0.3173    0.3173
     1.2534    0.0528    0.0528    0.2399    0.2399    0.2399    0.2399
     1.2662    0.0354    0.0354    0.1609    0.1609    0.1609    0.1609
     1.2740    0.0178    0.0178    0.0807    0.0807    0.0807    0.0807
     1.2765         0         0         0         0         0         0
! Aerodynamic paramters
! SD7073 : XFOIL analysis done at 2 Reynolds number ie 50 000 and 150 000
       t      CLmin      CLmax       Cdf       Cdp        Cm      dCLda     alpha
*      1.         1.         1.       1.0       1.0       1.0       1.0       1.0
          0   -0.4412    1.3463    0.0074    0.0054   -0.0813    5.9100    3.3000
     0.0578   -0.4412    1.3463    0.0074    0.0054   -0.0813    5.9100    3.3000
     0.1156   -0.4412    1.3463    0.0074    0.0054   -0.0813    5.9100    3.3000
     0.1733   -0.4412    1.3463    0.0074    0.0054   -0.0813    5.9100    3.3000
     0.2311   -0.4412    1.3463    0.0074    0.0054   -0.0813    5.9100    3.3000
     0.2889   -0.4412    1.3463    0.0074    0.0054   -0.0813    5.9100    3.3000
     0.3467   -0.4412    1.3463    0.0074    0.0054   -0.0813    5.9100    3.3000
     0.4044   -0.4412    1.3463    0.0074    0.0054   -0.0813    5.9100    3.3000
     0.4622   -0.4412    1.3463    0.0074    0.0054   -0.0813    5.9100    3.3000
     0.5200   -0.4412    1.3463    0.0074    0.0054   -0.0813    5.9100    3.3000
     0.5200   -0.4405    1.3432    0.0074    0.0055   -0.0807    5.9227    3.2614
     0.5825   -0.4404    1.3428    0.0074    0.0056   -0.0806    5.9246    3.2557
     0.6445   -0.4401    1.3415    0.0075    0.0056   -0.0803    5.9302    3.2387
     0.7057   -0.4395    1.3392    0.0075    0.0057   -0.0799    5.9395    3.2105
     0.7656   -0.4388    1.3361    0.0075    0.0058   -0.0793    5.9524    3.1713
     0.8239   -0.4379    1.3322    0.0076    0.0060   -0.0785    5.9688    3.1214
     0.8801   -0.4368    1.3274    0.0076    0.0062   -0.0775    5.9887    3.0611
     0.9338   -0.4355    1.3219    0.0077    0.0065   -0.0764    6.0118    2.9908
     0.9847   -0.4340    1.3156    0.0077    0.0067   -0.0751    6.0381    2.9110
     1.0324   -0.4323    1.3085    0.0078    0.0070   -0.0737    6.0674    2.8223
     1.0766   -0.4305    1.3009    0.0079    0.0074   -0.0722    6.0993    2.7252
     1.1170   -0.4286    1.2926    0.0080    0.0077   -0.0705    6.1339    2.6204
     1.1533   -0.4265    1.2837    0.0081    0.0081   -0.0687    6.1707    2.5087
     1.1854   -0.4244    1.2744    0.0082    0.0085   -0.0669    6.2095    2.3907
     1.2128   -0.4221    1.2647    0.0083    0.0090   -0.0649    6.2502    2.2674
     1.2355   -0.4197    1.2546    0.0084    0.0094   -0.0629    6.2923    2.1394
     1.2534   -0.4173    1.2442    0.0085    0.0099   -0.0608    6.3357    2.0078
     1.2662   -0.4148    1.2335    0.0087    0.0103   -0.0586    6.3799    1.8735
```

```
    1.2740   −0.4122    1.2228  0.0088  0.0108   −0.0565  6.4248    1.7372
    1.2765   −0.4097    1.2119  0.0089  0.0113   −0.0543  6.4700    1.6000
! Flap derivatives : ailerons has index 1 and airvreak 4
! XFOIL analysis done at Reynolds number of 50 000
! with a hinge mean position of 0.8 chord
! Airbreaks were disable in speed polars analysis
      t       dCLdF1  dCMdF1  dCDdF1   dCLdF4  dCMdF4  dCDdF4
*     1.      0.0302    −0.006   0.000      0       0       0
  −1.2765     0       0       0        0       0       0
   −1.13      0       0       0        0       0       0
   −1.13      −1       1       1        0       0       0
   −0.75      −1       1       1        0       0       0
   −0.75      0       0       0        0       0       0
   −0.36      0       0       0        0       0       0
   −0.36      0       0       0        1       1       1
   −0.12      0       0       0        1       1       1
   −0.12      0       0       0        0       0       0
    0.0       0       0       0        0       0       0
    0.12      0       0       0        0       0       0
    0.12      0       0       0        1       1       1
   0.36       0       0       0        1       1       1
   0.36       0       0       0        0       0       0
   0.75       0       0       0        0       0       0
   0.75       1.0      −1.0       1        0       0       0
   1.13       1.0      −1.0       1        0       0       0
   1.13       0       0       0        0       0       0
   1.2765     0       0       0        0       0       0
End
#==========
Beam 2
V stab
! V−stab is considered stiffer than the main wing
! Elliptical distribution with an unswept 0.56 chord line (hinge axis
! location)
! All stiffness parameters are set to infinite and coupling terms to 0.
! Geometric parameters
      t          x          y          z          chord      Xax      twist
*     1.0          1.0        1.0        1.0        1.0        0.0      0.0
        0     0.7600          0          0     0.1500     1.0000     1.0000
    0.0434    0.7613     0.0347     0.0261     0.1477     1.0000     1.0000
    0.0855    0.7651     0.0683     0.0515     0.1410     1.0000     1.0000
    0.1250    0.7714     0.0998     0.0752     0.1299     1.0000     1.0000
    0.1607    0.7799     0.1283     0.0967     0.1149     1.0000     1.0000
    0.1915    0.7904     0.1529     0.1153     0.0964     1.0000     1.0000
    0.2165    0.8025     0.1729     0.1303     0.0750     1.0000     1.0000
    0.2349    0.8159     0.1876     0.1414     0.0513     1.0000     1.0000
    0.2462    0.8302     0.1966     0.1482     0.0260     1.0000     1.0000
    0.2500    0.8450     0.1997     0.1505          0     1.0000     1.0000
! Aerodynamic paramters (NACA0008, obtained from a XFOIL analysis at 2
! Reynolds number ie 50 000 and 150 000)
   t       CLmin      CLmax     Cdf      Cdp       Cm       dCLda      alpha
*  1.0     1.0        1.0       1.0      1.0       0.0      1.0        1.0
        0    −0.8300     0.8300     0.0075     0.0038     0     6.0900          0
    0.0434   −0.8291     0.8291     0.0075     0.0038     0     6.0889          0
    0.0855   −0.8264     0.8264     0.0077     0.0038     0     6.0858          0
    0.1250   −0.8220     0.8220     0.0079     0.0039     0     6.0806          0
    0.1607   −0.8160     0.8160     0.0082     0.0040     0     6.0736          0
    0.1915   −0.8086     0.8086     0.0086     0.0041     0     6.0650          0
    0.2165   −0.8000     0.8000     0.0091     0.0042     0     6.0550          0
    0.2349   −0.7905     0.7905     0.0096     0.0044     0     6.0439          0
    0.2462   −0.7804     0.7804     0.0101     0.0045     0     6.0322          0
    0.2500   −0.7700     0.7700     0.0107     0.0047     0     6.0200          0
! Flap derivative, V−tail flap is used as rudder and elevator
! NACA0008, obtained from a XFOIL analysis at 2 Reynolds number
! ie 50 000 and 150 000. Hinge location is 0.56 of the root chord
      t       dCLdF2  dCMdF2   dCLdF3  dCMdF3
*     1.0          1.0        1.0       1.0     1.0
   −0.2500    0.0521    −0.0060   −0.0521    0.0060
   −0.2462    0.0662    −0.0079   −0.0662    0.0079
   −0.2349    0.0800    −0.0098   −0.0800    0.0098
   −0.2165    0.0928    −0.0116   −0.0928    0.0116
```

```
   −0.1915    0.1045   −0.0131   −0.1045    0.0131
   −0.1607    0.1145   −0.0145   −0.1145    0.0145
   −0.1250    0.1227   −0.0156   −0.1227    0.0156
   −0.0855    0.1287   −0.0164   −0.1287    0.0164
   −0.0434    0.1323   −0.0169   −0.1323    0.0169
         0    0.1336   −0.0171   −0.1336    0.0171
         0    0.1336   −0.0171    0.1336   −0.0171
    0.0434    0.1323   −0.0169    0.1323   −0.0169
    0.0855    0.1287   −0.0164    0.1287   −0.0164
    0.1250    0.1227   −0.0156    0.1227   −0.0156
    0.1607    0.1145   −0.0145    0.1145   −0.0145
    0.1915    0.1045   −0.0131    0.1045   −0.0131
    0.2165    0.0928   −0.0116    0.0928   −0.0116
    0.2349    0.0800   −0.0098    0.0800   −0.0098
    0.2462    0.0662   −0.0079    0.0662   −0.0079
    0.2500    0.0521   −0.0060    0.0521   −0.0060


End
#==========
Beam 3
Fuselage
! The fuselage is considered stiffer than the wing
! Cross section and radius distribution obtained from side view scanning
! All stiffness paramters are set to infinite and cpupling terms to 0
! Geometric paramters
       t          x          z      radius
*    1.0        1.0        1.0         1.0
   −0.2352    −0.2352    −0.0257      0.0007
   −0.2295    −0.2295    −0.0252      0.0060
   −0.2118    −0.2118    −0.0248      0.0132
   −0.1791    −0.1791    −0.0227      0.0192
   −0.1259    −0.1259    −0.0192      0.0261
   −0.0762    −0.0762    −0.0162      0.0304
   −0.0198    −0.0198    −0.0137      0.0328
    0.0322     0.0322    −0.0111      0.0317
    0.0704     0.0704    −0.0092      0.0295
    0.1291     0.1291    −0.0073      0.0219
    0.1737     0.1737    −0.0055      0.0147
    0.2204     0.2204    −0.0054      0.0054
    0.2204     0.2204    −0.0054      0.0054
    0.2971     0.2971    −0.0054      0.0054
    0.3737     0.3737    −0.0054      0.0054
    0.4503     0.4503    −0.0054      0.0054
    0.5269     0.5269    −0.0054      0.0054
    0.6035     0.6035    −0.0054      0.0054
    0.6801     0.6801    −0.0054      0.0054
    0.7568     0.7568    −0.0054      0.0054
    0.8334     0.8334    −0.0054      0.0054
    0.9100     0.9100    −0.0054      0.0054
! Aerodynamic paramters
       t        Cdf        Cdp
*    1.0        0.0        0.5
   −0.2352     1.0000     1.0000
   −0.2295     1.0000     1.0000
   −0.2118     1.0000     1.0000
   −0.1791     1.0000     1.0000
   −0.1259     1.0000     1.0000
   −0.0762     1.0000     1.0000
   −0.0198     1.0000     1.0000
    0.0322     1.0000     1.0000
    0.0704     1.0000     1.0000
    0.1291     1.0000     1.0000
    0.1737     1.0000     1.0000
    0.2204     1.0000     1.0000
    0.2204     1.0000     1.0000
    0.2971     1.0000     1.0000
    0.3737     1.0000     1.0000
    0.4503     1.0000     1.0000
    0.5269     1.0000     1.0000
    0.6035     1.0000     1.0000
```

```
354      0.6801      1.0000      1.0000
355      0.7568      1.0000      1.0000
356      0.8334      1.0000      1.0000
357      0.9100      1.0000      1.0000
358 End
```

Listing 7.1: Aeronaut Triple Thermic Neo ASWING file (Aeronaut.asw)

Chapter 8

Dynamic soaring on flexible UAVs

Abstract

This chapter proposes an extension of the current dynamic soaring analysis methods aiming at taking into account the UAV flexibility effects on its performances. The idea here is to use 2 different frameworks to set up a new optimisation problem. In a first time, thanks to the use of ASWING, up to 7 levels of new conservative constraints are introduced into the current 6-degrees of freedom point mass model.Those level brings modelling fidelity, and are evaluated against experimental data from the literature. Each level impact on dynamic soaring performances is then discussed. Follow a section on the unsteady flow and structural modal response involvement in the trajectory. Finally, a comparison between a rigid and flexible version of a RC glider is proposed. The performance compasses are compared between them and also with the baseline problem formulation to highlight what brings each new constraint level. In light of the flexible version performances, a new travelling strategy is proposed to improve them. From this first analysis, it seems that when a flexible aircraft allows high structural deflections, its dynamic soaring performances are negatively impacted. High-load manoeuvres tend to deform the structure leading to earlier stall and degraded aerodynamic performances. Also, the loss of ailerons and elevator effectiveness with the flight speed, reduce the performances. Finally, it seems that unsteady flow and structural modes effects can be neglected in the analysis. Finally, the new travelling strategy drastically improves the flexible UAV dynamic soaring performance.

Publications:

This chapter has been submitted as a journal paper to the International Journal of Micro Air Vehicles. The latter has been submitted with the title:

R.Jan, J-M. Moschetta and J-P. Condomines, New dynamic soaring formulation for the assessment of flexibility effects on the Mini UAVs performances, International of Micro Air Vehicles, 2024.

Contents

Nomenclature

b	m	wing span
S	m^2	UAV wetted area
m	kg	UAV mass
AR		UAV aspect ratio
W_x	m/s	wind horizontal speed
$W_{x,min}$	m/s	minimal required wind speed
z	m	aircraft inertial vertical position
z_r	m	wind field reference altitude
z_0	m	PBL roughness
V_{travel}	m/s	mean travel speed
ϕ	deg	UAV bank angle
ψ	deg	heading angle
γ	deg	climb angle
C_L		lift and drag coefficient
$V_{R,A}$	m/s	Ailerons reversal speed
$V_{R,E}$	m/s	Elevator reversal speed
V	m/s	air-relative speed
n		load factor
$h_\perp$	m	maximum distance to path
$C_{l,max}$		max rolling moment coeff
$C_{L,max}$		maximum lift coefficient
I_{xx}	kgm^2	x-moment of inertia
G_{clear}	m	Ground clearance altitude

Résumé du chapitre en français

Ce dernier chapitre, présente une nouvelle méthode d'analyse des performances de vol de gradient d'un drone flexible. Ici, l'étude proposée se concentre sur les trajectoires dites en boucle ouverte assurant une neutralité sur l'énergie totale de l'aéronef. Le phénoème atmostphérique dont le drone tire son énergie considéré dans ce travail est la couche limite planétaire. Sur le plan numérique, le vol de gradient consiste principalement à déterminter des trajectoires dites optimales qui assure la neutralité de l'énergie totale du drone. Jusqu'à présent un modèle de point matériel à 6 degrées de liberté est utilsé pour résoudre ce genre de problème. Aux vus des performances et de l'efficacité d'ASWING, il fut considérer dans un premier temps de l'utiliser comme outil de génération de trajectoire. En ce sens une discussion sur la non faisabilité d'utiliser ASWING comme outil de génération de trajectoire est proposée. En particulier une analyse d'ordre de grandeur de la compléxité algorithmique est présentée pour appuyer ce propos. Sur ce constat, une méthodologie adaptée est proposée pour tirer profit des 2 modèles.
En ce sens, ce travail s'appuie sur une formulation de base du problème issue de la littérature. Par la suite des niveaux de fidélité sont introduits pour prendre en compte les effets aérodynamiques et ceux d'une structure souple non pris en compte jusqu'à présents. Parmis eux les,

- effets de décrochages locales sur l'aile et le stabilisateur horizontal, impactant les performances en roulis et tangage
- une contrainte sur l'angle d'hélice d'une aile et non plus sur le taux de roulis
- la perte d'efficacité des gouvernes aérodynamiques sous l'effet du gauchissement variable de l'aile et de l'élévateur.
- la dégradation des performances aérodynamiques due à la variation de la géométrie sous l'effet du facteur de charge variable.

Chaque nouveau niveau de fidélité est comparé au problème de base pour apprécier son impact. De la même manière, l'ajout d'un niveau est comparé relativement au précédent pour identifier les éléments dominant la dégradation au l'amélioration des performances. Via l'analyse fréquentielle de la trajectoire, une discussion est proposée autour de l'implication ou non des phènomènes aérodynamiques instationnaires et de la réponse modale de la struture.
Par la suite une comparaison entre une version rigide et flexible du drone étudié est présentée La construction de la boussole de performances (vitesse minimale requise pour une trajectoire ayant une cap moyen fixé) de chaque version est présentée afin de donner un élément de réponse sur l'apport ou non de la flexibilité sur les performances en vol de gradient.
A première vue, la flexiblité d'un aéronef semble avoir un impact significatif sur les performances en vol de gradient. La variation des performances aérodynamiques due aux déformations structurelles semble avoir un effet au premier ordre. Ensuite la perte de performances en roulis due au gauchissement progressif de l'aile semble réduire la capacité du drone en manoeuvre. La diminution du taux de tangage a un impact mais est de second ordre devant les 2 effets précédents. Concernant les niveaux de conservatisme "aérodynamiques", imposer une contrainte sur le taux d'hélice (taux de roulis adimentionnel) plutôt que sur le taux de roulis à un impact significatif. Enfin les effets de dimmunutions de performances en roulis et tangage dus au décrochage ont des impacts variables suivant la trajectoire considérée mais invariablement négatifs. A la lumière de la comparaison avec le modèle rigide, la version flexible semble sous performer en particulier sur des trajectoires à haut facteur de charge. En ce sens nous proposons une nouvelles méthode de "parcours" de sorte à se rapprocher au mieux du cas rigide. Cependant malgré cette dernière, le drone rigide semble rester dominant. De toute évidence, ce genre d'étude doit être poussée plus en profondeur. Différentes configurations flexibles doivent être étudiées pour statuer en toute rigeur sur l'apport ou non de la flexiblité. Néanmois cette étude montre l'apport important de la nouvelle formulation du problème de génération de trajectoire pour le vol de gradient appliqué aux drones flexibles.

8.1 Introduction

With the miniaturisation of inboard electronics, the Unmanned Aerial Vehicle (UAV) market has been rising at a 2 figures exponential rate for the 2 past decades. To remain competitive, long-endurance and maximum payload are the two main keywords to drone manufacturer. There are many ways and devices to improve a UAV's range and efficiency. When all of them are used in a multi-disciplinary optimisation tool, an optimal geometry can be designed (Pollet et al.-2022,Bronz-2012 and Fayez et al.-2021). Or as there is a penalty on the payload, to save mass, fewer materials must be used on the aircraft structure. Moreover, optimisers tend generally to high aspect ratio wing configurations as they are much more efficient aerodynamically speaking. In consequence, long-endurance UAVs are very likely flexible and their geometry can be subject to important deformations.

Once a UAV is optimally designed, it is still possible to extend its endurance. To do so, the UAV must rely on the surrounding environment where potential energy can be harvested. There are various existing techniques but dynamic soaring shows a real potential to extend the range and the endurance of an existing drone. This problem has been widely treated numerically, where various atmospheric phenomena and types of trajectories have been studied. Also, on the experimental side, feasibility has been shown. Basically, all the works, initially bio-inspired by the flight of albatrosses (Rayleigh, Froude) , propose trajectory optimisation under constraints (maximum load factor, flying in the linear lift range, minimum and maximum altitude and speed, etc). The numerical analysis of Liu et al., Gao et al., Cutler et al., Mears, Bonnin et al., Deittert et al., Bencatel et al. (2012 and 2012) can be mentioned. The approach remains the same, a point mass or inertial simplified aircraft model is used to run an optimisation program for a given bounded wind shear profile. The aircraft and wind profiles vary, but they all show the feasibility of dynamic soaring on mini-UAVs. The latter work has been confirmed experimentally by Bronz et al. (2021 and 2021). As shown by Lawrance and Bonnin et al., there are 4 main families of trajectories, the inclined ellipse and three open cycle trajectories, which allow to fly cross wind, towards and backward the wind. On each cycle, the UAV gains kinematic energy, by repeating the process, the world record in speed was broken with a reported ground speed greater than 800km/h. At this speed, and in such a compressed trajectory, the drone faced a load factor of up to 100G, as reported by Richardson. Apart from this case, the "travelling" trajectories (open-loop) mentioned earlier imply a reasonable load factor of up to 2G to 6G. Also, Zikmund and Matějů and Zikmund showed that it was possible for a fighter jet, or what they called a transonic glider, to "surf" into the wake of an airliner. As the latter conclusion is entirely numerical, it is considered exotic.

Dynamic soaring is possible in hurricanes, cyclones or planetary Von Karman streets, where an optimal trajectory can be established, as shown by Grenestedt et al. However, according to the author, the existence of a solution depends on the nature and intensity of the atmospheric phenomena mentioned. Due to the high level of turbulence in a hurricane, no experimental evaluation has yet been proposed.

Grenestedt and Spletzer has shown numerically that it is possible to perform perpetual flight in shear layers of the jet stream.

Finally, Long et al. suggested using dynamic soaring to recharge the UAV's battery using the propeller in windmill mode. Thus the kinematic energy gain in a dynamic cycle is transformed into electric energy.

So far, it is difficult to find work where the effect of the structure deformation along the trajectory is taken into account. In consequence in this work, a new optimisation problem definition is proposed. To assess this problem, ASWING (Drela-1999-2008 and 2009) is used as a pre-analysis tool to set up new types of conservative constraints on a "lower fidelity but fast" model from Bonnin et al., Long et al.. Also, a discussion is proposed on which aeroelastic phenomena are important to rigorously evaluate the performances of a UAV in dynamic soaring flight.

8.2 Application example: Aeronaut Triple Thermic Neo

In order to present this new methodology, the Aeronaut Triple Thermic Neo is used. The latter has been chosen and bought by the author to perform numerical and further experimental analysis. It was chosen as it is relatively cheap and spare wings can be bought separately in case of a crash. A first model was crafted by the author and is depicted in figure 8.1 in flight condition. The mass, wing span, wetted area, and aspect ratio are respectively 1.0kg, 2.55 meters, 0.49 m^2, and 13.5. Because of its high aspect ratio, ASWING numerical predictions of the UAV behaviour are expected to be reasonable in regard to the model's theoretical limits. In this work freedom is taken on the structural parameters as the idea here is to highlight what could be the benefit or drawbacks brought by a highly deformable structure. Thus the latter parameters are not provided. However for the aerodynamic parameters, XFOIL (Drela-1989) analysis of the wing and V-stab profile were performed to

Figure 8.1: Application example: Aeronaut triple thermic (in flight)

feed ASWING for further analysis.

8.3 Type of trajectories considered in this work

Dynamic soaring is a very wide topic, however from a numerical perspective, no matter the atmospheric phenomena and aircraft considered, the main idea consists of looking for optimal trajectories that maximise or minimise a cost function. As seen in the introduction, there exist various types of trajectories that ensure harvesting energy from atmospheric phenomena. Two main types can be defined, neutral and non-neutral total energy.

Non-neutral total energy trajectory: Here the idea is to find a trajectory ensuring that the total energy at the end of the cycle is greater than the one at the initial time. If no thrust is invested in the system, energy has been necessarily harvested from the environment. The most famous example of this type of trajectory is the inclined circle over ridges. Gliders come back to their initial position with a greater inertial speed than the previous cycle. Speed world records have been broken many times using these techniques (Richardson-2012).

Neutral energy trajectory: In this case, the idea is to find a trajectory that will ensure that the final total energy is equal to the initial one. Again if no thrust is invested in the aircraft, energy is harvested from the wind field. There exist various trajectories fulfilling the neutral energy cycle, but only the one in Open loop are of interest in this work. They are useful for travelling. Figure 8.2 highlights how looks like such a trajectory. There are various types of atmospheric phenomena that can be harvested using gradient soaring. In this work, only the Planetary Boundary Layer is considered. The wind field of the PBL can be reasonably expressed as :

$$W_x(z) = W_n \frac{\log\left(\frac{z}{z_0}\right)}{\log\left(\frac{z_r}{z_0}\right)} \tag{8.1}$$

where $z_r = 10m$ is the reference altitude such that $W_x(z_r) = W_n$. Ten meters are chosen as most of the weather satellite data and models provide mean wind speed at this altitude. The PBL roughness $z_0 = 0.03m$ defines how strong is the wind gradient at low altitude. This value has been chosen from the literature (Bonnin). As the wind profile numerically diverges, the altitude of the aircraft is bounded ($G_R < z < 100m$). For the next sections, the reference altitude and PBL roughness will remain constant. The 10-meter wind speed will be defined as a cost function in this work.

When the type of aircraft, trajectory, and wind field have been chosen, the overall problem can be summarised as follows:

$$\begin{aligned} &\text{Minimize } W_x(z = 10m) \\ &\text{over } f(x,u) = 0 \\ &\text{and } g_l \leq g(x,u) \leq g_u \end{aligned} \tag{8.2}$$

where $W_x(z = 10m)$ is the wind speed at 10 meters required to ensure a neutral energy cycle. The discretised equations of motion are lumped into the non-linear functions $f(x,u)$. The level of "fidelity" will drastically impact the computational time, so care must be taken when the equations of motion of the aircraft are defined. So far most of the literature work uses a 6-degree-of-freedom point mass model. Then all the different non-linear constraints are defined into $g(x,u)$. Among them, there are, for example, the final and initial energy states, the rolling and pitching rate constraints, the lift coefficient bounds, etc. In the next sections, it is shown how by adding a new set of constraints, it is possible to create a more conservative problem to capture more rigorously the aerodynamic and aeroelastic effects.

8.4 On the non-feasibility of using ASWING for in-the-loop path planning

ASWING is a aeroelasticity software. Initially developed as part of the MIT Daedalus project, it can predict the unsteady and steady behaviour of flexible aircraft. Based on the coupling of extensions of the lifting line, slender body and Euler-Bernoulli beam theories, the latter is a very efficient and precise software. So its use was considered for the generation of optimal open-loop trajectories ensuring a neutral

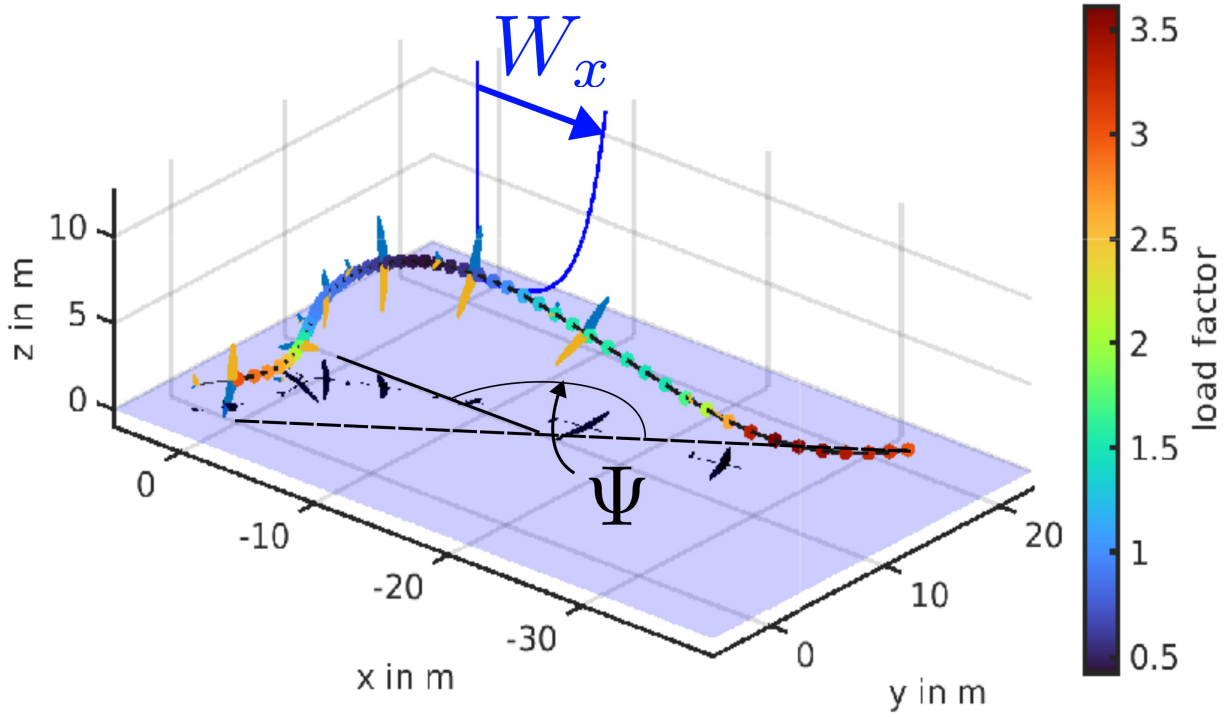

Figure 8.2: Typical Aeronaut dynamic soaring trajecotory $\psi = 150°$ (illustration)

total energy cycle. However, it is not suitable for direct path planning. To understand this statement, an algorithmic complexity analysis is proposed. In the dynamic soaring field, the literature mainly presents an optimisation algorithm where the aircraft equations of motion form a set of non-linear constraints on each discretized state variables. So far, most of the works use a 6-degree-of-freedom point mass model, where the state vector size varies between 8 and 12. The latter is then discretized into 50-time steps [1] rising the number of unknowns to 400-600. Depending on the level of conservatism expected, around 800 to 1000 non-linear constraints are associated with the optimization problem. When the best optimization algorithms are used (AMPL, SNOPT: Gill et al.-2005 and Fourer et al.-1995), the computational time on a modern laptop is between 3.5 to 20s for 1 trajectory generation.

To measure the performances of a UAV in dynamic soaring [2], a "basic" analysis can be summarised in 2 steps.

- **Step 1:** The minimal wind speed $W_x(z = 10m)$ ensuring a neutral energy open loop trajectory is the cost function. The mean heading angle (defining the travelling direction) is randomly setup in order to initialise the compass-building analysis. This step is long to converge has the initial trajectory (steady glide in the heading direction) is quite far away from the optimal solution. (trajectory count: 1)
- **Step 2:** From the step 1 heading angle Ψ (cf figure 8.2), the minimum wind speed compass is generated ($W_x(z = 10m)$ against Ψ). The same cost function as step 1 is used. A constraint on the aircraft mean heading angle Ψ is set up in order to build the minimal wind speed compass. In the literature work the resolution of the compass can vary but usually 1 to 5 degrees are chosen. The algorithm runs until the optimisation is not able to converge anymore. The last heading angle defines the tightness of the compass. The number of trajectories to be computed can rise up to 100. (trajectory count: 101).

The count is stopped here even if further analysis should be performed such as sensitivity analysis as Flanzer et al. has proposed. Thus to perform a "basic analysis" the computational time needed rises up to 300-1500 seconds (5 minutes to 25 minutes).
Now let us consider that ASWING might be used to set up the non-linear constraints defining the equations of motion of a flexible aircraft. From a numerical scheme convergence analysis, a minimal number of state variables is needed to ensure converged predictions. In the case of the Aeronaut Triple Thermic, for example, 1200 variables are needed. Then those

[1] for open loop trajectories only. For closed loop, the most common time steps number is between 100 and 150.
[2] Performances in the open loop only

variables must be temporally discretized to define the trajectory. As the aeroelastic modes are of interest, a Shannon criterium must be applied on at least the first 3 modes drastically decreasing the time steps used on the 6-degree of freedom model (from a factor of 10 to 100). The complete optimization state vector size thus rises to 600 000 (1500 bigger). Now assuming that the computational time evolves linearly with the state vector size (extremely optimistic) the basic analysis presented earlier would take around 13 to 52 days. Despite the extremely optimistic assumptions, it is clear that ASWING can not be used to force the equation of motions in the optimisation algorithm. Especially if a future purpose is to study the effect of structural parameters on dynamic soaring performances, the "basic" analysis should be performed each time a new structural parameter is changed exploding the computational time.
Consequently, despite the excellent performances of ASWING, it can not be used directly for path planning and dynamic soaring analysis.
Despite this pessimistic conclusion, it is still possible to use ASWING to perform dynamic soaring analysis. Indeed, the main idea of this work is to take the benefit of each model (6DOF and ASWING). The 6DOF model is used to generate very quickly the trajectories while ASWING is used to set up new types of non-linear constraints on the "low fidelity model" (6DOF) in order to capture the effect of aeroelasticity. The next sections aim to introduce the new constraints and why and how they can affect the performances. Finally, every new level of "fidelity" has been evaluated against experimental data to highlight the benefit of this methodology.

8.5 Level 0 : Baseline optimisation problem

In order to propose the new set of non-linear constraints, a baseline optimisation problem has been chosen from the literature. Thus the work of Bonnin et al. improved later by Long et al. has been chosen. Their code has been used directly and modified in consequence for convenience. The reader can find the 6 degrees of freedom point mass model equations of motion in eq IV 23 to 28 of Bonnin et al.'s PhD script (page 103). Those equations take into account the wind field user-defined in equation 8.1. Among the mandatory parameters there are the UAV mass, its wetted area, its span, and the drag polynomial coefficients such that the total drag coefficient is expressed as a function of the lift coefficient C_L

$$C_D(C_L) = C_{D,0} + C_{D,1}C_L + C_{D,2}C_L^2 + C_{D,3}C_L^3 + C_{D,4}C_L^4 \tag{8.3}$$

As the 6-DOF model is very simple, non-linear constraints are associated with it to recover the inertia, stall, rolling, and pitching performances of the aircraft. Then a periodicity constraint is defined on the air-relative speed, the inertial altitude, and the Euler angle to ensure a neutral energy cycle such that

$$\begin{gathered}\mathcal{E}(t=0) = \mathcal{E}(t_f) \\ \frac{1}{2}mV^2(t_0) + mgz_i(t_0) = \frac{1}{2}mV^2(t_f) + mgz_i(t_f)\end{gathered} \tag{8.4}$$

The x and y inertial position periodicity constraint has been released to ensure an open-loop trajectory and allow travel. To avoid crashing into the sea and avoid the wind field model from diverging a ground clearance constraint has been implemented. Bonnin has showed that the performances are very sensitive with the ground clearance as stronger gradient can be exploited. Or even if ASWING can captures accurately the ground effects[3], the ground clearance constraint has been set up high enough to avoid them. The major reason was that it was too difficult to model them in the 6-DOF model. Finally, a net travelling direction has been set to impose a mean heading angle Ψ about the wind direction (cf figure 8.2). Bonnin et al. were releasing this constraint to find the overall minimal wind speed, however the minimum wind speed of the performance compass is not a convex function in Ψ (heading direction), the optimiser is thus very likely to converge to a local minimum depending on the initial guess. The choice of imposing a travelling direction is adopted in this work. The overall minimal wind speed required ($min(W_x(z = 10m))$) is computed later from the performance compass. Overall the Baseline problem constraints have been summarised in the table 8.1. In order to introduce the new set of constraints, a single case will be used. The latter consists of finding the minimal wind speed required to fulfil a neutral energy open loop trajectory with a 150° net travelling direction with 0° defined as flying headwind and thus 180° as a tailwind (cf figure 8.2).

[3] Here the ground effect refers to the change in the flow field due to the ground, and not the strong wind gradient near the ground.

Constraint	Formulation	Parameters
A : EOF	equations IV 23-28 of Bonnin et al.	
B : Flight path bound	$\gamma_i \leq \gamma_{max}$	$65°$
C : Final time bounds	$t_{min} \leq t_f \leq t_{max}$	
D : Neutral energy	$V(t_0) = V(t_f) \mid z(t_0) = z_(t_f)$	
E : Net traveling direction	$\Delta y = tan\psi_{net}\Delta x$	$\psi_{default} = 150°$
F : Rolling round	$\lvert\phi\rvert \leq \phi_{max}$	$\phi_{max} = 75°$
G : No stall	$0 \leq C_L \leq C_{L,max}$	$C_{L,max} = 1.3$
I : Max load factor	$\frac{\rho S C_L (V_a)^2}{2mg} \leq n_{max}$	$n_{max} = 7$
J : Ground clearance	$\lvert z + \frac{b}{2} sin\phi cos\gamma \rvert \leq G_{clear}$	$G_{clear} = 0.5m$
K : Rolling rate	$\lvert\dot{\phi}\rvert \leq \dot{\phi}_{max}$	$40°/s$
L : Rolling acceleration	$\lvert\ddot{\phi}_{max}\rvert = \frac{\rho S b}{2I_{xx}} C_{l,max} V^2$	$C_{l,max} = 0.45$
M : C_L rate (pitching rate)	$\lvert\dot{C_L}\rvert \leq \dot{C}_{L,max}$	$0.5s^{-1}$
N : C_L double continuous	$\lvert\ddot{C_L}\rvert \leq \ddot{C}_{L,max}$	$2s^{-2}$

Table 8.1: Level 0 set of non linear constraints

8.6 New problem

8.6.1 Level 1 and 2: Helix angle and rolling cut-off

The first 2 new non-linear constraints to be presented are related to aerodynamics non-linear phenomenon. In the 6-DOF model, the lift coefficient C_L and bank angle ϕ are the control variables. So far in the literature, constraints are set up on the bank rate $\dot{\phi}$ and bank acceleration $\ddot{\phi}$. Bonnin et al. for example proposed the following constraints:

$$\dot{\phi}(t) \leq \dot{\phi}_{max} \tag{8.5}$$

where $\dot{\phi}_{max}$ is set by the user and constant

$$|\ddot{\phi}(t)| \leq |\ddot{\phi}_{max}| = \left| \frac{\rho S b}{2I_{xx}} C_{l,max} V^2 \right| \tag{8.6}$$

where I_{xx} is the rolling axis moment of inertia, $C_{l,max}$ is the maximum rolling moment coefficient (given for the maximum ailerons deflection amplitude). The biggest problem of the above non-linear constraints is that they do not take into account the local stall that could occur reducing the aileron rolling effectiveness. Flanzer et al. highlighted the problem in their work and proposed to implement a VLM code into their optimization problem to ensure no local stall. However because they were using more state variables to describe the problem, the computational time raise significantly (from 3.5s to 25s). In this work, a different approach is proposed.

In a first time, ASWING has been evaluated against experimental data to make sure it captures well the effect of a deflected control surfaces on the flight mechanic derivatives. To do so the work of Heald and Strother has been used. They placed a straight wing

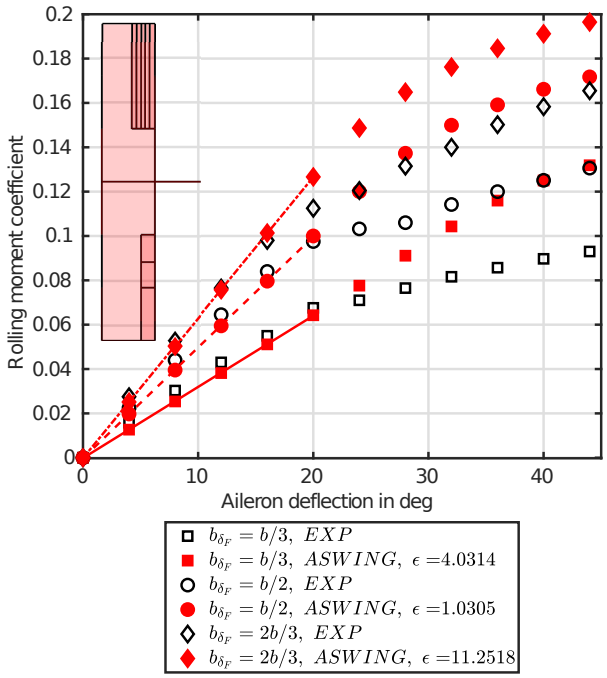

Figure 8.3: Rolling moment ASWING prediction in linear lift range against experimental data of Heald and Strother. $\alpha = 3°$

with various ailerons configurations (span and chord length varying) into a wind-tunnel. Ailerons were then deflected on a wide range and the rolling moment was measured. The wing was set up at 3 different angle of attack (linear, pre and post stall condition). Figure 8.3 presents how ASWING captures well the rolling moment induced by each configuration. Also in Appendix of this chapter, figure 8.19 presents the rolling moment prediction where the wing is in post-stall condition. It can clearly be seen a loss in the rolling moment coefficient of the wing that is capture by ASWING with a reasonable level of accuracy. Linear slope were computed and compared to the one of the experiments. As long as the wing is un-stall or in pre-stall configuration, ASWING provides good agreements [4] if flap deflections are not exceeding 20°. After this evaluation work, an ASWING analysis of the Aeronaut tripe thermic rigid rolling performance has been performed. Four aileron deflections were studied that are 5, 10, 15, and 20 degrees. The rolling moment was computed for various lift coefficient values and dynamic pressure. Figure 8.4 depicts the results and clearly highlights the effect of the total lift coefficient on the rolling performances. When the wing has a lift coefficient near its stall limits, when the ailerons are deflected, one of them can stall has it is near the local stall lift coefficient. The more the aileron is deflected the earlier it will stall in terms of C_L. As a consequence, a polynomial function of the rolling moment in the function of the lift coefficient is proposed to make the non-linear constraint **L** of table 8.1 (equation 8.6) more conservative:

$$|\ddot{\phi}(t)| \leq |\ddot{\phi}_{max}(C_L)| = \left|\frac{\rho S b}{2I_{xx}} C_{l,max}(C_L) V^2\right| \quad (8.7)$$

From the analysis of figure 8.4 the polynomial rolling moment function in C_L of the Aeronaut Triple Thermic rigid is

$$C_{l,max}(C_L) = 0.038C_L^2 - 0.033C_L - 0.037 \quad (8.8)$$

To define the constraint on the bank rate $\dot{\phi}$, the helix angle formulation is preferred as it does not vary with the dynamic pressure and is a function of the maximum rolling rate coefficient as follows

$$\left|\frac{\dot{\phi}(t) b}{2V}\right| \leq \left|\frac{C_{l,max}(C_L)}{C_{l\dot{\phi}}}\right| \quad (8.9)$$

where $C_{l\dot{\phi}}$ is the rolling wing damping coefficient which is computed with ASWING. The modification of the rolling rate constraint **K** into a helix angle constraint defines **Level 1**. When the stall "cut-off" effect is added to constraint **K** and **L** it defines the **Level 2**.

[4] only the configuration where ailerons span length was varying are presented.

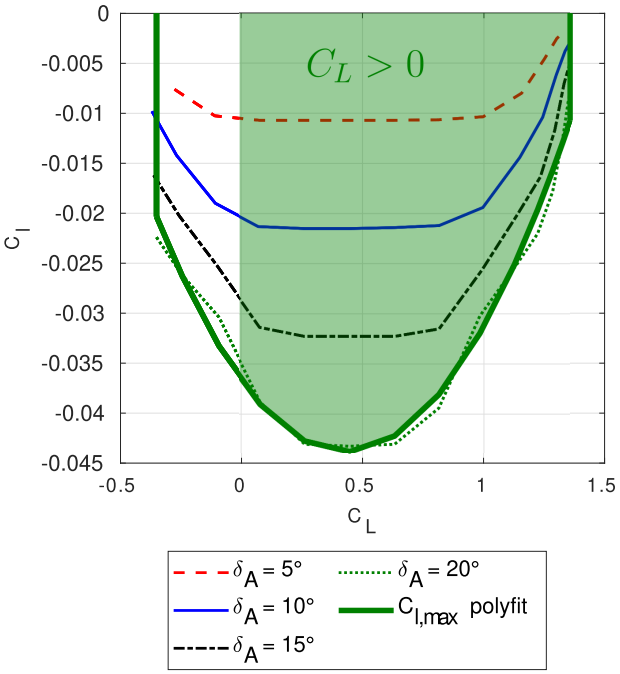

Figure 8.4: Ailerons cut off due to local stall, effect on the rolling moment

To highlight how the new non-linear constraints bring conservatism to the analysis, some trajectory computations have been performed on the Aeronaut Triple Thermic with the 3 levels of constraints summed up in the table 8.2. The first level of constraints is the one used in Bonnin's work with the parameters adapted to the glider considered in this work. The second level of constraint proposed in this work is to set up a constraint on the rolling rate using the helix angle (**Level 1**). The latter does not vary with the dynamic pressure on rigid aircraft and is a function of the roll rate and the air-relative speed. This constraint seems to be more rigorous than imposing an upper limit to the rolling rate as it varies with the speed of the aircraft (lower maximum rolling rate at a lower speed). The third level of constraints consists of adding the cut-off function to the **level 2**. In this case, the cost function was the minimal wind speed at 10 m required to ensure a neutral total energy cycle. The optimisation problem was solved using AMPL and SNOPT: some MATLAB libraries (also used in Bonnin et al.'s work). The results of the analysis are summed up in table 8.2. The change in the minimal speed relative to Bonnin et al.'s set of constraints (level 0) is also presented. From table 8.2 it is clear that level 1 and 2 bring much more conservatism than level 0 as there is an increase of more than 30% in the minimum required speed. The change from level 1 to 2 has been also computed and is below 3%. This small change can be explained as the trajectory generated is very "smooth" and so the aircraft is flying quite far away from its stall limits where the loss of rolling

effectiveness is important. However as reported by Bonnin et al., depending on the travelling direction imposed, the trajectory varies quite a lot. For some, the UAV can fly more near its stall limits increasing the rolling cut-off effects. That is why, this set of constraints is kept for the following analysis.
Regarding the computation time, the optimisation problem was run on a 2.5 GHz single-core processor. Depending on the initial condition the computational times were varying against 2.8 to 5s on the 2nd constraint level (more conservative). Flanzer et al. implemented a rolling cut-off function using a VLM (Vortex Lattice Method) formulation leading to the same conservative observations. Their computational time in similar conditions was varying between 18 and 300 seconds. Thus the advantage of keeping the 6 degrees of freedom model and implementing more conservative constraints is clearly highlighted.

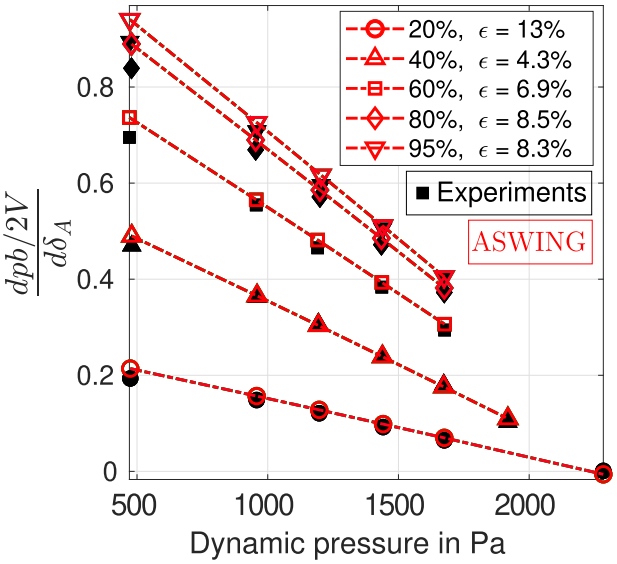

Figure 8.5: helix angle variation with dynamic pressure for various ailerons configuration (ailerons length). ASWING prediction against experimental data of Cole

8.6.2 Level 3: Ailerons effectiveness change

As it has been shown by Cole and Ganzer (1951), the rolling performances of a flexible aircraft can vary along its flight envelope up to the point when the ailerons are strictly inefficient. When the torsional deformations are small, the helix angle and rolling moment coefficients vary linearly with the dynamic pressure. Figure 8.5 shows how ASWING recovers the experimental conclusion of Cole and Ganzer. Helix angle measurements were performed at various dynamic pressure on a trapezoidal low aspect ratio wing. Several ailerons span length were tested (denoted as a % of the wing half span). Figure 8.5 presents the measurements in comparison with the ASWING predictions. Linear slopes have been computed and compared to the one of the experiments, and the mean predictions error is below 8%. Note that figure 8.20 in appendix of this chapter, presents the same comparison but for the rolling moment measurements. Same conclusions can be drawn: ASWING can predict accurately the losses of efficiency up to the reversal behaviour of any control surface. In consequence, the losses of efficiency of the ailerons can be expressed as a function of the reversal speed $V_{R,A}$ translated into the rolling rate $\dot{\phi}$ (ie helix angle) and acceleration constraints $\ddot{\phi}$ as follows:

$$\begin{aligned}\left|\frac{\dot{\phi}(t)b}{2V}\right| &\leq \left|\frac{C_{l,max}(C_L)}{C_{l\dot{\phi}}}\left(1-\frac{q}{q_R}\right)\right| \\ &\leq \left|\frac{C_{l,max}(C_L)}{C_{l\dot{\phi}}}\left(1-\frac{V^2}{V_R^2}\right)\right|\end{aligned} \tag{8.10}$$

$$\begin{aligned}|\ddot{\phi}(t)| &\leq \left|\ddot{\phi}_{max}(C_L)\right| \\ &\leq \left|\frac{\rho Sb}{2I_{xx}}C_{l,max}(C_L)V^2\left(1-\frac{V^2}{V_R^2}\right)\right|\end{aligned} \tag{8.11}$$

where $\left(1-\frac{V^2}{V_R^2}\right)$ is the "elasticity" loss factor varying linearly with the dynamic pressure up to zero when the reversal speed is reached. The blue terms in the above equations correspond to the rigid aircraft's maximum rolling performances. When the aileron reversal speed is defined, another constraint on the maximum flight speed must be imposed. Indeed, by definition near the aileron reversal speed, the aircraft becomes uncontrollable on its rolling axis. Thus, it is reasonable and safe to avoid reaching this speed. To be sure that imposing a maximum speed does not influence the effect of the aileron loss of effectiveness, simulations were performed on Level 2 with maximum speed varying and then done on Level 3. The table 8.3 sums up the simulation results. As it can be seen imposing a maximum flight speed, has no impact on the minimum required speed relative to Level 2. However, when the aileron loss of effectiveness is taken into account, some change can be witnessed, with an increase of up to 10% of the minimum required speed in comparison to level 2.

8.6.3 Level 4 : Elevator cut off

The aileron cut-off is not an isolated case. Actually, every aerodynamic control surface can be subject to

	Rolling constraints	$W_{x,min}$ (in m/s)	change (in %)
Level 0	$\dot{\phi}(t) \leq \dot{\phi}_{max}$ $\lvert\ddot{\phi}(t)\rvert \leq \left\lvert \frac{\rho Sb}{2I_{xx}} C_{l,max} V^2 \right\rvert$	9.36	0
Level 1	$\left\lvert \frac{\dot{\phi}(t)b}{2V} \right\rvert \leq \left\lvert \frac{C_{l,max}}{C_{l\dot{\phi}}} \right\rvert$ $\lvert\ddot{\phi}(t)\rvert \leq \left\lvert \frac{\rho Sb}{2I_{xx}} C_{l,max} V^2 \right\rvert$	10.59	13.1 to #0
Level 2	$\left\lvert \frac{\dot{\phi}(t)b}{2V} \right\rvert \leq \left\lvert \frac{C_{l,max}(C_L}{C_{l\dot{\phi}}} \right\rvert$ $\lvert\ddot{\phi}(t)\rvert \leq \left\lvert \frac{\rho Sb}{2I_{xx}} C_{l,max}(C_L) V^2 \right\rvert$	10.89	2.73 to #1 | 16.2 to #0

Table 8.2: Effect of the rolling cut off on open loop dynamic soaring performances. Constraint on travel direction released.

	Parameters	$W_{x,min}(in\ m/s)$	change (in %)
Level 3	$V_{R,A} = 20m/s$	11.88	9.1 to #2 | 26.9 to #0
	$V_{R,A} = 30m/s$	11.32	3.9 to #2 | 20.9 to #0
	$V_{R,A} = 60m/s$	11.31	3.8 to #2| 20.8 to #0
Level 3 (OFF)	$V_{max} = 20m/s$	10.88	-0.1 to #2
	$V_{max} = 30m/s$	10.89	0 to #2
	$V_{max} = 60m/s$	10.89	0 to #2

Table 8.3: Ailerons effectiveness change effect on the minimal wind speed required

stall reducing its efficiency. In consequence, the same principle is applied to the elevator. Figure 8.6 depicts the pitching moment bounds resulting from an ASWING analysis of the pitching moments induced by various deflections of the elevator. The analysis has been performed over the linear C_L range. As for the ailerons, the more the wing of the aircraft is closed to its maximum /minimum lift coefficient, the quicker will stall the elevator. However, this behaviour is not symmetric as for ailerons. For example, let us consider the case where the aircraft fly with a high lift coefficient. To pitch the aircraft nose down, the V-Stab must generate a positive lift, or the V-Stab is already at high C_L so it will stall easily if the elevator is deflected down. The opposite phenomenon will occur for negative C_L.From a polynomial fitting of the pitching moment boundaries, they have been translated into constraints over the lift coefficient rate and acceleration from the pitching moment equilibrium equation. The 2 elevator cut-off constraints defining **level 4** are given as follows

$$\begin{aligned} &\dot{C}_{L,min}(C_L) \leq \dot{C}_L \leq \dot{C}_{L,max}(C_L) \\ &\dot{C}_{L,max}(C_L) = -0.2288C_L^2 + 0.5366 \\ &\dot{C}_{L,min}(C_L) = -0.2288C_L^2 - 0.1134 \end{aligned} \tag{8.12}$$

where $\dot{C}_{L,min}(C_L)$ and $\dot{C}_{L,max}(C_L)$ are second-order polynomials computed from the ASWING analysis presented in figure 8.6. Following the same way, the lift coefficient acceleration is defined as

$$\begin{aligned} &\ddot{C}_{L,min}(C_L) \leq \ddot{C}_L \leq \ddot{C}_{L,max}(C_L) \\ &\ddot{C}_{L,max}(C_L) = -0.6863C_L^2 + 1.6098 \\ &\ddot{C}_{L,min}(C_L) = -0.6863C_L^2 + -0.3402 \end{aligned} \tag{8.13}$$

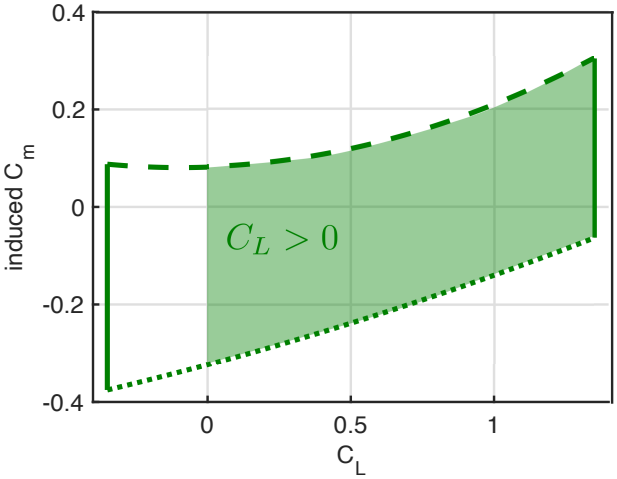

Figure 8.6: Elevator induced pitching moment cut-off due to local stall

Based on the ASWING analysis and the polynomial constraint function computed, simulations have been performed. To really assess, the effect of the elevator cut-off, the level 2 and 3 have been disabled. The table 8.4 presents the results. Again a rise in the minimal required wind speed is witnessed with a 25.7 % increase from Level 0.

	Parameters	$W_{x,min}(in\ m/s)$	change (in %)
Level 4 (2-3 OFF)		11.79	25.7 to #0
Level 5 (2-3 OFF)	$V_{R,E} = 20m/s$	12.10	2.6 to #4 | 29.3 to 0
	$V_{R,E} = 30m/s$	12.00	1.8 to #4 | 28.2 to #0
	$V_{R,E} = 60m/s$	11.82	0.3 to #4 | 26.2 to #0

Table 8.4: Elevator cut off and effectiveness effect on the minimum speed required

8.6.4 Level 5: elevator effectiveness

This section aims to introduce a new set of non-linear constraints to take into account the elevator aerodynamic effectiveness change through the trajectory. The figure 8.7 is used as a motivating example. For the same elevator flap deflection angle ($\delta_F = 10°$), the pitching moment coefficient produced varies with the air-relative speed as shown by figure 8.7. As for the aileron effectiveness section, this decrease is due to a local twist of the horizontal stabiliser elevator structure reducing the effective angle of attack and thus the lift produced by the elevator. Similarly, there is a moment when the air-relative speed is enough to lead to a reversal behaviour (black dash-dot lines in figure 8.7). In this example, the elevator reversal speed is 36 m/s which is quite high in regards to the Aeronaut flight envelope. However, the elevator pitching moment varies by 50% between 10 and 20 m/s which lies into the flight envelope. Thus, it is clear that the change in effectiveness within the flight envelope must be taken into account during dynamic soaring analysis; mainly because the trajectory involves a wide range of air-relative speed. As for the ailerons, the

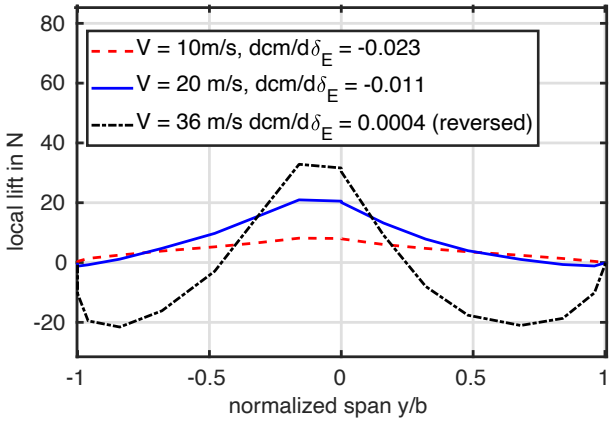

Figure 8.7: Aeronaut triple thermic: elevator effectiveness change with air-relative speed at 3 different speed when $\delta_E = 10°$

pitch moment flap derivatives vary linearly with the dynamic pressure as follows

$$\frac{dCm}{d\delta_E}(q) = \frac{q_R - q}{q_R}\frac{dCm0}{d\delta_E}\delta_E \tag{8.14}$$

where $\frac{dCm,r}{d\delta_E}$ is the rigid aircraft pitch flap derivative and q_R the reversal dynamic dynamic pressure. Thus the maximum pitch coefficient given by the maximum elevator flap deflection allowable is

$$\frac{dCm}{d\delta_E}(q) < \frac{q_R - q}{q_R}\frac{dCm0}{d\delta_E}\delta_{E,max} \tag{8.15}$$

As the pitch angle is not directly used in the 6-DOF point mass model, the above constraints must be translated in terms of control or state variables of the system. Or the pitch mainly impacts the lift coefficient and thus its acceleration. The lift coefficient acceleration can be related to the pitch acceleration as follows:

$$\ddot{C_L} \leq \frac{C_L, \alpha}{Iyy}\frac{q_R - q}{q_R}\frac{dCm0}{d\delta_E} \tag{8.16}$$

where $C_{L,\alpha}$ is the 3D aircraft lift slope, and Iyy is the y moment of inertia about the centre of gravity. As there are already many parameters, a simplification of the above expression is proposed.

$$\ddot{C_L} \leq \ddot{C_{L,r}}\frac{q_R - q}{q_R} = \ddot{C_{L,r}}\left(1 - \left(\frac{V}{V_{r,E}}\right)^2\right) \tag{8.17}$$

where $\ddot{C_{L,r}}(C_L)$ is the lift acceleration limits of the rigid aircraft previously defined. The above constraint is non-denationalised by the reversal speed for more convenience. Based on this idea, the constraint on the lift rate is proposed as follows:

$$\dot{C_L} \leq \dot{C_{L,r}}\frac{q_R - q}{q_R} = \dot{C_{L,r}}\left(1 - \left(\frac{V}{V_{r,E}}\right)^2\right) \tag{8.18}$$

where $\dot{C_{L,r}}$ is the lift rate limit of the rigid aircraft previously defined. The table 8.4 presents the results of simulation done with various elevator reversal speeds. When the latter decreases, an increase in the minimum required speed is witnessed. Note that the difference from **Level 4** is not that significant. This means that the elevator pitching cut off due to local stall seems to have more effect than the loss of effectiveness because of the structure deformation. This level of conservatism could be neglected for analysis but, in this work, each level has been kept just in case.

8.6.5 Level 6: Stall limits variation

Along the trajectory, various loads are applied to the aircraft. On a flexible one, the structure deforms modifying quite a lot the aerodynamic performances. For example, on a "high flexible" version of the Aeronaut (low bending stiffness), the geometry changes a lot with the load factor as depicted in figure 8.8. When a stall analysis is performed in ASWING against the load factor, a drop of the maximum lift coefficient with the load factor has been identified. Figure 8.9 highlights this change. This drop is due to the deformation of the structure. When a look is taken at the figure 8.8, the most deflected geometry (blue) sees its lift reduced as the section normal vectors are tilted by the local dihedral angle, reducing the contribution of the lift to the vertical axis. Thus the wing is more likely to stall earlier. As the change in stall limits can be quite significant (31 % in this case), a new non-linear constraint is proposed to take into account the stall limits variation with the load factor. To do so the following constraints are proposed.

$$\begin{aligned} 0 \leq C_L &\leq C_{L,max}(n) \\ C_{L,max}(n) &= -0.0161n^2 + 0.0715n + 1.3275 \end{aligned} \tag{8.19}$$

where $C_{L,max}(n)$ is a polynomial function with its order being user-defined. Here a second-order polynomial was enough to recover correctly the stall drop.

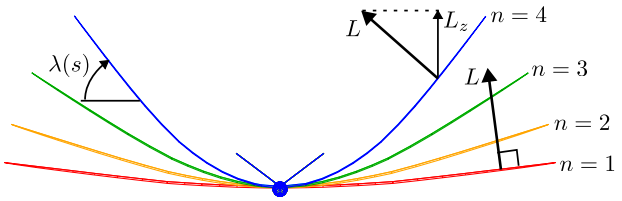

Figure 8.8: Aeronaut Triple Thermic Neo flexible change of the geometry with the load factor

The effect of the **6th level** is compared to level 3 in table 8.5. An increase of 7.2% is witnessed and 35.6% to level 0. Again depending on the trajectory, this effect is expected to vary a lot but always negatively.

8.6.6 Level 7 : Aerodynamic performances variation

The last level of conservatism to be introduced in this work is the variation of the aerodynamic performances within the flight envelope. Indeed as for the stall section introduced previously, the total drag coefficient of an aircraft can drastically vary as the structure deforms. It is no longer a function of the lift

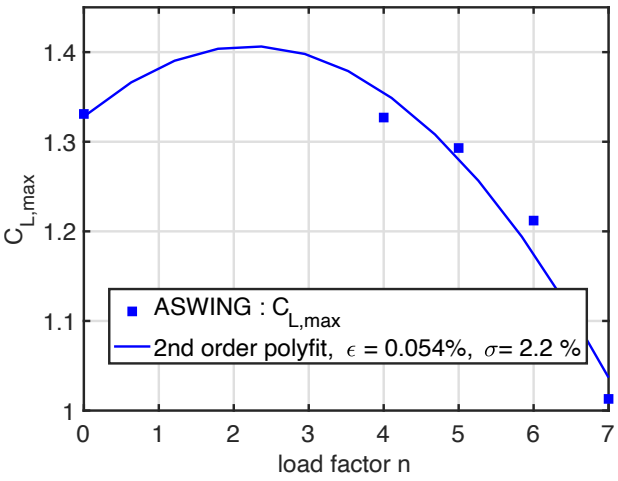

Figure 8.9: change of lift coefficient bounds with the load factor

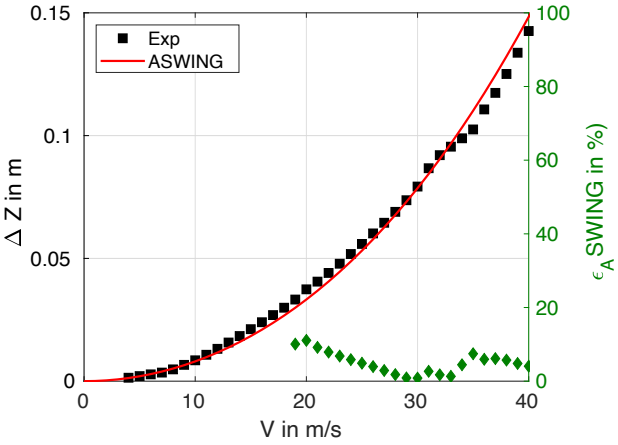

Figure 8.10: Pazy wing, tip deflection prediction against wind speed at $\alpha = 7°$. ASWING prediction against experiments of Avin et al.

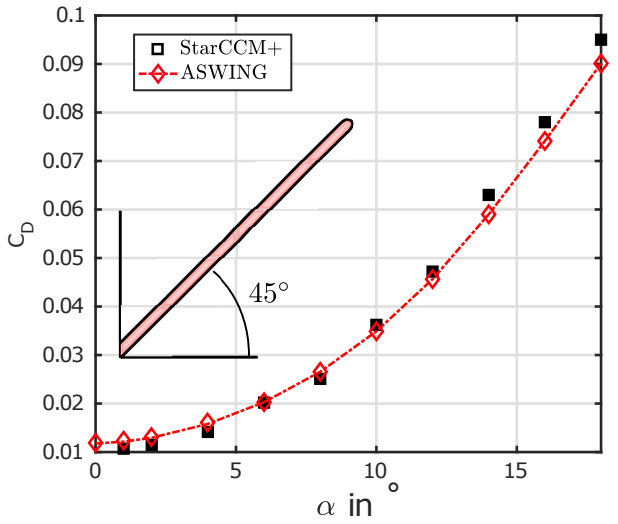

Figure 8.11: Drag coefficient of a rectangular wing with a 45° dihedral angle. ASWING prediction agsint StarCCM+ data (higher fidelity)

	Parameters	$W_{x,min}(z_{10})$	change (in %)
Level 6	$0 \leq C_L \leq C_{L,max}(C_L)$	12.73	+7.2 to worst 3 | +35.6 to 0
Level 7	$C_D(n, C_L)$	13.9481	+9.56 to 6 + 48 to 0

Table 8.5: Effect of lift and drag coefficients variation with the load factor on the minimal wind speed required.

coefficient alone, as it is rigorously on rigid aircraft. The structure deforms mainly because of the aerodynamic loads, this change of the geometry can induce a dramatic change in the drag polar. To make sure that Aswing captures well the change in aerodynamic performances of an aircraft deforming towards the trajectory, 2 evaluations have been performed:

- ASWING must captures the deformations of a structure due to aerodynamic loads. To do so the experimental data of Avin et al. have been used. The Pazy wing (straight wing of moderate aspect ratio allowing large deformations) was placed into a wind tunnel at various angle angle of attack. The wind tunnel speed was then varying and tip deflections and twist were measured. In this chapter only the tip deflections measurements in comparison with the ASWING prediction are presented for a wing root angle of attack of 7°. Figure 8.10 presents the results and the predictions errors. For large deformations the predictions error are below 10% which is satisfying. Similar conclusions were made for the other cases.

- For a given deformed geometry, ASWING must captures well its aerodynamic performances (ie drag in this case). Assuming that large deformation are expected and specially (out of the plane), a high dihedral angle wing case has been created in StarCCM+. Figure 8.11 presents a comparison between the ASWING predictions and the higher fidelity data. On a large range of angle of attack, it captures well the change in the drag coefficient of the wing. To make sure that Aswing also captures well the drag coefficient on undeformed geometry, a straight wing has also been used and is presented in Appendix in figure 8.21. Similar conclusions are drawn.

From the above evaluation, an ASWING analysis of the Aeronaut has been performed on a wide range of angles of attack and speed (cf figure 8.12). Here the results are presented in the function of n and C_L. It seems, that the drag polar keeps a convex and quadratic shape but tends to contract with the load factor. The stall limits can be identified also bounding the drag polar. It is clear that the drag drastically changes at the high lift coefficient and load factor. Thus a last non-linear constraint (**Level 7**) is proposed. From now on, the drag coefficient is non longer a polynomial function of the lift coefficient only but of the load factor also. From the data of figure 8.12 a polynomial fitting was performed leading to the following drag coefficient function

$$\begin{aligned} C_D(n) &= C_{D,0}(n) + C_{D,1}(n)C_L + C_{D,2}(n)C_L^2 \\ C_{D,0}(n) &= -0.0004n^2 + 0.0031n + 0.0139 \\ C_{D,1}(n) &= 0.0035n^2 - 0.0203n + +0.0097 \\ C_{D,2}(n) &= -0.001n^2 + 0.0106n + +0.0183 \end{aligned} \tag{8.20}$$

Note that 2nd order polynomials in C_L and n were enough as the mean error to the ASWING raw data is below 1% with a standard deviation lower than 5%. Also, it is important to note, that the polynomial function has been built from the positive lift coefficient data, as only positive load factor trajectories are considered in this work. The maximum load factor n_max must be wisely imposed so that the polynomial function remains "realistic". In our case, it was set from 0 to 7. When the new drag function is implemented into the flight mechanics equations of the aircraft, some change in the minimal wind speed requirement can be witnessed from the **Level 6**. Results are presented in the table 8.5. In this example (150° heading angle constraints), the minimum required wind speed rises by almost 10% from the **level 6** to **7**. In consequence, taking into account the effect of the geometry deformation along the trajectory is mandatory as it can have a huge impact on the performance predictions.

8.7 Unsteady flow and aeroelastic transient response in dynamic soaring trajectory

In this section, a discussion is proposed about unsteady flow and aeroelastic transient response involvement in dynamic soaring trajectories. Indeed, if they were important they would drastically change the performance of the aircraft. Let us start with the unsteady aerodynamic effects. To estimate if they are necessary to model, a frequency analysis of the "worst" trajectory is proposed. By worst,

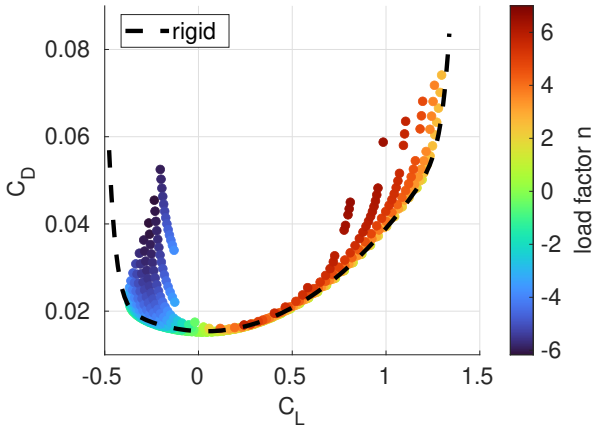

(a) ASWING raw data

Figure 8.12: Drag polar variation with the load factor. ASWING analysis and polynomial fitting

it means, the trajectory that involves the biggest and fastest change in the lift coefficient and rolling acceleration of the aircraft that are the translation of the unsteadiness of the flow. From numerical investigation, the "worst" trajectory was the one with a travel direction of 180° with an aggressive climb and turn involved. Before performing the FFT analysis of the lift coefficient and $\phi(\ddot{t})$, the optimisation problem was run again with a time step much smaller, to avoid a "low pass" effect. Here the number of time steps has been raised to 200 allowing the capture of reduced frequency up to 2.6 (enough to detect unsteady flow). Then FFT analysis has been performed on the $C_L(t)$ and $\ddot{\phi}$ signals. From the set of frequencies obtained, the feasible reduced frequencies have been computed using the air-speed signal $V(t)$. The blue zone in figures 8.13(a) and (b) depicts every reduced frequency possible. The red line shows the reduced frequency computation based on the mean air speed while the dashed red line is the one based on the standard deviation to the mean speed. Most of the reduced frequencies are contained in those bounds. As depicted in figure 8.13, even for the worst trajectory, the unsteadiness of the flow is very low and accounts for a very small amount of the spectrum. Thus for this aircraft only, it is reasonable to neglect unsteady aerodynamics.

Regarding, the structural modal response involvement, the figures 8.13 (a) and (b) provide useful information. The upper x-axis translates the reduced frequencies into the "real" frequencies. The energy of the lift coefficient and rolling acceleration signal is bounded into a frequency range between 0 and 5Hz. From a modal analysis of the Aeronaut flexible (not presented here), the first aeroelastic mode of the aircraft has a frequency of 10Hz. In consequence, the aeroelastic modes are very unlikely to be excited and will have no significant effect on the trajectory and performance of the aircraft.

From those, remarks it seems that a quasi-steady approach is reasonable to treat the effect of the flexibility of an aircraft on its dynamic soaring performances.

8.8 Comparison between a flexible and rigid aircraft

In light of the previous sections, it is clear that introducing new conservative constraints drastically modifies the minimal wind speed requirements. From table 8.6 the change from Level 0 is clearly highlighted with a change up to 50% on the flexible aircraft. Also, a change between 18.6% is witnessed between the rigid and flexible aircraft. At first sight, the flexible aircraft seems to under perform in dynamic soaring than the rigid aircraft. To push this a little bit further the analysis, the performance compass building of both rigid and flexible aircraft is proposed to provide a more rigorous analysis. The **Level 0** compass has also been built to highlight what brings the new set of constraints. The results are presented in figure 8.14. First of all, the new rigid and flexible constraints bring conservatism on the travelling direction feasibility. The travelling direction cone is tighter in comparison to Level 0 ($-2.5°$). Secondly, the Aeronaut Triple Thermic, no matter its version can only harvest energy for tailwind travelling configuration. Thirdly, the new set of constraints introduces conservatism on the minimal required speed no matter the travelling direction in comparison to **Level 0**. Fourthly and finally, the flexible version seems to under-perform the rigid version with a dramatic increase of the minimal required wind speed when the net travelling direction reaches 180° (tailwind). The more the heading angle is closed to this value, the more agressive is the trajectory, more high load turn and climb are involved to catch the pathline. Thus, the effects of **Level 6** and especially **7** are much more present reducing drastically the aerodynamic performances of the aircraft. For this specific case, the rigid aircraft seems to outperform the flexible one in dynamic soaring. Of course, further analysis must be performed, because a single set of structural parameters have been tested. So far, the only conclusion to be drawn is that the important geometry deformation of an aircraft in dynamic soaring has a negative impact on the performance.

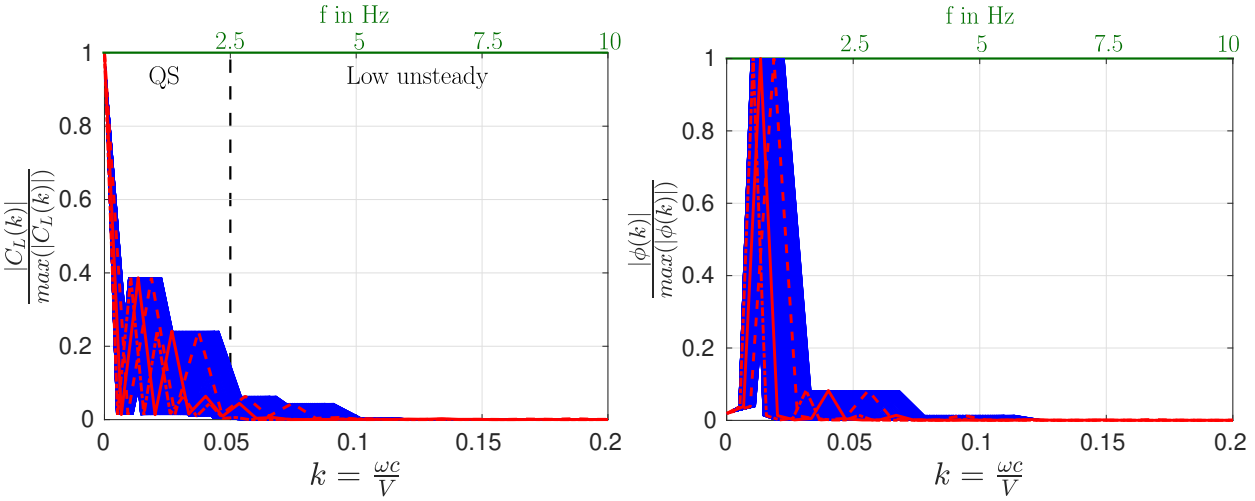

(a) lift coefficient *(b) rolling acceleration*

Figure 8.13: Fast Fourier Transform analysis of the command signals

	Combined levels	$W_{x,min}(z_{10})(in\ m/s)$	change (in %)
Bonnin 0	0	9.39	0
Rigid	2 & 4	11.75	25.2 to #0
Flexible	3 & 5-7	13.9481	18.6 to rigid, 48 to #0

Table 8.6: Final comparison between a flexible aircraft and a rigid one and Bonnin et al. method

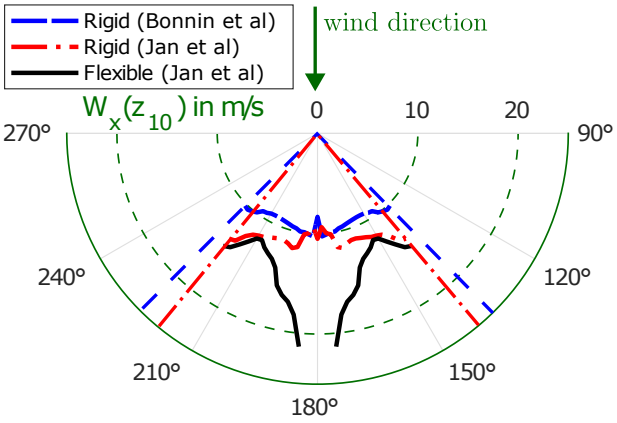

Figure 8.14: Dynamic Soaring performances compass, comparison between rigid and flexible Aeronaut

A first guess to improve the performance of the flexible version was to impose a constraint on the maximum load factor allowable. Thus it was expected to avoid high geometry deformation that drastically degrades the aerodynamic performances. However, no improvement has been witnessed. Figure 8.15 depicts the sensitivity analysis to the load factor on the 3 versions of the Aeronaut (**Level 0**, rigid and flexible). Despite the load factor reduction, no improvement can be identified in the flexible version. It seems that the aerodynamic degradation has more weight in the optimisation process than the maximum load factor. In other words, the optimiser will avoid high G manoeuvres as it knows it will not reach a global minimum. The maximum load factor constraints become redundant. Also from figure 8.15 it is interesting to notice that the minimal required speed increases when the maximum load factor reaches 1. Indeed by reducing it, the aircraft is much less manoeuvrable and thus is less efficient to harvest energy from the wind field. Finally, it is interesting to note that the minimum required wind speed reaches quickly an asymptote with the maximum load factor. In consequence, from this kind of analysis, a UAV manufacturer could reconsider the UAV design. Of course, the latter analysis should be performed over the performance compass. Especially near tail wind trajectories that need higher G manoeuvre, the asymptotic establishment could be later.

8.9 Travelling performances improvement proposition

So far from the compass analysis, the flexible aircraft is weaker than the rigid one. In this section, a "corrected" compass is proposed. Here the main idea is to improve the travelling performances of the flexible aircraft. To do so, the vision of how the aircraft should travel must be reconsidered. For example, it is possible to fly with a 180° heading angle by alterna-

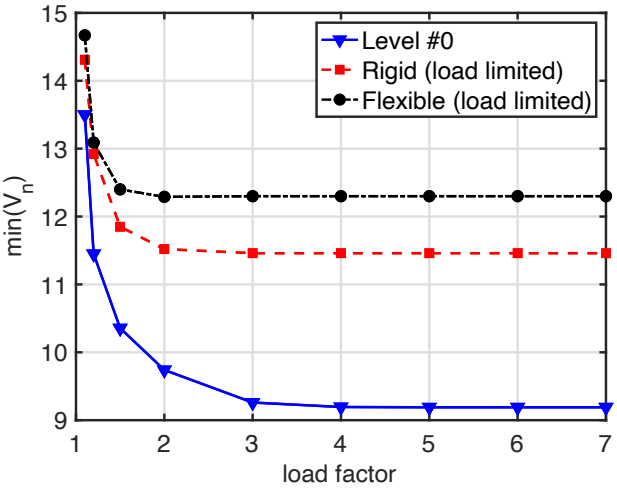

Figure 8.15: load factor sensitiity

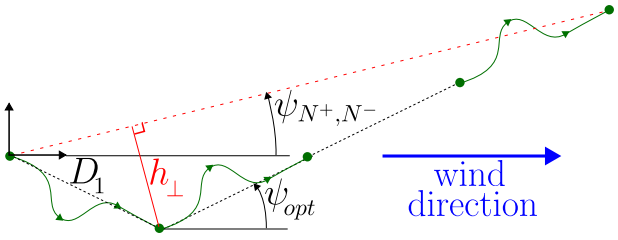

Figure 8.16: Travelling strategy illustration

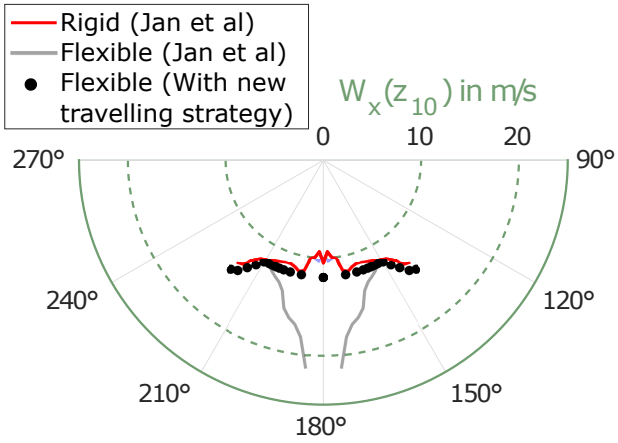

Figure 8.17: New travelling strategy results with corrected compass

tively following 150° and −150° trajectories. Based on this idea it is possible to fly in a finite number of directions contained in the feasibility cone. Let ψ_{opt} be the heading angle where the flexible aircraft performs the best. In this case $\psi_{opt} = 150°$. Let N^- and N^+ the number of times, negative and positive ψ_{opt} trajectory will be followed. Let fix N^- to 1 so that the trajectory is as depicted in figure 8.16. As N^- and N^+ must be integers, the number of feasible trajectories between $\psi = -150°$ and $\psi = 150°$ are necessarily finite. As expected the distance $h_\perp$ (depicted in figure 8.16) rises with the achievable heading angle and it becomes quickly irrelevant to adopt such strategies when ψ_{N^-,N^+} reaches ψ_{opt}. However, for lower angles, the strategies show real benefit as the UAV can use ψ_{opt} which requires much less wind to ensure a neutral energy cycle. When this strategy is adopted a new performance compass can be built. The latter is presented in figure 8.17, where the new strategy performance is compared to every case considered previously. In light of the results, the new strategy drastically improves the performance of the flexible aircraft without modifying any of its structural or geometrical parameters. However, despite the improvement, the rigid aircraft remains better, but the difference in performance is no longer huge for near-tail wind trajectories. Considering the previous results a more convenient illustration of each aircraft's performance is proposed in figure 8.18 (a) and (b). The idea here was to rely on a Windy weather forecast of the 10-meter altitude mean wind speed over the globe. From the performance compass, the zone on the planet where dynamic soaring is feasible could be built. As it is depicted, the rigid aircraft can perform dynamic soaring trajectories on a wider zone than the flexible one. For example, it could travel from Australia to South America flying "with" the wind stream while the flexible version could not.

8.10 Conclusions

In conclusion, in this work, it has been shown that ASWING can not be used directly to generate optimal trajectories. However, it can be coupled to a lower fidelity model, and be used as an off-line analysis tool to provide more conservative non-linear constraints. Then up to 7 levels of new constraints have been proposed for whom their impact on the performances has been quantified. Among the seven, 3 are aerodynamic new constraints while the 4 remaining have been introduced to take into account the effect of a deformable geometry. The following findings can be summarised

- On the flexible example chosen, important variations of the aircraft stall and drag with the load factor have been witnessed where their impacts are extremely important for near-tail wind trajectories because of a greater number of high load factor climbs and turns, degrading the aerodynamic performances.
- The loss of effectiveness of the ailerons because of the flexibility has an important impact, while the elevator is of second order. Both losses induce a lack of manoeuvrability which is mandatory to perform an efficient energy harvesting cycle.
- The wing ailerons and elevator cut-off because of local stalls have also an impact on global perfor-

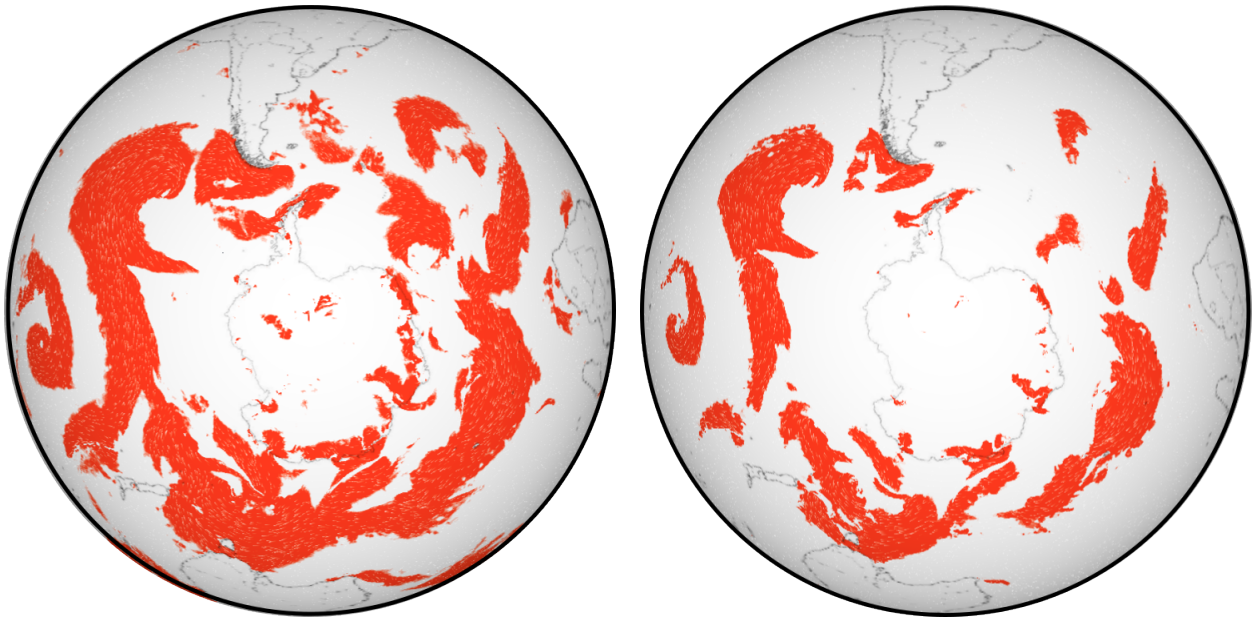

(a) rigid (b) flexible

Figure 8.18: Comparison of the zone size where dynamic soaring is feasible with the Aeronaut triple thermic Neo. Data adapted from Windy taken the May 25th 2023 at 13:38 pm UTC)

mances as they reduce the rolling and pitching performances of the UAV at high lift coefficient.

- When all the constraints are implemented and compared to the baseline model, a significant change between the performances predicted has been witnessed showing the interest in introducing new levels of fidelity.

- A more detailed analysis and comparison have been performed between a "high" flexible version of the UAV considered and its "unfeasible" rigid version. The performance compass shows that the rigid geometry always outperformed the flexible one.

- Allowing the biggest load factor possible is not mandatory to maximise the energy harvested from the planetary boundary layer. Making a very stiff aircraft is thus not necessary. What must be avoided at all costs, is the aeroelastic phenomena mentioned earlier. This analysis provides leads on the trade-off that must be made during a UAV pre-design process.

- From an FFT analysis of the control inputs rolling (rate and lift coefficient), it seems that no unsteady aerodynamic or structural modal response is involved in the trajectory. The signal power spectrum is mostly dominated by low frequency (and reduced frequencies). It is reasonable in this specific case to neglect them. Moreover, a constraint has been defined on the maximum airspeed that is below the flutter speed. There is little chance that the flutter mode will be excited (that involves unsteady aerodynamic and structural modes).

- It is possible to reduce the loss of efficiency of the flexible UAV without changing its structural parameters or geometry. Indeed, a new "travelling" strategy has been proposed to increase the performance of the aircraft by exploiting the "best" trajectory of the performance compass. Flying alternatively in a positive and negative heading direction allows to build a finite number of trajectories that lie in the performance compass, getting rid of the previous very low performing trajectories. Nevertheless, the rigid aircraft remains better.

From now on, more flexible versions of the UAV must be analysed to provide better conclusions on performance improvement or degradation brought by the flexibility. This type of problem should be lumped into an optimisation algorithm that would try to find the best structural parameters that maximise the performance compass. Moreover, the analysis should be performed on other types of trajectories mentioned earlier (closed loop, ride soaring etc).

8.11 Appendices

This appendix presents extra experimental evaluations of AWSING. Figure 8.19 add a complement on

the ailerons effects on the rolling performances of a straight wing. Here the wing is in post stall condition. Three ailerons configurations are presented (span length). Figure 8.20 presents the rolling moment induced by deflected ailerons (various span length). The trapezoidal wing is anchored. The rolling moment is given against the dynamic pressure to highlight the loss of effectiveness of the control surfaces. Finally, figure 8.21 presents how ASWING predicts well the drag coefficient of a flat straight wing.

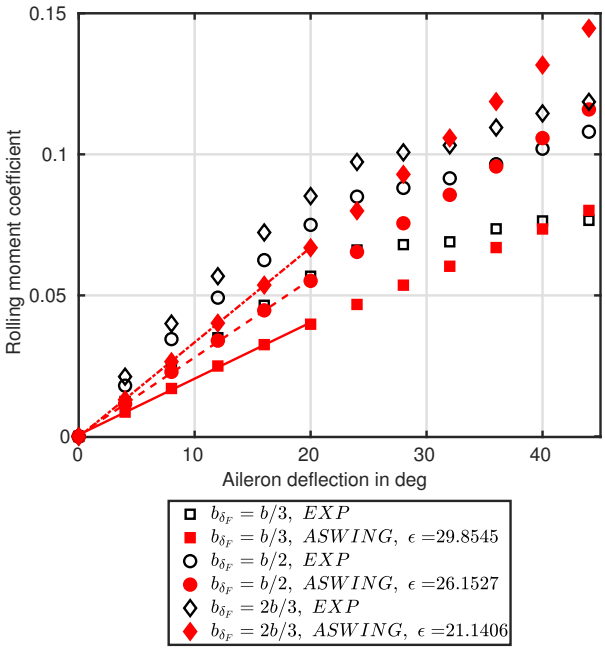

Figure 8.19: Rolling moment ASWING prediction in post stall condition against experimental data of Heald and Strother

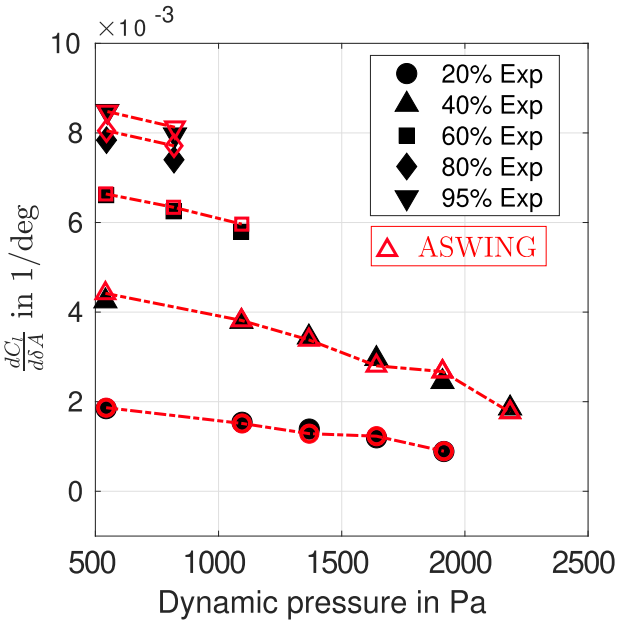

Figure 8.20: Rolling moment efficiency ASWING prediction for various ailerons configuration (span length). Experimental data of Cole

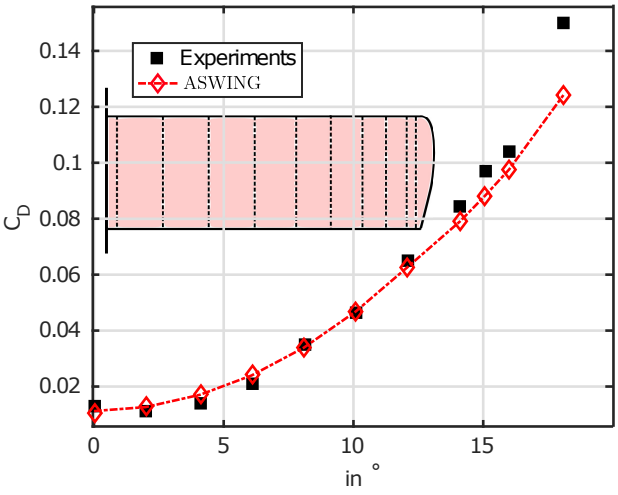

Figure 8.21: Drag coefficient ASWING prediction against experiments of Applin for a straight wing

Bibliography

[1] Applin ZT (1995) Pressure Distributions From Subsonic Tests of a NACA 0012 Semispan Wing Model. NASA Technical Memorandum 110148, NASA, Langley Research Center, Hampton, Virginia. 18, 280

[2] Avin O, Raveh DE, Drachinsky A, Ben-Shmuel Y and Tur M (2022) Experimental aeroelastic benchmark of a very flexible wing. *AIAA Journal* 60(3): 1745–1768. 18, 274, 275

[3] Bencatel R, Kabamba P and Girard A (2014) Perpetual dynamic soaring in linear wind shear. *Journal of Guidance, Control, and Dynamics* 37(5): 1712–1716. 265

[4] Bonnin V (2016) *From albatross to long range*

UAV flight by dynamic soaring. PhD Thesis, University of the West of England. 266, 268, 270

[5] Bonnin V, Bénard E, Moschetta JM and Toomer C (2015) Energy-harvesting mechanisms for uav flight by dynamic soaring. *International Journal of Micro Air Vehicles* 7(3): 213–229. 20, 265, 268, 269, 270, 271, 277

[6] Bronz M (2012) *A contribution to the design of long endurance mini unmanned aerial vehicles*. PhD Thesis, Institut Supérieur de l'Aéronautique et de l'Espace-ISAE. 265

[7] Bronz M, Gavrilovic N, Drouin A, Hattenberger G and Moschetta JM (2021) Flight testing of dynamic soaring part-2: open-field inclined circle trajectory. In: *AIAA AVIATION 2021 FORUM*. p. 2803. 265

[8] Bronz M, Gavrilovic N, Drouin A, Hattenberger G and Moschetta JM (2021) Flight testing of dynamic soaring part-2: open-field inclined circle trajectory. In: *AIAA AVIATION 2021 FORUM*. p. 2803. 265

[9] Cole HA (1951) Experimental investigation of rolling performance of straight and sweptback flexible wings with various ailerons. *NACA Technical Note* (2563): 46. 18, 271, 280

[10] Cole HA and Ganzer VM (1951) Experimental investigations of rolling performance of straight and sweptback flexible wings with various ailerons. Technical report, NACA. 271

[11] Cutler M, McLain T, Beard R and Capozzi B (2010) Energy harvesting and mission effectiveness for small unmanned aircraft. In: *AIAA guidance, navigation, and control conference*. p. 8037. 265

[12] Deittert M, Richards A, Toomer CA and Pipe A (2009) Engineless unmanned aerial vehicle propulsion by dynamic soaring. *Journal of guidance, control, and dynamics* 32(5): 1446–1457. 265

[13] Drela M (1989) Xfoil: An analysis and design system for low reynolds number airfoils. In: *Low Reynolds Number Aerodynamics: Proceedings of the Conference Notre Dame, Indiana, USA, 5–7 June 1989*. Springer, pp. 1–12. 265

[14] Drela M (1999) Integrated simulation model for preliminary aerodynamic, structural, and control-law design of aircraft. In: *40th Structures, Structural Dynamics, and Materials Conference and Exhibit*. St. Louis,MO,U.S.A.: American Institute of Aeronautics and Astronautics. DOI: 10.2514/6.1999-1394. 265

[15] Drela M (2008) ASWING 5.81 Technical Description — Unsteady Extension : 42. 265

[16] Drela M (2009) ASWING 5.86 Technical Description — Steady Formulation : 57. 265

[17] Fayez K, Leng Y, Jardin T, Bronz M and Moschetta JM (2021) Conceptual design for long-endurance convertible unmanned aerial system. In: *AIAA Scitech 2021 Forum*. p. 1059. 265

[18] Flanzer T, Bower G and Kroo I (2012) Robust trajectory optimization for dynamic soaring. In: *AIAA guidance, navigation, and control conference*. p. 4603. 267

[19] Flanzer T, Bunge R and Kroo I (2012) Efficient six degree of freedom aircraft trajectory optimization with application to dynamic soaring. In: *12th AIAA Aviation Technology, Integration, and Operations (ATIO) Conference and 14th AIAA/ISSMO Multidisciplinary Analysis and Optimization Conference*. p. 5622. 269, 271

[20] Fourer R, Gay DM and Kernighan BW (1995) *Ampl*. Boyd & Fraser Danvers, MA. 267

[21] Froude R (1889) Sailing flight of the albatross. *Nature* 40(1022): 102–102. 265

[22] Gao XZ, Hou ZX, Guo Z and Chen XQ (2015) Energy extraction from wind shear: reviews of dynamic soaring. *Proceedings of the Institution of Mechanical Engineers, Part G: Journal of Aerospace Engineering* 229(12): 2336–2348. 265

[23] Gill PE, Murray W and Saunders MA (2005) Snopt: An sqp algorithm for large-scale constrained optimization. *SIAM review* 47(1): 99–131. 267

[24] Grenestedt J, Montella C and Spletzer J (2012) Dynamic soaring in hurricanes. *Proceedings of the ICUAS* 12. 265

[25] Grenestedt J and Spletzer J (2010) Optimal energy extraction during dynamic jet stream soaring. In: *AIAA Guidance, navigation, and control conference*. p. 8036. 265

[26] Heald R and Strother D (1929) Report No. 298. Effect of variation of chord and span of ailerons on rolling and yawing moments in level flight. *Journal of the Franklin Institute* 207(5): 715–716. DOI:10.1016/S0016-0032(29)91609-4. 18, 269

[27] Heald R and Strother D (1930) Report No. 343. Effect of variation of chord and span of ailerons on rolling and yawing moments at several angles of pitch. *Journal of the Franklin Institute* 210(1): 126–127. DOI:10.1016/S0016-0032(30)90844-7. 18, 280

[28] Lawrance NR (2011) *Autonomous soaring flight for unmanned aerial vehicles*. PhD Thesis. 265

[29] Liu DN, Hou ZX, Guo Z, Yang XX and Gao XZ (2017) Bio-inspired energy-harvesting mechanisms and patterns of dynamic soaring. *Bioinspiration & biomimetics* 12(1): 016014. 265

[30] Long N, Watkins S, Moschetta JM and Bonnin V (2019) Regenerative dynamic soaring trajectory augmentation over flat terrains. In: *AIAA Scitech 2019 Forum*. p. 0569. 265, 268

[31] Mears M (2012) Energy harvesting for unmanned air vehicle systems using dynamic soaring. In: *50th AIAA Aerospace Sciences Meeting Including the New Horizons Forum and Aerospace Exposition*. p. 851. 265

[32] Pollet F, Delbecq S, Budinger M, Moschetta JM and Liscouët J (2022) A common framework for the design optimization of fixed-wing, multicopter and vtol uav configurations. In: *33rd Congress of the International Council of the Aeronautical Sciences*. 265

[33] Rayleigh L (1883) The soaring of birds. *Nature* 27(701): 534–535. 265

[34] Richardson PL (2012) High-speed dynamic soaring. *R/C Soaring Digest* 29(4): 36–49. 265, 266

[35] Richardson PL (2012) High-speed robotic albatross: Unmanned aerial vehicle powered by dynamic soaring. *R/C Soaring Digest* 29(6): 4–18. 265

[36] Zikmund P (2015) Wake vortex gliding. In: *6th EUCASS Conference, Krakow*. 265

[37] Zikmund P and Matějů J (2017) Dynamic soaring of unmanned aerial vehicle within airliner wake vortex in climb regime. *Proceedings of the Institution of Mechanical Engineers, Part G: Journal of Aerospace Engineering* 231(13): 2479–2486. 265

Chapter 9

Conclusion, additional work and perspectives

Abstract

In this chapter, a summary of the work done in this PhD program is proposed. In light of the results found, some ideas of perspectives work are listed.

Contents

9.1 Summary of the findings

The initial goal of this PhD program was to find if the flexibility of a UAV or an aircraft could benefit the performances in energy harvesting strategies. Various methods exist but in this work, only atmospheric energy harvesting strategies were of interest. A literature review has been performed to understand how they are working and what are metrics of performance needed to measure a UAV's performance. From the different features needed, ASWING has been chosen as the numerical framework of this thesis. The latter proposes a lot of interesting features however it has not been evaluated against experimental data and so it was not used by the community. Thus, before going too deeply into the PhD topic, a complete evaluation campaign of ASWING has been performed against experimental and higher fidelity data gathered from the peer-reviewed literature. On the way, some extensions and modifications of the code have been proposed in light of the modern work. This work has been separated into 4 dedicated chapters and is planned to be published so that the community can be aware of how ASWING is still a very efficient and precise predesign and analysis tool. The author put an effort to illustrate the theoretical model. For each evaluation part, a quick summary is proposed

- **Aerodynamics:** The unsteady slender body and lifting line theory have been evaluated against experimental cases. The latter were picked up in order to stress the theoretical limits of each model. Also, tandem configurations have been tested, to evaluate ASWING wake interactions predictions. Unsteady 2D and 3D data have been used to highlight the limits of the unsteady lifting line theory. A vicious loop has been modelled to improve a bit the drag and lift decambering predictions. And finally, a computational benchmark has been proposed against similar and higher fidelity existing tools. Overall, it has been shown that ASWING is an excellent tool, predictions error to experiments was reasonable and enough for our topic and it is extremely efficient from a computational time point of view.

- **Propellers and their jets:** This chapter has evaluated the ASWING propeller model, where jet/lifting-surface interactions can be modelled. In this work, experimental data have been gathered from the literature. The extended actuator theory shows good agreement with experiments in static and advanced flow conditions. It has been improved by a new formulation providing more accuracy on the shaft power to thrust transfer function. The unsteady formulation of the propeller (derived from a blade element theory) has been evaluated against high-pitch flow conditions. The latter shows limitations after 10-20 degrees of pitching angle which remains reasonable for fixed-wing aircraft. The jet model also shows good agreements with experiments especially for axial velocity predictions. The swirl velocity profile forecast is reasonable. When coupled to a lifting surface, ASWING predicts correctly the lift distribution change due to the propeller jet and swirl, no matter its rotation direction, and spanwise location. However, ASWING is not able to capture the effect of the propeller vertical position

- **Structural model:** This chapter sums up the structural model evaluation of ASWING. Static tip deflections and modal response of cantilevered beams with various composite tailoring were tested. The effect of concentrated masses position on a low aspect ratio beams on its modal response has been evaluated. Overall ASWING shows good agreement with experiments and captures well the effect of bending torsion coupling terms

- **Aeroelastic model:** When the 3 previous models are coupled, ASWING proposes a lot of features. In this chapter, experimental data from the literature have been gathered in order to evaluate a lot of them. Steady tip deflections and twists due to aerodynamic loads have been tested. Control loss of effectiveness up to reversal behaviour has been studied. Flutter speed predictions also with a study on the concentrated masses. Whirl flutter has also been discussed in regard to the literature. Results from the community were also invoked for gust response predictions. Finally, a section has been dedicated to folding wingtip devices. Again, it has been shown that ASWING shows excellent to reasonable agreements with the experiments gathered from the literature. It is excellent and fast for the features needed in this thesis so its choice.

In light of the good predictions results and efficiency, ASWING has been chosen to provide a beginning of an answer to the thesis topic. In consequence, 2 chapters have been proposed, focusing on thermal and dynamic soaring, the most promising energy harvesting techniques. Optimization problems have been proposed where ASWING has been used as an in-the-loop and out-of-the-loop analysis tool. From those early results, it seems that the flexibility is beneficial only to unsteady thermal or gust soaring. However, the set of structural parameters and tailoring enhancing the performances seem to degrade and contract a

lot of the flight envelope. Also, it has been shown that active control of a stiffer aircraft in unsteady thermal soaring is more efficient than the passive gain brought by flexibility. Of course, further analysis must be performed in order to provide a rigorous conclusion.

9.2 Not presented work:

In this manuscript, some work has not been presented. This section aims to summarize them.

- **Toulouse Tech Transfer:** During my PhD program I have applied and been selected for an entrepreneurship program called Toulouse Tech Transfer. The latter aims at creating companies from research ideas. In my case, based on the work I have done, I proposed a tandem UAV fitting in the mini UAV category. The prototype has been named Möwe as a tribute to Miyazaki's Nausicaa: valley of the Wind and an artist's view is presented in figure 9.1. I have used actually for preliminary design and presented a communication at ICAS 2022 in Stockholm entitled *Predicting Steady Lift and Drag Coefficient of Tandem aircraft using Prandtl's Extended Lifting-Line Theory implemented under ASWING*

- **Gust generator for wind tunnel:** Early in the PhD program, I started to design a gust generator device in order to explore experimentally some ideas regarding gust soaring strategies. As ENAC and ISAE-SUPAERO are used to working together, the idea here was to design a gust generator that could fit in both institute low Reynolds number wind tunnels that are Sabre and Windshape. The gust generator consists of 2 naca0012 wings actuated by 2 synchronized electric engines. The bench has been designed to sustain the hinge loads and moments on the full wind tunnel speed and reduced frequencies expected. The gust generator has been successfully tested on the windshape. A 5-hole probe windfield mapping was expected but because of covid crisis and funds cut off, this campaign has been cancelled. The gust generator is depicted in the figure

- **ASWING control law tool box:** Initially, this PhD program was aiming at treating the energy harvesting problem from a control point of view. When ASWING was chosen as the numerical framework, we figured out that only PID controllers could be implemented. I have decided then to modify the source code to be able to implement modern non-linear and linear control laws. Or among the advantages of ASWING, its computational efficiency is due to the way its solver has been built. Indeed, the latter uses a Newton descent method to solve the residual set of equations at each time step. The overall system Jacobian matrix has to be inverted. Professor Drela identified several patterns that could accelerate the inversion of the Jacobian matrix using different sub-matrix block algorithms. The new control law implementation had to not break this efficient pattern. The modification has been done in 2 parts. The first one consists of implementing a subroutine that would add the dynamic of a non-linear control law of the form.

$$\begin{aligned} \dot{x_u} &= f(\dot{x}, x, x_u, y) \\ u &= h(x, x, \dot{x_u}, y) \end{aligned} \tag{9.1}$$

The problem with this modification was that it was not really user-friendly as the non-linear function and its jacobian had to be implemented into the source code and recompiled each time a new configuration was tested. Instead of that, based on the fact that the modern literature on aircraft flight control mentions a lot of linear controllers.s A linear pattern has been implemented and is depicted in figure 9.3. Overall it is now possible to implement interpolated linear controllers, actuators, sensors and anti-wind-up systems. Also, the actuators and sensors saturations could be modelled. All the block information is given to ASWING as new control input files. Of course, when a block is not used in the loop, it is automatically ignored by ASWING. Unfortunately, I did not get the time to test and implement control laws related to energy harvesting strategy. This work has been presented at IMAV 2020 in conference proceedings entitled : *Fast simulation model for control law design and benchmark of high aspect ratio flexible UAVs*

9.3 Summary of the publications projects

- **Conference paper (accepted)** *R. Jan, J-M. Moschetta and J-P Condomines, Fast simulation model for control law design and benchmark of high aspect ratio flexible UAVs, IMAV 2021, Mexico City, Mexico*

- **Conference paper (accepted)** *R. Jan, J-M. Moschetta and J-P Condomines, Predicting Steady Lift and Drag Coefficient of Tandem aircraft using Prandtl's Extended Lifting-Line The-*

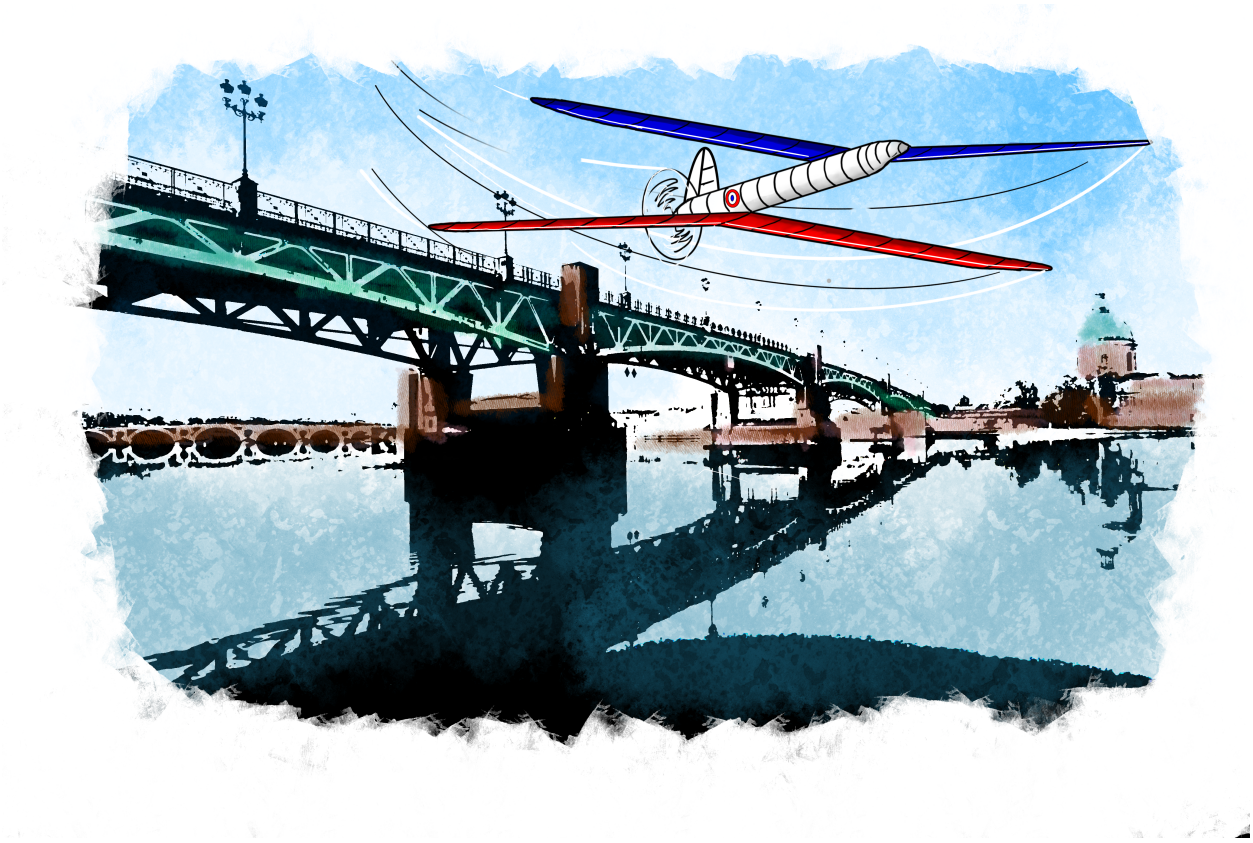

Figure 9.1: Möwe prototype : artist view (author : Romain JAN)

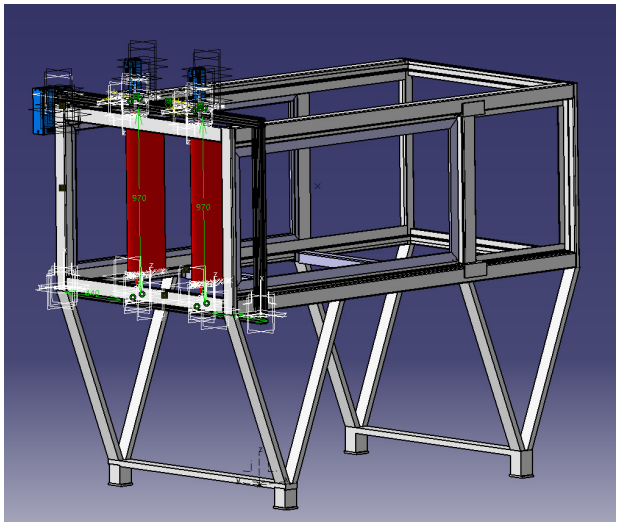

gust generated adapted to SABRE

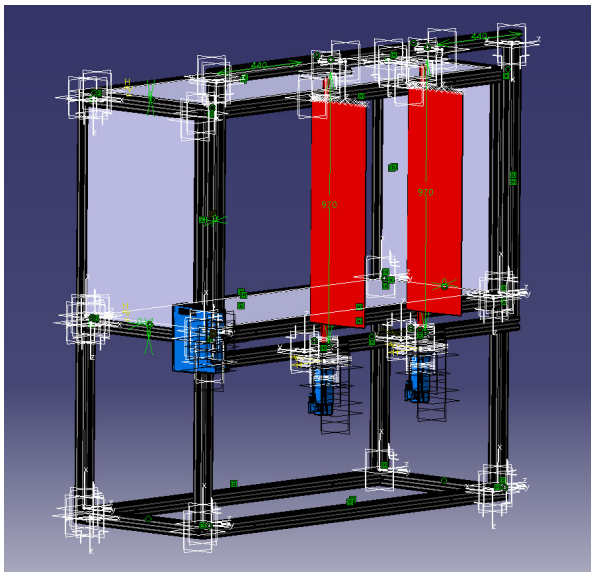

gust generated adapted to WINDSHAPE

Figure 9.2: gust generator mount on SABRE (closed loo) and windshape (open throat) wind tunnel

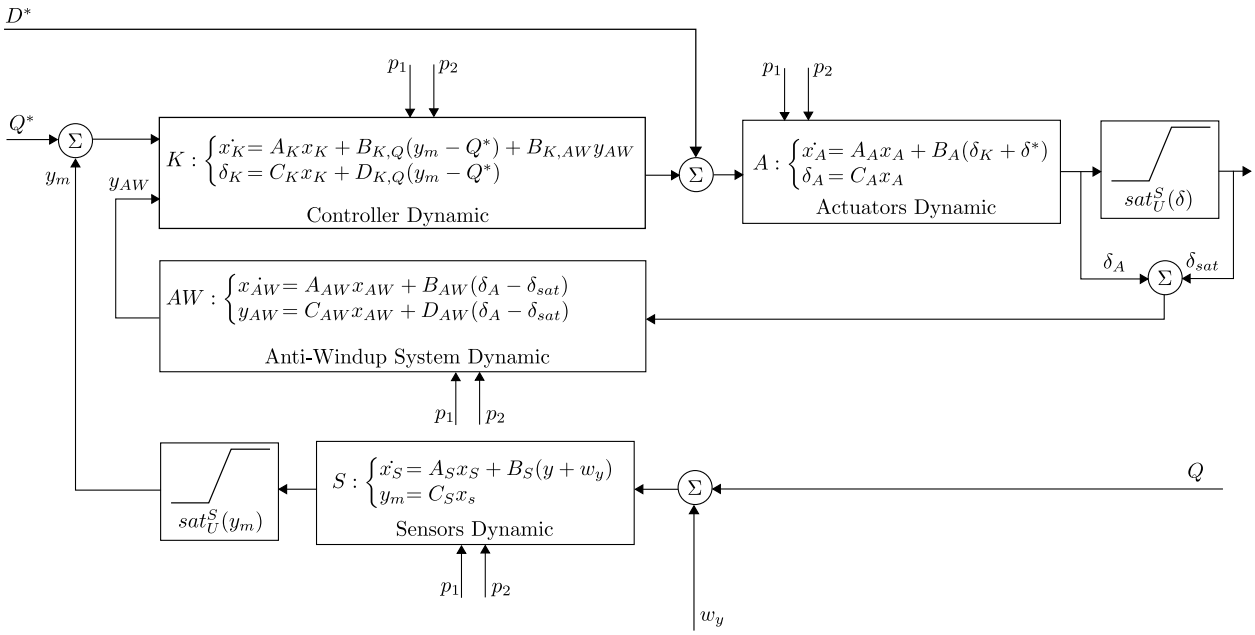

Figure 9.3: Linear control law pattern proposed

ory implemented under ASWING, ICAS 2022, Stockholm, Sweden

- **Journal paper (in project)** *R. Jan, J-M. Moschetta and J-P Condomines, Experimental evaluation of ASWING for preliminary design of flexible aircraft:* ***aerodynamic*** *model, AIAA Journal of Aircraft, 2024*

- **Journal paper (in project)** *R. Jan, J-M. Moschetta and J-P Condomines, Experimental evaluation of ASWING for preliminary design of flexible aircraft:* ***structural*** *model, AIAA Journal of Aircraft, 2024*

- **Journal paper (submitted)** *R. Jan, J-M. Moschetta and J-P Condomines, Experimental evaluation of ASWING for preliminary design of flexible aircraft:* ***aeroelastic*** *model, AIAA Journal of Aircraft, 2024*

- **Journal paper (submitted)** *R. Jan, J-M. Moschetta and J-P Condomines, Mini-UAV structure optimisation for efficient thermal soaring, International of Micro Air Vehicles, 2024*

- **Journal paper (submitted)** *R. Jan, J-M. Moschetta and J-P Condomines, New dynamic soaring formulation for the assessment of flexibility effects on the Mini UAVs performances, International of Micro Air Vehicles, 2024*

9.4 Future work and perspectives

- **On the impact of flexibility on Energy harvesting in general:** As it has been seen, a lot of time has been spent on the experimental evaluation and modification of ASWING. In consequence, the contributions on the thesis topic must be strengthened to really draw a rigorous conclusion on the benefit or not of the flexibility on static, dynamic and gust soaring strategies. Now ASWING and its modification seem to be a good candidate to answer the questions as it has been shown in chapters 7 and 8. More atmospheric phenomena must be studied, and more sophisticated optimization problems must be set up to explore more deeply this large topic.

- **On the use of ASWING:** Along this PhD journey, during the experimental evaluation work, I have studied features that I did not need to answer the question raised by the thesis. However, I thought that evaluating them could benefit the community. I have been hired by ISAE-SUPAERO DCAS as a postdoc researcher to couple ASWING with OpenMDAO in-house framework (FASTOAD-GA). This work aims to develop a future short-range regional hybrid aircraft sponsored by the European project HERA. ASWING will be used as an in-the-loop aeroelastic analysis tool, lumped into a multidisciplinary optimization tool.

- **Real flight dynamic soaring on Mermoz:** The Mermoz prototype (cf figure 9.4) aiming

at crossing the Atlantic Sea from Dakar Senegal to Natal Brasil successively passed its first flight tests last year. The real flight is now soon and among the second objectives of this project (once it would have flown) is to test path planning strategy and dynamic soairng endurance improvement technic. For dynamic soaring and in regards to the aggressive trajectories that are involved, here the idea, as suggested by Professor Moschetta is to fly into a safety cylinder. The idea in consequence would be to generate trajectory harvesting energy from the local wind field that stays in this cylinder. The trajectory generated is not expected to ensure a neutral cycle of the total energy but to minimize the power invested along the path. The range of Mermoz would be slightly extended. From a numerical point of view, ASWING could be used to generate those trajectories following the methodology presented in chapter 8. Then the control toolbox developed (and not presented in this manuscript) could be used to evaluate some modern robust control laws that ensure proper trajectory tracking.

Second successful flight with liquid hydrogen powered

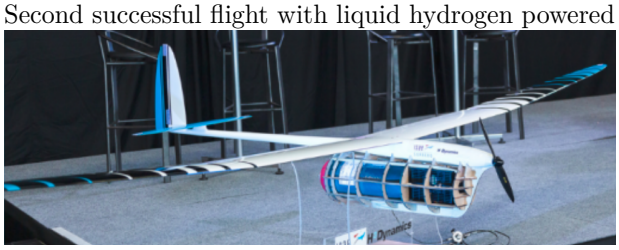

Image source : Mermoz-LH2

Figure 9.4: Mermoz team and prototype : From left to right, Dominique Benard, Dr Nikola Gavrilovic, Prof Jean-Marc Moschetta

Résumé — Le marché des drones à voilure fixe est en plein essor depuis les 2 dernières décennies. Pour rester compétitif un aéronef se doit d'être endurant et proposer une charge utile la plus importante possible. A la lumière de la littérature scientifique, l'ensemble des techniques d'optimisation multi-disciplinaires convergent vers des configurations de fort allongement et flexibles. Il est possible d'étendre encore l'endurance d'un drone en exploitant les perturbations atmosphériques rencontrées lors du vol. Cette thèse vise à montrer si la flexibilité d'une voilure peut améliorer les performances d'extraction d'énergie. Il existe 3 grandes stratégies, le vol d'ascendance, de gradient et de turbulence qui soulèvent des besoins numériques distincts. A la lumière de ces derniers, un espace de travail numérique a été retenu et a fait l'objet d'une validation sur le plan expérimental renforçant les éventuelles conclusions liées au sujet. A l'issue de ces travaux, l'impact de la flexibilité sur les performances, de vol d'ascendance, de gradient et turbulence ont été étudiées. Il semble que la souplesse de la voilure ne soit bénéfique qu'au vol de turbulence mais la géométrie optimisée pour cette stratégie tend à contracter significativement l'enveloppe de vol. Enfin pour le vol de gradient, les résultats préliminaires semblent montrer que la souplesse dégradent les performances.

Mots clés : Aéroélasticité, extraction d'énergie, vol de gradient, drone à voilure fixe, mécanique de vol, méthodes potentielles

Abstract — The fixed-wing drone market has been growing rapidly over the past 2 decades. To remain competitive, an aircraft must be efficient and carry the heaviest possible payload. In light of the literature, all multi-disciplinary optimization methods converge to high aspect ratio and flexible configurations. It is possible to extend a drone's endurance by exploiting the atmospheric disturbances encountered during flight. This thesis aims to show whether wing flexibility can improve energy extraction performance. There are 3 main strategies, static, dynamic and gust soaring, which raise distinct numerical needs. In light of these, a numerical framework was selected and experimentally validated, reinforcing any conclusions related to the subject. In the end, the impact of flexibility on static, dynamic, and turbulence soaring performance was studied. It seems that flexibility is only beneficial for turbulence soaring, but the optimized geometry for this strategy tends to significantly contract the flight envelope. Finally, for gradient flight, preliminary results seem to show that flexibility degrades performance.

Keywords : Aeroelasticity, energy harvesting, dynamic static and gust soaring, fixed wing UAV, flight mecanics, potential methods.

10 Av. Edouard Belin, 31400 Toulouse, France